Composition, structure, and formation of the lower crust in continental and oceanic arc settings: Insights from the xenolith record

Thesis by

Emma Sofia Sosa

In Partial Fulfillment of the Requirements for the Degree of

Doctor of Philosophy

CALIFORNIA INSTITUTE OF TECHNOLOGY

Pasadena, California

2024

(Defended April 26, 2024)

Emma Sofia Sosa
ORCID: 0000-0002-1765-6191

ACKNOWLEDGEMENTS

When I reflect on my academic journey and the circumstances that have brought me to this point, the proverb “It takes a village to raise a child” comes to mind. I am eternally indebted to all the people who have supported me on this journey. The list below is by no means exhaustive, as there are too many people for me to thank everyone individually, but know that I am very grateful for all of you.

First, I must thank my thesis advisor, Claire Bucholz, for your unceasing support and all you have taught me. You have helped me grow as a scientist and independent thinker more than anyone. I would also like to thank the other members of my thesis committee, Paul Asimow, Francois Tissot, and John Eiler, with whom I have had very helpful and constructive conversations over the years. I wish to extend a special thank you to Francois for your endless support during the many long days I spent in the clean lab. I would also like to thank Julie Lee, Jen Shechet, Julia Zuckerman, and all of the GPS staff who have helped me during my time at Caltech.

As anyone who routinely uses a Neptune Plus MC-ICP-MS for their work knows, this instrument rarely behaves as intended, and I must also thank Michael Kipp and Rosa Grigoryan for their help with the data collection process and troubleshooting the Neptune. I would not have been able to make these measurements without you both. I would also like to thank Chi Ma, Nathan Dalleska, Oliver Wilner, Kyle McCarthy, Lee Saper, Linda Godfrey, Jill VanTongeren, and Jacob Setera for their help with instrumentation over the years. The samples described in this thesis were collected and graciously shared by Sue Kay, Robert Kay, and Andrés Rodríguez-Vargas, to whom I extend my deepest thanks. I would also like to thank Barbara Ratschbacher and Jennifer Jackson for sharing their amphibole Mössbauer data with me, which significantly improved the third chapter of my thesis.

I would not be where I am today without the support and mentorship of the truly amazing scientists I worked with and learned from as an undergrad at Lafayette College. Thank you to everyone in the Lafayette College Geology and Environmental Geosciences

Department. I must give a special thanks to Tamara Carley, Guy Hovis, David Sunderlin, Lawrence Malinconico, and Rohana Meyerson, who made the department feel like home for me during my time at Lafayette. Thank you also to Tim McCoy, Nicole Lunning, and Liz Cottrell for your mentorship during my time at the Smithsonian and for an experience that I know opened many doors for me.

Thank you to all the friends I have made at Caltech over the years who have brought so much joy into my life, especially my first-year cohort. Thank you also to Gabriel Valencia, Jim Barry, Jaime Reyes, and everyone involved in the Caltech Arts Committee who helped bring the arts to Caltech. I owe an extra special thank you to Gabriel Valencia, Freya Morris, and Juan David Hernández-Montenegro, whose friendships have truly transformed my time at Caltech. Gabriel, thank you for being my artistic partner at Caltech and encouraging me to be big and bold in my creative pursuits. Freya, you have been on this academic journey with me since the beginning and have consistently been the most supportive friend I could ask for. I'm not sure if I would ever have taken a geology class had it not been for you, and I don't know where I would be today if we hadn't met in Gates our freshman year. Juan, you have brought more fun and adventure into the last three years of my life than I could have imagined. You support and comfort me in hard times while also continually challenging me to grow and be a better person. You are like no one I have met before, and I guess I must also thank Fe isotope geochemistry for bringing you into my life.

Lastly, thank you to my family and my amazing parents, Susan and Victor. I love you more than anything in this world, and I owe everything I am and have accomplished to you. I will eternally be grateful for the sacrifices you made to pay for my undergraduate education and the support you have given me to pursue my passions. Thank you for the freedom you gave me to make my own choices in life, for celebrating my success with me, and for helping me move on from my failures. Mom, you are probably the only person who will ever voluntarily read every single word of this document, so this thesis is for you.

ABSTRACT

The compositional variability of lavas erupted in subduction zone settings results from a multitude of deep crustal processes acting in concert, reflecting variations among arcs in source rock composition, water content, oxidation state (fO_2), temperature, pressure, and crystallization sequence across arcs. Lower to mid-crustal xenoliths—deeply sourced rock fragments entrained and brought to the surface by ascending melts—provide a robust record of the chemistry and structure of their inaccessible source regions. This thesis combines a variety of laboratory techniques and modeling approaches to explore the origins of two xenolith suites from vastly different arc settings: the oceanic Aleutian Arc off the coast of Alaska and the continental Andean Arc in Colombia. While all samples are fully characterized in terms of their petrography and the major and trace element chemistry (of both minerals and whole-rock), special attention is given to stable Fe isotope ratios, which are particularly sensitive to the fractionation of important Fe-bearing minerals like olivine, magnetite, amphibole, and garnet.

In the first chapter, we document the major and trace element compositions of 39 previously undescribed xenoliths from the Mt. Moffett and Mt. Adagdak volcanic centers on Adak Island, Central Aleutians. This data is then used to evaluate the P-T-fO_2-H_2O conditions under which the cumulates formed and interrogate the nature of their parental melts. The second chapter builds upon this first study, presenting Fe isotope data of whole-rock powders and mineral separates (spinel, clinopyroxene, olivine, amphibole, and magnetite) from the Adagdak xenoliths. Our data show that the Adak crust is stratified in terms of Fe isotopes, with an isotopically light lower-crust and an isotopically heavy middle to upper-crust. The implications of this compositional structure and its relation to the evolution of Adagdak magmas is then explored through mass-balance fractional crystallization modeling. In the final chapter, we apply the same methods used in the first two chapters to characterize a suite of lower to mid-crustal xenoliths from the Mercaderes region of Colombia in the Central Andean Cordillera. In contrast to Adagdak, the Mercaderes samples show a nearly constant whole-rock Fe isotope composition throughout our ~50 km crustal section. Through thermodynamic modeling, we show that the most likely explanation for this data is that the Mercaderes suite represents a prograde metamorphic sequence

PUBLISHED CONTENT AND CONTRIBUTIONS

Chapter 2: Sosa, E. S., Bucholz, C. E., Barickman, M. H., VanTongeren, J. A., Setera, J. B., Kay, S. M., & Kay, R. W. (2023). Petrology and geochemistry of Adak Island plutonic xenoliths: implications for primitive magma generation and crustal differentiation in the Aleutian Island arc. *Journal of Petrology*, 64(10), doi: 10.1093/petrology/egad073.

ESS participated in the conceptual development of this project, data collection and interpretation of results, completed the modeling, prepared the manuscript, and revised the manuscript.

MANUSCRIPTS IN REVISION AND PREPARATION

Chapter 3: Sosa, E. S., Bucholz, C. E., Hernández-Montenegro, J.D., Kipp M. A., Tissot, F. L. H., Ratschbacher, B. C., Jackson, J. M., Kay, S. M., Kay, R. W. (*submitted to GCA, Dec 2023*). Lower crustal control in the iron isotope systematics of plutonic xenoliths from Adak Island, Central Aleutians, with implications for arc magma geochemistry. (*In revision for Geochimica et Cosmochimica Acta*).

ESS participated in the conceptual development of this project and led sample preparation, Fe isotope data collection, interpretation of Fe isotope results, Fe isotope modeling, prepared the manuscript, and revised the manuscript.

Chapter 4: Sosa, E. S., Bucholz, C. E., Hernández-Montenegro, J.D., Rodriguez-Vargas A., Kipp M. A., Tissot, F. L. H. (*submitted to EPSL in May 2024)* Garnet clinopyroxenite formation via amphibole-dehydration in continental arcs: evidence from Fe isotopes.

ESS participated in the conceptual development of this project and led sample preparation, data collection, interpretation of results, modeling, and prepared the manuscript.

TABLE OF CONTENTS

LIST OF FIGURES

Chapter 2

Chapter 3

Chapter 4

LIST OF TABLES

Chapter 2

Chapter 3

Chapter 4

SUPPLEMENTARY TABLES AND FILES

Supplementary tables for this thesis are given in three supplementary data files (.xlsx):

Chapter 2: Supplementary_Data_File_1.xlsx
Chapter 3: Supplementary_Data_File_2.xlsx
SMS experiments and spectral fits.zip
Chapter 4: Supplementary_Data_File_3.xlsx

Supplementary tables for Chapter 2

Supplementary tables for Chapter 3

Supplementary tables for Chapter 4

Chapter 1

INTRODUCTION

1.1 Background and motivation

The process(es) responsible for the formation of Earth's andesitic continental crust remains a fundamental question in geology. Over the past 50 years, general agreement has emerged that subduction zone settings represent the best natural laboratories to study continental crust formation due to **1)** broad similarities in trace element chemistry between arc lavas and estimates of the bulk composition of the continental crust, **2)** the fact that the vast majority of andesites erupt in arc settings, **3)** the fact that both regions (arcs and continental cratons) are characterized by thickened crust (at least for continental arc settings) (Taylor, 1967; Grove and Kinzler, 1986; Wedepohl, 1995; Rudnick and Fountain, 1995; Jagoutz and Kelemen, 2015; Gazel et al., 2015)

This analogy is complicated, however, by a primary distinction between subduction zone magmas and estimates of the bulk composition of continental crust. While arcs do represent the primary locus for the generation of andesitic melts, most lavas erupted in subduction zone settings are, in fact, basaltic. This dichotomy has led to the so-called "andesite paradox" and spurred decades of research into the dynamics of convergent margins and the mechanisms by which juvenile crust is created (or, in some cases, destroyed) in these complex settings. Some proposed models for how a net andesitic crust may be created in arc settings arc: **1)** deep crustal differentiation may result in the creation of eclogite lower crust, either through primary garnet clinopyroxenite crystallization or eclogitization of gabbroic protoliths, and the loss of this mafic, density-unstable material could leave behind a more felsic (possibly andesitic) crustal composition (Kay and Kay, 1991, 1993; Jull and Kelemen, 2001); **2)** basaltic magmas may assimilate upper crustal granitic material before crystalizing, increasing their silica content (McBirney et al., 1987); or **3)** the dominant mode of arc magmatism may have changed through time, and the processes by which arc crust is created today

may differ greatly from how continental cratons were created during the Archean. In this framework, arc magmas may have been primarily andesitic in the past due to elevated Archean geothermal gradients, which could have resulted in high extents of slab melting (i.e., "adakite" production: Defant and Drummond, 1990; Shirey & Hanson, 1984; Martin, 1986).

Of first-order importance to resolving this paradox is a detailed understanding of how the arc crust is created, destroyed, and chemically stratified in modern arc environments. This recognition has spurred considerable research on the dynamics of subduction zone settings over the past decades. The compositional diversity of arc magmas and the considerable thickness of crustal material they must, in some cases, traverse before erupting make it challenging to disentangle the effects of different processes and the relative contributions of individual end members challenging. For example, arc magmas are distinguished from mid-ocean ridge basalts (MORBs) and intra-plate ocean island basalt (OIBs) by their elevated oxygen fugacities (fO_2, expressed here as log deviation from the fayalite-magnetite-quartz redox buffer: ΔFMQ) (Cottrell et al., 2022) and high water contents (Grove et al., 2012). Water can enhance Fe depletion (i.e., calc-alkaline) trends, which are prevalent in many convergent margin magmas, particularly those from the thickest arc settings (Miyashiro, 1974), by suppressing the saturation of plagioclase and enhancing that of amphibole (e.g., Zimmer et al., 2010). Elevated oxygen fugacity can also enhance the development of calc-alkaline differentiation trends, however, by promoting early magnetite saturation (e.g., Osborn, 1959). There is also debate on whether the elevated oxygen fugacities of arc magmas are inherited from their mantle source regions (e.g., Kelley and Cottrell, 2009) or acquired during differentiation (e.g., Tang et al., 2018).

Within the past two decades, studies have shown that the stable isotope geochemistry of arc magmas (particularly Fe, K, Ca, Si, and Ti) may offer additional insights into subduction zone processes, as the isotopes of these elements can be strongly fractionated by differentiation (e.g., Savage et al., 2011; Williams et al., 2018; Aarons et al., 2020). Iron isotope ratios (expressed in $\delta^{56}Fe$ notation, where $\delta^{56}Fe_{sample} = 1000 \times [(^{56}Fe/^{54}Fe)_{sample}/(^{56}Fe/^{54}Fe)_{standard} -1]$ holds particular promise

for deciphering the effects of oxygen fugacity and differentiation on arc magmas due to the preferences of important rock-forming minerals (e.g., garnet, olivine, pyroxene, amphibole, magnetite) for heavy or light isotopes of Fe. This preference arises from the respective affinity of isotopically light ^{54}Fe for the reduced Fe^{2+} valence state and heavy Fe isotopes (e.g., ^{56}Fe, ^{57}Fe, and ^{58}Fe) for the oxidized Fe^{3+} valance state, both in melts and minerals (Polyakov and Mineev, 2000). Iron isotope studies of lavas have, however, yielded highly variable results with often conflicting interpretations of the data. While it is agreed that arc lavas extend to isotopically lighter values than those observed in those from MORBs or OIBs, the reason why arc magmas exhibit these light $\delta^{56}Fe$ compositions remains debated. Some have argued that subarc mantle peridotite has experienced more extraction of heavy Fe isotopes than MORB or OIB mantle regimes due to extensive removal of Fe^{3+} by high extents of water-fluxed melting in arc settings (e.g., Nebel et al., 2015; Foden et al., 2018). It has also been suggested that isotopically light fluids released from subducting slabs in arc environments may react with subarc mantle peridotite, creating an isotopically light source region (e.g., Debret et al., 2016; Chen et al., 2023). Alternatively, protracted wet or high-pressure lower to mid-crustal differentiation in arc settings may fractionate Fe isotopes (Li et al., 2020; Cooper and Inglis, 2022; Du et al., 2022). Lower to mid-crustal differentiation could produce isotopically light or heavy melts depending on what phases are fractionated and the affinity of those phases for heavy vs. light isotopies of Fe.

Answering these questions requires constraining the composition of primary melts and their earliest crystallization products. To date, most of the work aimed at understanding and disentangling the complex processes occurring in subduction zones has focused on arc magmas. The utility of the lava record in accurately recording deep crustal processes, however, can be hindered by several factors:

1. Primitive arc melts may assimilate country rock during their ascent to the surface, particularly in regions where they must traverse over-thickened crust (e.g., Huppert et al., 1985; Sparks, 1986; Reiners et al., 1995).

2. Melt inclusions may re-equilibrate with their host crystal or external environment on short timescales and thus may not accurately reflect their source magmatic conditions or composition (e.g., Blundy et al., 2010; Gaetani et al., 2013; Reubi et al., 2013).

3. Degassing can significantly alter the oxygen fugacity and volatile content of magmas during ascent (e.g., Moussallam et al., 2014).

An alternative approach to studying lavas is direct analyses of lower crustal rocks, which have not been modified by the supracrustal processes discussed above. This may be done in areas where paleo-arcs have been exhumed (e.g., Talkeetna: DeBari and Coleman, 1989; Greene et al., 2006; Kohistan: Jagoutz et al., 2011; Jagoutz and Schmidt, 2013) or through the study of lower to mid-crustal xenoliths (i.e., rock fragments entrained by deeply sourced magmas during an eruption). Xenoliths may therefore offer direct insights into deep crustal structure and composition (e.g., Conrad and Kay, 1984; Debari et al., 1987; Rudnick, 1992; Lee et al., 2001; Weber et al., 2002; Cooper et al., 2016; Chin et al., 2017). Of particular relevance to constraining magmatic processes in arc settings are cumulate xenoliths, rocks formed by the accumulation of minerals precipitated from a melt (Wager et al., 1960).

The following chapters combine major and trace element chemistry, petrography, and Fe isotope geochemistry of lower to mid-crustal xenoliths with modeling to improve our understanding of the chemistry, structure, and formation of the lower to middle-crust in two localities, Adak Island in the oceanic Aleutian Arc and Mercaderes in the continental Andean Arc. Comparing lower to mid-crustal xenoliths from these two vastly different arc settings allows us to evaluate and contrast crustal structure and evolution in thin vs. thickened arc crusts. A takeaway from these chapters is that lower crustal xenoliths provide robust records of deep crustal processes and, when available, should be studied in concert with the lava record.

1.2 Dissertation summary

The second and third chapters of this work focus on the petrology and geochemistry of two lower to mid-crustal cumulate xenolith suites from Adak Island, Central Aleutians. The xenolith suites were collected by Sue and Robert Kay (Cornell University) in the 1970s and first described in a series of papers published over the following decade (Conrad et al., 1983; Conrad and Kay, 1984; Debari et al., 1987). The first suite is from the larger (1200 m) Mt. Moffett volcanic center, whose lavas carry a suite of small (up to 4 cm in diameter but usually ~2 cm across) cumulate xenoliths ranging from primitive olivine pyroxenite to more evolved amphibole gabbro and hornblendite. These samples were first described by Conrad et al. (1983) (n = 8). The second suite is from the smaller (650 m) Mt. Adagdak volcano; they were brought to the surface by a primitive (11.83 wt.% MgO) olivine-phyric basalt flow and were originally described by Debari et al. (1987) (n = 10). The xenoliths from this suite are considerably larger (generally 6-10 cm in diameter, but up to 54 kg) and range from ultramafic dunite and wehrlite to more evolved amphibole gabbro and hornblendite. After the initial works of Debari et al. (1987) and Conrad et al. (1983), the suites received little attention until the mid-2000s, when Yogodzinski and Kelemen (2007) obtained clinopyroxene trace element profiles from olivine clinopyroxenite cumulates (n = 2), lava phenocrysts (n = 1), and one gabbroic sample from Mt. Moffett.

In the second chapter, we expand upon these previous studies and characterize an extensive collection of previously undescribed xenoliths from the Mt. Moffett (n = 12) and Mt. Adagdak (n = 33) collections. The xenoliths are characterized in terms of their petrography, major element, and trace element mineral chemistry. With this data, we calculate pressure, temperature, and fO_2 of equilibration for the xenoliths, the latter representing only the second set of direct oxygen fugacity estimates for lower crustal oceanic arc cumulates obtained through olivine-spinel oxybarometry. These estimates are then compared to data from experimental studies to understand the crystallization sequence and P-T-fO_2-H_2O conditions of formation of the cumulate suites. Consistent with the previous study of Yogodzinski and Kelemen (2007), we find that the trace element

characteristics of clinopyroxene in the most primitive cumulates from both volcanic centers (especially Mt. Moffett) indicate a contribution from a basaltic eclogite melt to their parent magmas. However, this signature is obscured in the more evolved lithologies by the effects of progressive differentiation. Previous studies have attributed these signatures to partial melting of the subducting slab beneath Adak (i.e., adakite formation: Kay, 1978; Defant and Drummond, 1990; Yogodzinski and Kelemen, 1998; 2007) or forearc subduction erosion (Jicha and Kay, 2018; Kay et al., 2019). As our data are unsuitable for distinguishing between the two processes, the term "basaltic eclogite melt" is used throughout this thesis to refer to situations where the source of these signatures is ambiguous or irrelevant to our discussion. In the last section of this chapter, we explore the origins of these basaltic eclogite melt signatures, calculate the likely composition of the parental melts of the cumulates, and assess the relationship between the cumulates and upper crustal plutonic rocks on Adak Island.

Our olivine–spinel oxybarometry of the Adagdak cumulates shows that they are oxidized relative to MORB (ΔFMQ = +0.1 to +2.1 vs. ΔFMQ = 0 ± 0.2; Cottrell and Kelley, 2011; Kelley and Cottrell, 2012), consistent with the previous hypothesis that arc lavas (and by extension, their crystallization products) are oxidized at the earliest stages of their genesis (Parkinson and Arculus 1999; Kelley and Cottrell; 2009; Brounce et al. 2014; Bucholz and Kelemen, 2018). Notable differences in mineral chemistry and crystallization sequence between cumulates from the Mt. Moffett and Mt. Adagdak suites point to a complex magma plumbing system beneath the island, with these two volcanic centers either sampling melts derived from a spatially heterogenous mantle or a source region that has changed through time. For example, the Mt. Moffett crystallization sequence is defined by early amphibole saturation and a prevalence of olivine + cpx + amphibole-bearing rocks, while plagioclase and amphibole saturate together in the Adagdak suite, an event that corresponds to the loss of olivine from the fractionating assemblages. This would be consistent with the parental melt of the Moffett suite being more hydrous or more oxidized than that of the Adagdak cumulates. Clinopyroxene from the most primitive cumulates from both suites shows signatures suggesting the parental melts contain a component in equilibrium with garnet: fractionation between

light and heavy rare earth elements (LREE and HREE), high Sr/Y ratios, and positive Sr-anomalies ($Sr/Sr^* = Sr_N/[Pr_N \times Nd_N]^{0.5}$, where *N* designates normalization to chondrite) (Defant and Drummond, 1990). However, these characteristics are stronger in the ultramafic lithologies from Mt. Moffett (e.g., Sr/Y = 24-42, Sr/Sr* 1.8-2.8) than those from Mt. Adagdak (Sr/Y = 6-14, Sr/Sr* 1.3-2.2). This would suggest that the parental melt of the Moffett suite contains a greater contribution from a basaltic eclogite endmember. Importantly, we show in the second chapter, through mass-balance fractional crystallization modeling, that while the diminution in these signatures between the ultramafic and plagioclase/amphibole-bearing lithologies can be modeled by plagioclase fractionation for Adagdak, the strong Sr-anomalies observed in the most primitive Moffett samples cannot be erased by fractional crystallization. Connecting the characteristics of the Moffett suite with the relatively unfractionated trace element chemistry of the upper crustal lithologies on Adak would, therefore, require open-system processes like magma-mixing or country rock assimilation for this volcanic center.

In the third chapter, we build upon the work of the previous section and measure Fe isotope ratios of mineral separates (spinel, clinopyroxene, olivine, amphibole, and magnetite) and whole-rock powders of the Adagdak xenoliths to explore the utility of cumulate records for chronicling the stable isotopic evolution of arc systems. This chapter also aims to understand the source of the Fe isotope variability of arc systems ($\delta^{56}Fe$ = –0.09 to +0.20‰, Dauphas et al., 2009; Foden et al., 2018; Williams et al., 2018; Chen et al., 2023) as compared to MORBs ($\delta^{56}Fe$ = +0.06 to +0.18‰, Weyer and Ionov, 2007; Teng et al., 2013). Our results represent the second whole-rock Fe isotope measurements of cumulates and the first measurements of mineral separates from arc cumulates. These data are supplemented with Fe isotope measurements of five basaltic to andesitic Adagdak lavas and data from one mantle residue. Due to the small size of the Moffett xenoliths and a paucity of inclusion-free grains, we were unable to measure Fe isotopes in this suite.

Our whole-rock cumulate data show an increase in $\delta^{56}Fe$ from the most primitive dunite samples ($\delta^{56}Fe$ = –0.09 to –0.02‰) to the more evolved amphibole gabbro and hornblendite

xenoliths (δ^{56}Fe = +0.04 to +0.08‰). This evolution is not observed in the lavas, which show a narrow range of δ^{56}Fe from +0.03 to +0.06‰, highlighting the utility of cumulates in chronicling effects of fractional crystallization that may be omitted from the lava record. We use previously determined Fe force constants (<*F*>) (i.e., measurements of the bonding strength of Fe in different lattice sites, expressed in N/m) for olivine, magnetite, and spinel, together with estimated values for clinopyroxene and amphibole, to calculate the isotopic compositions of the parental melts of the cumulates. With this result, we construct a mass balance Fe isotope model for the Adagdak suite and track the evolution of the melts as fractional crystallization progresses. Importantly, because we measured mineral separates as well as whole-rock powders, our data allow us to assess the degree to which the fractionation of specific phases drives Fe isotope trends in the system as a whole.

Our results point to an important crustal control in the isotopic evolution of Adagdak magmas and their crystallization products, with the increases in whole-rock δ^{56}Fe between lower and mid to upper-crustal lithologies reflecting a shift from fractionation dominated by isotopically light olivine to isotopically heavy amphibole and magnetite. In terms of the Fe isotope variability observed in arc magmas, our modeling suggests that convergent margin magmas may experience periods of enrichment as isotopically light phases like olivine are fractionated, followed by depletion once heavy phases like amphibole and magnetite saturate and begin to control the Fe budget of the system. An isotopically depleted arc source is, therefore, not a prerequisite for isotopically light erupted melts, and the fractionated assemblages in each arc system need to be considered when evaluating isotopic trends in lava records. Importantly, while previous studies have also argued that isotopically heavy magnetite fractionation exerts a strong control on the trends toward light Fe isotope ratios observed in some arc lavas (Williams et al., 2018), our results suggest that amphibole may also represent a previously overlooked yet significant reservoir of heavy Fe isotopes in the mid-to-upper arc crust, and a key player in dictating the isotopic evolution of convergent margin magmas.

If we focus on Adagdak specifically, the data in the two chapters discussed above paint a relatively clear picture of the evolution and structure of the oceanic crust for this particular system.

Primitive basalts crystallize dunite and wehrlite cumulates in the lower crust, with gabbro and hornblendite assemblages later crystallizing from more evolved melts, presumably at shallower, mid-crustal depths. This shift from olivine and clinopyroxene-rich fractionating assemblages to those dominated by amphibole, plagioclase, and magnetite, is evidenced by changes in whole-rock and mineral chemistry (both major and trace element) and an increase in whole-rock δ^{56}Fe. A natural extension to this work would be a detailed petrographic and geochemical study of a lower to mid-crustal xenolith suite from a thick, continental arc setting, which is the subject of the fourth chapter. In that work, we interrogate the petrography, mineral and whole-rock major and trace element chemistry, and Fe isotope systematics of a xenolith suite from the continental Colombian Andes to explore the evolution and structure of a thickened arc crust.

The xenolith suite in question is from the Mercaderes region of the Northern Volcanic Zone in the Central Cordillera of the Colombian Andes. The Mercaderes xenolith suite was first described in detail by Marion Weber in the late 1990s for her PhD thesis at the University of Leicester, United Kingdom. The samples we studied were collected by Andres Rodriguez-Vargas in the early 2000s for his master's thesis at the National University of Colombia, Bogotá. Another sample suite was recently collected by Mauricio Ibañez-Mejia (University of Arizona) and colleagues in the late 2010s. The Mercaderes suite contains an array of crustal lithologies, ranging from lower-crustal garnet clinopyroxenite to mid-crustal garnet and plagioclase-bearing hornblendite and upper-crustal diorite (Weber, 1998; Weber et al., 2002; Rodriguez Vargas et al., 2005). Based on a detailed petrographic and major element study, Weber (1998) initially interpreted the Mercaderes suite as representing a prograde metamorphic sequence, in which amphibole dehydration reactions drive densification of upper-crustal diorite protoliths and the formation of garnet clinopyroxenite. In more recent years, the suite has been reinterpreted to represent igneous garnet clinopyroxenite cumulates (or "arclogites," Lee and Anderson, 2015) formed at the base of the crust, or possibly as partial melting residues of such cumulates (Bloch et al., 2017). This change in perception likely reflects the publication of several influential works by Cin-Ty Lee (Rice University) and colleagues over the past two decades, which focused on the role garnet clinopyroxenite cumulates and their partial

melting residues may play in driving lower-crustal delamination in continental arc settings. In this framework, arclogites are divided into high-MgO and low-MgO groups, with the former representing igneous (cpx-rich) cumulates formed from primary arc melts, and the latter interpreted as either garnet-rich cumulates formed from more evolved melts or as partial melting residues of high-MgO arclogite protoliths (Lee et al., 2006).

In the fourth chapter, we measured Fe isotope ratios of whole-rock powders (n = 21) and mineral separates of amphibole (n = 10), clinopyroxene (n = 17), and garnet (n = 17) from a suite of Mercaderes xenoliths, ranging in lithology from lower-crustal garnet clinopyroxenite to mid/upper-crustal diorite. We also fully characterized these samples in terms of their petrography and mineral and whole chemistry (both major and trace element). We note that all measured xenoliths in our sample suite would be classified as low-MgO arclogites based on the criteria of Lee et al. (2006) and, unfortunately, do not represent the full compositional spread observed in this system.

Under the prevailing theory that the Mercaderes suite represents a fractional crystallization sequence (albeit with some partial melting and densification of the deepest garnet clinopyroxenite cumulates), we expected to see pronounced trends in major and trace element chemistry and Fe isotope composition in the transition from garnet and clinopyroxene-rich lower-crustal lithologies to amphibole and plagioclase-dominated upper-crustal rocks. However, surprisingly little variability is observed in either the major, trace element, or Fe isotope chemistry of whole-rock samples within the suite, and the variations that do exist are not correlated to mineralogy. For example, within our sample suite, whole-rock δ^{56}Fe ranges from –0.02 to +0.11‰ and MgO from 5.5 to 13.8 wt.%, with no correlation observed between composition and lithology. While increased Fe isotope fractionation is observed between garnet and clinopyroxene/amphibole mineral separates in the mid/upper-crustal lithologies as compared to the lower crustal garnet clinopyroxenite, this is better explained by lower equilibrium temperatures than any systematic shift in parental melt chemistry during fractional crystallization.

Considering these results, we constructed two potential Fe isotope models with Perple_X to explore the origin of these samples: **1)** a fractional crystallization model, in which we crystallize a primitive Colombian basalt along the Mercaderes geothermal gradient (~1300 °C and 2 GPa to 800 °C and 1 GPa), and **2)** an amphibole dehydration model, in which a representative Mercaderes diorite is brought to higher pressures and temperatures along the same *P-T* path. Sensitivity tests were performed for each model, in which initial composition, fO_2, water content, and other model parameters were varied. We consistently found that amphibole dehydration melting of diorite protoliths reproduced the Fe isotope trends of both whole-rock samples and mineral separates, while the fractional crystallization models failed to reproduce our data. With 35% melting (by mass) of the protolith, the $\delta^{56}Fe$ of the metamorphic residues decreased modestly by 0.03‰ in our amphibole dehydration model. In contrast, crystallization modeling resulted in highly fractionated cumulate compositions, with ~0.32‰ variability in whole-rock Fe isotope composition from 1300 to 800 °C. The solid assemblages in our amphibole dehydration and fractional crystallization models show dissimilar trends in Fe isotope composition because Fe behaves very differently in these two systems. While only 21% of the initial Fe in the system is lost to the melt in the amphibole dehydration model, 95% of the initial Fe is fractionated by the cumulate in the crystallization model, with Fe primarily sequestered by garnet crystallization.

Our Fe isotope data and modeling suggest that our Mercaderes xenolith suite most likely represents a prograde metamorphic sequence as opposed to fractional crystallization products. As our samples are limited to more evolved "low-MgO" arclogites, our data do not prohibit the existence of high-MgO garnet clinopyroxenite cumulates at the base of the Andean crust but instead point to another mechanism by which garnet + clinopyroxenite ± amphibole assemblages may be created in continental arc settings. While previous studies have long argued that eclogitization of gabbro and basalt may play an important role in promoting lower crustal densification and delamination (e.g., Kay and Kay, 1991, 1993; Wolf and Wyllie, 1993; Jull and Kelemen, 2001), our data provide the first Fe isotope evidence for such processes. Eclogitization of upper to mid-crustal lithologies and garnet clinopyroxenite crystallization in the lower crust likely act in concert, with amphibole

dehydration melting occurring in response to burial and the formation of dense crustal roots. Eclogitization of the middle crust would, in turn, drive densification of the cumulate roots of thickened arc crusts.

A more appropriate model for crustal growth in the Andes may be one where primitive mantle melts fractionate high-MgO garnet clinopyroxenite at the base of the crust before rapidly ascending to mid/upper crustal depths, where they fractionate gabbro or diorite cumulates that may later descend to greater depths and undergo densification reactions in response to burial or the pull of lower crustal garnet clinopyroxenite cumulates being delaminated into the mantle. Recent experimental studies have also shown that garnet may not readily crystallize from basaltic melts at intermediate crustal depths (0.9-1.2 GPa: Blatter et al., 2013, 2023), which would favor the formation of the Mercaderes garnet + clinopyroxene + amphibole + plagioclase assemblages (for which geothermobarometry yields equilibrium pressures between 0.8 and 1.7 GPa) through incomplete amphibole dehydration reactions. Importantly, our results suggest that arclogites should not ubiquitously be used as archives of deep magma conditions in continental arcs because not all garnet clinopyroxenite forms through purely igneous processes.

While much of the early work on Fe isotopes in igneous systems performed in the early 2000s focused on their potential to chronicle changes in oxygen fugacity across time and space (e.g., Williams et al., 2004; Dauphas et al., 2009), the data presented here suggest that Fe isotopes may also represent a powerful tool to distinguish between rocks created through igneous vs. metamorphic processes. Thin oceanic crusts formed through cumulate processes may display pronounced isotopic stratification, reflecting the change in fractionating assemblages as parental melts evolved from primitive basalts in the lower crust to more silicious andesites or dacites at shallower depths. Thick crust formed in continental arcs, where amphibole dehydration may play an important role in crustal evolution, might be compositionally uniform for large stratigraphic sections because metamorphic processes do not fractionate Fe isotopes as efficiently as fractional crystallization. For example, assuming a pressure-to-depth conversion of 35 km/GPa, geothermobarometry suggests that our

Mercaderes xenoliths are sampling material from ~70 to 20 km below the surface, and yet the suite displays only 0.13‰ variability in $\delta^{56}Fe$.

1.3 Future directions

The data presented in this thesis raise further questions and highlight potential avenues for future study. Due to limitations on sample availability, we were not able to measure all the rocks we wanted to from both systems. Ideally, one would measure a full suite of crustal rocks, mantle rocks, and lavas from each system, but this is not often feasible. For example, there are three large plutonic bodies exposed on Adak Island: The Finger Bay pluton (~38 Ma), the Hidden Bay pluton (~35-31 Ma), and the Kagalaska pluton (~14 Ma) (Kay et al., 1990, 2019a; Kay and Kay, 1994; Jicha et al., 2006). The rocks in these suites are more evolved than the lithologies observed in the Adagdak xenolith suite, including monzonite (±quartz), monzodiorite, diorite, and granodiorite with minor amounts of Fe-bearing phases including hornblende, biotite, pyroxene, magnetite, and ilmenite (Fraser and Snyder, 1959; Citron *et al*., 1979, 1980; Kay et al., 2019). In chapter 2, we show through trace element modeling that these more evolved plutonic lithologies could be related to the primitive Adagdak cumulates through fractional crystallization (consistent with the conclusions of Kay et al., 2019). It would be interesting to measure Fe isotopes of the exposed plutonic units on Adak Island as well to assess their possible relationship to the Adagdak cumulate suite. Our modeling in chapter three suggested that further fractionation of amphibole and magnetite might deplete late-stage Adagdak melts and, by extension, their crystallization products, in heavy Fe isotopes. It would be interesting to test this theory by measuring the Fe isotope composition of rocks from the plutonic rocks of Adak.

It would also be interesting to measure Fe isotopes from the Adagdak xenolith's host lava, which is the most primitive melt composition measured to date from Adak Island (olivine-phyric basalt selvage from xenolith ADAG81-DR: Debari et al., 1987). As we did not have data from this sample, we had to estimate an appropriate starting composition for our Fe isotope mass-balance model in Chapter 3. Measuring the sample directly would allow us to place tighter constraints on our

modeling parameters. As this sample is also thought to represent a near-primary mantle melt (Debari et al., 1987), measuring it would also provide insights into the Fe isotope composition of near-primary arc melts.

Finally, a future study should date the Adagdak and Moffett xenolith suites. As discussed above, our analysis suggests that the Adagdak and Moffett xenolith suites crystallized from distinct parental melts under different crystallization conditions. This would be consistent with **1)** a heterogeneous mantle beneath Adak or **2)**, if the xenoliths did not crystallize concurrently, a source region that has changed through time. The likelihood of either scenario could be evaluated by simply dating the xenoliths. If the Moffett and Adagdak cumulates formed contemporaneously, this may imply spatial heterogeneity beneath Adak, possibly the results of variable degrees of mantle metasomatism from melts or fluids derived from the subducting slab. If the xenolith suites are of different ages, then the differences in chemistry between the two suites may reflect changes in the mantle source region through time with the maturation of the Aleutian arc.

For the Mercaderes suite, a critical future step would be performing Fe isotope analysis of high-MgO garnet clinopyroxenite. Though regional political unrest makes future sample collection from the area dubious (e.g., Weber, 1998), a limited number of high-MgO garnet clinopyroxenite samples have been collected and described in previous studies (Weber, 1998; Bloch et al., 2017; Zieman et al., 2023). If this high-MgO garnet clinopyroxenite represent igneous cumulates, we might expect them to be isotopically depleted relative to those from the low-MgO group measured here (δ^{56}Fe = –0.02 to +0.11‰). In addition, obtaining Fe isotope data from mantle xenoliths and erupted lavas from Mercaderes would allow for a more robust characterization of the behavior of Fe in the system and would provide additional constraints for the modeling in Chapter 4. Measuring the Fe isotope composition of mantle xenoliths from Mercaderes would allow us to calculate the composition of theoretical primary melts of the Andean subarc mantle, which we could use as a starting composition for our fractional crystallization modeling.

It would also be interesting to measure the Fe isotope composition of erupted lavas associated with the Mercaderes xenolith suite, which include andesite, dacite, and lamprophyre, although interpreting the results may not be straightforward. Both our amphibole dehydration and fractional crystallization models result in the production of andesitic to dacitic melts, representing either partial melts of the metamorphic protoliths or evolved magmas formed through cumulate garnet clinopyroxenite removal. Andesite and dacite produced in both scenarios would be expected to be isotopically heavy, although our modeling suggests that those produced through fractional crystallization may show more isotopic variability (~0.17‰ variation in $\delta^{56}Fe$) compared to those produced through amphibole dehydration (~0.07‰ variation in $\delta^{56}Fe$).

Another avenue to explore concerning the Mercaderes xenoliths is their trace element systematics. Due to the affinity of garnet for HREE, whole-rock trace element data of garnet clinopyroxenite xenoliths from Mercaderes unsurprisingly shows enrichment in HREE relative to LREE (La/Yb = 0.1 to 0.6). Prolonged crystallization of garnet clinopyroxenite xenoliths would, therefore, be expected to deplete more evolved melts in HREEs. Samples of diorite, clinopyroxene hornblendite, and garnet-bearing gabbro and hornblende clinopyroxenite from Mercaderes do not, however, display pronounced depletions in HREE, and in fact, look quite similar to each other on primitive mantle-normalized spider diagrams (La/Yb = 1 to 4). Conceptually, the similarities in trace element chemistry across different lithologies in the Mercaderes suite is more consistent with an amphibole dehydration melting scenario. Future studies could explore this further through modeling exercises. Indeed, the major element constraints from the amphibole dehydration and fractional crystallization models presented in Chapter 4 could be the foundation for future trace element modeling.

Regarding Fe isotopes more broadly, there are other rock suites that may provide interesting comparisons to Adak or Mercaderes. For Adagdak, it would be interesting to compare our Fe isotope data to other cumulate xenolith suites or exhumed lower-crustal terrains containing a large range of lithologies, particularly suites with different crystallization conditions and sequences. Do other

cumulate suites follow a similar trend of initial heavy Fe isotope enrichment during olivine-dominated fractionation followed by heavy Fe depletion during amphibole and magnetite-dominated crystallization? Or do changes in crystallization sequence or *P*-*T*-fO_2-H_2O result in these melts taking different evolutionary paths? To date, the only arc cumulate suites that have been the subject of Fe isotope studies are Adagdak (this thesis) and the Lesser Antilles (Cooper and Inglis, 2022).

Future studies should also measure Fe isotopes from clinopyroxene and amphibole grains for which the $Fe^{3+}/\sum Fe$ ratio is known. A major limitation of the modeling exercises in chapters 3 and 4 was a lack of published force constants for clinopyroxene and amphibole. Determining the appropriate Fe force constant for models involving amphibole will always be more challenging than for other common Fe-bearing phases like garnet, olivine, or orthopyroxene because amphibole can structurally accommodate significant quantities of Fe^{3+} and, unlike Fe-Ti oxides, recalculating amphibole Fe^{3+} from electron microprobe analysis (EPMA) generally yields inaccurate results (Lamb et al., 2012). While the efficacy of recalculating clinopyroxene $Fe^{3+}/\sum Fe$ ratios from EPMA is debated, it will be strongly controlled by the quality of the original analysis (Neave et al., 2024). Nevertheless, a detailed Mössbauer-based study of amphibole and clinopyroxene with varying $Fe^{3+}/\sum Fe$ ratios would go far in improving our understanding of the potential for these phases to drive Fe isotope trends in igneous and metamorphic systems.

1.4 References

Aarons, S. M., Reimink, J. R., Greber, N. D., Heard, A. W., Zhang, Z., & Dauphas, N. (2020). Titanium isotopes constrain a magmatic transition at the Hadean-Archean boundary in the Acasta Gneiss Complex. *Science Advances,* 6(50), eabc9959.

Arculus, R. J., & Smith, D. J. (1979). Eclogite, pyroxenite and amphibolite inclusions in the Sullivan Buttes Latite, Chino Valley, Yavari County, Arizona. *The Mantle Sample: Inclusion in Kimberlites and Other Volcanics,* 16, 309-317.

Blatter, D. L., Sisson, T. W., & Hankins, W. B. (2013). Crystallization of oxidized, moderately hydrous arc basalt at mid-to lower-crustal pressures: Implications for andesite genesis. *Contributions to Mineralogy and Petrology,* 166, 861-886.

Blatter, D. L., Sisson, T. W., & Hankins, W. B. (2023). Garnet stability in arc basalt, andesite, and dacite - an experimental study. *Contributions to Mineralogy and Petrology,* 178(6), 33.

Bloch, E., Ibañez-Mejia, M., Murray, K., Vervoort, J., & Müntener, O. (2017). Recent crustal foundering in the Northern Volcanic Zone of the Andean arc: Petrological insights from the roots of a modern subduction zone. *Earth and Planetary Science Letters,* 476, 47-58.

Blundy, J., Cashman, K. V., Rust, A., & Witham, F. (2010). A case for CO_2-rich arc magmas. *Earth and Planetary Science Letters,* 290(3-4), 289-301.

Brounce, M. N., Kelley, K. A., & Cottrell, E. (2014). Variations in $Fe^{3+}/\sum$ Fe of Mariana Arc basalts and mantle wedge fO_2. *Journal of Petrology,* 55(12), 2513-2536.

Bucholz, C. E., & Kelemen, P. B. (2019). Oxygen fugacity at the base of the Talkeetna arc, Alaska. *Contributions to Mineralogy and Petrology,* 174, 1-27.

Chen, Z., Chen, J., Tamehe, L. S., Zhang, Y., Zeng, Z., Zhang, T., ... & Yin, X. (2023). Light Fe isotopes in arc magmas from cold subduction zones: Implications for serpentinite-derived fluids oxidized the sub-arc mantle. *Geochimica et Cosmochimica Acta,* 342, 1-14.

Chin, E. J., Shimizu, K., Bybee, G. M., & Erdman, M. E. (2018). On the development of the calc-alkaline and tholeiitic magma series: A deep crustal cumulate perspective. *Earth and Planetary Science Letters,* 482, 277-287.

Citron, G. P., Kay, R. W., & Kay, S. M. (1979). Geology and geochemistry of the Hidden Bay Pluton, Adak Island, Aleutian Islands, Alaska (Abstr.). *Geological Society of America,* 11, 402.

Citron, G. P., Kay, R. W., Kay, S. M., Snee, L. W., & Sutter, J. F. (1980). Tectonic significance of early Oligocene plutonism on Adak Island, central Aleutian Islands, Alaska. *Geology,* 8(8), 375-379.

Cooper, G. F., Davidson, J. P., & Blundy, J. D. (2016). Plutonic xenoliths from Martinique, Lesser Antilles: Evidence for open system processes and reactive melt flow in island arc crust. *Contributions to Mineralogy and Petrology,* 171, 1-21.

Cooper, G. F., & Inglis, E. C. (2022). A crustal control on the Fe isotope systematics of volcanic arcs revealed in plutonic xenoliths from the Lesser Antilles. *Frontiers in Earth Science,* 9, 795858.

Conrad, W. K., & Kay, R. W. (1984). Ultramafic and mafic inclusions from Adak Island: crystallization history, and implications for the nature of primary magmas and crustal evolution in the Aleutian Arc. *Journal of Petrology,* 25(1), 88-125.

Cottrell, E., & Kelley, K. A. (2011). The oxidation state of Fe in MORB glasses and the oxygen fugacity of the upper mantle. *Earth and Planetary Science Letters,* 305(3-4), 270-282.

Cottrell, E., Birner, S. K., Brounce, M., Davis, F. A., Waters, L. E., & Kelley, K. A. (2021). Oxygen fugacity across tectonic settings. *Magma Redox Geochemistry,* 33-61.

Dauphas, N., Craddock, P. R., Asimow, P. D., Bennett, V. C., Nutman, A. P., & Ohnenstetter, D. (2009). Iron isotopes may reveal the redox conditions of mantle melting from Archean to Present. *Earth and Planetary Science Letters,* 288(1-2), 255-267.

Debari, S., Kay, S. M., & Kay, R. W. (1987). Ultramafic xenoliths from Adagdak volcano, Adak, Aleutian Islands, Alaska: Deformed igneous cumulates from the Moho of an island arc. *The Journal of Geology,* 95(3), 329-341.

DeBari, S. M., & Coleman, R. G. (1989). Examination of the deep levels of an island arc: Evidence from the Tonsina ultramafic-mafic assemblage, Tonsina, Alaska. *Journal of Geophysical Research: Solid Earth,* 94, 4373-4391.

Debret, B., Millet, M. A., Pons, M. L., Bouilhol, P., Inglis, E., & Williams, H. (2016). Isotopic evidence for iron mobility during subduction. *Geology,* 44(3), 215-218.

Defant, M. J., & Drummond, M. S. (1990). Derivation of some modern arc magmas by melting of young subducted lithosphere. *Nature,* 347(6294), 662-665.

Dodge, F. C. W., Lockwood, J. P., & Calk, L. C. (1988). Fragments of the mantle and crust from beneath the Sierra Nevada batholith: Xenoliths in a volcanic pipe near Big Creek, California. *Geological Society of America Bulletin,* 100(6), 938-947.

Esperança, S., Carlson, R. W., & Shirey, S. B. (1988). Lower crustal evolution under central Arizona: Sr, Nd and Pb isotopic and geochemical evidence from the mafic xenoliths of Camp Creek. *Earth and Planetary Science Letters,* 90(1), 26-40.

Foden, J., Sossi, P. A., & Nebel, O. (2018). Controls on the iron isotopic composition of global arc magmas. *Earth and Planetary Science Letters,* 494, 190-201.

Fraser, G. D., & Snyder, G. L. (1959). Geology of southern Adak Island and Kagalaska Island, Alaska. U.S. *Geological Survey Bulletin,* 1028, 371-408.

Gaetani, G. A., O'Leary, J. A., Shimizu, N., Bucholz, C. E., & Newville, M. (2012). Rapid reequilibration of H2O and oxygen fugacity in olivine-hosted melt inclusions. *Geology,* 40(10), 915-918.

Gazel, E., Hayes, J. L., Hoernle, K., Kelemen, P., Everson, E., Holbrook, W. S., ... & Yogodzinski, G. M. (2015). Continental crust generated in oceanic arcs. *Nature Geoscience,* 8(4), 321-327.

Greene, A. R., DeBari, S. M., Kelemen, P. B., Blusztajn, J., & Clift, P. D. (2006). A detailed geochemical study of island arc crust: The Talkeetna arc section, south–central Alaska. *Journal of Petrology,* 47(6), 1051-1093.

Grove, T. L., & Kinzler, R. J. (1986). Petrogenesis of andesites. *Annual Review of Earth and Planetary Sciences,* 14(1), 417-454.

Grove, T. L., Till, C. B., & Krawczynski, M. J. (2012). The role of H2O in subduction zone magmatism. *Annual Review of Earth and Planetary Sciences* 40, 413-439.

Huppert, H. E., Stephen, R., & Sparks, J. (1985). Cooling and contamination of mafic and ultramafic magmas during ascent through continental crust. *Earth and Planetary Science Letters,* 74(4), 371-386.

Jagoutz, O., Müntener, O., Schmidt, M. W., & Burg, J. P. (2011). The roles of flux-and decompression melting and their respective fractionation lines for continental crust formation: Evidence from the Kohistan arc. *Earth and Planetary Science Letters,* 303(1-2), 25-36.

Jagoutz, O., & Schmidt, M. W. (2013). The composition of the foundered complement to the continental crust and a re-evaluation of fluxes in arcs. *Earth and Planetary Science Letters,* 371, 177-190.

Jagoutz, O., & Kelemen, P. B. (2015). Role of arc processes in the formation of continental crust. *Annual Review of Earth and Planetary Sciences,* 43, 363-404.

Jicha, B. R., Scholl, D. W., Singer, B. S., Yogodzinski, G. M. & Kay, S. M. (2006). Revised age of Aleutian Island Arc formation implies high rate of magma production. *Geology,* 34, 661.

Jull, M., & Kelemen, P. Á. (2001). On the conditions for lower crustal convective instability. *Journal of Geophysical Research: Solid Earth,* 106, 6423-6446.

Kay, R. W. (1978). Aleutian magnesian andesites: Melts from subducted Pacific Ocean crust. *Journal of Volcanology and Geothermal Research,* 4, 117-132.

Kay, R. W., & Mahlburg-Kay, S. (1991). Creation and destruction of lower continental crust. *Geologische Rundschau,* 80, 259-278.

Kay, R. W., & Kay, S. M. (1993). Delamination and delamination magmatism. *Tectonophysics,* 219(1-3), 177-189.

Kay, S.M. and R.W. Kay, 1994, Aleutian magmatism in space and time, in G. Plafker and H.C. Berg (eds.), The Geology of Alaska, Decade of North American Geology (DNAG), *Geological Society of America,* 1, 687-722.

Kay, S. M., Kay, R. W., Citron, G. P., & Perfit, M. R. (1990). Calc-alkaline plutonism in the intra-oceanic Aleutian arc, Alaska. Plutonism from Antarctica to Alaska: *Geological Society of America Special Paper,* 241, 233-255.

Kay, S. M., Jicha, B. R., Citron, G. L., Kay, R. W., Tibbetts, A. K. & Rivera, T. A. (2019). The Calc-Alkaline Hidden Bay and Kagalaska Plutons and the Construction of the Central Aleutian Oceanic Arc Crust. *Journal of Petrology,* 60, 393–439.

Kelemen, P. B., Yogodzinski, G. M., & Scholl, D. W. (2003). Along-strike variation in the Aleutian island arc: Genesis of high Mg# andesite and implications for continental crust. *Inside the Subduction Factory,* 138, 223-276.

Kelley, K. A., & Cottrell, E. (2009). Water and the oxidation state of subduction zone magmas. *Science,* 325(5940), 605-607.

Kelley, K. A., & Cottrell, E. (2012). The influence of magmatic differentiation on the oxidation state of Fe in a basaltic arc magma. *Earth and Planetary Science Letters,* 329, 109-121.

Lamb, W. M., Guillemette, R., Popp, R. K., Fritz, S. J., & Chmiel, G. J. (2012). Determination of Fe3+/Fe using the electron microprobe: A calibration for amphiboles. *American Mineralogist,* 97(5-6), 951-961.

Lee, C. T., Rudnick, R. L., & Brimhall Jr, G. H. (2001). Deep lithospheric dynamics beneath the Sierra Nevada during the Mesozoic and Cenozoic as inferred from xenolith petrology. *Geochemistry, Geophysics, Geosystems,* 2(12).

Lee, C. T. A., Cheng, X., & Horodyskyj, U. (2006). The development and refinement of continental arcs by primary basaltic magmatism, garnet pyroxenite accumulation, basaltic recharge and delamination: Insights from the Sierra Nevada, California. *Contributions to Mineralogy and Petrology,* 151, 222-242.

Lee, C. T. A., & Anderson, D. L. (2015). Continental crust formation at arcs, the arclogite "delamination" cycle, and one origin for fertile melting anomalies in the mantle. *Science Bulletin,* 60(13), 1141-1156.

Martin, H. (1986). Effect of steeper Archean geothermal gradient on geochemistry of subduction-zone magmas. *Geology,* 14(9), 753-756.

Marxer, F., Ulmer, P., & Müntener, O. (2022). Polybaric fractional crystallisation of arc magmas: An experimental study simulating trans-crustal magmatic systems. *Contributions to Mineralogy and Petrology,* 177(1), 3.

McBirney, A. R., Taylor, H. P., & Armstrong, R. L. (1987). Paricutin re-examined: A classic example of crustal assimilation in calc-alkaline magma. *Contributions to Mineralogy and Petrology,* 95, 4-20.

Miyashiro, A. (1974). Volcanic rock series in island arcs and active continental margins. *American Journal of Science,* 274(4), 321-355.

Moussallam, Y., Oppenheimer, C., Scaillet, B., Gaillard, F., Kyle, P., Peters, N., ... & Donovan, A. (2014). Tracking the changing oxidation state of Erebus magmas, from mantle to surface, driven by magma ascent and degassing. *Earth and Planetary Science Letters,* 393, 200-209.

Neave, D. A., Stewart, A. G., Hartley, M. E., & McCammon, C. (2024). Re-evaluating stoichiometric estimates of iron valence in magmatic clinopyroxene crystals. *Contributions to Mineralogy and Petrology,* 179(1), 1-17.

Nebel, O., Sossi, P. A., Bénard, A., Wille, M., Vroon, P. Z., & Arculus, R. J. (2015). Redox-variability and controls in subduction zones from an iron-isotope perspective. *Earth and Planetary Science Letters,* 432, 142-151.

Osborn, E. F. (1959). Role of oxygen pressure in the crystallization and differentiation of basaltic magma. *American Journal of Science,* 257(9), 609-647.

Parkinson, I. J., & Arculus, R. J. (1999). The redox state of subduction zones: Insights from arc-peridotites. *Chemical Geology,* 160(4), 409-423.

Polyakov, V. B., & Mineev, S. D. (2000). The use of Mössbauer spectroscopy in stable isotope geochemistry. *Geochimica et Cosmochimica Acta,* 64(5), 849-865.

Reiners, P. W., Nelson, B. K., & Ghiorso, M. S. (1995). Assimilation of felsic crust by basaltic magma: Thermal limits and extents of crustal contamination of mantle-derived magmas. *Geology,* 23(6), 563-566.

Reubi, O., Blundy, J., & Varley, N. R. (2013). Volatiles contents, degassing and crystallization of intermediate magmas at Volcan de Colima, Mexico, inferred from melt inclusions. *Contributions to Mineralogy and Petrology,* 165, 1087-1106.

Rodriguez-Vargas, A., Koester, E., Mallmann, G., Conceição, R. V., Kawashita, K., & Weber, M. B. I. (2005). Mantle diversity beneath the Colombian Andes, northern volcanic zone: Constraints from Sr and Nd isotopes. *Lithos,* 82(3-4), 471-484.

Rudnick, R. L., & Fountain, D. M. (1995). Nature and composition of the continental crust: A lower crustal perspective. *Reviews of Geophysics,* 33(3), 267-309.

Rudnick, R. L. (1992). Xenoliths—samples of the lower continental crust. *Continental Lower Crust,* 23(797), 269-316.

Savage, P. S., Georg, R. B., Williams, H. M., Burton, K. W., & Halliday, A. N. (2011). Silicon isotope fractionation during magmatic differentiation. *Geochimica et Cosmochimica Acta,* 75(20), 6124-6139.

Shirey, S. B., & Hanson, G. N. (1984). Mantle-derived Archaean monzodiorites and trachyandesites. *Nature,* 310(5974), 222-224.

Sparks, R. S. J. (1986). The role of crustal contamination in magma evolution through geological time. *Earth and Planetary Science Letters* ,78(2-3), 211-223.

Tang, M., Erdman, M., Eldridge, G., & Lee, C. T. A. (2018). The redox "filter" beneath magmatic orogens and the formation of continental crust. *Science Advances,* 4(5), eaar4444.

Taylor, S. R. (1967). The origin and growth of continents. *Tectonophysics,* 4(1), 17-34.

Teng, F. Z., Dauphas, N., Huang, S., & Marty, B. (2013). Iron isotopic systematics of oceanic basalts. *Geochimica et Cosmochimica Acta,* 107, 12-26.

Wager, L. R., G. M. Brown, and W. J. Wadsworth. (1960). Types of igneous cumulates. *Journal of Petrology,* 1(1), 73-85.

Weber, M. B. (1998). The Mercaderes-Rio Mayo xenoliths, Colombia: Their bearing on mantle and crustal processes in the Northern Andes. University of Leicester (United Kingdom).

Weber, M. B., Tarney, J., Kempton, P. D., & Kent, R. W. (2002). Crustal make-up of the northern Andes: Evidence based on deep crustal xenolith suites, Mercaderes, SW Colombia. *Tectonophysics,* 345(1-4), 49-82.

Wedepohl, K. H. (1995). The composition of the continental crust. *Geochimica et Cosmochimica Acta,* 59(7), 1217-1232.

Weyer, S., & Ionov, D. A. (2007). Partial melting and melt percolation in the mantle: The message from Fe isotopes. *Earth and Planetary Science Letters,* 259(1-2), 119-133.

Williams, H. M., McCammon, C. A., Peslier, A. H., Halliday, A. N., Teutsch, N., Levasseur, S., & Burg, J. P. (2004). Iron isotope fractionation and the oxygen fugacity of the mantle. *Science*, 304(5677), 1656-1659.

Williams, H. M., Prytulak, J., Woodhead, J. D., Kelley, K. A., Brounce, M., & Plank, T. (2018). Interplay of crystal fractionation, sulfide saturation and oxygen fugacity on the iron isotope composition of arc lavas: An example from the Marianas. *Geochimica et Cosmochimica Acta,* 226, 224-243.

Wolf, M. B., & Wyllie, P. J. (1991). Dehydration-melting of solid amphibolite at 10 kbar: Textural development, liquid interconnectivity and applications to the segregation of magmas. *Mineralogy and Petrology,* 44(3-4), 151-179.

Yogodzinski, G. M., & Kelemen, P. B. (1998). Slab melting in the Aleutians: Implications of an ion probe study of clinopyroxene in primitive adakite and basalt. *Earth and Planetary Science Letters,* 158(1-2), 53-65.

Yogodzinski, G. M., & Kelemen, P. B. (2007). Trace elements in clinopyroxenes from Aleutian xenoliths: Implications for primitive subduction magmatism in an island arc. *Earth and Planetary Science Letters,* 256(3-4), 617-632.

Zimmer, M. M., Plank, T., Hauri, E. H., Yogodzinski, G. M., Stelling, P., Larsen, J., ... & Nye, C. J. (2010). The role of water in generating the calc-alkaline trend: New volatile data for Aleutian magmas and a new tholeiitic index. *Journal of Petrology,* 51(12), 2411-2444.

Chapter 2

PETROLOGY AND GEOCHEMISTRY OF ADAK ISLAND PLUTONIC XENOLITHS: IMPLICATIONS FOR PRIMITIVE MAGMA GENERATION AND CRUSTAL DIFFERENTIATION IN THE ALEUTIAN ISLAND ARC

2.1 ABSTRACT

Deep crustal cumulates in arcs offer a window into the chemistry and crystallization conditions (*P*-*T*-H_2O-fO_2) of primitive basalts in the upper mantle and lower crust and can be studied in ancient exhumed terranes or in xenoliths erupted in young arc lavas. Here, we expand on previous studies and thoroughly characterize the extensive xenolith suites erupted from the Mt. Moffett and Mt. Adagdak volcanic centers (Adak Island, Central Aleutians), which range from primitive ultramafic cumulates to more evolved amphibole gabbro and hornblendite. We present detailed petrography as well as in situ trace and major element mineral chemistry. We use these data to calculate pressure, temperature, and fO_2 estimates for the xenoliths, and compare these findings to experimental results to understand the crystallization sequence and P-T-H_2O-fO_2 under which the cumulates formed. The Moffett crystallization sequence is defined by early amphibole fractionation and an abrupt shift in oxide compositions from chromite to magnetite, while the Adagdak suite is characterized by simultaneous saturation of amphibole+plagioclase and oxide compositions that become increasingly aluminous before magnetite saturation. Olivine–spinel oxybarometry of the Adagdak xenoliths indicates that they are oxidized relative to MORB (FMQ +0.1 to +2.1). Highly fractionated REE and elevated Sr/Y ratios are observed in clinopyroxene from the most primitive cumulates, consistent with a contribution from a basaltic eclogite melt. This basaltic eclogite melt is hypothesized to come from partial melting of the slab or through melting of basalt introduced into the subarc mantle through forearc subduction erosion. These signatures are greatly diminished in the more evolved lithologies, which can be explained through fractionation of plagioclase and amphibole. Our findings support the presence of a complex

magmatic plumbing system beneath Adak, with Mt. Moffett and Mt. Adagdak volcanic centers tapping compositionally distinct sources. More broadly, our results are consistent with studies suggesting that low-degree basaltic eclogite melts formed through slab melting or forearc subduction erosion contribute to arc magmas in the Aleutians, though the associated geochemical signatures are easily obscured by differentiation in the crust.

2.2 INTRODUCTION

Partial melting of subducted oceanic crust has long been invoked in models pertaining to the origin of convergent-margin magmas (Ringwood and Green, 1966; Green and Ringwood, 1968; Kay, 1978, 1980; Defant and Drummond, 1990; Drummond and Defant, 1990). Experimental studies show that low degree partial melting of oceanic basalts metamorphosed to eclogite facies produces magmas with fractionated REE patterns (La/Yb = 40-55), depletions in high field strength elements (HFSE, Nb/La = 0.1-0.4), and high Sr concentrations (800-1500 ppm) (Rapp et al., 1999). These signatures are attributed to the presence of garnet and rutile and a lack of plagioclase in the eclogitic protoliths (Rapp et al., 1999; Sisson and Kelemen, 2018). However, numerical modeling studies in the 1990s questioned both the capacity of dehydrated ocean crust to melt under conditions relevant to the subduction channel (Davies and Stevenson, 1992; Peacock et al., 1994; Yasuda et al., 1994) and the effectiveness by which these melts could segregate from their residues (Vigneresse et al., 1996).

Thermal modeling (van Keken et al., 2002; Peacock et al., 2005; Wada and Wang, 2009; Syracuse et al., 2010; Peacock, 2020) however, suggests that slab-top geotherms may intersect the wet-solidus of basaltic eclogite (Supplementary Figure 1, Schmidt and Poli, 1998; Poli and Schmidt, 2002; Sisson and Kelemen, 2018). Furthermore, refined models of partial melts of eclogite reacting with mantle wedge peridotite can reproduce major and trace element characteristics of primitive arc magmas (e.g., Sisson and Kelemen, 2018). Recently, Turner and Langmuir (2022a, 2022b) support a general model, accounting for global variations in arc magma geochemistry, in which subducted altered oceanic crust (AOC) and sediment ubiquitously melt and are mixed into a mantle wedge that varies in composition from a depleted MORB source to an

enriched mantle. In this model, variable degrees of melting of these hybridized mantle compositions account for geochemical variations across and within arc systems. Slab melt signatures may also be introduced into the mantle wedge through subduction erosion, a process in which crustal material from the upper plate is eroded and brought to the subarc mantle via the subduction channel. Metamorphism and partial melting of this material with increased pressure and temperature may also create "slab-melt" signatures (Bourgois et al., 1996; Goss and Kay, 2006; Jicha and Kay, 2018; Kay et al., 2019).

The Aleutians have been extensively studied to understand the contribution of subducted slab melts and forearc subduction erosion to the geochemistry of lavas and plutonic rocks (Kay, 1978, 1980, Yogodzinski et al., 1994; Kay and Kay, 1994; Yogodzinski and Kelemen, 1998; Kelemen et al., 2003b; Yogodzinski and Kelemen, 2007; Yogodzinski et al., 2017; Jicha and Kay, 2018; Kay et al., 2019; Bezard et al., 2021). Slab melts in the source region of magmas have been inferred both from the presence of primitive high magnesium andesites (i.e., adakites; Kay, 1978; Yogodzinski et al., 1994; Yogodzinski and Kelemen, 1998; Kelemen et al., 2003b) and from studies of primitive lower crustal cumulates with adakite-like trace element signature (e.g., fractionated REE patterns, high Sr/Y; Yogodzinski and Kelemen, 2007). Although primitive adakites rarely erupt in the central arc around Adak and are not observed in the eastern arc, some authors have suggested that some degree of slab melting may be common across the entire arc (Kelemen et al., 2003b; Yogodzinski et al., 2015).

Lower crustal, ultramafic cumulate xenoliths from Mt. Moffett on Adak Island have been used to support the inference that slab melting has occurred in the central Aleutians by Yogodzinski and Kelemen (2007), who analyzed trace elements in clinopyroxene from two olivine+amphibole clinopyroxenite xenoliths and found that they had elevated Sr/Y (5.1-47.2) and La/Yb (1.2-2.6) ratios which were positively correlated with Mg#. They proposed the correlation between high Sr/Y, La/Yb and Mg# suggested that the slab melt component was strongest in the parental melts to the most primitive xenoliths but was then diluted by reactions within the mantle or mixing with diverse melts within the crust or upper mantle (similar to inferences from previous

studies: Kay, 1978, Yogodzinski et al., 1994; Kelemen et al., 2003b). Others have used the plutonic record on Adak Island to suggest that slab melting signatures on Adak may reflect subduction erosion and partial melting of mafic forearc material, at least locally (Jicha and Kay, 2018; Kay et al., 2019). Pairing pluton Ar/Ar ages with trace element chemistry, Jicha and Kay (2018) and Kay et al. (2019) showed that arc migration, a feature associated with periods of increased forearc subduction erosion (Stern, 1991; von Huene and Scholl, 1991; Kay and Kay, 1994; Kay et al., 2005; Goss et al., 2013), coincided with the emplacement of the plutonic units with the strongest adakite-like signatures. In summary, while it is generally agreed that the geochemical characteristics of high-Mg andesites and xenoliths found on Adak necessitate mixing/reaction with partial melts of a basaltic eclogite, different possible sources for this end-member component have been proposed in the literature.

Here, we further explore the origin and characteristics of the parental magmas to xenoliths found in lava flows from Mt. Moffett and Adagdak volcano on Adak Island and their chemical evolution during differentiation. Although the mineralogy and chemistry of the xenoliths have been studied in the past (Conrad and Kay, 1984; Debari et al., 1987) we characterize a larger suite of Adak xenoliths than previously described, including a previously undocumented mantle xenolith, in terms of major (Moffett: $n = 12$, Adagdak: $n = 34$) and trace element (Adagdak: $n = 15$, Moffett: $n = 6$) mineral chemistry. With these data, we calculate crystallization conditions (P, T, H_2O, fO_2) and parental melt trace element compositions. We then model the origin of the parental melts through basaltic eclogite melt-peridotite reactions and discuss the effect of fractional crystallization on the geochemical signatures of these hybridized melts. As the processes of slab melting and forearc subduction erosion should create melts with the same major and trace element characteristics, and the data we present here are not suitable to distinguish between the two processes, we use the term basaltic eclogite melt to refer to situations in which the source of this endmember component is ambiguous and could have resulted from either (or both) process(es).

2.3 GEOLOGIC SETTING AND PREVIOUS WORK

2.3.1 Adak Island

Adak Island is part of the Andreanof crustal block in the central Aleutian arc (Fig. 1a) (Geist et al., 1988). The island has two young stratovolcanoes, Mount Moffett and Mount Adagdak, which are located in the northern part of the island ~ 5 km apart (Fig. 1b). Mount Moffett has erupted in the Holocene (Jicha and Kay, 2018) and Mount Adagdak was active during the Pleistocene (Baten, 2002). Lavas from Adagdak and Moffett range from high-Mg basalt to dacite (Coats, 1956). Plutonic rocks exposed on Adak Island include the ~38 Ma Finger Bay pluton in the north-central part of the island, the ~35-31 Ma Hidden Bay pluton to the south, and the ~14 Ma Kagalaska pluton on the far eastern terminus of the island (Kay et al., 1990, 2019a; Kay and Kay, 1994; Jicha et al., 2006). The Finger Bay pluton comprises amphibole-poor tholeiitic gabbro with subordinate quartz monzonite, and (quartz) monzodiorite (Kay et al., 1983). The Hidden Bay and Kagalaska plutons consist of amphibole-rich calc-alkaline gabbro, diorite, granodiorite, and minor leucogranodiorite (Fraser and Snyder, 1959; Citron et al., 1979; Citron, 1980; Kay et al., 2019).

2.3.1 Adak Island xenoliths—geologic context and previous work

The Moffett xenolith suite was collected from a ~100 m thick lava flow on the north/northeastern slopes of Mount Moffett (Coats, 1956; Conrad et al., 1983; Conrad and Kay, 1984). A bulk-rock analysis of the xenolith-bearing flow is provided in the appendix of Kay and Kay (1994) (sample MFHOS). The Mount Adagdak xenoliths are exposed in an olivine-phyric, high-MgO (11.8 wt.%) Holocene basaltic flow on the western slopes of the volcano (Debari et al., 1987; Fig. 1b). Xenoliths from the Moffett and Adagdak flows have been the subject of thorough petrographic and geochemical studies (Conrad et al., 1983; Conrad and Kay, 1984; Debari et al., 1987) with additional trace element studies from two Moffett xenoliths documented by Yogodzinski and Kelemen (2007). We briefly describe these previous studies and their findings to establish a baseline for our further investigation of these xenoliths. The petrography and mineral chemistry of Adak xenoliths provided by these earlier works are summarized in Table 1.

Mount Adagdak: Debari et al. (1987) described the petrography and major element mineral chemistry of 10 cumulate xenoliths from Mount Adagdak, including dunite, wehrlite, clinopyroxenite, and hornblendite (Table 1). Reported olivine and clinopyroxene Mg# varies from 83.2 to 86.6 and 75 to 92, respectively. Debari et al. (1987) suggested that the parental magma to these cumulates was similar to the host basalt and that the xenoliths represent the deep crustal (>0.8 GPa) cumulate complements to low-Mg, high-Al basalts typically found in the Central Aleutian arc.

Mount Moffett: Conrad et al. (1983) divided the xenoliths from Mount Moffett into (1) cumulate textured xenoliths, (2) cognate inclusions (i.e., megacrystic minerals crystallizing either within the host lava or entrained from deeper in the crust), and (3) 'composite' xenoliths (i.e., inclusions of quenched magmas of a different origin than the host). Conrad and Kay (1984) present mineral analyses for 7 cumulate xenoliths, including 2 ultramafic and 5 gabbroic samples. In this study, we focus exclusively on cumulate xenoliths which have been classified into three petrologic groups: (1) olivine pyroxenite (±amphibole); (2) hornblende gabbro (±olivine); and (3) orthopyroxene-bearing gabbro (±olivine) (Conrad and Kay, 1984). Xenoliths in groups 1 and 2 were interpreted as part of a cogenetic crystallization sequence resulting from the differentiation of a primary hydrous basalt in the lower crust. Yogodzinski and Kelemen (2007) measured trace element abundances in clinopyroxene from two olivine clinopyroxenite specimens (MM-102 and MM-43) (Table 1) as well as clinopyroxene phenocrysts from a magnesian andesite (MM79A) in the Cornell collection. Trace element characteristics of clinopyroxene from Mount Moffett xenoliths, such as elevated Sr/Y and Nd/Yb ratios, resemble phenocrysts from primitive, enriched high-Mg andesite described by Kay (1978). Yogodzinski and Kelemen (2007) found that these eclogite-melt trace element characteristics were strongest in most magnesian clinopyroxene.

2.4 METHODS

Olivine, clinopyroxene, amphibole, plagioclase, and spinel major element mineral compositions from 46 samples from Mt. Adagdak (n = 34) and Mt. Moffett (n = 12) from the Cornell collection were obtained with a JEOL JXA-8200 electron microprobe at Caltech (Supplemental Data File 1,

Ch2-T2 - Ch2-T6). For 11 of the more primitive Adagdak xenoliths, spinel compositions were analyzed separately following the methods of Wood and Virgo (1989), recently revisited by Davis et al. (2017) (Supplemental Data File 1, Ch2-T6). Each 150 to 200 spinel analyses were bracketed by analyses of standards whose $Fe^{3+}/\Sigma Fe$ ratios ($Fe^{3+}/[Fe^{3+}+ Fe^{2+}]$) are known from Mössbauer spectroscopy (Wood and Virgo, 1989; Bryndzia and Wood, 1990). The bracketing procedure consisted of 3 core analyses from each of our 11 spinel standards. Adagdak spinel $Fe^{3+}/\Sigma Fe$ ratios were then adjusted using the Wood and Virgo (1989) correction (Supplemental Data File 1, Ch2-T7). High-precision measurements of calcium in olivine cores for 15 of our most primitive xenoliths were obtained in a separate session (Supplemental Data File 1, Ch2-T2). Clinopyroxene, amphibole, and plagioclase trace element concentrations were obtained via Laser Ablation Inductively Coupled Plasma Mass Spectrometry (LA-ICP-MS) at Rutgers University using a Photon Machines 193 nm excimer laser coupled to a Thermo Scientific iCAPQc (Supplemental Data File 1, Ch2-T8 - Ch2-T10). All measurements represent grain cores that had previously been queried with respect to their major element chemistry via electron microprobe analysis. A more detailed description of these methods is given in the Appendix.

2.5 RESULTS

A total of 59 xenoliths from Adagdak (n = 42) and Moffett (n = 17) were studied in thin section. Modal mineralogy and petrographic descriptions of each sample are given in Table 2 and Figures 2 and 3. Representative thin section photomicrographs are presented in Figure 4. We highlight the salient features of each lithology below and provide detailed descriptions of each sample in the Appendix (sections 2.13-2.14, Supplementary Figures 2-4).

2.5.1 Adagdak petrography

***Lherzolite*:** ADG-CB-9 is the only lherzolite in the Adagdak sample suite. By volume, the xenolith consists of olivine (77%), clinopyroxene (14%), orthopyroxene (8%), and spinel (1%) and has a protogranular texture (Fig. 4a). Spinel occurs both interstitially and poikilitically within clinopyroxene.

***Dunite*:** These samples (n = 3) have protogranular textures and are composed of olivine (93-94%), spinel (3-4%), and clinopyroxene (2-3%). Spinel is present both interstitially and as poikilitic inclusions in clinopyroxene and olivine.

***Wehrlite*:** These samples (n = 8) are composed of olivine (40-83%), clinopyroxene (14-58%), and spinel (0-7%). Textures vary from adcumulate to protogranular. Clinopyroxene varies considerably in size from 0.10 to 4.5 mm across. When present, spinel is interstitial or poikilitically included in clinopyroxene or olivine (Fig. 4b).

***Olivine clinopyroxenite*:** These xenoliths (n = 5) contain clinopyroxene (62-88%), olivine (12-37%), and spinel (~1%) and have adcumulate to protogranular textures. Except for ADG-32, which contains olivine up to 9.8 mm across, olivine in these xenoliths generally ranges from 0.10 to 2.2 mm in diameter. Traces of amphibole are observed as veins in samples ADG-CB-7, ADG-8, and ADG-32 along clinopyroxene grain boundaries.

***Clinopyroxenite*:** These samples (n = 2) contain clinopyroxene (93-94%), olivine (5-6%), and spinel (~1%). Sample ADG-82-15 has a protogranular texture and ADG-82-1 has an adcumulate texture. Small (<10 μm) euhedral spinel crystals are interstitial in both samples. Sample ADG-82-15 contains thin veins of amphibole along clinopyroxene grain boundaries.

Amphibole gabbro: These xenoliths (n = 19) are composed of plagioclase (8-53%), amphibole (24-64%), clinopyroxene (1-55%), Fe-Ti oxides (0-9%), and traces of olivine (0-3%), with adcumulate (n = 8) and mesocumulates (n = 11) textures. Plagioclase is generally elongate (0.10-8.0 mm long); however, three samples contain distinct poikilitic plagioclase enclosing amphibole and clinopyroxene (Fig. 4c). In most samples (n = 13), amphibole poikilitically encloses plagioclase, clinopyroxene, and Fe-Ti oxides (Fig. 4d). Amphibole grains are generally elongate and euhedral although anhedral intercumulus amphibole is observed in sample ADG-22a. In samples ADG-4, ADG-38, ADG-73, and ADG-82-6, anhedral clinopyroxene is surrounded by 0.2-1 mm amphibole rims (Fig. 4d). Most xenoliths (n = 15) contain two petrographically distinct

Fe-Ti oxide populations: 1) small (10-150 μm) euhedral Fe-Ti oxides present as inclusions in amphibole or clinopyroxene, and 2) larger (0.10–1.2 mm) anhedral, interstitial Fe-Ti oxides.

***Hornblendite*:** These xenoliths (n = 4) have modal amphibole abundances exceeding 70% and contain amphibole (79-95%), clinopyroxene (3-14%), plagioclase (0-11%), and Fe-Ti oxides (~1%). In samples ADG-26 and ADG-52, some amphibole (~35-50%) poikilitically envelops rounded 0.1 to 1.8 mm clinopyroxene, small (<0.02 mm) Fe-Ti oxides, or other distinct amphibole grains, while amphibole in samples ADG-CB-10 and ADG-82-18 is mostly inclusion free. Plagioclase is only present in samples ADG-52 and ADG-CB-10, where it occurs as a continuous intercumulus fill without defined grain boundaries. Small (<0.25 mm) Fe-Ti oxides occur interstitially in all samples or as poikilitic inclusions in amphibole and clinopyroxene.

2.5.2 Moffett petrography

Olivine clinopyroxenite (+ amphibole): These samples (n = 6) are comprised of clinopyroxene (32-81%), olivine (9-36%), and oxide phases (0-3%) with orthocumulate textures. Samples MM-77-35, MM-77-76, and MOF-81X-G, also contain amphibole (modally 32-48%) (Fig. 4e). Amphibole from samples MM-77-67 and MM-77-35 has 25-125 μm thick opacitic rims (Fig. 4e). Most amphibole (>60%) in these samples is euhedral and prismatic, although some crystals display an intercumulus texture around pre-existing olivine and clinopyroxene. Amphibole from MOF-81X-G is anhedral and interstitial, often present as veins at the interface between olivine and clinopyroxene and does not show opacitic rims. MOF-81X-C and MM-77-35 contain Fe-Ti oxides and samples MM-77-67, MM-CB-2, and MOF-81X-A contain Cr-spinel.

Clinopyroxenite: These xenoliths (n = 2) have orthocumulate textures and contain clinopyroxene (90-97%), olivine (3-9%), and Fe-Ti oxides (~1%). Small Fe-Ti oxides (<40 μm) occur interstitially or as inclusions in olivine and clinopyroxene.

Amphibole gabbro: These samples (n = 4) contain plagioclase (42-68%), amphibole (23-43%), clinopyroxene (0-21%), and Fe-Ti oxides (0-10%) and show orthocumulate textures. Plagioclase in MOF-81X-D and MM-76-4 often poikilitically encloses small (<10 μm) Fe-Ti oxides or larger

(50-150 μm) amphibole or clinopyroxene (Fig. 4f), while plagioclase from MM-76-9 and MOF-81X-F is generally inclusion free. Amphibole from samples MM-76-4 and MOF-81X-D has 50-125 μm thick opacitic rims (Fig. 4f). Clinopyroxene in MM-76-9 has experienced uralitization. When present, Fe-Ti oxides occur poikilitically.

Hornblendite: Moffett hornblendite ($n = 5$) contains amphibole (74-99%), clinopyroxene (0-16%), plagioclase (0-7%), and Fe-Ti oxides (0-4%) and shows mesocumulate to orthocumulate textures. Amphibole is highly altered, especially along cleavage planes, with pervasive fracturing observed in all grains. Opacitic rims (10-25 μm thick) are observed on amphibole from samples MM-CB-1 and MOF-81X-E.

2.5.3 Adagdak major and trace element mineral chemistry

Olivine: Sample average Mg# ($[Mg/(Mg + Fe^T)] \times 100$ for all phases but spinel) for olivine cores range from 84.1 to 87.1 for ultramafic Adagdak cumulates (Fig. 5a). Lherzolite ADG-CB-9 and amphibole gabbro ADG-CB-1 have average olivine core Mg# of 91.3 and 73.5, respectively (Fig. 5a). Including literature data, average core NiO concentrations positively correlate with Mg# and range from 0.03 to 0.30 wt.% (Fig. 5a). In samples analyzed for high precision Ca-in-olivine (n = 13), core Ca concentrations range from 290 to 645 ppm (0.04 to 0.09 wt.% CaO). Core-to-rim zoning was only observed in the more evolved samples (amphibole gabbro, clinopyroxenite, and olivine clinopyroxenite), with Mg# typically decreasing by 0.5-1.0 from core to rim.

Pyroxene: Clinopyroxene is the only phase present throughout the entire Adagdak suite and consists predominantly of diopside. Sample average Mg# of clinopyroxene cores ranges from 93.8 to 81.6 for the ultramafic xenoliths and from 73.6 to 77.8 in the amphibole gabbro and hornblendite (Fig. 5b, c). $K_{D,Ol-CPX}^{Fe^T/Mg}$ (molar $\frac{(Fe^T/Mg)_{Ol}}{(Fe^T/Mg)_{CPX}}$) varies from 0.77 to 1.53 (Fig. 5b). Average Al_2O_3 concentrations range from 1.34 to 5.44 wt.% in the ultramafic lithologies and reach their highest values in the hornblendite (6.9-8.5 wt.%; Fig. 5c). All clinopyroxene is depleted in Nb and Ta, with negative Zr-anomalies ($Zr/Zr^* = Zr_N/[Nd_N \times Sm_N]^{0.5}$, where N designates normalization to chondrites), which range from 0.2 to 0.6 and are negatively correlated to Mg#. Eu-anomalies

(Eu/Eu* = $Eu_N/[Sm_N \times Gd_N]^{0.5}$) are not observed in Adagdak xenolith clinopyroxene (Fig. 6). Sr-anomalies (Sr/Sr* = $Sr_N/[Pr_N \times Nd_N]^{0.5}$) correlate with Mg# and are generally positive (>1) in the ultramafic lithologies (0.96-2.18) and negative (<1) in clinopyroxene from the amphibole gabbro and hornblendite (0.61-0.74) (Fig. 7a). Clinopyroxene Sr/Y and La/Yb ratios are positively correlated with Mg# and vary from 3.4 to 21.3 and from 0.5 to 2.7, respectively (Fig. 7b).

Amphibole: Average amphibole core Mg# ranges from 64.3 to 71.3 and does not correlate with rock type or the concentration of any major element. Seven of the Adagdak amphibole gabbro samples contain magnesio-hastingsite and one contains pargasitic amphibole (based on the nomenclature of Leake, 2004). All Adagdak hornblendite contains pargasitic amphibole. Amphibole is consistently enriched in Cs, Rb, Ba, and Sr (Sr/Sr* 1.9-8.8: Supplemental Figure 5).

Plagioclase: Plagioclase in the Adagdak amphibole gabbro and hornblendite is anorthite-rich (An_{91-96}) and unzoned. Plagioclase is consistently enriched in LREE and LILE, particularly Sr (530-830 ppm) relative to the HREE (La/Yb = 0.1-0.3) and HFSE. All samples show positive Ba, Pb, Sr, and Eu anomalies on primitive mantle normalized spider diagrams (Supplemental Figure 6).

Spinel: Average Cr# (100 × molar Cr/[Cr+Al]) from spinel cores ranges from 4 to 60 and decreases with increasing Mg# (for spinel only, we define Mg# as [Mg/(Mg + Fe^{2+})] × 100) (Fig. 5d). Spinel core Cr# for olivine clinopyroxenite, wehrlite, and dunite xenoliths ranges from 22.3 and 47.0. Lower Cr#, ranging from 0.4 to 11, is observed in amphibole gabbro and clinopyroxenite xenoliths. Average core Mg# varies from 50.4 to 72.9 in the Adagdak suite. Calculated sample average $Fe^{3+}/\Sigma Fe$ ratios from spinel cores range from 0.3 to 0.5 and do not correlate with Mg#, Cr#, (Fig. 5e) or the concentration of any major oxide. Magnetite is the dominant oxide in the more evolved amphibole gabbro and hornblendite cumulates.

2.5.4 Moffett major and trace element mineral chemistry

***Olivine*:** Olivine core Mg# and NiO range from 84.8 to 89.0 and from 0.13 to 0.23 wt.%, respectively (Fig. 5a). Normal zoning in Mg# is observed in the outer 20-60 μm rims of olivine

from samples MM-77-35 and MOF-81X-C. Reverse zoning is only observed in olivine from sample MOF-81X-A, where the outer 50 μm rims show increased Mg# adjacent to clinopyroxene. Ca concentrations (750-970 ppm) are higher in olivine from Moffett that from Adagdak and do not correlate with Mg# or other major element concentrations.

Pyroxene: Clinopyroxenite (±olivine) have clinopyroxene core Mg# between 88.5 and 90.7. Clinopyroxene consists of diopside in all samples except olivine clinopyroxenite MOF-81X-C, which contains augite. Amphibole-bearing samples have Mg# between 72.7 and 78.1. Sample average Al_2O_3 concentrations range from 1.1 to 8.0 wt.% and negatively correlate with Mg# (Fig. 5c). Sample $K_{D,Ol-CPX}^{Fe^T/Mg}$ ranges from 0.70 to 1.88 (Fig. 5b). Strontium anomalies range from 0.7 to 2.8 and positively correlate with Mg# (Fig. 7a). Sample average Sr/Y and La/Yb ratios positively correlate with Mg# and range from 6.4 to 41.7 and from 1.2 to 2.5, respectively (Fig. 7b, c). All samples are depleted in LREE and HREE relative to MREE (Fig. 8).

Amphibole: Samples MM-77-35 and MM-77-67 contain populations of both euhedral and intercumulus amphibole. In both samples, the major element chemistry of the two groups is similar (Table S4). All Moffett samples contain magnesio-hastingsite except for MM-CB-1 and MOF-81X-G, which contain pargasitic amphibole. We do not observe the high Cr concentrations Conrad and Kay (1984) reported for amphibole from ultramafic xenoliths (up to 0.55 wt.% Cr_2O_3), with Cr_2O_3 concentrations in the amphibole cores we analyzed never exceeding 0.07 wt.%. Amphibole is enriched in Sr and Ba and depleted in the LREE relative to the MREE and HREE (La/Sm = 0.3-0.5, La/Yb = 0.6-1.1; Supplemental Figure 5).

Plagioclase: Moffett plagioclase is consistently anorthite-rich (An_{91}-An_{93}) and unzoned. Plagioclase from amphibole gabbro MM-76-4 shows similar trace element chemistry to those from Adagdak, with enrichment in the LILE and LREE but depletion in HREE and HFSE. All analyses from this sample show positive Ba, Pb, Sr, and Eu anomalies on primitive mantle normalized trace element diagrams (Supplemental Figure 6).

Spinel: Magnetite is the dominant oxide phase in the Moffett cumulates. Chromium-rich spinel is only present in olivine clinopyroxenite samples MOF-81X-A, MM-CB-2, and MM-77-67, with core Cr# ranging from 73.5 to 82.3 (Fig. 5d). Average calculated $Fe^{3+}/\Sigma Fe$ ranges from 0.25 to 0.42 for spinel cores (note: the Wood and Virgo correction was not applied to these analyses) and does not correlate with Mg# or Cr# (Fig. 5e).

2.6 DISCUSSION

2.6.1 Crystallization Sequence

Determining the crystallization sequences of the Moffett and Adagdak cumulate suites is critical to understanding their petrogenesis, as it is controlled in part by the P-T-H_2O-fO_2 conditions of their parental magmas. Although both cumulate suites show evidence for some subsolidus Fe-Mg exchange, we infer the same crystallization sequence for both suites—based on olivine, clinopyroxene, and amphibole Mg#, spinel Cr#, and modal mineralogy (Fig. 9)—as those inferred in earlier studies. Both sequences were constructed under the assumption that the most primitive samples should contain the most magnesian silicates, Cr-rich oxides, and the highest modal abundances of olivine. Petrographic examination indicates that, when present, olivine and spinel were the first phases to crystallize, then joined by clinopyroxene.

Adagdak: The dunite represents the initial crystallization products of the Adagdak suite. These samples have the highest modal abundances of olivine (93-94%) and the most Mg-rich olivine (Mg# ~ 87) and clinopyroxene (Mg# = 90-91). The modal abundance of olivine decreases as clinopyroxene becomes the dominant phase in the cumulates, represented by the wehrlite and clinopyroxenite xenoliths. Amphibole and plagioclase then join the cumulate assemblage together as the abundance of cumulus clinopyroxene and olivine decreases abruptly (Fig. 2). Magnetite also replaces spinel as the dominant oxide phase. This final phase of the crystallization sequence is represented by the amphibole gabbro and hornblendite cumulates. Although trace amounts of olivine are present in only half of these samples, clinopyroxene persists to the end of the observed sequence. While the amphibole veins observed in some of the ultramafic samples are interpreted to be peritectic in origin, amphibole in all but four of the hornblendite and amphibole gabbro

samples is inferred to be a primary cumulate phase (consistent with the interpretation of Debari et al., 1987). This interpretation is supported petrographically, with amphibole in these more evolved cumulates usually present as large euhedral grains in no apparent reaction relationship with clinopyroxene or olivine (Fig. 4c). Amphibole in samples ADG-4, -38, -73, and -82-6 is texturally distinct, poikilitically enclosing rounded clinopyroxene (Fig. 4d). This texture could be interpreted two ways: 1) late-stage cumulate amphibole fractionation, with amphibole enveloping pre-existing clinopyroxene grains, or 2) amphibole forming through peritectic reactions between melts percolating through the cumulate mush and preexisting clinopyroxene (e.g., Blatter et al., 2017; Cooper et al., 2016). The petrography suggests, however, that the vast majority of amphibole in the Adagdak amphibole gabbro and hornblendite co-crystallized with clinopyroxene without evidence for a peritectic relationship. Thus, the dominant inferred crystallization sequence for the Adagdak xenolith suite is olivine + clinopyroxene + spinel $\rightarrow$ clinopyroxene + amphibole + plagioclase + Fe-Ti oxide.

Moffett: The most primitive crystallization assemblage in the Moffett suite is olivine clinopyroxenite with minor Cr-spinel. Half of these samples also contain amphibole. While the altered appearance of amphibole in MOF-81X-G suggests a secondary or peritectic origin, the petrography of amphibole in samples MM-77-35 and MM-77-67 is consistent with amphibole being a primary cumulate phase (Fig. 4e, Supplementary Figures 2-4). The co-crystallization of high-magnesium amphibole, clinopyroxene, and olivine is consistent with derivation from a hydrous primitive basalt or basaltic andesite (Conrad and Kay, 1984; Krawczynski et al., 2012). Conrad and Kay (1984) came to a similar conclusion, suggesting (based on high Cr concentrations in amphibole from Moffett xenolith MM-102) that amphibole was a near-liquidus phase. Plagioclase subsequently enters the crystallization assemblage while amphibole and magnetite modal abundances increase, as observed in the amphibole gabbro and hornblendite xenoliths. The onset of plagioclase crystallization coincides with a decrease in clinopyroxene abundance (21 to 0%; Fig. 3) and the loss of olivine from the cumulate assemblage. The inferred crystallization assemblage for the Moffett cumulates, as also suggested by Conrad and Kay (1984), is olivine +

clinopyroxene + spinel → olivine + clinopyroxene + spinel + amphibole → clinopyroxene + amphibole + plagioclase + Fe-Ti-oxide → amphibole + plagioclase + Fe-Ti oxide.

2.6.2 Crystallization conditions

We estimate crystallization conditions (H_2O, P, T, fO_2) through (1) comparison with experimental studies where these variables are controlled, (2) comparison to xenoliths from other localities where crystallization conditions have been inferred or calculated, and (3) calculation of temperature and fO_2 where geothermometers and oxybarometers suitable for use with the xenolith mineral assemblages are available.

2.6.2.1 Water contents

Adagdak: Crystallization assemblages from the experimental studies of Nandedkar et al. (2014) (N14) and Ulmer et al. (2018) (U18) resemble the Adagdak xenolith assemblages. These studies performed equilibrium and fractional crystallization experiments on primitive basalts (Mg# 69.0-76.4) at 0.7-1 GPa, 0 to 2 log units above the Ni-NiO buffer, and hydrous (~3 wt.% H_2O initial) conditions. The crystallization sequence, modal proportions, and mineral chemistry of crystallization assemblages produced in these experiments are summarized in the Appendix. The ultramafic cumulates from Adagdak likely crystallized from a primitive basalt with a similar water content to that of the high temperature (1200-1060 ºC), initial crystallization interval of basalt in U18 and N14 (3-7 wt.% H_2O). Characteristics of the Adagdak suite such as the modal dominance of olivine in the early crystallizing assemblages and the late appearance of plagioclase are also consistent with derivation from a hydrous melt (Nicholls and Ringwood, 1973; Gaetani et al., 1993; Pichavant and Macdonald, 2007; Ulmer et al., 2018). The modal mineralogy and mineral chemistry of the Adagdak amphibole gabbro and hornblendite are similar to lower-temperature (920-730 ºC) experimental assemblages of N14 which contained 8-12 wt.% H_2O. We suggest that during the crystallization of the Adagdak suite, early olivine, spinel, and clinopyroxene crystallization from a relatively hydrous basalt (3-7 wt.% H_2O) produced the dunite, wehrlite, and clinopyroxenite. Fractionation of these nominally anhydrous phases increased the water content of

later-stage melts to 8-12 wt.% H_2O, at which point the amphibole gabbro and hornblendite cumulates crystallized.

Moffett: The presence of amphibole in Moffett ultramafic olivine clinopyroxenite and the absence of early plagioclase suggests that the parental melt to the suite had higher water contents than parental melts to the Adagdak suite. The experiments of Krawczynski et al. (2012) on basaltic starting materials provide a close experimental comparison to the ultramafic Moffett crystallization assemblage of olivine + clinopyroxene ± amphibole. These experiments show that water-saturated basalts may simultaneously stabilize olivine, clinopyroxene, and amphibole at 500-800 MPa and water-saturated conditions after about 30% solidification and at <1000 ºC. Plagioclase-free assemblages of clinopyroxene and amphibole (±olivine and spinel) have also been produced in crystallization experiments of hydrous (>7 wt.% H_2O) basalts by Melekhova et al (2015) and Ulmer et al (2018). The phase assemblage and mineral chemistry of Moffett amphibole gabbro and hornblendite are very similar to those from Adagdak. We therefore estimate that the parental melts to the Moffett amphibole gabbro and hornblendite cumulates were also saturated with an H_2O-rich fluid in the lower to middle crust.

2.6.2.2 Pressure

As is common for garnet-free ultramafic and mafic igneous assemblages, the mineralogy of the Adak xenoliths does not lend itself well to thermodynamic geobarometry (Debari et al., 1987; Bryndzia and Wood, 1990; Wood et al., 1990; Davis et al., 2017; Bucholz and Kelemen, 2019). We therefore derive pressure estimates by comparing our samples to experimental studies where pressure was controlled and xenoliths from other locations where pressure is well constrained.

Adagdak: We infer that the Adagdak ultramafic cumulates crystalized at ~1 GPa. This estimate is consistent with experimental studies that have produced assemblages modally and geochemically similar to the Adak cumulates (Blatter et al., 2013; Ulmer et al., 2018) as well as previous studies of Adak and central Aleutian magmatism that place crystallization of the most primitive lithologies at the base of the arc crust (Gust and Perfit, 1987; Kay and Kay 1994, Kay et al., 2019). Our ~1 GPa estimate is also consistent with previous studies of Aleutian magmas, which have suggested

that plagioclase-free ultramafic cumulate fractionation in the upper mantle and lower crust leads to the formation of the high-Al basalts found on Adak Island and throughout the Aleutians (Kay and Kay, 1985a, 1985b). The high-Mg basalt crystallization experiments from U18 that we use as our primary experimental comparison for these most primitive Adagdak cumulates were also conducted at 1 GPa.

The negative correlation between clinopyroxene Mg# and Al_2O_3 observed in the ultramafic cumulates (Fig. 5c) is also consistent with plagioclase-free crystallization under high-pressure or high-water conditions (DeBari et al., 1987; DeBari and Coleman, 1989; Melekhova et al., 2015). Similar trends are seen in clinopyroxene from intermediate to high-pressure exhumed arc sections (e.g., the Chilas Complex, Kohistan, 0.5-0.8 GPa: Jagoutz et al., 2007; Talkeetna, 0.95-1.1 GPa: DeBari and Coleman, 1989), but are not observed in clinopyroxene from low-pressure cumulates (e.g., the Lesser Antilles, 0.2-0.5 GPa: Stamper et al., 2014b; Cooper et al., 2016). Due to the expanded stability field of clinopyroxene at higher pressures (e.g., Blatter et al., 2013; Stamper et al., 2014a), early fractionation of clinopyroxene + olivine assemblages also result in the Adagdak wehrlite containing more magnesian olivine (Mg# = 84.1 to 86.7) than is observed in wehrlites from lower pressure systems (e.g., Lesser Antilles, wehrlite olivine Mg# = 82.5 ± 2, Stamper et al., 2014b)

Due to the similarities discussed previously between 0.7 GPa experiments from N14 and the Adagdak amphibole gabbro and hornblendite cumulates, it is tempting to assert that this pressure regime is also an appropriate estimate for these lithological groups. However, because amphibole-plagioclase-magnetite assemblages are ubiquitous in rocks from various crustal depths (e.g., Lesser Antilles, 0.2-0.5 GPa: Cooper et al., 2016; Kohistan, 0.5-0.8 GPa: Jagoutz et al., 2007; Talkeetna, 0.95-1.1 GPa: DeBari and Coleman, 1989) comparisons based on similarities in phase proportions are not as useful. Due to the lack of available thermodynamic geobarometers, we also implement empirical amphibole-only geobarometry for both Adagdak and Moffett cumulates. Empirical amphibole-only geobarometry (Ridolfi et al., 2021) yields pressure estimates between 390 and 910 MPa for the Adagdak amphibole gabbro and hornblendite, consistent with mid- to

deep crustal pressures and the large range of pressures over which amphibole gabbro can crystallize (Table 3).

Moffett: The ultramafic olivine + clinopyroxene ± amphibole ± Fe-Ti oxide Moffett assemblage has been produced by experimental studies over a pressure interval of 0.2 to 0.8 GPa (Holloway and Burnham, 1972; Cawthorn et al., 1973; Helz, 1973; Sisson and Grove 1993; Krawczynski et al., 2012). The amphibole-only geobarometer of Ridolfi et al. (2021) yields pressure estimates of 0.4 to 0.7 GPa for these lithologies, within this range (Table 3). For the amphibole gabbro and hornblendite, amphibole-only geobarometry yields pressures between 0.6 to 0.7 GPa (Ridolfi et al., 2021) (Table 3). In summary, the mineral chemistry and phase assemblages observed in the Moffett cumulate suite are generally consistent with crystallization in the lower to middle crust, between 0.4 and 0.7 GPa.

2.6.2.3 Temperature

For ultramafic xenoliths containing the assemblage olivine + clinopyroxene + spinel, we use the olivine-spinel Fe-Mg exchange thermometers of Ballhaus et al. (1991) and Li et al. (1995) (n = 11). For samples from which we obtained high-precision analyses of the Ca content of olivine (n = 15), we also calculated temperature with the Ca-in-olivine thermometers of Shejwalkar and Coogan (2013) and Köhler and Brey (1990). The empirical amphibole-only thermometers of Putirka (2016) and Ridolfi and Renzulli (2012) were used to obtain temperature estimates for amphibole gabbro and hornblendite (n = 17). For xenoliths for which we had both amphibole and plagioclase mineral chemistry, we used the amphibole-plagioclase thermometer of Holland and Blundy (1994) to estimate temperature (n = 10). Results of these calculations are given in Table 3.

Adagdak: For the lherzolite, both olivine-spinel Fe-Mg exchange thermometers yield temperatures that are within error of each other, ranging from 1080 to 1100 ºC. For the ultramafic cumulate xenoliths (n = 11), Fe-Mg exchange temperatures obtained with the Ballhaus et al. (1991) and Li et al. (1995) thermometers are generally within error of each other (Supplemental Figure 7), ranging from 1000 to 1150 ºC. Temperature estimates were also obtained with the olivine-clinopyroxene calcium exchange thermobarometers of Shejwalkar and Coogan (2013) (their

equation 13) and Köhler and Brey (1990) (their equation 5). Both thermobarometers are calibrated on experiments ranging from 0.1 to 6 GPa and both were evaluated at 1 GPa. Temperature estimates obtained with the Ca-in-olivine thermometer range from 920 to 1040 ºC for the ultramafic cumulates (n = 12) and were generally 40 to 230 ºC lower than temperature estimates obtained through Fe-Mg exchange thermometry. The low Ca-in-olivine temperature estimates may reflect subsolidus diffusion of Ca from olivine (Dohmen et al., 2017) or variations in the monticellite activity coefficient in forsterite with changing bulk composition or pressure (Shejwalkar and Coogan, 2013).

Taken together, the temperatures these samples preserve (950-1150 ºC) are consistent with experimental studies of hydrous basalts that produced similar assemblages of olivine + clinopyroxene + spinel (1050 -1200 ºC, Pichavant and Macdonald, 2007; Nandedkar et al., 2014; Ulmer et al., 2018) and suggests that Fe-Mg exchange thermometry broadly preserves magmatic crystallization temperatures. Amphibole-only thermometry for the amphibole gabbro and hornblendite yields temperatures from 920 to 970 ºC (n = 11). Amphibole-plagioclase thermometry (n = 8; Holland and Blundy, 1994) yields temperatures between 920 and 1070 ºC. Amphibole-plagioclase temperatures are generally 60 to 140 ºC higher than those obtained with amphibole-only thermometry.

Moffett: The Moffett cumulates broadly preserve crystallization temperatures between 900 and 1100 ºC. Fe-Mg olivine-spinel exchange thermometry in ultramafic samples (MM-77-67, MOF-81X-A, and MM-CB-2) yielded temperatures of 855^{+4}_{-2} ºC, 1045±3 ºC, and 1140^{+10}_{-17} ºC. We consider 860ºC and 1140 ºC to be erroneous estimates, as they are inconsistent with experimental studies that have crystalized olivine + cpx + amphibole assemblages over a limited temperature range (900-1050 °C; Holloway and Burnham, 1972; Cawthorn et al., 1973; Helz, 1973; Krawczynski et al., 2012). Low olivine-spinel temperatures may be due to subsolidus Fe-Mg exchange in the Moffett samples, as evidenced by the large variations in $K_{D,Ol-CPX}^{Fe^T/Mg}$ observed in the Moffett suite (Fig. 5b), or re-equilibration of small chromite grains with the surrounding olivine (e.g., Peltonen, 1995). Moffett Ca-in-olivine thermometry (n = 3) was conducted at 0.7 GPa (based

on the discussion in the previous section) and yielded temperature estimates between 1040 and 1105 ºC. Amphibole-only thermometry ranged from 920 to 960 ºC (Supplemental Figure 7). Amphibole-plagioclase thermometry for samples MM-77-61 and MM-76-4 yields respective temperatures of 900 ºC and 920 ºC.

2.6.2.4 Oxygen fugacity

Adagdak: Thermodynamic oxybarometers for mantle rocks typically rely on phase equilibrium among the fayalite component of olivine, the ferrosilite component of orthopyroxene, and the magnetite component of spinel. The ferrosilite component of orthopyroxene is employed to estimate silica activity in the redox reaction between fayalite and magnetite (Mathez, 1984; Mattioli and Wood, 1988; Wood and Virgo, 1989; Ballhaus et al., 1991). Because our Adagdak cumulates do not contain orthopyroxene, we estimated silica activity using diopside-monticellite equilibria following the methods of Bucholz and Kelemen (2019). High-precision Ca-in-olivine analyses were used to determine the monticellite component of olivine (X_{Mo}) for these calculations, obtaining fO_2 values 0.1 to 1.8 log units above the fayalite-magnetite-quartz (FMQ) buffer for the cumulates (n = 9) and a value of ΔFMQ +1.2 for lherzolite ADG-CB-9 (method A in Table 3, Supplemental Figure 8).

Using the oxybarometer of Ballhaus et al. (1991), we calculate fO_2 from ΔFMQ +1.2 to +2.1 for the Adagdak cumulates and ΔFMQ +1.3 for the lherzolite (method B in Table 3). While this oxybarometer can be implemented on samples with only spinel and olivine present, reduced silica activity in these systems can lead to overestimates of fO_2 up to +0.6 log units. For samples lacking orthopyroxene (i.e., all but ADG-CB-9), these estimates must therefore be taken as upper fO_2 limits. For the lherzolite, we also calculated fO_2 with olivine-orthopyroxene-spinel oxybarometry using the parameterization of Davis et al. (2017), yielding a value of ΔFMQ $+1.02^{+0.43}_{-0.25}$.

These are the second direct estimates of fO_2 for oceanic arc lower crustal cumulates through olivine-spinel oxybarometry. Consistent with a previous study of Talkeetna arc cumulates (ΔFMQ +0.4 to +2.3: Bucholz and Kelemen, 2019), our fO_2 estimates (ΔFMQ +0.1 to +2.1) support other

studies indicating that the lower crust and upper mantle of oceanic arcs are oxidized relative to MORB (ΔFMQ = 0.16±0.01; Cottrell and Kelley, 2011). These values are consistent with studies of sub-arc mantle xenoliths (ΔFMQ +0.5 to +2.9: Parkinson and Pearce, 1998; Parkinson and Arculus, 1999; Parkinson et al., 2003; Bryant et al., 2007; Ichiyama et al., 2016) and arc lavas, which studies consistently show to be oxidized relative to MORB (ΔFMQ + 0.5 to + 3.5; Kelley and Cottrell, 2009; Brounce et al., 2014; Richards, 2015; Cottrell et al., 2020).

While the mineral assemblage in the amphibole gabbro and hornblendite (clinopyroxene + amphibole + plagioclase + magnetite) does not allow us to rigorously interrogate their fO_2 through phase equilibria, the high amphibole/clinopyroxene ratios in these samples and the shift in oxide compositions from spinel to magnetite is consistent with fractionation from an oxidized melt. Ulmer et al. (2018) found, in their equilibrium crystallization experiments of high-Mg basalts, that as the melt fraction decreased in lower temperature runs, the fO_2 of the remaining liquid in the charges increased from ~ΔFMQ +2 to +6. They attributed this apparent auto-oxidation of the system to the removal of Fe^{2+} from the melt by olivine and clinopyroxene fractionation, increasing the $Fe^{3+}/\Sigma Fe$ ratio of the remaining late-stage melts. A similar scenario may be envisioned for Adagdak, in which olivine and clinopyroxene fractionation leads to auto-oxidation of the melt, increasing fO_2 in the late-stage magmas that crystalized the amphibole gabbro and hornblendite cumulates (e.g., Kelley and Cottrell, 2012).

Moffett: Due to the paucity of spinel in Moffett xenoliths, we cannot confidently estimate fO_2 for the Moffett cumulates. Taking our Fe-Mg exchange temperature estimates and mineral chemistry for spinel-bearing samples MM-CB-2, MM-77-67, and MOF-81X-A, and applying the Ballhaus et al. (1991) oxybarometer at 0.7 GPa yields fO_2 estimates between ΔFMQ +1.4 and +2.1. Although the lack of satisfactory temperature constraints renders these values approximate, they are broadly consistent with comparisons to experimental studies, which also suggest the ultramafic cumulates crystalized under oxidizing conditions. The experimental studies that produced assemblages similar to the Moffett cumulates were all conducted at oxygen fugacities between the NNO and hematite-magnetite (HM) redox buffers (ΔFMQ +0.25 to +4.4; Holloway and Burnham,

1972; Helz, 1973; Krawczynski et al., 2012). We therefore infer that the Moffett xenolith suite also crystalized under oxidizing conditions, perhaps more so than the Adagdak suite, although we cannot give precise or quantitative estimates.

2.6.3 Trace elements

For the purposes of discussion, we break our cumulate samples into four compositional groups based on similarities in clinopyroxene trace element chemistry, while the lherzolite is discussed separately. These groupings are based on the degree of LREE-HREE fractionation, HFSE depletion, the presence or absence of a Sr-anomaly, and clinopyroxene Mg#. The average compositions of clinopyroxene from each group are shown in Figure 10, and each sample is categorized in Supplemental Data File 1 (Ch2-T8). We compare our results to clinopyroxene trace element data from cumulate and peridotite xenoliths from other arc settings where trace element signatures have been attributed to interactions between mantle melts/rocks and basaltic eclogite melts.

Adagdak lherzolite: Clinopyroxene from lherzolite ADG-CB-9 shares trace element characteristics with clinopyroxene from the cumulate xenoliths, such as LREE-HREE fractionation ($La/Yb = 2.7\pm0.6$) and positive Sr-anomalies ($Sr/Sr^* = 1.83\pm0.48$). HFSE behavior is variable, with lower Ta and Nb ($\leq$11 ppb) but higher concentrations of Zr and Hf (9.5 and 0.3 ppm, respectively) compared to the most primitive Adagdak and Moffett cumulates (0.9-4.3 and 0.1-0.2 ppm, respectively). Clinopyroxene from the lherzolite also has higher Th and U concentrations than observed in the cumulate xenoliths.

Clinopyroxene from mantle xenoliths from Cerro del Fraile (Southern Patagonia) has REE patterns similar to ADG-CB-9 (e.g., $La/Yb = 3.9$; Kilian and Stern, 2002). While this clinopyroxene shows some discrepancies with ADG-CB-9 clinopyroxene regarding absolute HFSE and large ion lithophile element (LILE) concentrations, it shows the same general pattern of Th, U, and Sr enrichment with Ta, Nb, and Zr depletion (Fig. 10a). The trace element signatures in the Cerro del Fraile xenoliths were attributed to both cryptic and modal metasomatism of mantle peridotite by a basaltic eclogite melt (Kilian and Stern, 2002). Notably, clinopyroxene from ADG-

CB-9 is compositionally distinct from that found in both fluid metasomatized and unmetasomatized mantle xenoliths from the Honshu arc (Abe et al., 1998; Ichiyama et al., 2016); from Avacha, Southern Kamchatka (Ishimaru et al., 2006); from Mexico (Luhr and Aranda-Gómez, 1997; Mukasa et al., 2007); or from the Lesser Antilles (Parkinson et al., 2003; Vannucci et al., 2007). All of these are typically characterized by flat to HREE-enriched trace element profiles (La/Yb generally <1).

Group 1: Group 1 clinopyroxene is characterized by the greatest enrichment in LREE relative to HREE (La/Yb = 1.5-2.5), positive Sr-anomalies (Sr/Sr* = 1.8-2.8), and significant HFSE depletion (1-2 ppm Zr, ≤ 8 ppb Hf, Nb, Ta). This group is composed only of the most magnesian clinopyroxene in the Moffett suite (Mg# 90-91). Clinopyroxene in the most primitive (Mg# > 90) cumulate xenoliths from Kharchinsky, Central Kamchatka (Siegrist et al., 2019), as well as that from a previous study of Moffett cumulate xenoliths (Yogodzinski and Kelemen, 2007), is similar to Group 1 clinopyroxene with respect to trace element characteristics (Fig. 10b). Both studies invoked a basaltic eclogite melt component in the magma parental to the cumulates to explain their trace element characteristics. The presence of these signatures in clinopyroxene from Group 1 xenoliths may also suggest that an end-member component derived from the partial melting of a basaltic eclogite source was present in their parental magmas.

Group 2: This group includes Adagdak cumulates ADG-32 and ADG-42 and Moffett sample MM-CB-3. All these samples are ultramafic olivine and clinopyroxene-bearing cumulates. Clinopyroxene in this group shares characteristics with compositional Group 1, such as high Mg# (88-89), similar degrees of LREE-HREE fractionation (La/Yb = 0.9-1.5), and positive Sr-anomalies (Sr/Sr* = 1.8-2.3). However, this clinopyroxene consistently exhibits lower absolute concentrations in all trace elements except Rb, Th, U, and Ta (Fig. 10b). We are not aware of any previous study reporting clinopyroxene trace element compositions this depleted from an arc-derived lava or related cumulate xenolith.

Group 3: Clinopyroxene in our third group is characterized by more modest HFSE depletion (2.5-4.3 ppm Zr, ≤ 20 ppb Na, Ta, Hf), LREE-HREE fractionation (La/Yb = 0.6-1.5), and smaller

(although still positive) Sr-anomalies (Sr/Sr* = 1.3-2.2) than are observed in compositional groups 1 and 2. This group contains Adagdak dunite, wehrlite, and (olivine) clinopyroxenite. The trace element profiles of this clinopyroxene resemble clinopyroxene phenocrysts from Moffett adakite lavas (Yogodzinski and Kelemen, 2007), and the less magnesian clinopyroxene (Mg# < 90) in cumulate xenoliths from Kamchatka (Siegrist et al., 2019; Fig.10c) and from the previous study of Moffett xenoliths by Yogodzinski and Kelemen (2007). The less pronounced basaltic eclogite melt signatures in these cumulates could imply that while the same endmember ascribed to groups 1 and 2 may have been present in the parental magmas of Group 3 samples, its characteristics were diluted by mixing, assimilation, or fractionation processes.

Group 4: Clinopyroxene from the most evolved Adagdak xenoliths (clinopyroxene Mg# < 82) and amphibole-bearing Moffett samples fall into this group. This clinopyroxene has lower Mg# (73-82), more subtle LREE-HREE fractionation (La/Yb = 0.5-1.3), and significantly less HFSE depletion (8-15 ppm Zr, 0.5-1 ppm Hf) compared to groups 1-3 (Fig. 10d). Group 4 clinopyroxene displays negative Sr-anomalies (0.6-0.9). Similar trace element characteristics are observed in clinopyroxene from basaltic lavas from Seguam Island (east of Adak: Yogodzinski and Kelemen, 1998), cumulate xenoliths from the basement of Kanaga Island (west of Adak: Yogodzinski and Kelemen, 2007), and from Martinique island in the Caribbean (Cooper et al., 2016) (Fig. 10d). The trace element characteristics of clinopyroxene from these studies are attributed to crystallization from basaltic arc magmas with little to no input from an eclogite melt.

Taken together, our clinopyroxene trace element data suggests the basaltic eclogite melt component or “adakite” signature was strongest in the most primitive Moffett and Adagdak cumulates and was diluted or overprinted by the time the more evolved lithologies crystallized. These results are consistent with the previous study of Yogodzinski and Kelemen (2007), who observed positive correlations between Mg# and Sr/Y and La/Yb ratios in the Moffett clinopyroxene. The similarities in clinopyroxene trace element data between lherzolite ADG-CB-9 and the mantle xenoliths from Patagonia and Kamchatka also suggest the contribution of a metasomatic agent with an adakite-like trace element signature.

2.6.4 Equilibrium melt compositions

Trace element compositions of parental melts to the xenoliths were calculated using basalt-clinopyroxene partition coefficients (K_d). The partition coefficients are given in Table 4 and plotted in Supplemental Figure 9. The average calculated equilibrium melt compositions for each group are shown in Fig. 11 and given in Supplemental Data File 1 (Ch2-T12). Primitive mantle normalized spider diagrams for all calculated equilibrium melt compositions are given in supplemental figures 10 and 11.

Group 1: The equilibrium melt compositions for Group 1 clinopyroxene are within the adakite field as defined by Castillo (2012) and others (Supplemental Figure 12). Adakite lavas from the Santa Clara volcanic field in Baja (Aguillón-Robles et al., 2001) show remarkably similar trace element systematics to this group in terms of La/Yb ratios (14-32) and Sr enrichment (Sr/Y = 62-164), although with notably higher Th, U, and HFSE concentrations (Fig. 11a). Group 1 melt compositions are also broadly similar to high-Mg andesite ADK-53 from Adak Island (Sun et al., 1980; Kay et al., 1986; Münker et al., 2004). Although the absolute concentrations of most trace elements are higher in ADK-53 (e.g., 1780 ppm Sr), the sample shows a similar degree of LREE-HREE fractionation (La/Yb = 30-31) and HFSE depletion (Nb/La = 0.1, Zr/Zr* = 0.27). The trace element similarities between our calculated melt compositions and these adakites support our hypothesis that a basaltic eclogite melt contributed to the parental magmas of the most primitive Moffett xenoliths.

Group 2: Melt compositions calculated from the Group 2 clinopyroxene are generally depleted in all trace elements (Fig. 11a). While these compositions still show significant LREE-HREE fractionation (La/Yb = 8-12), Sr enrichment (Sr/Sr* = 2.5-2.9) and HFSE depletion (Zr/Zr* = 0.25-0.66), they do not meet the required criteria to be classified as “adakites” (e.g., Sr > 300 ppm: Castillo, 2012).

Group 3: Calculated equilibrium melt compositions for Group 3 clinopyroxene show more modest LREE-HREE fractionation (La/Yb = 5-12) and Sr enrichment (Sr/Sr* = 1.9-2.8) than those from groups 1 and 2 and are more akin to typical Aleutian calc-alkaline basalts (Fig. 11b). Absolute

HREE concentrations in Group 3 equilibrium melts are lower, but within error, of previously identified primitive melts from the Aleutians (Kay et al., 1982; Kay and Kay, 1994; and Schmidt and Jagoutz, 2017; Fig. 11). Group 3 equilibrium melt compositions are similar to magnesian andesites from Piip volcano in the western Aleutians (Yogodzinski et al., 1994). Yogodzinski et al. (1994) proposed a model for the petrogenesis of Piip magnesian andesites where a low-degree slab melt stalls in the subarc mantle, creating an enriched source rock. Subsequent melting of this hybridized peridotite then produces basalts with trace element characteristics inherited from the original slab melt. Because these signatures are less pronounced in the Group 3 melts (e.g., less HREE-LREE fractionation, lower Sr), and the mineralogy of ultramafic xenoliths from this group suggests fractionation from a primitive basalt, a similar petrogenetic scenario may be appropriate for this group: hybridization or mixing of silicic basaltic eclogite derived magmas and mantle peridotite/melts.

Group 4: Group 4 equilibrium melts show the least LREE-HREE fractionation (La/Yb = 4-10) and HFSE depletion (Zr/Zr* = 0.5 – 1.45: Fig. 11c). Melt compositions calculated for five samples in this group show negative Sr-anomalies (Sr/Sr* = 0.8 to 0.9), in contrast to groups 1-3, due to the co-crystallization of clinopyroxene with plagioclase. Group 4 equilibrium melts are similar to the bulk compositions of non-cumulate granodiorite from Adak's Hidden Bay pluton (Kay et al., 1983, 1990, 2019a) (Fig.11c). Kay et al. (2019) suggests a model for the formation of the Hidden Bay pluton in which a high-Al basalt ascends to mid-crustal depths (11-13 km) and fractionates the cumulate gabbro and diorite units. The granodiorite and leucogranodiorite units then formed during further crystallization of the residual magma in the upper crust (2-4 km). A similar mid-crustal origin from an evolved basalt or basaltic andesite may be an appropriate petrogenetic model for the Group 4 cumulates.

2.6.5 Modeling the origin of parental melts to the Adak xenoliths

The trace element systematics of our equilibrium melt compositions for groups 1-3 show similarities to those produced by melting experiments on basaltic eclogites (Rapp et al., 1999; Sisson and Kelemen, 2018) and sediments (Hermann and Spandler, 2008; Mallik et al., 2015,

2016); however, these experimental partial melts are also characterized by high-silica contents (Ringwood, 1990; Rapp et al., 1991, 1999; Sen and Dunn, 1994; Rapp and Watson, 1995; Johnson and Plank, 1999; Hermann and Rubatto, 2009). Thus, interactions between basaltic eclogite and mantle melts or peridotite were critical to the origin of the melts parental to the most primitive cumulates. In this section, we model and explore interactions between melts of the depleted mantle, basaltic eclogites, and subducted sediments. All partition coefficients, melting modes, source rock compositions, and modal proportions used are given in the Appendix (see supplementary figures 13 and 14 and tables Ch2-T13 to Ch2-T15 in Supplementary Data File 1). The models given below represent end-member scenarios, none of which fully reproduce all characteristics of our data, and all of which require assumptions about the subarc mantle beneath Adak. We emphasize that it is likely that several of these processes were operating contemporaneously. We focus on the elements most relevant for exploring these interactions and for which our equilibrium melt calculations are the most robust (i.e., elements present in clinopyroxene in concentrations well above detection limits, with well-constrained mineral-melt partition coefficients for all required phases).

2.6.5.1 Model components

Depleted mantle melt: We implement a non-modal batch melting model (Kinzler and Grove, 1992, using equations of Shaw, 2006) and the depleted mantle composition of Salters and Stracke (2004). Calculated equilibrium melts for 5 to 15% depleted mantle partial melting are shown in Figure 12a.

Basaltic eclogite melt: We modeled the non-modal fractional melting of a basaltic eclogite with an altered oceanic basalt composition. Results for 2.5-10% partial melting of a basaltic eclogite are shown in Fig. 12a. All modeled melts display positive Sr-anomalies (Sr/Sr* = 2.0-3.9) and extreme LREE-HREE fractionation (La/Yb = 70-190).

Sediment melt: The metamorphism of subducted sediment may result in the formation of many incompatible element-rich accessory phases including garnet, amphibole, biotite, magnetite, coesite, kyanite, apatite, zircon, phengite, allanite, and monazite (Johnson and Plank, 1999; Hermann and Spandler, 2008; Skora and Blundy, 2010). Partial melting (10-60%) experiments on

trench sediments under conditions relative to the top of subducting slabs (600-900ºC, 2-4.5 GPa) have produced hydrous rhyolitic to basaltic melts with highly variable trace element compositions (Johnson and Plank, 1999; Hermann and Spandler, 2008; Hermann and Rubatto, 2009; Skora and Blundy, 2010). This means that minor variations in metasedimentary phase assemblages and slab-top P-T-H_2O-fO_2 can significantly affect trace element partitioning between residues and melts. We therefore calculated a range of possible Aleutian sediment melt compositions using an array of bulk sediment-melt partition coefficients (Johnson and Plank, 1999) (Fig. 12a). We take the melt composition calculated using the 700 ºC (experiment PC36) bulk partition coefficients from Johnson and Plank (1999) as our sediment-melt component. This set of partition coefficients was chosen because (a) it is roughly the temperature at which the solidus for subducted sediment (Nichols et al., 1994; Hermann and Spandler, 2008) crosses the slab-top geotherm for the central Aleutians (Syracuse et al., 2010) (Supplemental Figure 1) and (b) the melt composition calculated using these partition coefficients is close to the average of our range of possible sediment melts. We add this sediment melt component to the 5% basaltic eclogite melt in a 1:19 sediment: basaltic eclogite melt ratio, referred to as the "subduction-derived component" in all subsequent modeling (Fig. 12a).

We explore three possible scenarios of how our subduction-derived components interact with depleted mantle melts or peridotite to form mafic to intermediate magmas with slab-derived trace element signatures: 1) reactions between mantle peridotite and subduction-derived melts, 2) mixing of subduction-derived and depleted mantle melts, and 3) metasomatism of the depleted mantle by a subduction-derived melt, followed by partial melting of the hybridized mantle.

2.6.5.2 Reactions between mantle peridotite and basaltic eclogite melts

Experimental studies have demonstrated that reactions between basaltic eclogite melt and mantle peridotite provide an effective means for silicic magmas to develop more primitive major element characteristics while maintaining their highly fractionated trace element patterns. For example, Rapp et al. (1999) found that when a dacitic partial melt of an eclogite reacted with depleted peridotite in a 2:1 melt:rock ratio, melt SiO_2 concentrations decreased from 67.5 to 61.1 wt.% and

Mg# increased from 44 to 56. These changes in major element composition were accompanied by only minor changes in trace element concentrations (e.g., Y decreased from 6.7 to 5.8 ppm, Yb increased from 0.9 to 1.3 ppm; Rapp et al., 1999).

We first explore reactions between our subduction-derived melt and mantle peridotite with the AFC model of DePaolo (1981). We modeled a scenario in which the rate of assimilation of mantle peridotite is greater than the rate of crystallization, and the mass of the magma increases during assimilation. As the melt mass increases, it acquires characteristics of the peridotite it consumes, resulting in a general decrease in the degree of LREE/HREE fractionation in the hybridized melts. In general, the AFC model results provide a good fit for our Group 1 melt compositions (Fig. 12b). We also implemented an open-system critical melting model (Shaw, 2000), in which peridotite is melted at the same time as a subduction-derived melt is added to the system, while a hybridized melt is expelled. The more subduction-derived melt is added, the less effect the peridotite melt has on the expelled hybridized magma composition, consistent with channelized ascent. Interaction with peridotite is primarily observed in the HREEs, which are closer to mantle values when small quantities of melt are reacted with peridotite. The model results for the open-system critical melting also reproduce the HREE depletions observed in the Group 1 melt compositions (Fig. 12b). Based on these results, we consider reactions between subduction-derived melts and mantle peridotite a viable mechanism for the petrogenesis of the melts parental to our Group 1 xenoliths.

2.6.5.3 Mixing of basaltic eclogite and mantle melts

Previous studies have also invoked mixing between basaltic eclogite melts and mantle-derived magmas to explain the geochemistry of mafic to intermediate arc lavas and their phenocrysts (e.g., Mount Shasta: Streck et al., 2007; Northern Andean Volcanic zone: Schiano et al., 2010). We used a simple binary mixing model to combine our subduction-derived melt with a 10% mantle melt, considers mass ratios of the two melts spanning a range from 1:3 to 3:1 (Fig. 12c). Although we explore magma mixing over a large range of mixing ratios, the modeled compositions containing over a 50% subduction-derived melt component would be too silicic to crystallize our mafic

xenoliths. These model results provide a reasonable fit for some of our less fractionated Group 3 melts (Fig. 12c). While experimental and modeling studies have shown that silicic and mafic melts might not readily mix due to viscosity differences (Campbell and Turner, 1985; Sparks and Marshall, 1986), mixing of felsic and mafic melts in the upper mantle or lower crust may be possible, given sufficient time under an appropriate thermal regime and in the presence of water. If water-saturated basaltic eclogite melts are sufficiently heated as they ascend through the inverted geothermal gradient of the lower mantle wedge, or if such a high-silica melt is added slowly to the mantle melt, the viscosity of the basaltic eclogite melt may approach that of a mantle basalt, facilitating mixing.

2.6.5.4 Partial melting of metasomatized mantle

Metasomatism of mantle peridotite by a basaltic eclogite melt, followed by partial melting of the hybridized rock, may be an appropriate petrogenetic model when the degree of basaltic eclogite melting is low (Rapp et al., 1999). To illustrate this, we generated a bulk metasomatized peridotite composition by mixing our subduction-derived melt with a depleted mantle composition with a melt:rock ratio ranging from 1:9 to 1:1. These new mantle compositions display greater LREE/HREE fractionation (La/Yb = 2.3-25) than the original depleted source (La/Yb = 0.6), as well as positive Sr-anomalies (Sr/Sr* = 2.2 to 2.9) (Supplemental Figure 15). Experimental studies have shown that reactions of basaltic eclogite melt and peridotite often result in precipitation of orthopyroxene, amphibole, and garnet and consumption of olivine (Sekine and Wyllie, 1982; Johnston and Wyllie, 1989; Sen and Dunn, 1995; Rapp et al., 1999). We therefore modeled 5-15% melting of a garnet-amphibole peridotite with each of our metasomatized mantle compositions. The best match for our Group 1 melt compositions were produced through ~10% melting of a modally metasomatized mantle composition generated through reactions between our subduction-derived melt and the depleted mantle in a 1:9 melt:rock ratio (Fig. 12d).

2.6.5.5 Modeling conclusions

The strongly fractionated trace element characteristics of the equilibrium melts for the Group 1 xenoliths require a significant contribution (>5%) from a basaltic eclogite melt. This is consistent

with the recent study of Turner and Langmuir (2022a), which suggests that a 5-7% slab melt component is ubiquitous in convergent margin magmas. Reactions between a basaltic eclogite melt and peridotite (Fig. 12b), or partial melting of a metasomatized mantle (Fig. 12d) may have been important processes in the petrogenesis of the melts parental to these samples. The melts parental to the Group 3 cumulates may have formed through the mixing of slab and mantle melts (Fig. 12c) or partial melting of a less metasomatized mantle. All three models fail, however, to reproduce the Zr and Hf depletions observed in Group 1 and 2 melt compositions. Previous studies have suggested that, in addition to rutile, zircon may be an important phase in controlling the HFSE budget of subduction zones (Rubatto and Hermann, 2003; Hirai et al., 2018; Turner and Langmuir, 2022a). Zircon has also been observed in the residues of partial melting experiments of metasedimentary rocks (Johnson and Plank, 1999; Rubatto and Hermann, 2003). The depletions in Hf and Zr observed in the calculated equilibrium melt compositions could therefore reflect the presence of zircon in their melting residues (basaltic eclogites and/or metasediments).

These results can be interpreted two ways: 1) the mantle beneath Adak is heterogenous, with Adagdak and Moffett volcanoes sampling melts generated in regions of the mantle that have experienced variable degrees of interaction with a subduction-derived component, or 2) if the Moffett and Adagdak cumulates are not contemporaneous, the dynamics of the mantle source region beneath Adak may have changed in the elapsed time between the crystallizations of the two separate cumulate suites (Supplemental Figure 16). Temporal changes in the strength of the basaltic eclogite melt signature, particularly if the changes correlate to periods of arc migration, may suggest that the source of these signatures is forearc subduction erosion. Testing these hypotheses requires high-precision chronology of cumulates, which is beyond the scope of this paper.

2.6.6 Relationship to upper crustal plutonic rocks on Adak

A notable feature of all models explored above is that the positive Sr-anomaly of the original slab-derived component persists in melt compositions produced through peridotite-eclogite melt interactions. This finding has been emphasized by previous models of peridotite-eclogite melt

reactions (Sisson and Kelemen, 2018). Positive Sr-anomalies are typical features of primitive arc magmas including basalts (Perfit et al., 1980; Kelemen et al., 2003a; Schmidt and Jagoutz, 2017; Turner and Langmuir, 2022a) and adakites (Kay, 1978; Kay et al., 1986; Yogodzinski et al., 1994). However, as arc magmatism is thought to be the primary mechanism by which continental crust is generated, a conundrum arises in that the average bulk continental crust has a Sr/Sr* value of 0.94 (preferred value of Rudnick and Gao, 2003). Furthermore, the upper continental crust has an even larger negative Sr-anomaly, with estimated Sr/Sr* of 0.67. This implies that if magmas with positive Sr-anomalies are parental to the continental crust, then (intra-) crustal processes must erase the primary positive Sr-anomalies of primitive arc magmas and replace them with negative Sr-anomalies. Removal of excess Sr could occur through differentiation of plagioclase-bearing cumulates, which could eventually be removed via density foundering (Kay and Kay, 1991; Kay and Kay, 1993; Kelemen et al., 2003a; Jagoutz and Schmidt, 2013). This process is consistent with observations from preserved paleo-arcs where densification reactions involving the transformation of plagioclase (+ olivine) to produce garnet, pyroxene, and spinel are observed (e.g., Kohistan: Jagoutz and Schmidt, 2013). Alternatively, Sr may be preferentially lost from the crust during chemical weathering (Rudnick, 1995; Rudnick and Gao, 2003).

We use the xenolith suite studied here and the upper crustal plutonic rocks from Adak (namely the calc-alkaline Hidden Bay pluton; Kay et al., 1990, 2019) to understand the differentiation process within the arc and the evolution of Sr-anomalies in near-primitive melts with a strong basaltic eclogite melt component. We model fractional crystallization of Adagdak and Moffett primitive melts through stepwise removal of calculated bulk cumulate trace element assemblages (see Appendix for details). For Adagdak, this consisted of removing 18% of an ultramafic assemblage and 30% of a gabbroic assemblage from our most primitive equilibrium melt composition. The results of this modeling are shown in Figure 13. Fractionation of the Adagdak ultramafic cumulates results in increased concentrations of all trace elements in the remaining liquid with little modification to Sr-anomalies (Sr/Sr* = 1.60-1.61). Once amphibole gabbro fractionation begins, and we remove Sr-rich plagioclase-bearing lithologies, Sr-anomalies begin to decline and are absent after 22% amphibole gabbro fractionation (Sr/Sr* = 1). After 30%

amphibole gabbro fractionation, Sr-anomalies are in fact negative (Sr/Sr* = 0.76). Another notable feature of the model is that the final compositions are very similar to non-cumulate granodiorite assemblages from the Hidden Bay pluton on Adak Island (Fig. 13). While most of the Hidden Bay diorite is interpreted as cumulate, some of the granodiorite and leucogranodiorite is thought to represent the magmatic compositions (Kay et al., 2019). We further screened the granodiorite compositions from Kay et al. (2019) to remove compositions showing signs of plagioclase accumulation (Sr/Sr* and Eu/Eu* > 1).

We employed the same method for studying the Moffett suite, starting with the equilibrium melt composition for our most primitive cumulates (MM-CB-2) and removing representative cumulate assemblages through a mass balance model (see Appendix for details). Because the Sr concentrations in these melt compositions are very high (>500 ppm), fractionation of lower Sr phases like clinopyroxene (30-80 ppm Sr) and amphibole (230-350 ppm Sr) serves to further increase Sr in the remaining melt. By the time plagioclase-bearing assemblages begin to fractionate, Sr concentrations in the remaining melt are >600 ppm. Although Moffett amphibole gabbro has high (~400 to 600 ppm) Sr, even after 30% fractionation, strong positive Sr-anomalies remain (Sr/Sr* decreased from 2.01 to 1.50, Supplemental Figure 17).

Although undoubtedly an oversimplification, these results suggest that 1) the trace element chemistry of the Adagdak cumulate suite can be related to that of the non-cumulate Hidden Bay plutonic rocks through fractional crystallization, and the cumulates may represent lower crustal complements to the Hidden Bay granodiorite, and 2) the loss of positive Sr-anomalies from primitive arc lavas to their more evolved, intrusive equivalents may be achieved by fractionation of plagioclase bearing lithologies. With respect to Moffett, these results suggest that Sr-anomalies in melts with strong basaltic eclogite melt components may persist throughout differentiation, even when plagioclase is part of the fractionated assemblage. The diminution of Sr-anomalies within the Adagdak fractionation suite affirms the idea that reconciling geochemical differences between arc magmas (and their crystallization products) with estimates of the bulk continental crust can be achieved through the removal of plagioclase-rich cumulates through densification reactions.

2.7 CONCLUSIONS

The petrography and mineral chemistry of primitive cumulates from Moffett and Adagdak volcanoes are consistent with fractionation from hydrous, oxidized parental melts in the upper mantle or lower crust, however important differences exist. Primitive cumulates from both suites are distinct from those in arcs where the slab-derived component has previously been attributed to an aqueous fluid (e.g., Lesser Antilles), but are similar to those from locations where the parental melt has been interpreted to contain a slab-melt component (e.g., Kamchatka). This relationship suggests that the melts parental to the most primitive Adak cumulates contain a basaltic eclogite melt component from slab melting and/or forearc subduction erosion.

Clinopyroxene from the most primitive cumulates in both suites displays positive Sr-anomalies, which are not observed in the more evolved lithologies. The loss of the positive Sr-anomaly can be modeled through the fractionation of plagioclase-bearing cumulates for the Adagdak suite. However, the differences between the pronounced Sr-anomalies and depletions in HREEs and HFSEs observed in the most primitive Moffett samples cannot be reconciled with the relatively unfractionated trace element patterns observed in the more evolved samples. This relationship suggests that supracrustal processes, or injection of a compositionally distinct basaltic melt, may be an important process for the Moffett volcanic system. Together, the differences in major and trace element systematics between the two xenolith suites suggest a complex magma plumbing system beneath Adak Island, with the two volcanoes either tapping a heterogenous mantle source characterized by variable degrees of interaction with an eclogite melt or a mantle source region that has chemically evolved through time.

2.8 ACKNOWLEDGEMENTS

We thank C. Ma and L. Saper for their assistance with electron microprobe analyses, L.V. Godfrey for her assistance with the LA-ICP-MS, and B. Wood for providing the spinel standards. Constructive reviews from T.W. Sisson and an anonymous reviewer significantly improved the quality of the manuscript and are gratefully acknowledged. E.S.S. was supported by the National

Science Foundation Graduate Research Fellowship under Grant No. DGE-1745301. Special thanks to T.L. Carley and the Lafayette College Department of Geology and Environmental Geosciences for the use of their petrographic microscopes, which allowed this work to continue during the COVID-19 pandemic.

2.9 REFERENCES

Abe, N., Arai, S. & Yurimoto, H. (1998). Geochemical characteristics of the uppermost mantle beneath the Japan island arcs: Implications for upper mantle evolution. *Physics of the Earth and Planetary Interiors,* 107, 233–248.

Aguillón-Robles, A., Calmus, T., Benoit, M., Bellon, H., Maury, R. C., Cotten, J., Bourgois, J. & Michaud, F. (2001). Late Miocene adakites and Nb-enriched basalts from Vizcaino Peninsula, Mexico: Indicators of East Pacific Rise subduction below southern Baja California? *Geology,* 29, 531.

Ballhaus, C., Berry, R. F. & Green, D. H. (1991). High pressure experimental calibration of the olivine-orthopyroxene-spinel oxygen geobarometer: Implications for the oxidation state of the upper mantle. *Contributions to Mineralogy and Petrology,* 107, 27–40.

Baten Soyini, K. (2002). Eruptive History and Assessment of Volcanic Hazards of Mt. Adagdak, Adak Island, Aleutian Islands, Alaska. PhD thesis, Northern Arizona University.

Beattie, P. (1993). The generation of uranium series disequilibria by partial melting of spinel peridotite: Constraints from partitioning studies. *Earth and Planetary Science Letters*, 117, 379–391.

Beyer, B. J. (1980). Petrology and geochemistry of ophiolite fragments in a tectonic melange, Kodiak Islands, Alaska. PhD Thesis, University of California, Santa Cruz.

Bezard, R., Turner, S., Schaefer, B., Yogodzinski, G., & Hoernle, K. (2021). Os isotopic composition of western Aleutian adakites: Implications for the Re/Os of oceanic crust processed through hot subduction zones. *Geochimica et Cosmochimica Acta,* 292, 452–467.

Blatter, D. L., Sisson, T. W. & Hankins, W. B. (2013). Crystallization of oxidized, moderately hydrous arc basalt at mid- to lower-crustal pressures: Implications for andesite genesis. *Contributions to Mineralogy and Petrology,* 166, 861–886.

Bourgois, J., Martin, H., Lagabrielle, Y., Le Moigne, J. & Frutos Jara, J. (1996). Subduction erosion related to spreading-ridge subduction: Taitao peninsula (Chile margin triple junction area). *Geology,* 24, 723.

Brounce, M. N., Kelley, K. A. & Cottrell, E. (2014). Variations in Fe3+/∑Fe of Mariana Arc Basalts and Mantle Wedge fO2. *Journal of Petrology,* 55, 2513–2536.

Bryant, J. A., Yogodzinski, G. M. & Churikova, T. G. (2007). Melt-mantle interactions beneath the Kamchatka arc: Evidence from ultramafic xenoliths from Shiveluch volcano. *Geochemistry, Geophysics, Geosystems,* 8(4), Q04007.

Bryndzia, L. T. & Wood, B. J. (1990). Oxygen thermobarometry of abyssal spinel peridotites; the redox state and C-O-H volatile composition of the Earth's sub-oceanic upper mantle. American Journal of Science. *American Journal of Science,* 290, 1093–1116.

Bucholz, C. E. & Kelemen, P. B. (2019). Oxygen fugacity at the base of the Talkeetna arc, Alaska. *Contributions to Mineralogy and Petrology,* 174, 1-27.

Campbell, I. H. & Turner, J. S. (1985). Turbulent mixing between fluids with different viscosities. *Nature,* 313, 39–42.

Castillo, P. R. (2012). Adakite petrogenesis. *Lithos,* 134–135, 304–316.

Cawthorn, R. G., Curran, E. B. & Arculus, R. J. (1973). A Petrogenetic Model for the Origin of the Calc-alkaline suite of Grenada, Lesser Antilles. *Journal of Petrology,* 14, 327–337.

Coats, R. (1956). Geology of northern Adak Island, Alaska. *U.S. Geological Survey Bulletin*, 1028, 45–67.

Conrad, W. K. & Kay, R. W. (1984). Ultramafic and mafic inclusions from Adak Island: Crystallization history and implications for the nature of primary magmas and crustal evolution in the Aleutian arc. *Journal of Petrology,* 88–125.

Conrad, W. K., Kay, S. M. & Kay, R. W. (1983). Magma mixing in the Aleutian arc: Evidence from cognate inclusions and composite xenoliths. Jour*nal of Volcanology and Geothermal Research,* 18, 279–295.

Cooper, G. F., Davidson, J. P. & Blundy, J. D. (2016). Plutonic xenoliths from Martinique, Lesser Antilles: Evidence for open system processes and reactive melt flow in island arc crust. *Contributions to Mineralogy and Petrology,* 171, 87.

Cottrell, E., Birner, S., Brounce, M., Davis, F., Waters, L. & Kelley, K. (2020). Oxygen fugacity across tectonic settings. preprint. In *Magma redox geochemistry,* 33–61.

Cottrell, E. & Kelley, K. A. (2011). The oxidation state of Fe in MORB glasses and the oxygen fugacity of the upper mantle. *Earth and Planetary Science Letters,* 305, 270–282.

Dalton, J. A. & Lane, S. J. (1996). Electron microprobe analysis of Ca in olivine close to grain boundaries: The problem of secondary X-ray fluorescence. *American Mineralogist,* 81, 194–201.

Davies, J. H. & Stevenson, D. J. (1992). Physical model of source region of subduction zone volcanics. *Journal of Geophysical Research: Solid Earth,* 97, 2037–2070.

Davis, F. A., Cottrell, E., Birner, S. K., Warren, J. M. & Lopez, O. G. (2017). Revisiting the electron microprobe method of spinel-olivine-orthopyroxene oxybarometry applied to spinel peridotitesk. *American Mineralogist,* 102, 421–435.

Debari, S., Kay, S. M. & Kay, R. W. (1987). Ultramafic xenoliths from Adagdak Volcano, Adak, Aleutian Islands, Alaska: Deformed igneous cumulates from the Moho of an Island Arc. *The Journal of Geology*, 95, 329–341.

DeBari, S. M. & Coleman, R. G. (1989). Examination of the deep levels of an island arc: Evidence from the Tonsina Ultramafic-Mafic Assemblage, Tonsina, Alaska. *Journal of Geophysical Research: Solid Earth,* 94, 4373–4391.

Defant, M. J. & Drummond, M. S. (1990). Derivation of some modern arc magmas by melting of young subducted lithosphere. *Nature,* 347, 662–665.

DePaolo, D. J. (1981). Trace element and isotopic effects of combined wallrock assimilation and fractional crystallization. *Earth and Planetary Science Letters,* 53, 189–202.

Dohmen, R., Faak, K. & Blundy, J. D. (2017). Chronometry and Speedometry of Magmatic Processes using Chemical Diffusion in Olivine, Plagioclase and Pyroxenes. *Reviews in Mineralogy and Geochemistry,* 83, 535–575.

Drummond, M. S. & Defant, M. J. (1990). A model for Trondhjemite-Tonalite-Dacite Genesis and crustal growth via slab melting: Archean to modern comparisons. *Journal of Geophysical Research: Solid Earth,* 95, 21503–21521.

Fraser, G. D., & Snyder, G. L. (1959). Geology of southern Adak Island and Kagalaska Island, Alaska. U.S. *Geological Survey Bulletin,* 1028, 371–408.

Frost, T. P. & Mahood, G. A. (1987). Field, chemical, and physical constraints on mafic-felsic magma interaction in the Lamarck Granodiorite, Sierra Nevada, California. *Geological Society of America Bulletin,* 99, 272.

Gaetani, G. A., Grove, T. L. & Bryan, W. B. (1993). The influence of water on the petrogenesis of subductionrelated igneous rocks. *Nature,* 365, 332–334.

Geist, E. L., Childs, J. R. & Scholl, D. W. (1988). The origin of summit basins of the Aleutian Ridge: Implications for block rotation of an arc massif. *Tectonics*, 7, 327–341.

Goss, A. R., & Kay, S. M. (2006). Steep REE patterns and enriched Pb isotopes in southern Central American arc magmas: Evidence for forearc subduction erosion? *Geochemistry, Geophysics, Geosystems,* 7(5).

Goss, A. R., Kay, S. M. & Mpodozis, C. (2013). Andean Adakite-like high-Mg Andesites on the Northern Margin of the Chilean–Pampean Flat-slab (27–28·5°S) Associated with Frontal Arc Migration and Fore-arc Subduction Erosion. *Journal of Petrology,* 54, 2193–2234.

Green, T. H. & Ringwood, A. E. (1968). Genesis of the calc-alkaline igneous rock suite. *Contributions to Mineralogy and Petrology,* 18, 105–162.

Greene, A. R., DeBari, S. M., Kelemen, P. B., Blusztajn, J., & Clift, P. D. (2006). A detailed geochemical study of island arc crust: The Talkeetna arc section, south–central Alaska. *Journal of Petrology,* 47, 1051–1093.

Grove, T. L., Till, C. B. & Krawczynski, M. J. (2012). The Role of H2O in Subduction Zone Magmatism. *Annual Review of Earth and Planetary Sciences,* 40, 413–439.

Gust, D. A. & Perfit, M. R. (1987). Phase relations of a high-Mg basalt from the Aleutian Island Arc: Implications for primary island arc basalts and high-Al basalts. *Contributions to Mineralogy and Petrology,* 97, 7–18.

Hauri, E. H., Wagner, T. P., & Grove, T. L. (1994). Experimental and natural partitioning of Th, U, Pb and other trace elements between garnet, clinopyroxene and basaltic melts. *Chemical Geology,* 117, 149–166.

Hart, S. R., & Dunn, T. (1993). Experimental cpx/melt partitioning of 24 trace elements. *Contributions to Mineralogy and Petrology,* 113, 1–8.

Helz, R. T. (1973). Phase Relations of Basalts in their Melting Range at PH2O = 5 kb as a Function of Oxygen Fugacity1: Part I. Mafic Phases. *Journal of Petrology,* 14, 249–302.

Hermann, J. & Rubatto, D. (2009). Accessory phase control on the trace element signature of sediment melts in subduction zones. *Chemical Geology,* 265, 512–526.

Hermann, J. & Spandler, C. J. (2008). Sediment Melts at Sub-arc Depths: An Experimental Study. *Journal of Petrology,* 49, 717–740.

Hirai, Y., Yoshida, T., Okamura, S., Tamura, Y., Sakamoto, I. & Shinjo, R. (2018). Breakdown of residual zircon in the Izu arc subducting slab during backarc rifting. *Geology,* 46, 371–374.

Holland, T. & Blundy, J. (1994). Non-ideal interactions in calcic amphiboles and their bearing on amphibole-plagioclase thermometry. *Contributions to Mineralogy and Petrology,* 116, 433–447.

Holloway, J. R. & Burnham, C. W. (1972). Melting Relations of Basalt with Equilibrium Water Pressure Less Than Total Pressure1. *Journal of Petrology,* 13, 1–29.

Ichiyama, Y., Morishita, T., Tamura, A. & Arai, S. (2016). Peridotite xenoliths from the Shiribeshi Seamount, Japan Sea: Insights into mantle processes in a back-arc basin. *Contributions to Mineralogy and Petrology,* 171, 86.

Ishimaru, S., Arai, S., Ishida, Y., Shirasaka, M. & Okrugin, V. M. (2006). Melting and Multi-stage Metasomatism in the Mantle Wedge beneath a Frontal Arc Inferred from Highly Depleted Peridotite Xenoliths from the Avacha Volcano, Southern Kamchatka. *Journal of Petrology,* 48, 395–433.

J. Wood, B. & Virgo, D. (1989). Upper mantle oxidation state: Ferric iron contents of Iherzolite spinels by 57Fe Mössbauer spectroscopy and resultant oxygen fugacities. *Geochimica et Cosmochimica Acta* 53, 1277–1291.

Jacobson, C. E., Grove, M., Pedrick, J. N., Barth, A. P., Marsaglia, K. M., Gehrels, G. E. & Nourse, J. A. (2011). Late Cretaceous-early Cenozoic tectonic evolution of the southern California margin inferred from provenance of trench and forearc sediments. *Geological Society of America Bulletin,* 123, 485–506.

Jagoutz, O., Müntener, O., Ulmer, P., Pettke, T., Burg, J.-P., Dawood, H. & Hussain, S. (2007). Petrology and Mineral Chemistry of Lower Crustal Intrusions: The Chilas Complex, Kohistan (NW Pakistan). *Journal of Petrology,* 48, 1895–1953.

Jagoutz, O. & Schmidt, M. W. (2013). The composition of the foundered complement to the continental crust and a re-evaluation of fluxes in arcs. *Earth and Planetary Science Letters,* 371–372, 177–190.

Jicha, B. R. & Kay, S. M. (2018). Quantifying arc migration and the role of forearc subduction erosion in the central Aleutians. *Journal of Volcanology and Geothermal Research,* 360, 84–99.

Jicha, B. R., Scholl, D. W., Singer, B. S., Yogodzinski, G. M. & Kay, S. M. (2006). Revised age of Aleutian Island Arc formation implies high rate of magma production. *Geology,* 34, 661.

Johnson, M. C. & Plank, T. (1999). Dehydration and melting experiments constrain the fate of subducted sediments. *Geochemistry, Geophysics, Geosystems,* 1(12), 1007.

Johnston, A. D. & Wyllie, P. J. (1989). The system tonalite-peridotite-H2O at 30 kbar, with applications to hybridization in subduction zone magmatism. *Contributions to Mineralogy and Petrology,* 102, 257–264.

Kay, R. W. (1978). Aleutian magnesian andesites: Melts from subducted Pacific Ocean crust. *Journal of Volcanology and Geothermal Research,* 4, 117–132.

Kay, R. W. (1980). Volcanic arc magmas: Implications of a melting-mixing model for element recycling in the crust-upper mantle system. *The Journal of Geology*, 88(5), 497–522.

Kay, R. W. & Mahlburg Kay, S. (1993). Delamination and delamination magmatism. *Tectonophysics,* 219, 177–189.

Kay, R. W. & Mahlburg-Kay, S. (1991). Creation and destruction of lower continental crust. *Geologische Rundschau,* 80, 259–278.

Kay, R. W., Rubenstone, J. L. & Kay, S. M. (1986). Aleutian terranes from Nd isotopes. *Nature,* 322, 605–609.

Kay, S. M., & Kay, R. W. (1985a). Role of crystal cumulates and the oceanic crust in the formation of the lower crust of the Aleutian arc. *Geology,* 13, 461–464.

Kay, S. M., & Kay, R. W. (1985b). Aleutian tholeiitic and calc-alkaline magma series I: The mafic phenocrysts. *Contributions to Mineralogy and Petrology,* 90, 276–290.

Kay, S.M. and R.W. Kay, 1994, Aleutian magmatism in space and time, in G. Plafker and H.C. Berg (eds.), The Geology of Alaska, Decade of North American Geology (DNAG), *Geological Society of America,* 1, 687–722.

Kay, S., Kay, R., Citron, G. P. & Perfit, M.R., (1990). Calc-alkaline plutonism in the intra-oceanic Aleutian arc, Alaska. *Plutonism from Antarctica to Alaska*, 233–256.

Kay, S. M., Godoy, E. & Kurtz, A. (2005). Episodic arc migration, crustal thickening, subduction erosion, and magmatism in the south-central Andes. *Geological Society of America Bulletin,* 117, 67.

Kay, S. M., Jicha, B. R., Citron, G. L., Kay, R. W., Tibbetts, A. K. & Rivera, T. A. (2019). The calc-alkaline Hidden Bay and Kagalaska Plutons and the construction of the Central Aleutian oceanic arc crust. *Journal of Petrology,* 60, 393–439.

Kay, S. M., Kay, R. W., Brueckner, H. K. & Rubenstone, J. L. (1983). Tholeiitic Aleutian arc plutonism: The Finger Bay pluton, Adak, Alaska. *Contributions to Mineralogy and Petrology,* 82, 99–116.

Kay, S. M., Kay, R. W. & Citron, G. P. (1982). Tectonic controls on tholeiitic and calc-alkaline magmatism in the Aleutian Arc. *Journal of Geophysical Research: Solid Earth,* 87, 4051–4072.

Kelemen, P. B., Hanghøj, K. & Greene, A. R. (2003a). One view of the geochemistry of subduction-related magmatic arcs, with an emphasis on primitive andesite and lower crust. *Treatise on Geochemistry,* 3, 659.

Kelemen, P. B., Shimizu, N. & Dunn, T. (1993). Relative depletion of niobium in some arc magmas and the continental crust: Partitioning of K, Nb, La and Ce during melt/rock reaction in the upper mantle. *Earth and Planetary Science Letters,* 120, 111–134.

Kelemen, P. B., Yogodzinski, G. M. & Scholl, D. W. (2003b). Along-strike variation in the Aleutian Island Arc: Genesis of high Mg# andesite and implications for continental crust. *Washington DC American Geophysical Union Geophysical Monograph Series,* 138, 223–276.

Kelley, K. A. & Cottrell, E. (2009). Water and the Oxidation State of Subduction Zone Magmas. *Science,* 325, 605–607.

Kelley, K. A. & Cottrell, E. (2012). The influence of magmatic differentiation on the oxidation state of Fe in a basaltic arc magma. *Earth and Planetary Science Letters,* 329–330, 109–121.

Kelley, K. A., Plank, T., Ludden, J. & Staudigel, H. (2003). Composition of altered oceanic crust at ODP Sites 801 and 1149. *Geochemistry, Geophysics, Geosystems,* 4(6), 8910.

Kilian, R. & Stern, C. R. (2002). Constraints on the interaction between slab melts and the mantle wedge from adakitic glass in peridotite xenoliths. *European Journal of Mineralogy,* 14, 25–36.

Kinzler, R. J. & Grove, T. L. (1992). Primary magmas of mid-ocean ridge basalts 1. Experiments and methods. *Journal of Geophysical Research: Solid Earth,* 97, 6885–6906.

Klemme, S., Blundy, J. D., & Wood, B. J. (2002). Experimental constraints on major and trace element partitioning during partial melting of eclogite. *Geochimica et Cosmochimica Acta,* 66, 3109–3123.

Köhler, T. P. & Brey, G. P. (1990). Calcium exchange between olivine and clinopyroxene calibrated as a geothermobarometer for natural peridotites from 2 to 60 kb with applications. *Geochimica et Cosmochimica Acta,* 54, 2375–2388.

Krawczynski, M. J., Grove, T. L. & Behrens, H. (2012). Amphibole stability in primitive arc magmas: Effects of temperature, H2O content, and oxygen fugacity. *Contributions to Mineralogy and Petrology,* 164, 317–339.

Leake, B. E. et al. (2004). Nomenclature of amphiboles: Additions and revisions to the International Mineralogical Association's amphibole nomenclature. *Mineralogical Magazine,* 68, 209–215.

Li, J., Kornprobst, J., Vielzeuf, D. & Fabriès, J. (1995). An improved experimental calibration of the olivine-spinel geothermometer. *Chinese Journal of Geochemistry,* 14, 68–77.

Luhr, J. F. & Aranda-Gómez, J. J. (1997). Mexican Peridotite Xenoliths and Tectonic Terranes: Correlations among Vent Location, Texture, Temperature, Pressure, and Oxygen Fugacity. *Journal of Petrology,* 38, 1075–1112.

Mallik, A., Dasgupta, R., Tsuno, K. & Nelson, J. (2016). Effects of water, depth and temperature on partial melting of mantle-wedge fluxed by hydrous sediment-melt in subduction zones. *Geochimica et Cosmochimica Acta,* 195, 226–243.

Mallik, A., Nelson, J. & Dasgupta, R. (2015). Partial melting of fertile peridotite fluxed by hydrous rhyolitic melt at 2–3 GPa: Implications for mantle wedge hybridization by sediment melt and generation of ultrapotassic magmas in convergent margins. *Contributions to Mineralogy and Petrology,* 169, 48.

Marsh, B. D. (1976). Some Aleutian andesites: Their nature and source. *The Journal of Geology,* 84, 27–45.

Mathez, E. A. (1984). Influence of degassing on oxidation states of basaltic magmas. *Nature,* 310, 371–375.

Matsui, Y., Onuma, N., Nagasawa, H., Higuchi, H., & Banno, S. (1977). Crystal structure control in trace element partition between crystal and magma. *Bulletin de Minéralogie,* 100, 315–324.

Mattioli, G. S. & Wood, B. J. (1988). Magnetite activities across the MgAl2O4-Fe3O4 spinel join, with application to thermobarometric estimates of upper mantle oxygen fugacity. *Contributions to Mineralogy and Petrology,* 98, 148–162.

McDonough, W. F., & Sun, S. S. (1995). The composition of the Earth. *Chemical Geology,* 120, 223–253.

Mukasa, S. B., Blatter, D. L. & Andronikov, A. V. (2007). Mantle peridotite xenoliths in andesite lava at El Peñon, central Mexican Volcanic Belt: Isotopic and trace element evidence for melting and metasomatism in the mantle wedge beneath an active arc. *Earth and Planetary Science Letters,* 260, 37–55.

Münker, C., Wörner, G., Yogodzinski, G. & Churikova, T. (2004). Behaviour of high field strength elements in subduction zones: Constraints from Kamchatka–Aleutian arc lavas. *Earth and Planetary Science Letters* 224, 275–293.

Nandedkar, R. H., Ulmer, P. & Müntener, O. (2014). Fractional crystallization of primitive, hydrous arc magmas: An experimental study at 0.7 GPa. *Contributions to Mineralogy and Petrology,* 167, 1015.

Nicholls, I. A. & Ringwood, A. E. (1973). Effect of Water on Olivine Stability in Tholeiites and the Production of Silica-Saturated Magmas in the Island-Arc Environment. *The Journal of Geology,* 81, 285–300.

Nichols, G. T., Wyllie, P. J. & Stern, C. R. (1994). Subduction zone melting of pelagic sediments constrained by melting experiments. *Nature,* 371, 785–788.

Parkinson, I. J. & Arculus, R. J. (1999). The redox state of subduction zones: Insights from arc-peridotites. *Chemical Geology,* 160, 409–423.

Parkinson, I. J., Arculus, R. J. & Eggins, S. M. (2003). Peridotite xenoliths from Grenada, Lesser Antilles Island Arc. *Contributions to Mineralogy and Petrology,* 146, 241–262.

Parkinson, I. J. & Pearce, J. A. (1998). Peridotites from the Izu–Bonin–Mariana forearc (ODP Leg 125): Evidence for mantle melting and melt–mantle interaction in a supra-subduction zone setting. *Journal of Petrology,* 39(9), 1577-1618.

Paster, T. P., Schauwecker, D. S., & Haskin, L. A. (1974). The behavior of some trace elements during solidification of the Skaergaard layered series. *Geochimica et Cosmochimica Acta,* 38, 1549–1577.

Peacock, S. M., Rushmer, T. & Thompson, A. B. (1994). Partial melting of subducting oceanic crust. *Earth and Planetary Science Letters,* 121, 227–244.

Peacock, S. M., Keken, P. E. van, Holloway, S. D., Hacker, B. R., Abers, G. A. & Fergason, R. L. (2005). Thermal structure of the Costa Rica – Nicaragua subduction zone. *Physics of the Earth and Planetary Interiors,* 149, 187–200.

Peacock, S. M. (2020). Advances in the thermal and petrologic modeling of subduction zones. *Geosphere,* 16, 936–952.

Peltonen, P. (1995). Crystallization and re-equilibration of zoned chromite in ultramafic cumulates, Vammala Ni-belt, southwestern Finland. *The Canadian Mineralogist,* 33(3), 521–535.

Perfit, M. R., Gust, D. A., Bence, A. E., Arculus, R. J. & Taylor, S. R. (1980). Chemical characteristics of island-arc basalts: Implications for mantle sources. *Chemical Geology,* 30, 227–256.

Pichavant, M. & Macdonald, R. (2007). Crystallization of primitive basaltic magmas at crustal pressures and genesis of the calc-alkaline igneous suite: Experimental evidence from St Vincent, Lesser Antilles arc. *Contributions to Mineralogy and Petrology*, 154, 535–558.

Plank, T., Cooper, L. B. & Manning, C. E. (2009). Emerging geothermometers for estimating slab surface temperatures. *Nature Geoscience,* 2, 611–615.

Plank, T. & Langmuir, C. H. (1998). The chemical composition of subducting sediment and its consequences for the crust and mantle. *Chemical Geology,* 145, 325–394.

Poli, S. & Schmidt, M. W. (2002). Petrology of Subducted Slabs. *Annual Review of Earth and Planetary Sciences,* 30, 207–235.

Putirka, K. (2016). Amphibole thermometers and barometers for igneous systems and some implications for eruption mechanisms of felsic magmas at arc volcanoes. *American Mineralogist,* 101, 841–858.

Rapp, R. P., Shimizu, N., Norman, M. D. & Applegate, G. S. (1999). Reaction between slab-derived melts and peridotite in the mantle wedge: Experimental constraints at 3.8 GPa. *Chemical Geology,* 160, 335–356.

Rapp, R. P. & Watson, E. B. (1995). Dehydration melting of metabasalt at 8-32 kbar: Implications for continental growth and crust-mantle recycling. *Journal of Petrology,* 36, 891–931.

Rapp, R. P., Watson, E. B. & Miller, C. F. (1991). Partial melting of amphibolite/eclogite and the origin of Archean trondhjemites and tonalites. *Precambrian Research,* 51, 1–25.

Richards, J. P. (2015). The oxidation state, and sulfur and Cu contents of arc magmas: Implications for metallogeny. *Lithos,* 233, 27–45.

Ridolfi, F. & Renzulli, A. (2012). Calcic amphiboles in calc-alkaline and alkaline magmas: Thermobarometric and chemometric empirical equations valid up to 1,130°C and 2.2 GPa. *Contributions to Mineralogy and Petrology,* 163, 877–895.

Ridolfi, F., Renzulli, A. & Puerini, M. (2010). Stability and chemical equilibrium of amphibole in calc-alkaline magmas: An overview, new thermobarometric formulations and application to subduction-related volcanoes. *Contributions to Mineralogy and Petrology,* 160, 45–66.

Ringwood, A. E. (1990). Slab-mantle interactions: 3. Petrogenesis of intraplate magmas and structure of the upper mantle. *Chemical Geology,* 82, 187–207.

Ringwood and Green, A. (1966). An experimental investigation of the gabbro-eclogite transformation and some geophysical implications. *Tectonophys,* 3, 383–427.

Rubatto, D. & Hermann, J. (2003). Zircon formation during fluid circulation in eclogites (Monviso, Western Alps): Implications for Zr and Hf budget in subduction zones. *Geochimica et Cosmochimica Acta,* 67, 2173–2187.

Rudnick, R. L. (1995). Making continental crust. *Nature,* 378, 571–578.

Rudnick, R. L. & Gao, S. (2003). Composition of the continental crust. *Treatise on Geochemistry,* 3, 659.

Schiano, P., Monzier, M., Eissen, J.-P., Martin, H. & Koga, K. T. (2010). Simple mixing as the major control of the evolution of volcanic suites in the Ecuadorian Andes. *Contributions to Mineralogy and Petrology,* 160, 297–312.

Schmidt, M. W. & Jagoutz, O. (2017). The global systematics of primitive arc melts. *Geochemistry, Geophysics, Geosystems,* 18, 2817–2854.

Schmidt, M. W. & Poli, S. (1998). Experimentally based water budgets for dehydrating slabs and consequences for arc magma generation. *Earth and Planetary Science Letters,* 163, 361–379.

Scholl, D. W., Vallier, T. L. & Stevenson, A. J. (1987). Geologic Evolution and Petroleum Geology of the Aleutian Ridge. In *Geology and Resource Potential of the Western North America and Adjacent Ocean Basins—Beaufort Sea to Baja California*. Circum Pacific Council Publications.

Sekine, T. & Wyllie, P. J. (1982). The system granite-peridotite-H2O at 30 kbar, with applications to hybridization in subduction zone magmatism. *Contributions to Mineralogy and Petrology,* 81, 190–202.

Sen, C. & Dunn, T. (1994). Dehydration melting of a basaltic composition amphibolite at 1.5 and 2.0 GPa: Implications for the origin of adakites. *Contributions to Mineralogy and Petrology,* 117, 394–409.

Sen, C. & Dunn, T. (1995). Experimental modal metasomatism of a spinel lherzolite and the production of amphibole-bearing peridotite. *Contributions to Mineralogy and Petrology,* 119, 422–432.

Shaw, D. M. (2000). Continuous (dynamic) melting theory revisited. *The Canadian Mineralogist*, 38(5), 1041–1063.

Shaw, D. M. (2006). *Trace Elements in Magmas: A Theoretical Treatment.* Cambridge University Press.

Shejwalkar, A. & Coogan, L. A. (2013). Experimental calibration of the roles of temperature and composition in the Ca-in-olivine geothermometer at 0.1MPa. *Lithos,* 177, 54–60.

Siegrist, M., Yogodzinski, G., Bizimis, M., Fournelle, J., Churikova, T., Dektor, C. & Mobley, R. (2019). Fragments of Metasomatized Forearc: Origin and Implications of Mafic and Ultramafic Xenoliths from Kharchinsky Volcano, Kamchatka. *Geochemistry, Geophysics, Geosystems,* 20, 4426–4456.

Sisson, T. W. & Kelemen, P. B. (2018). Near-solidus melts of MORB + 4 wt% H2O at 0.8–2.8 GPa applied to issues of subduction magmatism and continent formation. *Contributions to Mineralogy and Petrology,* 173, 70.

Skora, S. & Blundy, J. (2010). High-pressure Hydrous Phase Relations of Radiolarian Clay and Implications for the Involvement of Subducted Sediment in Arc Magmatism. *Journal of Petrology,* 51, 2211–2243.

Sparks, R. S. J. & Marshall, L. A. (1986). Thermal and mechanical constraints on mixing between mafic and silicic magmas. *Journal of Volcanology and Geothermal Research,* 29, 99–124.

Stamper, C. C., Melekhova, E., Blundy, J. D., Arculus, R. J., Humphreys, M. C. S., & Brooker, R. A. (2014a). Oxidised phase relations of a primitive basalt from Grenada, Lesser Antilles. *Contributions to Mineralogy and Petrology,* 167, 1–20.

Stamper, C. C., Blundy, J. D., Arculus, R. J., & Melekhova, E. (2014b). Petrology of plutonic xenoliths and volcanic rocks from Grenada, Lesser Antilles. *Journal of Petrology,* 55, 1353–1387.

Staudigel, H., Plank, T., White, B. & Schmincke, H.-U. (1996). Geochemical fluxes during seafloor alteration of the basaltic upper oceanic Crust: DSDP sites 417 and 418. *Geophysical Monograph Series,* 96, 19–38.

Stern, C. R. (1991). Role of subduction erosion in the generation of Andean magmas. *Geology,* 19, 78.

Streck, M. J., Leeman, W. P. & Chesley, J. (2007). High-magnesian andesite from Mount Shasta: A product of magma mixing and contamination, not a primitive mantle melt. *Geology,* 35, 351.

Sun, S. S., Bailey, D. K., Tarney, J. & Dunham, K. C. (1980). Lead isotopic study of young volcanic rocks from mid-ocean ridges, ocean islands and island arcs. *Philosophical Transactions of the Royal Society of London. Series A, Mathematical and Physical Sciences,* 297, 409–445.

Syracuse, E. M., van Keken, P. E. & Abers, G. A. (2010). The global range of subduction zone thermal models. *Physics of the Earth and Planetary Interiors,* 183, 73–90.

Tamura, A., & Arai, S. (2006). Harzburgite–dunite–orthopyroxenite suite as a record of supra-subduction zone setting for the Oman ophiolite mantle. *Lithos,* 90, 43–56.

Turner, S. J. & Langmuir, C. H. (2022a). Sediment and ocean crust both melt at subduction zones. *Earth and Planetary Science Letters,* 584, 117424.

Turner, S. J. & Langmuir, C. H. (2022b). A quantitative framework for global variations in arc geochemistry. *Earth and Planetary Science Letters* ,584, 117411.

Ulmer, P., Kaegi, R. & Müntener, O. (2018). Experimentally derived intermediate to silica-rich arc magmas by fractional and equilibrium crystallization at 1·0 GPa: An evaluation of phase relationships, compositions, liquid lines of descent and oxygen fugacity. *Journal of Petrology,* 59, 11–58.

van Keken, P. E., Kiefer, B. & Peacock, S. M. (2002). High-resolution models of subduction zones: Implications for mineral dehydration reactions and the transport of water into the deep mantle. *Geochemistry, Geophysics, Geosystems,* 3(10), 1056.

Vannucci, R., Tiepolo, M., Defant, M. J. & Kepezhinskas, P. (2007). The metasomatic record in the shallow peridotite mantle beneath Grenada (Lesser Antilles arc). *Lithos,* 99, 25–44.

Vigneresse, J. L., Barbey, P. & Cuney, M. (1996). Rheological transitions during partial melting and crystallization with application to felsic magma segregation and transfer. *Journal of Petrology,* 37, 1579–1600.

von Huene, R. & Scholl, D. W. (1991). Observations at convergent margins concerning sediment subduction, subduction erosion, and the growth of continental crust. *Reviews of Geophysics,* 29, 279–316.

Wada, I. & Wang, K. (2009). Common depth of slab-mantle decoupling: Reconciling diversity and uniformity of subduction zones. *Geochemistry, Geophysics, Geosystems,* 10(10), Q10009.

Wood, B. J., Bryndzia, L. T. & Johnson, K. E. (1990). Mantle oxidation state and its relationship to tectonic environment and fluid speciation. *Science,* 248, 337–345.

Yasuda, A., Fujii, T. & Kurita, K. (1994). Melting phase relations of an anhydrous mid-ocean ridge basalt from 3 to 20 GPa: Implications for the behavior of subducted oceanic crust in the mantle. *Journal of Geophysical Research: Solid Earth,* 99, 9401–9414.

Yogodzinski, G. M. & Kelemen, P. B. (1998). Slab melting in the Aleutians: Implications of an ion probe study of clinopyroxene in primitive adakite and basalt. *Earth and Planetary Science Letters,* 158, 53–65.

Yogodzinski, G. M. & Kelemen, P. B. (2007). Trace elements in clinopyroxenes from Aleutian xenoliths: Implications for primitive subduction magmatism in an island arc. *Earth and Planetary Science Letters,* 256, 617–632.

Yogodzinski, G. M., Volynets, O. N., Koloskov, A. V., Seliverstov, N. I. & Matvenkov, V. V. (1994). Magnesian andesites and the subduction component in a strongly calc-alkaline series at Piip Volcano, far Western Aleutians. *Journal of Petrology,* 35, 163–204.

Yogodzinski, G. M., Brown, S. T., Kelemen, P. B., Vervoort, J. D., Portnyagin, M., Sims, K. W., & Werner, R. (2015). The role of subducted basalt in the source of island arc magmas: Evidence from seafloor lavas of the western Aleutians. *Journal of Petrology,* 56, 441–492.

Yogodzinski, G. M., Kelemen, P. B., Hoernle, K., Brown, S. T., Bindeman, I., Vervoort, J. D., & Werner, R. (2017). Sr and O isotopes in western Aleutian seafloor lavas: Implications for the source of fluids and trace element character of arc volcanic rocks. *Earth and Planetary Science Letters,* 475, 169–180.

2.0 FIGURES AND CAPTIONS

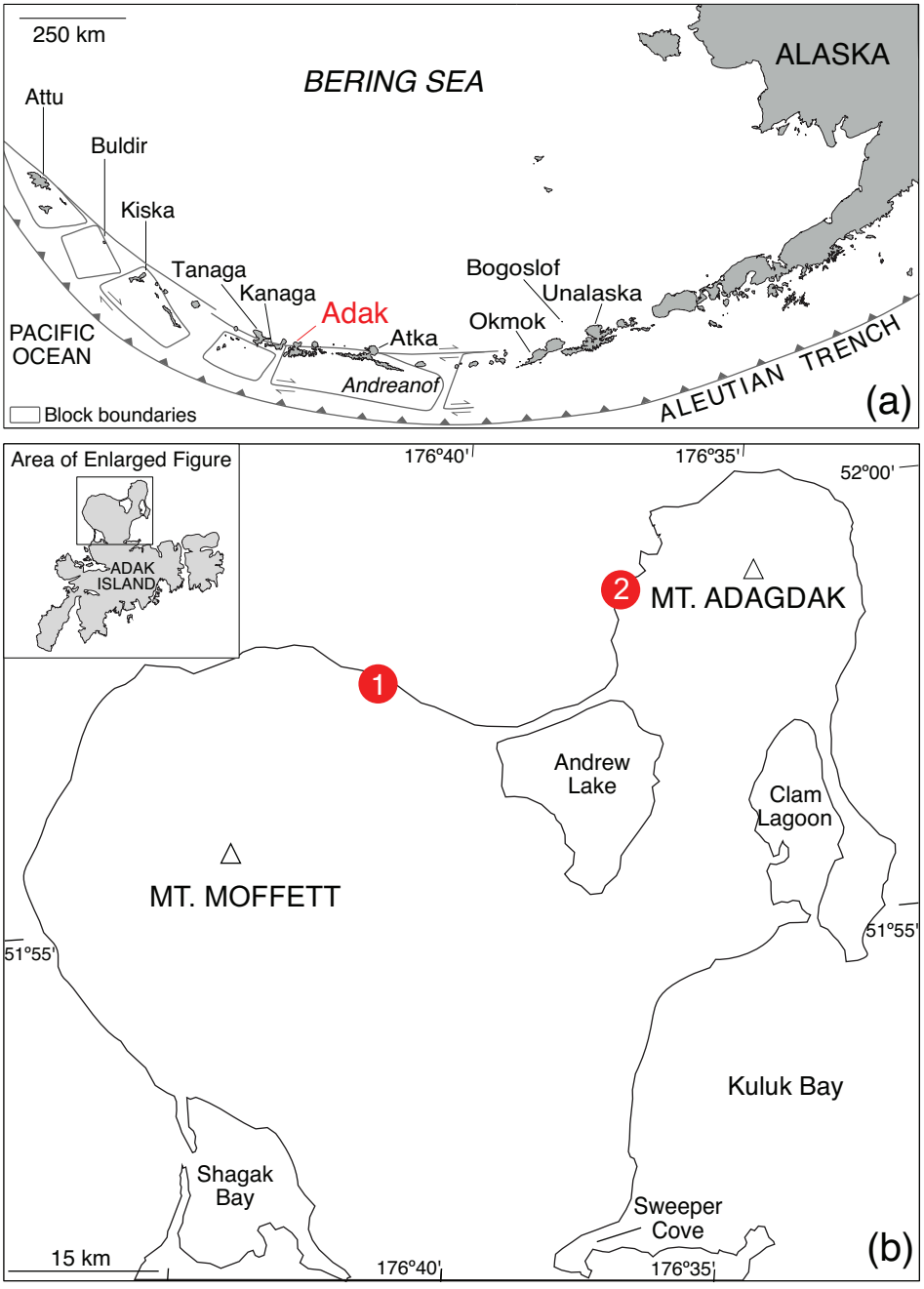

Figure 1: Map of xenolith source locations. **a)** Geological map of the Aleutian Arc. **b)** Enlarged map of Adak Island. The locations where the xenolith suites from 1) Mount Moffett (51°58.01' N, 176°43.55' W) and 2) Mount Adagdak (51°58.78' N, 176°37.36' W) were collected are designated with red circles.

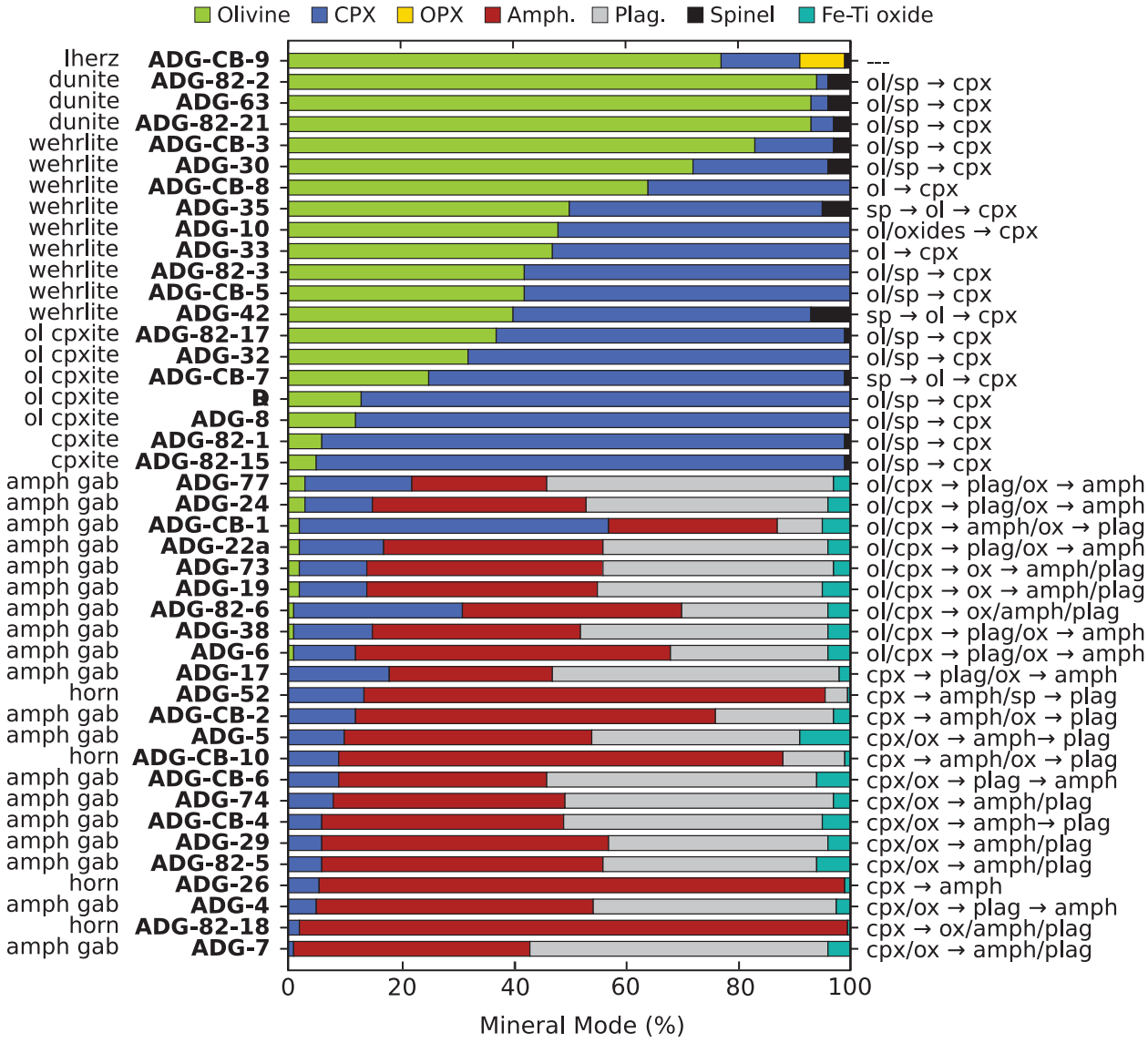

Figure 2: Adagdak xenolith modal mineral proportions (in vol. %). The crystallization sequence for cumulate samples is based on petrographic relationships observed in thin section. Abbreviations: lherz = lherzolite, ol cpxite = olivine clinopyroxenite, amph gab = amphibole gabbro, horn = hornblendite.

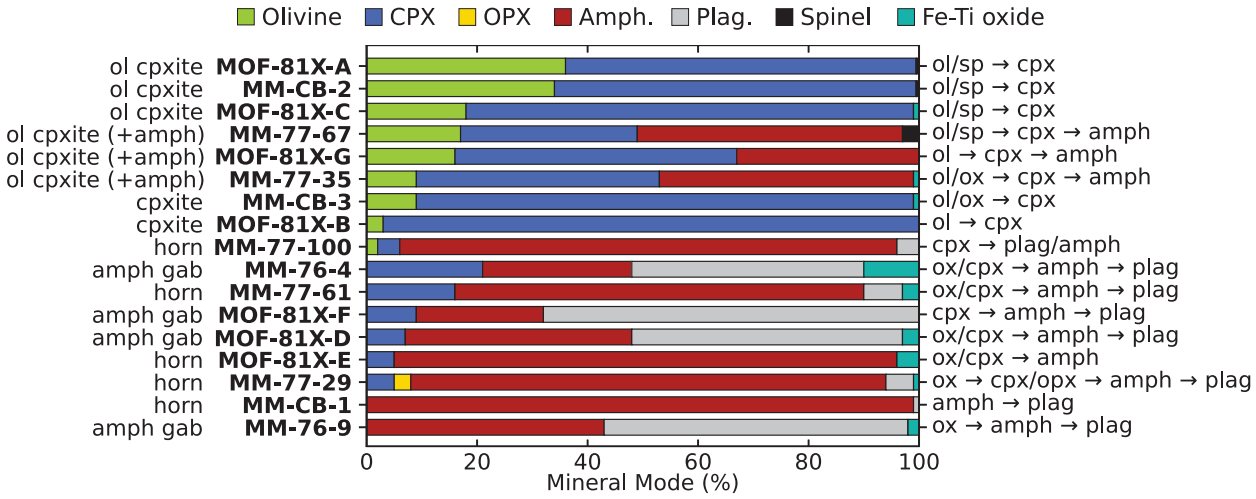

Figure 3: Modal mineral proportions of Moffett xenoliths (vol. %). The abbreviations used are the same as in Figure 2.

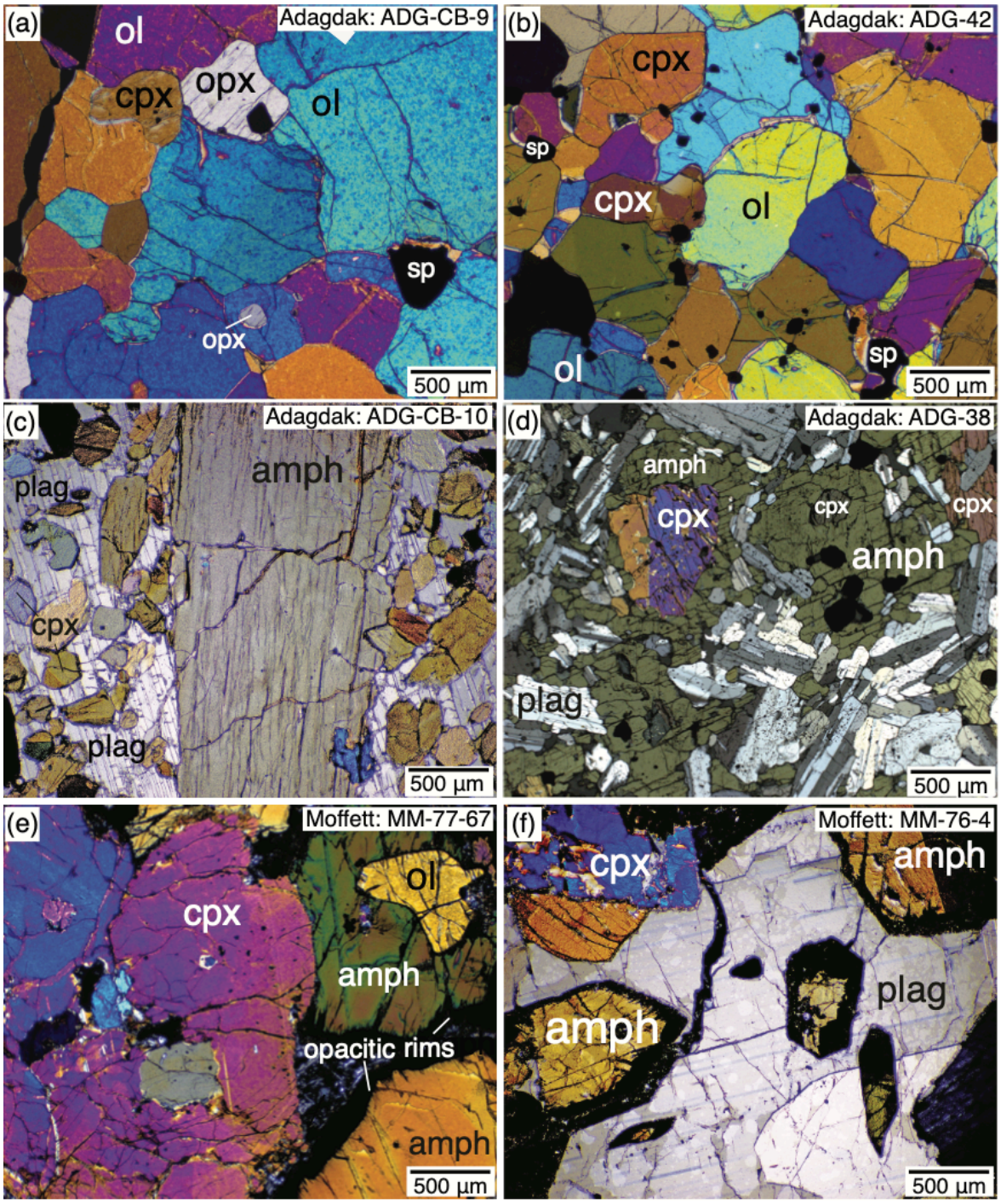

Figure 4: Photomicrographs of thin sections in cross-polarized light. **a)** Adagdak lherzolite ADG-CB-9. **b)** Adagdak wehrlite ADG-42. **c)** Adagdak hornblendite ADG-CB-10. **d)** Adagdak amphibole gabbro ADG-38. **e)** Moffett amphibole-bearing olivine clinopyroxenite MM-77-67. **f)** Moffett amphibole gabbro MM-76-4.

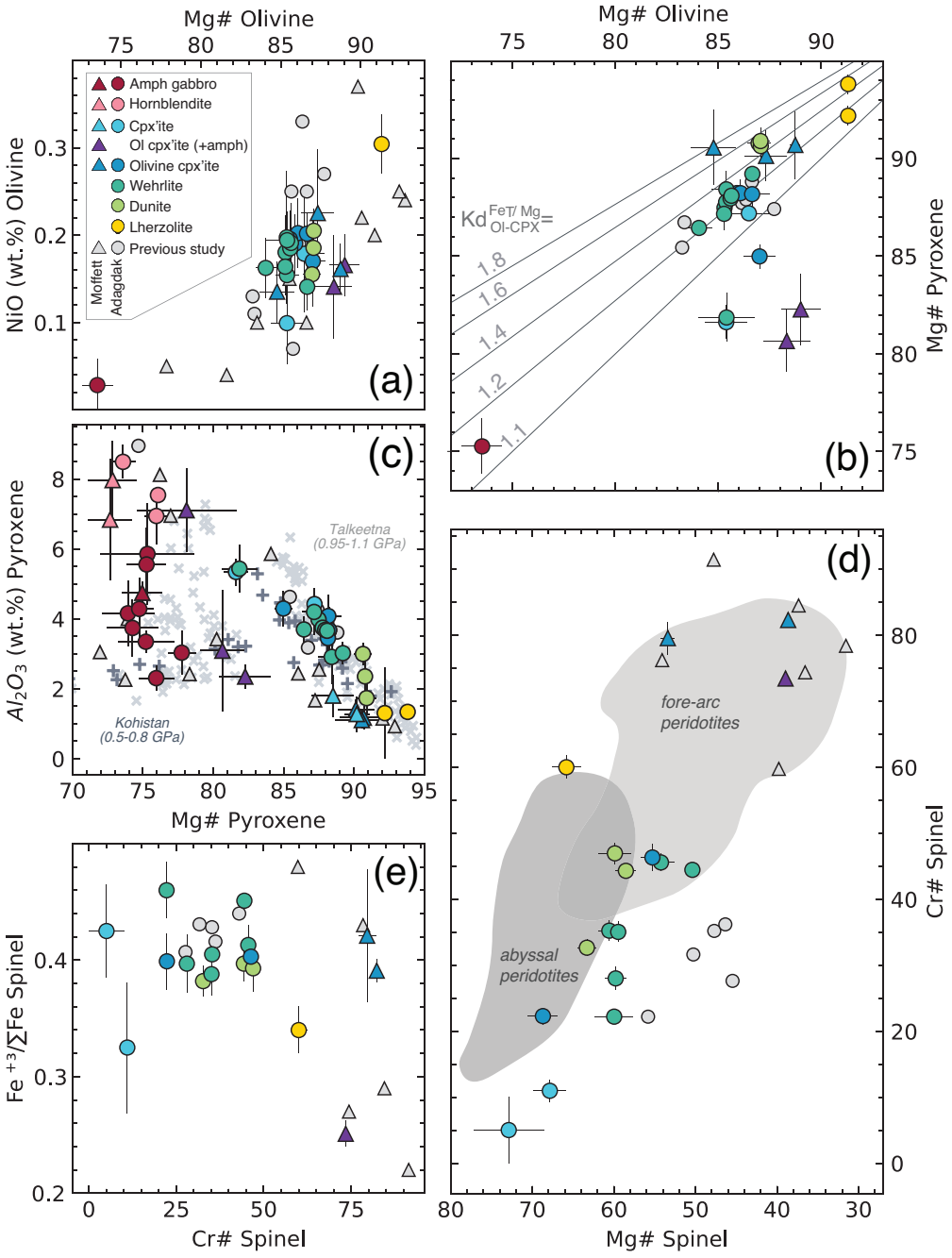

Figure 5: Summary of xenolith major element mineral chemistry. Error bars represent 2σ variations in sample composition. **a)** Olivine Mg# vs. NiO_2 (wt.%). **b)** Olivine Mg# vs. clinopyroxene Mg#. **c)** Pyroxene Mg# vs. Al_2O_3 (wt.%). Clinopyroxene data from the Chilas complex, Kohistan (Jagoutz et al., 2007) and Talkeetna (Beyer, 1980; DeBari and Coleman, 1989; Greene et al., 2006) are given for comparison. **d)** Spinel Mg# vs. Cr#. Abyssal and fore-arc peridotite fields after Tamura and Arai (2006). **e)** Spinel Cr# vs. Fe^{3+}/Fe^{T}.

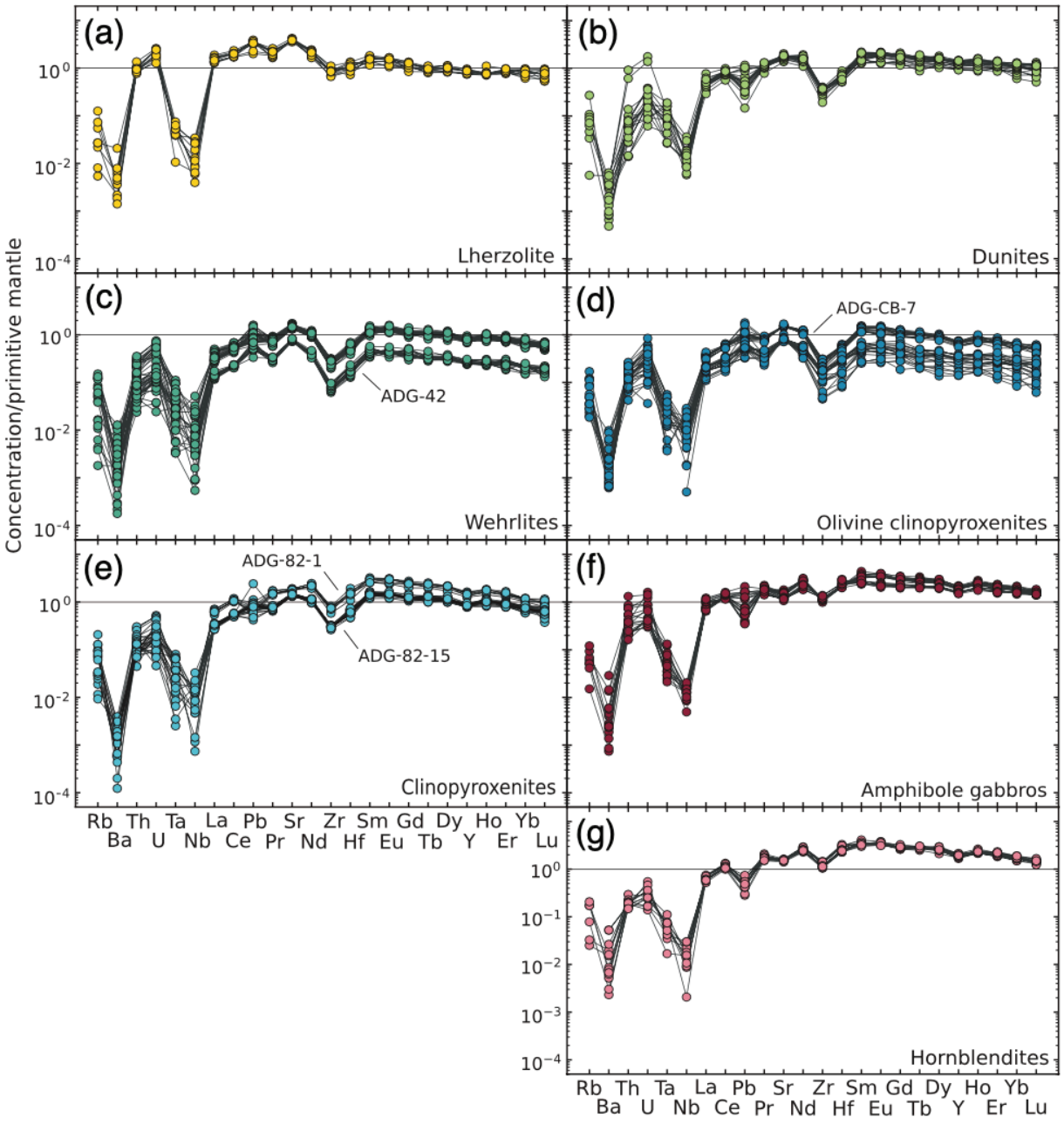

Figure 6: Primitive mantle normalized trace element concentrations in Adagdak xenolith clinopyroxene. **a)** Amphibole gabbro. b) Hornblendite. **c)** Clinopyroxenite. **d)** Olivine clinopyroxenite. **e)** Wehrlite. **f)** Dunite. **g)** Lherzolite.

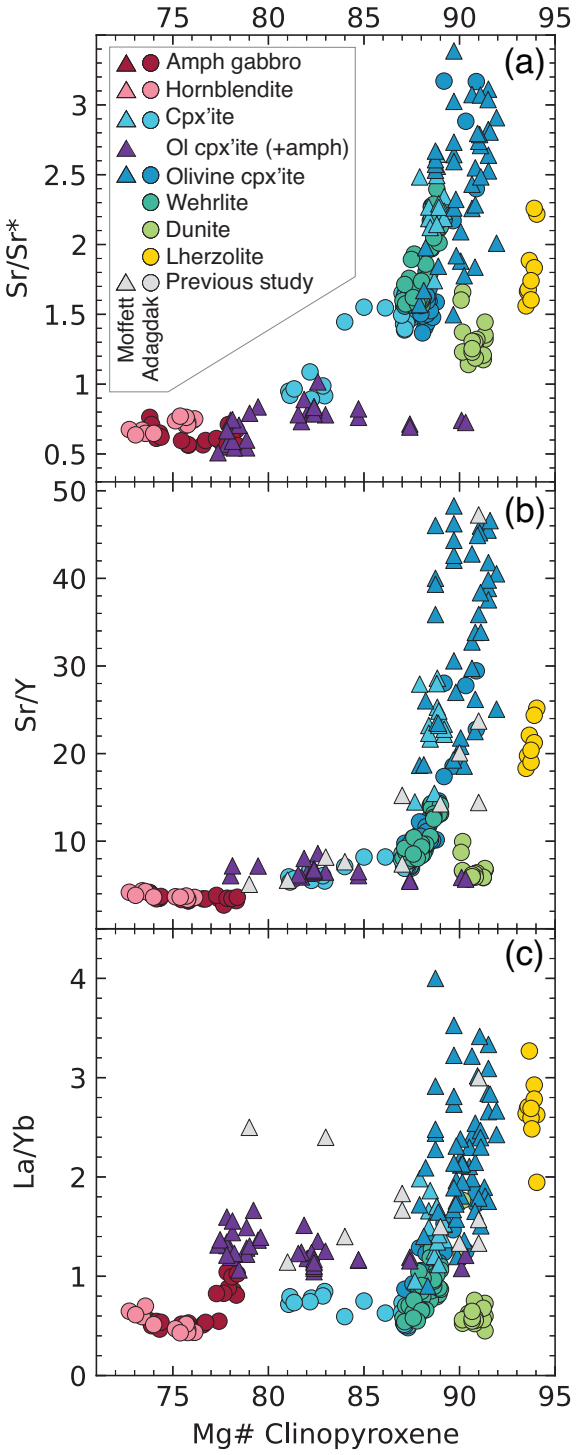

Figure 7: Clinopyroxene trace element ratios vs. Mg#. **a)** Sr/Sr* vs Mg#. **b)** Sr/Y vs. Mg#. **c)** La/Yb vs. Mg#.

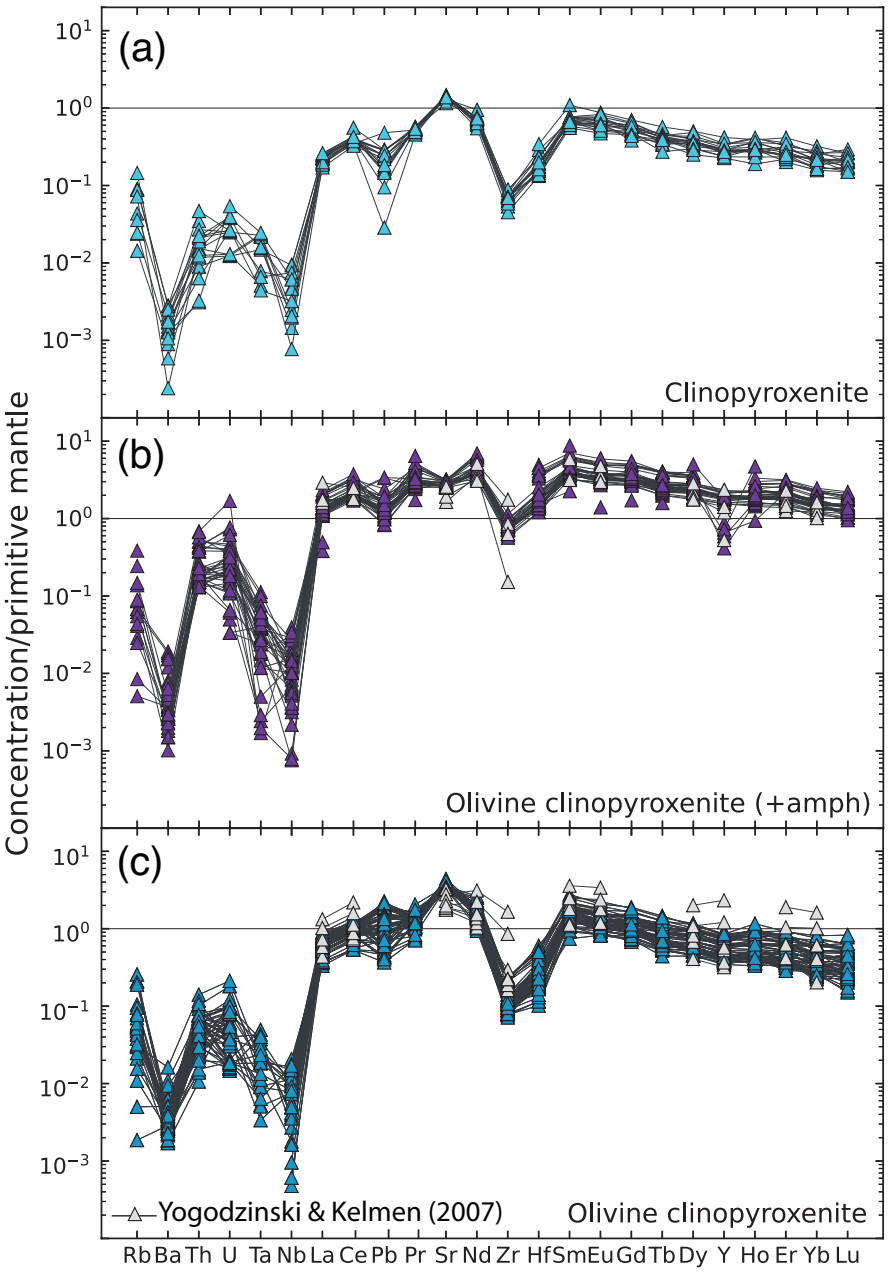

Figure 8: Primitive mantle normalized trace element concentrations in Moffett xenolith clinopyroxene. **a)** Clinopyroxenite. **b)** Amphibole-bearing olivine clinopyroxenite. **c)** Olivine clinopyroxenite.

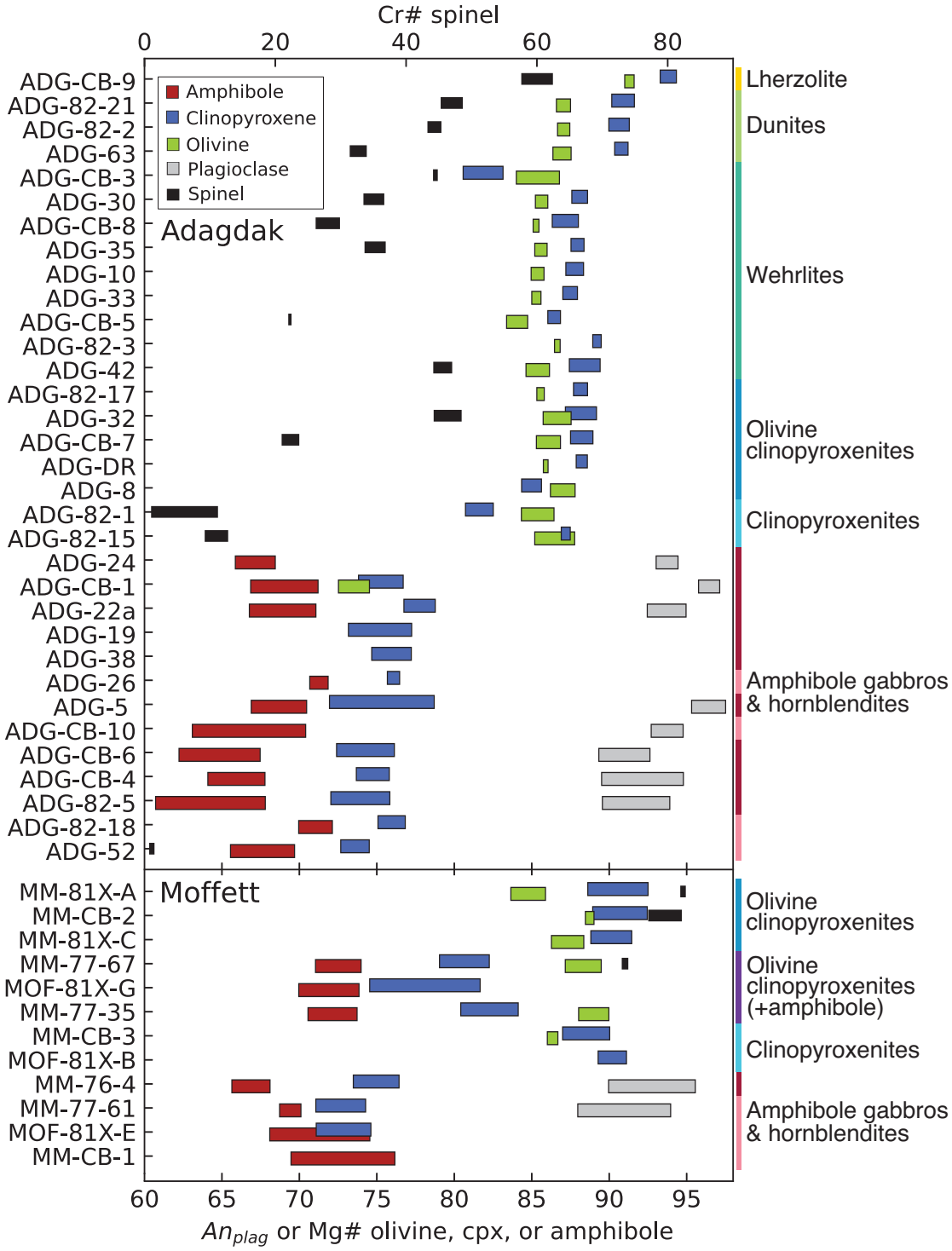

Figure 9: Summary of major element mineral chemistry for the Adagdak and Moffett xenoliths suites. Samples are ordered by modal abundance of olivine.

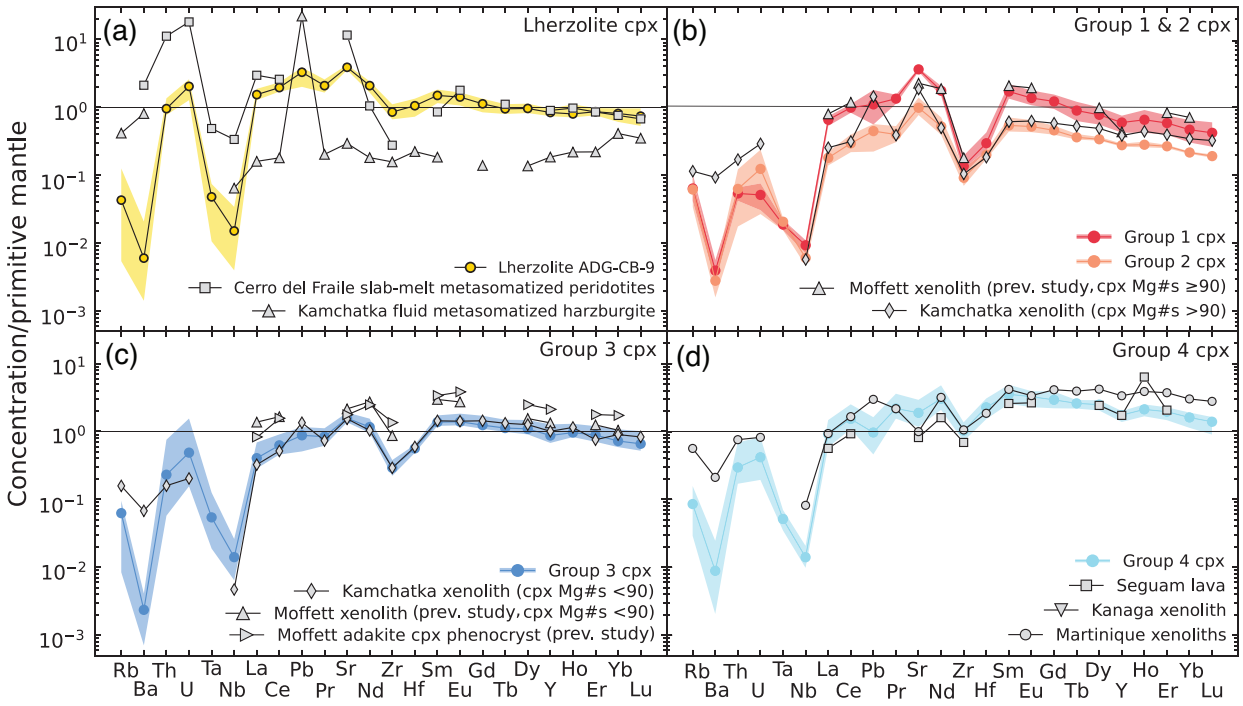

Figure 10: Clinopyroxene trace element concentrations organized by compositional groups. Solid lines and shaded regions represent the averages and variability observed in samples or compositional groups, respectively. **a)** Lherzolite ADG-CB-9 clinopyroxene. Trace element data from 1) slab-melt metasomatized mantle xenolith clinopyroxene, Cerro del Fraile, Southern Patagonia (Kilian and Stern, 2002) and 2) fluid metasomatized mantle xenolith clinopyroxene from Kamchatka (Ishimaru et al., 2006) are also shown. **b)** Clinopyroxene compositional Groups 1 and 2. High Mg# (>90) clinopyroxene trace element data from Kamchatka cumulate xenoliths (Siegrist et al., 2019) and a previous study of Moffett cumulates (Yogodzinski and Kelemen, 2007) are shown for comparison. **c)** Clinopyroxene compositional Group 3. Low Mg# (<90) clinopyroxene trace element data from the Kamchatka (Siegrist et al., 2019) and Moffett cumulates (Yogodzinski and Kelemen, 2007) are shown for comparison. **d)** Clinopyroxene compositional Group 4. Clinopyroxene trace elements from 1) Kanaga Island (Yogodzinski and Kelemen, 2007) and Martinique Island (Cooper et al., 2016) cumulate xenoliths and 3) Seguam Island basalts (Yogodzinski and Kelemen, 1998) are given for comparison.

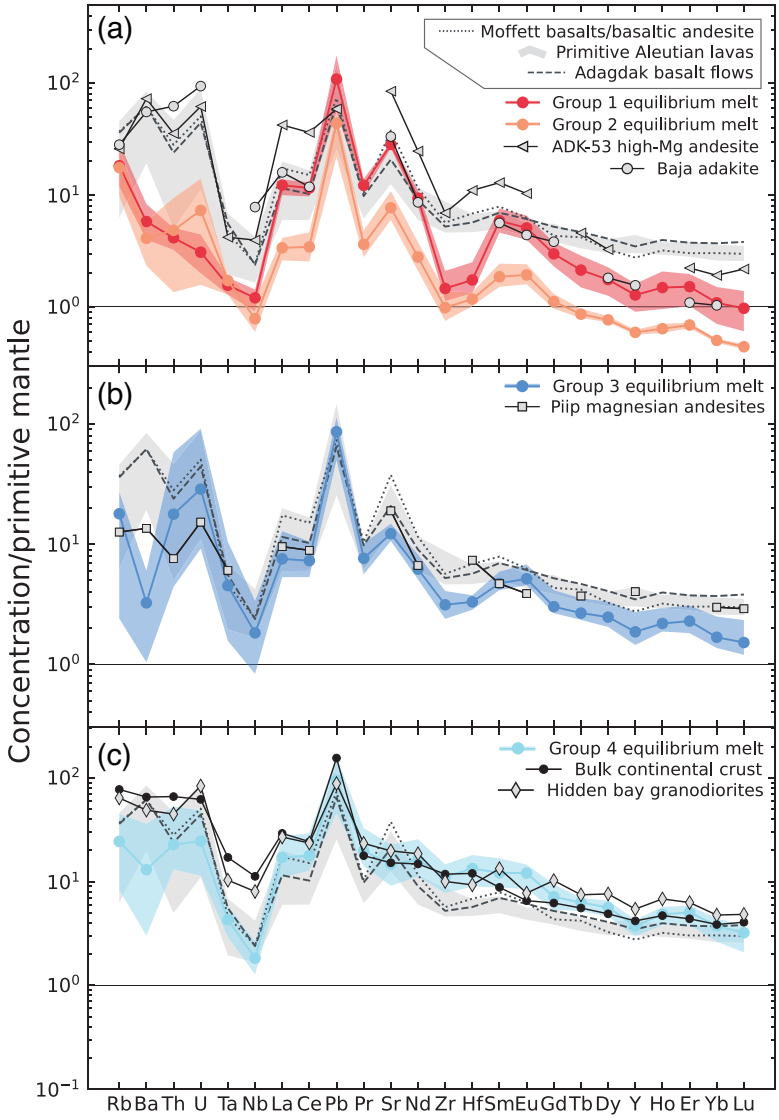

Figure 11: Equilibrium melt compositions calculated from clinopyroxene trace element data. Solid lines represent compositional group averages and shaded areas represent the variations observed in equilibrium melt compositions from each group. Whole-rock trace element data of Adagdak basalt flows (dashed lines) and Moffett basalts and basaltic andesites (dotted lines) are shown for comparison (Kay and Kay, 1994; Marsh, 1976). The compilation of primitive Aleutian calc-alkaline basalts and andesites (gray shaded field) is from Schmidt and Jagoutz (2017). **a)** Groups 1 and 2 equilibrium melt compositions. Whole-rock data from adakite ADK-53 (Adak Island, Sun et al., 1980; Kay et al., 1986; Kay and Kay, 1994; Münker et al., 2004) and adakites from the Santa Clara volcanic field, Baja California (Aguillon-Robles et al., 2001) is given for comparison. **b)** Group 3 equilibrium melt compositions. Data from Piip volcano magnesian andesites (Yogodzinski et al., 1994) is shown for comparison. **c)** Group 4 equilibrium melt compositions. Whole-rock data from the Hidden Bay pluton (Kay et al., 1990, 2019) is also shown.

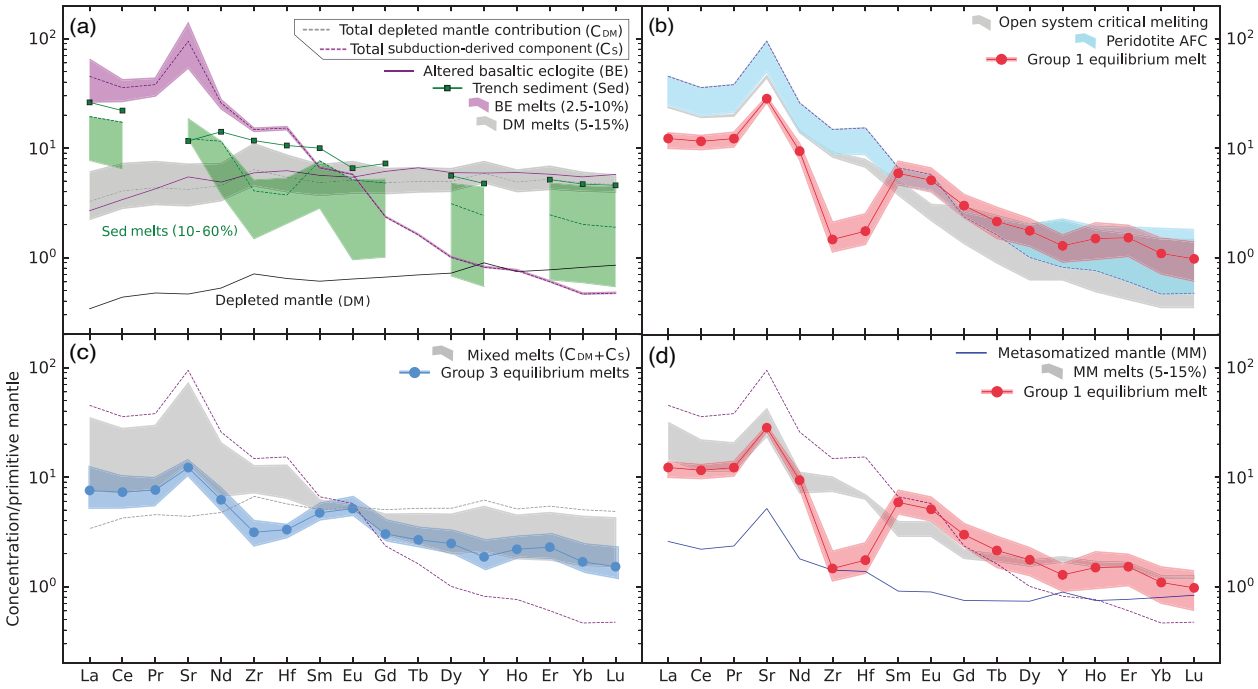

Figure 12: Trace element modeling results. Group 1, and 3 melt compositions overlay model results that give best fits. **a)** Compositions of source rocks and melts used in modeling. Dotted purple and gray lines represent the subduction-derived and mantle melt compositions used in models, while shaded fields represent compositional variations for different degrees of basaltic eclogite and mantle melting. **b)** Model results for subduction-derived melt (purple dotted line) reacting with the depleted mantle through AFC reactions (blue field: DePaolo, 1981) and open system critical melting (gray field: Shaw, 2000). **c)** Model results (gray field) for mixing subduction-derived melt (purple dotted line) with 10% depleted mantle melt (black dotted line). **d)** Model results (gray field) for 5-10% melting of a mantle composition (blue line) modal metasomatized by a subduction-derived melt (purple dotted line) in a 1:9 melt: rock ratio.

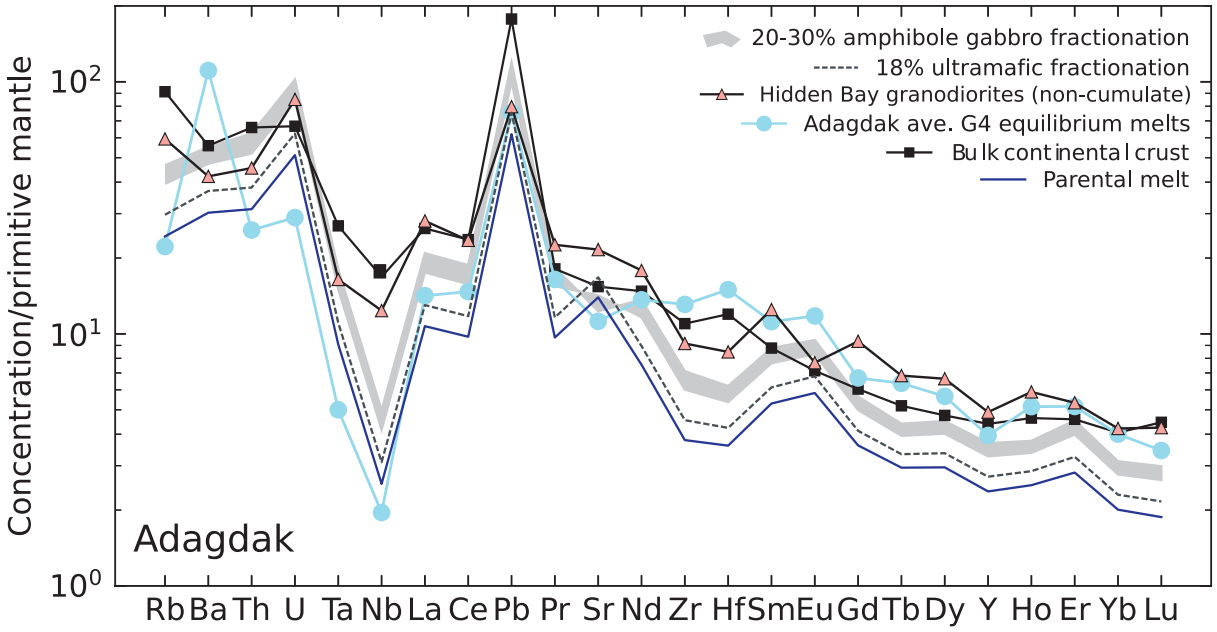

Figure 13: Trace element fractional crystallization model results for Adagdak. Bulk continental crust composition is from Rudnick and Gao (2003) and Hidden Bay pluton data is from Kay et al. (2019).

Table 1: Summary of data from previous studies of the Adak xenolith suites

		Modal abundance of cumulate phases						
Sample	**Lithology**	*Ol*	*Cpx*	*Spin*	*Mag*	*Amph*	*Plag*	*Glass*
Adagdak								
30	Dunite	95	4	1				
39	Dunite	92	8	minor		minor		
35	Dunite	90	9	1				
32	Wehrlite	50	50	<1		minor		
DR	Mixed dunite and clinopyroxenite	50	50	1				
ADAG81-X	Olivine clinopyroxenite	40	60	<1		minor		
34	Olivine clinopyroxenite	35	65					
8	Clinopyroxenite	2	95					3
ADG-1	Hornblendite	2			7	90	1	
ADAG82-18	Amphibolite					100		
Moffett								
78F-1	Hornblende gabbro							
MM-102	Olivine clinopyroxenite							
MM-43	Olivine clinopyroxenite							
MM-7610	Hornblende gabbro							
MM-76BB	Opx gabbro							
MM-78C	Opx gabbro							
MM-78F	Hornblende gabbro							
MM-DK	Hornblende gabbro							
MMG	Olivine pyroxenite							

Table 1: continued

	Mineral chemistry					
Sample	*Fo Ol*	*Mg# Cpx*	*Cr# Spin*	*Sr/Y Cpx*	**Crystallization sequence**	**Ref.**
Adagdak						
30	86	89	35			[1]
39	86	92	32			[1]
35	86	92	36			[1]
32	87	89	22			[1]
DR	86	88	43			[1]
ADAG81-X	83	87	27			[1]
34	86	88				[1]
8	83	86				[1]
ADG-1		75				[1]
ADAG82-18						[1]
Moffett						
78F-1					Mt + Amph, Cpx + Plag	[2]
MM-102	87 - 92	80 - 91	60 - 85	5.6 - 47.2	Crm, Ol + Cpx → Amph	[1, 2, 3]
MM-43		79 - 91		3.8 - 14.6		[3]
MM-7610					Mt, Amph +/- Cpx, Plag	[1, 2]
MM-76BB	69	74			Ol → Mt, Plag, Opx + Cpx	[2]
MM-78C		74	67		Mt, Cpx + Opx, Plag + Qtz	[2]
MM-78F					Mt, Amph, Cpx + Plag	[2]
MM-DK	76 - 80	77 - 78			Mt, Ol + Cpx → Plag + Amph + Mt	[1, 2]
MMG	84 - 90	88	76		Crm, Ol + Cpx, Mt + Cpx → Amph	[2]

[1] Debari et al., 1987; [2] Conrad & Kay, 1984; [3] Yogodzinski & Kelemen, 2007

Table 2: Summary of xenolith petrography

Sample	Phase	Mode (%)	Grain size (mm)	Description
Adagdak				
Dunite				
ADG-82-2	Olivine	94	0.1 - 2.2	Protogranular texture. Most spinel is observed as inclusions in cpx or olivine, interstitial spinel is rare.
	Oxide	4	0.01 - 0.18	
	Cpx	2	0.4 - 1.3	
ADG-82-21	Olivine	93	0.1 - 1.25	Protogranular texture. Pervasive fracturing observed throughout entire sample. Spinel < 0.15 mm is generally euhedral while larger grains are anhedral.
	Cpx	4	0.15 - 0.8	
	Oxide	3	0.05 - 0.3	
ADG-63	Olivine	93	0.1 - 3.25	Protogranular texture. Olivine is well preserved, free of fracturing, and with clearly defined edges. About 25% of spinel shows symplectic texture, the rest range from euhedral to anhedral. Clinopyroxene is subhedral to anhedral.
	Oxide	4	0.05 - 0.2	
	Cpx	3	0.1 - 0.8	
Lherzolite				
ADG-CB-9	Olivine	77	0.075 - 2.5	Protogranular texture. Subhedral to anhedral olivine and pyroxene. Olivine has serpentinized rims. Spinel is euhedral and interstitial.
	Cpx	14	0.15 - 1.375	
	Opx	8	0.25 - 1.2	
	Oxide	1	0.01 - 0.02	
Wehrlite				
ADG-CB-3	Olivine	83	0.1 - 0.85	Series of nested xenoliths. Innermost xenolith has adcumulate texture and is rimmed by a 7 mm thick amphibole clinopyroxenite with poikilitic amphibole. The outer-most rim is composed of a 5 mm thin section of coarse-grained amphibole crystals with inclusions of cpx and olivine.
	Cpx	14	1.1 - 0.2	
	Oxide	3	0.01 - 0.1	
ADG-30	Olivine	72	0.075 - 1.6	Adcumulate texture. About 50% of cpx have sieve textures. Spinel is observed interstitially and as poikilitic inclusions. Interstitial spinel is larger than that seen as poikilitic inclusions (0.05 - 0.18 mm vs 0.01 - 0.075 mm).
	Cpx	24	0.1 - 1.3	
	Oxide	4	0.01-0.18	

Table 2: continued

ADG-35	Olivine Cpx Oxide	50 45 5	0.12 - 2.1 0.1 - 1.8 0.01 - 0.12	Adcumulate texture. About 20% of cpx have sieve textures. Spinel is euhedral and occur interstitially and as poikilitic inclusion in clinopyroxene.
ADG-10	Cpx Olivine Oxide	52 48 trace	0.2 - 1.45 0.1 - 1.3 0.01 - 0.1	Adcumulate texture. About 15% of cpx have sieve textures. About 65% of olivine is anhedral, ~30% are subhedral, and ~5% are euhedral. The euhedral grains are smaller (0.1 – 0.2 mm) and primarily occur as inclusions in cpx.
ADG-33	Cpx Olivine	53 47	0.15 - 4.5 0.1 - 1. 75	Protogranular texture. No grains in sample contain poikilitic inclusion or display sieve textures.
ADG-82-3	Cpx Olivine Oxide	58 42 < 1	0.2 - 2.3 0.05 - 1.5 <0.01 - 0.05	Protogranular texture. Sieve textures or poikilitic inclusions of olivine and spinel are observed in cpx > 1 mm. Euhedral spinel is seen interstitially and as poikilitic inclusions in cpx and olivine.
ADG-CB-5	Cpx Olivine Oxide	58 42 < 1	0.1 - 6 0.05 - 1.7 0.01 - 0.05	Adcumulate texture. Clinopyroxene shows pervasive fracturing and partially reabsorbed rims. Larger olivine grains (> 1 mm) often contain inclusions of smaller olivine. Spinel observed interstitially and as poikilitic inclusions in cpx.
ADG-42	Cpx Olivine Oxide OPX	53 40 7 < 1	0.2 - 2 0.1 - 0.8 0.01 - 0.2 1.5 - 3	Protogranular texture. Subhedral to anhedral cpx and euhedral olivine. Spinel occurs as poikilitic inclusions in cpx.
Olivine clinopyroxenite				
ADG-82-17	Cpx Olivine Oxide	62 37 1	0.17 - 2.4 0.1 - 2.1 < 0.1	Adcumulate texture. Olivine and cpx are generally free of fracturing and crystalline edges are well preserved.
ADG-32	Cpx Olivine Oxide	68 32 < 1	1.25 - 19.3 0.1-9.8 0.6-2.1	Protogranular texture. Larger cpx (> 10 mm) is euhedral and smaller grains (< 4 mm) are subhedral to anhedral. Spinel is observed interstitially and as poikilitic inclusions in cpx and olivine.

Table 2: continued

ADG-CB-7	Cpx Olivine Oxide	74 25 1	0.08 - 0.9 0.1 - 1.1 < 0.01	Protogranular texture. Clinopyroxene is subhedral to anhedral and olivine is euhedral. Small euhedral spinel is seen interstitially.
DR	Cpx Olivine Oxide	87 13 < 1	0.2 to 4.2 0.1 to 2.2 0.01 - 0.05	Protogranular texture. Clinopyroxene is subhedral to anhedral and sometimes contains small (0.2 – 0.35 mm) inclusions of rounded olivine grains. Spinel is euhedral and seen interstitially.
ADG-8	Cpx Olivine Oxide	88 12 < 1	0.22 - 2.5 0.15 - 0.6 0.01 - 0.18	Adcumulate texture. About 50% of cpx have sieve textures. Most Fe-Ti oxides (> 90%) are present as poikilitic inclusions in cpx. In some areas, skeletal olivine fills the space between cpx grains.
Clinopyroxenite				
ADG-82-1	Cpx Olivine Oxide	93 6 1	0.1 - 3 0.1 - 1.2 < 0.01	Adcumulate texture. Clinopyroxene and olivine along the rim of the sample (outer 2-6 mm) show sieve textures. Most olivine is euhedral, although several skeletal olivine grains also observed. Small euhedral spinel seen interstitially.
ADG-82-15	Cpx Olivine Oxide	94 5 1	0.1 - 3.2 0.1 - 0.2 0.01	Protogranular texture. Clinopyroxene sometimes contains inclusions of olivine with serpentinized rims or smaller distinct cpx. Small euhedral spinel observed interstitially.
Amphibole gabbro				
ADG-77	Amph Plag Cpx Oxide Olivine	24 51 19 3 3	0.4 - 1.7 0.1 - 1.3 0.2 -1.4 0.1 - 0.7 0.1 - 0.6	Mesocumulate texture. Plagioclase is subhedral and individual grains interlock one another. Amphibole occurs poikilitically. All cpx have sieve textures and > 90% contain poikilitic inclusions of Fe-Ti oxides. All cpx show reabsorption along their rims. Oxides are subhedral to anhedral and occur interstitially and as inclusions in cpx and amphibole. Oxides with symplectic textures also observed. Olivine > 0.25 mm is usually skeletal. Smaller olivine is seen both interstitially and as inclusions in amphibole and cpx.

Table 2: continued

ADG-24	Plag	43	0.25 - 4.7	Mesocumulate texture. About 50% of amphibole > 3 mm occurs poikilitically and contain inclusions of plagioclase, cpx, and olivine. About 70% of cpx contain inclusions of Fe-Ti oxides, amphibole, and/or plagioclase. Small euhedral oxides (0.075 to 0.15 mm) are present as poikilitic inclusions in other phases. Larger oxides are generally anhedral.
	Amph	38	0.3 - 5	
	Cpx	12	0.2 - 3	
	Oxide	4	0.075 - 0.7	
	Olivine	3	0.1 - 1.1	
ADG-CB-1	Cpx	55	0.15 - 2.25	Adcumulate texture. Clinopyroxene often contains inclusions of olivine, amphibole, and Fe-Ti oxides. Small amphibole (<1 mm) is euhedral/subhedral and larger grains (>2 mm) occur poikilitically around cpx, plag, olivine, and other distinct amphiboles. Intercumulus plag contains olivine and cpx inclusions. Small euhedral Fe-Ti oxides (0.01 to 0.1 mm) present as inclusions in cpx. Larger anhedral Fe-Ti oxides (0.15 to 0.6 mm) appear as intercumulus phases.
	Amph	30	0.2 - 7	
	Plag	8	0.1 - 0.8	
	Oxide	5	0.01 - 0.6	
	Olivine	2	0.02 - 0.75	
ADG-22	Plag	40	0.2 - 8	Mesocumulate texture. Amphibole occurs poikilitically around large (0.25 - 1.5mm) plagioclase, cpx, and distinct amphibole. Poikilitic amphibole ranges from 9 mm to 1.5 cm in diameter, but 40-70% of their area is occupied by other phases. Approximately 20% of all cpx are skeletal and all cpx show partially reabsorbed rims. Fe-Ti oxides < 0.25 mm are euhedral and grains between 0.25 - 0.6 mm are subhedral or anhedral.
	Amph	39	--	
	Cpx	15	0.3 - 2.75	
	Oxide	4	0.02 - 0.6	
	Olivine	2	0.25 - 1.2	
ADG-73	Amph*	42	0.3 - 1.9	Adcumulate texture. > 80% of amphibole occurs poikilitically around Fe-Ti oxides, plag, cpx, and/or olivine. About 85% of plag have sieve textures and ~5% contain poikilitic inclusions small oxides (< 0.01 mm) or amphibole (0.02 and 0.06 mm). About 30% of all cpx over 1 mm in diameter are skeletal.
	Plag	41	0.075 - 0.8	
	Cpx	12	0.2 - 1.3	
	Oxide	3	0.03 - 0.6	
	Olivine	2	0.1 - 0.35	
ADG-19	Amph	41	0.1 - 2.3	Mesocumulate texture. Amphibole is euhedral and about 60% contains inclusions of plag, cpx, and/or Fe-Ti oxides. Small euhedral Fe-Ti oxides (0.05 – 0.1 mm) occur as poikilitic inclusions in cpx and amphibole and larger anhedral grains (>0.12 mm) appear as intercumulus phases.
	Plag	40	0.1 - 2.1	
	Cpx	12	0.1 - 2.1	
	Oxide	5	0.05 - 0.5	
	Olivine	2	0.15 - 0.3	

Table 2: continued

ADG-82-6	Amph*	39	--	Mesocumulate texture. Amphibole occurs as intercumulus phases or poikilitically and do not show distinct grain boundaries. Poikilitic amphibole contains inclusions of 0.1 - 0.4 mm plag, cpx, olivine, and distinct euhedral amphibole. Clinopyroxene pervasively shows sieve textures and partially reabsorbed rims. Many cpx (> 65%) contain poikilitic inclusions of small (0.02 to 0.1 mm) Fe-Ti oxides. Larger oxides (0.1 - 0.2 mm) are present interstitially. Olivine occurs as inclusions in amphibole.
	Plag	26	0.1 - 0.8	
	Cpx	30	0.2 - 0.7	
	Oxide	4	0.02 - 0.2	
	Olivine	1	0.15 - 0.2	
ADG-38	Plag	44	0.2 - 0.9	Mesocumulate texture. Plagioclase is lath-like and > 95% of grains have sieve textures. Amphibole is anhedral and does not show distinct grain boundaries. About 70% of amphibole occurs poikilitically around Fe-Ti oxides, plag, cpx, and olivine. Fe-Ti oxides show a great diversity of sizes and morphologies. About 20% of oxides have symplectic texture. Olivine is primarily present as inclusions in amphibole.
	Amph*	37	--	
	Cpx	14	0.2 - 1.1	
	Oxide	4	0.01 - 0.3	
	Olivine	1	0.1 - 0.2	
ADG-6	Amph	56	0.1 - 1.1	Mesocumulate texture. ~ 80% of amphibole occurs poikilitically around Fe-Ti oxides, plag, cpx, and olivine. Small cpx (0.1 - 0.25 mm) only present as inclusions in amphibole. Larger cpx (>0.25 mm) contain inclusions of Fe-Ti oxides and olivine. Larger oxides (> 0.25 mm) are subhedral to anhedral and appear as intercumulus phases. Smaller euhedral oxides (0.02 - 0.2 mm) are observed as inclusions in cpx and amphibole.
	Plag	28	0.2 - 1.2	
	Cpx	11	0.1 - 1.1	
	Oxide	4	0.02 - 0.9	
	Olivine	1	0.075 - 1	
ADG-74	Plag	48	0.08 - 1	Adcumulate texture. Amphibole < 0.4 mm is hexagonal and euhedral. Larger amphibole (0.4 - 1.8 mm) is anhedral and occurs poikilitically around cpx, plag, Fe-Ti oxides, and olivine. About 70% of plagioclase have sieve textures. Clinopyroxene contains poikilitic inclusions of Fe-Ti oxides. Oxides between 0.1 and 0.12 are euhedral and present as inclusions in other phases. Larger anhedral oxides (<0.25 mm) are interstitial. Olivine is only present as inclusions in amphibole or cpx.
	Amph	41	0.2 - 1.8	
	Cpx	8	0.15 - 0.8	
	Oxide	3	0.1 - 0.25	
	Olivine	< 1	0.1 - 0.4	

Table 2: continued

ADG-4	Amph*	49	--	Mesocumulate texture. Amphibole occurs poikilitically or as rims around other phases. Most cpx (> 90%) contain poikilitic inclusions of smaller (0.2 – 0.1 mm) euhedral oxides. Small (0.01 – 0.05 mm) euhedral Fe-Ti oxides are present as poikilitic inclusions in cpx and amphibole. Larger (0.25 – 0.7 mm) anhedral oxides are seen interstitially.
	Plag	43	0.17 - 2.1	
	Cpx	5	0.1 - 1.1	
	Oxide	3	0.01 - 0.7	
	Olivine	< 1	0.15 - 0.3	
ADG-17	Amph	29	0.15 to 8	Mesocumulate texture. Most (> 90%) amphibole over 2.25 mm occurs poikilitically and contains inclusions of oxides, plagioclase, and cpx. About 90% of oxides are anhedral, 0.1 and 0.25 mm in diameter, and occur interstitially. Smaller euhedral oxides (< 0.1 mm) are only seen as poikilitic inclusions.
	Plag	51	0.1-0.75	
	Cpx	18	0.15 - 1.1	
	Oxide	2	0.05 - 0.3	
ADG-CB-2	Amph	64	0.25 - 4.9	Mesocumulate texture. About 20% of amphibole contains inclusions of smaller distinct amphibole or cpx. Twelve large poikilitic grains of plagioclase were noted in this sample, ranging from 2.5 to 5.2 mm in diameter, each containing between 15 and 30 grains of amphibole and cpx. 5% of Fe-Ti oxides show symplectic textures.
	Plag	21	0.1 - 5.1	
	CPX	12	0.15 - 1.3	
	Oxide	3	0.01 - 0.8	
ADG-5	Amph	44	0.3 - 3.2	Adcumulate texture. Amphibole is euhedral to subhedral and ~ 20% has 0.02 to 0.03 mm thick opaque rims. Plagioclase is anhedral. All cpx have sieve textures and about 20% is skeletal. Fe-Ti oxides are anhedral.
	Plag	37	0.2 - 1.8	
	Cpx	10	0.18 - 1.25	
	Oxide	9	0. 1 - 1	
ADG-CB-6	Plag	48	0.025 - 0.7	Adcumulate texture. About 5% of plagioclase contain inclusions of amphibole or cpx. About 50% of amphibole occurs poikilitically and contain inclusions of Fe-Ti oxides, plag, or cpx. All cpx have partially reabsorbed rims and ~30% are skeletal in form. Small euhedral Fe-Ti oxides (<0.01 - 0.15 mm) occur as poikilitic inclusions in amphibole and larger anhedral oxides (0.075 - 0.4 mm) are seen interstitially.
	Amph	37	0.1 - 1.9	
	Cpx	9	0.075 - 0.2	
	Oxide	6	0.075 - 0.35	
ADG-82-5	Amph	50	0.1 - 1.2	Adcumulate texture. Amphibole is generally elongated. About 60% of plagioclase over 0.8 mm in length occurs poikilitically around small (< 0.25 mm) amphibole. Clinopyroxene shows partially reabsorbed rims. Subhedral Fe-Ti oxides.
	Plag	38	0.07 - 1.3	
	Cpx	6	0.05 - 0.3	
	Oxide	6	0.02 - 0.55	

Table 2: continued

ADG-CB-4	Plag	46	0.07 - 2.25	Mesocumulate texture. Smaller plag (< 0.3mm) is euhedral/subhedral and larger grains are anhedral and intercumulus, often containing inclusions of amphibole and cpx. Small euhedral Fe-Ti oxides (0.025 – 0.075 mm) present as poikilitic inclusions in amphibole and cpx while larger anhedral oxides (0.2 - 1.2 mm) are observed as intercumulus phases.
	Amph	43	0.1 - 2.75	
	Cpx	6	0.08 - 0.45	
	Oxide	5	0.025 - 1.2	
ADG-29	Amph	51	0.3 - 1.1	Adcumulate texture. Slight metamorphic fabric, with elongate plagioclase and amphibole grains consistently aligning along the same plane. Most amphibole (> 90%) has sieve textures and ~50% contain cpx inclusions. Individual plagioclase grains are anhedral and interlocking with one another.
	Plag	39	0.08 - 0.25	
	Cpx	6	0.15 - 0.5	
	Oxide	4	0.08 - 0.4	
ADG-7	Plag	53	0.1 - 3.4	Adcumulate texture. About 40% of amphibole grains have opaque rims between 0.025-0.05 mm thick and 80% have sieve textures. Most oxides (> 95%) are anhedral and > 0.1 mm. Small (0.01-0.02 mm) euhedral oxides present as poikilitic inclusions in plag, amphibole, and cpx.
	Amph	42	0.5 - 9	
	Oxide	4	0.01 - 1	
	Cpx	1	0.2 - 0.4	
Hornblendite				
ADG-26	Amph	93	0.15- 3	Mesocumulate texture. Amphibole < 1.5 mm in length is generally hexagonal, and that > 2 mm across is elongated. Olivine present as poikilitic inclusions in amphibole.
	Cpx	6	0.25 - 0.7	
	Olivine	< 1	0.075 - 0.8	
	Oxide	1	0.01 - 0.02	
ADG-82-18	Amph	98	0.25 - 3.25	Orthocumulate texture. Euhedral hexagonal amphibole. Clinopyroxene and olivine are rare and highly altered when present, with pervasive fracturing and partially reabsorbed rims. Fe-Ti oxides seen interstitially or as inclusions in amphibole.
	Cpx	2	0.2 - 1.3	
	Olivine	<1	0.2 - 0.8	
	Oxide	<1	<0.01	
ADG-52	Amph	82	0.15 - 2.75	Adcumulate texture. Contains both euhedral and poikilitic amphibole. Euhedral amphibole has partially reabsorbed rims and pervasive fracturing, while poikilitic grains are well preserved. Clinopyroxene contains inclusions of spinel. Plagioclase appears only as an intercumulus phase filling void space between amphibole and cpx and does not show distinct grain boundaries
	Cpx	14	0.1 - 1.8	
	Plag	4	--	
	Oxide	<1	0.02	

Table 2: continued

ADG-CB-10	Amph	79	0.1 - 2.5	Mesocumulate texture. Elongate and fractured amphibole with inclusions of cpx. Plagioclase only observed as an intercumulus phase. clinopyroxene has sieve textures. Oxides observed interstitially.
	Plag	11		
	Cpx	9	0.05 - 1.9	
	Oxide	1	0.025 - 0.25	
Moffett				
Olivine clinopyroxenite				
MOF-81X-A	Cpx	64	0.16 - 0.9	Orthocumulate texture. Clinopyroxene contains small inclusions of serpentinized olivine. Cr-spinel occurs interstitially and as poikilitic inclusions in cpx and olivine
	Olivine	36	0.1 - 0.6	
	Oxide	<1	<0.05	
MM-CB-2	CPX	66	0.12- 2.25	Orthocumulate texture. Clinopyroxene >0.25 mm in diameter occurs poikilitically, each containing 3 to ~40 small (>150 μm) inclusions of olivine and distinct cpx. Olivine has serpentinized rims and often occur as inclusions in cpx.
	Olivine	34	0.05 - 0.5	
	Oxide	<1	<0.01	
MOF-81X-C	Cpx	81	0.16- 01.1	Orthocumulate texture. Euhedral to subhedral cpx, often with partially reabsorbed rims. About 60% of cpx have sieve textures. Fe-Ti oxides occur interstitially or as poikilitic inclusions in cpx.
	Olivine	18	0.1 - 0.75	
	Oxide	1	0.12 - 0.04	
Olivine clinopyroxenite (+ amphibole)				
MM-77-67	Amph	48	0.25 - 1.3	Orthocumulate texture. Amphibole occurs both as euhedral inclusion-free grains and against olivine/cpx grain boundaries. Amphibole has 0.05-0.13 mm opaque rims. About 75% of cpx and anhedral and 25% is euhedral. The Euhedral cpx show oscillatory zoning. Olivine and Fe-Ti oxides occur as inclusions in cpx or amphibole.
	Cpx	32	0.125 - 1	
	Olivine	17	0.08 - 0.9	
	Oxide	3	0.02 - 0.08	
MOF-81X-G	Cpx	51	0.17-2.25	Adcumulate texture. Most cpx is highly fractured but those that are not show oscillatory zoning. Clinopyroxene contains inclusions of olivine and Fe-Ti oxides. Most amphibole (~90%) is anhedral and appear as an interstitial phase or poikilitically around cpx or olivine.
	Amph*	33	0.31-7	
	Olivine	16	0.05-0.46	
MM-77-35	Amph	46	0.32 - 1.75	Orthocumulate texture. Amphibole occurs both as euhedral grains without inclusions and poikilitically around 0.1 to 0.25 mm olivine and cpx. Clinopyroxene shows oscillatory zoning and is euhedral to subhedral. All Fe-Ti oxides occur as poikilitic inclusions in cpx or amphibole.
	Cpx	44	0.15 - 1.13	
	Olivine	9	0.075 - 1.25	
	Oxide	1	0.025 - 0.075	

Table 2: continued

Clinopyroxenite				
MM-CB-3	Cpx Olivine Oxide	90 9 1	0.6 - 2.4 1.1 < 0.04	Orthocumulate texture. Euhedral olivine and cpx, about half display sieve texture. Fe-Ti oxides occur interstitially or as poikilitic inclusions in cpx and olivine.
MOF-81X-B	Cpx Olivine Oxide	97 3 <1	0.1 - 1.5 0.07 - 0.12 < 0.02	Orthocumulate texture. Euhedral to subhedral cpx, some with embayed rims. About half of all cpx contain poikilitic inclusions of olivine or small (0.01 – 0.05 mm) oxides.
Amphibole gabbro				
MM-76-4	Plag Amph Cpx Oxide	42 27 21 10	0.25 - 2.4 0.2 - 2.6 0.4 -1.6 0.05 - 0.8	Orthocumulate texture. Subhedral plag. All amphibole has 0.05-0.075 mm thick opaque rims. Skeletal cpx. One grain of skeletal olivine ~1.2 mm in diameter observed. Fe-Ti oxides occur interstitially and as intercumulus phases.
MOF-81X-F	Plag Amph Cpx	68 23 9	0.15 - 1.25 0.17 - 1.3 0.3 - 1.75	Orthocumulate texture. Most amphibole has 0.01-0.025 mm opaque rims. Clinopyroxene is pervasively fractured with partially reabsorbed edges, sometimes showing sieve textures. Fe-Ti oxides are euhedral and observed as inclusion in amphibole.
MOF-81X-D	Plag Amph Cpx Oxide	49 41 7 3	0.2 - 1.2 0.2 - 1.4 0.1 - 0.3 0.025 - 0.3	Orthocumulate texture. Plagioclase often contains poikilitic inclusions of small oxides (< 0.01 mm) or larger (0.05-0.15 mm) grains of amphibole, cpx, or distinct plagioclase. All amphibole has 0.075 to 0.15 mm thick opaque rims. Clinopyroxene shows sieve textures.
MM-76-9	Plag Amph Oxide	55 43 2	0.15 - 0.5 0.25 - 2.5 <0.05	Orthocumulate texture. Plagioclase is euhedral to subhedral. Oxides only observed as poikilitic inclusions in amphibole. Clinopyroxene has experienced almost complete uralitization.
Hornblendite				
MM-77-100	Amph Cpx Plag Olivine	90 4 4 2	0.2 - 1.7 0.1 - 0.5 0.1 - 0.25 0.07 - 0.35	Orthocumulate texture. Plagioclase is equigranular. Clinopyroxene shows sieve textures. Olivine and cpx usually observed as inclusions in amphibole.

Table 2: continued

MM-77-61	Amph	74	0.3 - 3.5	Mesocumulate texture. Amphibole is pervasively fractured and have 0.05 to 0.1 mm thick opaque rims. Clinopyroxene is observed both as small (0.2 to 0.5 mm) euhedral to subhedral zoned grains and as larger (0.75 - 1.5 mm) fractured grains with embayed rims. Euhedral Fe-Ti oxides.
	Cpx	16	0.2 - 1.5	
	Plag	7	0.125 - 1.75	
	Oxide	3	0.025 - 0.1	
MOF-81X-E	Amph	91	0.3 - 11	Orthocumulate texture. Most amphibole has 0.01-0.025 mm thick opaque rims. Clinopyroxene and Fe-Ti oxides only observed as inclusion in amphibole. Clinopyroxene is pervasively fractured and has partially reabsorbed edges, sometimes showing sieve textures. Fe-Ti oxides are euhedral.
	Cpx	5	0.075 - 0.5	
	Oxide	4	0.01-0.075	
MM-77-29	Amph	86	0.25 - 3.75	Mesocumulate texture. About half of all amphibole grains have 0.05 and 0.1 mm thick opaque rims. cpx, opx, and olivine usually observed as poikilitic inclusions in amphibole. Fe-Ti oxides only present as inclusions in amphibole or pyroxene.
	Plag	5	0.2 - 1.3	
	Cpx	5	0.075 - 1.8	
	Opx	3	0.1 - 0.4	
	Oxide	1	0.015	
	Olivine	<1	<0.1	
MM-CB-1	Amph	99	0.1 - 9	Orthocumulate texture. Most amphibole has 0.01 mm thin opaque rims. Cracks in amphibole filled with fine-grained plagioclase and Fe-Ti oxides. Fine to medium-grained plagioclase occasionally fills intercumulus spaces between amphibole grains.
	Plag	1	0.17 - 1	
	Olivine	<1 (n = 1)	0.75	

More detailed descriptions of each sample are given in the Supplemental Data

Amph = amphibole, plag = plagioclase, cpx = clinopyroxene, cpx = orthopyroxene

**Petrography suggests amphibole may be peritectic in nature*

Table 3: Calculated temperature, silica activity, and oxygen fugacity estimates

Sample	Pressure (kbar)		Temperature estimates (˚C)					
	Amphibole-only		***Fe-Mg exchange***				***Ca-in-olivine***	
	R2021		*L1995*		*B1991*		*S&C2013*	
	Ave.	2σ[a]	Ave.	2σ[b]	Ave.	2σ[b]	Ave.	2σ[c]
ADG-82-5	4.77	±0.79						
ADG-CB-4	7.48	±1.89						
ADG-26	6.20	±0.56						
ADG-CB-6	3.94	±0.81						
ADG-5	5.88	±0.73						
ADG-CB-10	6.6	±1.97						
ADG-82-18	9.08	±0.66						
ADG-22a	4.79	±1.24						
ADG-24	4.65	±0.34						
ADG-52	6.41	±0.88						
ADG-CB-1	4.93	±0.78						
ADG-82-15			914	+42/-49	886	±50		
ADG-CB-7			1173	+40/-39	1127	±20	947	+21/-25
ADG-32			1029	+20/-27	1069	±23	965	+23/-10
ADG-82-17							935	+9/-4
ADG-42			1066	+38/-24	1133	±22	946	+19/-20
ADG-CB-5							943	+6/-8
ADG-35			1026	+25/-17	1113	±18	961	±6
ADG-30			1057	+35/-20	1053	±25	968	+12/-29
ADG-CB-3			998	+5/-11	1106	±4	1001	+7/-8
ADG-82-21			1106	+34/-35	1146	±31	923	+13/-15
ADG-63			1049	+28/-22	1060	±17	930	+42/-53
ADG-82-2			1051	+35/-25	1087	±14	990	+46/-52
ADG-CB-9			1080	+27/-23	1101	±25	942	+17/-45
MM-CB-1	6.38	±1.7						
MOF-81X-E	7.33	±1.85						
MM-77-61	6.79	±0.41						
MM-76-4	7.40	±2.65						
MM-77-35	3.90	±0.25					1107	+17/-50
MOF-81X-C							1044	+16/-30
MM-77-67	6.65	±0.38					1106	+8/-35

Table 3: continued

Sample	Temperature estimates (˚C)					
	Ca-in-olivine		***Amphibole-only***		***Amphibole-plagioclase***	
	K&B1990		*R2021*		*H&B1994*	
	Ave.	2σ[c]	Ave.	2σ[d]	Ave.	2σ[e]
ADG-82-5			925	±13	1022	+21/-31
ADG-CB-4			964	±15	996	+22/-23
ADG-26			933	±9		
ADG-CB-6			923	±12	1049	+22/-28
ADG-5			939	±12	917	+52/-43
ADG-CB-10			953	±18	1014	±31
ADG-82-18			968	±24		
ADG-22a			931	±23	1063	+44/-43
ADG-24			929	±12	1074	±23
ADG-52			927	±15		
ADG-CB-1			919	±9	1039	+27/-23
ADG-82-15						
ADG-CB-7	971	+24/-2				
ADG-32	991	+16/-17				
ADG-82-17	971	±4				
ADG-42	997	+11/-31				
ADG-CB-5	993	+48/-7				
ADG-35	978	-20/+23				
ADG-30	977	±4				
ADG-CB-3	1040	±8				
ADG-82-21	961	+19/-22				
ADG-63	1012	+23/-26				
ADG-82-2	944	+15/-26				
ADG-CB-9	936	+15/-16				
MM-CB-1			940	±20		
MOF-81X-E			954	±25		
MM-77-61			951	±11	895	+34/-35
MM-76-4			959	±38	921	+29/-30
MM-77-35	1107	+35/-43	917	±8		
MOF-81X-C	1070	+23/-27				
MM-77-67	1104	+21/-23	963	±16		

Table 3: continued

Sample	Silica activity estimates			Oxygen fugacity estimates								
	log(aSiO₂)			**method A**			**method B**			**method C**		
	B&K2019			*B&K2019*			*B1991*			*D2017*		
	Ave	$2\sigma^f$	ΔEn-Fo	log(fO_2)	$2\sigma^f$	ΔFMQ	log(fO_2)	$2\sigma^f$	ΔFMQ	log(fO_2)	$2\sigma^f$	ΔFMQ
ADG-82-15							-10.15	+0.47/-1.00	1.32			
ADG-CB-7	-0.406	+0.05/-0.11	-0.010	-6.09	+0.42/-0.55	1.76	-6.66	+0.33/-0.52	1.19			
ADG-32	-0.476	+0.15/-0.5	-0.018	-9.09	+0.29/-0.49	0.60	-7.96	+0.27/-0.37	1.73			
ADG-42	-0.441	+0.09/-0.08	0.001	-8.17	+0.63/-0.39	1.02	-7.48	+0.47/-0.32	1.71			
ADG-35	-0.471	±0.03	-0.011	-9.13	+0.46/-0.31	0.61	-8.24	+0.40/-0.16	1.49			
ADG-30	-0.456	+0.05/-0.04	-0.011	-8.54	+0.55/-0.38	0.77	-7.85	+0.44/-0.26	1.46			
ADG-CB-3	-0.521	±0.03	-0.042	-10.10	+0.21/-0.40	0.10	-8.06	+0.05/-0.23	2.14			
ADG-82-21	-0.404	+0.06/-0.05	0.019	-7.15	+0.50/-0.56	1.51	-7.19	+0.41/+0.44	1.48			
ADG-63	-0.444	+0.21/-0.16	0.005	-8.29	+0.39/-0.36	1.13	-7.98	+0.35/-0.28	1.44			
ADG-82-2	-0.431	+0.03/-0.15	0.017	-8.79	+0.54/-0.41	0.60	-7.78	+0.45/-0.33	1.61			
ADG-CB-9	-0.388	+0.15/-0.11	0.047	-7.84	+0.35/-0.56	1.16	-7.71	+0.34/-0.30	1.30	-8.05	+0.43/-0.25	1.02

R2021 Ridolfi, 2021; *L1995* Li et al. (1995); *B1991* Ballhaus et al. (1991); *S&C2013* Shejwalkar and Coogan (2013); *K&B1990* Kohler and Brey (1990); *B&K2019* Bucholz and Kelemen (2019); *D2017* Davis et al. (2017).

[a]Pressure estimates were obtained for each amphibole core analysis. Uncertainties represent 2 standard deviations the range for those calculated pressures per sample.

[b]Uncertainties calculated using average olivine compositions and calculating a different temperature for each core spinel analysis (15-50 per sample).

[c]Uncertainties calculated by varying X_{Mo} to the minimum and maximum values obtained for each sample (for S&C2013, X_{Fo} was fixed to its average value)

[d]Temperature was calculated for each amphibole analysis. Uncertainties represent 2 standard deviations the range for those calculated temperatures per sample.

[e]Uncertainties calculated by fixing the plagioclase composition and calculating a different temperature for each amphibole analysis.

[f]Uncertainties calculated by varying temperatures obtained through olivine-spinel thermometry (L1995) to their maximum and minimum values.

Table 4: Basalt-cpx partition coefficients

Element	K_d	Reference
Rb	0.0035	Klemme *et al.* (2002)
Ba	0.00068	Hart & Dunn (1993)
Th	0.013	Matsui *et al.* (1977)
U	0.017	Matsui *et al.* (1977)
Ta	0.012	Klemme *et al.* (2002)
Nb	0.0077	Hart & Dunn (1993)
La	0.0536	Hart & Dunn (1993)
Ce	0.0858	Hart & Dunn (1993)
Pb	0.0102	Hauri *et al.* (1994)
Pr	0.11	Klemme *et al.* (2002)
Sr	0.1283	Hart & Dunn (1993)
Nd	0.1873	Hart & Dunn (1993)
Zr	0.093	Klemme *et al.* (2002)
Hf	0.170	Klemme *et al.* (2002)
Sm	0.291	Hart & Dunn (1993)
Eu	0.27	Paster *et al.* (1974)
Gd	0.41	Paster *et al.* (1974)
Tb	0.42	Paster *et al*. (1974)
Dy	0.442	Hart & Dunn (1993)
Y	0.467	Hart & Dunn (1993)
Ho	0.44	Paster *et al.* (1974)
Er	0.39	Hart & Dunn (1993)
Yb	0.43	Hart & Dunn (1993)
Lu	0.433	Hart & Dunn (1993)

APPENDIX TO CHAPTER 2

2.12 Analytical methods

Electron microprobe analysis: Counting times for olivine, pyroxene, and spinel analysis were 40 seconds for elements Fe, Ca, K, Mn, Zn, and Ni, 50 seconds for elements Si and Na, and 60 seconds for Al. Elements Mg, Cr, and V were counted for 50 seconds in olivine and pyroxene analyses and for 60 seconds in spinel analyses. Titanium was counted for 60 seconds in olivine and pyroxene and 50 seconds in spinel. Background counting times were half of the peak counting times for Al and equal to peak counting times for Fe, Ca, K, Mn, Zn, and Ni in all olivine, pyroxene, and spinel analyses. A complete description of the standards and electron microprobe conditions is given in Supplemental Data Table S1. Data were reduced with a modified ZAF procedure (CITIZAF, Armstrong, 1995). The detection limits for the olivine, clinopyroxene, amphibole, and plagioclase sessions were: <0.01 wt.% for Si, Al, Mg, Ca, Na, Cr, K, V, and Ti, <0.02 wt.% for Fe, Mn, and Ni, and <0.04 wt.% for Zn.

As described in the main test, separate analytical sessions were conducted for the most primitive xenoliths to measure spinel compositions and the calcium content of olivine. For the spinel session, the detection limits for elements Si, Al, Mg, Ca K, and V were all under 0.01 wt.% and the detection limits Ti, Na, Mn, and Cr were all under 0.02 wt.%. The detection limits for Fe, Zn, and Ni were 0.02, 0.04, and 0.03 wt.%, respectively for these analyses. Except for the lherzolite, application of the Wood and Virgo correction to $Fe^{3+}/\Sigma Fe$ calculations lowered the $Fe^{3+}/\Sigma Fe$ ratio by 0.065 to 0.003. For the lherzolite, the Wood and Virgo correction increased the $Fe^{3+}/\Sigma Fe$ from 0.32 to 0.34. For the Ca in olivine session, the cores of previously analyzed olivine grains were measured only for their calcium content using synthetic anorthite standard P-80, a 10kV accelerating voltage, a 200 nA beam current, and a 10 μm spot size. Ca was measured for a total of 1200 seconds (20 minutes) for each analysis during this session. Calcium was counted for 600 seconds on peak and for 300 seconds on either side of the peak. Four to five of these measurements were made from separate olivine cores for each sample. Analyses focused on the cores of larger olivine grains, at least

500 μm from the rim, to avoid the effects of secondary X-ray fluorescence (Dalton and Lane, 1996). Fifteen to 40 core analyses were typically collected for each measured phase in each sample. Five to 10 analyses were also often collected from the outer 20-70 μm rims of each measured phase.

Laser ablation inductively coupled mass spectrometry (LA-ICP-MS): Variable laser settings were used for each mineral phase, with plagioclase analyses using a spot size and fluence of 65 μm and 5.32 J/cm^2, clinopyroxene analyses using a spot size and fluence of 40 μm and 2.95 J/cm^2, and amphibole analyses using a spot size and fluence of 155 μm and 4.30 J/cm^2. Each laser spot consisted of 300 shots performed at a 10 Hz repetition rate, totaling 30s of ablation. Approximately 10 s of gas background (0.800 L min^{-1} He carrier gas) was collected before each ablation spot, which was then followed by a 25 s washout. NIST 610, 612, and 614 standards were used to construct calibration curves, as well as monitor any drift during analytical sessions, while USGS basalt glasses BCR-2g and BIR-1g were regularly analyzed as unknowns to ensure accuracy (Table S1).

2.13 Sample descriptions—Adagdak xenoliths

ADG-CB-9: Xenolith ADG consists of olivine (77%), clinopyroxene (14%), orthopyroxene (8%), and spinel (1%). The sample has a protogranular texture with interlocking grains of pyroxene and olivine. Olivine ranges from 0.075 to 2.5 mm in diameter, with an average grain size of 0.75 mm. Some degree of serpentinization is observed in olivine grains along their rims. Clinopyroxene ranges from 0.15 to 1.375 mm in diameter, with an average grain size of 0.625 mm. Exsolution lamellae and simple twinning are observed in about 10% of all clinopyroxene. Orthopyroxene typically ranges from 0.25 to 1.2 mm, with an average diameter of 0.65 mm. Spinel is generally very small, between 0.01 and 0.02 mm in diameter, although several larger grains between 0.2 and 0.4 mm in diameter are observed.

ADG-82-2: Xenolith ADG-82-2 has a protogranular texture and consists of olivine (94%), spinel (4%), and clinopyroxene (2%). Olivine ranges from subhedral to anhedral and vary from 0.1 to 2.2 mm in diameter, with an average grain size of 0.6 mm. Spinel ranges from 0.01 to 0.18 mm in

diameter and has an average grain size of 0.02 mm. Most spinel is observed as inclusions in clinopyroxene or olivine, and interstitial oxides are rare. Clinopyroxene is rare but relatively large, ranging from 0.4 to 1.3 mm with an average grain size of 0.5 mm.

ADG-63: Sample ADG-63 is primarily composed of interlocking grains of subhedral to anhedral olivine and has a protogranular texture. The sample is composed of olivine (93%), spinel (4%), and clinopyroxene (3%). Olivine grains are generally subhedral or anhedral and range from 0.1 to 3.25 mm in diameter with an average grain size of 0.8 mm. These grains are generally well preserved, unfractured, and show clearly defined edges. Spinel is observed both interstitially and as poikilitic inclusions in olivine. Spinel ranges from euhedral to anhedral in morphology. About 25% of all spinel grains observed in this sample shows symplectic textures. Spinel ranges from 0.05 to 0.2 mm in diameter and has an average grain size of 0.1 mm. Clinopyroxene grains range from 0.1 to 0.8 mm in diameter and have an average grain size of 0.3 mm. Clinopyroxene is usually subhedral to anhedral and are often fractured.

ADG-82-21: Xenolith ADG-82-21 has a protogranular texture and consists of olivine (93%), clinopyroxene (4%), and spinel (3%). Pervasive fracturing is observed throughout the entire sample. Olivine ranges from 0.1 to 1.25 mm in diameter, with an average grain size of 0.3 mm. Clinopyroxene ranges from 0.15 to 0.8 mm in diameter and has an average grain size of 0.25 mm. Spinel occurs interstitially and ranges from 0.05 to 0.3 mm in diameter, with an average grain size of 0.1 mm. Spinel grains under 0.15 mm are generally euhedral. About half of all spinel crystals over 0.15 mm in diameter are anhedral and the rest are euhedral.

ADG-CB-3: Sample ADG-CB-3 consists of a series of nested xenoliths. The innermost xenolith is a triangular-shaped wehrlite, approximately 3 cm wide at the base with a height of 2 cm, which is composed of olivine (83%), clinopyroxene (14%), and spinel (3%). All mineral chemistry was conducted on this inner-most lithology, which shows an adcumulate texture. Olivine ranges from 0.1 to 0.85 mm in diameter, with an average grain size of 0.4 mm. Clinopyroxene ranges from 1.1 to 0.2 mm in diameter, with an average grain size of 0.3 mm. Spinel ranges from 0.01 to 0.1 mm in

diameter, with an average grain size of 0.025 mm. This innermost xenolith is enclosed by a ~ 7 mm thick amphibole-bearing olivine clinopyroxenite rim that is composed of clinopyroxene (47%), olivine (32%), amphibole (17%), and spinel (2%). Clinopyroxene is subhedral and contains inclusions of olivine and oxides. Clinopyroxene ranges from 0.2 to 1.25 mm in diameter and has an average grain size of 0.7 mm. Olivine is euhedral and shows alteration coronas and pervasive fracturing. Olivine ranges from 0.01 to 0.8 mm in diameter and has an average grain size of 0.12 mm. Amphibole occurs poikilitically, usually containing inclusions of olivine that are between 0.1 and 0.2 mm in diameter. Amphibole ranges from 0.12 to 1.75 mm in diameter, with an average grain size of 0.25 mm. The outer-most rim of the sample is composed of a 5 mm thin section of coarse-grained amphibole. The amphibole contains inclusions of highly altered clinopyroxene, olivine, and oxide phases. The olivine and clinopyroxene inclusions generally range from 0.4 to 0.1 mm in diameter, and the oxides are usually between 0.01 and 0.2 mm across.

ADG-30: Xenolith ADG-30 shows an adcumulate texture and consists of olivine (72%), clinopyroxene (24%), and spinel (4%). Olivine ranges from euhedral to anhedral and is generally well preserved, with clearly defined grain boundaries and a lack of fracturing. Olivine ranges from 0.075 to 1.6 mm in diameter, with an average grain size of 0.4 mm. Clinopyroxene ranges from euhedral to subhedral and is pervasively fractured. About 15% of clinopyroxene has exsolution lamellae and roughly 50% shows some degree of sieve texture. Clinopyroxene ranges from 0.1 to 1.3 mm in diameter, with an average grain size of 0.25 mm. Spinel is observed interstitially and as poikilitic inclusions. Those present as interstitial phases tend to be slightly larger than those seen as poikilitic inclusions (0.05 to 0.18 mm in diameter vs. 0.01 to 0.075 mm in diameter).

ADG-35: Xenolith ADG-35 has an adcumulate texture and is composed of olivine (50%), clinopyroxene (45%), and spinel (5%). Olivine is generally euhedral and slightly serpentinized around the rims. Olivine ranges from 0.12 to 2.1 mm in diameter, with an average grain size of 0.75 mm. Clinopyroxene is subhedral to anhedral and sometimes shows fracturing (50% of grains) or exsolution lamellae (~10% of grains). A few clinopyroxene crystals (~ 20%) show a slight sieve

texture or contain poikilitic inclusions of spinel. Clinopyroxene ranges from 0.1 to 1.8 mm in diameter, with an average grain size of 0.4 mm. Spinel appears interstitially or as poikilitic inclusions in olivine, and generally varies between 0.01 and 0.12 mm in diameter, with an average grain size of 0.08 mm.

ADG-10: Sample ADG-10 has an adcumulate texture and contains clinopyroxene (52%), olivine (48%), and traces of spinel (< 1%). Clinopyroxene ranges from 0.2 to 1.4 mm in diameter and has an average grain size of 0.8 mm. About 70% of clinopyroxene is anhedral and ~ 27% are subhedral. Euhedral clinopyroxene (~ 3% of all grains) is small (generally < 0.3 mm) and often observed as ingrowths in larger olivine crystals. Sieve textures are observed in approximately 15% of all clinopyroxene grains. Olivine has serpentinized rims and ranges from 0.1 to 1.3 mm in diameter with an average grain size of 0.7 mm. Small euhedral olivine (0.1 – 0.2 mm in diameter, ~ 5% of grains) is present interstitially and as inclusions in clinopyroxene. Most olivine is anhedral (~ 65%) or subhedral (~ 30%). Small euhedral spinel is seen interstitially and about 80% are ~ 0.01 mm in diameter. Some larger spinel grains, between 0.02 and 0.1 mm in diameter, are also observed but these are not common (~ 20% of all grains).

ADG-33: Xenolith ADG-33 contains clinopyroxene (53%) and olivine (47%). Pervasive grain fracturing is seen throughout the entirety of the sample. Grains range from subhedral to anhedral and are interlocking, with a protogranular texture. Clinopyroxene ranges from 0.15 to 4.5 mm in diameter, with an average grain size of 0.55 mm. Olivine ranges from 0.1 to 1.75 mm in diameter, with an average grain size of 0.625 mm. No grains in this sample contain poikilitic inclusions or display sieve textures.

ADG-82-3: Sample ADG-82-3 has a protogranular texture and is primarily composed of clinopyroxene (58%) and olivine (42%), with traces of spinel (< 1%). Clinopyroxene ranges from euhedral to subhedral and shows pervasive fracturing. Sieve textures or poikilitic inclusions of olivine and spinel are only observed in larger clinopyroxene grains (> 1 mm in diameter). Clinopyroxene varies from 0.2 to 2.3 mm in diameter, with an average grain size of 0.4 mm. Olivine

ranges from subhedral to anhedral and are generally well-preserved, being relatively free of fractures and with clearly defined grain boundaries. Olivine ranges from 0.05 to 1.5 mm in diameter, with an average grain size of 0.3 mm. Larger olivine grains sometimes contains inclusions of oxides or smaller distinct olivine crystals. Spinel is euhedral and very small, never exceeding 0.05 mm in diameter and usually under 0.01 mm across. Spinel is observed interstitially and as poikilitic inclusions in other phases.

ADG-CB-5: Xenolith ADG-CB-5 has an adcumulate texture and consists of clinopyroxene (58%) and olivine (42%). Traces of oxide phases are also observed, but these account for under 1% of the modal mineralogy. Sieve textures are occasionally observed in clinopyroxene, but this is not a pervasive feature. Clinopyroxene ranges from 0.1 to 6 mm in diameter, with an average grain size of 0.45 mm. Olivine ranges from 0.05 to 1.7 mm in diameter, with an average grain size of 0.3 mm. Larger olivine grains (0.4 to 1.7 mm) are generally subhedral or anhedral, whereas smaller grains (< 0.3 mm) are usually euhedral or subhedral. Larger olivine grains (> 1 mm) often contain smaller olivine inclusions. Oxides are observed interstitially and as poikilitic inclusions, usually under 0.01 mm in diameter and never exceeding 0.05 mm. Because olivine and clinopyroxene tend to occur as clusters/pods within this sample, the modal mineralogy in these phases in thin section may not reflect their proportions in the bulk cumulate.

ADG-42: Xenolith ADG-42 has a protogranular texture and is composed of clinopyroxene (53%), olivine (40%), and spinel (7%). Two massive grains of orthopyroxene (diameters of 3 mm and 1.5 mm) were noted, but these account for well under 1% of the modal mineralogy of the sample. The large orthopyroxene crystals have clinopyroxene ingrowths along their rims and contain poikilitic inclusion of spinel. Clinopyroxene ranges from subhedral to anhedral and is generally between 0.2 and 2 mm in diameter, with an average grain size of 0.6 mm. Olivine grains are usually euhedral and range from 0.1 to 0.8 mm in diameter, with an average grain size of 0.3 mm. Spinel occurs as poikilitic inclusions in pyroxene and ranges from 0.01 to 0.2 mm in diameter, with an average grain size of 0.1 mm. In thin section, this sample contains spinel-dense areas as well as sections that are

nearly devoid of spinel, so the modal mineralogy of spinel in thin section may not reflect that of the bulk cumulate.

ADG-82-17: Sample ADG-82-17 has an adcumulate texture and contains clinopyroxene (62%), olivine (37%), and spinel (~ 1%). Clinopyroxene is subhedral to anhedral and ranges from 0.17 to 2.4 mm in diameter, with an average grain size of 0.6 mm. Smaller olivine (0.1-0.25 mm) is usually euhedral or subhedral but larger olivine (0.25 – 2.1 mm) is anhedral. Neither olivine nor clinopyroxene is significantly altered, with grains being relatively free of fracturing and showing well-preserved crystal edges. Oxides are consistently small and are generally under 0.01 mm in diameter.

ADG-32: Sample ADG-32 consists of several massive clinopyroxene grains (> 10 mm) separated by regions of smaller (usually < 4 mm) interlocking grains of olivine and clinopyroxene. Approximately 68% of the sample is composed of clinopyroxene and 32% consists of olivine. The xenolith has a protogranular texture. Traces of spinel account for less than 1% of the sample. Larger clinopyroxene crystals (those > 10 mm) are euhedral and smaller grains (< 4 mm) are subhedral to anhedral. The largest clinopyroxene in the sample is 19.3 mm in diameter and the smallest is 1.25 mm. About ~ 70% of all olivine is anhedral, ~ 25% are subhedral, and only ~ 5% are euhedral. Olivine grains are well preserved, with clearly defined edges, and are generally unfractured. Olivine ranges from 0.1 to 9.8 mm in diameter, with an average grain size of 0.75 mm. One small triangular-shaped grain, about 2 mm in width and height, of skeletal olivine was noted. Spinel is rare and observed interstitially and as poikilitic inclusions with diameters from 0.6 to 2.1 mm; the average grain size is 1.1 mm. Thin veins of peritectic amphibole are sometimes observed at the interface between olivine and clinopyroxene. Due to the coarse nature of this sample, the modal mineralogy of the thin section itself does not necessarily reflect that of the bulk sample.

ADG-CB-7: Xenolith ADG-CB-7 has a protogranular texture and is composed of clinopyroxene (74%), olivine (25%), and spinel (1%). Clinopyroxene ranges from 0.1 to 1.1 mm in diameter, with an average grain size of 0.7 mm. Olivine is usually euhedral and shows pervasive fracturing. Olivine

ranges from 0.08 to 0.9 mm in diameter, with an average grain size of 0.22 mm. When present, spinel is generally < 0.01 mm in diameter. Traces of peritectic amphibole are observed at some olivine-clinopyroxene interfaces. This amphibole accounts for well under 1% of the modal mineralogy of the sample.

ADG-DR: Sample ADG-DR (Doug's rock) has a protogranular texture and contains clinopyroxene (87%), olivine (13%), and traces of spinel (< 1%). Clinopyroxene grains range from 0.2 to 4.2 mm in diameter with an average grain size of 1.2 mm. About 5% of clinopyroxene shows exsolution lamellae. Clinopyroxene ranges from subhedral to anhedral and sometimes contains small (0.2 – 0.35 mm) rounded olivine inclusions. Olivine is also subhedral to anhedral and range from 0.1 to 2.2 mm in diameter, with an average grain size of 0.7 mm. Spinel is euhedral and seen interstitially, ranging from 0.01 to 0.05 mm in diameter. Olivine tends to occur as pods within an otherwise clinopyroxene-dominated matrix, and as such the modal mineralogy of this thin section does not necessarily reflect that of the bulk sample.

ADG-8: Sample ADG-8 has an adcumulate texture and contains clinopyroxene (88%), olivine (12%), and traces of Fe-Ti oxides (< 1%). Clinopyroxene has pervasive fracturing and ranges from 0.22 to 2.5 mm in diameter, with an average grain size of 0.8 mm. Grains range from subhedral to anhedral. About half of all clinopyroxene has sieve textures. Olivine grains are euhedral to subhedral and range from 0.15 to 0.6 mm in diameter, with an average grain size of 0.35 mm. Most oxides (> 90%) are present as poikilitic inclusions in clinopyroxene and are between 0.01 and 0.03 mm in diameter. Olivine tends to occur as pods within an otherwise clinopyroxene-dominated matrix, and as such the modal mineralogy of this thin section does not necessarily reflect that of the bulk cumulate. Peritectic amphibole is sometimes present at the interface between olivine and clinopyroxene.

ADG-82-1: Xenolith ADG-82-1 consists of clinopyroxene (93%), olivine (6%), and spinel (1%) and has an adcumulate texture. Grains along the rim of the sample (outer 2-6 mm) show sieve textures. Clinopyroxene ranges from 0.1 to 3 mm in diameter, with an average grain size of 0.85 mm. Olivine

is generally euhedral and ranges from 0.1 to 1.2 mm in diameter, with an average grain size of 0.25 mm. Several grains of skeletal olivine are also observed throughout the sample. Small euhedral spinel is only seen interstitially and is usually under 0.01 mm in diameter.

ADG-82-15: Xenolith ADG-82-15 consists of clinopyroxene (94%), olivine (5%), and spinel (1%). The sample is primarily composed of interlocking clinopyroxene crystals and has a protogranular texture. Clinopyroxene is pervasively fractured and subhedral to anhedral in form. These grains sometimes contain inclusions of serpentinized olivine or smaller distinct clinopyroxene crystals. Clinopyroxene ranges from 0.1 to 3.2 mm in diameter, with an average grain size of 0.45 mm. Serpentinized olivine is usually observed as 0.1 – 0.2 mm inclusions in clinopyroxene. One large grain of highly altered, triangular-shaped skeletal olivine with poikilitic inclusions of spinel was noted. The base of this grain was approximately 1 mm wide and it had a height of about 0.75 mm. Small euhedral spinel is observed interstitially throughout the sample and is generally under 0.01 mm in diameter. Small veins of peritectic amphibole are also observed throughout this sample at olivine-clinopyroxene grain boundaries, although they account for <1% of the modal mineralogy of the sample.

ADG-CB-1: Xenolith ADG-CB-1 has an adcumulate texture and consists of clinopyroxene (55%), amphibole (30%), plagioclase (8%), Fe-Ti oxides (5%), and traces of olivine (2%). Clinopyroxene often has embayed rims and sieve textures. Some clinopyroxene contains inclusions of olivine, amphibole, and oxide phases. Clinopyroxene ranges from 0.15 mm to 2.25 mm, with an average grain size of 0.7 mm. Two populations of amphibole are observed in this sample: the first consists of 0.2 to 1.1 mm fractured, euhedral to subhedral grains. The second population consists of larger (2.5-7 mm) unfractured amphibole occurring poikilitically around clinopyroxene, plagioclase, olivine, and distinct euhedral amphibole. Plagioclase is the most well-preserved silicate in the sample and usually occurs as an intercumulus phase. These grains are generally subhedral to anhedral and show exsolution lamellae. Plagioclase ranges from 0.1 to 0.8 mm in diameter, with an average grain size of 0.3 mm. Small (< 1 mm) inclusions of olivine and clinopyroxene are observed in some

plagioclase grains. Many of the smaller oxides (0.01 to 0.1 mm) in this sample are euhedral in form and are observed as poikilitic inclusions in clinopyroxene. Larger oxides (0.15 to 0.6 mm) are generally observed as intercumulus phases and are anhedral in shape. Olivine grains are highly altered, usually occurring as small (0.02-0.25 mm) inclusions in clinopyroxene or amphibole or as larger skeletal phases (0.2-0.75 mm).

ADG-52: Xenolith ADG-52 has an adcumulate texture and is comprised of amphibole (82%) and clinopyroxene (14%), plagioclase (4%), and traces of Fe-Ti oxides (<1%). Amphibole ranges from euhedral to anhedral and is between 0.15 and 2.75 mm in diameter, with an average grain size of 0.9 mm. Clinopyroxene often contains poikilitic inclusions of oxides. Some clinopyroxene also shows sieve textures. Clinopyroxene range from 0.1 to 1.8 mm in diameter, with an average grain size of 0.47 mm. Plagioclase is only observed as an intercumulus phase filling the void space between clinopyroxene and amphibole grains. Oxides are equigranular and about 0.02 mm in diameter.

ADG-77: Sample ADG-77 has a mesocumulate texture and contains amphibole (24%), plagioclase (51%), clinopyroxene (19%), Fe-Ti oxides (3%), and olivine (3%). Amphibole is anhedral, occurs poikilitically, and ranges from 0.4 to 1.7 mm in diameter, with an average grain size of 0.9 mm. Amphibole consistently contains plagioclase ingrowths, and sometimes also contain ingrowths of clinopyroxene or Fe-Ti oxides. Distinct amphibole grains are also seen interfingering with one another. Plagioclase ranges from 0.1 to 1.3 mm in along long axes and is 0.8 mm long on average. Plagioclase grains are subhedral and interlock with one another. Clinopyroxene ranges from 0.2 to 1.4 mm in diameter with an average grain size of 0.75 mm. All clinopyroxene has sieve textures and pervasive fracturing. Most clinopyroxene (> 90%) contains poikilitic inclusions of Fe-Ti oxides and about 35% also contain poikilitic inclusions of amphibole. All clinopyroxene shows some degree of reabsorption along rims. Exsolution lamellae are present in about 60% of all clinopyroxene. Oxides range from 0.2 to 0.45 mm in diameter with an average grain size of 0.15 mm. Oxides are subhedral to anhedral and occur both interstitially and as inclusions in clinopyroxene and amphibole. Size does not correlate with oxide shape or whether the oxide is present interstitially or as an inclusion. The

xenolith also contains several oxides with symplectic textures. Olivine ranges from 0.1 to 0.6 mm in diameter and have an average grain size of 0.3 mm. Olivine over 0.25 mm in diameter is usually skeletal. Small, rounded olivine (0.1 to 0.3 mm in diameter), with serpentinized rims, is seen both interstitially and as inclusions in amphibole and clinopyroxene.

ADG-17: Xenolith ADG-17 has a mesocumulate texture and contains amphibole (29%), plagioclase (51%), clinopyroxene (18%), and Fe-Ti oxides (2%). Amphibole ranges from 0.15 to 8 mm in diameter across long axes. Most (> 90%) amphibole is over 2.25 mm long and contains poikilitic inclusions of oxides, plagioclase, and clinopyroxene. Plagioclase and clinopyroxene inclusions are usually (for 90% of all inclusions) under 0.2 mm in diameter and oxide inclusions are consistently under 0.075 mm in diameter. Sieve textures are pervasive features in amphibole grains between 2 mm and 0.3 mm in length. Small amphibole grains under 0.35 mm in diameter are the most well-preserved and usually do not show sieve textures. Plagioclase appears as an intercumulus phase. These grains are lath-like and range from 0.1 to 0.75 mm in length, with an average length of 0.6 mm. About 75% of all plagioclase grains over 0.3 mm in length have sieve textures. Most plagioclase and clinopyroxene grains have exsolution lamellae. Clinopyroxene ranges from 0.15 to 1.1 mm in diameter, with an average grain size of 0.25 mm. Clinopyroxene has embayed rims and sieve textures. About 90% of all Fe-Ti oxides are anhedral, between 0.1 and 0.25 mm in diameter, and are present interstitially. Smaller euhedral oxides (< 0.1 mm in diameter) are only seen as poikilitic inclusions and account for ~10% of all oxides present. One symplectic oxide, about 0.3 mm in diameter, was noted in the xenolith.

ADG-24: Sample ADG-24 has a mesocumulate texture and contains plagioclase (43%), amphibole (38%), clinopyroxene (12%), Fe-Ti oxides (4%), and olivine (3%). Plagioclase ranges from 0.25 to 4.7 mm in diameter across longest axes, with an average length of 0.7 mm. Larger plagioclase grains (> 0.4 mm) are anhedral and smaller grains are euhedral to subhedral. Amphibole ranges from 0.3 to 5 mm in diameter and has an average grain size of 0.8 mm. About 40% of amphibole between 1.25 and 3 mm in diameter has sieve textures, embayed rims, and ingrowths of plagioclase along

rims. Amphibole under 1.25 mm is generally euhedral and well-preserved. About half of all amphibole grains over 3 mm occur poikilitically and contain inclusions of plagioclase, clinopyroxene, and olivine. Clinopyroxene ranges from 0.2 to 3 mm in diameter and has an average grain size of 0.8 mm. Clinopyroxene consistently has embayed rims and sieve textures, and most (> 60%) contains inclusions of Fe-Ti oxides, amphibole, and or/plagioclase. Euhedral oxides are present as poikilitic inclusions in other phases and range from 0.075 to 0.15 mm in diameter, with an average grain size of 0.1 mm. Anhedral oxides range from 0.1 to 0.7 mm in diameter, with an average grain size of 0.3 mm, and are present as intercumulus phases. Olivine grains range from 0.1 to 1.1 mm in diameter and have an average grain size of 0.5 mm.

ADG-22a: Xenolith ADG-22a has a mesocumulate texture and contains plagioclase (40%), amphibole (39%), clinopyroxene (15%), Fe-Ti oxides (4%), and olivine (2%). Plagioclase grains are equant and subhedral, ranging from 0.2 to 8 mm in diameter across the longest axis, with an average grain size of 1.7 mm. Amphibole occurs poikilitically, enclosing large (0.25 – 1.5 mm) grains of plagioclase and clinopyroxene as well as distinct amphibole crystals. Poikilitic amphibole ranges from 9 mm to 1.5 cm in diameter, but 40-70% of its area is occupied by other phases and these grains do not show distinct grain boundaries. Approximately 20% of all clinopyroxene is skeletal. Clinopyroxene ranges from 0.3 to 2.75 mm in diameter and has an average grain size of 1.6 mm. Oxides range from 0.02 to 0.6 mm in diameter and have an average grain size of 0.06 mm. Oxides under 0.25 mm in diameter are euhedral whereas most grains between 0.25 and 0.6 mm in diameter are subhedral or anhedral. Most oxides (~60% of all grains) occur as inclusions in clinopyroxene. Olivine ranges from 0.25 to 1.2 mm in diameter, although most (~ 90%) are under 0.6 mm.

ADG-73: Xenolith ADG-73 has an adcumulate texture and contains amphibole (42%), plagioclase (41%), clinopyroxene (12%), Fe-Ti oxides (3%), and olivine (2%). Amphibole is anhedral and ranges from 0.3 to 1.9 mm in diameter, with an average grain size of 1.2 mm. Amphibole shows embayed rims and pervasive grain fracturing. Most amphibole (> 80%) is poikilitic, containing inclusions of oxides, plagioclase, olivine, and especially clinopyroxene. Plagioclase is subhedral and

about 85% has sieve textures. A few plagioclase grains (~ 5%) contain poikilitic inclusions of very small oxides (< 0.01 mm) or amphibole (0.02 - 0.06 mm). The lengths of plagioclase laths range from 0.2 to 1.3 mm in length and are 0.5 mm long on average. The widths of plagioclase laths range from 0.07 to 0.3 mm and are 0.15 mm wide on average. Clinopyroxene ranges from 0.2 to 1.3 mm in diameter with an average grain size of 0.5 mm. About 30% of all clinopyroxene over 1 mm in diameter is skeletal. Larger clinopyroxene is also more likely to contain poikilitic oxide inclusions. Fe-Ti oxides are present as inclusions and between 0.03 and 0.1 mm in diameter. About 70% of all clinopyroxene grains with oxide inclusions only contain euhedral oxides and ~ 30% only contain anhedral oxides; no clinopyroxene contains both euhedral and anhedral oxides. Four clinopyroxene crystals between 0.8 and 1.75 mm in diameter were noted that contain poikilitic inclusions of amphibole between 0.01 and 0.07 mm in diameter. About 40% of all clinopyroxene has 0.2-0.5 mm thick amphibole rims. Texturally, these rims are consistent with either late-stage amphibole growth or amphibole forming through peritectic reactions between percolating melts and clinopyroxene. Oxides are present both interstitially and as poikilitic inclusions throughout the sample. Smaller oxides (0.03 – 0.05 mm) were consistently euhedral and larger oxides (up to 0.6 mm) were both euhedral and anhedral. A few oxides with symplectic texture were noted. Olivine is usually (~70% of all grains) seen interstitially but is also present as inclusions in amphibole. Olivine ranges from 0.1 to 0.35 mm in diameter with an average grain size of 0.15 mm. Olivine is generally small, rounded, and slightly serpentinized along rims.

ADG-19: Sample ADG-19 has a mesocumulate texture and consists of amphibole (41%), plagioclase (40%), clinopyroxene (12%), Fe-Ti oxides (5%), and olivine (2%). Amphibole grains range from 0.1 to 2.3 mm in diameter, although most grains (~80%) are over 0.5 mm in diameter and the average grain size is 0.75 mm. Most amphibole grains are hexagonal and equant (~ 70%) but some are elongate (~ 30%). Grain morphology does not correlate with grain size. Most (~ 80%) amphibole shows sieve textures and many (~ 60%) contain inclusions of plagioclase and/or clinopyroxene. Elongate amphibole usually contains plagioclase ingrowths along rims. Plagioclase grains range from 0.1 to 2.1 mm in diameter, with an average grain size of 0.8 mm. Clinopyroxene

ranges from 0.1 to 2.1 mm in diameter and has an average grain size of 0.6 mm. All clinopyroxene shows pervasive sieve textures, embayed rims, and fractures. Fe-Ti oxides range from 0.05 to 0.5 mm in diameter and have an average grain size of 0.1 mm. The sample contains roughly equal amounts of euhedral and anhedral oxides. Most anhedral oxides are over 0.12 mm in diameter and appear as an intercumulus phase, whereas euhedral oxides are primarily observed as poikilitic inclusions. Olivine is rare; when present it is seen as small grains with embayed edges between 0.15 and 0.3 mm in diameter. Olivine is observed both interstitially and as inclusions in amphibole and clinopyroxene. Amphibole tends to occur in clusters/pods, and so the modal mineralogy of amphibole in thin section may not reflect that of the bulk cumulate.

ADG-82-6: Sample ADG-82-6 has a mesocumulate texture and consists of amphibole (39%), plagioclase (26%), clinopyroxene (30%) Fe-Ti oxides (4%), and olivine (1%). Amphibole occurs as an intercumulus phase or poikilitically and does not show distinct grain boundaries. Poikilitic amphibole contains inclusions of larger (0.1 - 0.4 mm) grains of plagioclase, clinopyroxene, and olivine, as well as distinct euhedral amphibole crystals. The most common inclusion in amphibole is clinopyroxene. It is texturally inconclusive whether amphibole represents a late-stage cumulate phase for this sample or was produced by peritectic reactions as melts percolated through a clinopyroxene cumulate mush. Plagioclase is generally well-preserved, and grains are subhedral to anhedral in form. Plagioclase laths are elongated and range from 0.01 to 0.8 mm in length, with an average length of 0.35 mm. Clinopyroxene is very altered, with all grains showing pervasive fracturing, sieve textures, and embayed edges. Most (> 65%) clinopyroxene contains poikilitic inclusions of Fe-Ti oxides. Clinopyroxene ranges from 0.2 to 0.7 mm in diameter and has an average grain size of 0.3 mm. About 20% of all clinopyroxene occurs as inclusions in amphibole. Oxides present as poikilitic inclusions are euhedral and range from 0.02 to 0.1 mm in diameter with an average grain size of 0.08 mm. Interstitial oxides are larger and anhedral, reaching up to 0.2 mm in diameter. Most olivine (~ 80%) is observed as inclusions in amphibole. These grains are small with embayed rims and range from 0.15 to 0.3 mm in diameter, with an average grain size of 0.2 mm.

Amphibole tend to occur in clusters/pods, and so the modal mineralogy of amphibole in thin section may not reflect that of the bulk sample.

ADG-82-18: Sample ADG-82-18 has an orthocumulate texture and is comprised of amphibole (98%) with traces of clinopyroxene (~2%), olivine (< 1%), and traces of Fe-Ti oxides (< 1%). Amphibole grains are slightly altered along their cleavage planes and show pervasive fracturing and embayed edges. Most amphibole (~ 80% of all grains) is between 0.25 and 2 mm in diameter across longest axes, with an average length of 1.2 mm. Smaller amphibole grains (< 1 mm in diameter) are often hexagonal, while larger grains tend to be more elongated in morphology. The largest grain observed in this sample is 3.25 mm long and 1.2 mm wide. The few clinopyroxene grains observed in the sample vary greatly in size and morphology, varying from euhedral to subhedral and ranging from 0.2 to 1.3 mm in diameter. Olivine is generally euhedral and ranges from 0.2 to 0.8 mm in diameter, with an average grain size of 0.35 mm. Traces of very small oxides, never exceeding 0.01 mm in diameter, are observed interstitially and as poikilitic inclusions in amphibole.

ADG-38: Sample ADG-38 has a mesocumulate texture and contains plagioclase (44%), amphibole (37%), clinopyroxene (14%), Fe-Ti oxides (4%), and traces of olivine (~ 1%). Plagioclase is lath-like and almost all laths (> 95%) have sieve textures. Grain lengths vary from 0.2 to 0.9 mm and are 0.4 mm on average. Plagioclase widths vary from 0.05 to 0.25 mm and are 0.1 mm on average. Amphibole is slightly altered along cleavage planes, with pervasive fracturing and embayed rims. All amphibole is anhedral and most (~ 70%) is poikilitic. Poikilitic amphibole shows pervasive plagioclase ingrowths around the edges and contains inclusions of Fe-Ti oxides, plagioclase, clinopyroxene, and olivine. Clinopyroxene ranges from 0.2 to 1.1 mm in diameter and has an average grain size of 0.6 mm. Most clinopyroxene shows exsolution lamellae. About 70% of clinopyroxene grains display 0.2-0.5 mm thick rims of amphibole, suggesting that some amphibole in this sample may be peritectic in origin. Oxides show a great diversity of sizes and morphologies, and range from 0.01 to 0.3 mm in diameter, with an average grain size of 0.12 mm. About 20% of all oxides have symplectic textures. Grains under 0.08 mm are always euhedral, while larger grains (0.08-0.3 mm)

are about half anhedral and half euhedral. Most olivine forms small, rounded grains between 0.1 and 0.2 mm in diameter, primarily present as inclusions in amphibole. Only one larger olivine grain was observed in this sample. This grain was ~ 0.75 mm in diameter and fractured, with small amphibole crystals and oxide symplectites filling the cracks.

ADG-6: Sample ADG-6 has a mesocumulate texture and contains amphibole (56%), plagioclase (28%), clinopyroxene (11%), Fe-Ti oxides (4%), and olivine (1%). Amphibole ranges from 0.25 to 3.2 mm in diameter along longest axes and is 1.3 mm long on average, ranging from euhedral to subhedral. Most (> 90%) amphibole contains plagioclase ingrowths along rims. Plagioclase appears to be an intercumulus phase, often present as ingrowths in other phases. Plagioclase grains are the most well-preserved in the sample, usually free of fracturing or reaction rims. Plagioclase is lath-like and ranges from 0.2 to 1.25 mm long and 0.05 to 0.2 mm wide, with average lengths and widths of 0.8 and 0.1 mm, respectively. Clinopyroxene ranges from 0.1 to 1.1 mm in diameter and has an average grain size of 0.8 mm. Smaller clinopyroxene, between 0.1 and 0.25 mm in diameter, is only present as inclusions in amphibole. Larger clinopyroxene often contains inclusions of Fe-Ti oxides or small (0.1-0.2 mm), rounded olivine grains. One clinopyroxene containing poikilitic inclusions of amphibole was noted in the sample. This clinopyroxene was 0.9 mm in diameter and was rimmed by ingrowths of anhedral oxides. Exsolution lamellae are seen in about 30% of clinopyroxene crystals. Oxides range from 0.02 to 0.9 mm in diameter. Larger oxides (> 0.25 mm) are subhedral to anhedral are appear as intercumulus phases or as ingrowths in clinopyroxene or amphibole rims. Smaller euhedral oxides (0.02-0.2 mm) are usually observed as inclusions in clinopyroxene and amphibole. Olivine is present both interstitially and as inclusions in clinopyroxene and amphibole. Olivine ranges from 0.075 to 1 mm in diameter, with an average grain size of 0.2 mm.

ADG-CB-2: Sample ADG-CB-2 has a mesocumulate texture and contains amphibole (64%), plagioclase (21%), clinopyroxene (12%), and Fe-Ti oxides (3%). Amphibole ranges from 0.25 to 4.9 mm in diameter across longest axes, with an average length of 0.9 mm. Some amphibole grains (~20%) contains inclusions of smaller, distinct amphibole grains or clinopyroxene. Amphibole range

from subhedral to euhedral. About 30% of all amphibole grains have sieve textures and this feature is most prevalent in larger grains (diameter > 0.75 mm). Two amphibole crystals (1.6 and 2.2 mm across) contain rounded olivine inclusions between 0.1 and 0.25 mm across. This was the only instance in which olivine was observed in this sample. Plagioclase is present as an intercumulus phase and grains range from 0.1 to 5.1 mm in diameter, with an average grain size of 0.4 mm. Twelve large poikilitic grains of plagioclase were noted in this sample, ranging from 2.5 to 5.2 mm in diameter. Each of these crystals contained between 15 and 30 grains of amphibole and clinopyroxene. The amphibole inclusions were euhedral and ranged from 0.1 to 0.4 mm in length and the clinopyroxene inclusions were fractured with partially reabsorbed edges and ranged from 0.075 to 0.2 mm in diameter. Clinopyroxene containing poikilitic inclusions of Fe-Ti oxides was also noted. Clinopyroxene ranges from 0.15 to 1.3 mm in diameter, with an average grain size of 0.55 mm. Fe-Ti oxides range from 0.01 to 0.8 mm in diameter, with an average grain size of 0.18 mm. Most (> 95%) Fe-Ti oxides are under 0.4 mm. Small oxides (0.02 – 0.075 mm) are usually euhedral and larger oxides (> 0.1 mm) are usually anhedral. Fe-Ti oxides with symplectic textures are noted but account for less than 5% of all oxides.

ADG-CB-10: Xenolith ADG-CB-10 has a mesocumulate texture and contains amphibole (79%), plagioclase (11%), clinopyroxene (9%), and Fe-Ti oxides (1%). Amphibole is elongated and often contain inclusions of clinopyroxene. Amphibole ranges from 0.1 to 2.5 mm in length, with an average length of 0.35 mm. Plagioclase is only observed as an intercumulus phase, filling irregularly-shaped void spaces between amphibole and clinopyroxene, making it difficult to discern individual grain boundaries. Clinopyroxene ranges from 0.05 to 1.9 mm in diameter, with an average grain size of 0.25 mm. Oxides are observed interstitially and range from 0.025 to 0.25 mm in diameter, with an average grain size of 0.06 mm.

ADG-5: Sample ADG-5 has an adcumulate texture and consists of amphibole (44%), plagioclase (37%), clinopyroxene (10%), and Fe-Ti oxides (9%). Amphibole ranges from 0.3 to 3.2 mm in diameter across longest axes and has an average grain size of 1.1 mm. A few amphibole crystals (<

20%) have 0.02 to 0.03 thick opaque rims. Plagioclase is subhedral to anhedral and ranges from 0.2 to 1.8 mm in diameter with an average grain size of 0.6 mm. Clinopyroxene ranges from 0.18 to 1.25 mm in diameter, with an average grain size of 0.5 mm. Clinopyroxene is very altered, with pervasive fracturing and embayed rims. All clinopyroxene has sieve textures and about 20% is skeletal in form. Oxides are anhedral and range from 0.1 to 1 mm in diameter, with an average grain size of 0.2 mm.

ADG-CB-6: Xenolith ADG-CB-6 has an adcumulate texture and is composed of plagioclase (48%), amphibole (37%), clinopyroxene (9%), and Fe-Ti oxides (6%). Plagioclase grains range from euhedral to subhedral and vary from 0.7 to 0.025 mm in diameter, with an average grain size of 0.3 mm. Plagioclase is generally well preserved and shows exsolution lamellae. Plagioclase occasionally (< 5% of all grains) contain inclusions of amphibole or clinopyroxene, but this is not a pervasive feature. Approximately half of all amphibole grains occur poikilitically and contain inclusions of oxides, plagioclase, or clinopyroxene. About a quarter of all amphibole grains show sieve textures. Amphibole grains range from 0.1 to 1.9 mm in diameter, with an average grain size of 0.65 mm. All clinopyroxene has partially resorbed rims and about 30% is skeletal in form. Clinopyroxene range from 0.075 to 0.2 mm in diameter, with an average grain size of 0.1 mm. Two populations of oxides are observed in this xenolith: (1) small euhedral oxides occurring as poikilitic inclusions in amphibole, which range from < 0.01 to 0.15 mm in diameter and have an average grain size of 0.05 mm, and (2) interstitial anhedral oxides ranging from 0.075 to 0.4 mm in diameter, with an average grain size of 0.25 mm.

ADG-74: Sample ADG-74 has an adcumulate texture and consists of plagioclase (48%), amphibole (41%), clinopyroxene (8%), Fe-Ti oxides (3%), and traces of olivine (< 1%). Amphibole ranges from 0.2 to 1.8 mm in diameter with an average grain size of 0.85 mm. Amphibole under 0.4 mm is generally hexagonal and euhedral. Larger amphibole (0.4 - 1.8 mm) is anhedral and occurs poikilitically, containing inclusions of clinopyroxene, plagioclase, Fe-Ti oxides, and olivine. Poikilitic amphibole also has plagioclase ingrowths along the margins. Plagioclase laths are euhedral

to subhedral and range from 0.08 to 1 mm in diameter along their longest axis, with an average grain size of 0.2 mm. About 70% of all plagioclase have sieve textures. Clinopyroxene is euhedral to subhedral and ranges from 0.15 to 0.8 mm in diameter, with an average grain size of 0.3 mm. Clinopyroxene often contains poikilitic inclusions of Fe-Ti oxides and about 20% of grains have sieve textures. Fe-Ti oxides range from 0.01 to 0.25 mm in diameter. Oxides between 0.1 and 0.12 mm are usually euhedral and present as inclusions in other phases. Anhedral oxides range from 0.05 to 0.25 mm and are seen interstitially. Small, rounded olivine grains are sometimes seen as inclusions in amphibole and range from 0.1 to 0.4 mm in diameter with an average grain size of 0.2 mm.

ADG-26: Sample ADG-26 has a mesocumulate texture and contains amphibole (93%), clinopyroxene (6%), and traces of olivine (< 1%) and Fe-Ti oxides (1%). Amphibole has embayed rims and is slightly fractured. Sieve textures are rare in amphibole (present in < 5% of all grains). Amphibole ranges from 0.15 to 3 mm in diameter across longest axes and is 1.2 mm on average. Amphibole under 1.5 mm is generally equant and hexagonal, while that over 2 mm in length tends to be elongate and often contains ingrowths of clinopyroxene or distinct, smaller amphibole crystals. Clinopyroxene are mostly subhedral (~ 80% of all grains) and ranges from 0.25 to 0.7 mm in diameter, with an average grain size of 0.45 mm. Olivine with serpentinized rims ranges from 0.075 to 0.8 mm in diameter. Most (~ 90%) olivine is euhedral and between 0.075 and 0.15 mm across. About 40% of all olivine in the sample is observed as inclusions in amphibole. Traces of small euhedral Fe-Ti oxides, between 0.01 and 0.02 mm in diameter, are also observed in this sample.

ADG-CB-4: Xenolith ADG-CB-4 is fine to medium-grained with a mesocumulate texture and contains plagioclase (46%), amphibole (43%), clinopyroxene (6%), and Fe-Ti oxides (5%). Plagioclase is the most well-preserved phase in the sample. Smaller plagioclase grains (0.07 – 0.3 mm in diameter) are usually euhedral to subhedral. Larger plagioclase laths are usually (~70% of all grains) anhedral and appear as intercumulus phases. These intercumulus grains often contain poikilitic inclusions of amphibole or clinopyroxene. Plagioclase ranges from 0.07 to 2.25 mm in diameter with an average grain size of 0.4 mm. Amphibole generally occurs poikilitically around

Fe-Ti oxides, clinopyroxene, or smaller amphibole grains. These grains range from 0.1 to 2.75 mm in size, with an average diameter of 0.5 mm. Clinopyroxene has sieve textures and partially reabsorbed edges. Most clinopyroxene contains poikilitic inclusions of oxides. A few skeletal clinopyroxene grains are also observed. Clinopyroxene varies from 0.08 to 0.45 mm in diameter, with an average grain size of 0.3. Two populations of oxide phases are observed in this sample. Small, euhedral oxides are seen as poikilitic inclusions in amphibole and clinopyroxene, which range from 0.025 to 0.075 mm in diameter. Larger anhedral oxides are also observed as an intercumulus phase, which ranges from 0.2 to 1.2 mm in diameter.

ADG-29: Sample ADG-29 contains amphibole (51%), plagioclase (39%), clinopyroxene (6%), and Fe-Ti oxides (4%). The xenolith has an adcumulate texture and a slight metamorphic fabric, with elongated plagioclase and amphibole grains consistently aligning along the same plane. Amphibole is consistently elongated in form and the majority (> 80%) of crystals are between 0.3 and 1.1 mm in length and 0.1 to 0.2 mm in width. The longest amphibole in the sample is 8 mm long and 0.4 mm wide. Clinopyroxene ranges from 0.07 to 0.15 mm in diameter. Plagioclase ranges from 0.08 to 0.25 mm in length along longest axes. Individual plagioclase grains are anhedral and interlocking with one another. Clinopyroxene is present both as inclusions in amphibole and interstitially. Interstitial clinopyroxene ranges from 0.15 to 0.5 mm in diameter, with an average grain size of 0.3 mm. Oxides are anhedral and range from 0.08 to 0.4 mm in diameter, with an average grain size of 0.12 mm.

ADG-82-5: Xenolith ADG-82-5 consists of amphibole (50%), plagioclase (38%), clinopyroxene (6%), and Fe-Ti oxides (6%). The sample has an adcumulate texture. Amphibole is elongate and has embayed rims. Amphibole varies from 0.1 to 1.2 mm in length, with an average length of 0.5 mm. About 60% of all plagioclase laths over 0.8 mm in diameter occur poikilitically around small (< 0.25 mm) amphibole inclusions. Plagioclase grains often show exsolution lamellae or simple twinning. Plagioclase ranges from 0.07 to 1.3 mm in diameter and has an average grain size of 0.3 mm. Clinopyroxene is pervasively fractured and often has partially reabsorbed rims. Clinopyroxene ranges from 0.05 to 0.3 mm in diameter, with an average grain size of 0.1 mm. Oxides are usually

subhedral and range from 0.02 to 0.55 mm across, with an average diameter of 0.12 mm. Amphibole tends to occur in clusters/pods, and so the modal mineralogy of amphibole in thin section may not reflect that of the bulk cumulate.

ADG-4: Sample ADG-4 has a mesocumulate texture and contains amphibole (49%), plagioclase (43%), clinopyroxene (5%), Fe-Ti oxides (3%), and traces of olivine (< 1%). Amphibole is either poikilitic or forms rims around other phases, particularly clinopyroxene. About 60% of all amphibole grains have sieve textures. Plagioclase laths are elongated in form; grain lengths range from 0.17 to 2.1 mm and are 0.45 mm on average. Plagioclase grains are subhedral to anhedral in form. Clinopyroxene ranges from 0.1 to 1.1 mm in diameter and has an average grain size of 0.3 mm. Clinopyroxene consistently shows embayed rims, sieve textures, and pervasive fracturing. Most clinopyroxene (> 90%) contains poikilitic inclusions of smaller (0.2 – 0.1 mm) euhedral Fe-Ti oxides. About 40% of clinopyroxene shows exsolution lamellae. Most clinopyroxene (~80%) has 0.1-0.3 mm amphibole rims. These rims may reflect late-stage cumulate amphibole growth, following clinopyroxene saturation, or amphibole growth from peritectic reactions between relict pyroxene and melts percolating through a cumulate pile. Two populations of Fe-Ti oxides are present in this sample, the first being small (0.01 – 0.05 mm diameter), euhedral, and usually present as poikilitic inclusions in clinopyroxene or amphibole. The second group consists of larger (0.25 – 0.7 mm diameter) anhedral oxides that are usually seen interstitially. Small, rounded olivine grains with serpentinized rims, usually between 0.15 and 0.3 mm in diameter, are present in trace amounts and observed both interstitially and as inclusions in amphibole.

ADG-7: Sample ADG-7 has an adcumulate texture and consists of plagioclase (53%), amphibole (42%), Fe-Ti oxides (4%) and clinopyroxene (~ 1%). Plagioclase ranges from 0.1 to 3.4 mm in diameter, with an average grain size of 1.3 mm. Small plagioclase grains between 0.1 and 0.2 mm in diameter occur interstitially, filling the spaces between larger plagioclase and amphibole grains, or as inclusions. Most (> 85%) plagioclase is subhedral to anhedral in form. Grain fracturing is a pervasive feature in plagioclase. Amphibole is elongated and ranges from 0.5 to 9 mm in length,

with an average length of 2.3 mm. Most amphibole (> 70%) has pale reaction rims between 0.025 and 0.15 mm thick. About 40% of amphibole also shows opaque rims between 0.025 and 0.05 mm thick. Sieve textures are seen in approximately 80% of amphibole grains. Oxides range from 0.01 to 1 mm in diameter and have an average grain size of 0.25 mm. Most oxides (> 95%) are anhedral and over 0.1 mm in diameter. Very small euhedral oxides between 0.01 and 0.02 mm in diameter are present as poikilitic inclusions in plagioclase, amphibole, and clinopyroxene. Clinopyroxene is highly altered, often skeletal in form, with pervasive fracturing and embayed rims. These grains are usually between 0.2 and 0.4 mm in diameter.

2.14 Sample descriptions—Moffett xenoliths

MOF-81X-A: Xenolith MOF-81X-A has an orthocumulate texture and consists of clinopyroxene (64%), olivine (36%), and traces of Cr-spinel (< 1%). The xenolith is fine-to-medium-grained and primarily composed of subhedral grains, although a few are euhedral in form. Clinopyroxene ranges from 0.16 to 0.9 mm in diameter, with an average grain size of 0.4 mm. Olivine varies from 0.1 to 0.6 mm in diameter, with an average grain size of 0.25 mm. Small grains of serpentinized olivine are also observed as inclusions within large clinopyroxene crystals. Oxides occur interstitially and as poikilitic inclusions within clinopyroxene and olivine. Cr-spinel is generally under 0.05 mm across, except one grain which was noted with a diameter of 0.12 mm. Very fine-grained plagioclase is present only as an intercumulus phase near the periphery of the xenolith, and its interface with the volcanic groundmass, this plagioclase often displays a variolitic texture and is not interpreted to be part of the primary cumulate mineralogy. The xenolith is enclosed in a matrix of microlitic plagioclase containing phenocrysts of serpentinized olivine, skeletal amphibole, and clinopyroxene, and large plagioclase grains with oscillatory zoning.

MM-CB-2: Sample MM-CB-2 consists of a small xenolith, approximately 2.5 cm in diameter, surrounded by a matrix of microlitic plagioclase, pyroxene, and amphibole. The xenolith has an orthocumulate texture and is composed of clinopyroxene (66%), olivine (34%), and traces of Cr-spinel. Clinopyroxene shows embayed rims and is between 0.12 and 2.25 mm in diameter, with an

average grain size of 0.25 mm. Clinopyroxene over 0.25 mm in diameter occurs poikilitically, each containing between 3 and ~40 small (>150 μm) inclusions of olivine and distinct clinopyroxene crystals. Olivine has serpentinized rims and often occurs as inclusions in clinopyroxene. Olivine ranges from 0.05 to 0.5 mm in diameter, with an average grain size of 0.15 mm. The intercumulus space between grains along the rim of the xenolith is filled with fine-grained plagioclase (0.08 - 0.12 mm), which is not interpreted to be part of the primary cumulate mineralogy. Traces of small Cr-spinel, generally under 0.01 mm, are also observed as intercumulus phases.

MOF-81X-C: Sample MOF-81X-C consists of a fine-to-medium-grained xenolith surrounded by a microlitic matrix of plagioclase, clinopyroxene, and olivine. The xenolith has an orthocumulate texture and contains clinopyroxene (81%), olivine (18%), and Fe-Ti oxides (1%). Clinopyroxene is euhedral to subhedral and often (~70% of all grains) shows embayed edges. Some clinopyroxene also has sieve textures (~60% of all grains) or simple twinning (~25% of all grains). Clinopyroxene ranges from 0.16 to 1.1 mm in diameter and has an average grain size of 0.5 mm. Olivine grains have serpentinized rims and range from 0.1 to 0.75 mm in diameter, with an average grain size of 0.15 mm. Oxide phases occur interstitially or as poikilitic inclusions in clinopyroxene and range from 0.12 to 0.04 mm across, with an average diameter of 0.08 mm. Plagioclase is observed only in the surrounding groundmass and does not appear to be part of the primary cumulate mineralogy. Plagioclase grains have an average diameter of 0.075 mm.

MM-77-67: Xenolith MM-77-67 has an orthocumulate texture and is approximately 4 × 2 cm in size. The sample consists of amphibole (48%), clinopyroxene (32%), olivine (17%), and Cr-spinel (3%). Amphibole has 0.05-0.125 mm thick opaque rims surrounding all grains and ranges from 0.25 to 1.3 mm in diameter, with an average grain size of 0.625 mm. Most clinopyroxene (~ 75%) is subhedral or anhedral although some grains (~ 25%) are euhedral. The anhedral amphibole generally grew up against olivine or clinopyroxene grain boundaries, although they do not form rims around olivine and clinopyroxene, as is observed for peritectic amphibole. Texturally, amphibole appears to have saturated at the same time, or perhaps slightly after, clinopyroxene and olivine. Clinopyroxene

ranges from 0.125 to 1 mm across, with an average diameter of 0.4 mm. Euhedral clinopyroxene has oscillatory zoning. Exsolution lamellae are also seen in ~ 30% of all clinopyroxene grains. Olivine has serpentinized rims and often occurs as inclusions in clinopyroxene or amphibole. Olivine grains are subhedral to euhedral, and range from 0.08 to 0.9 mm in diameter, with an average grain size of 0.35 mm. A few skeletal olivine crystals are also observed in this sample. Oxides primarily occur as poikilitic inclusions in clinopyroxene or amphibole, and range from 0.02 to 0.08 mm in size, with an average grain size of 0.03 mm. MM-77-67 contains a significant amount of groundmass along the xenoliths' periphery, consisting of fine-grained plagioclase. These plagioclase grains are lath-like and range from 0.05 to 0.15 mm in length and are not interpreted to be part of the primary cumulate mineralogy.

MOF-81X-G: Sample MOF-81X-G consists of a 2 × 3 cm xenolith surrounded by a microcrystalline matrix with small phenocrysts of plagioclase, clinopyroxene, and amphibole. The xenolith has an adcumulate texture and contains clinopyroxene (51%), amphibole (33%), and olivine (16%). Most clinopyroxene grains are highly fractured and display sieve textures, although several less altered euhedral to subhedral grains are also observed. Clinopyroxene with less fracturing typically displays exsolution lamellae and oscillatory zoning. Clinopyroxene ranges from 0.17 to 2.25 mm in diameter, with an average grain size of 0.53 mm. Amphibole is generally very large, ranging from 0.31 mm to 7 mm in diameter across longest axes, with an average grain size of 1.35 mm. Most amphibole is anhedral and occurs poikilitically around large olivine and clinopyroxene grains. The amphibole appears very altered in hand sample and might be secondary or peritectic in origin. Olivine is serpentinized and sometimes appears as skeletal grains. Olivine is also occasionally observed as inclusions within clinopyroxene. Olivine ranges from 0.05 to 0.46 mm in diameter, with an average grain size of 0.2 mm. Very small oxide phases, generally under 0.01 mm in diameter, are often observed as poikilitic inclusions in clinopyroxene. Amphibole tends to occur in clusters/pods, and so the modal mineralogy of amphibole in thin section may not reflect that of the bulk sample.

MM-77-35: Xenolith MM-77-35 is 2.5 × 2 mm in size and has an orthocumulate texture. The xenolith consists of amphibole (46%), clinopyroxene (44%), olivine (9%), and Fe-Ti oxides (1%). Amphibole grains have 0.025 to 0.075 mm thick opacitic rims and pervasive fractures. Amphibole ranges from 0.32 to 1.75 mm in diameter, with an average grain size of 0.65 mm. The amphibole in sample MM-77-35 is texturally similar to those in sample MM-77-67. About 80% of amphibole grains are large (>1mm), euhedral, and prismatic. About 20% of amphibole crystals grow up against olivine grain boundaries but are again texturally distinct from peritectic amphibole, which is generally seen as rims around clinopyroxene or olivine cores. This amphibole also appears to have either co-crystalized with olivine and clinopyroxene or grown just after. Clinopyroxene ranges from 0.15 to 1.13 mm across, with an average diameter of 0.375 mm. Most clinopyroxene shows oscillatory zoning and is euhedral to subhedral in form. A few clinopyroxene grains (~ 5%) show exsolution lamellae. Olivine is slightly serpentinized along rims and ranges from 0.075 to 1.25 mm in diameter, with an average grain size of 0.25 mm. Oxides range from 0.025 to 0.075 mm in diameter, with an average grain size of 0.05 mm, and often occur as poikilitic inclusions in clinopyroxene and amphibole. Plagioclase is only present near the interface between the xenolith and the groundmass and is not interpreted to be part of the primary cumulate mineralogy. These plagioclase grains are lath-like and range from 0.07 to 0.12 mm in length.

MM-CB-3: Sample MM-CB-3 contains a small xenolith (~ 1.5 cm in diameter) surrounded by a matrix of microcrystalline plagioclase with fine to medium-grained phenocrysts of zoned plagioclase, amphibole, and highly serpentinized olivine. The xenolith itself has an orthocumulate texture and consists of clinopyroxene (90%), olivine (9%), and traces of Fe-Ti oxides (1%). Most of the olivine and clinopyroxene grains are euhedral and lack embayed edges. Approximately half of all olivine and clinopyroxene grains display sieve textures or contain poikilitic inclusions of oxides. Clinopyroxene varies from 0.6 to 2.4 mm in diameter, with an average grain size of 1.4 mm. Olivine ranges from 0.15 to 1.1 mm in diameter, with an average grain size of 0.4 mm. Oxides occur interstitially or as poikilitic inclusions and are generally less than 0.04 mm in diameter. Plagioclase is only present as an intercumulus phase near the periphery of the xenolith and its interface with the

volcanic groundmass and is not counted as part of the primary cumulate mineralogy. These plagioclase grains are microcrystalline, equigranular, and approximately 0.04 mm in diameter.

MOF-81X-B: Sample MOF-81X-B consists of a small (2.5 × 0.75 cm) xenolith surrounded by a matrix of microcrystalline plagioclase containing phenocrysts of olivine, clinopyroxene, and large euhedral plagioclase. The xenolith itself has an orthocumulate texture and consists of clinopyroxene (97%), olivine (3%), and traces of Fe-Ti oxides (< 1%). Most clinopyroxene is euhedral to subhedral, although some altered grains with embayed rims are also noted. Several clinopyroxene grains show exsolution lamellae (~ 15%) or slight sieve textures (~ 30%), but these are not pervasive features. A few euhedral clinopyroxene crystals also show simple twinning. About half of all clinopyroxene contains poikilitic inclusions of olivine or small (0.01 – 0.05 mm) oxides. Clinopyroxene grains range from 0.1 to 1.5 mm, with an average grain size of 0.75 mm. Olivine grains are generally much smaller, ranging from 0.07 to 0.12 mm with an average grain size of 0.1 mm.

MM-77-100: Pervasive grain fracturing makes discerning the original igneous texture challenging in some areas of the xenolith, although examination of the most well-preserved regions of the sample suggests an orthocumulate texture. The xenolith is composed of amphibole (90%), plagioclase (4%), clinopyroxene (4%), and olivine (2%). Amphibole grains have reaction rims and are pervasively fractured. Some amphibole shows sieve textures. Amphibole ranges from 0.2 to 1.7 mm in diameter, with an average grain size of 1.3 mm. Plagioclase is equigranular and has an average grain size of 0.1 mm. Clinopyroxene shows sieve textures and ranges from 0.1 to 0.5 mm in diameter, with an average grain size of 0.2 mm. Olivine is serpentinized along rims and ranges from 0.07 to 0.35 mm in diameter, with an average grain size of 0.2 mm. Olivine and clinopyroxene are usually observed as inclusions in amphibole. Individual grains in the xenolith are often separated by an intercumulus matrix consisting of plagioclase with a variolitic texture, which is not interpreted to be part of the primary cumulate mineralogy.

MM-76-4: Sample MM-76-4 consists of a small medium-to-coarse-grained xenolith, approximately 2.5 cm in diameter, surrounded by a matrix of microlitic plagioclase and amphibole containing

phenocrysts of skeletal olivine. The xenolith has an orthocumulate texture and is composed of plagioclase (42%), amphibole (27%), clinopyroxene (21%), and Fe-Ti oxides (10%). One grain of skeletal olivine, approximately 1.2 mm in diameter, was observed within the xenolith. Plagioclase grains are generally subhedral with well-preserved edges and range from 0.25 to 2.4 mm in diameter, with an average grain size of 1.5 mm. All amphibole has 0.05-0.075 mm thick opaque rims. Amphibole sometimes display simple twinning, and generally ranges from 0.2 to 2.6 mm across longest axes, with an average length of 1 mm. Grain fracturing and embayed rims are also common features in clinopyroxene. Clinopyroxene is generally between 0.4 and 1.2 mm in diameter, with an average grain size of 0.8 mm. Skeletal textures and amphibole ingrowths are also observed in some clinopyroxene. Oxides occur both interstitially and as intercumulus phases. Oxides are between 0.05 and 0.8 mm in diameter with an average grain size of 0.2 mm. Poikilitic inclusions of oxides are not observed within larger phases.

MM-77-61: Xenolith MM-77-61 is approximately 1.5 × 4 cm in size and is composed of amphibole (74%), clinopyroxene (16%), plagioclase (7%), and Fe-Ti oxides (3%). All phases are pervasively fractured, especially along their rims, making it difficult to discern the original igneous texture in some places, although the sample appears to have a mesocumulate texture in the less altered regions. Amphibole grains range from 0.3 to 3.5 mm in diameter, with an average grain size of 1.4 mm. Fractures in amphibole are concentrated along the cleavage planes and are often filled with microcrystalline plagioclase and small oxide phases. All amphibole has 0.05 to 0.1 mm thick opaque rims. Clinopyroxene is observed both as small (0.2 to 0.5 mm), euhedral to subhedral zoned grains, and as larger (0.75 - 1.5 mm) fractured grains with embayed rims. Plagioclase grains are anhedral and present as an intercumulus phase. Plagioclase grains range from 0.125 to 1.75 mm across, with an average diameter of 0.325 mm. Plagioclase grains are generally free of fractures with clearly defined rims. Oxides are euhedral and range from 0.025 to 0.1 mm in diameter, with an average grain size of 0.03 mm.

MOF-81X-F: Sample MOF-81X-F consists of a small (9 mm × 2 cm) xenolith surrounded by a matrix of microlitic plagioclase containing larger phenocrysts of olivine, clinopyroxene, and plagioclase. The xenolith itself shows an orthocumulate texture and consists of plagioclase (68%), amphibole (23%), and clinopyroxene (9%). Plagioclase grains are euhedral to subhedral and range from 0.15 to 1.25 mm in diameter, with an average grain size of 0.78 mm. Amphibole grains are highly fractured and have 0.05-0.075 mm thick opacitic rims. The cracks in amphibole grains are often filled with fine-grained plagioclase and small oxide phases. Amphibole ranges from 0.17 to 1.3 mm in diameter, with an average grain size of 0.6 mm. Clinopyroxene is also highly fractured and usually shows sieve textures. Clinopyroxene ranges from 0.3 to 1.75 mm in diameter, with an average grain size of 0.6 mm.

MOF-81X-D: Sample MOF-81X-D generally has an orthocumulate texture, but it is so fractured in places that it is difficult to discern what the original igneous texture was. The xenolith contains plagioclase (49%), amphibole (41%), clinopyroxene (7%), and Fe-Ti oxides (3%). Plagioclase grains are generally well preserved and are often euhedral to subhedral. Plagioclase often includes poikilitic inclusions of small oxides (< 0.01 mm) or larger (0.05-0.15 mm) grains of amphibole, clinopyroxene, or distinct plagioclase. Plagioclase grains range from 0.2 to 1.2 mm in diameter, with an average grain size of 0.8 mm. Amphibole grains show pervasive fracturing and sometimes sieve textures. All amphibole has opacitic rims, which are generally 0.075 to 0.15 mm thick. The cracks in amphibole are often filled with very fine-grained plagioclase and Fe-Ti oxides. Amphibole ranges from 0.2 to 1.4 mm across longest axes, with an average diameter of 0.8 mm. Clinopyroxene pervasively shows sieve textures and ranges from 0.1 to 0.3 mm in diameter, with an average grain size of 0.2 mm. Oxides occur interstitially and as poikilitic inclusions in clinopyroxene and amphibole and generally range from 0.025 to 0.3 mm in diameter, with an average grain size of 0.12 mm.

MOF-81X-E: Xenolith MOF-81X-E is composed of amphibole (91%), clinopyroxene (5%), and Fe-Ti oxides (4%). All silicate phases show pervasive fracturing and many display evidence of partial reabsorption along their rims, which makes discerning the original igneous texture difficult

in places. Study of the less altered regions of the sample, however, suggests it has an orthocumulate texture. Amphibole grains range from 0.3 to 11 mm across their longest axis, with an average grain size of 1.25 mm. Most amphibole has thin (0.01-0.025 mm) opacitic rims. Clinopyroxene is only observed as inclusions in amphibole. Clinopyroxene sometimes shows sieve textures and is generally between 0.075 and 0.5 mm in diameter, with an average grain size of 0.3 mm. Oxides are small, rarely exceeding 0.01 mm in diameter, and euhedral. Larger oxides, generally between 0.02 and 0.075 mm in diameter, are also observed as intercumulus phases. Very fine-grained plagioclase with a variolitic texture is also observed as an intercumulus phase in portions of the xenolith, but it does not appear to be part of the primary cumulate mineralogy.

MM-77-29: Xenolith MM-77-29 has a mesocumulate texture and is comprised of amphibole (86%), plagioclase (5%), clinopyroxene (5%), orthopyroxene (3%), Fe-Ti oxides (1%), and olivine (< 1 %). Amphibole grains are consistently fractured and sometimes show sieve textures. Amphibole ranges from 0.25 to 3.75 mm in diameter, with an average grain size of 1.6 mm. Opacitic rims, between 0.05 and 0.1 mm in diameter, are observed on approximately half of all amphibole crystals. Plagioclase is observed as an intercumulus phase and is generally the most well-preserved phase in the sample. Plagioclase typically shows exsolution lamellae and grains range from 0.2 to 1.3 mm in diameter, with an average grain size of 0.7 mm. Clinopyroxene, orthopyroxene, and olivine are observed as poikilitic inclusions in amphibole. Clinopyroxene varies from 0.075 to 1.8 mm in diameter, with an average grain size of 0.3 mm. Larger clinopyroxene grains are usually more altered than smaller grains, often showing sieve textures and highly irregular, embayed edges. Orthopyroxene grains are generally small with embayed edges, and generally range from 0.1 to 0.4 mm in diameter, with an average grain size of 0.18 mm. Intercumulus space in the sample is filled with a very fine-grained microcrystalline matrix in which specific mineral phases are hard to identify, possibly containing plagioclase, clinopyroxene, and Fe-Ti oxides. Oxides are usually equigranular and approximately 0.015 to 0.025 mm in diameter, although a few larger grains between 0.075 and 0.1 mm across are noted. Oxides are only present as poikilitic inclusions in amphibole or pyroxene.

Olivine is only observed as very small inclusions in amphibole or pyroxene. Individual olivine grains are generally under 0.1 mm in diameter.

MM-CB-1: Xenolith MM-CB-1 has an orthocumulate texture and is almost entirely composed of highly altered amphibole (~99%). The sample also contains traces of plagioclase (~ 1%) and olivine (< 1%). Amphibole is highly fractured and ranges from 0.1 to 9 mm in diameter, with an average grain size of 1.2 mm. Most amphibole has thin opaque rims, usually about 0.01 mm thick. The cracks in amphibole are sometimes filled with very fine-grained plagioclase and Fe-Ti oxides. Only a few grains of plagioclase were observed in this sample, ranging from 0.17 to 1 mm in diameter with an average grain size of 0.25 mm. This plagioclase is subhedral and appears to be filling intercumulus spaces between amphibole grains. One grain of highly altered skeletal olivine was also observed in this sample. This crystal has an approximate diameter of 0.75 mm. Most of the intercumulus space is filled with microcrystalline plagioclase and small grains (< 0.05 mm) of highly altered pyroxene and olivine. These intercumulus phases were not interpreted as part of the primary cumulate mineralogy.

MM-76-9: Xenolith MM-76-9 contains amphibole (55%), plagioclase (43%), and Fe-Ti oxides (2%). The sample appears to have an orthocumulate texture, although the grains are so fractured in places that it is difficult to discern the original igneous texture. Amphibole ranges from 0.25 to 2.5 mm across longest axes and has an average diameter of 1.2 mm. Amphibole is highly fractured and sometimes shows sieve textures. Plagioclase shows considerably less fracturing than amphibole and is often euhedral to subhedral in form. Plagioclase often shows exsolution lamellae and grains range from 0.15 to 0.8 mm in diameter, with an average grain size of 0.5 mm. Oxides are typically very small (< 0.05 mm) and are only observed as poikilitic inclusions in amphibole. Traces of clinopyroxene that have experienced almost complete uralitization are also noted in this sample.

2.15 Additional model results and information

Partition Coefficients: Our choice to use basalt-clinopyroxene K_ds was based on comparisons to experimental studies and the mineralogy and geochemistry of the xenoliths, all of which suggest that the ultramafic xenoliths from Moffett and Adagdak crystallized from basalts to basaltic andesites. For internal consistency, we use the same set of partition coefficients to calculate the equilibrium melt compositions for all clinopyroxenes. Because trace elements generally become increasingly incompatible as silica content and the degree of melt polymerization increases (Schmidt et al., 2006), these partition coefficients are likely not strictly appropriate for calculating the equilibrium melts for our amphibole gabbro and hornblendite xenoliths (compositional Group 4). The magma compositions we calculated from clinopyroxene in these more evolved lithologies should therefore be taken as maximum estimates. The high absolute trace element concentrations we calculate for melts in compositional Group 4 likely reflect 1) fractionation of the cumulates from more evolved melts, in which differentiation increased the concentration of incompatible elements in the magma, and to a lesser extent, 2) an artifact of applying basalt-clinopyroxene partition coefficients to lithologies that crystallized from more evolved melts later in the crystallization sequence, such as basaltic andesites or Mg-andesites.

We were not able to obtain all 24 basalt-clinopyroxene K_ds of interest from a single study. Our approach was to use the available partitioning data from the experimental study of Hart and Dunn (1993), and then supplement the missing K_ds with values obtained from the Geochemical Earth Reference Model (GERM) database (*kdd.earthref.org/KdD*). Partition coefficients from GERM were selected based on the following criteria: 1) that they be generally consistent with values given by other studies listed in the database, and 2) that when taken together, the selected K_ds reproduce the expected trends in trace element compatibility in clinopyroxene (i.e., Ba, Nb, Pb, Zr, Hf are incompatible, HREE are more compatible than LREE: Hart and Dunn, 1993; Hauri *et al.*, 1994).

Major element modeling: A simple mass balance fractionation model was used to further constrain the crystallization sequences for Adagdak and Moffett. Specifically, this model focused on the approximate amount of each lithological group fractionated in the cumulate sequence. To this end, we started with the initial melt compositions (major elements) of the experimental studies that best reproduced the crystallization sequences observed for each suite. For Adagdak, we used high-Mg basalt RC158c from (Ulmer *et al.*, 2018) and for Moffett, we used basalt 85-44 from (Krawczynski *et al.*, 2012). A more detailed account of this modeling than was presented in the main text is given below.

Adagdak: Using an $K_{D,Fe^{2+}/Mg}^{ol/melt}$ of 0.3 (Roeder and Emslie, 1970), we calculated the composition of olivine which would be in equilibrium with a melt of our starting composition. This olivine would have a Mg# of 90.18, higher than that observed in our most primitive dunite (Mg# = 87.06 for ADG-82-2 and 87.05 for ADG-82-21). We crystallized 1% of our initial melt, removing olivine from this equilibrium composition, and recalculated the composition of the remaining melt and the olivine that would be in equilibrium with that melt. This process was repeated until we had crystalized 10% of the melt, removing only olivine. By this point, the olivine in equilibrium with the residual liquid had a Mg# of 86.51, which is very close to that observed in our most primitive wehrlite, ADG-82-3 (Mg# = 86.65 ± 0.15). Using $K_{D,Fe^{2+}/Mg}^{cpx/melt}$ of 0.23 (Toplis and Carroll, 1995), we calculated that the clinopyroxene in equilibrium with this melt would have a Mg# of 89.32, which is also very close to that observed in ADG-82-3 clinopyroxene (Mg# = 89.21 ± 0.24). We therefore marked this as the end of olivine-dominated fractionation and began to remove a cumulate with modal proportions typical of the Adagdak wehrlite and olivine clinopyroxenite (50% olivine and 50% clinopyroxene).

We continued to crystalize the melt in 1% increments, removing a cumulate containing equal proportions of clinopyroxene and olivine. As before, the compositions of the remaining melt and the olivine and clinopyroxene in equilibrium with that melt were re-calculated each time. After an additional 8% of crystallization, the olivine and clinopyroxene in equilibrium with the remaining liquid had respective Mg#s of 83.06 and 86.48. These values are close to those observed in the most

evolved of the ultramafic cumulate, sample ADG-CB-5 (Mg# olivine = 84.06, CPX = 86.45). We therefore marked this as the end of ultramafic fractionation for Adagdak. For the last iteration of the model, we removed a representative amphibole gabbro composition (40% amphibole, 40% plagioclase, 15% cpx, 5% magnetite). The clinopyroxene Mg#s of the amphibole gabbro and hornblendite cumulates range from 77.76 to 73.59. After an additional 5% amphibole gabbro crystallization the equilibrium clinopyroxene would have a Mg# of 77.65 and after 17% it would have a Mg# of 73.67. We therefore conclude the amphibole gabbro likely represents an additional 5-17% crystallization of the residual melt after the cessation of ultramafic cumulate fractionation.

Moffett: We used the same methods to constrain the Moffett crystallization sequence with respect to major elements. The olivine and clinopyroxene in equilibrium with our starting composition would have Mg#s of 88.99 and 91.34, respectively. This is similar to that observed in our most primitive Moffett cumulate, olivine clinopyroxenite MM-CB-2 (olivine Mg# = 88.74 ± 0.24, CPX Mg# = 90.70 ± 1.17). We again began to crystalize the melt in 1% increments, removing olivine and clinopyroxene in the approximate modal proportions observed in our most primitive Moffett cumulates (40% olivine and 60% CPX). After 10% crystallization, the olivine and clinopyroxene in equilibrium with the remaining melt would have Mg#s of 86.23 and 89.09, respectively. This is similar to that observed in clinopyroxenite xenolith MM-CB-3 (Mg# olivine = 86.35 ± 0.31, CPX Mg# = 88.51 ± 0.79). This suggests that the most primitive Moffett olivine clinopyroxenite can be genetically tied to the clinopyroxenite by 10% olivine + clinopyroxene fractionation of a mafic melt. Placing the amphibole-bearing olivine clinopyroxenite on the Moffett fractionation sequence is more difficult. The clinopyroxene in these samples has higher Mg# than the olivine, suggesting that the phases are not in equilibrium with each other or may have experienced some subsolidus exchange. The clinopyroxene in the amphibole-bearing cumulates is however, markedly less magnesian than those observed in the amphibole-free lithologies (Mg# 82.27-78.10 vs 90.70-88.51), suggesting crystallization from a more evolved, further fractionated melt.

Trace Element Modeling

Adagdak: For the trace element modeling, we started with the equilibrium melt composition of dunite ADG-82-2, our most primitive sample (94% olivine, olivine Mg# = 87.06 ± 0.36, Sr/Sr* = 2.08 ± 0.10). We used a simple mass balance model and removed 8% of a representative wehrlite trace element composition from the ADG-82-2 equilibrium melt. Because we are assuming that clinopyroxene controls the distribution of trace elements between melt and the fractionating assemblage, we normalize the bulk composition removed, assuming the 50% modal olivine in the cumulate contains negligible quantities of the trace elements modeled (Figure S14b). Because clinopyroxene has lower absolute concentrations of all trace elements modeled than the equilibrium melt (as all CPX-basalt K_ds are <1), removing ultramafic assemblages effectively increases the concentration of all trace elements in the residual melt with little modification to the trace element profile or Sr-anomaly (Figure S14a).

Following our major element modeling, we then removed a representative amphibole gabbro composition (Figure S14). We used the average trace element composition of plagioclase, amphibole, and clinopyroxene from the amphibole gabbro, and normalized the composition of the bulk cumulate removed to mimic the modal proportions of a representative amphibole gabbro (~40% amphibole, 45% plagioclase, 10% cpx). Using a mass balance model, we removed 20-30% of this cumulate from the residual melt. Because strontium concentrations are higher in plagioclase (600-800 ppm) than in clinopyroxene (25-33 ppm), adding this phase to the assemblages greatly increases the Sr of the bulk cumulate removed (>500ppm). Once the strontium concentration of the cumulate removed exceeds that of the melt, mass balance dictates that Sr concentrations in the residual liquid must decrease. As seen in Figure S14a, the most profound change in the trace element profile after plagioclase saturation occurs is the diminution of the Sr-anomaly from 1.58 to 0.76.

Moffett: We employed the same approach to explore the decrease in Sr-anomalies and degree of HREE-LREE fractionation observed between the most primitive Moffett cumulates and the more evolved amphibole-bearing lithologies. Specifically, we aim to understand whether these changes

can be explained by fractionation in a closed system. For Moffett, we started with the trace element equilibrium melt composition we calculated from clinopyroxene in sample MM-CB-2. Using the same mass balance approach, we first crystalized 10% of a representative olivine clinopyroxenite (80% CPX, 20% olivine). Again, we assume the trace element budget of the system is controlled by clinopyroxene and normalize the bulk composition of the cumulate removed accordingly, effectively diluting the absolute concentrations of elements in the fractionating assemblage. As observed previously in the Adagdak model, because clinopyroxene has lower absolute abundances of all trace elements than the equilibrium melt, its removal serves to increase the concentration of these elements in the remaining liquid.

For the second iteration of crystallization, we removed a representative amphibole-bearing olivine clinopyroxenite (45% amphibole, 45% CPX, 10% olivine). Because amphibole has higher concentrations of MREE and HREE than the equilibrium melt, fractionating amphibole-bearing lithologies in fact depletes the remaining melt in these elements. Furthermore, although Sr concentrations are higher in Moffett amphibole (290-350 ppm) than they are in clinopyroxene (30-80 ppm), they are still less than what should be present in the parental melts to the most primitive cumulates (>550 ppm). The fractionation of amphibole and clinopyroxene bearing cumulates thus cannot explain the diminution of Sr-anomalies and increase in MREE and HREE concentrations observed between the primitive Moffett olivine clinopyroxenite and more evolved amphibole bearing cumulates (Figure S15). Reconciling these differences would require early fractionation of a Sr-rich and HREE-depleted phase like plagioclase, which is not observed in the Moffett suite.

The compositional differences between the most primitive and most evolved Moffett cumulates cannot be explained by closed system fractionation of amphibole + olivine + clinopyroxene bearing assemblages. It is possible that 1) a piece of the fractionation sequence is missing, such as a plagioclase-rich cumulate which might sequester Sr and whose removal would elevate the HREE in the remaining melt, or 2) that the olivine clinopyroxenite and amphibole-bearing lithologies do not represent close system fractionation and the composition of the parental

melt was modified by mixing or reaction with another melt or the mantle peridotite/wall rock between fractionating these two lithological groups.

2.16 Supplemental Figures

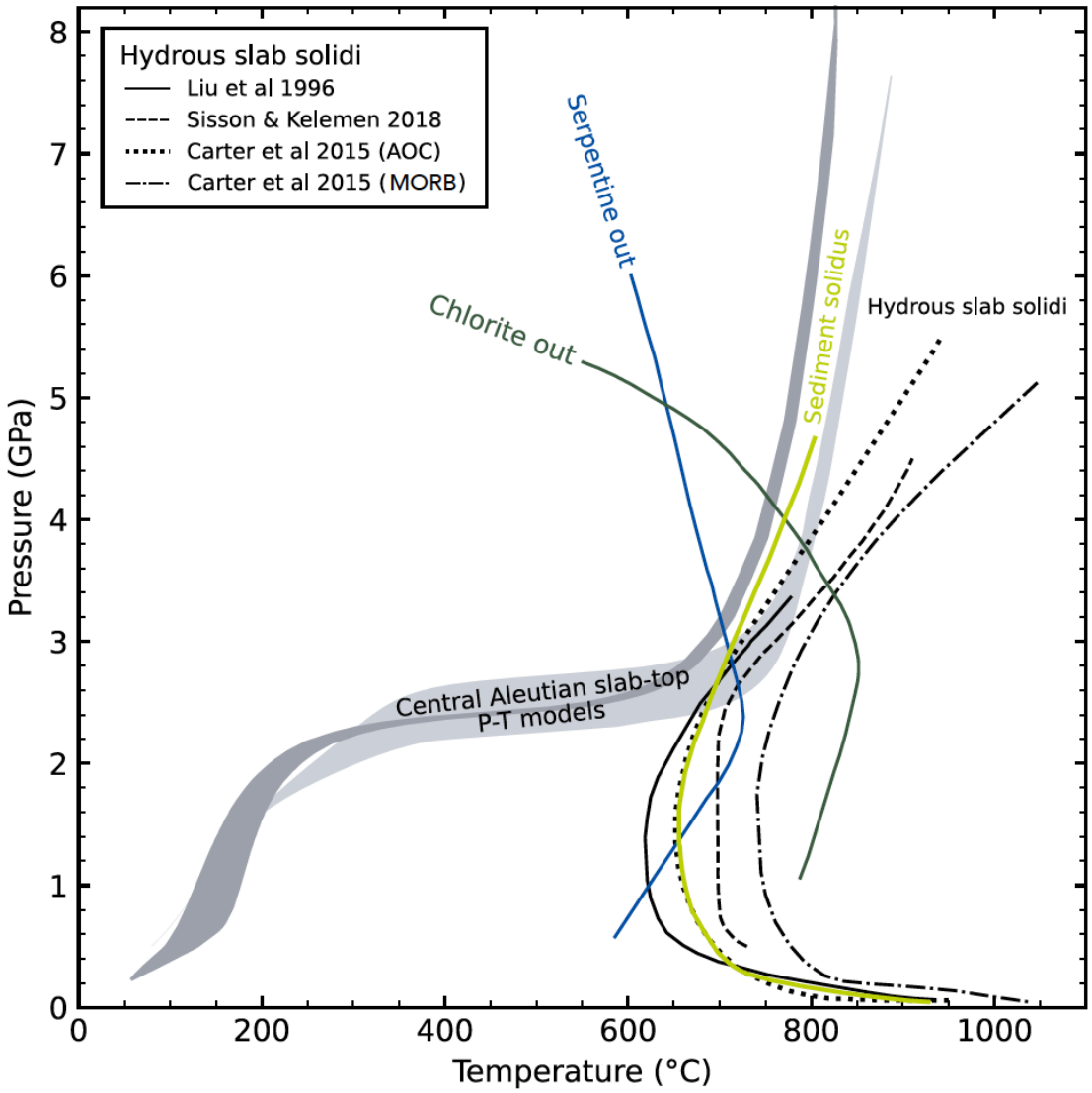

Supplemental Figure 1: Relations between slab-surface models, dehydration reactions, and solidi for subducted lithologies in P-T space. Central Aleutian slab-top P-T models are from Syracuse et al. (2010) (light gray field) and van Keken et al. (2018) (dark gray field). Dehydration reactions for serpentine and chlorite are from Ulmer and Trommsdorff (1995) and Till et al. (2012), respectively. Estimates for the H_2O-saturated solidus of subducted slabs are from Liu et al. (1996, solid line), Sisson and Kelemen (2018: dashed line), and Carter et al. (2015) (altered oceanic crust – dotted line, K-free MORB, dot-dashed line). Solidus for subducted sediment is from Nichols et al. (1994). Multiple estimates for Central Aleutian slab-top P-T and the solidus of hydrous subducted slabs are given to show the range of values present in the literature.

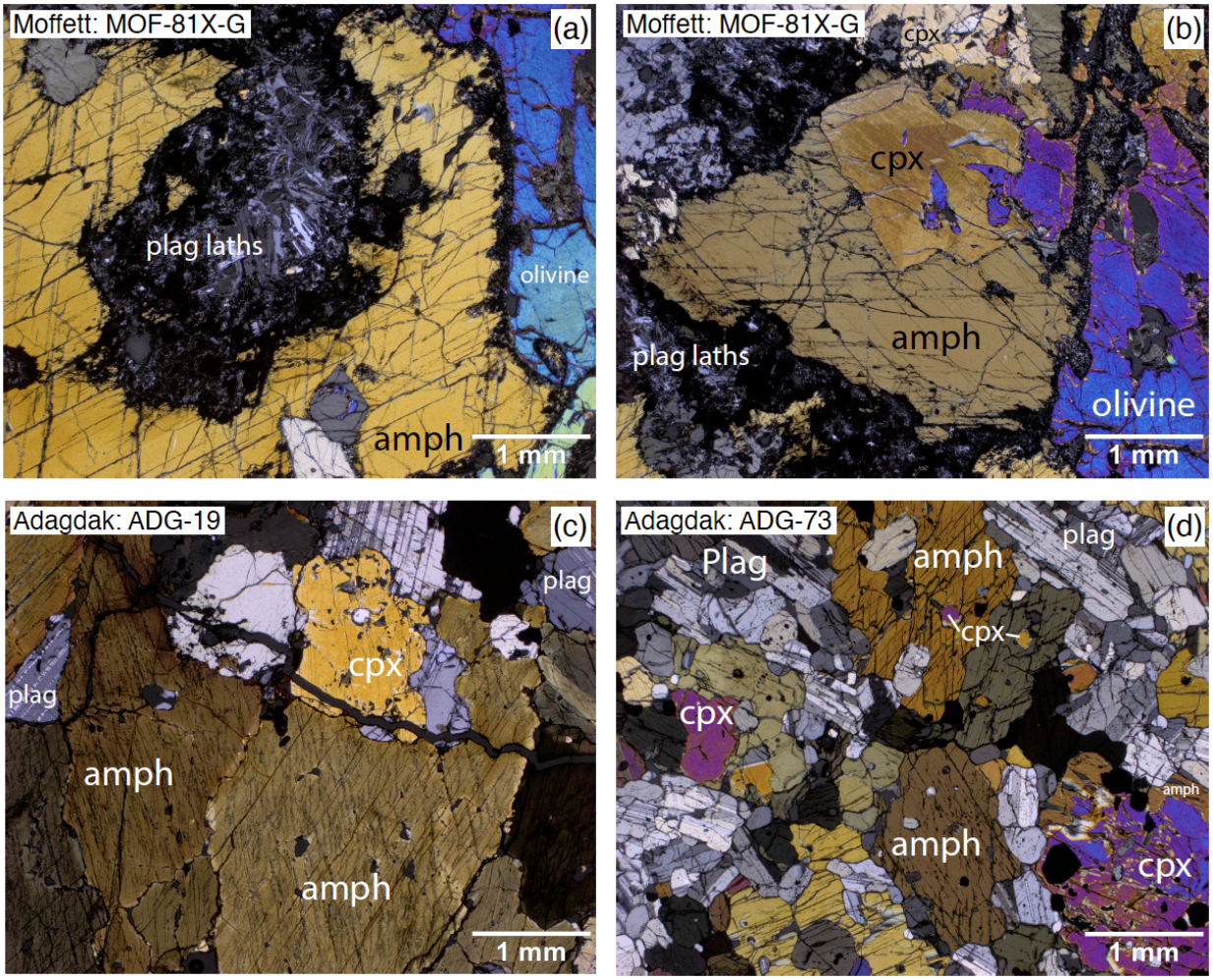

Supplemental Figure 2: Additional photo micrographs of amphibole. **A)** Plagioclase laths from xenolith matrix infiltrating sample MOF-81X-G. **B)** Amphibole partially surrounding clinopyroxene in sample MOF-81X-G. **C)** Inclusion-free amphibole in sample ADG-19. **D)** Amphibole partially surrounding cpx in sample ADD-73.

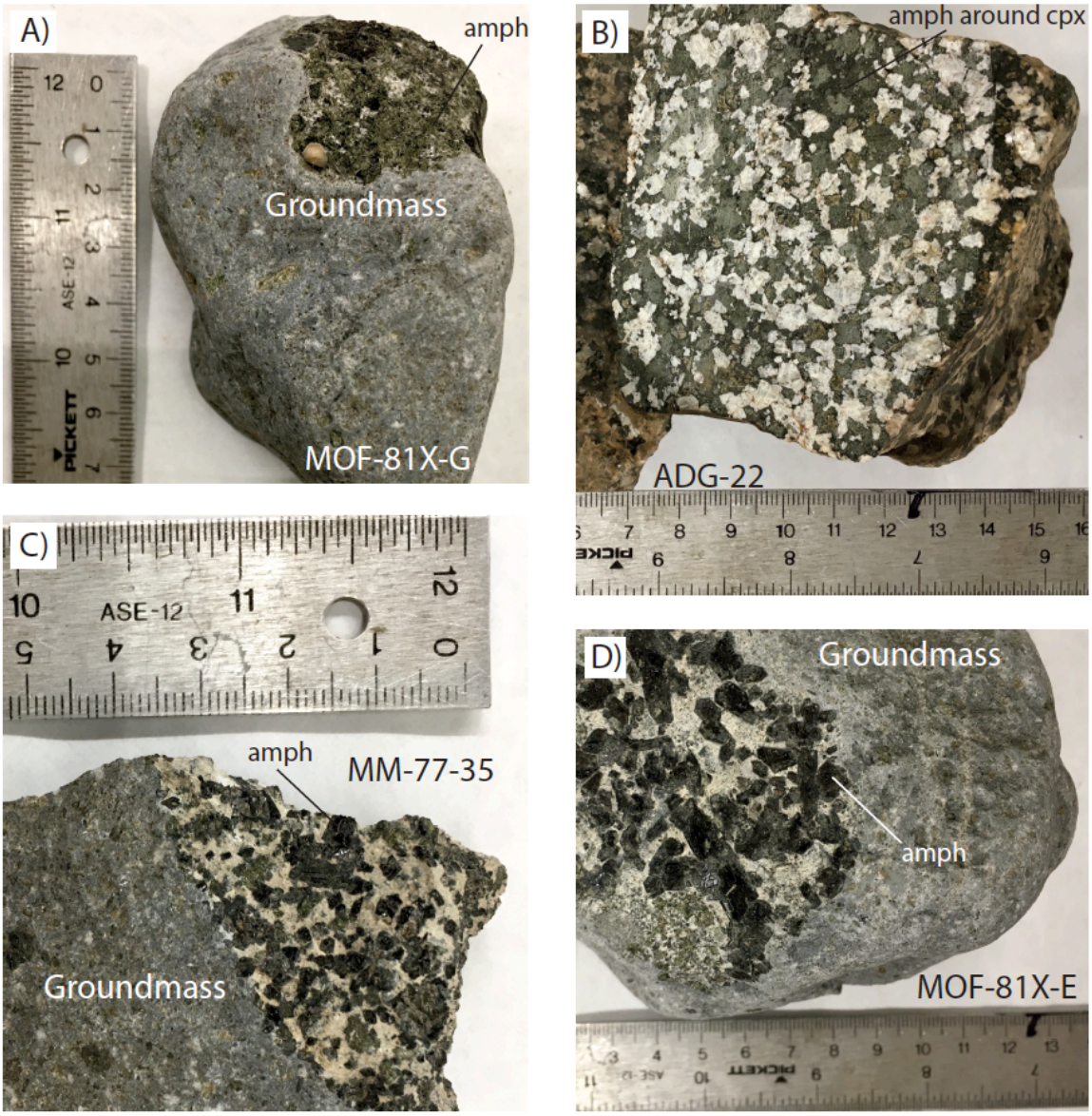

Supplemental Figure 3: Hand sample photos of xenoliths. A) Moffett xenolith MOF-81X-G, with possible secondary or peritectic amphibole. B) Adagdak xenolith ADG-22, with cumulate poikilitic amphibole rimming clinopyroxene. C) Moffett xenolith MM-77-35 with cumulate amphibole. D) Moffett xenolith MOF-81X-E with cumulate euhedral amphibole grains.

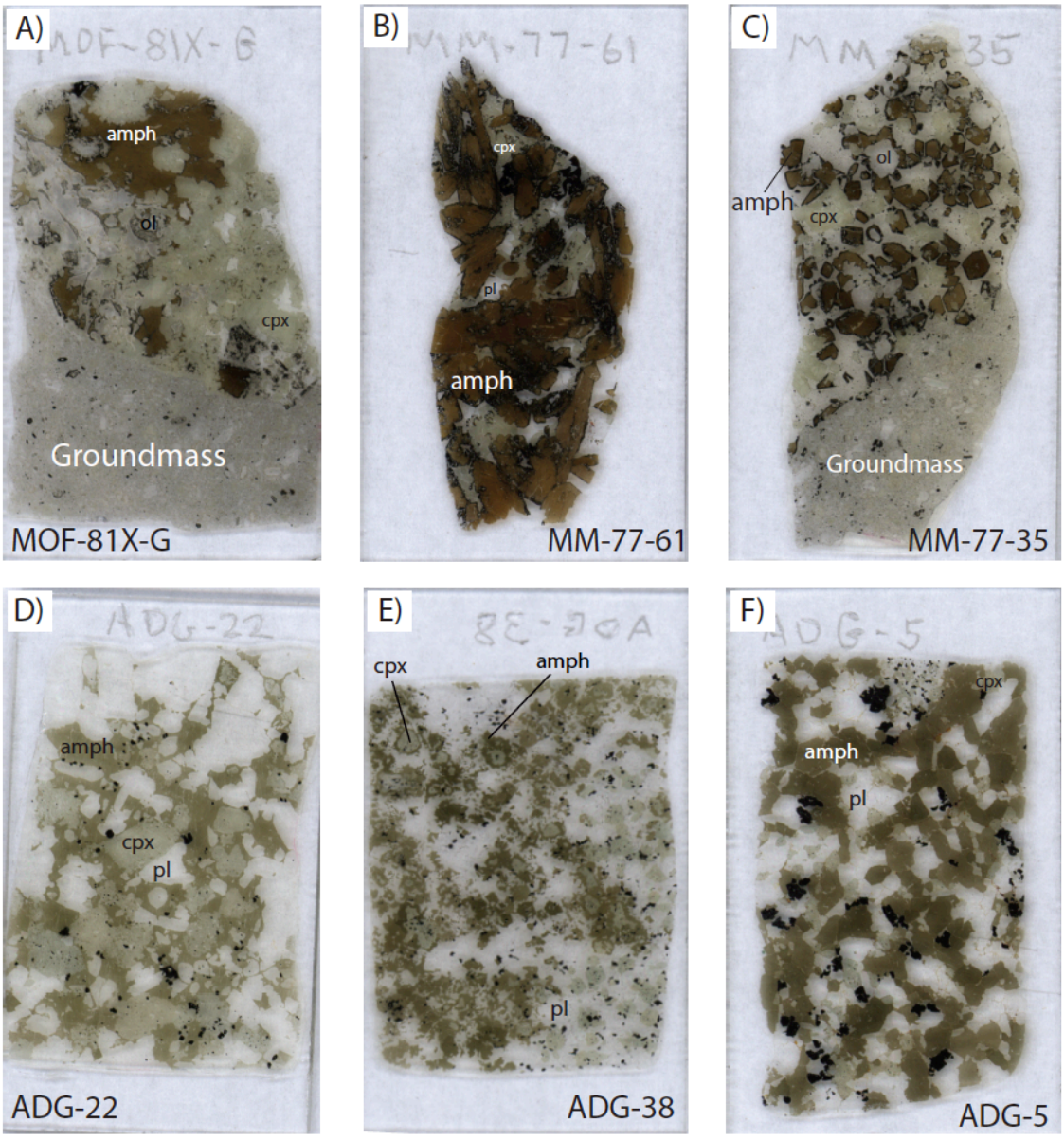

Supplemental Figure 4: Thin section scans of xenoliths showing variety of observed amphibole textures. **A)** Moffett xenolith MOF-81X-G with possible secondary or peritectic amphibole. **B)** Moffett xenolith MM-77-61 with large euhedral cumulate amphibole. **C)** Moffett xenolith MM-77-35 with well-defined cumulate amphibole grains. **D)** Adagdak xenolith ADG-22, with intercumulus amphibole. **E)** Adagdak xenolith ADG-38 with possible peritectic amphibole forming rims around clinopyroxene. Similar textures are seen in amphibole from samples ADG-4, ADG-73, and ADG-82-6. **F)** Adagdak xenolith ADG-5, with well-formed euhedral amphibole that is interpreted as cumulate in origin.

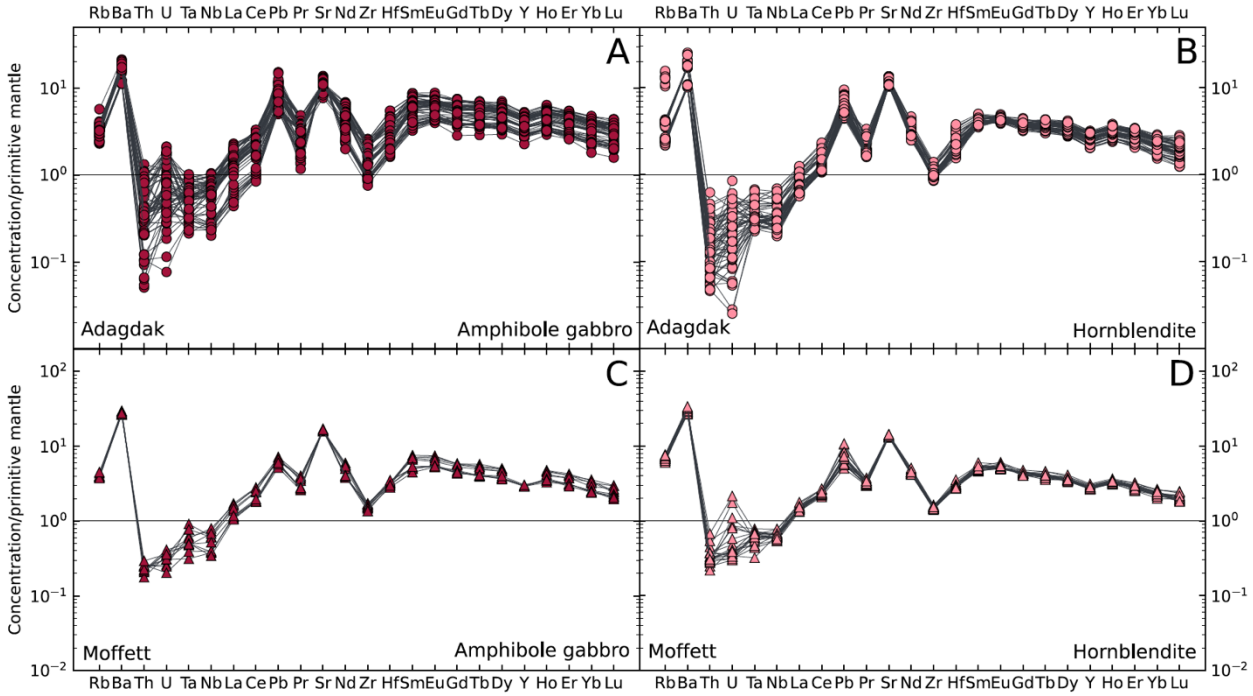

Supplemental Figure 5: Primitive mantle normalized trace element concentrations in amphibole. **A)** Adagdak amphibole gabbro. **B)** Adagdak hornblendite. **C)** Moffett amphibole gabbro. **D)** Moffett hornblendite.

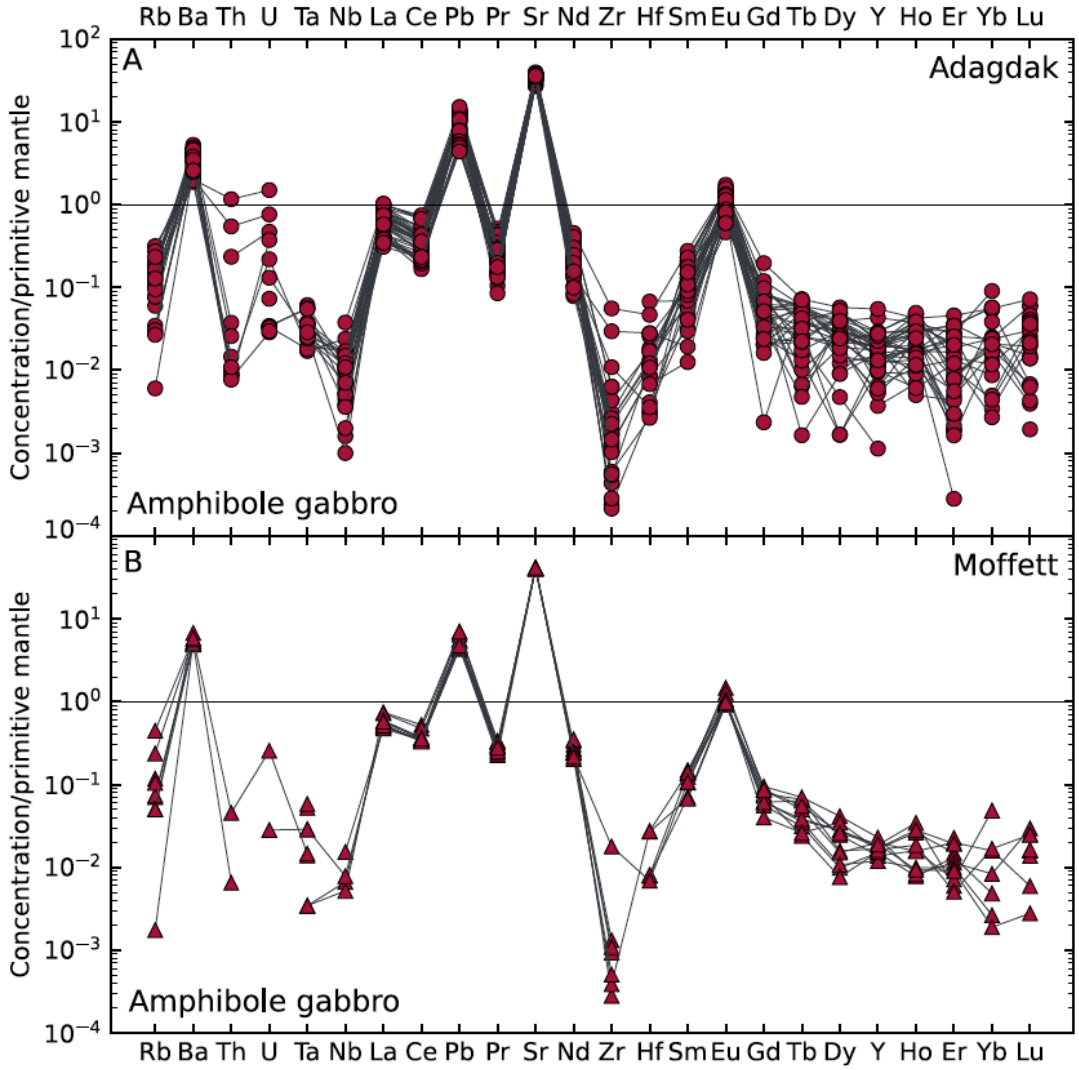

Supplemental Figure 6: Primitive mantle normalized trace element concentrations in plagioclase. **A)** Adagdak amphibole gabbro. **B)** Moffett amphibole gabbro.

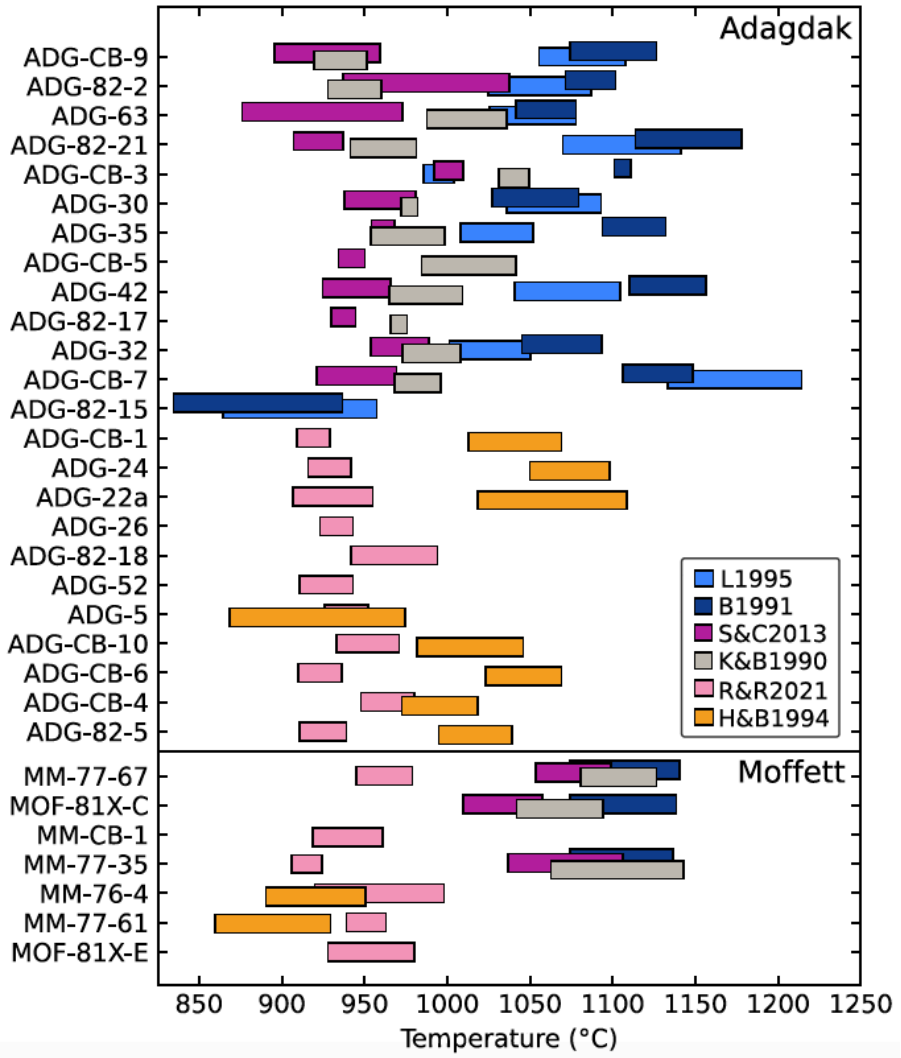

Supplemental Figure 7: Temperature estimates for Adagdak and Moffett xenoliths. Thermometers used: *K&B1990* - Kohler and Brey (1990), *L1995* - Li et al. (1995), *B1991* - Ballhaus et al. (1991), *S&C2013* - Shejwalkar and Coogan (2013), *R2021* - Ridolfi (2021). Samples are ordered by modal abundance of olivine. Note that for the Li *et al.* (1995) thermometer, ADG-82-15 preserves a lower temperature of 885-915ºC, and ADG-CB-7 yields a higher temperature of 1170ºC. This is due to the high Al_2O_3 of spinel in ADG-82-15 (49.93 wt.%) and high MgO of spinel from ADG-CB-7 (16.52 wt.%), respectively, resulting in low and high temperature estimates when the Li *et al.* (1995) parameterization is applied. While both crystallization temperatures are reasonable estimates for ultramafic lithologies, the Al_2O_3 content of spinel in both samples is higher than the Li *et al.* (1995) parameterization is calibrated for (see Table 1, Li *et al*., 1995). Fe-Mg exchange thermometry for ADG-82-15 and ADG-82-17 must therefore be taken as minimum and maximum estimates, respectively.

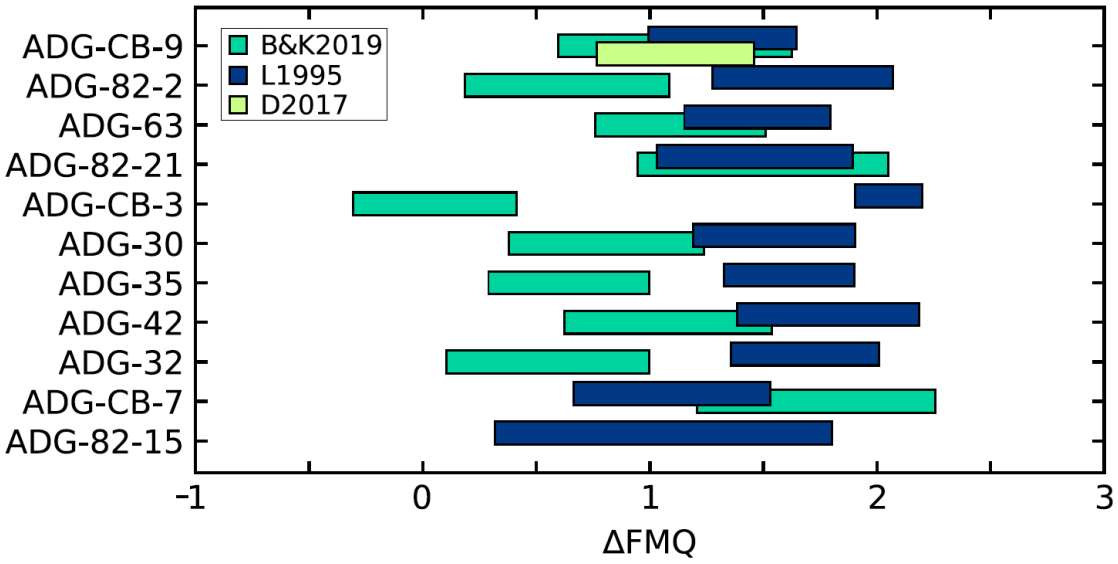

Supplemental Figure 8: fO_2 estimates for Adagdak xenoliths. *B&K2019* - Bucholz and Kelemen (2019), *B1991* - Ballhaus et al. (1991), *D2017* - Davis et al. (2017).

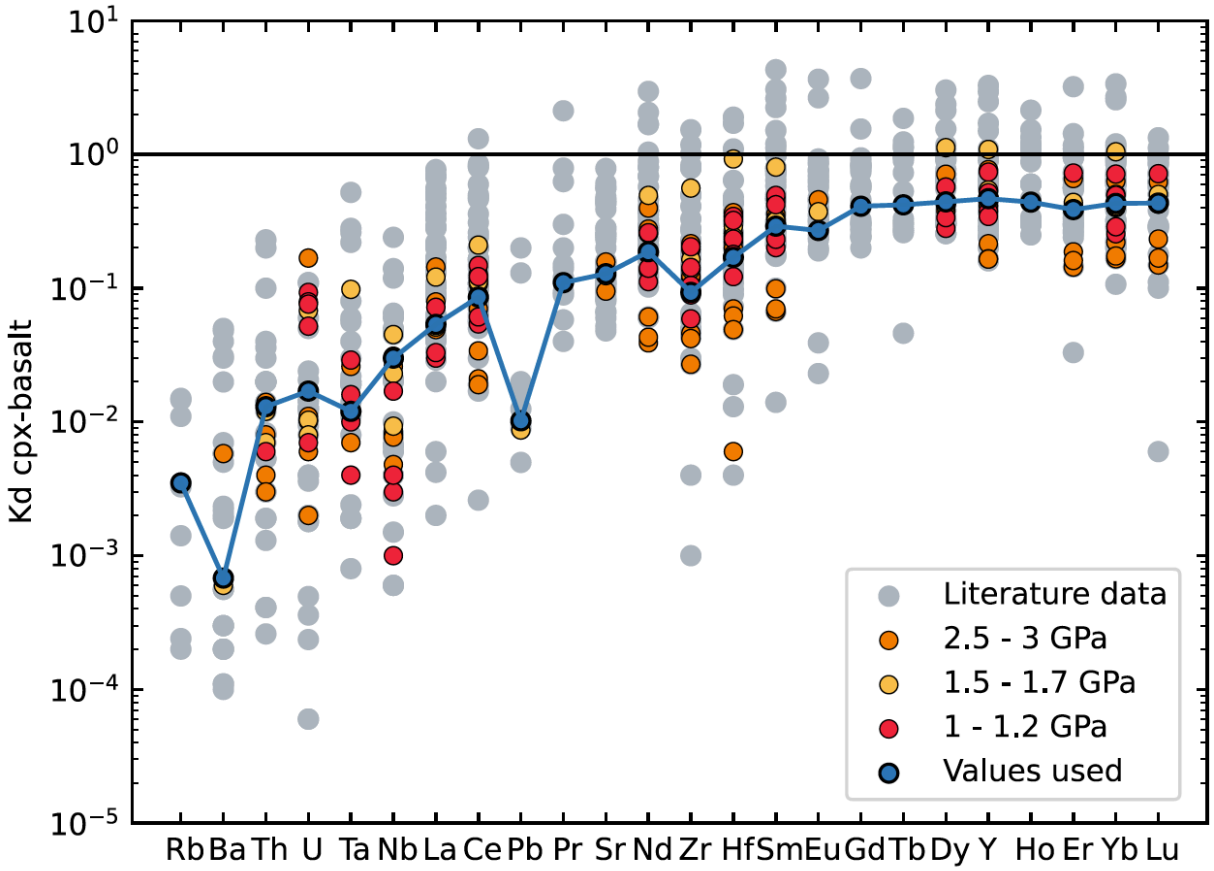

Supplemental Figure 9: Basalt-clinopyroxene partition coefficients. Gray symbols represent the range of values found on the GERM database and blue symbols show the values used to calculate equilibrium melt compositions (*https://kdd.earthref.org/KdD/search*). Sources of data used in modeling are given in Table S13.

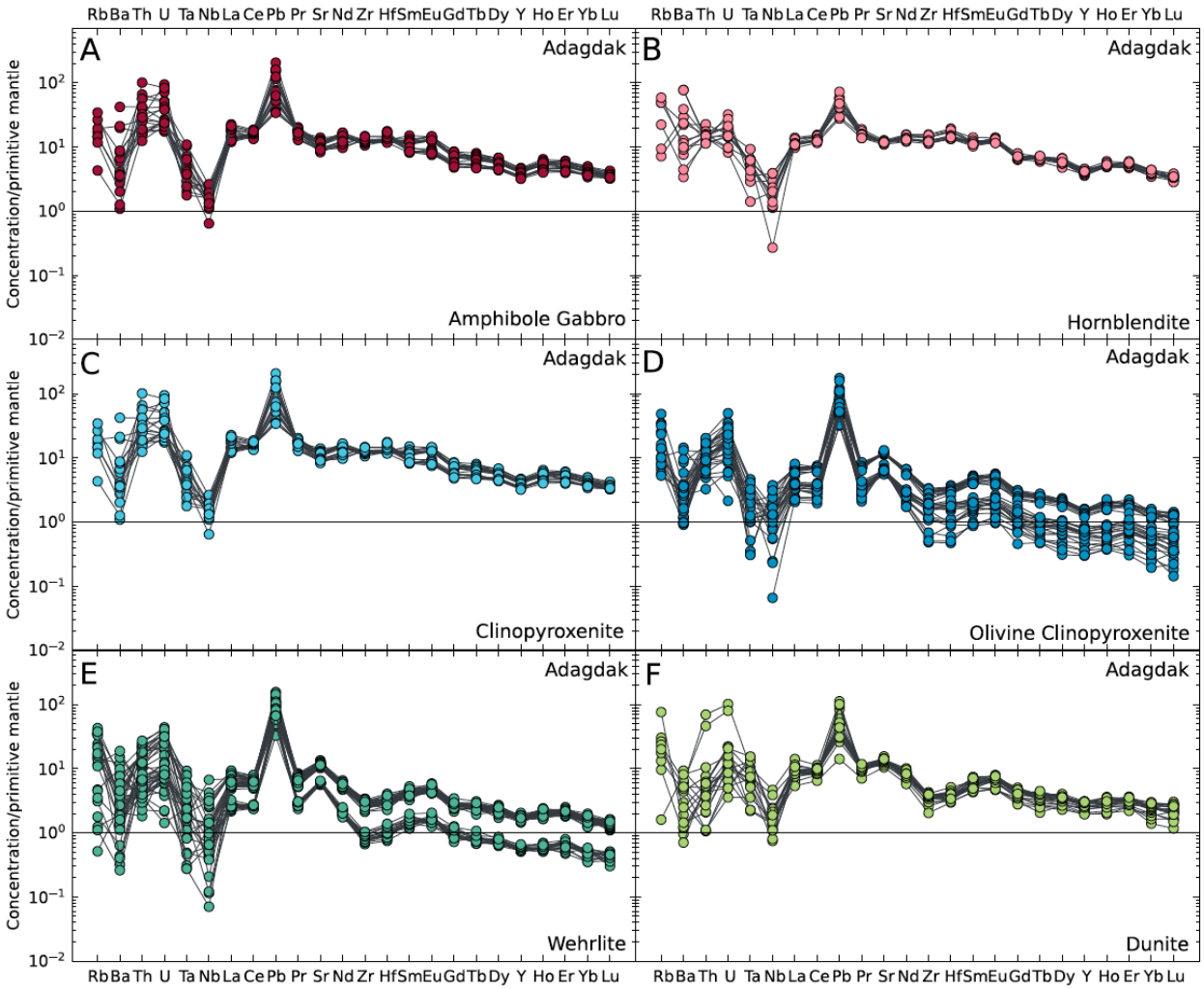

Supplemental Figure 10: Equilibrium melt compositions calculated from Adagdak clinopyroxene trace element data. **A**) Amphibole gabbro. **B**) Hornblendite. **C**) Clinopyroxenite. **D**) Olivine clinopyroxenite. **E**) Wehrlite. **F**) Dunite.

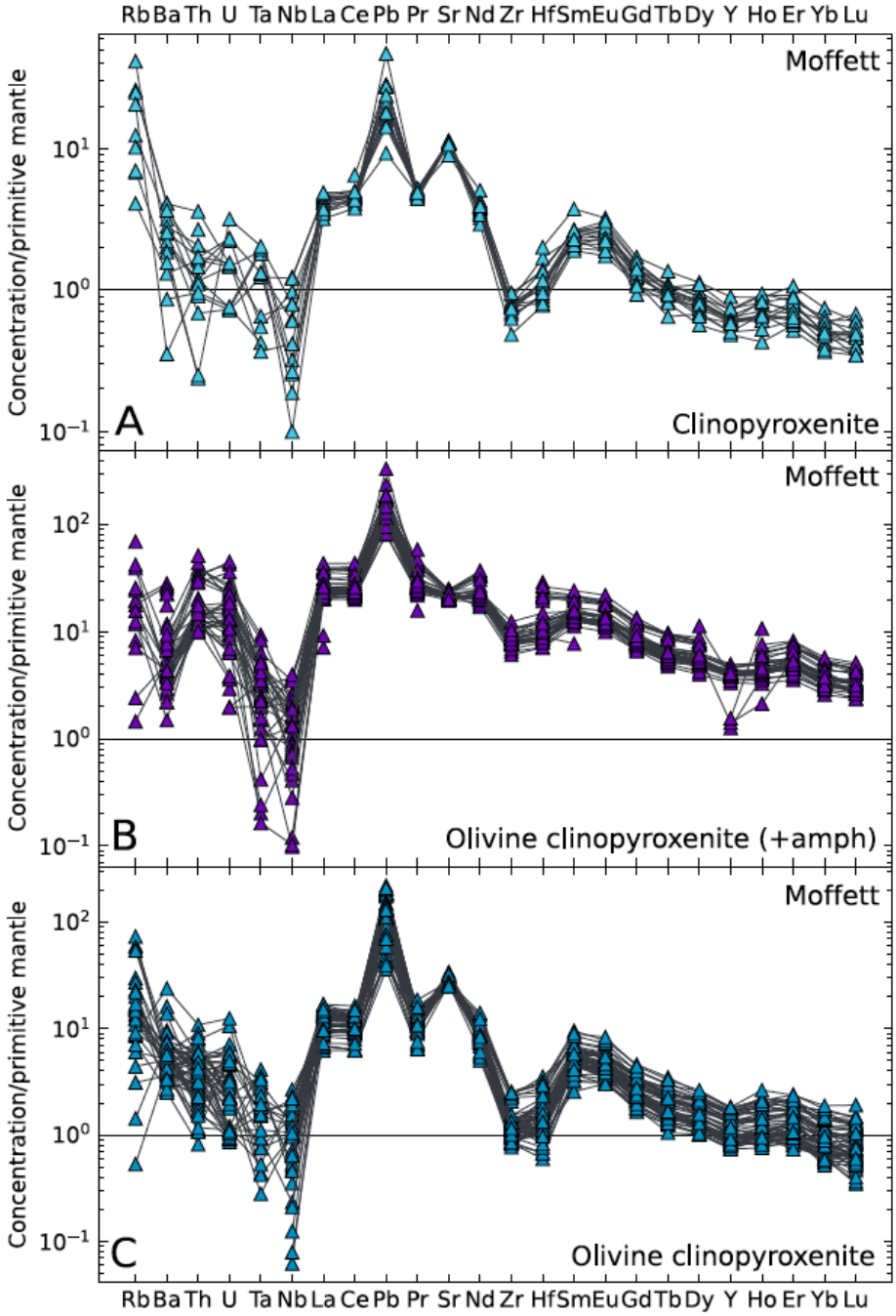

Supplemental Figure 11: Equilibrium melt compositions calculated from Moffett clinopyroxene trace element data. **A**) Clinopyroxenite. **B**) Amphibole-bearing olivine clinopyroxenite. **C**) Olivine clinopyroxenite.

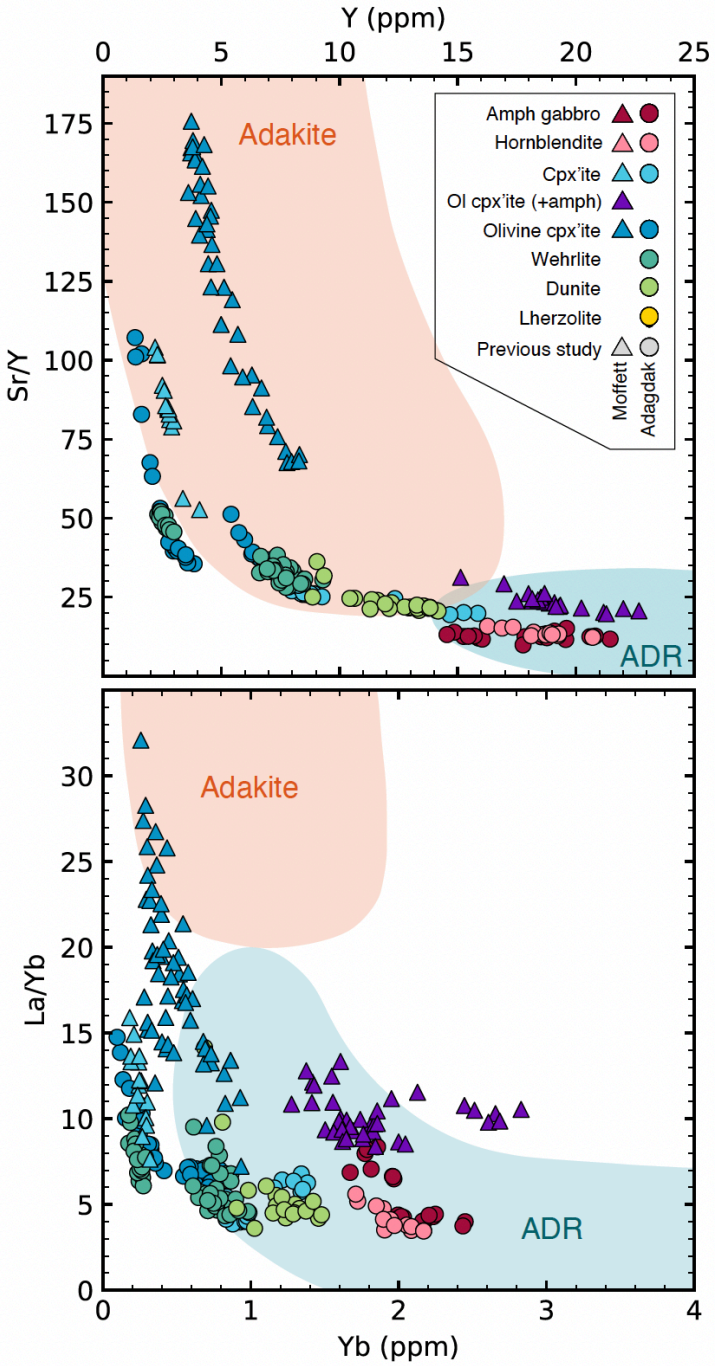

***Supplemental Figure 12*:** Typical adakite classification diagram. Boundaries for adakites and the normal arc andesite, dacite, and rhyolite (ADR) fields from Richards and Kerrich (2007). **A)** Sr/Y vs Y and **B)** La/Yb vs Yb.

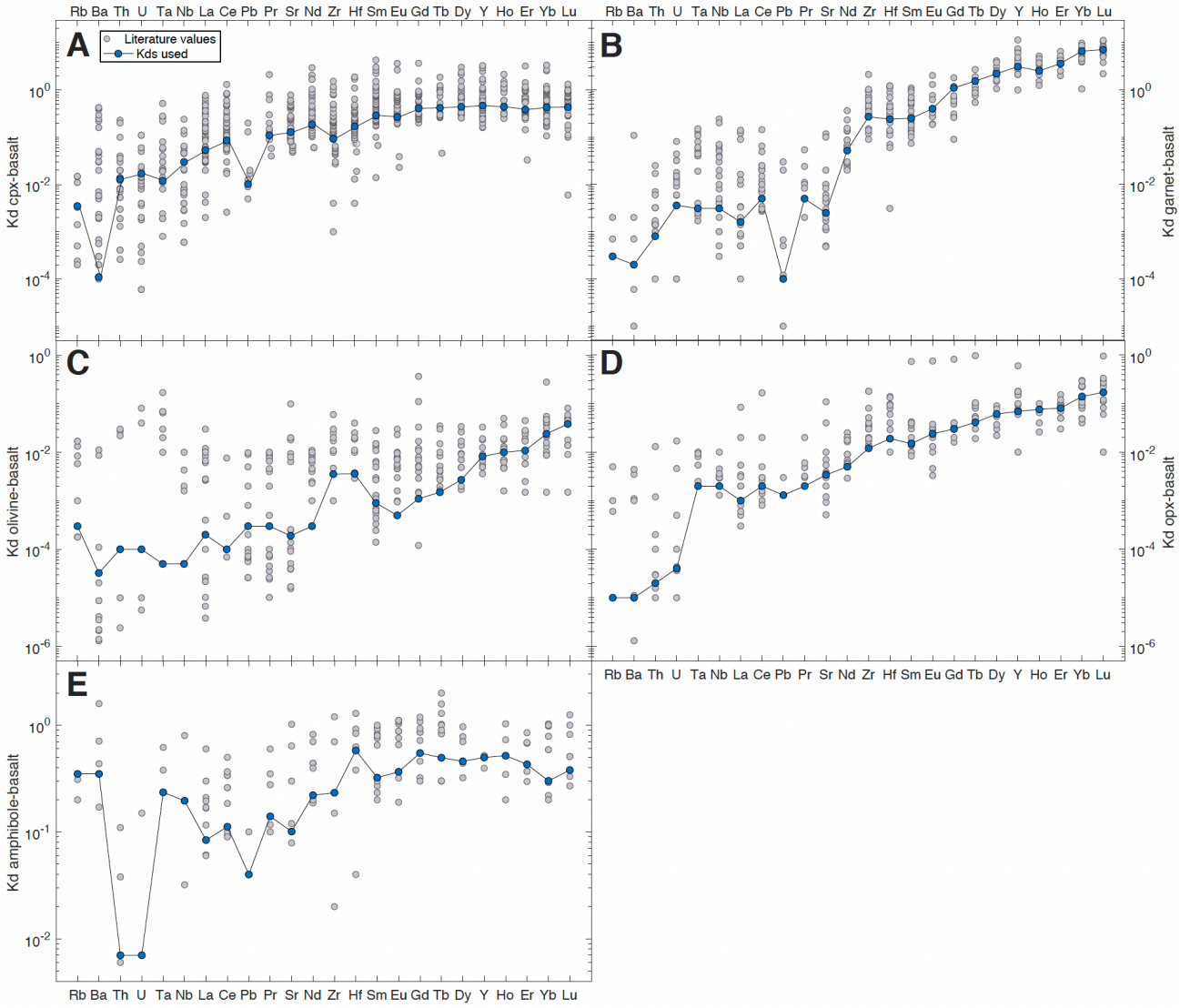

Supplemental Figure 13: Summary of basalt-mineral partition coefficients used in modeling for A) clinopyroxene, B) garnet, C) olivine, D) orthopyroxene, and E) amphibole. Gray symbols represent literature data and blue symbols show the values used in modeling. Sources of data used in modeling are given in Table S13. The same clinopyroxene-basalt partition coefficients used to calculate equilibrium melt compositions (Figure S6) were used in modeling.

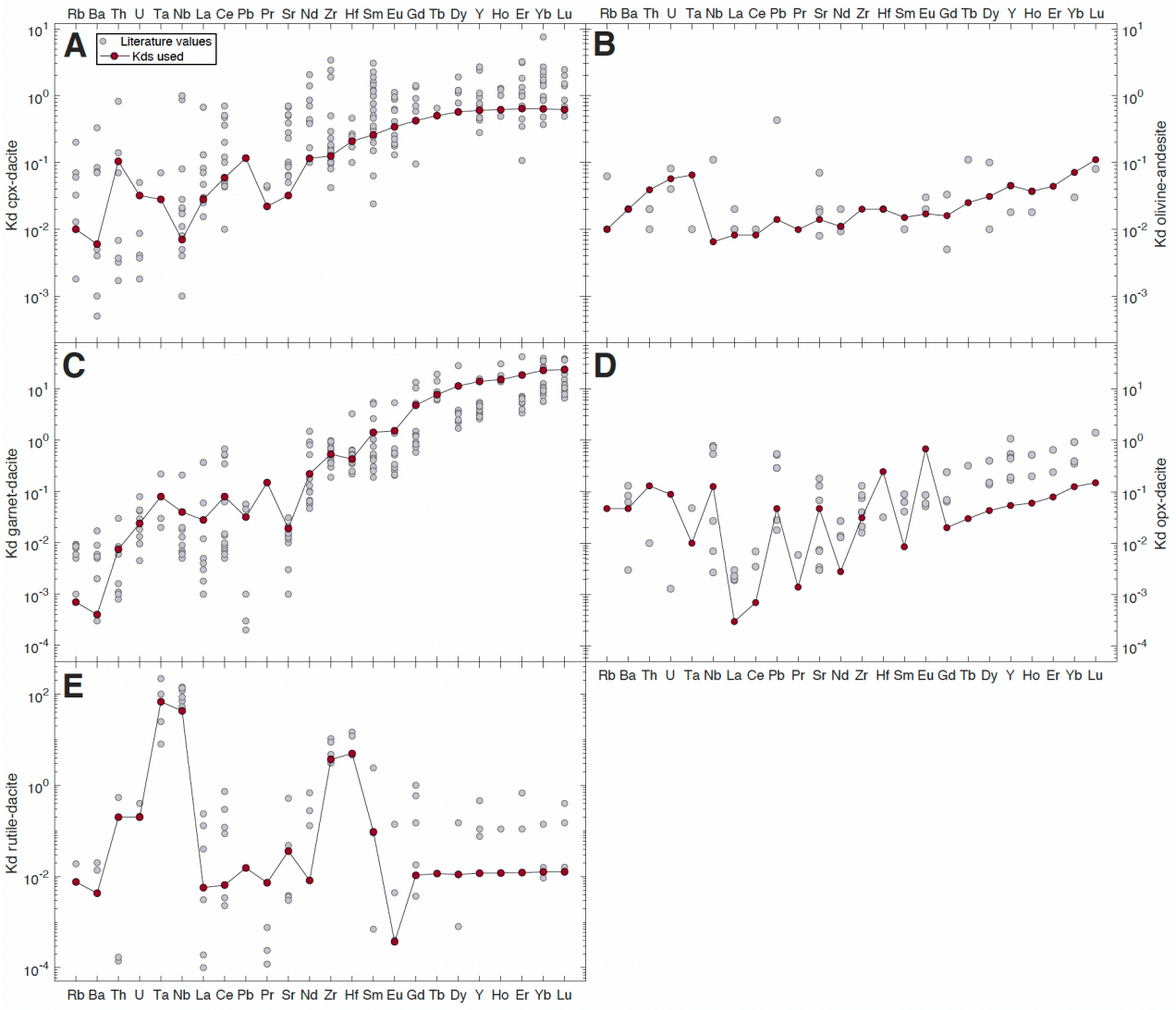

***Supplemental Figure 14*:** Summary of dacite-mineral partition coefficients used in modeling for A) clinopyroxene, B) olivine, C) garnet, D) orthopyroxene, and E) rutile. Gray symbols represent literature data from the GERM database and red symbols show the values used in modeling. Sources of data used in modeling are given in Table S13.

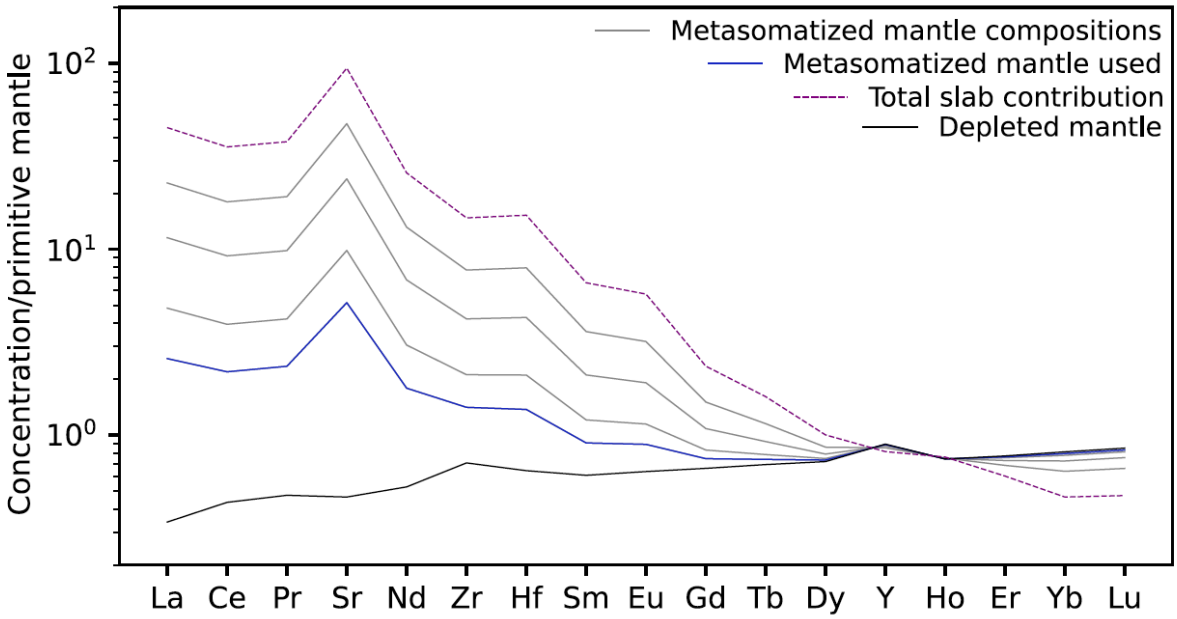

Supplemental Figure 15: Metasomatized mantle compositions, depleted mantle (black) metasomatized by a 5% slab melt (purple dotted line) over a 1:9 to 1:1 melt: rock ratio. The composition used in modeling (1:9 melt rock ratio) is shown in blue.

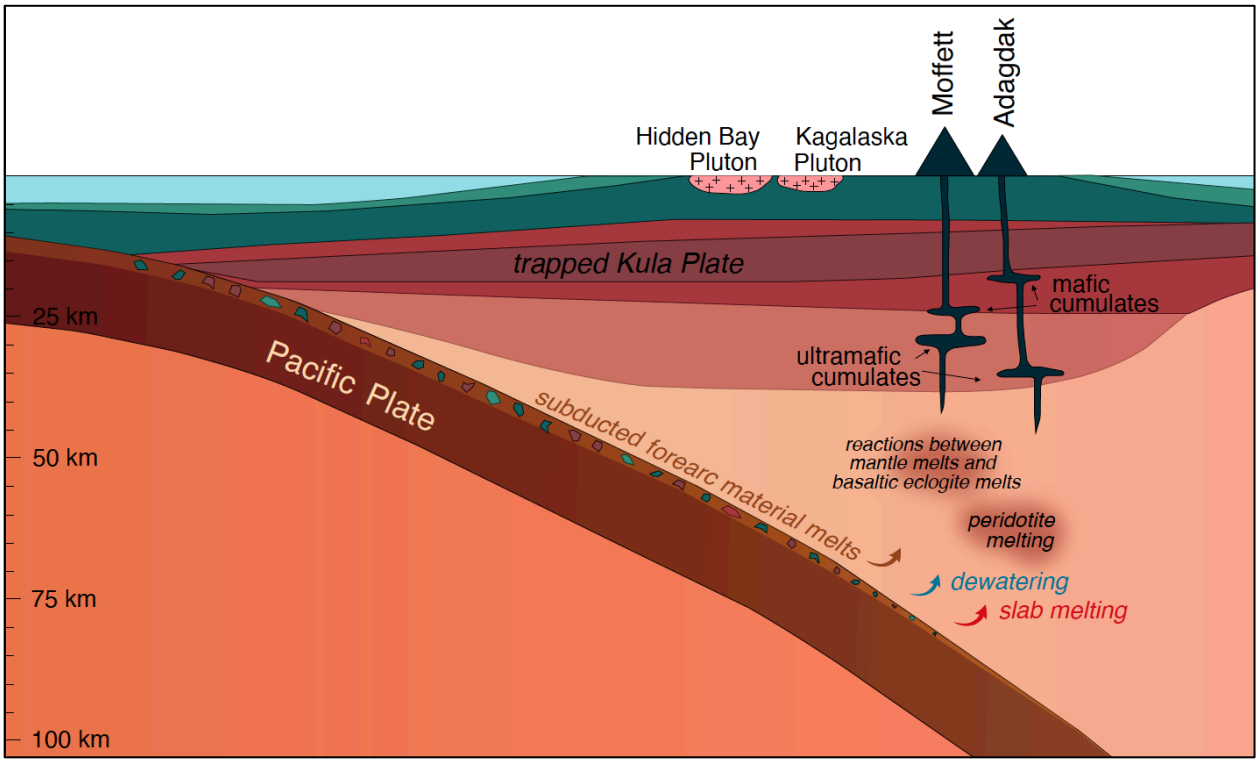

Supplemental Figure 16: Schematic cross section of Adak Island and its magmatic plumbing system. Melts of subducted forearc material and possible contributions from slab melts are shown in brown and red arrows, respectively. The source region beneath Moffett is shown to have a larger contribution from reactions between basaltic eclogite melts and the mantle peridotite, resulting in more fractionated trace element patterns. This diversity in mantle source regions could either reflect spatial mantle heterogeneity beneath Adak, or temporal changes in source composition if the Moffett and Adagdak cumulate suites are of different ages. Modified after Jicha and Kay (2018) and Kay et al. (2019).

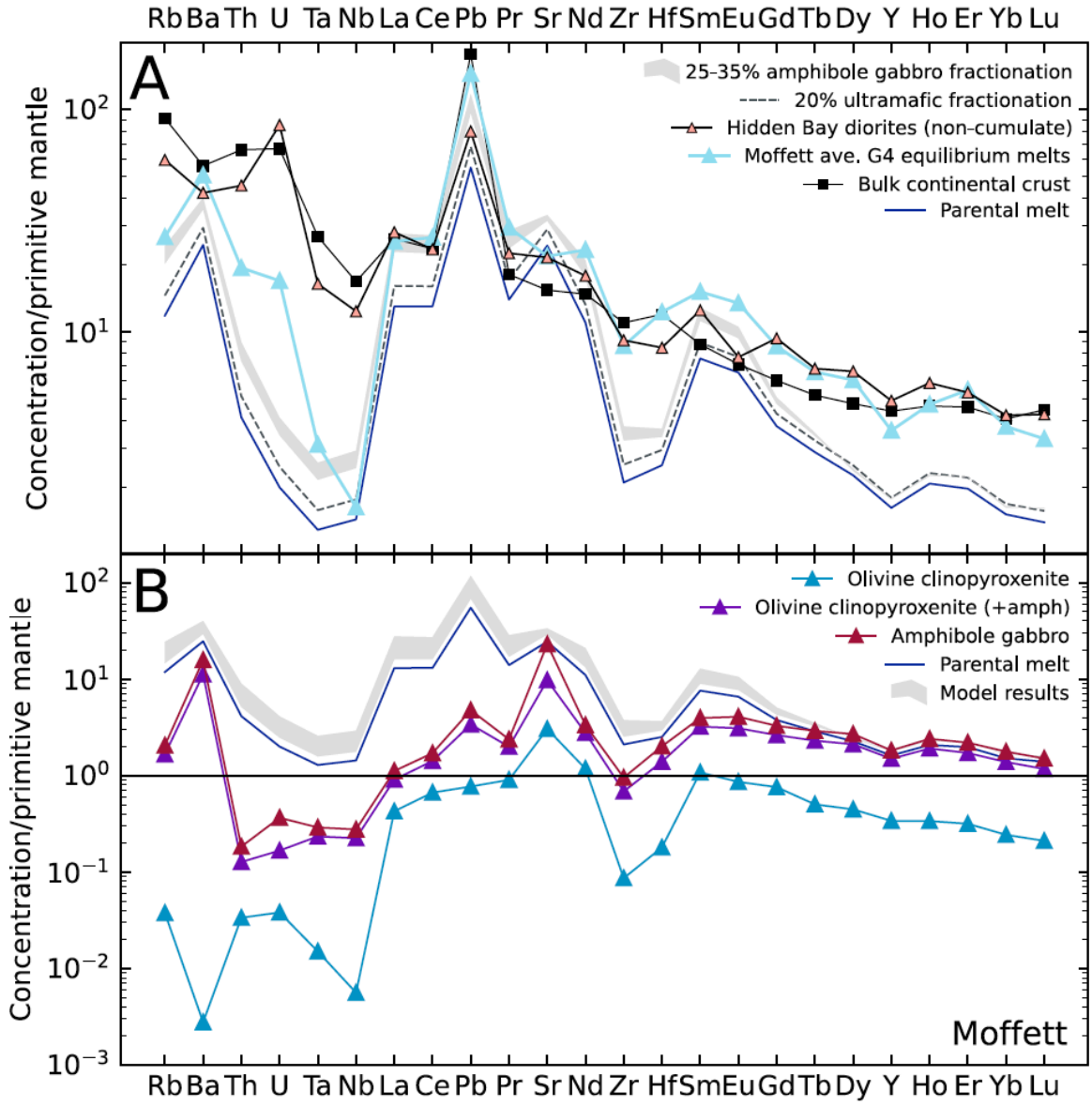

Supplemental Figure 17: **A)** Trace element fractional crystallization model results for Moffett. Bulk continental crust composition is from Rudnick and Gao (2003) and non-cumulate Hidden Bay pluton data is from Kay *et al.* (2019). Pluton compositions from Kay *et al.* (2019) were further screened for signs of cumulate plagioclase accumulation (Sr/Sr*>1.1, Eu/Eu*>1). The average calculated equilibrium melt composition for the Adagdak samples in compositional Group 4 is also given. **B)** Parental melt composition (blue line with circles), model results (gray field) and representative bulk olivine clinopyroxenite (dark blue solid line), amphibole bearing olivine clinopyroxenite (purple line), and amphibole gabbro (red line) compositions for Moffett.

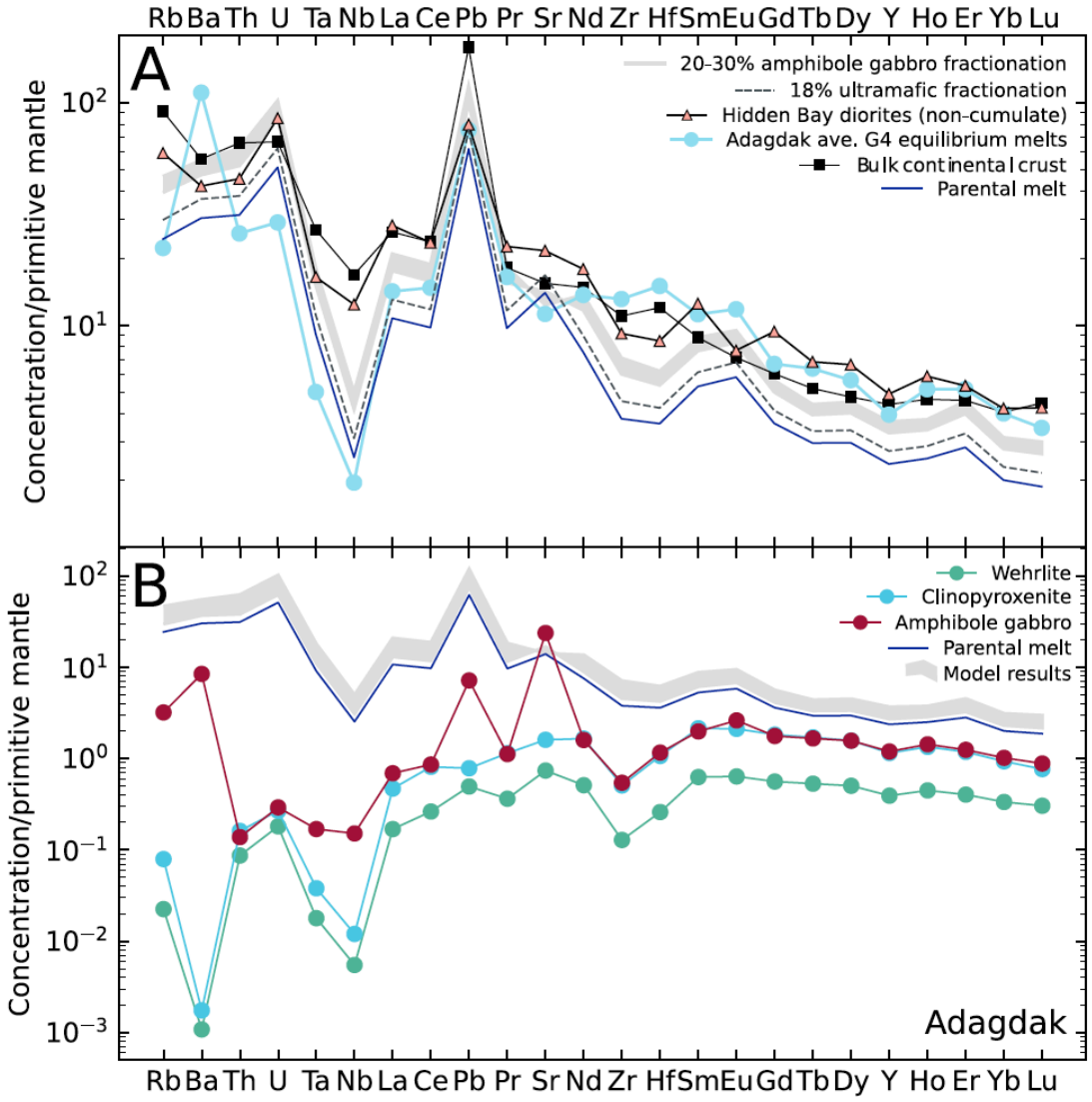

Supplemental Figure 18: **A**) Trace element fractional crystallization model results for Adagdak. Bulk continental crust composition (black line) is from (Rudnick and Gao, 2003) and Hidden Bay pluton data (pink triangles) is from (Kay *et al.*, 2019). Hidden Bay pluton data were further screened to remove samples showing signs of plagioclase accumulation (Sr/Sr* and Eu/Eu*>1). The average calculated equilibrium melt composition for the Adagdak samples in compositional Group 4 is also given (light blue line). Model results for 18% ultramafic cumulate fractionation from the parental melt and a further 20-30% amphibole gabbro fractionation are represented with a light gray field and dotted dark dray line, respectively. **B**) Parental melt composition (dark blue line), model results (gray field), and representative bulk wehrlite (green line), clinopyroxenite (light blue line), and amphibole gabbro (red line) compositions for Adagdak.

2.17 Additional References

Adam, J., & Green, T. (2006). Trace element partitioning between mica-and amphibole-bearing garnet lherzolite and hydrous basanitic melt: 1. Experimental results and the investigation ofcontrols on partitioning behaviour. *Contributions to Mineralogy and Petrology* 152, 1-17.

Bédard, J. H. (2006). A catalytic delamination-driven model for coupled genesis of Archaean crust and sub-continental lithospheric mantle. *Geochimica et Cosmochimica Acta* 70*,*1188-1214.

Beattie, P. (1993). The generation of uranium series disequilibria by partial melting of spinel peridotite: constraints from partitioning studies. *Earth and Planetary Science Letters* 117, 379-391.

Carter, L. B., Skora, S., Blundy, J. D., De Hoog, J. C. M., & Elliott, T. (2015). An experimental study of trace element fluxes from subducted oceanic crust. *Journal of Petrology* 56, 1585-1606.

Chazot, G., Menzies, M. A., & Harte, B. (1996). Determination of partition coefficients between apatite, clinopyroxene, amphibole, and melt in natural spinel lherzolites from Yemen: Implications for wet melting of the lithospheric mantle. *Geochimica et Cosmochimica Acta* 60, 423-437.

Dantas, C., Grégoire, M., Koester, E., Conceição, R. V., & Rieck Jr, N. (2009). The lherzolite–websterite xenolith suite from Northern Patagonia (Argentina): Evidence of mantle–melt reaction processes. *Lithos* 107, 107-120.

Draper, D. S. (1992). Spinel lherzolite xenoliths from Lorena Butte, Simcoe mountains, southern Washington (USA). *The Journal of Geology* 100, 766-775.

Dunn, T., & Sen, C. (1994). Mineral/matrix partition coefficients for orthopyroxene, plagioclase, and olivine in basaltic to andesitic systems: A combined analytical and experimental study. *Geochimica et Cosmochimica Acta* 58, 717-733.

Grove, T., Parman, S., Bowring, S., Price, R., & Baker, M. (2002). The role of an H 2 O-rich fluid component in the generation of primitive basaltic andesites and andesites from the Mt. Shasta region, N California. *Contributions to Mineralogy and Petrology* 142, 375-396.

Frey, F. A. (1969). Rare earth abundances in a high-temperature peridotite intrusion. *Geochimica et Cosmochimica Acta* 33, 1429-1447.

Fujimaki, H., Tatsumoto, M., & Aoki, K. I. (1984). Partition coefficients of Hf, Zr, and REE between phenocrysts and groundmasses. *Journal of Geophysical Research: Solid Earth* 89, 662-672.

Hart, S. R. & Dunn, T. (1993). Experimental cpx/melt partitioning of 24 trace elements. *Contributions to Mineralogy and Petrology* 113, 1–8.

Hauri, E. H., Wagner, T. P. & Grove, T. L. (1994). Experimental and natural partitioning of Th, U, Pb and other trace elements between garnet, clinopyroxene and basaltic melts. *Chemical Geology* 117, 149–166.

Hofmann, A. W. (1988). Chemical differentiation of the Earth: the relationship between mantle, continental crust, and oceanic crust. *Earth and Planetary Science Letters* 90, 297-314.

Kay, S. M., Jicha, B. R., Citron, G. L., Kay, R. W., Tibbetts, A. K. & Rivera, T. A. (2019). The calc-alkaline Hidden Bay and Kagalaska plutons and the construction of the Central Aleutian oceanic arc crust. *Journal of Petrology* 60, 393–439.

Krawczynski, M. J., Grove, T. L. & Behrens, H. (2012). Amphibole stability in primitive arc magmas: Effects of temperature, H_2O content, and oxygen fugacity. *Contributions to Mineralogy and Petrology* 164, 317–339.

Irving, A. J., & Frey, F. A. (1984). Trace element abundances in megacrysts and their host basalts: Constraints on partition coefficients and megacryst genesis. *Geochimica et cosmochimica acta* 48, 1201-1221.

Johnson, K. (1998). Experimental determination of partition coefficients for rare earth and high-field-strength elements between clinopyroxene, garnet, and basaltic melt at high pressures. *Contributions to Mineralogy and Petrology* 133, 60-68.

Lehnert, K., Su, Y., Langmuir, C. H., Sarbas, B., & Nohl, U. (2000). A global geochemical database structure for rocks. *Geochemistry, Geophysics, Geosystems* 1(5).

Liu, J., Bohlen, S. R. & Ernst, W. G. (1996). Stability of hydrous phases in subducting oceanic crust. *Earth and Planetary Science Letters* 143, 161–171.

Luhr, J. F., & Carmichael, I. S. (1980). The colima volcanic complex, Mexico. *Contributions to Mineralogy and Petrology* 71, 343-372.

McDonough, W. F., & Sun, S. S. (1995). The composition of the Earth. *Chemical Geology* 120, 223-253.

McKenzie, D. A. N., & O'nions, R. K. (1991). Partial melt distributions from inversion of rare earth element concentrations. *Journal of Petrology* 32, 1021-1091.

Nichols, G. T., Wyllie, P. J. & Stern, C. R. (1994). Subduction zone melting of pelagic sediments constrained by melting experiments. *Nature*. **371**, 785–788.

Plank, T., & Langmuir, C. H. (1998). The chemical composition of subducting sediment and its consequences for the crust and mantle. *Chemical Geology* **145**, 325-394.

Richards, J. P. & Kerrich, R. (2007). Special Paper: Adakite-Like Rocks: Their diverse origins and questionable role in metallogenesis. *Economic Geology* **102**, 537–576.

Roeder, P. L. & Emslie, R. F. (1970). Olivine-liquid equilibrium. *Contributions to Mineralogy and Petrology* **29**, 275–289.

Rudnick, R. L. & Gao, S. (2003). Composition of the continental crust. *Treatise on Geochemistry* **3**, 659.

Salters, V. J., & Longhi, J. (1999). Trace element partitioning during the initial stages of melting beneath mid-ocean ridges. *Earth and Planetary Science Letters* **166**, 15-30.

Salters, V. J., & Stracke, A. (2004). Composition of the depleted mantle. *Geochemistry, Geophysics, Geosystems* **5**.

Schmidt, M. W., Connolly, J. A. D., Günther, D. & Bogaerts, M. (2006). Element partitioning: The role of melt structure and composition. *Science* **312**, 1646–1650.

Sisson, T. W. & Kelemen, P. B. (2018). Near-solidus melts of MORB + 4 wt% H2O at 0.8–2.8 GPa applied to issues of subduction magmatism and continent formation. *Contributions to Mineralogy and Petrology* **173**, 70.

Stamper, C. C., Blundy, J. D., Arculus, R. J., & Melekhova, E. (2014). Petrology of plutonic xenoliths and volcanic rocks from Grenada, Lesser Antilles. *Journal of Petrology* **55**, 1353-1387.

Staudigel, H., Plank, T., White, B., & Schmincke, H. U. (1996). Geochemical fluxes during seafloor alteration of the basaltic upper oceanic crust: DSDP Sites 417 and 418. *Washington D.C. American Geophysical Union Geophysical Monograph Series* **96**, 19-38.

Syracuse, E. M., van Keken, P. E. & Abers, G. A. (2010). The global range of subduction zone thermal models. *Physics of the Earth and Planetary Interiors* **183**, 73–90.

Till, C. B., Grove, T. L. & Withers, A. C. (2012). The beginnings of hydrous mantle wedge melting. *Contributions to Mineralogy and Petrology* **163**, 669–688.

Toplis, M. J. & Carroll, M. R. (1995). An experimental study of the influence of oxygen fugacity on Fe-Ti oxide stability, phase relations, and mineral-melt equilibria in ferro-basaltic systems. *Journal of Petrology* **36**, 1137–1170.

Ulmer, P., Kaegi, R. & Müntener, O. (2018). Experimentally Derived Intermediate to Silica-rich Arc Magmas by Fractional and Equilibrium Crystallization at 1·0 GPa: An evaluation of phase relationships, compositions, liquid lines of descent and oxygen fugacity. *Journal of Petrology* **59**, 11–58.

Ulmer, P. & Trommsdorff, V. (1995). Serpentine stability to mantle depths and subduction-related magmatism. *Science* **268**, 858–861.

van Keken, P. E., Wada, I., Abers, G. A., Hacker, B. R., & Wang, K. (2018). Mafic high-pressure rocksare preferentially exhumed from warm subduction settings. *Geochemistry, Geophysics, Geosystems* **19**, 2934-2961.

Chapter 3

LOWER CRUSTAL CONTROL IN THE IRON ISOTOPE SYSTEMATICS OF PLUTONIC XENOLITHS FROM ADAK ISLAND, CENTRAL ALEUTIANS, WITH IMPLICATIONS FOR ARC MAGMA GEOCHEMISTRY

3.1 ABSTRACT

We present bulk-rock and mineral Fe isotope data of ultramafic to mafic xenoliths and basaltic to andesitic lavas from Adagdak Volcano (Adak Island, Central Aleutians) to study the effects of early differentiation on the Fe isotopic evolution of island arc basalts and their crystallization products. The Fe isotope composition of ultramafic cumulate xenoliths increases from dunite (δ^{56}Fe = –0.09 to –0.02‰) to clinopyroxenite (δ^{56}Fe = +0.06 to +0.09‰), consistent with higher modal proportions of clinopyroxene (δ^{56}Fe = –0.05 to +0.11‰) relative to olivine (δ^{56}Fe = –0.10 to +0.06‰) in the latter. Mid-crustal cumulate amphibole gabbro and hornblendite cumulates also record heavier Fe isotope compositions (δ^{56}Fe = +0.04 to +0.08‰) due to the abundance of isotopically heavy amphibole (δ^{56}Fe = +0.07 to +0.09‰) and magnetite (δ^{56}Fe = +0.11 to +0.13‰) in these rocks. High inter-mineral fractionations observed in spinel-olivine and spinel-clinopyroxene pairs ($\Delta^{56}Fe_{spl\text{-}ol}$ = +0.12 to +0.28 and $\Delta^{56}Fe_{spl\text{-}cpx}$ = +0.06 to +0.19) suggest that spinel is not recording equilibrium crystallization conditions for the ultramafic assemblages, likely due to subsolidus Fe-Mg exchange. Our data also include Fe isotope measurements of one mantle dunite (δ^{56}Fe = +0.03 ± 0.05‰). Five Adagdak lavas, spanning from basalts to andesites, yield a narrow range of δ^{56}Fe between +0.03 and +0.06‰. Our results highlight the potential of amphibole in driving the Fe isotope depletion trends observed in many erupted arc lavas, as amphibole hosts 28-99% of the FeO_T budget in the amphibole gabbro and hornblendite cumulates. This is also supported by single-crystal synchrotron Mössbauer spectroscopy of two amphibole grains, the first from an amphibole gabbro and the second from a hornblendite, which yield $Fe^{3+}/\Sigma Fe$ ratios of 0.55

± 0.06 and 0.58 ± 0.02, respectively. Water content and hydrogen isotope compositions determined by secondary-ion mass spectrometry from the same amphibole grains indicate partial dehydrogenation. Using Rayleigh fractionation modeling to account for oxidation during post-crystallization dehydrogenation, we calculate magmatic $Fe^{3+}/\Sigma Fe$ ratios of 0.41 ± 0.04 for the amphibole gabbro and 0.30 ± 0.05 for the hornblendite. These data are then used to estimate an appropriate Fe force constant for Adagdak amphibole and quantitatively evaluate the effects of amphibole fractionation. Through a fractional crystallization model, we show how arc melts may experience periods of increasing $\delta^{56}Fe$ during olivine-dominated fractionation, followed by decreasing $\delta^{56}Fe$ once magnetite and amphibole saturate as cumulate phases. Notably, this dichotomy between fractionation of isotopically light versus heavy cumulate assemblages and its effects on the Fe isotope evolution of arc magmas is not captured by the Adagdak lava record, highlighting the utility of cumulates in chronicling the early isotopic evolution of magmatic systems.

3.2 INTRODUCTION

Iron isotope variations in lavas and mantle rocks are effective tracers of differentiation (Sossi et al., 2012; Nebel et al., 2015; Williams et al., 2018), partial melting (Weyer and Ionov, 2007; Williams and Bizimis, 2014), and changes in oxygen fugacity (fO_2) (Williams et al., 2005; Dauphas et al., 2014). The utility of Fe isotopes (expressed in delta notation as $\delta^{56}Fe = 1000 \times [(^{56}Fe/^{54}Fe)_{sample}/(^{56}Fe/^{54}Fe)_{standard} - 1)]$ in understanding these processes largely reflects the respective affinities of isotopically light versus heavy Fe for reduced (Fe^{2+}) and oxidized (Fe^{3+}) valence states (Polyakov and Mineev, 2000). Due to the oxidized nature of arc lavas (up to 3 log units above the fayalite-magnetite-quartz redox buffer [FMQ]) relative to mid-ocean ridge basalts (MORB: ~FMQ) (e.g., Cottrell et al., 2021, and references therein), and the preference for isotopically heavy Fe species in oxidized magmas (Dauphas et al., 2009, 2014; Roskosz et al., 2023), arc magmas are theoretically expected to display higher $\delta^{56}Fe$ than MORB. However, the Fe isotope compositions of arc lavas show more variability and extend to isotopically lighter values

than the observed range in MORB (arcs: $\delta^{56}Fe$ = –0.09 to +0.20‰, Dauphas et al., 2009; Foden et al., 2018; Williams et al., 2018; Chen et al., 2023; as compared to MORB: $\delta^{56}Fe$ = +0.06 to +0.18‰, Weyer and Ionov, 2007; Teng et al., 2013) (Fig. 1a).

The greater variability in $\delta^{56}Fe$ and the presence of isotopically light compositions in arc lavas may reflect a combination of several processes that distinctively operate in subduction zones, including (1) greater depletion in some arc sources due to higher extents of wet melting (e.g., Nebel et al., 2015; Foden et al., 2018; Chen et al., 2021), (2) reaction between subarc mantle peridotite and isotopically variable fluid fluxes from the subducted slab (Nebel et al., 2013; Debret et al., 2016; Deng et al., 2022; Chen et al., 2023), or (3) the effects of lower to mid-crustal differentiation in arcs (Li et al., 2020; Cooper and Inglis, 2022; Du et al., 2022). For example, subarc mantle peridotites are also isotopically light relative to those from mid-ocean ridges (Fig. 1b and references therein), which may reflect prior melt depletion of the subarc mantle (Williams et al., 2005; Williams and Bizimis, 2014) or metasomatism by isotopically light fluids derived from serpentinite breakdown in the slab (Debret et al., 2016, 2018, 2020). The latter process would suggest that the $\delta^{56}Fe$ of arc magmas may be inherited from their sources. In contrast, Foden et al. (2018) observed negative correlations between arc thermal parameter (φ, an expression of the slab temperature profile) and $\delta^{56}Fe$ in a globally distributed suite of mafic arc lavas, suggesting that light Fe isotope compositions in convergent margin magmas may instead reflect greater extents of flux melting in arcs with older and colder subducting slabs. This would imply that the isotopic depletion in some arc magmas reflects not only variable degrees of alteration of the mantle source but also differences in geodynamic regime.

In concert with the above processes, magmatic differentiation may also play an important role in the Fe isotope evolution of arc magmas due to the differences in bond strength between fractionating minerals (including silicates, oxides, and sulfides) and the melt (Dauphas et al., 2014; Sossi and O'Neill, 2017). Isotopically heavy Fe is preferentially incorporated into Fe^{3+}-bearing phases (e.g., oxides such as magnetite) over Fe^{2+}-bearing phases (e.g., olivine, orthopyroxene, garnet, and sulfides). The effects of magmatic differentiation on Fe isotope systematics in arcs

have primarily been studied through the volcanic record (Nebel et al., 2015; He et al., 2017; Foden et al., 2018; Williams et al., 2018; Johnson et al., 2023). For example, Williams et al. (2018) found that producing the major/trace element and Fe isotope trajectories ($\delta^{56}Fe$ = –0.04 to +0.09‰) of basaltic to dacitic lavas from Anatahan volcano (Marianas) requires three distinct stages with different crystallizing assemblages, including (1) olivine and pyroxene, (2) magnetite, and (3) sulfide fractionation. In comparison to the Marianas, which are built on relatively thin crust (~20 km; Calvert et al., 2008), the Fe isotope compositions of lavas from the Central Andes have higher $\delta^{56}Fe$ (+0.14 ± 0.04‰) and Sm/Yb (Du et al., 2022). This may suggest that early garnet fractionation at the base of the thick Andean crust (~60 km) drove later-stage melts to heavier Fe isotope compositions (Du et al., 2022). However, in a recent study of Indonesian calc-alkaline lavas, Johnson et al. (2023) found no correlations between indices of fractionation (e.g., SiO_2 and MgO) and $\delta^{56}Fe$. This led the authors to suggest that $\delta^{56}Fe$ of the melt was buffered by the crystallization of isotopically heavy magnetite, which prevented late-stage magmas from acquiring heavy Fe isotope compositions (Johnson et al., 2023). Taken together, these studies suggest that fractional crystallization may have variable effects on the Fe isotope evolution of magmas depending on the crystallizing assemblage and *P*-*T*-fO_2-H_2O conditions.

The plutonic record of differentiation in arcs and its effect on Fe isotope systematics in evolving melts has received comparatively less attention. Li et al. (2020) measured the Fe isotope compositions of gabbro and diorite samples from the Tongde region of Southern China. These rocks display an initial period of modest isotopic enrichment followed by a decrease in $\delta^{56}Fe$ as fractionation progresses, a pattern which Li et al. (2020) attribute to the removal of isotopically light garnet, pyroxene, and olivine in a deep crustal hot zone followed by crystallization of isotopically heavy amphibole at mid-crustal levels. Cooper and Inglis (2022) found that mid to upper-crustal (≤ 0.4 GPa) gabbro, gabbronorite, and hornblendite cumulate xenoliths from the Lesser Antilles had higher $\delta^{56}Fe$ compositions than upper-crustal non-cumulate gabbro xenoliths and erupted lavas, suggesting that mid-crustal fractionation depleted the melt in the heavy isotopes of Fe. However, this cumulate suite was restricted to mid to upper-crustal samples (≤ 15 km;

Cooper et al., 2016, 2019) and did not include lower crustal ultramafic assemblages (MgO <13.4 wt.% for all samples analyzed).

Understanding the source of the Fe isotope variability in arc lavas requires constraining the nature of primitive arc melts and how their δ^{56}Fe evolves during ascent through the entire crustal column. To address this, we measured Fe isotope compositions in ultramafic to mafic cumulate (*n* = 28) and mantle (*n* = 1) xenoliths from a well-documented lower to mid-crustal xenolith suite from the Adagdak Volcano on Adak Island, Central Aleutians (Fig. 2) (Debari et al., 1987; Sosa et al., 2023). We analyzed both minerals (spinel, clinopyroxene, olivine, amphibole, and magnetite) and whole-rock Fe isotope ratios. Amphibole Fe isotope data are complemented by single-crystal synchrotron Mössbauer spectroscopy of two amphibole grains, one from an amphibole gabbro (sample ADG-CB-1) and the other from a hornblendite (sample ADG-82-18). These measurements allow us to determine $Fe^{3+}/\Sigma Fe$ ratios for these grains and evaluate the potential of amphibole to drive the Fe isotopic evolution of Adagdak melts.

Our data extend to more primitive compositions than reported in the previous study of cumulate xenoliths (Cooper and Inglis, 2022), capturing a different, but complementary, interval of fractional crystallization (Fig. 3). We also measured δ^{56}Fe for five lavas from Mt. Adagdak, ranging from basalt to andesite (Kay and Kay, 1985, 1990, 1994). With this data, we construct a model to explore the effects of fractional crystallization of the isotopic evolution of arc magmas. Our results show that the cumulates chronicle a complex isotopic history that is not captured in the lava record.

3.3 GEOLOGICAL BACKGROUND AND SAMPLE DESCRIPTIONS

The Aleutian oceanic arc spans approximately 2000 km, extending from the western edges of the Alaskan Peninsula to its western terminus at the Kamchatka Peninsula. The arc consists of a largely submarine intra-oceanic ridge, which is only subaerial at volcanic centers (e.g., Scholl et al., 1975; Kay and Kay, 1994). Magmatism results from the northward subduction of the Pacific plate beneath the North American plate (e.g., Jicha and Kay, 2018). Although the arc has migrated

northward since 40 Ma, active magmatism in the Aleutians has occurred in a geometry similar to that of the present day for the past 52 to 46 million years (e.g., Kay et al., 1982, 1994; Davis et al., 1989; Jicha et al., 2006; Jicha and Kay, 2018). Crustal thicknesses show little variability and are approximately 39 ± 3 km all along the arc (Janiszewski et al., 2013). The xenolith suite from Mount Adagdak on Adak Island in the central Aleutians was collected in the late 1970s on the volcano's western slope from an olivine-phyric basalt flow (Fig. 2) (Debari et al., 1987). While the age of the Adagdak xenolith suite is unknown, exposed plutonic rocks on Adak Island have been dated from ~14 to 38 Ma (Citron et al., 1980; Jicha et al., 2006; Kay et al., 2019). The petrography, mineral chemistry, and crystallization conditions of the xenolith suite are extensively described in Debari et al. (1987) and Sosa et al. (2023), but we briefly highlight the most salient features here.

The samples described here were taken in 2017 from the Cornell collection, which includes extensive xenolith suites from both Mount Adagdak and Mount Moffett on Adak Island. The Adagdak xenolith suite is comprised of lower to mid-crustal cumulates, which range from primitive spinel dunite and wehrlite to more evolved amphibole gabbro and hornblendite. The crystallization sequence for the Adagdak cumulate suite is inferred to be olivine + clinopyroxene + spinel → clinopyroxene + amphibole + plagioclase + magnetite. The elongate and euhedral character of amphibole in the amphibole gabbro and hornblendite samples suggests a cumulate rather than peritectic origin (Debari et al., 1987; Sosa et al., 2023). peritectic amphibole is only observed as thin veins (< 1% by volume) along clinopyroxene grain boundaries in (± olivine) clinopyroxenite xenoliths (Sosa et al., 2023). The only oxide phase in the ultramafic cumulates is Fe-Cr-Al-Mg spinel (hitherto referred to simply as "spinel"), while the amphibole gabbro and hornblendite lithologies contain magnetite. The suite also contains one mantle lherzolite. Olivine-spinel-pyroxene oxybarometry of the ultramafic lithologies yields oxygen fugacity estimates of ΔFMQ = +0.1 to +2.1. Thermobarometry yields temperatures between 950 and 1150 °C for the ultramafic lithologies and 920 to 1070 °C for the amphibole gabbro and hornblendite samples (Sosa et al., 2023). The dunite, wehrlite, and clinopyroxenite xenoliths display adcumulate textures, whereas the amphibole gabbro and hornblendite samples have mesocumulate to

orthocumulate textures. Based on mineral chemistry, amphibole-only geobarometry, and comparisons to experimental studies, Sosa et al. (2023) interpreted the ultramafic assemblages (dunite and wehrlite cumulates) to be lower-crustal in origin, while the more evolved amphibole gabbro and hornblendite cumulates are likely sourced from the middle crust.

For this study, Fe isotope ratios were measured on whole-rock powders and/or mineral separates for 29 xenolith samples. These xenolith include dunite (n = 3), wehrlite (n = 8), olivine clinopyroxenite (n = 5), clinopyroxenite (n = 2), amphibole gabbro (n = 7), and hornblendite (n = 3) cumulates and one mantle xenolith, which is distinguished from the cumulate samples by highly magnesian olivine (Mg# = 91.3) 100 × [Mg/(Mg + Fe^T)] molar), clinopyroxene (Mg# = 93.8), and orthopyroxene (Mg# = 92.2) and chromium-rich spinel (Cr# = 60.0: where Cr# = 100 × Cr/[Cr+Al] molar) (Sosa et al., 2023). Representative photomicrographs and modal mineral proportions of thin sections for selected samples are given in the Appendix (Supplemental Figures 1 and 2), Supplementary Data File 2 (Ch3-T1), Sosa et al. (2023), and Debari et al. (1987). We also measured Fe isotope compositions of 5 lavas from Mt. Adagdak, which range from basalt to andesite (Supplementary Data File 2, Ch3-T7; Kay and Kay, 1985; 1994). Note that none of these samples represent the magnesium-rich host lava for the xenolith suite (Debari et al., 1987), but rather a more typical array of magma compositions erupted from Mt. Adagdak.

3.4 MATERIALS AND METHODS

3.4.1 Bulk-rock analyses

Samples were selected for bulk-rock analysis based both on grain size and the overall xenolith dimensions to ensure a representative measurement. Samples were cut into smaller aliquots (40-70 g per aliquot) to remove altered surfaces or veining. Samples were then polished with sandpaper to remove any saw marks and sonicated in deionized water. Cleaned aliquots were crushed and powdered in an agate grinding vessel. Powders were dried overnight at 110 ºC, then heated to 1050 ºC for one hour to determine loss on ignition (LOI). The LOI for amphibole-rich samples (n = 9)

was performed at 1100 ºC to ensure any structurally bound water was volatilized. Glass beads were prepared using a 10:1 mass ratio of Li-borate flux to sample powder and fused at 1200 ºC. Major elements (Si, Ti, Al, Fe, Mn, Mg, Ca, Na, K, P) were analyzed using a Panalytical Zetium 4 kW wavelength-dispersive X-ray fluorescence (XRF) spectrometer at Caltech following methods in Bucholz and Spencer (2019). Trace elements (Cr, Ni, Rb, Sr, Y, Zr, Ba, Nb, Cs, all REEs, Hf, Ta, Pb, Th, U) were measured from glass chips of the Li-borate beads through solution inductively-coupled plasma mass spectrometry following methods described in Lewis et al. (2021). Bulk-rock xenolith compositions (n =19) are given in Supplementary Data File 2 (Ch3-T2).

3.4.2 Mineral chemistry

Major element mineral compositions of olivine, clinopyroxene, amphibole, and magnetite were obtained from polished thin sections with a JEOL JXA-8200 Electron Probe MicroAnalyzer (EPMA) at Caltech. These analyses were combined with previously obtained major and trace element mineral compositions for the cumulate xenoliths (Sosa et al., 2023). The majority of the mineral major element data used in this study and all of the trace element data were presented in Sosa et al. (2023), which details the analytical conditions, detection limits, and data reduction of these analyses. The same analytical conditions and data reduction procedures were used here. All mineral data are provided in Supplementary Data File 2 (Ch3-T3 to Ch3-T6) along with the corresponding Fe isotope analyses, and the source of the major element data (i.e., Sosa et al., 2023 vs. this study) is noted for each analysis in the Appendix. The most salient features of these data are highlighted in Table 1.

3.4.3 Single-crystal Mössbauer spectroscopy

Single-crystal synchrotron Mössbauer spectroscopy (SMS) of amphibole grains (n = 2) was performed at the Advanced Photon Source, Argonne National Laboratory, USA, following the methodology described in Ratschbacher et al. (2023). Both amphibole grains were fully characterized through EPMA (major and minor elements), secondary-ion mass spectrometry

(SIMS) to determine water contents and hydrogen isotope composition, and single crystal-X-ray diffraction to determine unit cell parameters and identify twinning prior to SMS. Details of these analyses are given in the Appendix. Single-crystal time-domain Mössbauer spectra were collected at beamline 3ID-D during the hybrid mode filling pattern of the storage ring. For each grain, spectra were collected in two distinct crystallographic orientations with and without a stainless-steel reference foil (natural isotopic abundance of ^{57}Fe; thickness of 10 μm). Spectra were fitted using the CONUSS 2.3.0 software package (Sturhahn, 2000; 2021). Additional details related to the SMS experiments and the spectral fitting results—including the time window used to fit the spectra, the best-fit hyperfine parameters and their uncertainties, as well as the Euler angles and asymmetry parameters determined from the "K-H" hornblende crystal structure reported in Makino and Tomita (1989)—are given in the Appendix.

3.4.4 Iron isotopes

The Fe isotopic composition of mineral separates and whole-rock powders were measured at the Isotoparium, Caltech. Mineral separates were hand-picked using stainless steel tweezers under a binocular to ensure all grains were free of inclusions and visible alteration. Grains were then sonicated in isopropyl alcohol and deionized water to remove any surface contamination. Reference USGS rock powders AGV-2, BHVO-2, BCR-2, and COQ-1, whose Fe isotope compositions have previously been measured (Craddock and Dauphas, 2010), were prepared and analyzed alongside samples to confirm data accuracy. Sample digestion and Fe separation via ion chromatography followed the methods of Dauphas et al. (2004). Across all repeated analyses, USGS rock powders AGV-2, BHVO-2, BCR-2, and COQ-1 yielded average δ^{56}Fe of +0.100 ± 0.007, +0.113 ± 0.010, +0.104 ± 0.008, and –0.095 ± 0.026‰, respectively, in agreement with previously published values for these samples (AGV-2 = +0.105 ± 0.011‰, BHVO-2 = +0.114 ± 0.011‰, BCR-2 = +0.091 ± 0.011‰, and COQ-1 = –0.117 ± 0.030‰: Craddock and Dauphas, 2010). The measured Fe isotope ratios for each replicate analysis of the USGS standard powders are given in Supplementary Data File 2 (Ch3-T8). The measured compositions of these reference

rock powders show long-term reproducibility from January to December of 2022 (Supplementary Data File 2, Ch3-T8).

Whole-rock powders (1-2 mg) and mineral separates of olivine (1-2 mg), clinopyroxene (2-3 mg), amphibole (1-2 mg), and magnetite (~1 mg) were digested using a series of acid attacks on hot plates: (1) 1.5 mL concentrated 2:1 HF:HNO_3 solution for 5 hours at 100 °C, (2) 1.25 mL of 3:1 HCl:HNO_3 (aqua regia) overnight at 140 °C, (3) 1.5 mL of 2:1 HCl:HNO_3 overnight at 140 °C, (4) 1 mL concentrated HCl at 180 °C for two days. Samples were fully dried between each digestion step. After the final digestion, samples were dried, brought into a 6 M HCl solution, and refluxed overnight at 130 °C in preparation for column chemistry. We were not able to digest bulk spinel mineral separates using the methods presented above due to spinel's refractory nature, and instead opted to digest, chemically purify, and analyze single grains of spinel. Each spinel grain was individually digested in a Parr bomb for a total of eight days. First, each spinel grain was loaded into a separate 200 µL microcapsule and digested in three drops (~ 90 µL) of concentrated HF inside a Parr bomb for two days at 210 °C. While remaining inside the microcapsule, the spinel grains were then dried down on a hot plate, taken back into solution with three drops of 5 M HCl, and refluxed in the Parr bomb at 180 °C for two days. Each spinel grain went through an additional round of digestion, first in concentrated HF then (after being dried down again) in 5 M HCl, before being fully dried and brought into a 6 M HCl solution prior to column chemistry.

Iron purification was performed using 10 mL polyethylene chromatography columns (Biorad Polyprep) with 1 mL of BioRad AG1-X8 (200-400 mesh size) anion exchange resin. The samples were loaded in 0.5 ml of 6 M HCl. Matrix elements were eluted with 9 mL of 6 M HCl, and the purified Fe cut was then recovered with 8 mL of 0.4 M HCl. To ensure complete removal of all matrix-forming elements, column chemistry was performed twice for each sample. In preparation for analysis, samples were dried down and refluxed overnight at 140 °C in 0.5 mL of concentrated HNO_3. Samples were then dried to a drop (<25 µL), taken back up in 5 mL of 0.3 M HNO_3 run acid, and refluxed overnight at 130 °C.

Iron isotope measurements were made on a Neptune Plus (ThermoFisher) Multi-Collector Inductively-Coupled-Plasma Mass-Spectrometer (MC-ICP-MS) in wet plasma conditions (glass spray chamber). To resolve ArO interferences, measurements were performed in high mass resolution mode using ThermoFisher general Ni sample and skimmer cones and a static cup configuration monitoring masses 53 through 60. In addition to all four isotopes of Fe, we also measured ^{53}Cr, ^{55}Mn, ^{59}Co, and ^{60}Ni . Measurements of ^{53}Cr and ^{60}Ni were respectively used to account for and remove interferences of ^{54}Cr on ^{54}Fe and ^{58}Ni on ^{58}Fe, while ^{55}Mn and ^{59}Co were monitored to verify complete separation of Fe from matrix elements during column chemistry. All Faraday cups were assigned 10^{11} Ω feedback resistors, except for ^{60}Ni (H4 cup), which was assigned a 10^{12} Ω feedback resistor to improve the accuracy of Ni isobaric interference monitoring and corrections. Cup gains were calibrated at least weekly, and the instrument was tuned for optimal sensitivity and stability.

Standard and sample solutions diluted to a final Fe concentration of 5 µg/g in 3% vol HNO_3 were aspired using a PFA nebulizer with a nominal flow rate of 50 µl/min, yielding a typical beam intensity of 20-25 V on ^{56}Fe, corresponding to a sensitivity of 4-5 V/ppm. On-peak-zeros (OPZ) were measured before all samples and standards using a 90 second uptake and 40 seconds of on-peak measurement of clean acid solution from the same batch used to dilute the samples. This was done to monitor memory effects of the sample introduction system and remove background from all measurements. Typical background intensities were ~ 5-7 mV on ^{56}Fe. Sample and bracketing standard measurements consisted of 90 s of sample uptake, followed by 50 cycles of 4.192 second integration time for each measurement, for a total of 210 seconds of static on-peak sample measurement. The inlet system was then rinsed for 120 seconds between samples using 3 % vol HNO_3, before repeating the cycle for the next standard/unknown. Each unknown measurement was bracketed with the IRMM-524b metallic Fe standard diluted in the same run acid and at the same Fe concentration (within 5 %). Within each run, at least one USGS reference material was measured alongside the unknown samples.

Following the methods of Dauphas et al. (2009), we calculated the corresponding error for each measurement using the standard deviation (SD) of the IRMM-524b standard for each analytical session:

$$\text{Error} = 2 \times \text{SD}_{\text{IRMM-524b}}/(n_{\text{sample}})^{0.5}$$

where n_{sample} is the number of measurements performed for the sample. During standard bracketing, the IRMM-524b standard is measured more frequently than any one sample, and its standard deviation is therefore taken to be more representative of the actual uncertainty for the analytical session (Dauphas et al., 2009).

3.5 RESULTS

3.5.1 Xenoliths

Whole rock: The cumulate compositions display the characteristic Z-shaped pattern on a Mg# versus SiO_2 diagram that is typical for cumulates formed from the differentiation of hydrous, oxidized arc magmas (e.g., Müntener and Ulmer, 2018; Fig. 3). Silica concentrations (37.4-50.0 wt.% for all samples) are lowest in the dunite samples (37.4-38.7 wt.%) and increase to 49-50 wt.% in the clinopyroxenite xenoliths at a relatively constant Mg# (83-89) (Fig. 3). Amphibole accumulation then leads to a decrease in Mg# (51-72) and SiO_2 (43 wt.%) for both hornblendite and amphibole gabbro xenoliths. MgO varies from 7.2 to 45.9 wt.% for the cumulate xenoliths, while mantle xenolith ADG-CB-9 has 49.0 wt.% MgO (Fig. 4a). FeO_T ranges from 4.3 to 13.8 wt.% in the cumulate samples, with the lowest values observed in the (± olivine) clinopyroxenite xenoliths (4.3-5.6 wt.%). The one analyzed mantle xenolith has a Mg# of 90.5 and 38.6 wt.% SiO_2.

While thin section petrography of sample ADG-CB-9 indicated that the sample should be classified as a lherzolite (albeit at the lherzolite-dunite boundary on the IUGS ultramafic classification diagram), the high whole-rock MgO content of this sample suggests that in a bulk-rock content, this sample should be classified as a dunite. To estimate modal abundances for the

dunite sample, we used mineral compositions, our whole-rock chemistry, and the Log-ratio Inversion of Mixed End-members (LIME) model of Prissel et al. (2023) to balance our whole-rock data against the average compositions of measured mineral phases. The results of these calculations suggest that the sample is, by volume, composed of approximately 96-97% olivine, 1% clinopyroxene, 1-2% orthopyroxene, and 2% spinel. This discrepancy between thin section and bulk modal proportions may be attributed to the small size of the mounted and polished thin section (~1.5 × 1.5 cm) compared to the bulk sample (~8 cm^3) and the coarse nature of the sample (grains up to 2.5 mm in diameter). As we are interested in compositional trends rather than relating Fe isotope chemistry to specific petrographic characteristics, we chose to classify this sample as a dunite for our discussion. Dunite xenoliths are therefore categorized as "cumulate dunite" (i.e., samples ADG-82-2, ADG-82-21, and ADG-63) or mantle dunite (i.e., ADG-CB-9) in all future figures, tables, and discussion.

Cumulate whole-rock Fe isotope compositions (n = 19) range from δ^{56}Fe = –0.09 to +0.09‰ and are strongly correlated to lithology and MgO (Fig. 4a) but uncorrelated with FeO_T. Dunite, wehrlite, and olivine clinopyroxenite cumulates with MgO >30 wt.% display the lowest δ^{56}Fe (–0.09 to +0.04‰), while the more evolved clinopyroxenite, hornblendite, and amphibole gabbro samples display heavier isotopic compositions (δ^{56}Fe +0.04 to +0.09‰). The mantle dunite has a whole-rock δ^{56}Fe of –0.03 ± 0.05‰. Positive correlations are observed between whole-rock δ^{56}Fe and incompatible element concentrations (e.g., Nd, Sr; Fig. S6a, b), while compatible elements are negatively correlated with δ^{56}Fe (e.g., Cr; Fig. S6c).

Olivine: Iron isotope compositions were measured for olivine separates from 14 ultramafic cumulates and range from δ^{56}Fe = –0.10 to +0.07‰ (Fig. 4b, c). Olivine spans a limited compositional range in terms of major elements within the cumulates (Mg# = 84-87), with no apparent correlations between olivine composition and δ^{56}Fe.

Clinopyroxene: The Fe isotope composition of clinopyroxene mineral separates (n =16) from wehrlite, (± olivine) clinopyroxenite, and amphibole gabbro cumulates range from δ^{56}Fe = –0.05

to +0.11‰ (Fig. 4b). Clinopyroxene Mg# for these samples ranges from 72.6 to 88.2 and is highest in the ultramafic lithologies (Mg# = 85.0-88.2). Clinopyroxene δ^{56}Fe displays broad correlations with whole-rock MgO and modal mineralogy, with the highest clinopyroxene δ^{56}Fe generally observed in cpx-rich (>80% modally) samples with whole-rock MgO between 16-20 wt.%. Positive correlations are also observed between δ^{56}Fe in coexisting olivine and clinopyroxene (Fig. 4b).

Amphibole: Iron isotope compositions were measured in amphibole mineral separates from hornblendite (n = 2) and amphibole gabbro (n = 2) cumulates and range from δ^{56}Fe = +0.07 to +0.09‰ (Fig. 5a). Following the classification scheme of Hawthorne et al. (2012), the Adagdak cumulates contain pargasitic amphibole. Amphibole Mg# ranges from 64.7 to 71.0 for these samples. Single-crystal synchrotron Mössbauer spectra of amphibole yield $Fe^{3+}/\Sigma Fe$ ratios of 0.55 ± 0.06 for the grain from amphibole gabbro ADG-CB-1 (grain 6), and 0.58 ± 0.02 for the grain from hornblendite ADG-82-18 (grain 10). For ADG-CB-1 grain 6, water contents analyzed by SIMS for the same area as the SMS spectra reveal 1.60 ± 0.13 wt.% H_2O and δD = –45 ± 11‰ (relative to SMOW; average of grain 6 and grain 3 from ADG-CB-1). ADG-82-18 grain 10 contains 1.34 ± 0.11 wt.% H_2O. While we do not have D/H ratios of this grain, SIMS analyses of two other amphibole grains from ADG-82-18 yield an average δD = –21 ± 6‰. Both grains contain less than 0.1 wt.% Cl + F.

Oxides: The ultramafic cumulates contain aluminous spinel (Cr# = 33-47) with δ^{56}Fe ranging from +0.10 to +0.28‰ (Fig. 4d-f). For four cumulate samples, we performed single-grain Fe isotope analysis on two separate spinel grains from each sample (i.e., a total of 8 analyses from 4 samples). The measured values of δ^{56}Fe for spinel grains from the same sample were consistently within error of each other. For the samples in which we measured the composition of both spinel and coexisting olivine (n = 5), δ^{56}Fe in spinel is positively correlated with δ^{56}Fe in olivine (Fig. 4c). In the cumulate samples, spinel δ^{56}Fe shows a weak negative correlation with $Fe^{3+}/\Sigma Fe$ (r^2=0.55, Fig. 4d) and Cr# (r^2=0.45, Fig. 4e) and a stronger positive correlation with Mg# (r^2=0.73, Fig. 4f).

Spinel in the mantle dunite is more chromium-rich (Cr#=60) than in the cumulates. The two spinel grains analyzed from the mantle dunite have δ^{56}Fe of +0.18 ± 0.04‰ and +0.11 ± 0.02‰. Magnetite is the dominant oxide phase in the amphibole gabbro and hornblendite cumulates. The δ^{56}Fe of three bulk magnetite mineral separates ranges from +0.11 to +0.13‰ (Fig. 5a).

3.5.2 Lavas

Iron isotope compositions were obtained for five Adagdak lavas, ranging from basalt to andesite. The measured δ^{56}Fe of the lavas ranges from +0.03 to +0.06‰ (Figs 5a and 6a). These values are typical of δ^{56}Fe observed in arc lavas (Fig. 1) and are similar to previous analyses of Central Aleutian arc lavas reported by Foden et al. (2018) (δ^{56}Fe = 0.00 to +0.08‰; Fig. 6a). While our lava samples do not extend to the high silica concentrations reported for Adagdak dacites by Romick et al. (1992), they span much of the compositional range observed by previous studies (Coats, 1952; Myers et al., 1985; Debari et al., 1987; Kay and Kay, 1985, 1994) of Adagdak basalt and andesite (Fig 6b). Our samples also do not extend to the high MgO concentrations observed in sample ADAG-81DR (11.83 wt.% MgO; Debari et al., 1986), the olivine-phyric host basalt of the Adagdak cumulate suite.

3.6 DISCUSSION

3.6.1 Effects of dehydrogenation on $Fe^{3+}/\Sigma Fe$ in amphibole

Two lines of evidence suggest that cumulate amphibole experienced dehydrogenation after crystallizing: 1) the presence of an oxo-component (O^{2-}) in amphibole gabbro ADG-CB-1 grain 6 (0.21-0.47 wt.%) and hornblendite ADG-82-18 grain 10 (0.49-0.71 wt.%; dependent on the uncertainties of water concentrations), and 2) δD values (–16 to –52‰ for all measured grains) that are heavier than the average reported measurements for arc magmatic waters as determined from melt inclusions (–60 to –80‰; compilation in Ratschbacher et al., 2023) (e.g., Demény et al., 2012). Dehydrogenation is accompanied by oxidation of ferrous to ferric Fe in the amphibole structure through the following reaction: $Fe^{2+} + OH^- \rightleftharpoons Fe^{3+} + O^{2-} + H^+$. Thus, the $Fe^{3+}/\Sigma Fe$ ratios determined by SMS of amphibole that has experienced dehydrogenation likely do not reflect

primary magmatic values. In an effort to estimate the magmatic $Fe^{3+}/\Sigma Fe$ ratios of amphibole during crystallization, we constructed two Rayleigh fractionation inverse models, assuming an initial amphibole $\delta D = -80‰$ and H_2O content of 2 wt.% (calculations and further details given in the Appendix). These calculations suggest that the $Fe^{3+}/\Sigma Fe$ ratio of ADG-CB-1 grain 6 and ADG-82-18 grain 10 during crystallization were 0.41 ± 0.04 and 0.30 ± 0.05, respectively. Due to its structural complexity, previous studies have not attempted to rigorously constrain the amphibole force constant. Li et al. (2020) estimated an amphibole force constant of 250 N/m based on the relationship between mineral coordination number and $Fe^{3+}/\Sigma Fe$, as discussed by Sossi and O'Neill (2017), and assuming an amphibole $Fe^{3+}/\Sigma Fe$ ratio of 0.53. Using the same method and a representative amphibole gabbro $Fe^{3+}/\Sigma Fe$ ratio 0.41 ± 0.04, we estimate an amphibole force constant of 241 ± 9 N/m for an average Adagdak amphibole composition.

3.6.2 Preservation of magmatic mineral compositions

Iron-magnesium ratios in cumulate minerals are susceptible to diffusive exchange between coexisting phases during cooling and lower-crustal residence. Subsolidus equilibration in mafic and ultramafic rocks can result in underestimates of magmatic temperatures when olivine-spinel geothermometry is applied to these assemblages (e.g., Fabriès, 1979; Lehmann, 1983). Studies have shown that subsolidus exchange also affects the Fe and Mg isotope systematics of coexisting phases in igneous rocks, and that spinel group minerals are particularly susceptible to alteration through these processes (e.g., Chen et al., 2014; Bai et al., 2020). To assess whether major element systematics are recording magmatic conditions, we first compare calculated mineral-equilibria temperatures and Fe/Mg ratios of coexisting phases in the Adagdak xenoliths to high-temperature experimental data.

Experiments conducted at conditions relevant to the crystallization of basaltic magmas in the lower oceanic crust (i.e., 0.7-1 GPa, >3 wt.% H_2O, fO_2 > FMQ: Blatter et al., 2013; Nandedkar et al., 2014; Ulmer et al., 2018; Marxer et al., 2022) produce dunite, wehrlite, and (± olivine) clinopyroxenite assemblages between 1230 and 1020 ºC and an amphibole gabbro assemblage

between 1030 and 700 ºC (Fig. 7). Apart from clinopyroxenite ADG-82-15, which preserves an anomalously low temperature of 914 +42/–49 ºC, the temperatures calculated with Fe-Mg exchange thermometry for the ultramafic cumulates (1000 to 1170 ºC: Sosa et al., 2023) are consistent with experimental studies. Comparison to experimental data suggests that the temperatures calculated from olivine-spinel thermometry of the olivine clinopyroxenite cumulates (1030 ± 20 ºC) are more appropriate estimates for Adagdak clinopyroxenite samples ADG-82-1 and ADG-82-15. Temperature estimates for Adagdak amphibole gabbro cumulates calculated with amphibole-only thermobarometry (920-970 ºC) are also consistent with experimental data, while those obtained through amphibole-plagioclase thermometry (1075-920 ºC) are slightly higher but generally in agreement with the range over which experimental studies have crystallized these assemblages.

Co-crystallizing olivine and clinopyroxene from experimental studies of lavas ranging from basalts to Mg-andesites preserve $K_D(Fe^T/Mg)^{cpx\text{-}ol}$ (i.e., molar $[Fe^T/Mg]_{ol}/[Fe^T/Mg]_{cpx}$) between 0.7 and 1.6 (Fig. 7; Holloway and Burnham, 1972; Sisson and Grove, 1993; Müntener et al., 2001; Pichavant and Macdonald, 2007; Krawczynski et al., 2012; Blatter et al., 2013; Stamper et al., 2014; Ulmer et al., 2018), consistent with the range observed in coexisting olivine and clinopyroxene in the Adagdak xenoliths ($K_D(Fe^T/Mg)^{cpx\text{-}ol}$ = 0.7-1.3). We note that while most (89%) of the ultramafic Adagdak xenoliths preserve $K_D(Fe^T/Mg)^{cpx\text{-}ol}$ between 0.7 and 0.9, samples ADG-8 and ADG-82-1 are outliers with higher K_Ds of 1.2 and 1.3, respectively. While still within the range observed in experimental studies, this deviation in Fe-Mg partitioning from what is observed in other samples within the suite may indicate that these samples have been affected by subsolidus processes to such an extent that they no longer reflect magmatic conditions. Concerning the Adagdak mantle dunite, orthopyroxene-clinopyroxene pairs in partial melting experiments of mantle peridotites yield $K_D(Fe^T/Mg)^{cpx\text{-}opx}$ between 0.8 and 1.4 (Gaetani et al., 1998; Wasylenki et al., 2003; Green et al., 2014; Mandler and Grove, 2016), consistent with the value of $K_D(Fe^T/Mg)^{cpx\text{-}opx} = 0.8 \pm 0.1$ preserved by sample ADG-CB-9 (Fig. 7)

Taken together, comparisons to experimental studies suggest that—apart from the specific samples discussed above (ADG-8 and ADG-82-15)—the Adagdak cumulates appear to preserve magmatic conditions and appropriate temperature estimates for modeling purposes. Iron-magnesium partitioning between olivine-clinopyroxene and orthopyroxene-clinopyroxene pairs in Adagdak lherzolite ADG-CB-9 also appears to reflect upper-mantle equilibrium conditions.

3.6.3 Inter-mineral fractionation

We compare measured inter-mineral isotope fractionation factors between co-crystallizing phases in the Adagdak xenoliths to theoretical predictions based on the force constant for Fe in different phases ($<F>_{mineral}$) and estimates of crystallization temperature (Sosa et al., 2023). The force constants of olivine, spinel, and magnetite have been measured by previous studies (Polyakov et al., 2007; Dauphas et al., 2012, 2014; Roskosz et al., 2015; Sossi and O'Neill, 2017). Due to their complex crystallographic structures and ability to structurally incorporate both ferric and ferrous Fe, the force constants for clinopyroxene and amphibole have not been determined but can be estimated based on observed inter-mineral fractionation within the cumulates and data from previous studies. The force constants used in these calculations are given in Table 2 and discussed in greater detail in the Appendix.

Within the ultramafic cumulates, spinel is consistently the isotopically heaviest phase (δ^{56}Fe = +0.10 to +0.28‰), followed by clinopyroxene (δ^{56}Fe = –0.05 to +0.11‰), and olivine (δ^{56}Fe = –0.10 to +0.06‰) (Fig. 5). Coexisting clinopyroxene and olivine preserve fractionations of $\Delta^{56}Fe_{cpx\text{-}ol}$ = +0.05 to +0.10‰ (Fig. 4b). Similar degrees of clinopyroxene-olivine fractionation are observed in spinel lherzolite xenoliths from the Mexican Basin and Range province ($\Delta^{56}Fe_{cpx\text{-}ol}$ = +0.03 to +0.06‰; Williams et al., 2005) and un-metasomatized Mg-lherzolites from the North China Craton ($\Delta^{56}Fe_{cpx\text{-}ol}$ = +0.04 to +0.09‰; Zhao et al., 2015). The strong positive correlations between δ^{56}Fe in coexisting olivine and clinopyroxene in the Adagdak samples (R^2 = 0.76), and the similarity between our measured $\Delta^{56}Fe_{cpx\text{-}ol}$ for the cumulates and that from previous studies of equilibrated mantle rocks suggest, that the Adagdak cumulates also record isotopic equilibrium

between co-crystallizing clinopyroxene and olivine. Using the observed clinopyroxene-olivine fractionation, temperature constraints from Fe-Mg exchange thermometry (Sosa et al., 2023) comparisons to experimental studies, and the known relationship between inter-mineral fractionation factors and force constants ($\Delta_{B\text{-}A} = (\delta_B - \delta_A) = 2853[\langle F \rangle_B - \langle F \rangle_A]/T^2$; Dauphas et al., 2014), we can estimate an appropriate clinopyroxene force constant from our data. Using the range of observed values for $\Delta^{56}Fe_{cpx\text{-}ol}$ (0.05-0.10‰), an average crystallization temperature of 1060 °C for the ultramafic assemblages, and an olivine force constant of 197 ± 10 N/m (Dauphas et al., 2014), our data suggest the clinopyroxene force constant should be between 227 and 262 N/m. Taking the average observed clinopyroxene-olivine fractionation of $\Delta^{56}Fe_{cpx\text{-}ol} = 0.07 \pm 0.02$‰, we use an estimate of $\langle F \rangle_{cpx} \approx 239 \pm 13$ N/m in our modeling moving forward.

Force constants for Adagdak spinel were calculated using the parameterization of Roskosz et al. (2015), where $\langle F \rangle = 190 \pm 15$ N/m for Fe^{2+} in Mg-Fe-Al spinel and $\langle F \rangle = 302 \pm 18$ N/m for Fe^{3+}. Spinel $Fe^{3+}/\Sigma Fe$ ratios were taken from Sosa et al. (2023), who calculated Fe speciation following the methods of Wood and Virgo (1989). For these analyses, spinel is analyzed in a separate EPMA session, and every 150-200 spinel analyses are bracketed by measurements of spinel grains whose $Fe^{3+}/\Sigma Fe$ ratios have previously been determined through Mössbauer spectroscopy (Wood and Virgo, 1989; Bryndzia and Wood, 1990). Spinel $Fe^{3+}/\Sigma Fe$ ratios for unknown samples, which are initially calculated from EPMA data through charge balance, are then adjusted using the correction scheme of Wood and Virgo (1989) (see Davis et al., 2017 for a recent discussion of the method). Calculated $Fe^{3+}/\Sigma Fe$ ratios for the measured Adagdak cumulate spinel range from 0.39 to 0.41 (Supplementary Data File 2, Ch3-T6), and using the parameterization of Roskosz et al. (2015), yield spinel force constants between 233 and 236 N/m.

The fractionation factor between coexisting Adagdak spinel and olivine ranges from $\Delta^{56}Fe_{spl\text{-}ol} = +0.12$ to $+0.28$‰. Dunite, wehrlite, and olivine clinopyroxenite cumulates from Adagdak preserve equilibrium temperatures between 1000 and 1170 ºC (Sosa et al., 2023). Using the average spinel force constant of 235 N/m and an olivine force constant of 197 (Dauphas et al., 2014), calculated estimates for equilibrium spinel-olivine fraction over this temperature interval are considerably lower, ranging from $\Delta^{56}Fe_{spl\text{-}ol} = +0.05$ to $+0.07$‰. High degrees of spinel-olivine

fractionation have also been previously observed in mantle lherzolite xenoliths ($\Delta^{56}Fe_{spin\text{-}ol}$ of +0.2 to +0.4‰; Zhao et al., 2015; Williams et al., 2015) (Fig. 8). These large inter-mineral fractionations between spinel and other mantle minerals have been attributed to disequilibrium developed during metasomatism or partial melting (Williams et al., 2005; Zhao et al., 2015; Roskosz et al., 2015). Additionally, measured spinel-clinopyroxene fractionations in the Adagdak cumulates range from $\Delta^{56}Fe_{spl\text{-}cpx}$ = +0.06 to +0.19‰. Using our estimated clinopyroxene force constant of 239 N/m and an average spinel force constant of 235 N/m, the equilibrium fractionation between coexisting Adagdak spinel and clinopyroxene should be $\Delta^{56}Fe_{spl\text{-}cpx} \approx 0.0$‰ at 1050 ºC.

The large inter-mineral isotopic fractionation between spinel and other phases suggests that spinel Fe isotope ratios do not record equilibrium conditions during crystallization in the cumulates. Instead, their Fe isotopic composition may reflect subsequent (partial) re-equilibration via Fe-Mg diffusion during their residence in the lower crust. Subsolidus exchange of Mg and Fe^{2+} between spinel and olivine during cooling has been well documented in experimental studies (e.g., Ozawa, 1984; Liermann and Ganguly, 2002; Vogt et al., 2015), resulting in a loss of Fe from spinel to olivine. Small spinel grains, such as those in the Adagdak cumulates (10-300 μm in diameter), are particularly susceptible to Fe loss during cooling (Ozawa, 1984), and their Fe isotope composition would be more affected by this process as compared to modally dominant olivine. The greatest spinel-olivine fractionation is also observed in the most olivine-rich cumulates (dunite: $\Delta^{56}Fe_{spin\text{-}ol}$ = +0.20 to +0.28‰, wehrlite: $\Delta^{56}Fe_{spin\text{-}ol}$ = +0.12 to +0.24‰). Spinel from all Adagdak cumulates shows core-to-rim increases in Mg# (+0.2 to +1.4), consistent with the idea that the rims of these small grains were affected by subsolidus Fe-Mg diffusion with neighboring olivine. If the effects of post-cumulus Fe-Mg exchange were concentrated in grain rims, this may partially explain why temperatures obtained through Fe-Mg exchange thermometry appear to be recording magmatic conditions, as these temperatures were calculated exclusively with core compositions.

Using temperature estimates and the known force constant of spinel and olivine, we can estimate theoretical δ^{56}Fe values of cumulate spinel. Crystallization experiments on primitive basalts conducted under conditions relevant to the lower arc crust (0.7-1 GPa, 3-4 wt.% initial

H_2O, fO_2 = NNO to NNO+2) typically crystallize dunite and wehrlite assemblages between the liquidus (~1200 °C) and ~1050 °C (Blatter et al., 2013; Nandedkar et al., 2014; Ulmer et al., 2018). Between 1200 and 1050 °C, the calculated equilibrium fractionation between spinel with $Fe^{3+}/\Sigma Fe$ = +0.38 to +0.41 (the range observed in spinel from Adagdak cumulates) and olivine is $\Delta^{56}Fe_{spl\text{-}ol}$ = +0.05 to +0.07‰. This would imply that olivine in the Adagdak dunite and wehrlite cumulates ($\delta^{56}Fe$ = –0.08 to +0.06‰) would have been in equilibrium with spinel with $\delta^{56}Fe$ between –0.03 and +0.13‰ during crystallization. Even considering the errors on reported spinel and olivine force constants, the maximum force constants for the Adagdak spinel would be 250-257 N/m. Using a minimum olivine force constant of 187 N/m, this would yield $\Delta^{56}Fe_{spl\text{-}ol}$ = 0.07 to 0.10‰ and imply that olivine in the Adagdak dunite and wehrlite cumulates would have crystallized in equilibrium with spinel with $\delta^{56}Fe$ –0.01 to +0.16‰, values which are still below the observed range some cumulate spinel ($\delta^{56}Fe$ = +0.10 to +0.28‰).

In the amphibole gabbro and hornblendite xenoliths, magnetite is consistently the phase with the highest $\delta^{56}Fe$ (+0.10 to +0.13‰), followed by amphibole (+0.07 to +0.09‰) and clinopyroxene (+0.05 to +0.07‰). Although we only have measurements of coexisting clinopyroxene and amphibole from two cumulates (amphibole gabbro samples ADG-6 and ADG-CB-1), these samples show similar degrees of amphibole-clinopyroxene fractionation with $\Delta^{56}Fe_{amph\text{-}cpx}$ = –0.01 to +0.01‰. While Fe isotope measurements of coexisting amphibole and clinopyroxene are scarce in the literature, similarly small degrees of amphibole-clinopyroxene fractionation have also been observed in mineral separates from augite syenites in the Ilímaussaq Complex by Schoenberg et al. (2009) ($\Delta^{56}Fe_{amph\text{-}cpx}$ = +0.03 ± 0.05‰), who interpreted these samples as preserving near isotopic equilibrium.

As our estimated force constants of amphibole and clinopyroxene (241 and 239 N/m, respectively) are within error of each other, we predict $\Delta^{56}Fe_{amph\text{-}cpx} \approx 0.0$‰ at equilibrium assuming an average crystallization temperature of 970 °C for the amphibole gabbro cumulates. In conjunction with comparisons to literature data and considering the typical errors of these measurements (0.02-0.03‰), this suggests that amphibole-clinopyroxene pairs are recording isotopic equilibrium within the amphibole gabbro cumulates. While we only have measurements

of co-crystallizing clinopyroxene and magnetite from one cumulate (ADG-74) and no measurements of coexisting amphibole and magnetite, the average Fe isotope compositions of these phases in the amphibole gabbro cumulates preserve magnetite-silicate fractionations of $\Delta^{56}Fe_{mag\text{-}cpx}$ and $\Delta^{56}Fe_{mag\text{-}amph} \approx +0.05‰$. Using a magnetite force constant of 264 N/m (Roskosz et al., 2015) and our estimated force constants for clinopyroxene and amphibole, we calculate equilibrium fractionations of $\Delta^{56}Fe_{mag\text{-}cpx}$ and $\Delta^{56}Fe_{mag\text{-}amph} = +0.05‰$ at 970 °C, consistent with our measurements. Coexisting magnetite and amphibole phenocrysts in basaltic andesites and dacites from Mount Lassen, California, show similar degrees of magnetite-amphibole fractionation ($\Delta^{56}Fe_{mag\text{-}amph} = –0.02 \pm 0.09‰$; Beard and Johnson 2004). In summary, the observed inter-mineral fractionation suggests that—within the amphibole gabbro samples—amphibole, magnetite, and clinopyroxene are recording equilibrium conditions. Within the ultramafic cumulates, olivine and clinopyroxene appear to be recording crystallization conditions, while spinel does not, likely due to subsolidus Fe-Mg exchange.

3.6.4 Isotopic evolution of Adagdak cumulates

Combining our Fe isotope measurements of cumulate mineral separates and whole-rock powders, we can evaluate the extent to which fractionation of different phases drives the isotopic evolution of the cumulate suite and, by extension, their parental melts during differentiation. Within the ultramafic cumulates, our data suggest that whole-rock Fe isotope compositions are strongly dependent on the modal proportion of olivine and clinopyroxene. Because clinopyroxene is consistently 0.05-0.10‰ heavier than coexisting olivine, the increase in bulk $\delta^{56}Fe$ observed between the most primitive dunite xenoliths ($\delta^{56}Fe = –0.09$ to $–0.02‰$) and more evolved (± olivine) clinopyroxenite samples ($\delta^{56}Fe = +0.06$ to $+0.09‰$) reflects the increasing modal proportion of clinopyroxene relative to olivine. This transition from dunite to clinopyroxenite corresponds to an increase up to 0.18‰ in whole-rock $\delta^{56}Fe$ for the cumulates. Although spinel is the most Fe-rich phase in the ultramafic cumulates (21.0 to 33.7 wt.% FeO_T), its low modal abundance (0-7% modally for all samples, ≤1% by volume for 60% of cumulates) means that spinel never contains more than ~30% of the whole-rock FeO_T budget in the ultramafic cumulates

(Fig. 9). By contrast, olivine contains 59-93% of bulk FeO_T in the Adagdak dunite and wehrlite cumulates while clinopyroxene contains 30-90% of the bulk FeO_T in the (± olivine) clinopyroxenite cumulates (Fig. 9).

Within the amphibole and magnetite-bearing samples, there is no correlation between MgO and whole-rock δ^{56}Fe (Fig. 4a). The elevated and relatively uniform δ^{56}Fe of these samples (δ^{56}Fe = +0.04 to +0.08‰) reflects their high modal proportions of isotopically heavy magnetite (δ^{56}Fe = +0.11 to +0.13‰) and amphibole (δ^{56}Fe = +0.06 to +0.09‰). Although amphibole is not as isotopically heavy as coexisting magnetite and contains lower Fe concentrations (9.9 - 12.6 wt.% FeO_T for amphibole vs. 79-81 wt.% FeO_T for magnetite), the high modal abundance of amphibole in the Adagdak amphibole gabbro and hornblendite cumulates (30-97% by volume) means that amphibole contains between 28 and 99% of the FeO_T budget for these samples (Fig. 9). We therefore argue that, in addition to magnetite, amphibole fractionation should exert a strong effect on the isotopic evolution of these cumulates and their parental liquids.

Cooper and Inglis (2022) also argued that amphibole fractionation must play an important role in the Fe isotope evolution of cumulate and non-cumulate gabbro from the Lesser Antilles. The isotopically lightest samples from this suite also had the lowest Dy/Yb ratios, suggesting that they had crystallized from a melt that had been depleted in both Dy and heavy Fe isotopes by amphibole fractionation (Cooper and Inglis, 2022). Although the Adagdak cumulates are not as evolved as those from the Lesser Antilles (Fig. 3), given the isotopically heavy compositions of measured amphibole separates (δ^{56}Fe = +0.07 to +0.09‰) and whole-rock hornblendite powders (δ^{56}Fe = +0.07 to +0.08‰), it is also reasonable to predict that continued fractionation of amphibole-rich assemblages would deplete more evolved Adagdak melts in heavy isotopes of Fe. Although we cannot directly tie the lava record to the cumulates, correlations in Adagdak lavas between SiO_2 and Mg# and indices of amphibole fractionation like La/Yb are consistent with the idea that that amphibole fractionation may have driven the evolving parental melts of the cumulates towards lower δ^{56}Fe (Fig. S8). The implications of amphibole and magnetite

fractionation on the evolutions of Adagdak magmas will be discussed further in our analyses of the Fe isotope composition of Adagdak lavas and in modeling.

In summary, the Adagdak cumulate record preserves a complex history of lower- to mid-crustal differentiation and Fe isotope evolution. Lower crustal cumulates first evolved to heavier isotopic compositions as clinopyroxene replaced olivine as the dominant fractionating phase. Once magnetite and amphibole entered the cumulate assemblage, the Fe isotope composition of bulk assemblages remained heavy and relatively constant. Continued fractionation of these isotopically heavy magnetite and amphibole-rich assemblages should have driven late-stage melts towards light Fe isotope ratios, but our samples are not evolved enough to robustly assess this inference analytically.

3.6.5 Mantle dunite

Subarc mantle peridotites display a wide range of Fe isotope compositions (δ^{56}Fe = –0.37 to +0.11‰), which extend to isotopically lighter values than are observed in mid-ocean ridge (MOR) peridotite (Fig. 1, δ^{56}Fe = –0.09 to +0.11‰; Craddock et al., 2013; Sossi et al., 2016). While Adagdak mantle dunite ADG-CB-9 (δ^{56}Fe = –0.03 ± 0.05‰) falls within the range observed for MOR peridotites, it is likely isotopically lighter than the MOR peridotite average of +0.01 ± 0.01‰ (Craddock et al., 2013). Depletion in heavy Fe isotopes in arc peridotites may reflect one or a combination of the following processes: (1) incompatible Fe^{3+} behavior during partial melting, with the heavier isotopes of Fe preferentially being extracted from the residue (Williams et al., 2004; Williams and Bizimis, 2014); (2) metasomatism from isotopically light fluids or melts fluxed from the slab (Zhao et al., 2010, 2012; Poitrasson et al., 2013); or (3) disequilibrium isotopic diffusion between melts and mantle wall rock during channelized ascent (Weyer and Ionov; 2007; Teng et al. 2011; Foden et al. 2018; Turner et al., 2018). In this last scenario, because light isotopes of Fe diffuse faster than heavy isotopes, disequilibrium fractionation between percolating melts and mantle olivine results in a net transfer of isotopically light Fe to the peridotite.

Previous studies have shown that partial melts of metamorphosed subducted forearc material or possibly the subducted slab yielded important trace element contributions to the parental magmas of Adak cumulates (Yogodzinski and Kelemen, 2007; Sosa et al., 2023) and other plutonic rocks on Adak Island (Kay et al., 2019). Hence it is possible that the slight isotopic depletion observed in lherzolite ADG-CB-9 stems from melt-rock reactions with partial melts of altered oceanic crust (AOC) or subducted forearc material. The Fe isotope composition of a component derived from the slab itself may be highly variable and would strongly depend on where in the slab the contribution was sourced from and whether it took the form of a melt or fluid. For example, hydrothermal fluids fluxed from the slab are isotopically light, and their progressive removal during subduction should increase δ^{56}Fe in the remaining AOC (Rouxel et al., 2003, 2008). Partial melting of this enriched source would be expected to produce isotopically heavy melts, particularly if garnet remained in the residue, which would retain the light isotopes of Fe (He et al., 2017; Sossi and O'Neill 2017). However, reduced fluids leached from the slab may also precipitate veins of isotopically light secondary sulfides and Fe oxyhydroxides (δ^{56}Fe as low as –0.71‰ Rouxel et al., 2003) within the slab, creating regions with highly depleted Fe isotope compositions. It is however unlikely that sediment subduction significantly affected the Fe isotope composition of the mantle wedge beneath Adagdak, as previous studies have shown subducted sediments to be isotopically heavy (δ^{56}Fe = +0.05 to +0.18‰, Nebel et al., 2015). The radiogenic isotope systematics of arc lavas globally are also consistent with a small net transfer of subducted sediment to the subarc mantle (<4%, Hawkesworth et al., 1993), particularly for the Central Aleutians (0.2-0.6% by mass sediment transfer, Nielsen et al., 2016).

Regardless of whether the mantle dunite analyzed here experienced an isotopic depletion or metasomatic event, the sample provides our best constraints on the Fe isotope systematics of the subarc mantle beneath Adagdak. Using the mantle melting equations of Dauphas et al. (2009), the calculated Fe isotope composition of magmas generated by 10% buffered fractional melting at fO_2 = FMQ +1 of our mantle dunite (δ^{56}Fe = –0.03 ± 0.05‰) ranges from δ^{56}Fe = –0.08 to +0.02‰ (see Appendix for a full discussion of modeling). This is consistent with the previous study of

Aleutian magmas by Foden et al. (2018), who report a δ^{56}Fe value of 0.00 to +0.08‰ for Central Aleutian lavas.

3.6.6 Implications for Adagdak melts

While we cannot establish a direct petrogenic relationship between the cumulate xenoliths and Adagdak lavas, we can use comparisons to experimental studies to evaluate whether the lavas may represent a complement to the xenoliths over a given interval of differentiation. Cumulate assemblages with similar mineral chemistry, modal proportions, and bulk compositions to the Adagdak cumulate suite have been produced in experiments that fractionally crystallize primitive hydrous basalts ($H_2O_{initial}$ = 3-3.6 wt.%, Mg# = 67-76) at conditions relevant to the lower arc crust (1-0.7 GPa, fO_2 = NNO-NNO+2; Nandedkar et al., 2014; Ulmer et al., 2018). These experiments produced melt compositions similar to our most primitive measured Adagdak basalt (ADAG-81-4: 48.6 wt.% SiO_2, Mg# = 49.6, Kay and Kay, 1994) after 40-55% crystallization of olivine, clinopyroxene, and spinel, just before amphibole and magnetite saturated as cumulate phases (Nandedkar et al., 2014; Ulmer et al., 2018). This suggests that the Adagdak basalts and andesites measured here are capturing a complementary record of melt evolution to our more evolved cumulate compositions (namely, the amphibole gabbro and hornblendite cumulates).

In contrast to the cumulate data, which show pronounced evolutionary trends, Fe isotope compositions of the Adagdak lavas are all within error of each other (δ^{56}Fe = +0.03 ± 0.02 to +0.06 ± 0.02: Fig. 6a). While there are suggestions of slight positive correlations between average δ^{56}Fe and indices of differentiation like MgO (Fig. 6a), the resolution on the data are not suitable to assess whether the melts are in fact becoming isotopically lighter with decreasing MgO. These data reveal fundamental issues with studying the Fe isotope systematics of lavas in isolation. Mass balance dictates that δ^{56}Fe of the parental lavas should change gradually over restricted melt fractions if the majority of Fe in the system remains in the melt during crystallization. As our samples do not fully encompass the compositional diversity of all Adagdak lavas (Fig. 6b), it is perhaps not surprising that over this restricted range in melt composition (48.6 to 61 wt.% SiO_2,

5.7 to 2.5 wt.% MgO), the Fe isotope composition of the melt varies almost negligibly. The isotopic fractionation associated with crystallization and magmatic evolution may, therefore, be more apparent in the cumulate record than in their complementary lavas. The highly magnesian nature of the Adagdak dunite and wehrlite cumulates also suggests that these samples crystallized from a primitive basalt (Mg# = ~66-76) as compared to the more evolved lava compositions analyzed here (Debari et al., 1986; Sosa et al., 2023). Our data also show that most primitive cumulates were isotopically light (δ^{56}Fe = –0.02 to +0.09‰), and fractionation of these assemblages should serve to increase the δ^{56}Fe of the remaining melt. This implies that there was likely a period of enrichment in heavy Fe isotopes during early crystallization of Adagdak basalts that the lava record fails to capture.

3.6.7 Modeling the isotopic evolution of the melts parental to the Adagdak cumulates

To illustrate the effect that fractional crystallization can have on the Fe isotope systematics of arc magmas, we use our Adagdak data to construct a mass balance fractionation model, in which our bulk cumulate compositions are removed from a basaltic melt with an initial composition of δ^{56}Fe = 0.0‰. Note that changing δ^{56}Fe of the initial melt to any value within our predicted range (δ^{56}Fe = –0.03 to +0.05‰) merely serves to shift the isotopic composition of our modeled melts and cumulates to isotopically lighter or heavier values and does not affect the degree of predicted fractionation. The purpose of this model is to illustrate the complex isotopic evolution magmas and their crystallization products may experience as fractionated assemblages change from isotopically light dunite and wehrlite to heavier clinopyroxenite cumulates to isotopically heavy amphibole+magnetite-bearing rocks. Our discussion below focuses on the most salient features of this model and the insights it provides into the isotopic evolution of the Adagdak cumulates and their parental melts. An additional detailed discussion of this modeling approach and the parameters used is given in Supplementary Figures 12-14 and Supplementary Data File 2 (Ch3-T13 to Ch3-15).

Roskosz et al. (2022) showed that the force constant of glasses with basaltic and andesitic compositions is nearly a linear function of their $Fe^{3+}/\Sigma Fe$ ratio. Although we do not know the $Fe^{3+}/\Sigma Fe$ ratio of the melts parental to the cumulates, we can approximate an appropriate value based on fO_2 estimates for the xenoliths themselves (Sosa et al., 2023). Oxygen fugacity estimates for the Adagdak cumulates range from ΔFMQ +0.10 to +2.14, with an average value of ΔFMQ ≈ +1 (Sosa et al., 2023). Using the high-Mg basalt from Ulmer et al. (2018) as a reference basalt, a temperature of 1050 °C, a pressure of 1 GPa, and an fO_2 of FMQ+1, we used the parametrization of Kress and Carmichael (1991) to estimate an appropriate $Fe^{3+}/\Sigma Fe$ ratio for the parental melts to the cumulates, which yielded a value of $Fe^{3+}/\Sigma Fe = 0.22$. The parameterization of Roskosz et al. (2022) then yields an initial force constant of 230 N/m for our basaltic melt.

The major element evolution of the fractionating melt was modeled through stepwise removal of representative bulk cumulate assemblages from a high-Mg basalt (Ulmer et al., 2018) (Supplementary Data File 2, Ch3-T8). Based on these major element constraints, we constructed an isotope fractionation model in which a primary mantle melt at fO_2 = FMQ+1 with an initial $Fe^{3+}/\Sigma Fe$ of 0.22 fractionates 10% dunite, 9% wehrlite, 7% olivine clinopyroxenite, 3% clinopyroxenite, and 20% of an amphibole gabbro assemblage (Fig. 10). Representative whole-rock $Fe^{3+}/\Sigma Fe$ ratios estimated from the model proportions, chemistry, and density of minerals for each lithological group (Table 3). For these calculations, we assumed olivine contained negligible Fe^{3+}. Clinopyroxene $Fe^{3+}/\Sigma Fe$ ratios were estimated using the normalization scheme of Wood and Banno (1973), and magnetite and spinel $Fe^{3+}/\Sigma Fe$ ratios were calculated from EPMA data based on charge balance. For amphibole, we assumed a uniformed magmatic $Fe^{3+}/\Sigma Fe$ ratio of 0.4 based on our Mössbauer data. Published and estimated Fe force constants for clinopyroxene, olivine, spinel, magnetite, basalt, and amphibole were used to calculate bulk force constants for these cumulates (Table 2). Combined with previously published temperature estimates (Sosa et al., 2023), these bulk force constants were used to calculate cumulate-melt fractionation factors as each lithological group was fractionated from the melt. The representative whole-rock compositions for each lithological group and temperature estimates used in modeling are given in Table 3.

Due to the affinity of olivine for isotopically light Fe relative to basalt, fractionation of olivine-dominated assemblages slightly increases the δ^{56}Fe in the remaining basalt. Because our estimated clinopyroxene force constant is higher than that of olivine and the same as that of basalt (Table 2), as clinopyroxene replaces olivine as the modally dominant phase at lower melt fractions, cumulate force constants approach that of the melt. The result of this is that during the last interval of ultramafic cumulate crystallization, the degree of cumulate-melt fractionation decreases from $\Delta^{56}Fe_{melt\text{-}cumulate}$ = +0.04 to +0.01‰. Once amphibole and magnetite-bearing assemblages begin to crystallize, the force constant of the fractionated cumulates exceeds that of the melt, and δ^{56}Fe of the melt decreases, as heavier isotopes of Fe are preferentially incorporated into the cumulates ($\Delta^{56}Fe_{melt\text{-}cumulate}$ = –0.03 to –0.06‰). This dichotomy between the fractionation of isotopically light and heavy cumulates is shown in Figure 10, with the modeled ultramafic cumulates falling below the modeled magma composition at higher melt fractions (>70%), and the amphibole and magnetite-bearing assemblages falling above the modeled composition at lower melt fractions (50-70%).

A notable shortcoming of our model is its failure to reproduce the clinopyroxenite assemblages, which showed far higher measured values (δ^{56}Fe = 0.06 – 0.09‰) than are predicted by our model (δ^{56}Fe = -0.02 – 0.01‰). This discrepancy may come from two potential sources. First, it may be an artifact of applying the same clinopyroxene force constant throughout the entire model. If clinopyroxene in the clinopyroxenite cumulates have higher $Fe^{3+}/\Sigma Fe$ ratios than those in the wehrlite and olivine clinopyroxenite lithologies (which we used to calculate $\langle F \rangle_{cpx}$ from $\Delta^{56}Fe_{cpx\text{-}ol}$), then a higher clinopyroxene force constant should be used. A second possibility is that the clinopyroxenite cumulate pile was infiltrated by a percolating melt at sub-solidus temperature during lower crustal residence. This would be consistent with the anomalously low Fe-Mg exchange thermometry temperature estimates obtained for clinopyroxenite ADG-82-15 (914 +42/–49 ºC) and the presence of small quantities of peritectic amphibole (< 1% by volume) at clinopyroxene grain boundaries noted in samples from this lithological group (Sosa et al., 2023).

3.6.8 Implications for the Fe isotopic composition of the oceanic arc plutonic record

Our Fe isotope measurements of mineral separates show that different phases in the cumulate sequence have strong and systematic affinities for isotopically heavy versus light Fe. This means that the crystallization sequence and the proportions of specific phases fractionating from the melt exert first-order controls on the isotopic composition of the bulk cumulate removed from the magma, and by extension, the isotopic evolution of parental melts. Fractionation of isotopically light dunite and wehrlite cumulates might produce an interval of increasing δ^{56}Fe in primitive arc basalts, while the removal of isotopically heavy clinopyroxenite, hornblendite, and amphibole gabbro assemblages results in depletion of heavy Fe isotopes in more evolved basalts and andesites. Our data also imply the existence of (1) a lower crustal layer of low δ^{56}Fe (<0‰) ultramafic cumulates (dunite and wehrlite) in the Aleutian arc crust and (2) a mid-crustal reservoir of clinopyroxenite, hornblendite, and amphibole gabbro cumulates with higher δ^{56}Fe (>0.05‰).

This is consistent with the previous study of Cooper et al. (2016), who found mid-crustal amphibole+plagioclase-bearing cumulates from Statia, Lesser Antilles (δ^{56}Fe = +0.09 to +0.12‰), to be isotopically heavier than their complementary non-cumulate gabbros and lavas (δ^{56}Fe = +0.01 to +0.06‰), suggesting that fractionation of these isotopically heavy assemblages depleted later stage melts in heavy Fe isotopes. Li et al. (2020) also argue that mid-crustal amphibole fractionation played an important role in the isotopic evolution of intrusive rocks from the Tongde region, South China, depleting the more evolved diorite compositions in the heavy isotopes of Fe. If the plutonic non-cumulate rocks on Adak Island (namely the calc-alkaline Hidden Bay pluton, Kay et al., 1990, 2019) are an upper crustal complement to the mid-crustal cumulates (Sosa et al., 2023), and represent crystallized melts that have experienced prolonged Fe isotope depletion from magnetite and amphibole fractionation, then we might also suspect these rocks to be isotopically light relative to the amphibole gabbro and hornblendite cumulates. Furthermore, our results suggest that for oxidized hydrous arc systems, amphibole—independent of magnetite—may play a role in generating the depletion in heavy Fe isotopes observed in erupted lavas (consistent with the conclusions of Li et al., 2020, and Cooper and Inglis, 2022).

Our results also support previous studies that have suggested that amphibole may play a key role in driving Fe-depletion trends in calc-alkaline magmas (Kay et al., 1991; Romick et al., 1992; Kay and Mpodozis, 2001; Walters et al., 2020; Barber et al., 2021; Du et al., 2022), with the greatest proportion of the bulk Fe content for the hornblendite and amphibole gabbro cumulates typically (90% of studied cumulates) hosted in amphibole (28-99% of the FeO_T budget) rather than in magnetite (0-46% of the FeO_T budget) (Fig. 9). However, with regards to Fe isotopes, the role of amphibole in dictating the trajectory of isotopic evolution might be complicated by the fact that studies have shown amphibole $Fe^{3+}/\Sigma Fe$ ratios to be highly variable in arc systems ($Fe^{3+}/\Sigma Fe$ = 0.14-0.64, Ratschbacher et al., 2023). Previous studies have shown that oxidation state and Fe coordination number are equally important in governing the ability of phases to accept heavy versus light isotopes of Fe, with minerals having higher $Fe^{3+}/\Sigma Fe$ ratios and lower Fe coordination numbers preferring the heavier isotopes (Roskosz et al., 2015; Sossi and O'Neill, 2017; Nie et al., 2021). While garnet fractionation (which has been suggested to be important in continental arcs with thicker crusts) should drive the remaining melt to higher $\delta^{56}Fe$, and magnetite fractionation to lighter Fe isotope compositions, amphibole fractionation may have the potential to drive arc melts Fe isotope compositions to lighter of heavier $\delta^{56}Fe$ values depending on fO_2 and amphibole $Fe^{3+}/\Sigma Fe$. Clinopyroxene might also play a dual role in governing the Fe isotope trajectories of arc melts, as Mössbauer studies of mantle peridotites have shown variable clinopyroxene $Fe^{3+}/\Sigma Fe$ ratios ($Fe^{3+}/\Sigma Fe$ = 0.05 to 0.37: Dyar et al., 1992; Luth and Canil, 1993; Woodland, 2009; Hao et al., 2013). Given that amphibole and clinopyroxene are both modally abundant phases in arc-related cumulates, our understanding of the Fe isotope systematics of arc magmas would benefit greatly from future studies measuring the force constants of amphibole and clinopyroxene with a range of $Fe^{3+}/\Sigma Fe$ ratios.

Our findings do not contradict previous studies that have suggested that prior isotopic depletion of the subarc mantle (Williams and Bizimis, 2014), oxygen fugacity (Williams et al., 2005; Dauphas et al., 2009), melt-peridotite reactions (Weyer and Ionov; 2007; Teng et al., 2011; Foden et al., 2018; Turner et al., 2018) and mantle metasomatism (Chen et al., 2023; Debret et al., 2016, 2018, 2020) exert strong controls over the Fe isotope systematics of arc magmas. Indeed,

the Fe isotope composition of primary arc melts will be a function of the initial composition of the subarc mantle, temperature, and oxygen fugacity (Dauphas et al., 2009). Instead, we argue that the diversity in Fe isotope compositions observed in arc lavas also reflects important contributions from lower to mid-crustal fractionation, which act in concert with the variations in source composition discussed by many previous authors. The light Fe isotope ratios observed in many arc melts may also reflect fractionation of isotopically heavy magnetite and amphibole. At high melt fraction, mass balance dictates that the effects of fractionation on the Fe isotope composition of the crystallizing melt may be small if the majority of the system's Fe remains in the liquid. Cumulates may, therefore, also amplify trends towards lighter or heavier Fe isotope ratios that may not be resolvable in the lava record. Robust characterization of the Fe isotope dynamics in arcs requires integrating data from mantle residues, lavas, and cumulates for individual systems.

3.7 CONCLUSIONS

Fully characterizing the isotopic evolution of arc magmatic systems requires constraining $\delta^{56}Fe$ for the subarc mantle, erupted lavas, and crustal cumulates. We have shown that lower to mid-crustal cumulate xenoliths provide robust records of the Fe isotope systematics in evolving magmas. Our results highlight the important role differentiation may play in the isotopic evolution of arc systems. Fractionation of dunite and wehrlite cumulates may increase $\delta^{56}Fe$ of a differentiating melt, but once magnetite and amphibole saturation occur, removal of these isotopically heavy phases will decrease $\delta^{56}Fe$ in the melt. Only the latter interval of isotopic evolution (when melt MgO is <6 wt.%) is captured by the Adagdak lava record, emphasizing the importance of studying the complementary cumulate record. The light Fe isotope composition of a unique mantle dunite xenolith indicates that the subarc mantle beneath Adak experienced some depletion in heavy Fe isotopes, likely due to incompatible Fe^{3+} behavior during repeated episodes of partial melting, or reactions between mantle peridotite and mantle/slab-derived melts or fluids. Partial melting of this isotopically light mantle would have produced magmas with light $\delta^{56}Fe$ compositions, possible parental melts to the Adagdak dunite and wehrlite cumulates. Our results highlight the importance of amphibole fractionation in influencing the Fe isotope evolution of

hydrous arc systems. As an isotopically heavy phase (δ^{56}Fe = +0.07 to +0.09‰ in Adagdak cumulates) and major Fe reservoir in mid to upper-crustal cumulate assemblages (26-99% of the bulk FeO_T budget for Adagdak amphibole gabbro and hornblendite cumulates), amphibole fractionation may play an important role in explaining the depleted nature of some erupted arc lavas relative to MORB.

3.8 ACKNOWLEDGMENTS

We thank C. Ma (Caltech) for his assistance with the EPMA, O. Wilner (Caltech) for his help with the ICPMS, R. Grigoryan (Caltech) and G. Budde (Brown University) for their support with the Neptune, and R.T.C. Marquez (Caltech) for his guidance in the clean lab. For the single-crystal XRD analyses, we thank J. Fettinger (UC Davis) for assistance, T. S. Toellner (Argonne National Laboratory) for help with SMS data collection, W. Sturhahn (Caltech) for helping with SMS fits, and Y. Gao (Caltech) for his assistance during SIMS analyses. The SMS data collected during hybrid mode of the APS used a dual, fast-shutter spectrometer built by T.S.T. and supported by Laboratory Directed Research and Development (LDRD) funding from Argonne National Laboratory, provided by the Director, Office of Science, of the U.S. DOE under Contract No. DE-AC02-06CH11357. E.S.S. was supported by the National Science Foundation Graduate Research Fellowship under Grant No. DGE-1745301. This work was also supported by NSF grant EAR-1943629 awarded to C. Bucholz and NSF grant EAR-1841790 awarded to C. Bucholz and J. Jackson. Thoughtful and constructive reviews by K. Prissel and two anonymous reviewers greatly strengthened the manuscript.

3.9 REFERENCES

Bai, Y., Su, B. X., Xiao, Y., Cui, M. M., & Charlier, B. (2021). Magnesium and iron isotopic evidence of inter-mineral diffusion in ultramafic cumulates of the Peridotite Zone, Stillwater Complex. *Geochimica et Cosmochimica Acta*, 292, 152-169.

Barber, N. D., Edmonds, M., Jenner, F., Audétat, A., & Williams, H. (2021). Amphibole control on copper systematics in arcs: Insights from the analysis of global datasets. *Geochimica et Cosmochimica Acta*, 307, 192-211.

Beard, B. L., & Johnson, C. M. (2004). Inter-mineral Fe isotope variations in mantle-derived rocks and implications for the Fe geochemical cycle. *Geochimica et Cosmochimica Acta*, 68(22), 4727-4743.

Blatter, D. L., Sisson, T. W., & Hankins, W. B. (2013). Crystallization of oxidized, moderately hydrous arc basalt at mid-to lower-crustal pressures: Implications for andesite genesis. *Contributions to Mineralogy and Petrology*, 166, 861-886.

Bryndzia, L. T. & Wood, B. J. (1990). Oxygen thermobarometry of abyssal spinel peridotites; the redox state and C-O-H volatile composition of the Earth's sub-oceanic upper mantle. *American Journal of Science*. *American Journal of Science,* 290, 1093-1116.

Bucholz, C. E., & Spencer, C. J. (2019). Strongly peraluminous granites across the Archean-Proterozoic transition. *Journal of Petrology*, 60(7), 1299-1348.

Calvert, A. J., Klemperer, S. L., Takahashi, N., & Kerr, B. C. (2008). Three-dimensional crustal structure of the Mariana Island arc from seismic tomography. *Journal of Geophysical Research: Solid Earth,* 113(B1).

Chen, L. M., Song, X. Y., Zhu, X. K., Zhang, X. Q., Yu, S. Y., & Yi, J. N. (2014). Iron isotope fractionation during crystallization and sub-solidus re-equilibration: Constraints from the Baima mafic layered intrusion, SW China. Chemical Geology, 380, 97-109.

Chen, Y., Niu, Y., Xue, Q., Gao, Y., & Castillo, P. (2021). An iron isotope perspective on back-arc basin development: Messages from Mariana Trough basalts. *Earth and Planetary Science Letters*, 572, 117133.

Chen, Z., Chen, J., Tamehe, L. S., Zhang, Y., Zeng, Z., Zhang, T., & Yin, X. (2023). Light Fe isotopes in arc magmas from cold subduction zones: Implications for serpentinite-derived fluids oxidized the sub-arc mantle. *Geochimica et Cosmochimica Acta*, 342, 1-14.

Citron, G. P., Kay, R. W., Kay, S. M., Snee, L. W. & Sutter, J. F. (1980). Tectonic significance of early Oligocene plutonism on Adak Island, central Aleutian Islands, Alaska. *Geology,* 8, 375-379.

Coats, R. R. (1952). Magmatic differentiation in Tertiary and Quaternary volcanic rocks from Adak and Kanaga islands, Aleutian Islands, Alaska. *Geological Society of America Bulletin*, 63(5), 485-514.

Cooper, G. F., Davidson, J. P., & Blundy, J. D. (2016). Plutonic xenoliths from Martinique, Lesser Antilles: Evidence for open system processes and reactive melt flow in island arc crust. *Contributions to Mineralogy and Petrology*, 171, 1-21.

Cooper, G. F., Blundy, J. D., Macpherson, C. G., Humphreys, M. C., & Davidson, J. P. (2019). Evidence from plutonic xenoliths for magma differentiation, mixing and storage in a volatile-rich crystal mush beneath St. Eustatius, Lesser Antilles. *Contributions to Mineralogy and Petrology*, 174, 1-24.

Cooper, G. F., & Inglis, E. C. (2022). A crustal control on the Fe isotope systematics of volcanic arcs revealed in plutonic xenoliths from the Lesser Antilles. *Frontiers in Earth Science*, 9, 795858.

Cottrell, E., Birner, S. K., Brounce, M., Davis, F. A., Waters, L. E., & Kelley, K. A. (2021). Oxygen fugacity across tectonic settings. *Magma Redox Geochemistry*, 33-61.

Craddock, P. R., & Dauphas, N. (2011). Iron isotopic compositions of geological reference materials and chondrites. *Geostandards and Geoanalytical Research*, 35(1), 101-123.

Dauphas, N., Janney, P. E., Mendybaev, R. A., Wadhwa, M., Richter, F. M., Davis, A. M., ... & Foley, C. N. (2004). Chromatographic separation and multicollection-ICPMS analysis of iron. Investigating mass-dependent and-independent isotope effects. *Analytical Chemistry*, 76(19), 5855-5863.

Dauphas, N., Craddock, P. R., Asimow, P. D., Bennett, V. C., Nutman, A. P., & Ohnenstetter, D. (2009). Iron isotopes may reveal the redox conditions of mantle melting from Archean to Present. *Earth and Planetary Science Letters*, 288(1-2), 255-267.

Dauphas, N., Roskosz, M., Alp, E. E., Golden, D. C., Sio, C. K., Tissot, F. L. H., ... & Morris, R. V. (2012). A general moment NRIXS approach to the determination of equilibrium Fe isotopic fractionation factors: Application to goethite and jarosite. *Geochimica et Cosmochimica Acta*, 94, 254-275.

Dauphas, N., Roskosz, M., Alp, E. E., Neuville, D. R., Hu, M. Y., Sio, C. K., ... & Cordier, C. (2014). Magma redox and structural controls on iron isotope variations in Earth's mantle and crust. *Earth and Planetary Science Letters*, 398, 127-140.

Davis, A. S., Pickthorn, L. B. G., Valuer, T. L., & Marlow, M. S. (1989). Petrology and age of volcanic-arc rocks from the continental margin of the Bering Sea: Implications for Early Eocene relocation of plate boundaries. *Canadian Journal of Earth Sciences*, 26(7), 1474-1490.

Davis, F. A., Cottrell, E., Birner, S. K., Warren, J. M. & Lopez, O. G. (2017). Revisiting the electron microprobe method of spinel-olivine-orthopyroxene oxybarometry applied to spinel peridotitesk. *American Mineralogist,* 102, 421-435

Demény, A., Vennemann, T. W., Harangi, S., Homonnay, Z., & Fórizs, I. (2006). H2O-δD-FeIII relations of dehydrogenation and dehydration processes in magmatic amphiboles. *Rapid Communications in Mass Spectrometry*, 20(5), 919-925.

Dyar, M. D., McGuire, A. V., & Harrell, M. D. (1992). Crystal chemistry of iron in two styles of metasomatism in the upper mantle. *Geochimica et Cosmochimica Acta*, 56(6), 2579-2586.

Debari, S., Kay, S. M., & Kay, R. W. (1987). Ultramafic xenoliths from Adagdak volcano, Adak, Aleutian Islands, Alaska: Deformed igneous cumulates from the Moho of an island arc. *The Journal of Geology*, 95(3), 329-341.

Debret, B., Millet, M. A., Pons, M. L., Bouilhol, P., Inglis, E., & Williams, H. (2016). Isotopic evidence for iron mobility during subduction. *Geology*, 44(3), 215-218.

Debret, B., Bouilhol, P., Pons, M. L., & Williams, H. (2018). Carbonate transfer during the onset of slab devolatilization: New insights from Fe and Zn stable isotopes. *Journal of Petrology* , 59(6), 1145-1166.

Debret, B., Reekie, C. D. J., Mattielli, N., Beunon, H., Ménez, B., Savov, I. P., & Williams, H. M. (2020). Redox transfer at subduction zones: Insights from Fe isotopes in the Mariana forearc. *Geochemical Perspectives Letters*, 46-51.

Deng, J., He, Y., Zartman, R. E., Yang, X., & Sun, W. (2022). Large iron isotope fractionation during mantle wedge serpentinization: Implications for iron isotopes of arc magmas. *Earth and Planetary Science Letters*, 583, 117423.

Du, D. H., Tang, M., Li, W., Kay, S. M., & Wang, X. L. (2022). What drives Fe depletion in calc-alkaline magma differentiation: Insights from Fe isotopes. *Geology*, 50(5), 552-556.

Fabriès, J. (1979). Spinel-olivine geothermometry in peridotites from ultramafic complexes. *Contributions to Mineralogy and Petrology*, 69(4), 329-336.

Foden, J., Sossi, P. A., & Nebel, O. (2018). Controls on the iron isotopic composition of global arc magmas. *Earth and Planetary Science Letters*, 494, 190-201.

Gaetani, G. A., & Grove, T. L. (1998). The influence of water on melting of mantle peridotite. *Contributions to Mineralogy and Petrology,* 131, 323-346.

Green, D. H., Hibberson, W. O., Rosenthal, A., Kovács, I., Yaxley, G. M., Falloon, T. J., & Brink, F. (2014). Experimental study of the influence of water on melting and phase assemblages in the upper mantle. *Journal of Petrology*, 55(10), 2067-2096.

Hao, X. L., & Li, Y. L. (2013). 57Fe Mössbauer spectroscopy of mineral assemblages in mantle spinel lherzolites from Cenozoic alkali basalt, eastern China: Petrological applications. *Lithos*, 156, 112-119.

Hawkesworth, C. J., Gallagher, K., Hergt, J. M., & McDermott, F. (1993). Mantle and slab contributions in arc magmas. *Annual Review of Earth and Planetary Sciences*, 21(1), 175-204.

Hawthorne, F. C., Oberti, R., Harlow, G. E., Maresch, W. V., Martin, R. F., Schumacher, J. C., & Welch, M. D. (2012). Nomenclature of the amphibole supergroup. *American Mineralogist*, 97(11-12), 2031-2048.

He, Y., Wu, H., Ke, S., Liu, S. A., & Wang, Q. (2017). Iron isotopic compositions of adakitic and non-adakitic granitic magmas: Magma compositional control and subtle residual garnet effect. *Geochimica et Cosmochimica Acta*, 203, 89-102.

Holloway, J. R., & Burnham, C. W. (1972). Melting relations of basalt with equilibrium water pressure less than total pressure. *Journal of Petrology*, 13(1), 1-29.

Jackson, J. M., Hamecher, E. A., & Sturhahn, W. (2009). Nuclear resonant X-ray spectroscopy of (Mg, Fe) SiO3 orthoenstatites. *European Journal of Mineralogy*, 21(3), 551-560.

Janiszewski, H. A., Abers, G. A., Shillington, D. J., & Calkins, J. A. (2013). Crustal structure along the Aleutian island arc: New insights from receiver functions constrained by active-source data. *Geochemistry, Geophysics, Geosystems*, 14(8), 2977-2992.

Jicha, B. R., & Kay, S. M. (2018). Quantifying arc migration and the role of forearc subduction erosion in the central Aleutians. *Journal of Volcanology and Geothermal Research*, 360, 84-99.

Jicha, B. R., Scholl, D. W., Singer, B. S., Yogodzinski, G. M., & Kay, S. M. (2006). Revised age of Aleutian Island Arc formation implies high rate of magma production. *Geology*, 34(8), 661-664.

Johnson, A. C., Zhang, Z. J., Dauphas, N., Rudnick, R. L., Foden, J. D., & Toc, M. (2023). Redox and mineral controls on Fe and Ti isotopic fractionations during calc-alkaline magmatic differentiation. *Geochimica et Cosmochimica Acta*, 355, 1-12

Kay, S. M., Kay, R. W., & Citron, G. P. (1982). Tectonic controls on tholeiitic and calc-alkaline magmatism in the Aleutian Arc. *Journal of Geophysical Research: Solid Earth*, 87(B5), 4051-4072.

Kay, S. M., & Kay, R. W. (1985). Aleutian tholeiitic and calc-alkaline magma series I: The mafic phenocrysts. *Contributions to Mineralogy and Petrology*, 90, 276-290.

Kay, S.M. and R.W. Kay, 1994, Aleutian magmatism in space and time, in G. Plafker and H.C. Berg (eds.), The Geology of Alaska, Decade of North American Geology (DNAG), *Geological Society of America,* v. G-1, p. 687-722.

Kay, S. M., & Mpodozis, C. (2001). Central Andean ore deposits linked to evolving shallow subduction systems and thickening crust. *GSA today*, 11(3), 4.

Kay, S., Kay, R., Citron, G. P. & Perfit, M.R., (1990). Calc-alkaline plutonism in the intra-oceanic Aleutian arc, Alaska. Plutonism from Antarctica to Alaska. *Geological Society of America Special Paper*, 241, 233-256.

Kay, S. M., Mpodozis, C., Ramos, V. A., & Munizaga, F. (1991). Magma source variations for mid-late Tertiary magmatic rocks associated with a shallowing subduction zone and a thickening crust in the central Andes (28 to 33 S). *Geological Society of America Special Paper*, 265, 113-137.

Kay, S. M., Jicha, B. R., Citron, G. L., Kay, R. W., Tibbetts, A. K. & Rivera, T. A. (2019). The Calc-Alkaline Hidden Bay and Kagalaska Plutons and the Construction of the Central Aleutian Oceanic Arc Crust. *Journal of Petrology*, 60, 393-439.

Krawczynski, M. J., Grove, T. L., & Behrens, H. (2012). Amphibole stability in primitive arc magmas: Effects of temperature, H_2O content, and oxygen fugacity. *Contributions to Mineralogy and Petrology*, 164(2), 317-339.

Kress, V. C., & Carmichael, I. S. (1991). The compressibility of silicate liquids containing Fe 2 O 3 and the effect of composition, temperature, oxygen fugacity and pressure on their redox states. *Contributions to Mineralogy and Petrology,* 108, 82-92.

Lehmann, J. (1983). Diffusion between olivine and spinel: Application to geothermometry. *Earth and Planetary Science Letters*, 64(1), 123-138.

Lewis, M. J., Bucholz, C. E., & Jagoutz, O. E. (2021). Evidence for polybaric fractional crystallization in a continental arc: Hidden Lakes mafic complex, Sierra Nevada batholith, California. *Contributions to Mineralogy and Petrology,* 176, 1-27.

Li, Q. W., Zhao, J. H., Wang, Q., Zhang, Z. F., An, Y. J., & He, Y. T. (2020). Iron isotope fractionation in hydrous basaltic magmas in deep crustal hot zones. *Geochimica et Cosmochimica Acta*, 279, 29-44.

Liermann, H. P., & Ganguly, J. (2002). Diffusion kinetics of Fe2+ and Mg in aluminous spinel: Experimental determination and applications. *Geochimica et Cosmochimica Acta*, 66(16), 2903-2913.

Luth, R. W., & Canil, D. (1993). Ferric iron in mantle-derived pyroxenes and a new oxybarometer for the mantle. *Contributions to Mineralogy and Petrology*, 113(2), 236-248.

Makino, K., and Tomita, K. (1989): Cation distribution in the octahedral sites of hornblendes. *American Mineralogist*, 74, 1097-1105.

Mandler, B. E., & Grove, T. L. (2016). Controls on the stability and composition of amphibole in the Earth's mantle. *Contributions to Mineralogy and Petrology*, 171, 1-20.

Marxer, F., Ulmer, P., & Müntener, O. (2022). Polybaric fractional crystallisation of arc magmas: An experimental study simulating trans-crustal magmatic systems. *Contributions to Mineralogy and Petrology*, 177(1), 3.

Müntener, O., Kelemen, P. B., & Grove, T. L. (2001). The role of H 2 O during crystallization of primitive arc magmas under uppermost mantle conditions and genesis of igneous pyroxenites: An experimental study. *Contributions to Mineralogy and Petrology*, 141, 643-658.

Müntener, O., & Ulmer, P. (2018). Arc crust formation and differentiation constrained by experimental petrology. *American Journal of Science*, 318(1), 64-89.

Myers, J. D., Marsh, B. D., & Sinha, A. K. (1985). Strontium isotopic and selected trace element variations between two Aleutian volcanic centers (Adak and Atka): Implications for the development of arc volcanic plumbing systems. *Contributions to Mineralogy and Petrology*, 91, 221-234.

Nandedkar, R. H., Ulmer, P. & Müntener, O. (2014). Fractional crystallization of primitive, hydrous arc magmas: An experimental study at 0.7 GPa. *Contributions to Mineralogy and Petrology,* 167, 1015.

Nebel, O., Arculus, R. J., Sossi, P. A., Jenner, F. E., & Whan, T. H. (2013). Iron isotopic evidence for convective resurfacing of recycled arc-front mantle beneath back-arc basins. *Geophysical Research Letters*, 40(22), 5849-5853.

Nebel, O., Sossi, P. A., Bénard, A., Wille, M., Vroon, P. Z., & Arculus, R. J. (2015). Redox-variability and controls in subduction zones from an iron-isotope perspective. *Earth and Planetary Science Letters*, 432, 142-151.

Nie, N. X., Dauphas, N., Alp, E. E., Zeng, H., Sio, C. K., Hu, J. Y., ... & Spear, F. S. (2021). Iron, magnesium, and titanium isotopic fractionations between garnet, ilmenite, fayalite, biotite, and tourmaline: Results from NRIXS, ab initio, and study of mineral separates from the Moosilauke metapelite. *Geochimica et Cosmochimica Acta*, 302, 18-45.

Nielsen, S. G., Yogodzinski, G., Prytulak, J., Plank, T., Kay, S. M., Kay, R. W., & Kading, T. (2016). Tracking along-arc sediment inputs to the Aleutian arc using thallium isotopes. *Geochimica et Cosmochimica Acta*, 181, 217-237.

Ozawa, K. (1984). Olivine-spinel geospeedometry: Analysis of diffusion-controlled Mg-Fe2+ exchange. *Geochimica et Cosmochimica Acta*, 48(12), 2597-2611.

Pichavant, M., & Macdonald, R. (2007). Crystallization of primitive basaltic magmas at crustal pressures and genesis of the calc-alkaline igneous suite: Experimental evidence from St Vincent, Lesser Antilles arc. *Contributions to Mineralogy and Petrology*, 154, 535-558.

Poitrasson, F., Delpech, G., & Grégoire, M. (2013). On the iron isotope heterogeneity of lithospheric mantle xenoliths: Implications for mantle metasomatism, the origin of basalts and the iron isotope composition of the Earth. *Contributions to Mineralogy and Petrology*, 165, 1243-1258.

Polyakov, V. B., & Mineev, S. D. (2000). The use of Mössbauer spectroscopy in stable isotope geochemistry. *Geochimica et Cosmochimica Acta*, 64(5), 849-865.

Polyakov, V. B., Clayton, R. N., Horita, J., & Mineev, S. D. (2007). Equilibrium iron isotope fractionation factors of minerals: Reevaluation from the data of nuclear inelastic resonant X-ray scattering and Mössbauer spectroscopy. *Geochimica et Cosmochimica Acta*, 71(15), 3833-3846.

Prissel, K., Olive, J. A., & Krawczynski, M. J. (2023). A Log-Ratio-Based Algorithm for Petrologic Mass-Balance Problems and Uncertainty Assessment. *Geochemistry, Geophysics, Geosystems*, 24(12), e2023GC011234.

Ratschbacher, B. C., Jackson, J. M., Toellner, T. S., Bucholz, C. E., Sturhahn, W., & Solomatova, N. V. (2023). Fe^{3+}/Fe^{T} ratios of amphiboles determined by high spatial resolution single-crystal synchrotron Mössbauer spectroscopy. *American Mineralogist*, 108(1), 70-86.

Romick, J. D., Kay, S. M., & Kay, R. W. (1992). The influence of amphibole fractionation on the evolution of calc-alkaline andesite and dacite tephra from the central Aleutians, Alaska. *Contributions to Mineralogy and Petrology*, 112, 101-118.

Roskosz, M., Sio, C. K., Dauphas, N., Bi, W., Tissot, F. L., Hu, M. Y., ... & Alp, E. E. (2015). Spinel-olivine-pyroxene equilibrium iron isotopic fractionation and applications to natural peridotites. *Geochimica et Cosmochimica Acta*, 169, 184-199.

Roskosz, M., Dauphas, N., Hu, J., Hu, M. Y., Neuville, D. R., Brown, D., ... & Alp, E. E. (2022). Structural, redox and isotopic behaviors of iron in geological silicate glasses: A NRIXS study of Lamb-Mössbauer factors and force constants. *Geochimica et Cosmochimica Acta*, 321, 184-205.

Rouxel, O., Dobbek, N., Ludden, J., & Fouquet, Y. (2003). Iron isotope fractionation during oceanic crust alteration. *Chemical Geology*, 202(1-2), 155-182.

Rouxel, O., Shanks III, W. C., Bach, W., & Edwards, K. J. (2008). Integrated Fe-and S-isotope study of seafloor hydrothermal vents at East Pacific Rise 9-10 N. Chemical Geology, 252(3-4), 214-227.

Scholl, D. W., Buffington, E. C., and Marlow, M. S., 1975, Plate tectonics and the structural evolution of the Aleutian-Bering Sea region, in Forbes, R. B., ed., Contributions to the geology of the Bering Sea Basin and adjacent regions. *Geological Society of America Special Paper,* 151, 1-31.

Schoenberg, R., Marks, M. A., Schuessler, J. A., von Blanckenburg, F., & Markl, G. (2009). Fe isotope systematics of coexisting amphibole and pyroxene in the alkaline igneous rock suite of the Ilímaussaq Complex, South Greenland. *Chemical Geology*, 258(1-2), 65-77.

Sisson, T. W., & Grove, T. L. (1993). Experimental investigations of the role of H 2 O in calc-alkaline differentiation and subduction zone magmatism. *Contributions to Mineralogy and Petrology*, 113, 143-166.

Sosa, E. S., Bucholz, C. E., Barickman, M. H., VanTongeren, J. A., Setera, J. B., Kay, S. M., & Kay, R. W. (2023). Petrology and geochemistry of Adak Island plutonic xenoliths: Implications for primitive magma generation and crustal differentiation in the Aleutian Island arc. *Journal of Petrology*, 64(10).

Sossi, P. A., Foden, J. D., & Halverson, G. P. (2012). Redox-controlled iron isotope fractionation during magmatic differentiation: An example from the Red Hill intrusion, S. Tasmania. *Contributions to Mineralogy and Petrology*, 164(5), 757-772.

Sossi, P. A., & O'Neill, H. S. C. (2017). The effect of bonding environment on iron isotope fractionation between minerals at high temperature. *Geochimica et Cosmochimica Acta*, 196, 121-143.

Stamper, C. C., Melekhova, E., Blundy, J. D., Arculus, R. J., Humphreys, M. C. S., & Brooker, R. A. (2014). Oxidised phase relations of a primitive basalt from Grenada, Lesser Antilles. *Contributions to Mineralogy and Petrology*, 167, 1-20.

Sturhahn, W. (2000): CONUSS and PHOENIX: Evaluation of nuclear resonant scattering data. *Hyperfine Interactions*, 125, 149-172.

Sturhahn, W. (2021): CONUSS (Coherent Nuclear Scattering by Single crystals). Open-source software. http://www.nrixs.com.

Teng, F. Z., Dauphas, N., Helz, R. T., Gao, S., & Huang, S. (2011). Diffusion-driven magnesium and iron isotope fractionation in Hawaiian olivine. *Earth and Planetary Science Letters*, 308(3-4), 317-324.

Teng, F. Z., Dauphas, N., Huang, S., & Marty, B. (2013). Iron isotopic systematics of oceanic basalts. *Geochimica et Cosmochimica Acta*, 107, 12-26.

Turner, S., Williams, H., Piazolo, S., Blichert-Toft, J., Gerdes, M., Adam, J., & Maury, R. (2018). Sub-arc xenolith Fe-Li-Pb isotopes and textures tell tales of their journey through the mantle wedge and crust. *Geology*, 46(11), 947-950.

Ulmer, P., Kaegi, R. & Müntener, O. (2018). Experimentally Derived Intermediate to Silica-rich Arc Magmas by Fractional and Equilibrium Crystallization at 1·0 GPa: An Evaluation of Phase Relationships, Compositions, Liquid Lines of Descent and Oxygen Fugacity. *Journal of Petrology*, 59, 11-58.

Vogt, K., Dohmen, R., & Chakraborty, S. (2015). Fe-Mg diffusion in spinel: New experimental data and a point defect model. *American Mineralogist*, 100(10), 2112-2122.

Wasylenki, L. E., Baker, M. B., Kent, A. J., & Stolper, E. M. (2003). Near-solidus melting of the shallow upper mantle: Partial melting experiments on depleted peridotite. *Journal of Petrology*, 44(7), 1163-1191.

Waters, L. E., Cottrell, E., Coombs, M. L., & Kelley, K. A. (2021). Generation of Calc-alkaline magmas during crystallization at high oxygen fugacity: An experimental and petrologic study of Tephras from Buldir volcano, Western Aleutian Arc, Alaska, USA. *Journal of Petrology*., 62(3), egaa104.

Weyer, S., & Ionov, D. A. (2007). Partial melting and melt percolation in the mantle: The message from Fe isotopes. *Earth and Planetary Science Letters*, 259(1-2), 119-133.

Williams, H. M., & Bizimis, M. (2014). Iron isotope tracing of mantle heterogeneity within the source regions of oceanic basalts. *Earth and Planetary Science Letters*, 404, 396-407.

Williams, H. M., McCammon, C. A., Peslier, A. H., Halliday, A. N., Teutsch, N., Levasseur, S., & Burg, J. P. (2004). Iron isotope fractionation and the oxygen fugacity of the mantle. *Science*, 304(5677), 1656-1659.

Williams, H. M., Peslier, A. H., McCammon, C., Halliday, A. N., Levasseur, S., Teutsch, N., & Burg, J. P. (2005). Systematic iron isotope variations in mantle rocks and minerals: the effects of partial melting and oxygen fugacity. *Earth and Planetary Science Letters*, 235(1-2), 435-452.

Williams, H. M., & Bizimis, M. (2014). Iron isotope tracing of mantle heterogeneity within the source regions of oceanic basalts. *Earth and Planetary Science Letters,* 404, 396-407.

Williams, H. M., Prytulak, J., Woodhead, J. D., Kelley, K. A., Brounce, M., & Plank, T. (2018). Interplay of crystal fractionation, sulfide saturation and oxygen fugacity on the iron isotope composition of arc lavas: An example from the Marianas. *Geochimica et Cosmochimica Acta*, 226, 224-243.

Wood, B. J., & Virgo, D. (1989). Upper mantle oxidation state: Ferric iron contents of Iherzolite spinels by 57Fe Mössbauer spectroscopy and resultant oxygen fugacities. *Geochimica et Cosmochimica Acta*, 53(6), 1277-1291.

Woodland, A. B. (2009). Ferric iron contents of clinopyroxene from cratonic mantle and partitioning behaviour with garnet. *Lithos*, 112, 1143-1149.

Yogodzinski, G. M., & Kelemen, P. B. (2007). Trace elements in clinopyroxenes from Aleutian xenoliths: Implications for primitive subduction magmatism in an island arc. *Earth and Planetary Science Letters*, 256(3-4), 617-632.

Zhao, X., Zhang, H., Zhu, X., Tang, S., & Tang, Y. (2010). Iron isotope variations in spinel peridotite xenoliths from North China Craton: Implications for mantle metasomatism. *Contributions to Mineralogy and Petrology*, 160, 1-14.

Zhao, X., Zhang, H., Zhu, X., Tang, S., & Yan, B. (2012). Iron isotope evidence for multistage melt-peridotite interactions in the lithospheric mantle of eastern China. *Chemical Geology*, 292, 127-139.

Zhao, X. M., Zhang, H. F., Zhu, X. K., Zhu, B., & Cao, H. H. (2015). Effects of melt percolation on iron isotopic variation in peridotites from Yangyuan, North China Craton. *Chemical Geology*, 401, 96-110.

3.10 FIGURES AND CAPTIONS

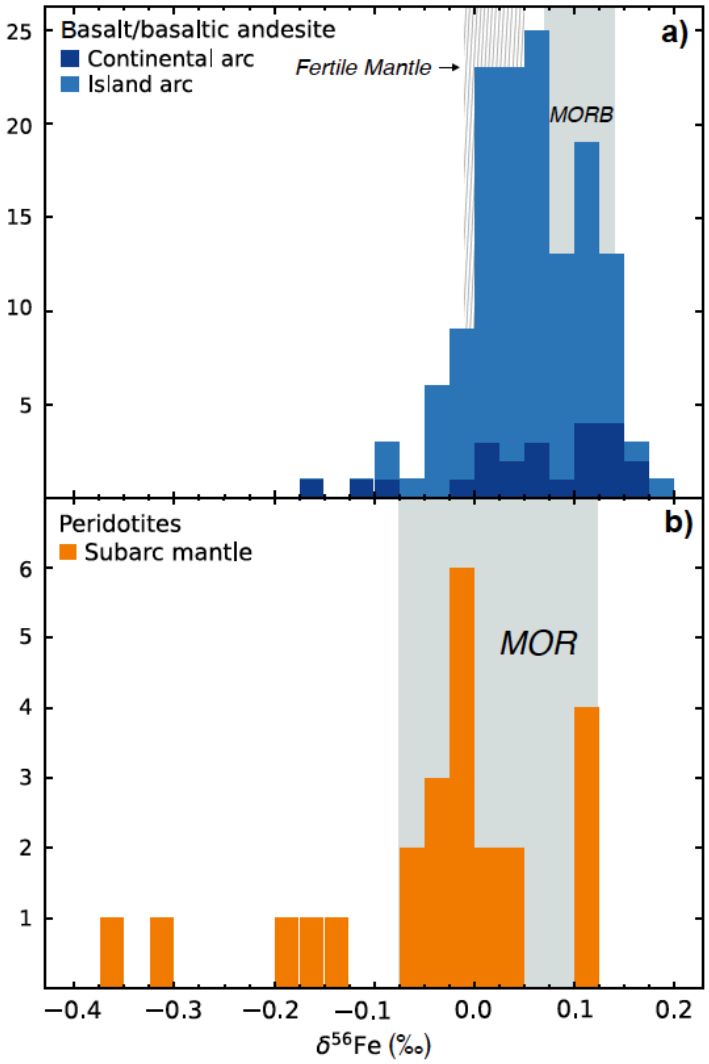

Figure 1: Frequency histograms of δ^{56}Fe (‰) in (**a**) arc basalts and basaltic andesites and (**b**) subarc mantle peridotites show the observed range in Fe isotope compositions for both rock types and how arc lavas and mantle rocks extend to more depleted compositions than observed in those from MOR environments. Arc lava data is from Dauphas et al. (2009), Foden et al. (2018), Williams et al. (2018), Du et al. (2022), and Chen et al. (2023). Subarc mantle peridotite data is from Williams et al. (2005), Poitrasson et al. (2013), Weyer and Ionov (2007), and Turner et al. (2018). MORB field (gray in panel a) is from Teng et al. (2013) and fertile upper mantle field (hatched lines) is from Weyer and Ionov (2007). MOR peridotite data (panel b) is from Craddock et al. (2013).

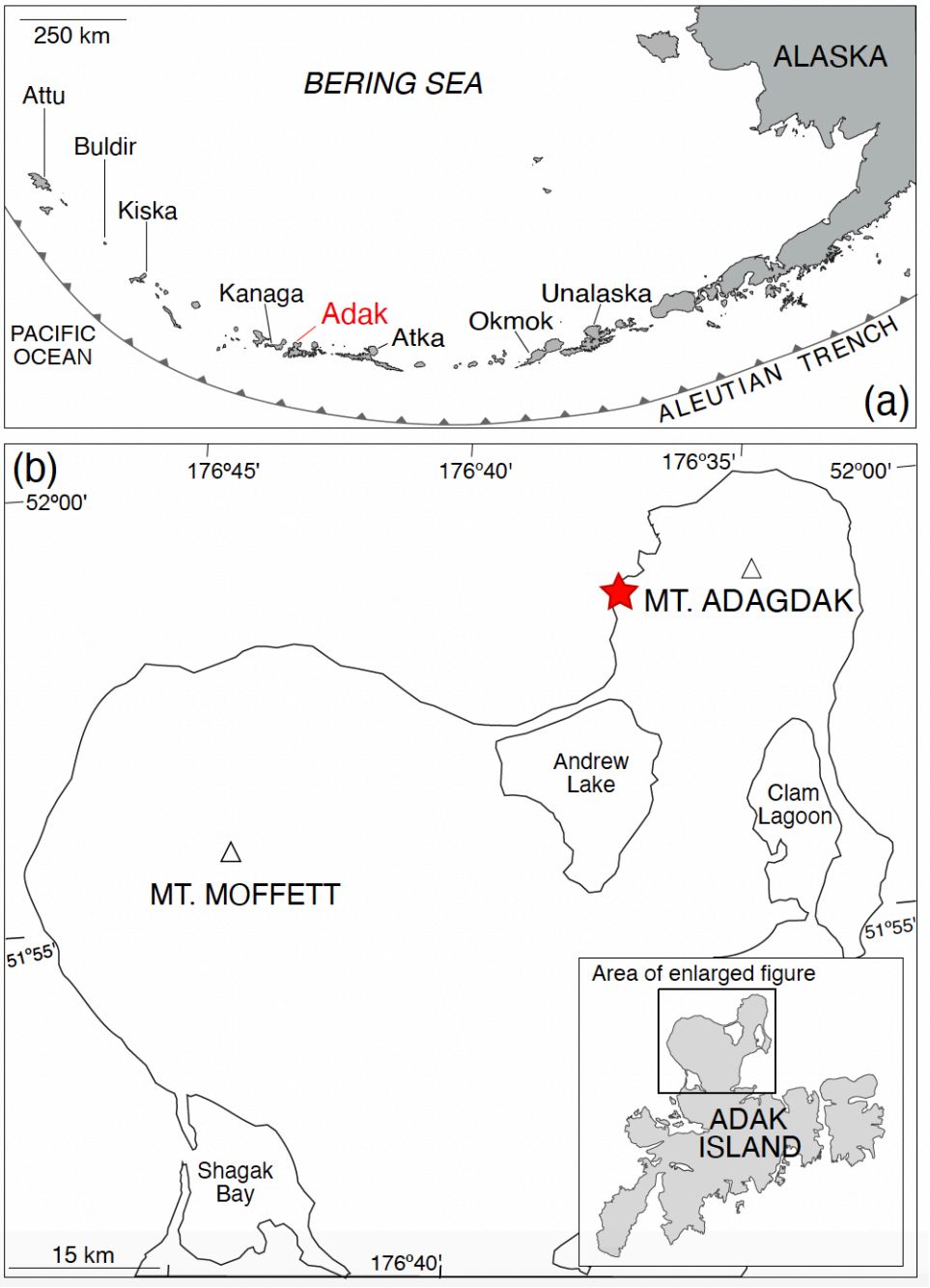

Figure 2: Simplified map of the Aleutian Arc (**a**) with enlargement of Adak Island (**b**). The location where the Mount Adagdak xenolith suite was collected from (51°58.78' N, 176°37.36' W) is designated with a red star. Modified from Sosa et al. (2023).

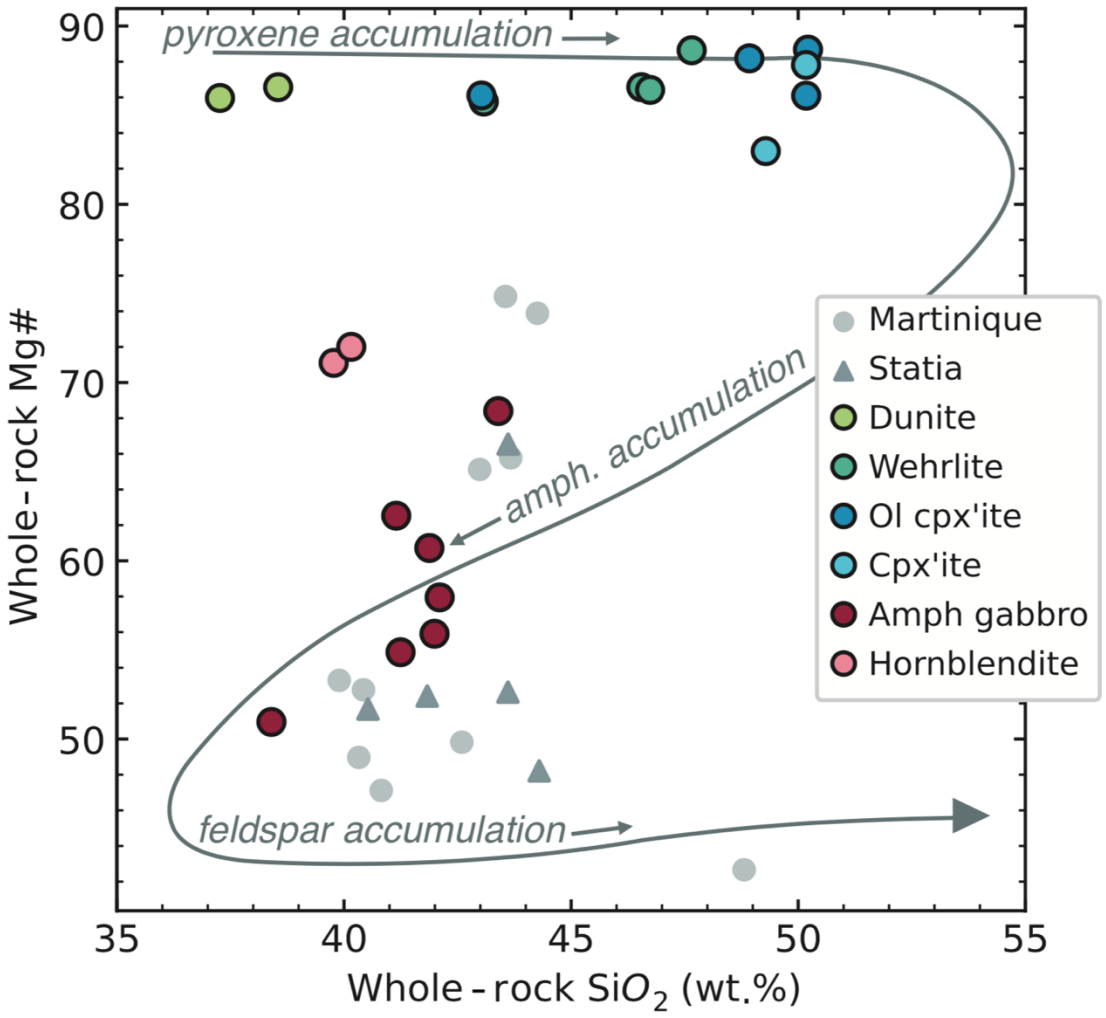

Figure 3: SiO_2 vs Mg# for whole-rock cumulate xenolith compositions from Martinique and Statia (Lesser Antilles; Cooper and Inglis, 2022) and Adagdak. Gray curve represents the experimental cumulate trend of hydrous arc basalts from Müntener and Ulmer (2018).

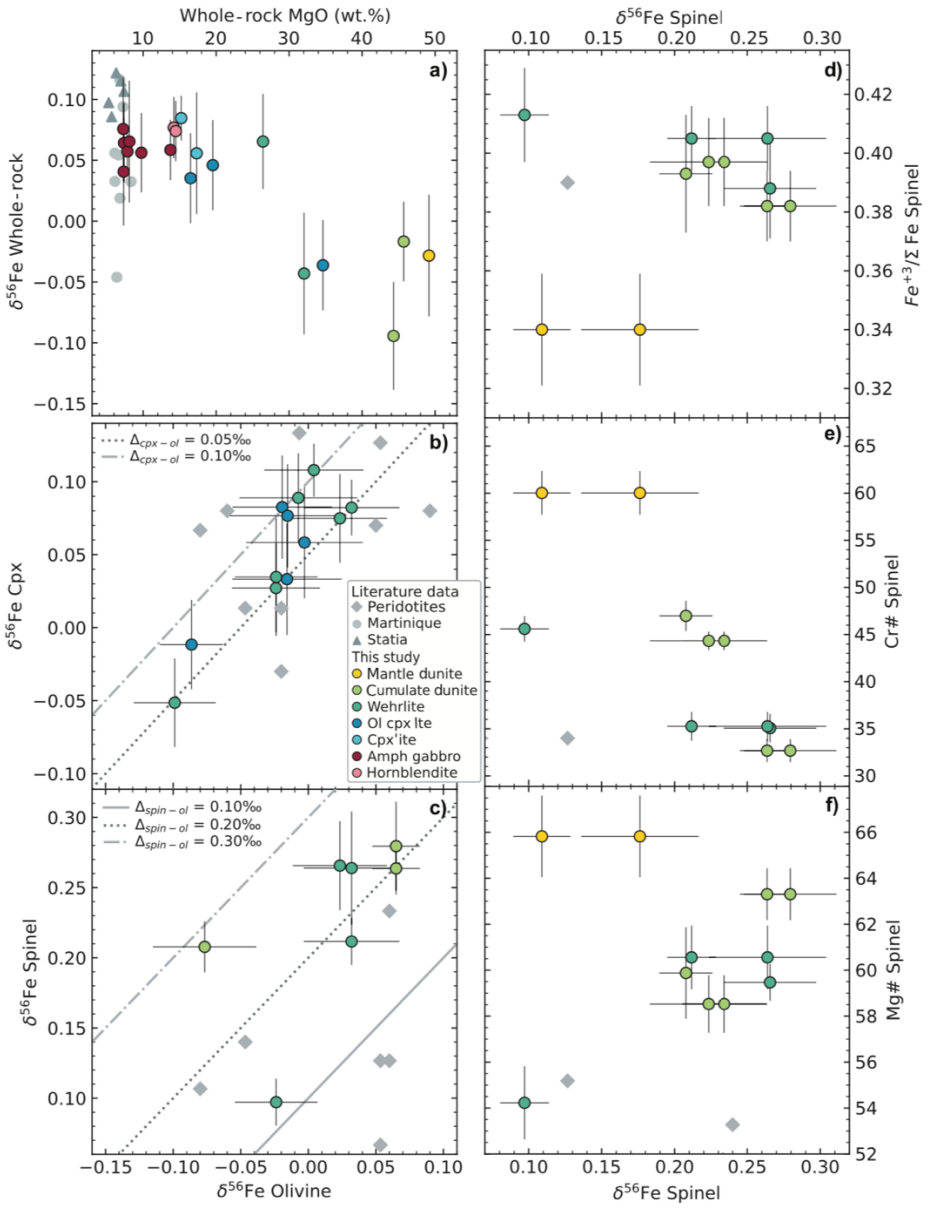

Figure 4: Adagdak xenoliths whole-rock and mineral chemistry vs. Fe isotope ratios. **(a)** Whole-rock δ^{56}Fe (‰) vs. MgO (wt.%). **(b)** δ^{56}Fe cpx vs. δ^{56}Fe of coexisting olivine. Grey dashed and dotted lines represent olivine-clinopyroxene fractionation for $\Delta^{56}Fe_{cpx\text{-}ol}$ of 0.05 and 0.10 ‰, respectively. **(c)** δ^{56}Fe spinel vs. δ^{56}Fe of coexisting olivine. Grey dashed, dotted, and solid lines represent spinel-olivine fractionation for $\Delta^{56}Fe_{spin\text{-}ol}$ of 0.10, 0.20, and 0.30‰, respectively. **(d)** δ^{56}Fe spinel vs. $Fe^{3+}/\Sigma Fe$ spinel. **(e)** δ^{56}Fe spinel vs. Cr# spinel. **(f)** δ^{56}Fe spinel vs. Mg# spinel. Literature data from arc mantle peridotites **(**Williams et al., 2005, 2014) and Lesser Antilles cumulates (Cooper and Inglis, 2022) are given for comparison.

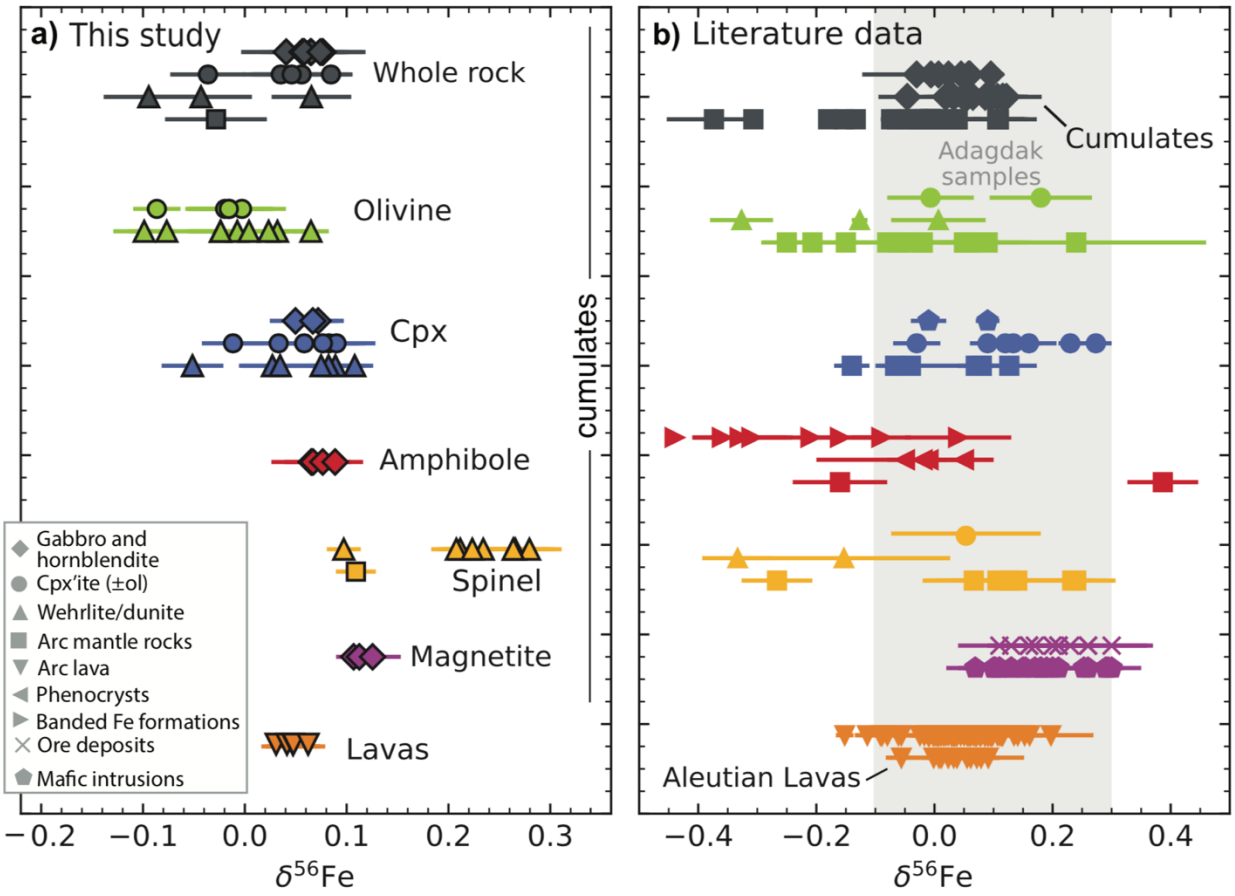

Figure 5: Summary of Adagdak Fe isotope data and comparisons to literature data. **(a)** δ^{56}Fe (‰) for Adagdak whole-rock samples, lavas, and olivine, clinopyroxene, amphibole, magnetite, and single-grain spinel mineral separates. Colors distinguish between different analyzed phases and symbols differentiate specific lithologies or rock types. **(b)** Literature data for δ^{56}Fe of igneous rocks and minerals. Aleutian lava data is from Foden et al. (2018) and cumulate data is from Cooper and Inglis (2022; Lesser Antilles). Other literature data are from Beard et al. (2004), Williams et al. (2005, 2014), Weyer and Ionov (2007), Sossi et al. (2012), Poitrasson et al. (2013), Chen et al. 2014, Zhao et al. (2015), Turner et al. (2018), Rodriguez-Mustafa et al, (2020), Tian et al. (2020), and Ye et al. (2020). Gray field in panel b represents the full range in δ^{56}Fe observed in the Adagdak samples.

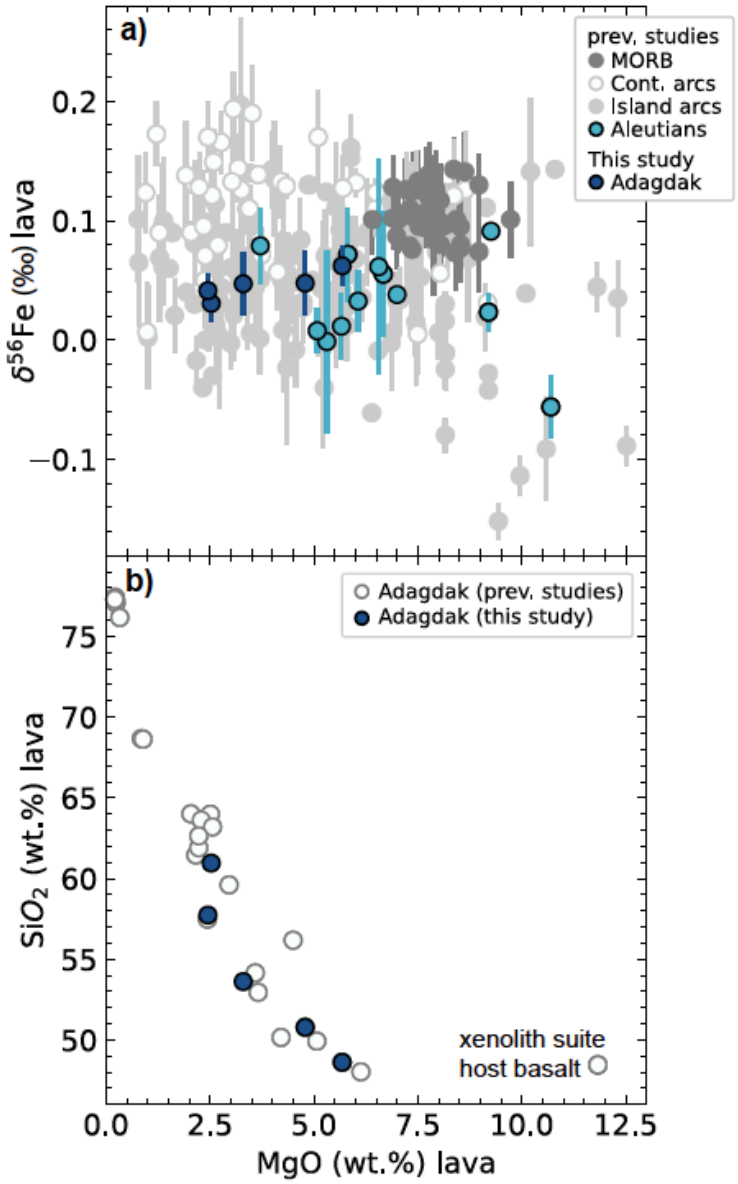

Figure 6: (a) δ^{56}Fe of Adagdak lavas vs. MgO (wt.%). The Fe isotope composition of lavas from other island arcs (Dauphas et al., 2009; Williams et al., 2018; Foden et al., 2018; Cooper and Inglis 2022; Chen et al., 2023; Johnson et al., 2023), continental arcs (Foden et al., 2018; Du et al., 2022), MORBs (Teng et al., 2013), and other Aleutian lavas (Foden et al., 2018) is given for comparison. **(b)** MgO vs SiO_2, (wt.%) for Adagdak lavas measured in this study compared to literature data (Coats, 1952; Kay and Kay, 1985, 1994; Myers et al., 1985; Romick et al., 1992; Hanna et al., 2020).

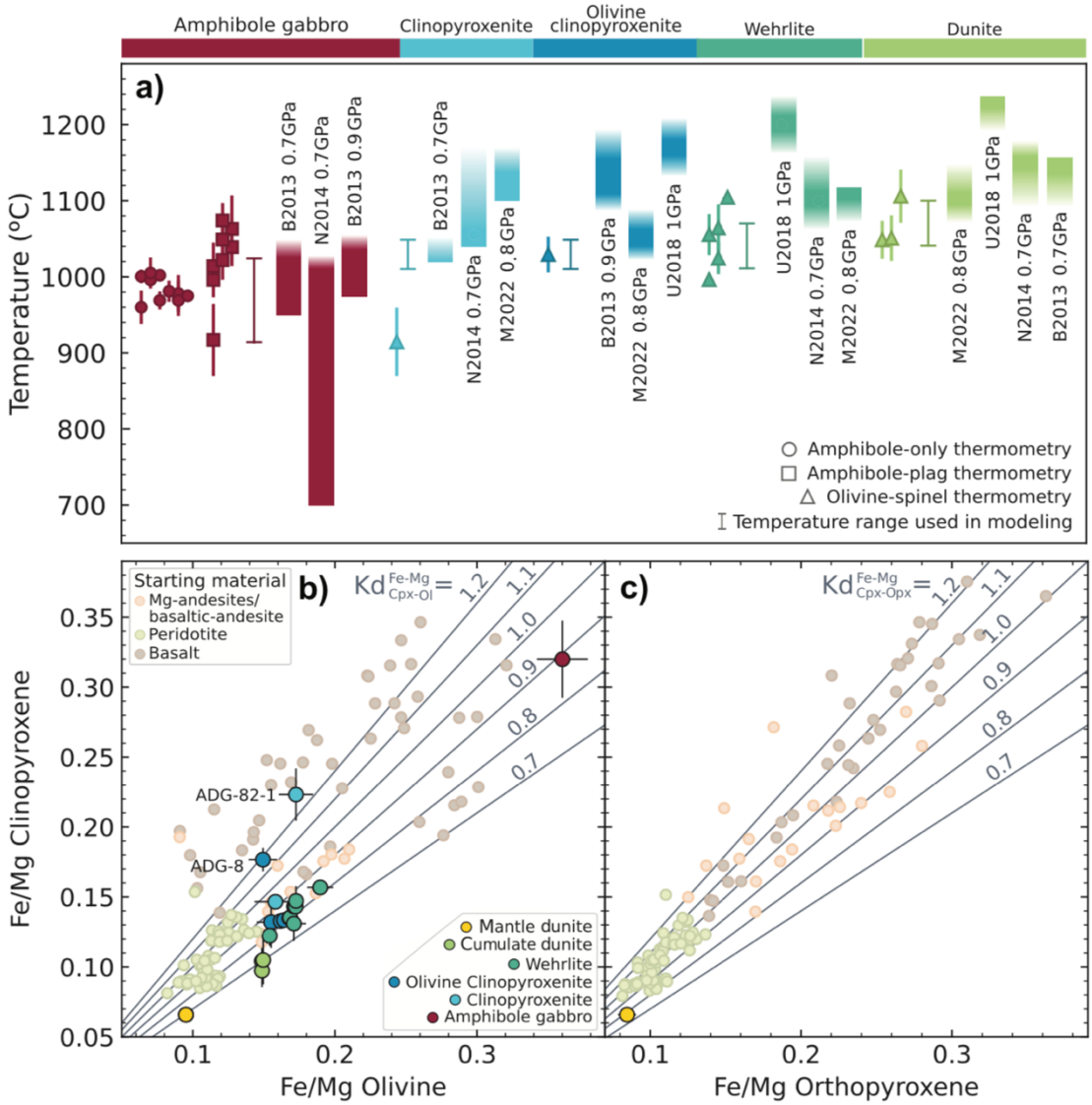

Figure 7: Comparison of Adagdak data to experimental studies. **A)** Temperature range over which experimental studies crystallized dunite, wehrlite, (± olivine) clinopyroxenite, and amphibole gabbro assemblages compared to calculated crystallization temperatures for cumulate xenoliths. **B)** Fe/Mg ratios in clinopyroxene and olivine from experimental studies compared to those from coexisting clinopyroxene and olivine in the Adagdak xenoliths. **C)** Fe/Mg ratios in clinopyroxene and orthopyroxene from experimental studies compared to those preserved in Adagdak lherzolite ADG-CB-9. Experimental data are from Holloway and Burnham (1972), Sisson and Grove (1993), Gaetani et al. (1998), Müntener et al. (2001), Wasylenki et al. (2003), Pichavant and Macdonald (2007), Krawczynski et al. (2012) Blatter et al. (2013), Green et al. (2014), Stamper et al. (2014), Mandler and Grove (2016), and Ulmer et al. (2018).

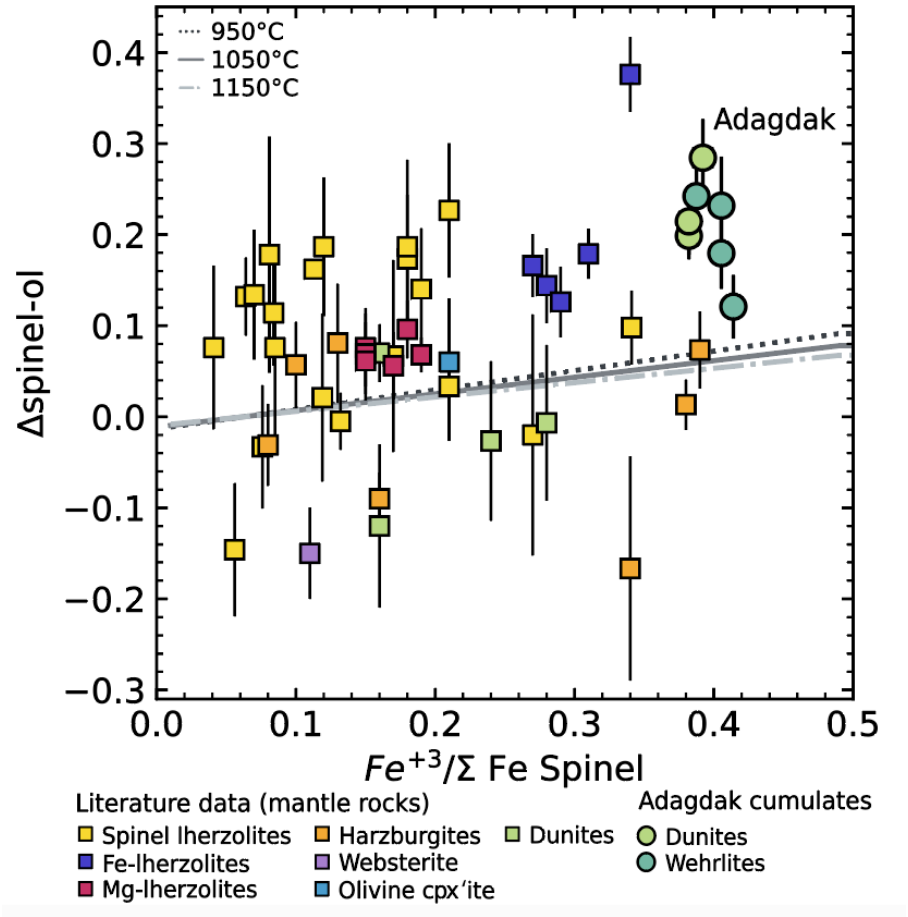

Figure 8: $\Delta^{56}Fe_{spinel\text{-}olivine}$ (‰) for Adagdak cumulates and mantle rock. Gray lines represent equilibrium fractionation at a given spinel $Fe^{3+}/\Sigma Fe$ (Roskosz et al., 2015) at 950 to 1150 °C, with an olivine force constant of 197 N/m. Literature data are from Macris et al. (2015), Williams et al. (2005), Xiao et al. (2016), Zhao et al. (2010, 2015).

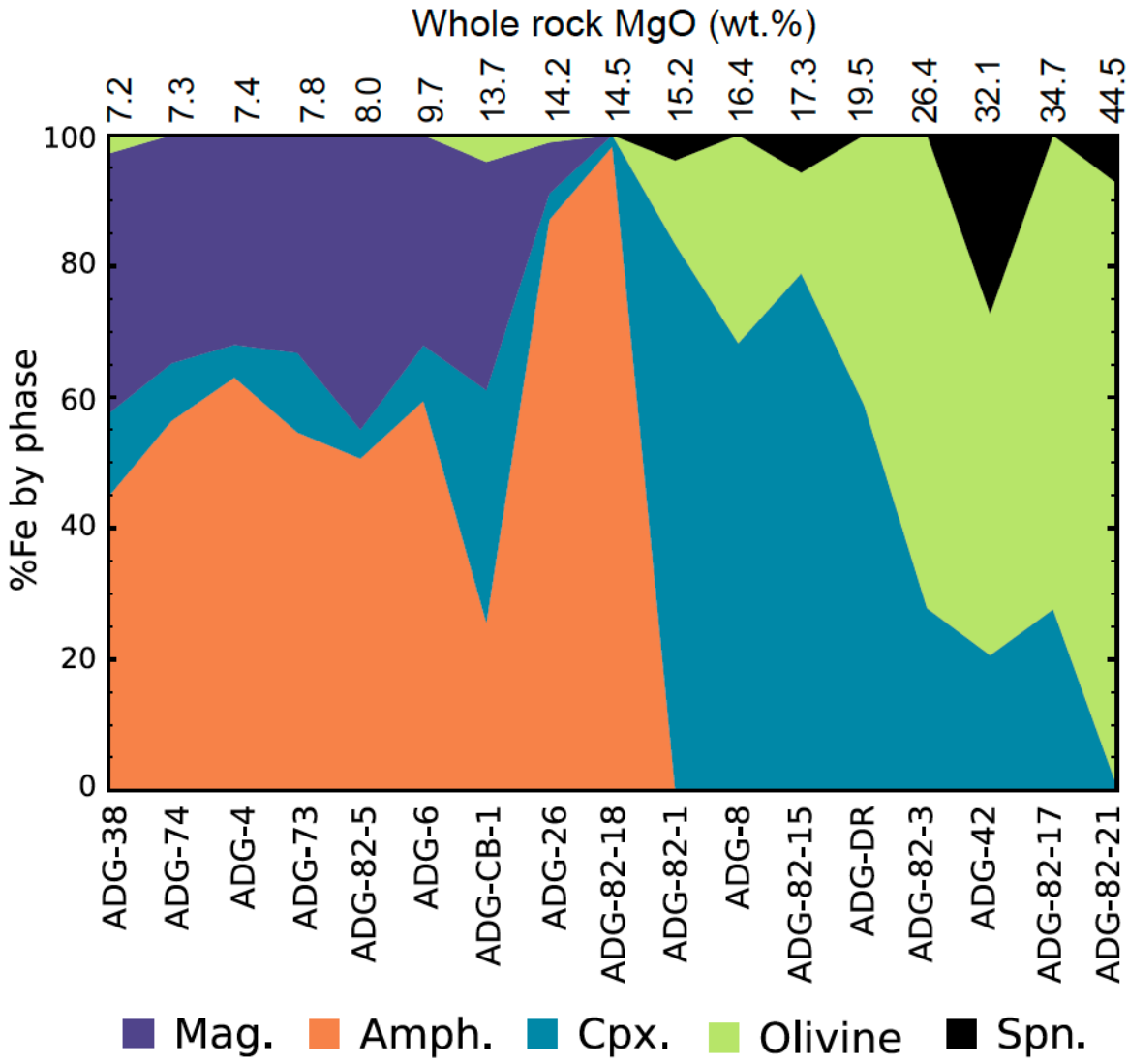

Figure 9: Percent of bulk whole-rock FeO_T budget held by each phase in Adagdak cumulates, calculated from modal abundances and mineral chemistry. Samples are organized by increasing MgO.

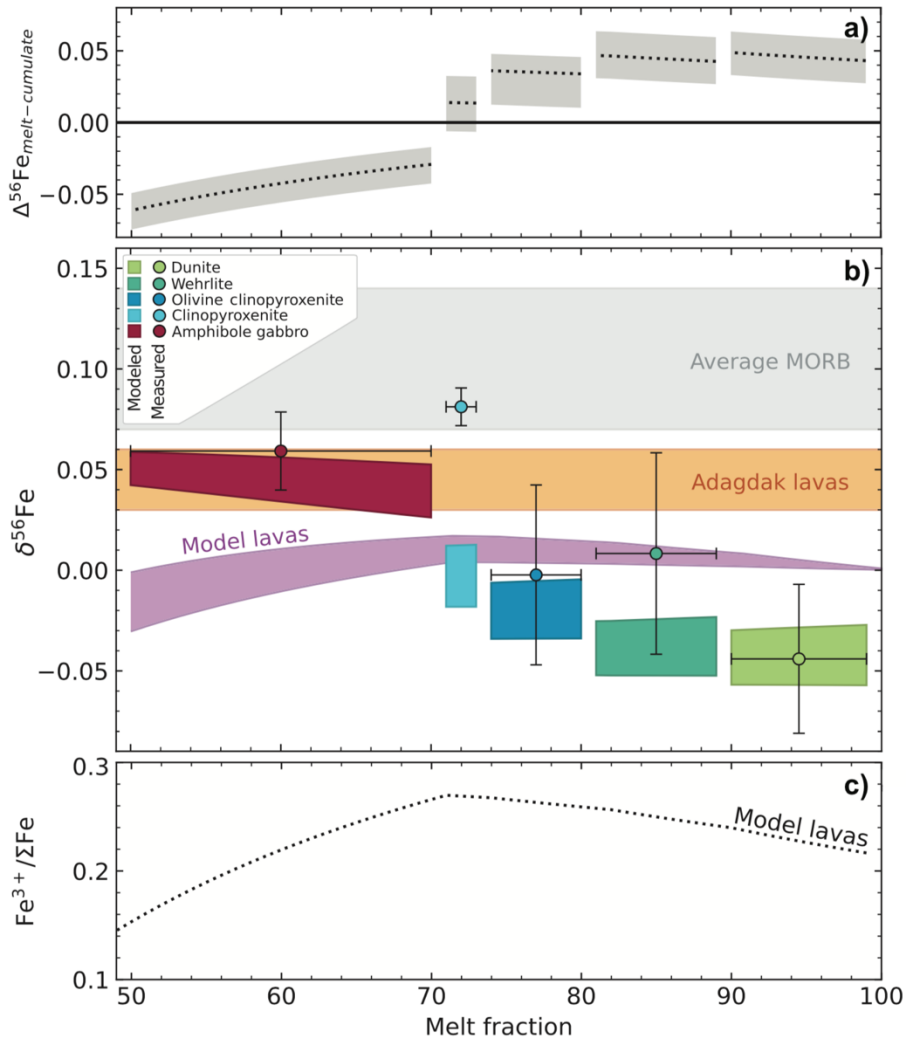

Figure 10: Mass balance model of Fe isotope evolution of Adagdak melts and cumulates during fractional crystallization. Results are shown as a function of melt fraction. **A)** Evolution of $\Delta^{56}Fe_{melt\text{-}cumulate}$ in model, with errors reflecting uncertainties on reported and estimated melt and mineral force constants **B)** $\delta^{56}Fe$ of modeled melts and cumulates. The weighted average measured cumulate composition for each lithological group is shown as data points with error bars over the interval where that lithology was fractionated in the model. Vertical error bars represent the uncertainty on the composition of the weighted average for each lithological group and horizontal bars represent the range over which each lithology was fractionated from the melt. Colored boxes represent the modeled cumulate compositions. The range in $\delta^{56}Fe$ of the modeled cumulates and the melts reflects the uncertainty on reported and estimated melt and mineral force constants. MORB field (gray) is from Teng et al. (2013) and Adagdak lava field represents the range in $\delta^{56}Fe$ of measured Adagdak lavas (this study). **C)** Evolution of $Fe^{3+}/\Sigma Fe$ in modeled melts.

3.11 FIGURES AND CAPTIONS

Table 1: Fe isotope compositions and select major element data for Adagdak samples

Sample	Phase	n	$\delta^{56}Fe$	Err	$\delta^{57}Fe$	Err	MgO (wt.%)	FeO_T (wt.%)	Mg#
Amphibole gabbro									
ADG-38	Whole rock	6	0.076	0.043	0.116	0.068	7.23	9.35	57.95
	Magnetite	10	0.107	0.017	0.159	0.027	2.93	79.76	14.01
ADG-74	Whole rock	8	0.041	0.044	0.070	0.069	7.30	8.42	60.72
	Clinopyroxene	6	0.050	0.025	0.078	0.041	12.28	8.27	72.58
	Magnetite	7	0.112	0.015	0.162	0.028	2.98	79.78	14.15
ADG-4	Whole rock	8	0.064	0.033	0.083	0.046	7.35	10.77	54.87
ADG-73	Whole rock	7	0.057	0.018	0.073	0.032	7.84	11.03	55.91
	Magnetite	6	0.125	0.028	0.191	0.051	2.79	80.50	13.25
ADG-82-5	Whole rock	8	0.065	0.050	0.090	0.074	8.04	13.79	50.96
ADG-6	Whole rock	8	0.056	0.033	0.093	0.046	9.67	10.32	62.53
	Clinopyroxene	7	0.072	0.025	0.100	0.041	13.24	8.27	74.04
	Amphibole	7	0.065	0.039	0.100	0.053			
ADG-CB-1	Whole rock	6	0.059	0.025	0.085	0.045	13.73	11.31	68.40
	Clinopyroxene	6	0.067	0.025	0.099	0.045	13.40	7.64	75.26
	Amphibole	7	0.076	0.021	0.110	0.048	13.81	11.03	69.03
Hornblendite									
ADG-26	Whole rock	6	0.077	0.025	0.104	0.041	14.21	10.29	71.10
ADG-82-18	Whole rock	6	0.074	0.025	0.114	0.045	14.47	10.03	72.00
	Amphibole	7	0.089	0.028	0.123	0.041	13.92	10.11	71.04
ADG-52	Amphibole	6	0.067	0.028	0.101	0.041	13.23	10.47	67.62
Clinopyroxenite									
ADG-82-1	Whole rock	7	0.085	0.018	0.138	0.032	15.21	5.56	82.98
ADG-82-15	Whole rock	8	0.049	0.050	0.074	0.074	17.27	4.27	87.82
	Clinopyroxene	6	0.090	0.038	0.140	0.067	15.52	4.05	87.2
Olivine clinopyroxenite									
ADG-8	Whole rock	8	0.035	0.037	0.059	0.061	16.41	4.72	86.10
	Whole rock*		0.050	0.054	0.072	0.077			
	Olivine	9	-0.019	0.037	-0.023	0.053	46.50	12.38	87
	Clinopyroxene	7	0.083	0.035	0.115	0.056	15.36	4.84	84.99

Table 1 continued

Sample	Phase	n	$\delta^{56}Fe$	Err	$\delta^{57}Fe$	Err	MgO (wt.%)	FeO_T (wt.%)	Mg#
ADG-DR	Whole rock	8	0.046	0.037	0.090	0.061	19.47	4.43	88.68
	Whole rock*		0.039	0.056	0.057	0.072			
	Olivine	9	-0.015	0.043	-0.023	0.046	46.13	13.50	85.90
	Clinopyroxene	7	0.077	0.035	0.113	0.056	16.22	3.86	88.23
ADG-CB-7	Olivine	9	-0.003	0.043	0.015	0.067	45.78	13.20	86.08
	Clinopyroxene	6	0.058	0.038	0.099	0.067	15.99	3.78	88.23
ADG-32	Olivine	5	-0.086	0.023	-0.129	0.040	46.44	12.84	86.64
	Clinopyroxene	8	-0.012	0.031	-0.019	0.043	15.93	3.75	88.18
ADG-82-17	Whole rock	8	-0.036	0.037	-0.049	0.061	34.72	9.98	86.11
	Whole rock*		-0.010	0.055	-0.001	0.090			
	Olivine	7	-0.016	0.040	-0.006	0.060	45.58	13.70	85.57
	Clinopyroxene	6	0.033	0.038	0.048	0.067	16.05	3.86	88.15
ADG-CB-8	Olivine	9	0.004	0.037	0.003	0.053	45.86	14.11	85.28
	Clinopyroxene	5	0.108	0.018	0.160	0.034	15.85	4.16	87.17
Wehrlite									
ADG-82-3	Whole rock	6	0.065	0.039	0.129	0.053	26.40	6.03	88.64
ADG-CB-5	Olivine	8	-0.099	0.030	-0.132	0.051	44.38	15.01	84.06
	Clinopyroxene	8	-0.051	0.030	-0.069	0.051	15.84	4.43	86.45
ADG-33	Olivine	6	-0.007	0.044	-0.017	0.065	45.48	13.97	85.3
	Clinopyroxene	8	0.089	0.031	0.127	0.043	15.90	4.06	87.48
ADG-10	Olivine	8	-0.024	0.033	-0.038	0.046	45.31	13.83	85.38
	Clinopyroxene	8	0.027	0.030	0.066	0.051	15.94	4.07	87.77
ADG-35	Olivine	7	0.032	0.035	0.041	0.056	45.40	13.63	85.59
	Clinopyroxene	7	0.082	0.019	0.113	0.030	15.63	3.77	87.96
	Spinel (vial 18)	7	0.212	0.017	0.302	0.034	13.63	15.82	60.56
	Spinel (vial 5)	6	0.264	0.040	0.394	0.064	13.63	15.82	60.56
ADG-42	Whole rock	8	-0.043	0.050	-0.060	0.074	32.14	9.51	85.77
	Whole rock*		0.014	0.053	0.019	0.082			
	Olivine	8	-0.024	0.031	-0.034	0.043	45.51	13.88	85.39
	Clinopyroxene	7	0.035	0.040	0.048	0.060	16.07	3.75	88.42
	Spinel (vial 16)	7	0.097	0.017	0.137	0.034	11.57	17.41	54.23

Table 1 continued

Sample	Phase	n	$\delta^{56}Fe$	Err	$\delta^{57}Fe$	Err	MgO (wt.%)	FeO_T (wt.%)	Mg#
ADG-30	Clinopyroxene	8	0.075	0.030	0.141	0.051	15.58	3.75	88.09
	Olivine	8	0.023	0.035	0.027	0.056	45.51	13.62	85.64
	Spinel (vial 13)	5	0.266	0.032	0.417	0.045	13.36	16.24	59.47
Cumulate dunite									
ADG-82-21	Whole rock	8	-0.094	0.044	-0.138	0.069	44.47	12.29	86.57
	Olivine	6	-0.077	0.038	-0.121	0.067	46.08	12.21	87.05
	Spinel (vial 11)	7	0.208	0.018	0.324	0.031	13.07	15.61	59.88
ADG-63	Olivine	6	0.065	0.018	0.101	0.027	46.24	12.32	86.95
	Spinel (vial 2)	5	0.279	0.032	0.416	0.045	14.39	14.86	63.31
	Spinel (vial 14)	6	0.264	0.019	0.401	0.035	14.39	14.86	63.31
ADG-82-2	Whole rock	8	-0.017	0.033	-0.042	0.046	45.89	13.35	85.97
	Spinel (vial 8)	6	0.234	0.029	0.362	0.041	12.63	15.96	58.53
	Spinel (vial 9)	6	0.223	0.040	0.334	0.064	12.63	15.96	58.53
Mantle dunite									
ADG-CB-9	Whole rock	8	-0.034	0.049	-0.055	0.072	48.95	9.13	90.52
	Spinel (vial 12)	6	0.109	0.020	0.167	0.033	13.88	12.85	65.83
	Spinel (vial 7)	6	0.176	0.040	0.284	0.064	13.88	12.85	65.83
Lavas									
ADAG-81-4	Whole rock	6	0.062	0.017	0.078	0.028	5.68	10.27	49.65
ADAG-81-2	Whole rock	6	0.0414	0.0146	0.066	0.022	2.45	6.78	39.18
ADAG-81-8	Whole rock	7	0.031	0.015	0.050	0.028	2.53	6.00	42.91
ADAG-81-7A	Whole rock	6	0.0476	0.0267	0.073	0.053	4.79	9.62	47.02
ADAG-81-7	Whole rock	6	0.0471	0.0267	0.071	0.053	3.30	7.96	42.50

*Whole rock values calculated from δ56Fe of all Fe-bearing phases based on mineral modes, densities, and major element chemistry.

Table 2: Force constants used in modeling

Phase	**<F> (N/m)**	**Source**
Olivine (Fo_{82})	197 ± 10	NRIXS, Dauphas et al. (2014)
Clinopyroxene	239 ± 13	Estimate from observed olivine-cpx fractionation
Orthopyroxene (En_{93})	195 ± 5	NRIXS, Jackson et al. (2009)
Spinel: Fe^{+2} in MgFeAl	190 ± 15	NRIXS, Roskosz et al. (2015)
Spinel: Fe^{+3} in MgFeAl	302 ± 18	NRIXS, Roskosz et al. (2015)
Amphibole	241 ± 9	Estimate from synchrotron Mössbauer spectroscopy
Magnetite	264 ± 6	NRIXS, Roskosz et al. (2015)
Fe^{+2} in basalt	193 ± 7	NRIXS, Roskosz et al. (2022)
Fe^{+3} in basalt	364 ± 23	NRIXS, Roskosz et al. (2022)

Table 3: Compositions, temperature estimates, and cumulate force constants

Lithology	*Dunite*	*Wehrlite*	*Olivine clinopyroxenite*	*Clinopyroxenite*	*Amphibole gabbro*
SiO_2	38.81	45.75	48.45	50.40	42.40
TiO_2	0.10	0.16	0.26	0.37	1.21
Al_2O_3	0.93	2.49	3.16	5.06	18.56
Fe_2O_3	0.49	0.57	0.69	0.85	6.45
FeO	12.09	8.63	5.86	4.23	5.20
MnO	0.00	0.15	0.00	0.09	0.02
MgO	46.08	30.06	23.91	16.49	8.97
CaO	0.97	12.03	17.36	22.19	15.74
Na_2O	0.00	0.13	0.24	0.20	1.30
K_2O	0.01	0.00	0.01	0.02	0.23
<F> (N/m)	200 ± 10	206 ± 8	215 ± 3	230 ± 7	256 ± 7
Temp (ºC)	1068 ± 33	1037 ± 31	1029 ± 20	1029 ± 20	973 ± 54

APPENDIX TO CHAPTER 3

3.12 Literature data used in Figure 5

Amphibole Fe isotope data - garnet-bearing websterites and clinopryoxenites: Williams et al. (2005); lava phenocrysts: Beard et al. (2004); banded iron formations: Ye et al. (2020).

Clinopyroxene data - mantle rocks: Williams et al. (2005, 2014); mafic intrusions: Tian et al. (2020).

Spinel data – mantle rocks: Williams et al. (2005), Zhao et al. (2015).

Olivine data -mantle rocks: Williams et al. (2005, 2014). Magnetite data - layered mafic intrusions: Chen et al 2014); Red Hills Sill diabase: Sossi et al 2012; Ore deposit: Rodriguez-Mustafa et al 2020.

Whole-rock data - Lesser Antilles cumulates and non-cumulate gabbros: Cooper and Inglis (2022); sub-arc mantle peridotites: Williams et al. (2005), Weyer and Ionov (2007), Poitrasson et al. (2013), Turner et al. (2018).

3.13 Additional Figures

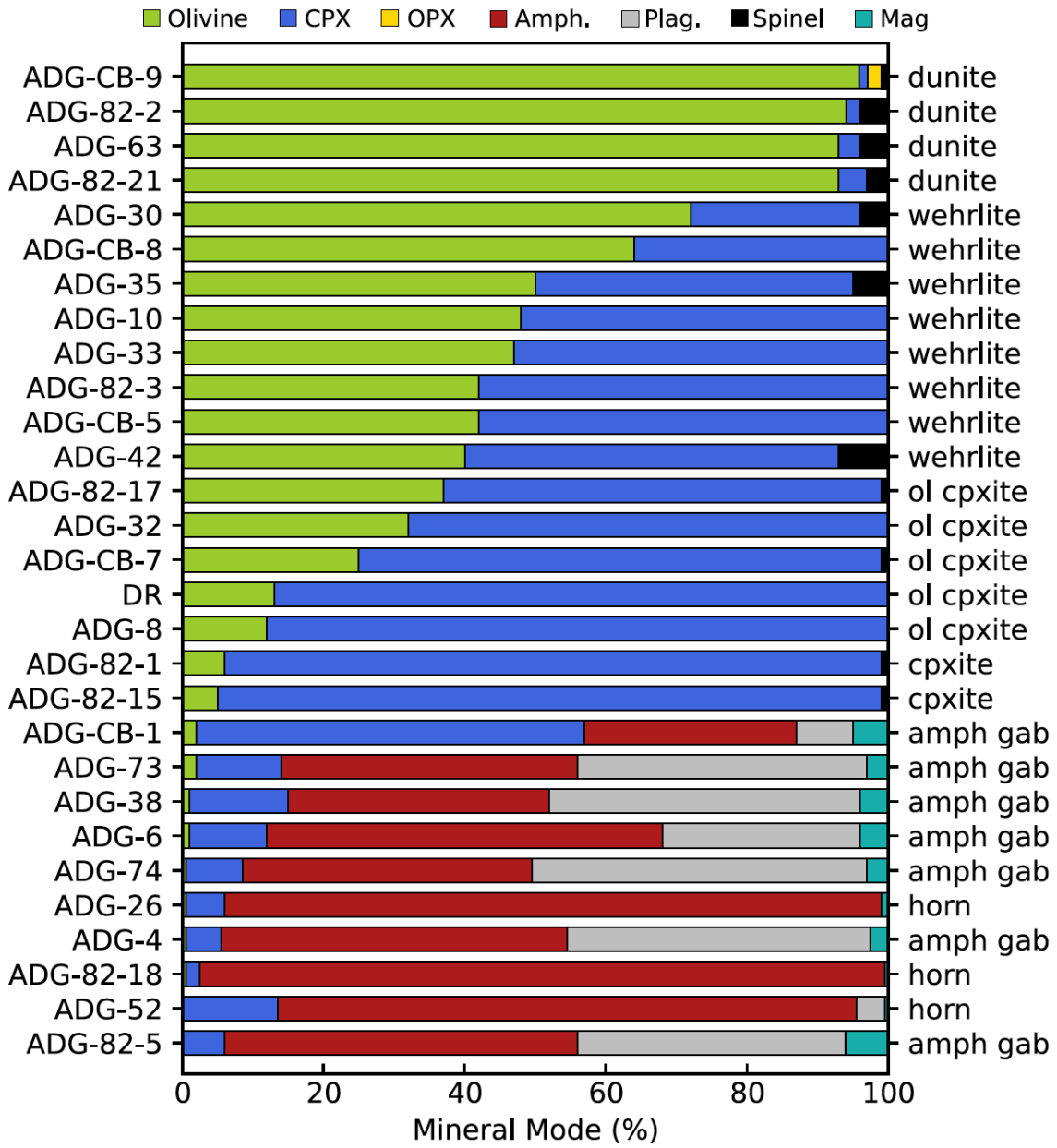

***Supplemental Figure 1*:** Modal proportions of studied xenoliths. The lithology for each xenolith is given to the left of the sample name and the crystallization sequence for cumulate samples inferred from petrography is noted to the right. Abbreviations: *ol cpxite* olivine clinopyroxenite, *amph gab* amphibole gabbro, *horn* hornblendite. Modified from Sosa et al. (2023).

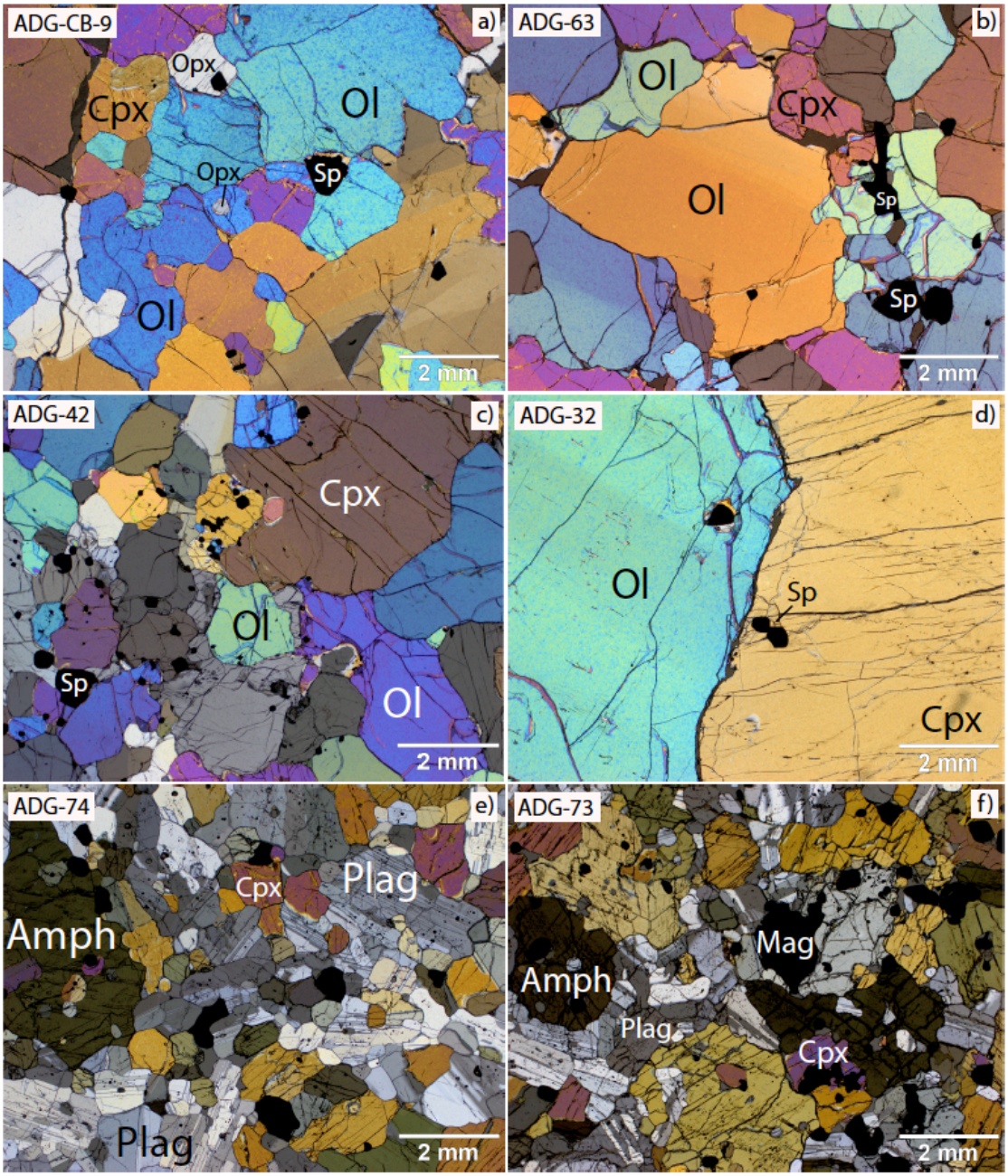

***Supplemental Figure 2*:** Representative photomicrographs of thin sections in cross-polarized light. **A)** Mantle dunite ADG-CB-9. **B)** Cumulate dunite ADG-63. **C)** Wehrlite ADG-42. **D)** Interface between coarse olivine and clinopyroxene crystals in olivine clinopyroxenite ADG-32. **E)** Amphibole gabbro ADG-74. **F)** Amphibole gabbro ADG-73.

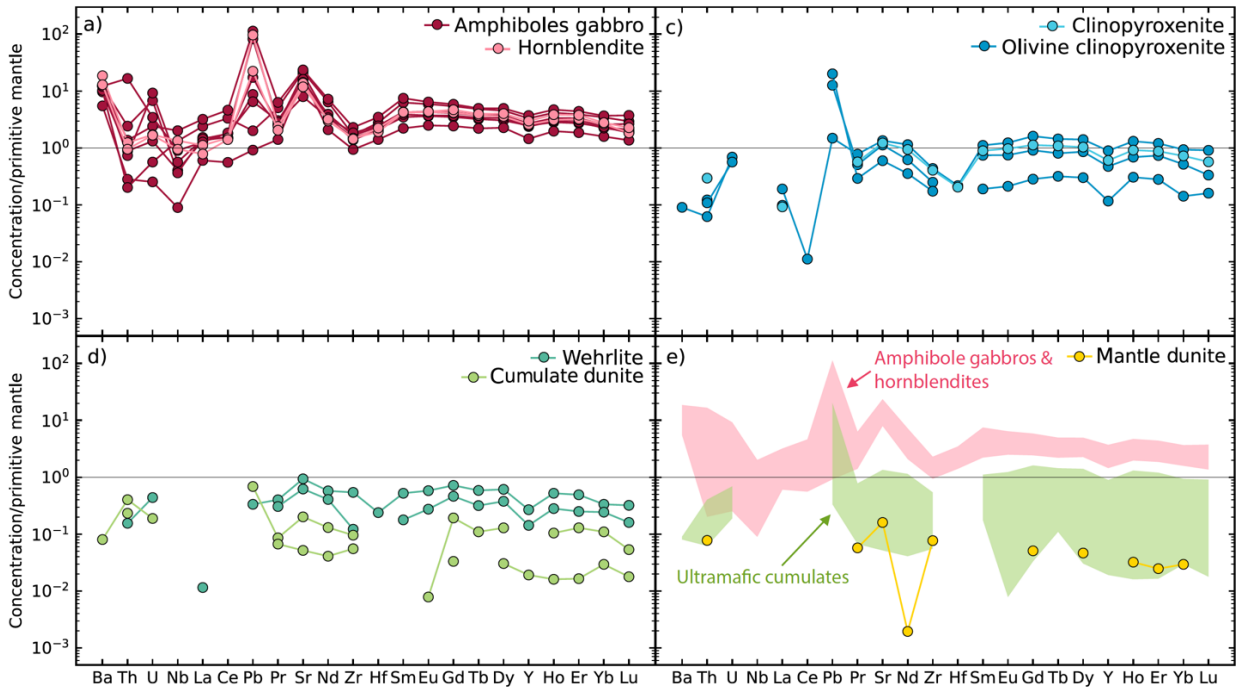

***Supplemental Figure 3*:** Whole-rock trace element compositions of Adagdak cumulates. **A)** Amphibole gabbro and hornblendite cumulates. **B)** Clinopyroxenite and olivine clinopyroxenite cumulates. **C)** Wehrlite and dunite cumulates. **D)** Mantle dunite residue compared to fields defined by the mafic and ultramafic cumulates**.**

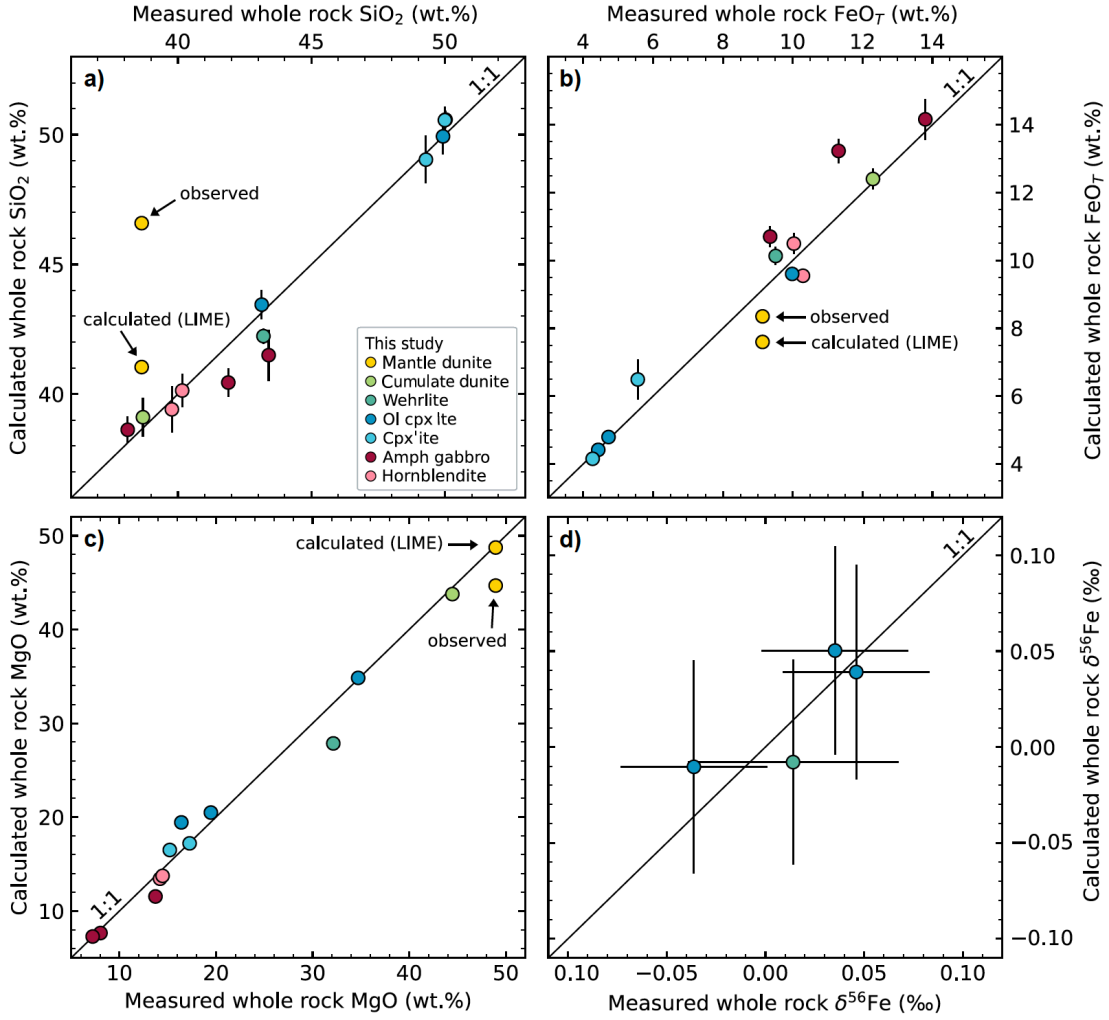

Supplemental Figure 4: Measured vs. calculated whole-rock compositions for Adagdak xenoliths. Major element compositions are shown in **A**, **B**, and **C**. Measured major element data are from XRF analyses of bulk-rock powders (section 3.1 of main text). Theoretical whole-rock compositions (wt.%) were calculated from modal mineralogy deduced from petrography, mineral chemistry, and inferred mineral densities. Error bars on calculated whole-rock compositions represent the propagated uncertainties in mineral chemistry. For mantle dunite ADG-CB-9, we calculated whole-rock compositions from observed mineral modes (i.e., in thin section) and modes calculated with LIME (Prissel et al., 2023), which are respectively labeled as "observed" and "calculated (LIME)". **D)** Calculated vs. measured whole-rock δ^{56}Fe for Adagdak cumulates. This was only done for ADG-8, ADG-DR, ADG-82-17, and ADG-42 because these are the only samples for which we obtained Fe isotope date from all Fe-bearing phases (in this case, olivine + clinopyroxene ± spinel) and whole-rock powders.

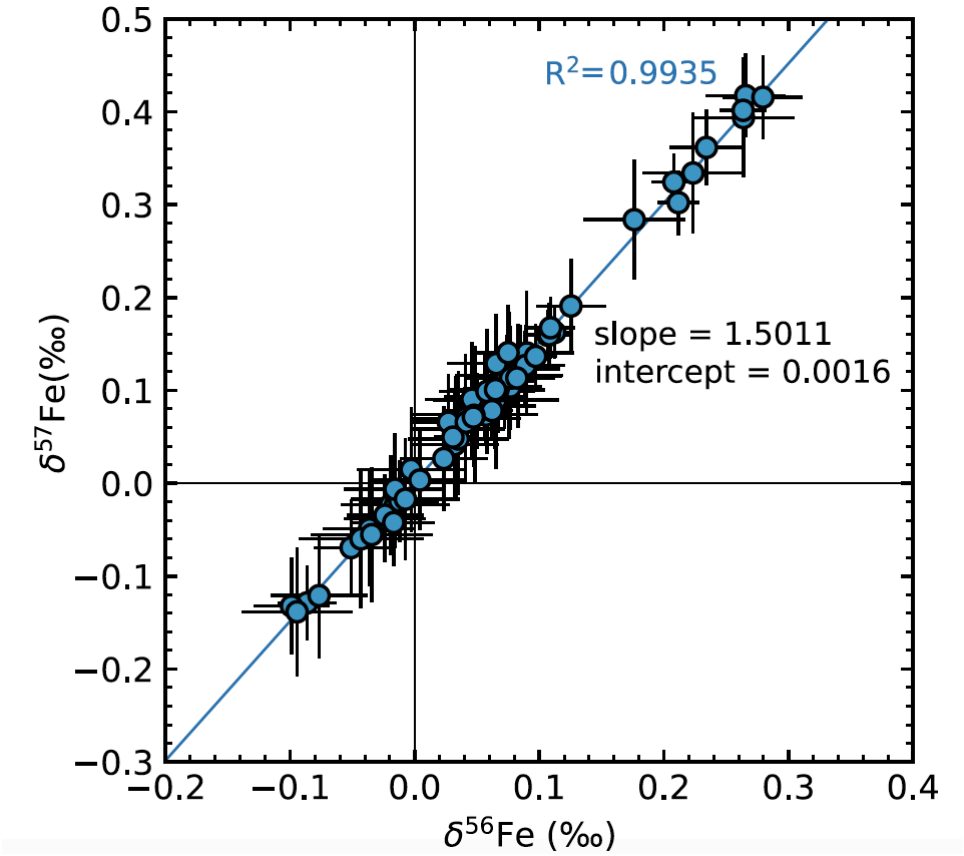

***Supplemental Figure 5*:** $\delta^{56}Fe$ vs. $\delta^{57}Fe$ (‰) of all measured samples. A linear regression through the data gives a slop of 1.5011 and an intercept of 0.0016, in excellent agreement with the expected mass-dependent fractionation ($\delta^{57}Fe \approx 1.5 \times \delta^{56}Fe$, Dauphas et al., 2017) and illustrating the accuracy of our Fe isotope measurements.

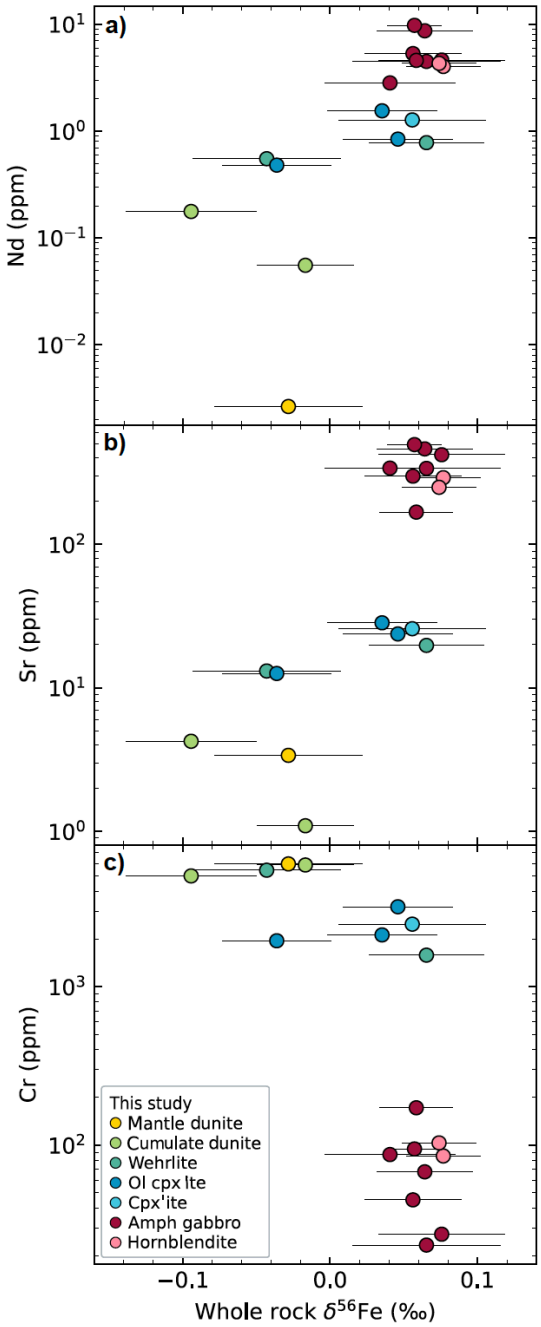

***Supplemental Figure 6*:** Whole rock δ^{56}Fe (‰) of Adagdak cumulates vs trace element composition (ppm). **A)** Whole rock δ^{56}Fe vs Nd. **B)** Whole rock δ^{56}Fe vs Sr. **C)** Whole rock δ^{56}Fe vs Cr.

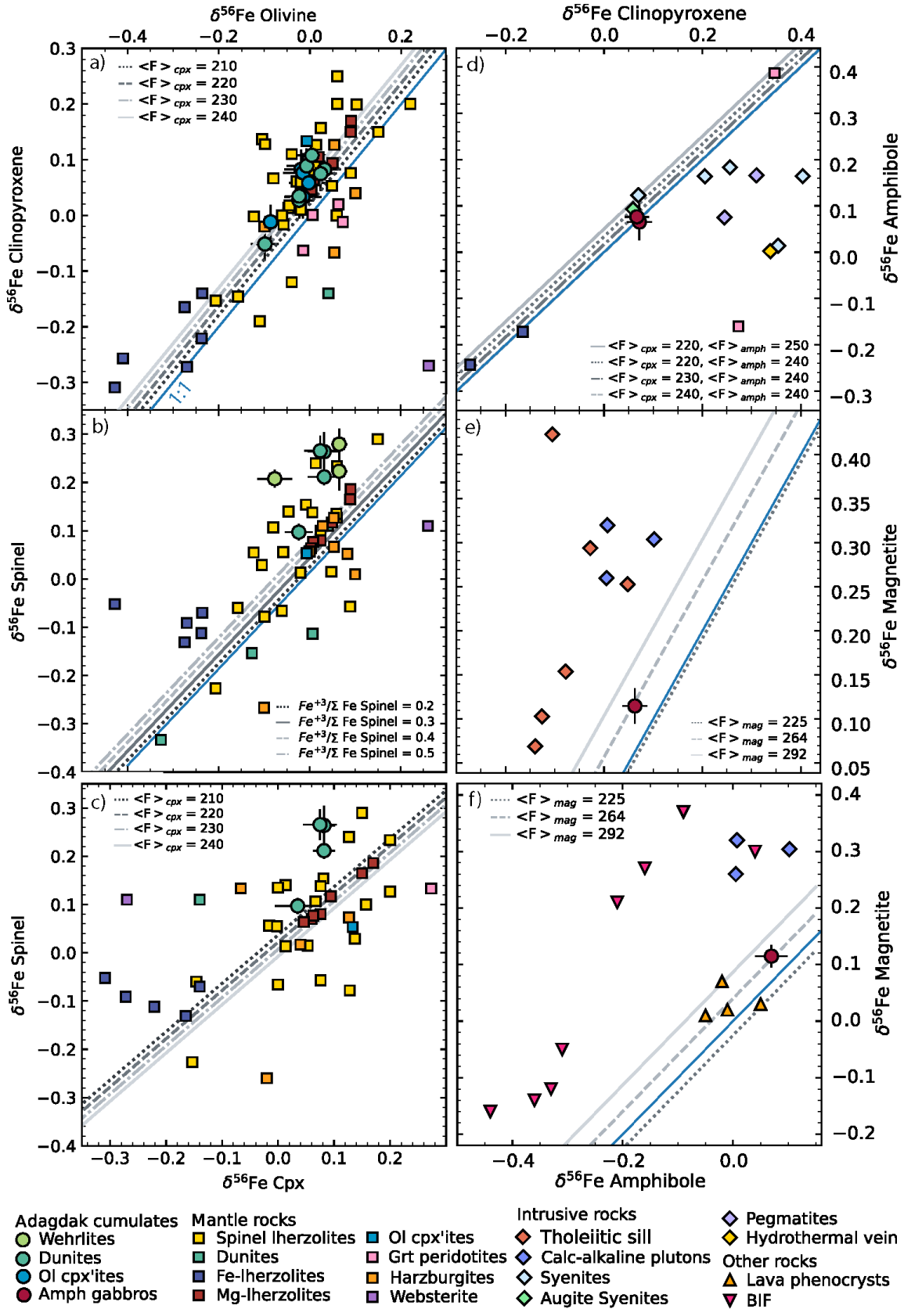
δ56Fe Olivine
δ56Fe Clinopyroxene
δ56Fe Amphibole
δ56Fe Spinel
δ56Fe Magnetite
δ56Fe Cpx
a)
b)
c)
d)
e)
f)
<F > cpx = 210
<F > cpx = 220
<F > cpx = 230
<F > cpx = 240
1:1
<F > cpx = 220, <F > amph = 250
<F > cpx = 220, <F > amph = 240
<F > cpx = 230, <F > amph = 240
<F > cpx = 240, <F > amph = 240
Fe+3/Σ Fe Spinel = 0.2
Fe+3/Σ Fe Spinel = 0.3
Fe+3/Σ Fe Spinel = 0.4
Fe+3/Σ Fe Spinel = 0.5
<F > mag = 225
<F > mag = 264
<F > mag = 292
Adagdak cumulates
Wehrlites
Dunites
Ol cpx'ites
Amph gabbros
Mantle rocks
Spinel lherzolites
Dunites
Fe-lherzolites
Mg-lherzolites
Ol cpx'ites
Grt peridotites
Harzburgites
Websterite
Intrusive rocks
Tholeiitic sill
Calc-alkaline plutons
Syenites
Augite Syenites
Pegmatites
Hydrothermal vein
Other rocks
Lava phenocrysts
BIF

***Supplemental Figure 7* (prev. page):** Inter-mineral Fe isotope fractionation in Adagdak cumulates compared to previous studies. Blue line in all figures represents no fractionation (i.e., 1:1 line). **A)** δ^{56}Fe olivine vs. δ^{56}Fe cpx for Adagdak cumulates compared to mantle rocks (Beard & Johnson 2004; Williams et al., 2005; Weyer and Ionov 2007; Zhao et al., 2010, 2012, 2015, 2021; Macris et al., 2015; Xiao et al., 2016). Gray lines represent equilibrium fractionation at 1050 °C with $<F>_{olivine}$ = 197 N/m (Dauphas et al., 2012) and varying $<F>_{cpx}$ from 210 N/m to 240 N/m. Similar degrees of cpx-olivine fractionation to that seen in the Adagdak cumulates ($\Delta^{56}Fe_{cpx\text{-}ol}$ = 0.05 to 0.10) are observed in Mg-lherzolite from the North China Craton ($\Delta^{56}Fe_{cpx\text{-}ol}$ = 0.04 to 0.09; Zhao et al., 2015) and spinel lherzolite from the Mexican Basin and Range province ($\Delta^{56}Fe_{cpx\text{-}ol}$ = 0.03 to 0.06; Williams et al., 2005). **B)** δ^{56}Fe olivine vs. δ^{56}Fe spinel for Adagdak cumulates compared to mantle rocks. Gray lines represent equilibrium fractionation at 1050 °C with $<F>_{olivine}$ = 197 N/m and varying $Fe^{+3}/\Sigma Fe$ spinel from 0.2 to 0.5. Similar degrees of spinel-olivine isotopic fraction to that observed in the Adagdak cumulates ($\Delta^{56}Fe_{spin\text{-}ol}$ = 0.12 to 0.28) are seen in Fe rich-lherzolite from the North China Craton ($\Delta^{56}Fe_{spin\text{-}ol}$ = 0.12 to 0.38; Zhao et al., 2015) and spinel lherzolite from the Cameroon Volcanic Line ($\Delta^{56}Fe_{spin\text{-}ol}$ = 0.07 to 0.23; Williams et al., 2005). **C)** δ^{56}Fe cpx vs. δ^{56}Fe spinel for Adagdak cumulates compared to mantle rocks. Gray lines represent equilibrium fractionation at 1050 °C with $<F>_{spinel}$ = 235 N/m (based on an average spinel $Fe^{+3}/\Sigma Fe$ of 0.4) and varying $<F>_{cpx}$ from 210 to 240 N/m. Similar degrees of spinel-cpx Fe isotope fractionation to that observed in the Adagdak cumulates ($\Delta^{56}Fe_{spin\text{-}cpx}$ = 0.06 to 0.19) are also seen in Fe rich-lherzolite from the North China Craton ($\Delta^{56}Fe_{spin\text{-}cpx}$ = 0.03 to 0.26; Zhao et al., 2015) and spinel lherzolite from San Carlos, AZ ($\Delta^{56}Fe_{spin\text{-}cpx}$ = 0.14 ± 0.04; Macris et al., 2015). **D)** δ^{56}Fe cpx vs. δ^{56}Fe amphibole for Adagdak cumulates compared to intrusive (Schoenberg et al., 2009) and mantle rocks from previous studies. Gray lines represent equilibrium fractionation at 970 °C varying $<F>_{amphibole}$ from 240 to 250 N/m and $<F>_{cpx}$ from 220 to 240 N/m. Similar low degrees of amphibole-cpx fractionation to that observed in the Adagdak cumulates ($\Delta^{56}Fe_{amph\text{-}cpx}$ = 0.01 to 0.01) are seen in garnet pargasite websterite from the Cameroon Volcanic Line ($\Delta^{56}Fe_{amph\text{-}cpx}$ = 0.04 ± 0.08; Williams et al., 2005), Fe rich-lherzolite from the North China Craton ($\Delta^{56}Fe_{amph\text{-}cpx}$ = –0.01 to 0.03; Zhao et al., 2015), and augite syenite from the Ilímaussaq Complex ($\Delta^{56}Fe_{amph\text{-}cpx}$ = 0.03 ± 0.05; Schoenberg et al., 2009). **E)** Average δ^{56}Fe cpx vs. δ^{56}Fe magnetite for Adagdak cumulates compared to intrusive rocks from previous studies. Less magnetite-amphibole fraction is seen in the Adagdak cumulates (taking lithology averages, $\Delta^{56}Fe_{mag\text{-}cpx}$ = 0.05 ± 0.03) compared to previous studies of rocks from the Boggy Plain Zoned Pluton, Australia ($\Delta^{56}Fe_{mag\text{-}cpx}$ = 0.20 ± 0.31; Schoenberg et al., 2009) and Red Hill Intrusion, Tasmania ($\Delta^{56}Fe_{mag\text{-}cpx}$ = 0.21 ± 0.53; Sossi et al., 2012). **F)** δ^{56}Fe amphibole vs. δ^{56}Fe magnetite for Adagdak cumulates compared to lava phenocrysts (Beard and Johnson, 2004**),** banded iron formations (BIFs; Ye et al., 2020), and plutonic data (Stow et al., 2021) from previous studies. Gray lines represent equilibrium fractionation at 970 °C with $<F>_{amphibole}$ = 240 N/m and using $<F>_{mag}$ of 225 (Dauphas et al., 2012), 264 (Roskosz et al., 2015), or 292 N/m (Sossi and O'Neill, 2017). Coexisting magnetite and amphibole phenocrysts in basaltic andesite and dacite from Mount Lassen, California, show similar degrees of magnetite-amphibole fractionation ($\Delta^{56}Fe_{mag\text{-}amph}$ = –0.02 ± 0.09; Beard & Johnson 2004) to what is observed in the Adagdak amphibole gabbro cumulates (taking lithology averages, $\Delta^{56}Fe_{mag\text{-}amph}$ = 0.05 ± 0.04).

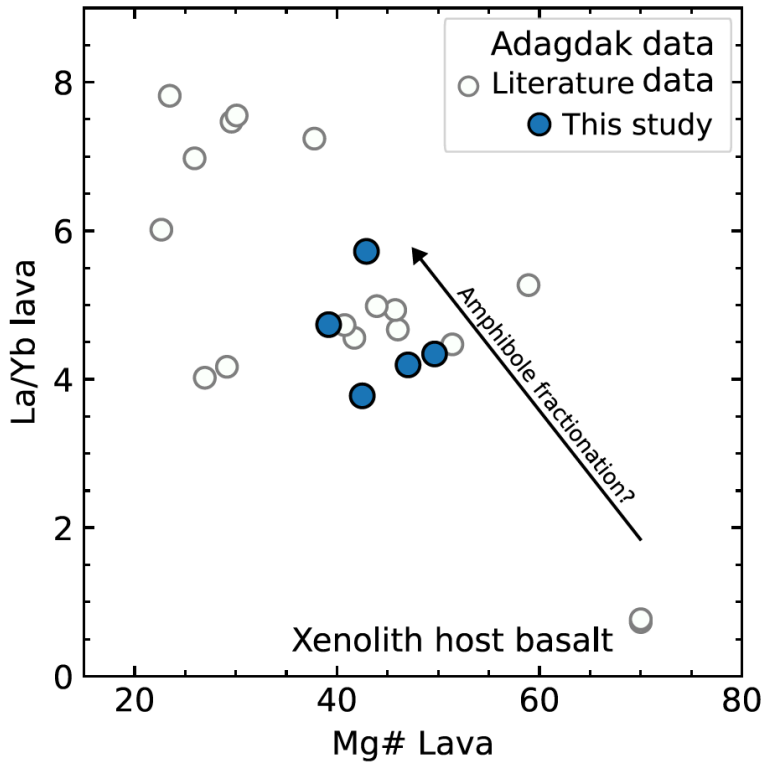

***Supplemental Figure 8*:** Mg# vs La/Yb for Adagdak lavas. Data for the samples used in this study is in blue and literature data for other Adagdak lavas is in grey. Data for other samples is from Coats (1952), Kay and Kay (1985, 1994), Myers et al. (1985), Romick et al. (1992); Hanna et al. (2020).

3.14 Single-crystal amphibole analyses

Methods

As the goal is to correlate all datasets, EMPA, SIMS, and SMS analyses were performed adjacent to each other or if possible, on top of each other (Fig. S9). The results of these analyses are provided in Supplementary Data File 2 (Ch3-T9 to Ch3-T12).

Electron microprobe analysis: Amphibole major and minor elements were analyzed at the California Institute of Technology using a JEOL JXA-8200 electron microprobe. Analyses conditions, a list of standards used for elemental peak calibration, and information about data reduction procedures are summarized in Ratschbacher et al. (2023). Multiple spots were analyzed in single grains along a core-rim transect to capture intra-grain compositional heterogenies. Major and minor element analyses and their 1 σ relative uncertainties (percent of absolute values) calculated from counting statistics are listed in Supplementary Data File 2 (Ch3-T9).

Secondary-ion mass spectrometry: Amphibole water contents were determined using a Cameca 7f-GEO secondary-ion microprobe (SIMS) at the California Institute of Technology following a protocol outlined in Ratschbacher et al. (2023). However, for D/H analyses, instead of using a Cs^+ primary beam and collecting negative secondary ions, we used a 13 keV O^- primary beam of ~16 nA current (~ 20 μm diameter) to pre-sputter the sample and then raster the analytical spot (5 × 5 mm^2) during sample data acquisition. Positive secondary ions (H+ and D+), energy filtered above 8.5 keV were collected with a Faraday cup (FC2) and an electronic multiplier (EM), respectively (e.g., Deloule et al., 1991). The mass spectrometer is set up with a mass resolving power (MRP) of 1800 to completely remove any possible contribution of $H2^+$ to D^+. Even though the ion yields of positive H and D are much lower than their negative ones, a 10-minute data collection for each spot is sufficient to achieve satisfying precision because of the high water

contents in amphibole. Analyses including counts, uncorrected, and corrected data are listed in Supplementary Data File 2 (Ch3-T10).

Single crystal-X-ray diffraction: Single crystal X-ray diffraction experiments were performed at the X-ray Crystallography Laboratory in the Chemistry Department at UC Davis on either a Bruker APEX2 platform (3-circle) sealed tube diffractometer or a Bruker D8 Venture with Kappa geometry (4-circle) and a IμS micro-source. Both X-ray diffractometers used MoKα radiation. Single amphibole grains were mounted and centered, followed by data collected and unit cell dimensions determination for each of the grains using the APEX3 software (Bruker 2012) and Cell_Now (Sheldrick, 2002) in cases where potential twinning may have been present. Grains that showed twinning were not used for single-crystal Mössbauer spectroscopy. Supplementary Data File 2 (Ch3-T11). lists unit cell parameters.

Single-crystal Mössbauer spectroscopy (SMS): Provided in the main text.

Results

Petrography: Amphibole in amphibole gabbro sample ADG-CB-1 is brown to light-green and form anhedral, interstitial, and in parts poikilitic grains enclosing clinopyroxene, olivine, plagioclase, and Fe-Ti oxides. Petrographic and back-scatter electron images show no intra-grain zonation. Amphibole in hornblendite sample ADG82-18 is brown to dark-green and forms an orthocumulate texture with ~97 vol.% amphibole. Larger grains are euhedral and can exhibit concentric zonation, simple twinning, and rare Fe-Ti oxide inclusions. Smaller grains are euhedral to anhedral.

Major and minor element chemistry: Amphibole in sample ADG-CB-1 and ADG-82-18 has a pargasitic composition (following the nomenclature after Hawthorne, 2012) with low F and Cl content (<1 wt.%). Crystals from the amphibole gabbro (ADG-CB-1) have slightly lower Al_2O_3

(~13.8 wt.%) and higher FeO_T (~11 wt.%) and Cr_2O_3 (~0.18 wt.%) contents compared to those from the hornblendite sample (ADG-82-18; ~14.70 wt.% Al_2O_3 and 9.6 wt.% FeO_T; Cr_2O_3 below the detection limit). Other major and minor element oxides are in a similar range between the two samples. Amphibole grains selected for SIMS and SMS analyses (ADG-CB-1 grain6 and ADG-82-18 grain10) do not show intra-grain compositional zonation in major and minor elements and they are inclusion-free as determined by back-scatter electron images (Fig. S9).

Water content and hydrogen isotope composition: Water content was determined in the same area as major and minor element compositions for selected amphibole grains (Fig. S9) resulting in 1.60 ± 0.13 wt.% H_2O in ADG-CB-1 grain6 and 1.34 ± 0.11 wt.% H_2O in ADG-82-18 grain10 (both these grains were then analyzed with SMS). Two additional grains have been analyzed in sample ADG-82-18: grain6: 1.40 ± 0.11 wt.% H_2O and grain15: 1.33 ± 0.11 wt.% H_2O. Calculations of anion occupancy on the W-sites in each amphibole grain shows the presence of an oxo-component for ADG-CB-1 grain6 between 0.21-0.47 wt.% and for ADG-82-18 grain10 between 0.49-0.71 wt.% dependent on the uncertainties of water concentrations. Additionally, the hydrogen isotope composition of ADG-CB-1 grain6 was determined in an adjacent area (Fig. S9) showing a composition of –37.2 ± 4.8‰ (relative to VSMOW). A second grain from sample ADG-CB-1 (grain3) has a hydrogen isotope composition of $\delta D = -52.6 \pm 4.7‰$ (relative to VSMOW). The two grains from sample ADG-82-18, which also have been analyzed for water contents, show a $\delta D = -16.4 \pm 6.1‰$ (grain6) and –25.1 ± 6.4‰ (grain15), respectively.

Single-crystal synchrotron Mössbauer spectroscopy: We fitted all spectra (i.e., spectra for each grain, collected in different orientations and for different durations of time) with a similar model using the approach described in Ratschbacher et al. (2023). Uncertainties for the weight fractions of ferric and ferrous sites of each fit reflect correlations between sites and are given in Supplementary File 2. The average Fe^{3+}/Fe^T ratio for each grain is determined from spectra collected in the same area (Supplemental Figure 9) and considers error propagation. The data

shows a correlation matrix for orientation 1 of grain ADG-82-18 grain10 (overnight spectra). Spectra for grain ADG-82-18 grain10 were fitted using 5 sites; these are (site and site weight): Fe^{2+} M(1) with 10%; Fe^{2+} M(2) with 26%; Fe^{2+} M(3) with 6%; Fe^{3+} M(2) with 11%; Fe^{3+} M(3) with 46-48%. The calculated Fe^{3+}/Fe^{T} ratio for this grain is 0.58 ± 0.02. Spectra for grain ADG-CB-1 grain6 were fitted with 6 sites (site and site weight): Fe^{2+} M(1) with 11%; Fe^{2+} M(2) with 25%; Fe^{2+} M(3) with 7%; Fe^{3+} M(2) with 12%; Fe^{3+} M(3) with 43%; Fe^{2+} M(4) with 2%. The calculated Fe^{3+}/Fe^{T} ratio for this grain is 0.55 ± 0.06.

Effects of amphibole dehydrogenation and Rayleigh fractionation modeling

Amphibole dehydrogenation can be expressed through the following equation (e.g., Demény et al., 2012):

$$Fe^{2+} + OH^{-} \rightleftharpoons Fe^{3+} O^{2-} + H^{+}$$

We used a Rayleigh fractionation model in combination with amphibole Fe^{3+}/Fe^{T} ratios determined with SMS, δD values and amphibole water contents determined by SIMS, and total Fe content determined by EPMA, to calculate the initial (non-dehydrogenated) Fe^{3+}/Fe^{T} ratios during amphibole crystallization. Initial amphibole water contents were assumed to be 2 wt.% in accordance with the low F and Cl contents in Adak amphibole (< 0.05 wt.%) and initial δD was set to –80‰. Experimentally constrained fractionation factors (for temperatures >540°C) for the Rayleigh fractionation model were taken from Kuroda et al. (1988). Calculated magmatic Fe^{3+}/Fe^{T} ratios are: 0.30±0.05 for ADG-82-18 grain 10 and 0.41±0.04 for ADG-CB-1 grain 6.

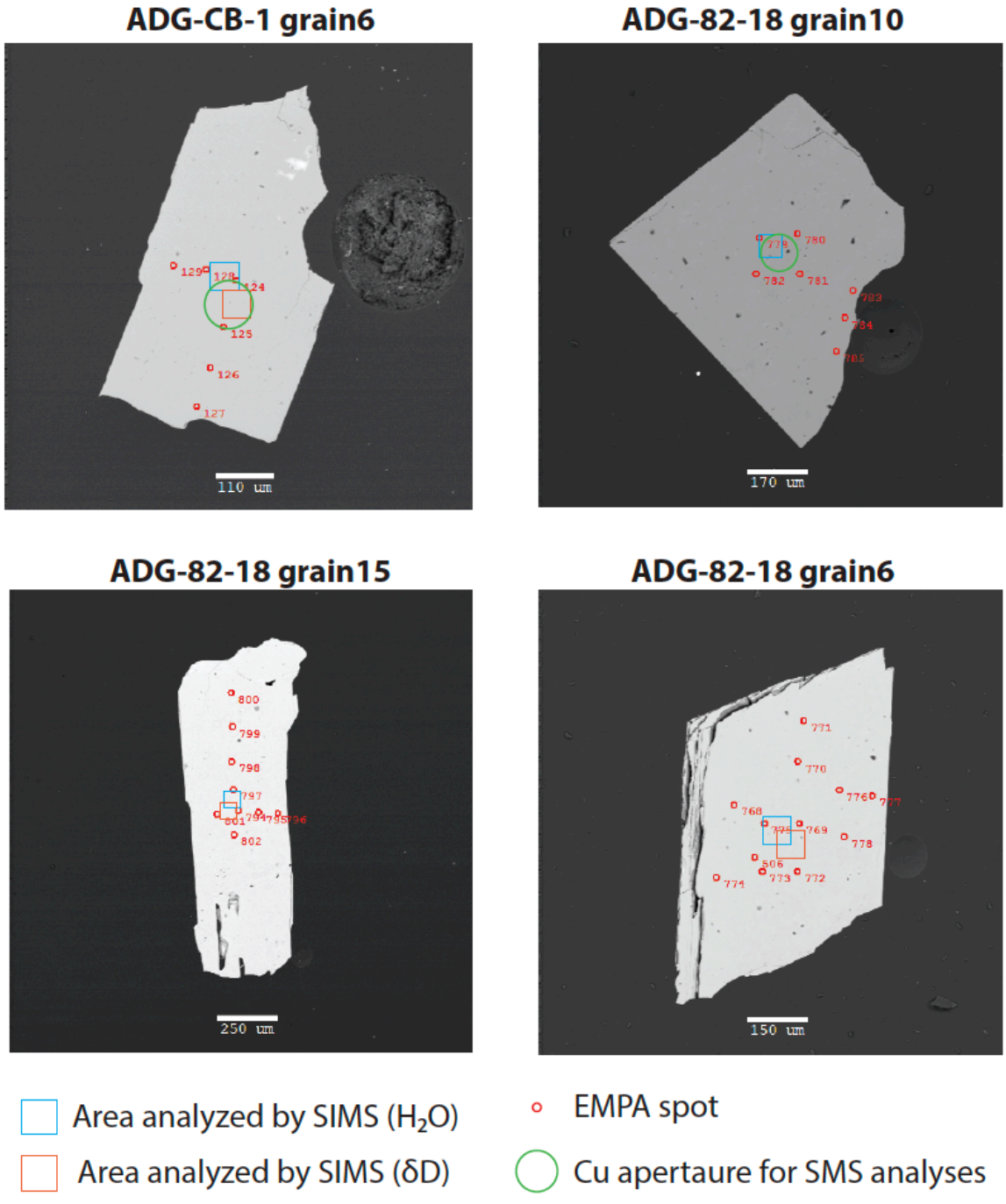

***Supplemental Figure 9*:** Back-scatter electron images of amphibole grains from samples ADG-CB-1 and ADG-82-18 showing EPMA and SIMS analyses were performed as well as Cu aperture area for SMS analyses.

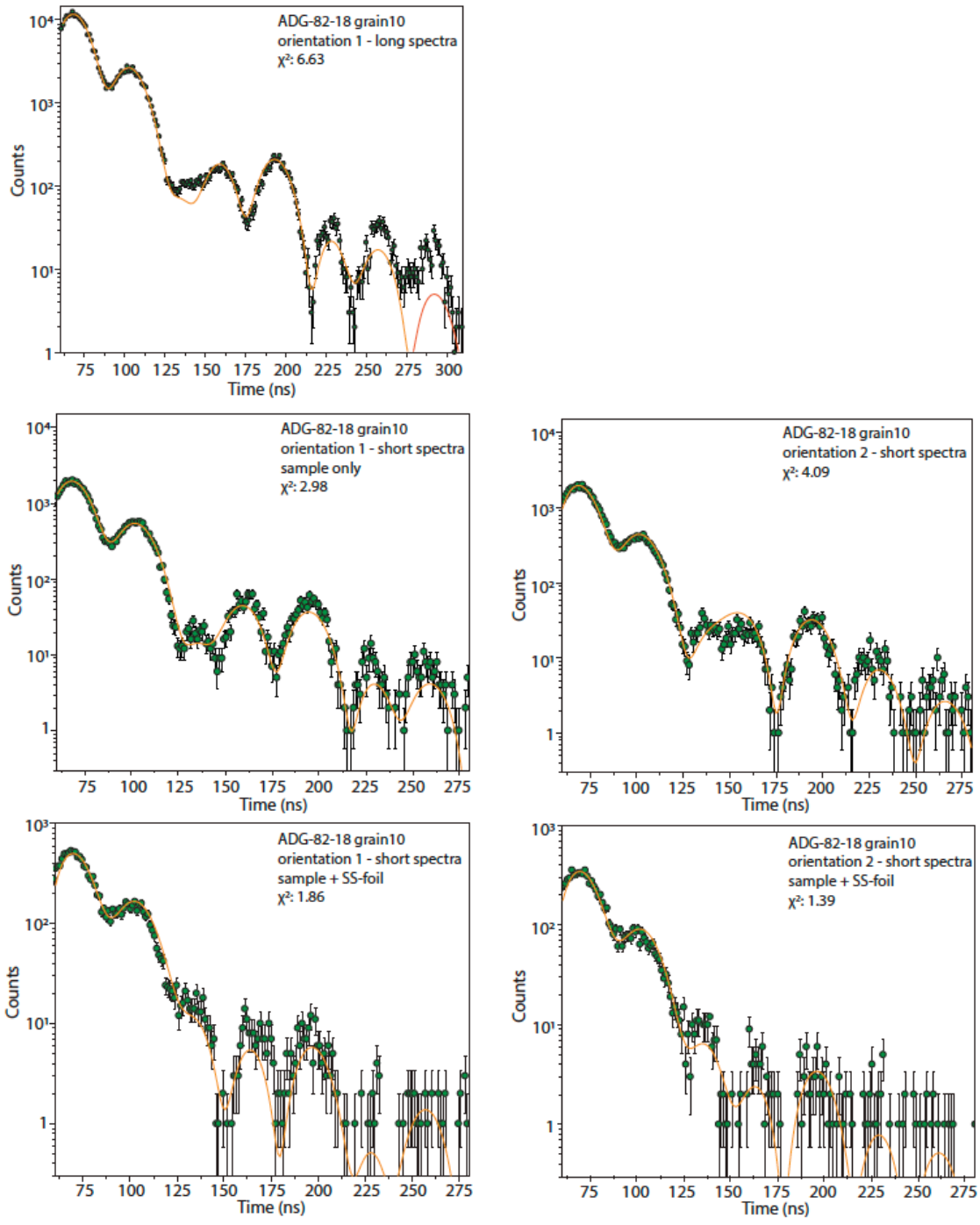

***Supplemental Figure 10*:** Fitted single-crystal amphibole Mössbauer spectra of sample ADG-82-18 grain10 and stainless-steel foil + sample.

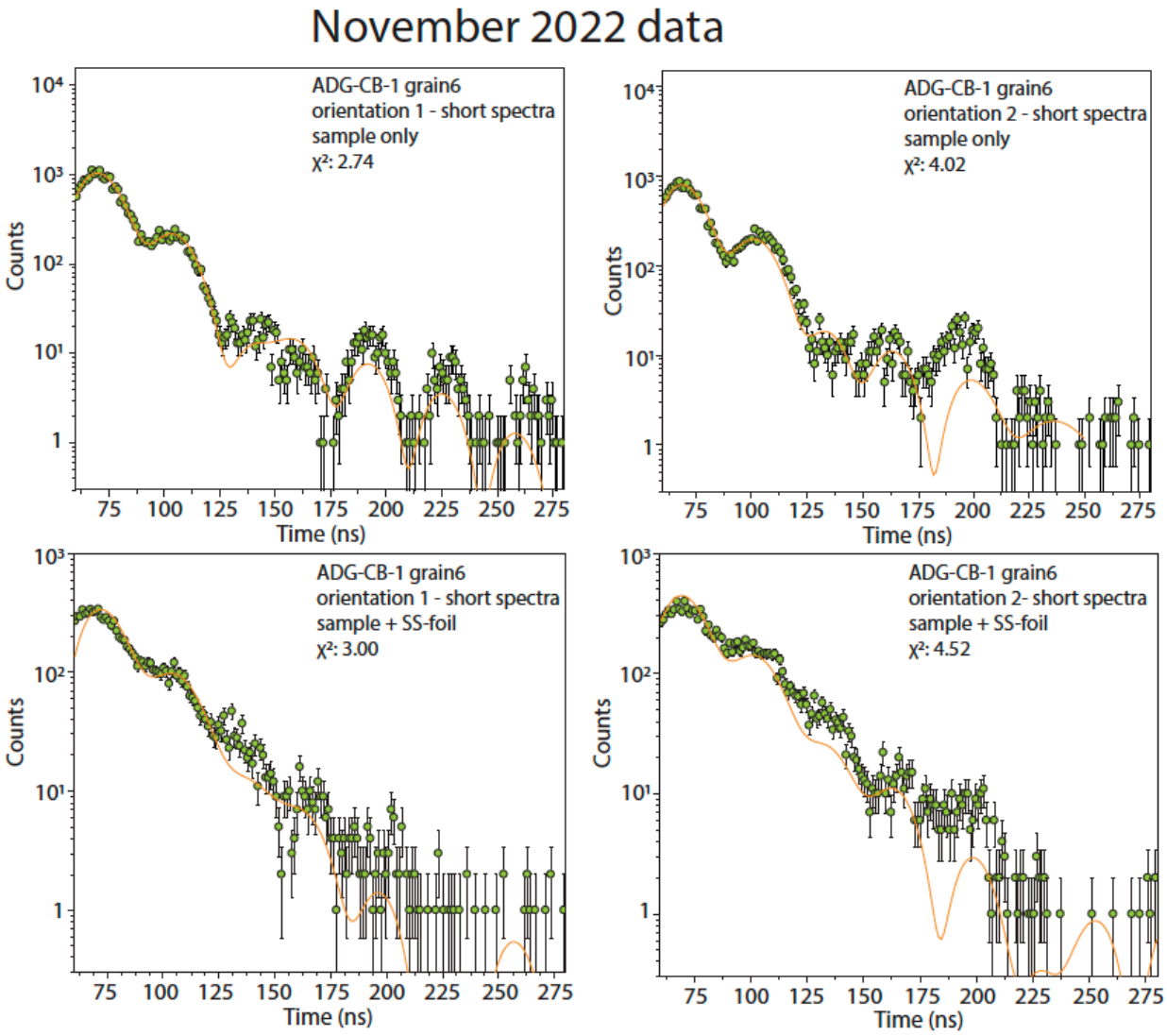

***Supplemental Figure 11a*:** Fitted single-crystal amphibole Mössbauer spectra of sample ADG-CB-1 grain6 and stainless-steel foil + sample (Nov 22).

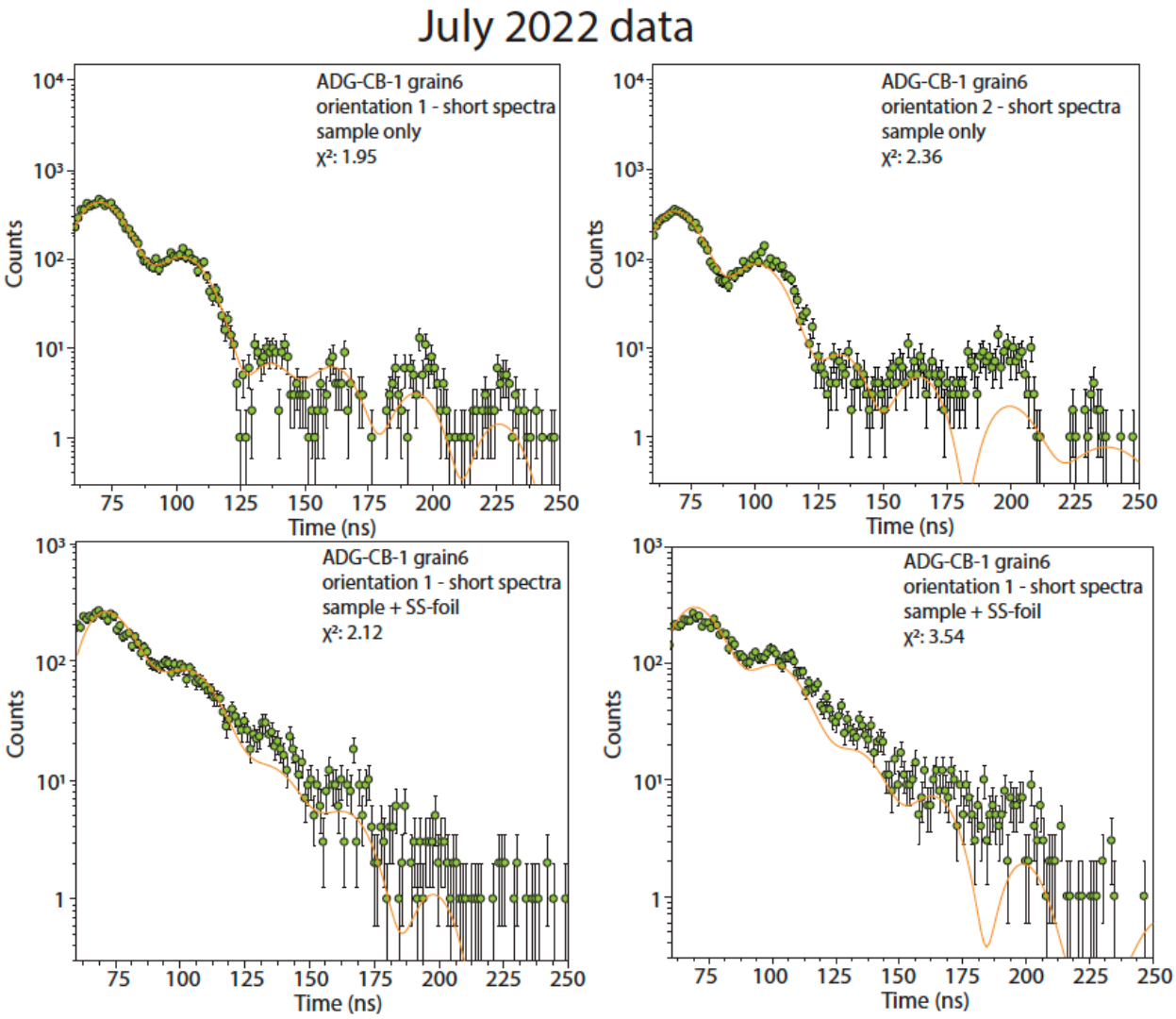

***Supplemental Figure 11b*:** Fitted single-crystal amphibole Mössbauer spectra of sample ADG-CB-1 grain6 and stainless-steel foil + sample (July 22).

3.15 Mass balance fractionation model

Major element mass balance modeling and comparison to experimental studies that reproduced the Adagdak cumulate assemblages serve as the foundation of our Fe isotope mass balance fractionation model. At any point in the crystallization sequence, *i*, the Fe isotope composition of the system, melt, and fractionating cumulate can be related through the equation:

$$\delta^{56}Fe^{i}_{system} = f^{i} \cdot \delta^{56}Fe^{i}_{melt} + (1 - f^{i}) \cdot \delta^{56}Fe^{i}_{cumulate} \quad (1)$$

where *f* is the fraction of the total Fe residing in the melt. Because the cumulate is removed from the system after each fractionating step, $\delta^{56}Fe_{system}$ is in effect the Fe isotope composition of the melt during the previous fractionation step:

$$\delta^{56}Fe^{i+1}_{system} = \delta^{56}Fe^{i}_{melt} \quad (2)$$

The bulk cumulate melt fractionation at step *i* can be calculated from:

$$\Delta^{56}Fe^{i}_{melt\text{-}cumulate} = \delta^{56}Fe^{i}_{melt} - \delta^{56}Fe^{i}_{cumulate} \quad (3)$$

Combining these equations, we can calculate the Fe isotope composition of the evolving melt from the following equation:

$$\delta^{56}Fe^{i+1}_{melt} = \delta^{56}Fe^{i}_{melt} + \Delta^{56}Fe^{i+1}_{melt\text{-}cumulate}\,(1 - f^{i+1}) \quad (4)$$

The fractional crystallization experiments of Nandedkar et al. (2014) and Ulmer et al. (2018) performed on magnesian basalts yield assemblages with similar bulk compositions, major element compositions, and modal mineralogy to the Adagdak cumulate suite (Fig. S12). The most primitive starting composition in these studies is the high-Mg basalt used by Ulmer et al. (2018) (SiO_2 47.65 wt.%, Mg# = 73). Starting with this composition, we used a simple mass balance fractionation

model to remove a representative Adagdak dunite (Supplementary Data File 2, Ch3-T14) from this melt in 1% increments. Using an olivine-melt $K_{D,Fe^{2+}/Mg}^{ol/melt}$ of 0.3 (Roeder and Emslie, 1970), the Mg# of the equilibrium olivine with the melt was recalculated at each step and compared to the Mg# of olivine in the dunite cumulates, until we reproduced the observed compositions after ~10% crystallization. We then began to remove a representative Adagdak wehrlite composition from the remaining melt, now calculating the Mg# of both the equilibrium olivine and clinopyroxene at each step using a clinopyroxene-melt $K_{D,Fe^{2+}/Mg}^{cpx/melt}$ of 0.23 (Toplis and Carroll, 1995). This process was repeated with our olivine clinopyroxenite, clinopyroxenite, and amphibole gabbro assemblages. Our data and comparisons to experimental studies suggest that an appropriate sequence for the model is ~10% dunite fractionation, ~9% wehrlite fractionation, ~7% olivine clinopyroxenite fractionation, ~3% clinopyroxenite fractionation, concluding with ~30% amphibole gabbro fractionation.

As an important constraint we wanted to obtain from this model is the change in $\langle F \rangle_{melt}$ as fractional crystallization progresses, we also had to estimate an initial $Fe^{3+}/\Sigma Fe$ ratio of the melt and the representative cumulate assembles. We used the high-Mg basaltic starting material from Ulmer et al. (2018) as our initial melt composition. Assuming a temperature of 1050°C, a pressure of 1GPa, and an fO_2 of FMQ+1, we used the parametrization of Kress and Carmichael (1991) to estimate an appropriate $Fe^{3+}/\Sigma Fe$ ratio for the initial melt composition, yielding a value of $Fe^{3+}/\Sigma Fe = 0.22$.

For the cumulates, we assumed the olivine contained negligible Fe^{3+}. Clinopyroxene $Fe^{3+}/\Sigma Fe$ ratios were estimated using the normalization scheme of Wood and Banno (1973). Magnetite and spinel $Fe^{+3}/\Sigma Fe$ ratios were calculated from EPMA data based on charge balance. For amphibole, we assumed a uniformed magmatic $Fe^{3+}/\Sigma Fe$ ratio of 0.4 based on our Mössbauer data. Using these estimated $Fe^{+3}/\Sigma Fe$ ratios for each phase, representative values for whole-rock $Fe^{3+}/\Sigma Fe$ were estimated from the model proportions, chemistry, and density of minerals for each lithology (Table 3). In this way, $Fe^{3+}/\Sigma Fe$ of the melt our mass balance model, and therefore $\langle F \rangle_{melt}$, was allowed to evolve as cumulates with different $Fe^{3+}/\Sigma Fe$ were fractionated. The system

is treated as closed to oxygen, and no external buffer is imposed; hence, Fe^{3+} and Fe^{2+} are separately conserved species in the mass balance. For simplicity, $\langle F \rangle_{cumulate}$ for each lithological group was held constant during fractional crystallization modeling (Table 3), even as $\langle F \rangle_{melt}$ was allowed to evolve. In each fractionation step, $\Delta_{melt\text{-}cumulate}$ was recalculated from $\langle F \rangle_{melt}$ and $\langle F \rangle_{cumulate}$.

Force constants and cumulate-melt fractionation

First, combining published and estimated Fe force constants for clinopyroxene, olivine, spinel, magnetite, and amphibole with xenolith mineral chemistry and modal proportions, we calculated a bulk Fe force constant ($\langle F \rangle$, with units of N/m) for each sample, normalizing $\langle F \rangle_{mineral}$ for each phase to 1) the molar proportion of Fe in the phase and 2) the molar proportion of each phase in the bulk assemblage. Force constants calculated through different methods do not always yield similar results (i.e., calculated from first principles as in Rabin et al., 2021, NRIXS like Polyakov et al., 2007), and thus for consistency, we only used reported force constant values obtained through NRIXS.

Clinopyroxene force constant: As discussed in the main text, estimating the force constant of both clinopyroxene and amphibole is difficult given the structural complexity of these minerals, the number of end-member components in their solid solution series, and their ability to take both the reduced and oxidized species of Fe. To our knowledge, there are currently no published values of the clinopyroxene force constant obtained through NRIXS. We can however estimate an appropriate value based on the observed fractionation between olivine and clinopyroxene (Fig. S13) at the temperature predicted by Fe-Mg exchange thermometry for the ultramafic cumulates (~1050 °C). Equilibrium fractionation between two phases can be related to force constants through the following equations:

$\Delta_{B\text{-}A} = (\delta_B - \delta_A)$ (Dauphas et al., 2017, equation 15)

$\delta_B - \delta_A = 2853[\langle F \rangle_B - \langle F \rangle_A]/T^2$ (Dauphas et al., 2014, equation 8)

Comparison of Fe-Mg ratios in coexisting olivine and clinopyroxene from the Adagdak cumulates to data from experimental studies (Fig. 7 of main text) suggests that mineral pairs from most samples are preserving equilibrium conditions with the notable exception of samples ADG-81-1 and ADG-8. Although we did not measure olivine-clinopyroxene pairs from ADG-82-1, we did for ADG-8. As it appears olivine and clinopyroxene from this sample are not recording equilibrium conditions, we did not use Fe isotope data from ADG-8 to estimate $\langle F \rangle_{cpx}$. The other samples for which we measured Fe isotopes from coexisting olivine and clinopyroxene pairs preserve an equilibrium temperature of 1061 ± 38 °C (weighted average). The typical $\Delta Fe^{56}_{cpx\text{-}olivine}$ observed in the Adagdak cumulates (0.07 ± 0.02‰) suggests that at 1060 °C (1333.15°K), the force constant of clinopyroxene should be approximately 239 ± 13 N/m if we use the olivine force constant of 197 N/m given by Dauphas et al. (2014).

These estimated force constants for amphibole and clinopyroxene were combined with previously published force constants for olivine, magnetite, and spinel, along with sample mineral chemistry and modal mineralogy, to calculate a bulk force constant for each cumulate. Using previously determined temperature estimates for the samples (Sosa et al., 2023), a basalt force constant of 230 N/m, and our calculated bulk cumulate force constants, we then calculated cumulate-melt fractionation factors and equilibrium melt compositions for each sample. These results are given in Supplementary Data File 2 (Ch3-T13).

Initial melt composition

Our modeling approach requires an estimate of the initial Fe isotope composition of a primary mantle melt. While mantle dunite ADG-CB-9 almost certainly represents a piece of the Aleutian subarc mantle, ascribing this one sample as the definitive source rock for the parental melts to the Adagdak cumulate suite would be overzealous. Nevertheless, it does represent our best estimate for the Fe isotope composition of the mantle beneath Adagdak. Using the melting equations of Dauphas et al. (2009), and our mantle dunite whole-rock composition as a starting value ($\delta^{56}Fe$ =

–0.03 ± 0.05‰), we calculate the Fe isotope composition of magmas generated by 10% mantle melting (Fig. S15). Melts generated by 10% fO_2 buffered fractional melting range from $\delta^{56}Fe$ = –0.08 to +0.02‰ (Fig S14).

We can derive additional constraints for our model with Fe isotope data of erupted Aleutian lavas. While the lavas we obtained Fe isotope measurements for span much of the compositional range observed in volcanic rocks from Adagdak (Figure 6b), they are far more evolved than primary mantle melts (e.g., MgO ≤ 5.68 wt.%). Reported Fe isotope compositions of primitive arc basalts and basaltic andesites span a wide compositional range (Figure 1a), from approximately $\delta^{56}Fe$ = –0.09 to +0.20‰. Previous measurements of Aleutian lavas specifically (Foden et al., 2018) center around $\delta^{56}Fe$ = 0.0‰ ($\delta^{56}Fe$ = –0.06 to +0.09‰). Based on the previous measurements of Aleutian lavas by Foden et al. (2018), and our mantle dunite melting model discussion above, we chose an initial $\delta^{56}Fe$ of 0.0‰ for our model. We note that increasing or decreasing $\delta^{56}Fe$ will not serve to change the degree of fractionation observed between cumulates and the melt, but merely serve to shift all values to more isotopically light or heavy values.

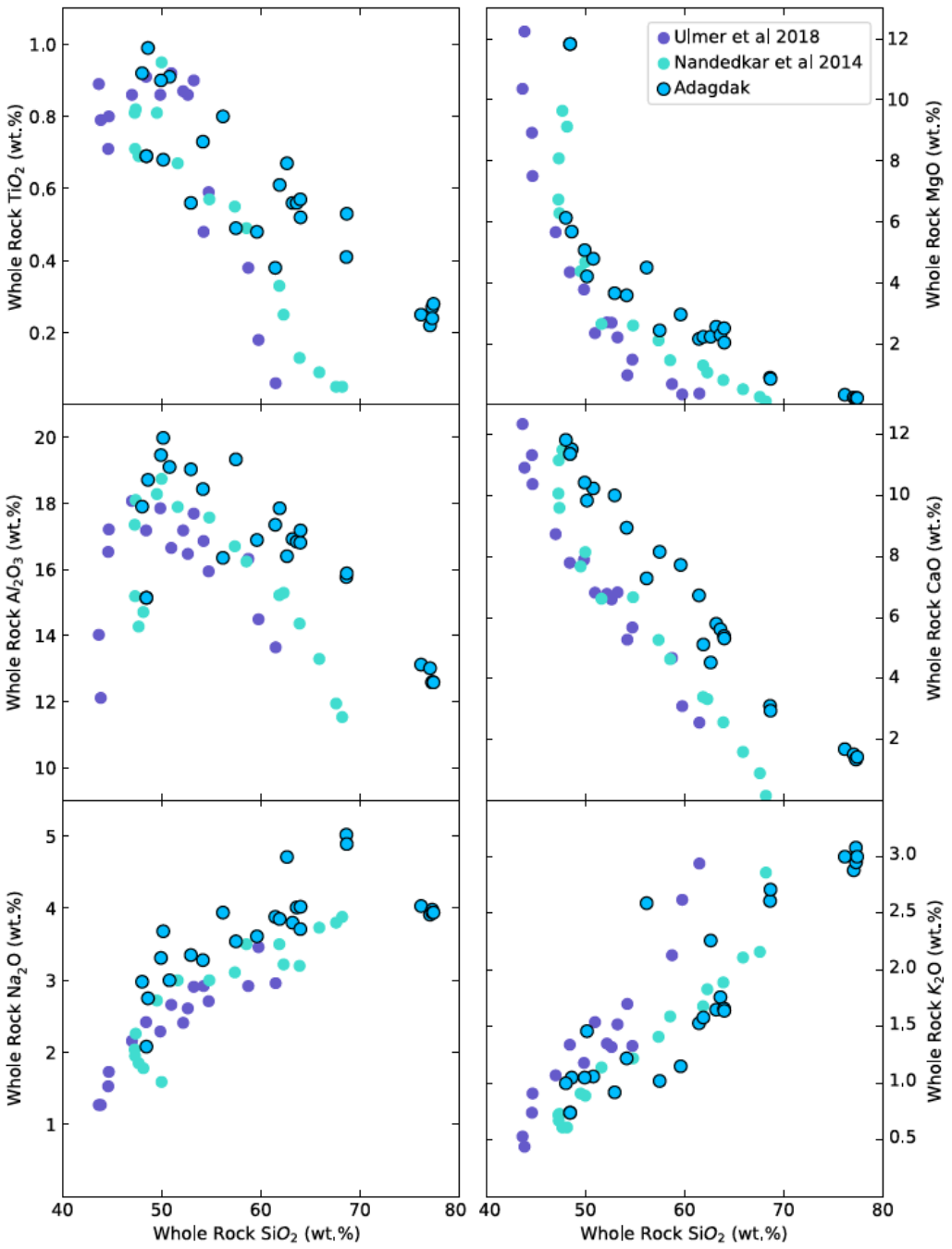

Supplemental Figure 12: Whole-rock composition of Adagdak cumulates compared to whole-rock composition of experimental cumulates formed at a known melt fraction from primitive basalt

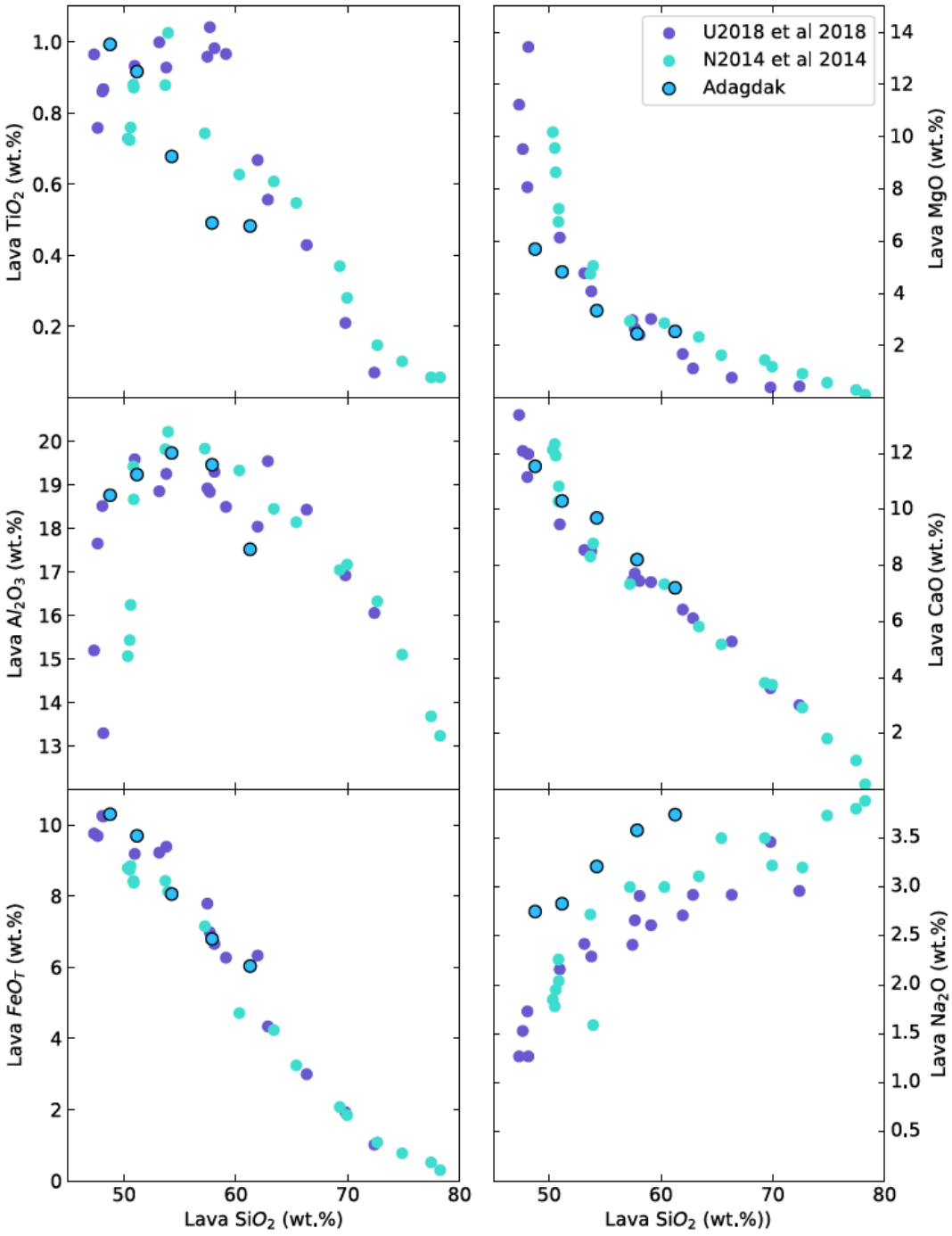

***Supplemental Figure 13*:** Adagdak lava compositions (normalized anhydrous) compared to experimental glasses from fractional crystallization experiments of Nandedkar et al. (2014) and Ulmer et al. (2018).

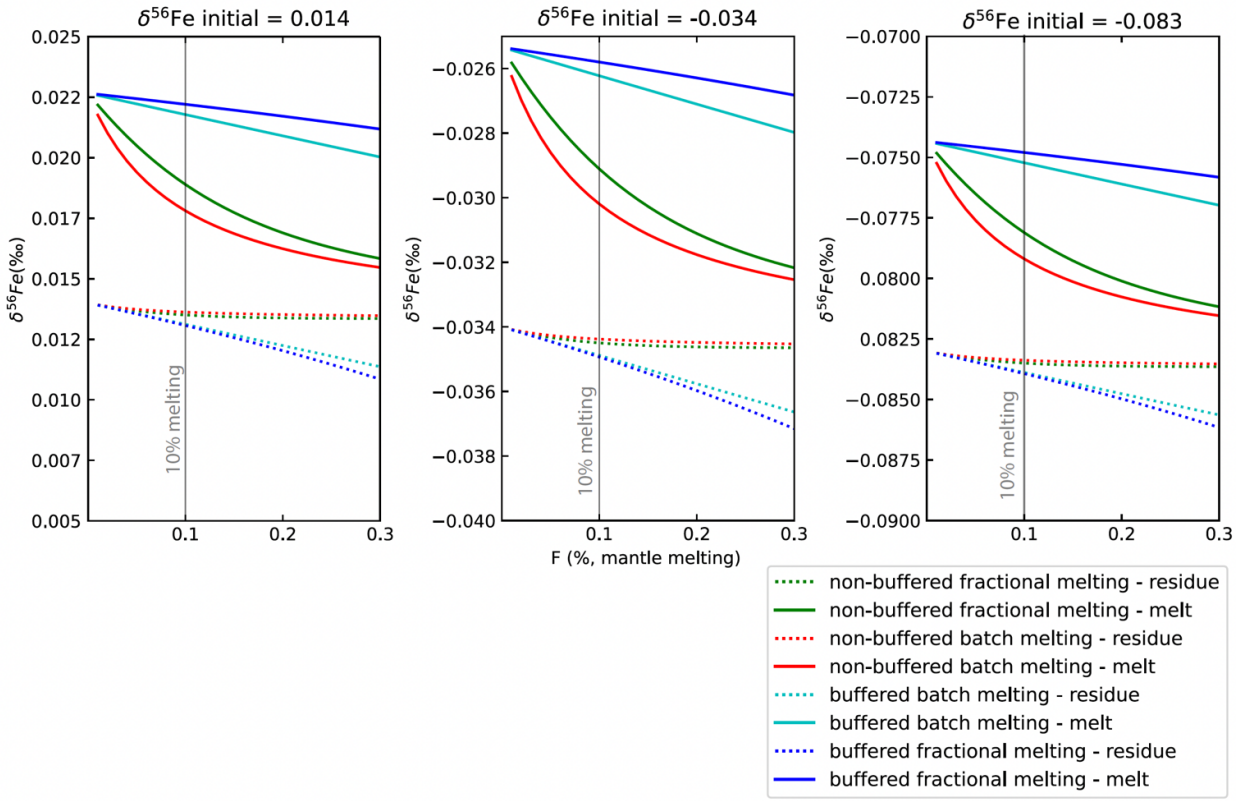

***Supplemental Figure 14*:** Mantle melting models for Adagdak mantle dunite ADG-CB-9 compositions ($\delta^{56}Fe = -0.03 \pm 0.05‰$). Note that each model has a different y-axis scale.

3.16 Additional References

Beard, B. L., & Johnson, C. M. (2004). Inter-mineral Fe isotope variations in mantle-derived rocks and implications for the Fe geochemical cycle. *Geochimica et Cosmochimica Acta*, 68(22), 4727-4743.

Blanchard, M., Dauphas, N., Hu, M. Y., Roskosz, M., Alp, E. E., Golden, D. C., Balan, E. (2015). Reduced partition function ratios of iron and oxygen in goethite. *Geochimica et Cosmochimica Acta*, 151, 19-33.

Chen, L. M., Song, X. Y., Zhu, X. K., Zhang, X. Q., Yu, S. Y., & Yi, J. N. (2014). Iron isotope fractionation during crystallization and sub-solidus re-equilibration: Constraints from the Baima mafic layered intrusion, SW China. *Chemical Geology*, 380, 97-109.

Dauphas, N., Craddock, P. R., Asimow, P. D., Bennett, V. C., Nutman, A. P., Ohnenstetter, D. (2009). Iron isotopes may reveal the redox conditions of mantle melting from Archean to Present. *Earth and Planetary Science Letters*, 288(1-2), 255-267.

Dauphas, N., Roskosz, M., Alp, E. E., Golden, D. C., Sio, C. K., Tissot, F. L. H., Morris, R. V. (2012). A general moment NRIXS approach to the determination of equilibrium Fe isotopic fractionation factors: Application to goethite and jarosite. *Geochimica et Cosmochimica Acta*, 94, 254-275.

Dauphas, N., Roskosz, M., Alp, E. E., Neuville, D. R., Hu, M. Y., Sio, C. K., Cordier, C. (2014). Magma redox and structural controls on iron isotope variations in Earth's mantle and crust. *Earth and Planetary Science Letters*, 398, 127-140.

Dauphas, N., John, S. G., & Rouxel, O. (2017). Iron isotope systematics. *Reviews in Mineralogy and Geochemistry*, 82(1), 415-510.

Deloule, E., C. France-Lanord, and F. Albarede, D/H analysis of minerals by ion probe, in "Stable Isotope Geochemistry: A Tribute to Samuel Epstein", *Geochemical Society Special Publication*, 3, 53–62, 1991.

Foden, J., Sossi, P. A., & Nebel, O. (2018). Controls on the iron isotopic composition of global arc magmas. *Earth and Planetary Science Letters*, 494, 190-201.

Hawthorne, F. C., Oberti, R., Harlow, G. E., Maresch, W. V., Martin, R. F., Schumacher, J. C., & Welch, M. D. (2012). Nomenclature of the amphibole supergroup. *American Mineralogist*, 97(11-12), 2031-2048.

Kress, V. C., & Carmichael, I. S. (1991). The compressibility of silicate liquids containing Fe 2 O 3 and the effect of composition, temperature, oxygen fugacity and pressure on their redox states. *Contributions to Mineralogy and Petrology*, 108, 82-92.

Kuroda, Y., Matsuo, S., & Yamada, T. (1988). D/H fractionation during dehydration of hornblende, mica and volcanic glass. *Journal of Mineralogy, Petrology and Economic Geology*, 83(3), 85-94.

Li, Q. W., Zhao, J. H., Wang, Q., Zhang, Z. F., An, Y. J., & He, Y. T. (2020). Iron isotope fractionation in hydrous basaltic magmas in deep crustal hot zones. *Geochimica et Cosmochimica Acta*, 279, 29-44.

Macris, C. A., Manning, C. E., & Young, E. D. (2015). Crystal chemical constraints on inter-mineral Fe isotope fractionation and implications for Fe isotope disequilibrium in San Carlos mantle xenoliths. *Geochimica et Cosmochimica Acta*, 154, 168-185.

Makino, K., and Tomita, K. (1989): Cation distribution in the octahedral sites of hornblendes. *American Mineralogist*, 74, 1097-1105.

Nandedkar, R. H., Ulmer, P., Müntener, O. (2014). Fractional crystallization of primitive, hydrous arc magmas: An experimental study at 0.7 GPa. *Contributions to Mineralogy and Petrology*, 167(6), 1015.

Nie, N. X., Dauphas, N., Alp, E. E., Zeng, H., Sio, C. K., Hu, J. Y., Spear, F. S. (2021). Iron, magnesium, and titanium isotopic fractionations between garnet, ilmenite, fayalite, biotite, and tourmaline: Results from NRIXS, ab initio, and study of mineral separates from the Moosilauke metapelite. *Geochimica et Cosmochimica Acta*, 302, 18-45.

Poitrasson, F., Delpech, G., & Grégoire, M. (2013). On the iron isotope heterogeneity of lithospheric mantle xenoliths: Implications for mantle metasomatism, the origin of basalts and the iron isotope composition of the Earth. *Contributions to Mineralogy and Petrology*, 165, 1243-1258.

Polyakov, V. B., Clayton, R. N., Horita, J., & Mineev, S. D. (2007). Equilibrium iron isotope fractionation factors of minerals: Reevaluation from the data of nuclear inelastic resonant X-ray scattering and Mössbauer spectroscopy. *Geochimica et Cosmochimica Acta*, 71(15), 3833-3846.

Rabin, S., Blanchard, M., Pinilla, C., Poitrasson, F., & Grégoire, M. (2021). First-principles calculation of iron and silicon isotope fractionation between Fe-bearing minerals at magmatic

temperatures: The importance of second atomic neighbors. *Geochimica et Cosmochimica Acta*, 304, 101-118.

Ratschbacher, B.C., J.M. Jackson, T.S. Toellner, C.E. Bucholz, W. Sturhahn, and N.V. Solomatova (2023): Fe^{3+}/FeT ratios of amphiboles determined by high-spatial resolution synchrotron Mössbauer spectroscopy. *American Mineralogist*, 108, 70-86.

Rodriguez-Mustafa, M. A., Simon, A. C., del Real, I., Thompson, J. F., Bilenker, L. D., Barra, F., ... & Cadwell, D. (2020). A continuum from iron oxide copper-gold to iron oxide-apatite deposits: Evidence from Fe and O stable isotopes and trace element chemistry of magnetite. Economic Geology, 115(7), 1443-1459.

Roeder, P. L., & Emslie, R. (1970). Olivine-liquid equilibrium. *Contributions to mineralogy and petrology*, 29(4), 275-289.

Roskosz, M., Sio, C. K., Dauphas, N., Bi, W., Tissot, F. L., Hu, M. Y., & Alp, E. E. (2015). Spinel–olivine–pyroxene equilibrium iron isotopic fractionation and applications to natural peridotites. *Geochimica et Cosmochimica Acta*, 169, 184-199.

Roskosz, M., Dauphas, N., Hu, J., Hu, M. Y., Neuville, D. R., Brown, D., & Alp, E. E. (2022). Structural, redox and isotopic behaviors of iron in geological silicate glasses: A NRIXS study of Lamb-Mössbauer factors and force constants. *Geochimica et Cosmochimica Acta*, 321, 184-205.

Schoenberg, R., Marks, M. A., Schuessler, J. A., von Blanckenburg, F., & Markl, G. (2009). Fe isotope systematics of coexisting amphibole and pyroxene in the alkaline igneous rock suite of the Ilímaussaq Complex, South Greenland. *Chemical Geology*, 258(1-2), 65-77.

Sossi, P. A., Foden, J. D., & Halverson, G. P. (2012). Redox-controlled iron isotope fractionation during magmatic differentiation: An example from the Red Hill intrusion, S. Tasmania. *Contributions to Mineralogy and Petrology*, 164(5), 757-772.

Sossi, P. A., & O'Neill, H. S. C. (2017). The effect of bonding environment on iron isotope fractionation between minerals at high temperature. *Geochimica et Cosmochimica Acta*, 196, 121-143.

Stow, M. A., Prytulak, J., Humphreys, M. C., & Nowell, G. M. (2022). Integrated petrological and Fe-Zn isotopic modelling of plutonic differentiation. *Geochimica et Cosmochimica Acta*, 320, 366-391.

Sturhahn, W. (2000): CONUSS and PHOENIX: Evaluation of nuclear resonant scattering data. *Hyperfine Interact*. 125, 149–172 (2000).

Sturhahn, W. (2021): CONUSS (Coherent Nuclear Scattering by Single crystals). Open source software. http://www.nrixs.com.

Teng, F. Z., Dauphas, N., & Helz, R. T. (2008). Iron isotope fractionation during magmatic differentiation in Kilauea Iki lava lake. *Science*, 320(5883), 1620-1622.

Tian, H. C., Zhang, C., Teng, F. Z., Long, Y. J., Li, S. G., He, Y., ... & Yang, W. (2020). Diffusion-driven extreme Mg and Fe isotope fractionation in Panzhihua ilmenite: Implications for the origin of mafic intrusion. *Geochimica et Cosmochimica Acta*, 278, 361-375.

Toplis, M. J., & Carroll, M. R. (1995). An experimental study of the influence of oxygen fugacity on Fe-Ti oxide stability, phase relations, and mineral—melt equilibria in ferro-basaltic systems. *Journal of Petrology*, *36*(5), 1137-1170.

Turner, S., Williams, H., Piazolo, S., Blichert-Toft, J., Gerdes, M., Adam, J., ... & Maury, R. (2018). Sub-arc xenolith Fe-Li-Pb isotopes and textures tell tales of their journey through the mantle wedge and crust. *Geology*, 46(11), 947-950.

Ulmer, P., Kaegi, R., & Müntener, O. (2018). Experimentally derived intermediate to silica-rich arc magmas by fractional and equilibrium crystallization at 1.0 GPa: An evaluation of phase relationships, compositions, liquid lines of descent and oxygen fugacity. *Journal of Petrology*, 59(1), 11-58.

Weyer, S., & Ionov, D. A. (2007). Partial melting and melt percolation in the mantle: the message from Fe isotopes. *Earth and Planetary Science Letters*, 259(1-2), 119-133.

Williams, H. M., Peslier, A. H., McCammon, C., Halliday, A. N., Levasseur, S., Teutsch, N., & Burg, J. P. (2005). Systematic iron isotope variations in mantle rocks and minerals: The effects of partial melting and oxygen fugacity. *Earth and Planetary Science Letters*, 235(1-2), 435-452.

Williams, K. B., Krawczynski, M. J., Nie, N. X., Dauphas, N., Couvy, H., Hu, M. Y., Alp, E. E. (2016, March). The role of differentiation processes in mare basalt iron isotope signatures. In *Lunar Planet Science Conference*, 47, 2779.

Wood, B. J., & Banno, S. (1973). Garnet-orthopyroxene and orthopyroxene-clinopyroxene relationships in simple and complex systems. *Contributions to Mineralogy and Petrology*, 42, 109-124.

Xiao, Y., Teng, F. Z., Su, B. X., Hu, Y., Zhou, M. F., Zhu, B., He, Y. S. (2016). Iron and magnesium isotopic constraints on the origin of chemical heterogeneity in podiform chromitite from the Luobusa ophiolite, Tibet. *Geochemistry, Geophysics, Geosystems*, *17*(3), 940-953.

Ye, H., Wu, C., Brzozowski, M. J., Yang, T., Zha, X., Zhao, S., Li, W. (2020). Calibrating equilibrium Fe isotope fractionation factors between magnetite, garnet, amphibole, and biotite. *Geochimica et Cosmochimica Acta*, 271, 78-95.

Zhao, X., Zhang, H., Zhu, X., Tang, S., Tang, Y. (2010). Iron isotope variations in spinel peridotite xenoliths from North China Craton: Implications for mantle metasomatism. *Contributions to Mineralogy and Petrology*, 160, 1-14.

Zhao, X., Zhang, H., Zhu, X., Tang, S., Yan, B. (2012). Iron isotope evidence for multistage melt–peridotite interactions in the lithospheric mantle of eastern China. *Chemical Geology*, 292, 127-139.

Zhao, X. M., Zhang, H. F., Zhu, X. K., Zhu, B., Cao, H. H. (2015). Effects of melt percolation on iron isotopic variation in peridotites from Yangyuan, North China Craton. *Chemical Geology*, 401, 96-110.

Zhao, X., Li, Z., Jia, X., Evans, N. J., Zhang, Z., Zhang, H. (2021). Multi-stage metasomatism revealed by trace element content and Fe isotopic composition of minerals in peridotite xenoliths from Niutoushan in the Cathaysia Block, South China. *Lithos*, 406, 106506.

Chapter 4

GARNET CLINOPYROXENITE FORMATION VIA AMPHIBOLE-DEHYDRATION IN CONTINENTAL ARCS: EVIDENCE FROM FE ISOTOPES

4.1 ABSTRACT

Lower-crustal garnet clinopyroxenite (sometimes termed "arclogite") fractionation in thick-crustal (>35 km) arc settings presents a compelling model to explain Fe-depletion trends, high oxygen fugacity, and evidence of recent delamination observed in many continental arcs. However, the origin of the garnet clinopyroxenites via igneous or metamorphic processes remains unclear. Due to preferential incorporation of light Fe isotopes in garnet relative to clinopyroxene or amphibole, Fe isotopes are ideally suited for studying the effects of garnet fractionation on magmatic systems. Here, we present whole-rock and mineral Fe isotope data from a suite of lower to mid/upper-crustal Andean xenoliths from Mercaderes, Colombia. This data is combined with petrography, major and trace element mineral and whole-rock chemistry, geothermobarometry, and thermodynamic modeling to explore the petrogenesis of the xenoliths and the crustal structure of the Northern Andes. Whole-rock samples display a narrow range of Fe isotope compositions (δ^{56}Fe = –0.02 to +0.11‰), which do not correlate with lithology, chemistry, or pressure-temperature conditions. This result is inconsistent with previous studies predicting the existence of an isotopically light Fe in the garnet-rich lower Andean crust. Through thermodynamic modeling, we show that the lack of isotopic fractionation in the Mercaderes xenoliths is more consistent with the suite representing a prograde metamorphic sequence, in which amphibole dehydration reactions drive eclogitization of mid/upper-crustal diorite protoliths. While our data do not preclude the presence of garnet clinopyroxenite cumulates at the base of the Andean crust, or that the delamination of such cumulates played an important role in the evolution of the Andes, they do indicate that not all garnet clinopyroxenites are cumulate in origin. Instead, the lower Andean crust may represent an amalgamation of igneous and metamorphic rock, with eclogitization of mid-crustal lithologies and partial melting of mafic

cumulate roots acting in tandem to drive densification and delamination of the lower crust in a self-feeding mechanism.

4.2 INTRODUCTION

Deep-crustal garnet formation in convergent margin (or arc) systems exerts a fundamental influence on processes related to continental differentiation and stability (e.g., Kay and Kay, 1993; Ducea and Saleeby, 1998; Jull and Kelemen, 2001; Ducea et al., 2021a, b). Lower-crustal garnet production results in compositional and density sorting in the crust, separating a more evolved, lower-density upper crust from an (ultra-)mafic, lower crust that may be denser than the underlying mantle and hence unstable (Rudnick and Fountain, 1995). Over the past decade, there has been renewed debate on the effects of garnet fractionation on the development of Fe-depletion trends and the redox state of magmas from continental arcs (Tang et al., 2018; Blatter et al., 2023; Holycross and Cottrell, 2023). Due to the preference of garnet for Fe^{2+} relative to Fe^{3+}, it has been posited that garnet fractionation results in Fe-depleted melts with elevated $Fe^{3+}/\Sigma Fe$ ratios (Green and Ringwood, 1968; Tang et al., 2018; Du et al., 2022).

Magmas from thick (>45 km) arcs have geochemistry consistent with residual garnet in their source regions (e.g., Sr/Y > 40, La/Yb >20), potentially reflecting (1) crystallization-differentiation of garnet from magmas in the uppermost mantle to lower crust (>1 GPa) (e.g., Bryant et al., 2006) or (2) partial melting of lower-crustal amphibolites and mafic granulites forming residual or peritectic garnet (e.g., Kay and Kay, 1991). Although there is limited direct exposure or evidence of the first two processes, field exposures of exhumed arcs support an important role for the latter two processes in the lower crust of both oceanic arcs such as Kohistan (Pakistan; Yamamoto & Yoshino, 1998; Yoshino et al., 1998; Ringuette et al., 1999; Jagoutz et al., 2011) and continental arcs such as Fiordland (New Zealand; Daczko et al., 2001; Stowell et al., 2010).

Garnet pyroxenite xenoliths from continental arcs (i.e., “arclogites;” Lee and Anderson, 2015) also provide evidence of lower-crustal garnet-bearing cumulate or restitic assemblages.

Garnet clinopyroxenites have been interpreted both as magmatic cumulates (Lee et al., 2006; Lee and Anderson, 2015; Bloch et al., 2017; Tang et al., 2018) and residues of lower-crustal melting of mafic plutonic precursors (Wolf and Wyllie, 1993; Weber et al., 2002; Bowman et al., 2021; Gianola et al., 2023). As with field exposures of exhumed arcs, uncertainty in their genetic origins arises from high-temperature metamorphic re-equilibration, erasing textural and compositional information concerning their origin. However, distinguishing between these two origins is paramount for correctly interpreting their chemistry and implications for the evolution of arc magmas.

Here, we present the first Fe isotope measurements on a suite of lower to mid-crustal garnet-bearing xenoliths, including garnet clinopyroxenites, from Mercaderes, Colombia. Although we integrate petrography and mineral/whole-rock chemistry in our discussion, we focus on Fe isotopes as they are sensitive to garnet fractionation, with garnet preferentially incorporating isotopically light Fe compared to other phases (Nie et al., 2021). Previous studies have, in fact, argued that heavy Fe isotope compositions in some Andean magmas indicate that primitive arc melts experienced prolonged light Fe isotope depletion during garnet fractionation (Du et al., 2022). Using our dataset, we 1) evaluate the magmatic versus metamorphic origin of these xenoliths, leveraging the differential behavior of Fe partitioning between melts and cumulates/restites during fractional crystallization versus partial melting, and 2) discuss the implications for the Fe isotope composition of the lower to mid-Andean crust.

4.3 GEOLOGICAL BACKGROUND AND PREVIOUS WORK

The Mercaderes region is in the northern volcanic zone (NVZ) of the Central Cordillera of the Colombian Andes. The xenolith suite is hosted in the Granatífera Tuff, a pyroclastic deposit located south of the town of Mercaderes. The tuff contains xenoliths of both mantle and crustal affinities, which have been the focus of several petrographic and geochemical studies (Weber, 1998; Weber et al., 2002; Rodriguez-Vargas et al., 2005; Bloch et al., 2017; Gianola et al., 2023; Zieman et al., 2023; 2024). The lower to mid-crustal lithologies range from garnet-free

gabbronorites and diorites to garnet-bearing hornblendites, clinopyroxenites, and garnetites (Weber et al., 2002; Rodriguez-Vargas et al., 2005). Amphibole is modally dominant in the crustal rocks; other common phases include garnet, clinopyroxene, orthopyroxene, plagioclase, and scapolite (Weber, 1998; Weber et al., 2002; Rodriguez-Vargas et al., 2005).

Weber et al. (2002) suggest that the transition from amphibole-rich lithologies to garnet clinopyroxenites represents a change from amphibolite to granulite facies metamorphism. In this framework, amphibole-bearing lithologies dehydrate along two metamorphic paths based on the presence or absence of CO_2. On the CO_2-free path, amphibole and plagioclase react to form clinopyroxene, garnet, and melt. In the presence of CO_2, amphibole, plagioclase, and garnet could react to form clinopyroxene and scapolite. Thus, the different lithologies observed in the Mercaderes suite are considered snapshots taken at different locations along a prograde metamorphic path. The suite has subsequently been reinterpreted as primarily high-pressure igneous cumulates (e.g., Bloch et al., 2017), though studies of andesitic to rhyolitic melt inclusions in garnets from the xenoliths support the original interpretation that they are restitic (Gianola et al., 2023).

4.4 METHODS

4.4.1 Petrography

Mineral modal proportions for the Mercaderes xenoliths were determined through optical petrography and micro-X-ray fluorescence (XRF) spectroscopy at Caltech. Phase maps were generated from thin sections using a Bruker M4 Tornado μ-XRF energy dispersive spectrometer. Modal volume fractions were assumed equal to the area fractions calculated with the Bruker M4 TORNADO software using the phase cluster analysis mode (Supplemental Data File 3, Ch4-T1). Additional details for the XRF mapping (and all analytical methods discussed below) are given in the Appendix.

4.4.2 Whole-rock chemistry

Mercaderes xenoliths selected for whole-rock analyses (*n*=21) were spheroidal and ranged from 9 to 13 cm in diameter. Altered surfaces and veining were removed with a rock saw. Samples were then cut into aliquots, crushed, and powdered with an agate grinding vessel. Powders were dried for 12 hours at 110ºC to remove any absorbed water, then heated to 1050ºC for one hour to determine loss on ignition. Glass beads were prepared from the ignited powders and mixed with a Li-borate flux in a 10:1 flux:sample ratio then fused at 1200ºC. Major elements were analyzed using a Panalytical Zetium 4 kW wavelength-dispersive XRF spectrometer at Caltech following the methods in Bucholz and Spencer (2019). Trace elements were obtained from chips of glass beads through solution inductively coupled plasma mass spectrometry (ICP-MS) at Caltech following methods of Lewis et al. (2021). These results are given in the Supplemental Data File 3 (Ch4-T2).

4.4.3 Mineral chemistry

Major element mineral compositions of 38 Mercaderes samples were obtained using a field-emission iHP-200F electron microprobe at Caltech. A complete description of the standards used, detection limits, instrument setup, and count time for each measured element is given in the Supplemental Data File 3 (Ch4-T3). Core and rim averages and standard deviations of each phase are given in the Supplemental Data File 3 (Ch4-T4 to Ch4-T8). For samples containing garnet and clinopyroxene, pressure and temperature were estimated with garnet-clinopyroxene geothermobarometry using the calibrations of Beyer et al. (2015) and Ravna (2000). Core-to-rim electron microprobe transects of adjacent clinopyroxene-garnet pairs were used to evaluate the changes in pressure-temperature conditions recorded along these profiles. For samples containing garnet and amphibole, we also calculated temperature with garnet-amphibole thermometry (Graham and Powell, 1984). For plagioclase and amphibole-bearing samples, we used amphibole-plagioclase thermometry (Holland and Blundy, 1994) and barometry (Anderson and Smith, 1995) to calculate pressure-temperature conditions. Amphibole-only geothermobarometry (Ridolfi, 2021) was used to estimate pressure-temperature conditions for clinopyroxene hornblendites due

to the lack of a phase assemblage in this lithology facilitating a thermodynamic assessment of these variables. These results were combined with whole-rock compositions to estimate densities using the *meemum* function of Perple_X. Pressure, temperature, and density estimates for each sample are given in the Supplemental Data File 3 (Ch4-T9).

For samples where classical thermobarometry gave unrealistic results, or where precise temperature constraints were necessary to calculate mean force constants $\langle F \rangle_{amph}$ and $\langle F \rangle_{cpx}$ for Fe isotope modeling, we also estimated equilibrium conditions by constructing pseudosections with Perple_X for each whole-rock composition. From these models, endmember isopleths for garnet and clinopyroxene were extracted and compared to measured data, with the intersection of matching isopleths representing our best estimate of equilibrium conditions. These calculations are further discussed in the Appendix, where model results for each sample are also given and compared to mineral equilibria thermobarometry (Supplemental Figures 1 and 2).

Trace element concentrations from garnet, clinopyroxene, and amphibole were obtained via laser ablation inductively coupled plasma mass spectrometry (LA-ICP-MS) at Pomona College in the David W. and Claire Oxtoby Environmental Isotope Laboratory using an Agilent 8900 triple quadrupole ICP-MS paired with an ESI NWR193 laser ablation system. Standards NIST 610 and BCR-2 were used to construct calibration curves and Al concentrations obtained through electron microprobe analysis (EMPA) were used as an internal standard. These data were later supplemented with additional LA-ICP-MS measurements at the Resnick Water and Environment Laboratory Science at Caltech using an Agilent 8800 Triple Quadrupole ICP-MS coupled to a New Wave Research UP 193 Solid State Laser System. Mineral trace element data is given in Supplemental Data File 3 (Ch4-T10 to Ch4-T13).

4.4.4 Fe isotopes

Iron isotope compositions were obtained from whole-rock powders and mineral separates at the Isotoparium, Caltech (Supplemental Data File 3, Ch4-T14). Garnet, clinopyroxene, and amphibole mineral separates were hand-picked to ensure grains did not contain inclusions or show signs of alteration. Grains were sonicated in 1) isopropyl alcohol and 2) deionized water to remove surface

contamination. Sample digestion and Fe purification were performed in the Isotoparium clean lab following the established methods of Dauphas et al. (2004, 2009). Samples were chemically purified alongside USGS rock powders AGV-2, BCR-2, BHVO-2, and COQ-1, whose Fe isotope compositions have been previously measured (Craddock and Dauphas, 2010), to confirm data accuracy. Measured Fe isotope compositions of samples and USGS standards are reported in the Supplemental Data File 3 (Ch4-T15).

Iron isotope measurements were made in wet plasma mode on a Neptune Plus (ThermoFisher) multi-collector ICP-MS. Isotopes ^{54}Fe, ^{56}Fe, ^{57}Fe, ^{58}Fe, ^{53}Cr, ^{55}Mn, ^{59}Co, and ^{60}Ni were measured for each sample and standard. Interferences of ^{54}Cr on ^{54}Fe and ^{58}Ni on ^{58}Fe were corrected with our ^{53}Cr and ^{60}Ni measurements, respectively, assuming natural isotopic abundances. We monitored ^{55}Mn and ^{59}Co to ensure complete matrix separation during column chemistry. Each unknown sample measurement was bracketed with the IRMM-524b metallic iron standard diluted in the same run acid and at the same Fe concentration (5 ppm, within 5%). We measured between 2 and 5 unknown and 1-2 USGS reference materials for each analytical run. Following the methods of Dauphas et al. (2009), we gauge instrumental uncertainty and calculate the errors reported in all figures and discussion using the standard deviation (SD) of the IRMM-524b standard for each session:

$$\text{Error} = 2*\text{SD}_{\text{IRMM-524b}}/(n_{\text{sample}})^{0.5}$$

where n_{sample} is the number of replicate analyses per solution.

4.5 RESULTS

4.5.1 Rock types and petrography

Rocks were classified with the IUGS plagioclase-pyroxene-hornblende ternary (Supplemental Figure 3). Because sample XC-MP1-1 also contains orthopyroxene, it was classified with the IUGS olivine-clinopyroxene-orthopyroxene ternary for ultramafic rocks as a garnet hornblende

websterite. Neither ternary was used for rocks comprising over 75% garnet (vol%), which were classified as garnetite. The sample classification is outlined in Table 1. For discussion, we organize the Mercaderes xenoliths into six groups:

(1) Diorites: Diorites (*n*=3) contain amphibole (62-59%), plagioclase (38-41%), and magnetite (0-3%) with traces of apatite, titanite, and titanomagnetite (Fig. 1a).

(2) Clinopyroxene-hornblendites: Samples XC-MP1-3 and XC-MP1-4 are the only examples of clinopyroxene-hornblendites in the xenolith suite and contain amphibole (89-90%) and clinopyroxene (11-10%) with traces of magnetite, apatite, and ilmenite (Fig. 1b).

(3) Plagioclase/scapolite-bearing garnet clinopyroxene hornblendites and gabbros: Garnet-bearing hornblende gabbros (*n*=3) and plagioclase/scapolite-bearing garnet clinopyroxene hornblendites (*n*=3) contain amphibole (34-79%), garnet (8-52%), plagioclase (0-20%), clinopyroxene (0-19%), scapolite (0-8%), allanite (0-3%), and titanite (0-2.6%) with traces of rutile, magnetite, apatite, ulvöspinel, and titanite. In plagioclase-bearing hornblendite samples XC-M-4 (Fig. 1c) and XC-M-5 and scapolite-bearing hornblendite XC08-1/17, clinopyroxene is present as 200-700 μm coronas around garnet at the garnet-amphibole interface.

(4) Garnet hornblendites (± cpx): These samples (*n*=3) contain amphibole (27-68%), garnet (16-49%), and clinopyroxene (16-28%) with traces of rutile, apatite, and titanite (Fig. 1d). Clinopyroxene is only observed at the interface between garnet and amphibole in garnet hornblendite samples XC-MH-8 and XC-MP2-3.

(5) Garnet hornblende clinopyroxenites/websterite: These samples (*n*=8) contain clinopyroxene (60-21%), garnet (19-50%), amphibole (5-29%), orthopyroxene (0-8%), scapolite (0-1.8%), and plagioclase (0-1.1%) with traces of rutile, apatite, magnetite, titanite, ulvöspinel, ilmenite, and quartz (Fig. 1e). Amphibole is consistently only observed as an anhedral interstitial phase,

generally confined to grain boundaries between clinopyroxene and garnet. 120° triple junctures between amphibole, garnet, and clinopyroxene are common in rocks from both groups 4 and 5.

(6) Amphibole-poor garnet clinopyroxenites and garnetite: There are ten garnet clinopyroxenites (32-74% garnet, 26-66% clinopyroxene, 0-4% amphibole) (Fig. 1f) and one plagioclase-bearing clinopyroxene garnetite (75.3% garnet, 8.1% plagioclase, 13.7% clinopyroxene, 2.9% scapolite) in our suite. Rutile is the most common accessory phase in these samples, although magnetite, ulvöspinel, titanite, and apatite are also observed.

4.5.2 Whole-rock chemistry

Compositionally, the Mercaderes garnet clinopyroxenites (± amphibole) are similar to "low-MgO" (MgO < 13 wt.%) pyroxenite xenoliths from the Sierra Nevada (California) and central Arizona (Dodge et al., 1988; Lee et al. 2006; Erdman et al. 2016) and to previously analyzed xenoliths from Mercaderes (Weber et al., 2002; Bloch et al., 2017; Fig. 2). Whole-rock Mg# (100*[Mg/(Mg + Fe_T)] molar) ranges from 42 to 69 and is positively correlated with SiO_2 (38.2-49.1 wt.%). The range in Mg# and SiO_2 overlap with feldspar-bearing plutonic lithologies of xenoliths from modern island arcs and of exhumed paleo-arcs (Fig. 2a), as well as calculated feldspar-bearing "cumulate" compositions from fractional crystallization experiments on hydrous basalts. (Fig. 2b). Despite their differences in phase assemblage, garnet clinopyroxenites (±amph) span a similar compositional range to the plagioclase and scapolite-bearing garnet clinopyroxene hornblendites and gabbros in terms of Mg# and other major elements, with no apparent correlation between composition and sample lithology. Enrichment in the heavy rare earth elements (HREE) relative to the light heavy rare earth elements (LREE) is only observed in the garnet clinopyroxenite xenoliths (Group 6; La/Yb = 0.1-0.6, Sm/Yb = 0.3-0.4), while enrichment in the LREE relative to the HREE is only observed in hornblendite and gabbro xenoliths (La/Sm = 1.0-4.4, La/Yb = 1.0-18.3) (Supplemental Figure 4).

4.5.3 Mineral chemistry

Garnet: Although core-to-rim zoning is not observed in garnets from Group 6, it is present in ~80% of samples from groups 3, 4, and 5. These samples consistently show core-to-rim decreases in MnO (-0.3 to -2.0 wt.%) and increases in MgO (+0.2 to +4.0 wt.%) (e.g., Fig. 3a, b). Core Mg# ranges from 22.7 to 64.1 and is highest in the Group 6 samples (40.6 – 64.1). The plagioclase and scapolite-bearing lithologies (Group 3) have the lowest garnet core Mg#s (22.7 – 53.0) and highest core MnO concentrations (i.e., spessartine component: X_{sps}, Fig. 3c) (0.4 – 2.3 wt.% MnO). Core-to-rim zoning in trace elements is only observed in garnet from Group 3 (plagioclase/scapolite-bearing), where rims have gently sloped HREE profiles on primitive mantle normalized spider diagrams (Dy_N/Yb_N 5 – 12, normalized to chondrite) and cores show steep HREE profiles (Dy_N/Yb_N 30 – 155) (Supplemental Figures 5 and 6).

Clinopyroxene: Core Mg#s and Na_2O concentrations range from 57 to 78 and 0.78 to 2.9 wt.%, respectively, and do not correlate with lithology (Figs. 3d, 4). All clinopyroxene from garnet-bearing samples show concave-down trace element profiles on primitive mantle normalized spider diagrams, with pronounced HREE depletion (Supplemental Figures 5 and 6).

Amphibole: Amphibole in the Mercaderes xenolith suite is calcic, including pargasite and pargasitic hornblende in samples from groups 3-5 and edenite in the diorites (Group 1) (Hawthorne et al., 2012). Core amphibole Mg#s range from 51.8 to 76.8 and are generally higher in the plagioclase and scapolite-free assemblages (56.2 – 76.8). Amphibole core Mg# is positively correlated to clinopyroxene core Mg# (Fig. 3d). Trace element concentrations in amphibole are highly variable and don't correlate with Mg# or sample lithology (Supplemental Figures 5 and 6).

4.5.4 Calculated pressures and temperatures

The highest pressures and temperatures are recorded by the garnet clinopyroxenites (1.5-2.2 GPa, 1100-1280 °C), followed by the garnet (± cpx) hornblendites and garnet hornblende clinopyroxenites (1.0-1.9 GPa, 900-1080 °C). Garnet-clinopyroxene geothermobarometry yields

a wide array of peak pressure-temperature conditions for the plagioclase and scapolite-bearing hornblendites, ranging from 1.4 to 2.3 GPa and 930 to 1230 °C, with rim compositions generally recording higher pressures and temperatures than the corresponding grain cores (40-500 MPa and 10-150 °C higher). For these amphibole-rich samples, we prefer the pressure-temperature estimates obtained through Perple_X modeling, ranging from 700 to 975 °C and 0.9-1.5 GPa, as our modeling suggests these compositions would contain high modal proportions of garnet (>50 vol%) at pressures over ~1.2-1.5 GPa. For the clinopyroxene hornblendites, amphibole-only geothermobarometry gives pressure-temperature estimates between 1.6-1.8 GPa and 1010-1050 °C while Perple_X modeling yields equilibrium conditions between 0.9-1.2 GPa and 700-975 °C. We consider the latter to be more realistic estimates as garnet should stabilize above ~1.3 GPa for these compositions. Amphibole-plagioclase thermometry and barometry for the diorites (n=4) yielded temperature estimates between 650 and 690 °C and pressures from 0.6 to 0.8 GPa. The geothermal gradient defined by these calculations is consistent with previous studies that have estimated crustal storage conditions with garnet–clinopyroxene geothermobarometry for Mercaderes xenoliths (Bloch et al., 2017; Gianola et al., 2023; Zieman et al., 2023) (Fig. 5a). Density estimates for the xenoliths range from 2.9 to 3.6 g/cm^3 and are highest for garnet clinopyroxenites (3.3 to 3.6 g/cm^3) and the lowest for diorites (2.9 – 3.0 g/cm^3).

4.5.5 Fe isotopes

4.5.5.1 Whole-rock: Whole-rock δ^{56}Fe ranges from –0.02 to 0.11‰ and does not correlate with MgO or SiO_2 concentration (Fig. 5b). For the samples where we measured Fe isotope compositions of all modally abundant Fe-bearing phases (n=15), we also calculated theoretical whole-rock δ^{56}Fe values from modal proportions and mineral chemistry. Except for xenoliths XC-MP2-1 and XC-2-09/16, which are coarse-grained and heterogranular such that modal proportions could not be confidently determined, these calculated whole-rock δ^{56}Fe values are within error (<0.03‰) of measured whole-rock compositions (Supplemental Data File 3, Ch4-T15, Supplemental Figure 7).

4.5.5.2 Minerals: Clinopyroxene (n=17, $\delta^{56}Fe$ = +0.08 to +0.23‰) and amphibole (n=10, $\delta^{56}Fe$ = +0.02 to +0.21‰) are the isotopically heaviest phases in all samples, while garnet is the isotopically lightest (n=17, $\delta^{56}Fe$ = –0.17 to +0.03‰) (Fig. 5c). Garnets from the plagioclase and hornblende-bearing rocks (groups 3-5) are the isotopically lightest ($\delta^{56}Fe$ = –0.11 to –0.02‰) while those from garnet clinopyroxenites are slightly heavier ($\delta^{56}Fe$ = –0.05 to +0.02‰). Coexisting clinopyroxene and garnet preserve fractionations ($\Delta^{56}Fe_{cpx\text{-}gar}$) of +0.07 to +0.33‰ (Supplemental Figure 8). In general, the garnet clinopyroxenites are characterized by lower $\Delta^{56}Fe_{cpx\text{-}gar}$ (+0.07 to +0.19‰) than the hornblendites (± scapolite/plagioclase) (+0.17 to +0.33‰). Inter-mineral isotopic fractionation between coexisting amphibole and garnet ranges from $\Delta^{56}Fe_{amph\text{-}gar}$ = +0.17 to +0.30‰ and is higher in hornblendite (± scapolite/plagioclase) xenoliths ($\Delta^{56}Fe_{amph\text{-}gar}$ = +0.23 to +0.30‰) compared to clinopyroxenites ($\Delta^{56}Fe_{amph\text{-}gar}$ = +0.17 to +0.23‰) (Supplemental Figure 8). Coexisting clinopyroxene and amphibole in the Mercaderes xenoliths show markedly less inter-mineral isotopic fractionation, with $\Delta^{56}Fe_{cpx\text{-}amph}$ ranging from –0.03 to +0.07‰ (Supplemental Figure 8).

4.5.5.3 Force constant estimates

Consistent with our data, previous studies of Fe isotopes in igneous and metamorphic rocks have found amphibole and clinopyroxene to be isotopically heavier than coexisting garnet ($\Delta^{56}Fe_{cpx\text{-}gar}$ and $\Delta^{56}Fe_{Amph\text{-}gar}$ +0.1 to +0.5‰: Beard & Johnson, 2004; Williams et al., 2005, 2009; Li et al., 2016; Liang et al., 2022), suggesting the amphibole and clinopyroxene force constants should both be significantly higher than that of garnet ($\langle F \rangle_{almandine}$ =110 N/m: Nie et al., 2021). We can estimate appropriate force constants for clinopyroxene and amphibole from our Fe isotope data and temperature estimates for each sample. These calculations were performed using the relationship between the permil fractionation (Δ) and force constants of two phases (A and B) at equilibrium at a given temperature for each sample (Dauphas et al., 2014):

$$\Delta^{56}Fe_{B\text{-}A} = \delta^{56}Fe_B - \delta^{56}Fe_A = 2853[\langle F \rangle_B - \langle F \rangle_A]/T^2$$

Given the sensitivity of these calculations to changes in temperature, thermobarometry and Perple_X modeling were rigorously interrogated for each sample used in estimating $\langle F \rangle_{amph}$ or $\langle F \rangle_{cpx}$ (Supplemental Figures 1 and 2). From these data, we calculated weighted average values of $\langle F \rangle_{cpx}$ = 227±17 N/m and $\langle F \rangle_{amph}$ = 232±21 N/m, with errors derived from temperature uncertainties for each sample. There is no systematic difference in calculated $\langle F \rangle_{amph}$ or $\langle F \rangle_{cpx}$ for each sample based on lithology or equilibrium temperature, suggesting that the observed increase in inter-mineral isotopic fractionation ($\Delta^{56}Fe_{cpx\text{-}grt}$ and $\Delta^{56}Fe_{amph\text{-}grt}$) in the hornblendite xenoliths reflect lower equilibrium temperatures for these samples and that our temperature estimates are associated with Fe isotope equilibrium (Supplemental Figure 9).

4.6. DISCUSSION

4.6.1 Textural and chemical evidence for restitic garnet clinopyroxenite origins

The textural and mineralogical variations observed in the Mercaderes xenoliths are consistent with previous conclusions that the Mercaderes xenoliths preserve an amphibolite to granulite facies transition in the lower crust, with amphibole-dehydration melting leading to the formation of garnet clinopyroxenite residues (Weber et al., 2002; Gianola et al., 2023). The transition from amphibole and plagioclase-dominated lithologies (groups 1 and 2: diorites and clinopyroxene-hornblendites) to those dominated by clinopyroxene and garnet is marked by strongly zoned porphyroblastic garnet with coronae of clinopyroxene in a matrix of amphibole and plagioclase (Group 3: Fig. 3a), suggesting incomplete transformation and equilibration to a garnet clinopyroxenite assemblage. Common features of retrograde metamorphism, such as plagioclase + clinopyroxene or plagioclase + amphibole symplectites/coronas around garnet (Zhao et al., 2001), are not observed in the Mercaderes xenoliths, consistent with a prograde metamorphic origin. Most garnets from the transitional metamorphic assemblages (groups 3-5) also show core-to-rim decreases in MnO and HREEs and increases in MgO, characteristic zoning patterns of prograde metamorphic garnet (e.g., Spear and Selverstone, 1983; Rubatto et al., 2020). These

textural observations are consistent with amphibole dehydration reactions involving the consumption of amphibole and plagioclase:

Amphibole + Plagioclase → Melt + Clinopyroxene + Garnet ± Orthopyroxene

In addition, other geochemical characteristics of the Mercaderes xenoliths are inconsistent with a cumulate origin, such as the lack of correlation between major/trace element data and lithology or modal assemblage (for both whole-rock and mineral analyses). For example, experimental studies have shown that with increased pressure, clinopyroxene in equilibrium with melt develops a greater jadeite component, increasing Al and Na concentrations (e.g., Blundy et al., 1995). Clinopyroxenes from experimental studies, therefore, show strong positive correlations between Al, Na, and pressure (Fig. 4). No correlations are observed, however, between Al and Na composition in clinopyroxenes or Al and Na as a function of calculated pressure (Fig. 4). Clinopyroxenes from Mercaderes xenoliths equilibrated between 0.9 and 2.2 GPa also have higher Na compositions than clinopyroxenes from experimental studies of basalts and andesites conducted up to 3 GPa (Fig. 4). These data can be explained if clinopyroxene Al and Na content in the garnet-bearing rocks (groups 3-6) is controlled by the composition and modal proportions of plagioclase and amphibole in their diorite protoliths rather than crystallization pressure.

These lines of evidence are consistent with the following model, in which garnet-free diorites (Group 1) and clinopyroxene hornblendites (Group 2) represent the least metamorphosed starting compositions, and garnet-bearing gabbros, hornblendites, and clinopyroxenites (groups 3 to 5) represent transitional (disequilibrium) metamorphic assemblages. Within this framework, the garnet clinopyroxenite and garnetite xenoliths (Group 6) represent the full consumption of amphibole rather than cumulates from basalt crystallization. Previous documentation of high silica melt inclusions in garnet (65.3-72.4 wt.% SiO_2; Gianola et al., 2021) from Mercaderes xenoliths is consistent with this model and is strong evidence that the host minerals grew in the presence of a felsic melt, likely generated through amphibole dehydration reactions. We now turn to the Fe isotope data, which adds a new dimension of support to this argument, as well as the implications

of our findings for the Fe isotopic evolution of arc magmas and the composition of the Andean crust.

4.6.2 Fe isotopes

A first-order observation of the Mercaderes dataset is that there is little variability in the whole-rock Fe isotope composition of the Mercaderes suite across all lithologies (average whole-rock $\delta^{56}Fe = 0.06\pm0.04$), suggesting that the process responsible for the formation of the suite resulted in limited Fe isotope fractionation. We explore the two competing models of garnet clinopyroxenite formation via 1) crystal accumulation from a melt or 2) as restitic products from amphibole dehydration. The predicted behavior of Fe in these systems is dramatically different. To conceptually illustrate this, we briefly examine the behavior of Fe in crystallization and partial melting experiments relevant to these two models. Blatter et al. (2023) show that a primitive arc basalt with ~9.5 wt.% FeO crystallizing at ~1.7 GPa saturates with clinopyroxene (and minor orthopyroxene) at ~1250 ºC, followed shortly by garnet at ~1200 ºC. By 1150ºC, ~40% of the initial magma has crystallized and FeO in the melt begins to drop precipitously due to the onset of garnet crystallization, with ~80% of the melts initial Fe incorporated into cumulate minerals by 1050 ºC.

In contrast, for a dehydration melting scenario, melt production is much more limited because it is constrained by the amount of amphibole in the protolith available to break down. Mafic amphibolite partial melting experiments conducted at 1.5-2 GPa and 850-1150 ºC by Sen and Dunn (1994) chronicle the transformation of amphibole and plagioclase-dominated assemblages to garnet clinopyroxenites. As melt was produced, the whole-rock Mg# of the residue increased from 53 to 69, similar to what is observed between the Mercaderes diorites and garnet clinopyroxenites (Mg# increases from 56 to 67). These experiments generated a maximum of ~25% melting, with only 14% of the initial Fe of the protolith lost to the liquid. Conceptually, although isotopic fractionations will be large at low temperatures during amphibole dehydration melting, mass balance dictates that the Fe isotopic composition of the residue should not be significantly affected due to the small volumes of Fe-poor melt being extracted. Progressive

eclogitization of diorite protoliths should, therefore, produce a suite of residues with relatively unfractionated Fe isotope compositions, similar to what is observed in our whole-rock measurements of the Mercaderes xenoliths.

We quantitatively explore whether the Fe isotope data is consistent with formation through crystallization from a melt (Model A; Fig. 6) versus metamorphic dehydration reactions (Model B; Fig. 7) by modeling the Fe isotope trajectories expected for each process. The most salient features of these models are discussed below, while greater details of model parameters, justification of starting compositions, and additional results are given in the Appendix.

4.6.2.1 Fractional crystallization (Model A)

We first construct a model to explore the evolution of primitive arc basalts undergoing fractional crystallization as they ascend through thickened arc crust using Perple_X. We start with a representative primitive Colombian basalt (Supplemental Figure 10) with 3 wt.% H_2O at an oxygen fugacity of FMQ+1 and fractionally crystallize the melt along the Mercaderes geothermal gradient (~1300 °C, 2 GPa to 800 °C, 1 GPa). While we prefer the parameters chosen in this model as they most accurately reproduce the observed mineralogy of the Mercaderes suite, sensitivity tests exploring the effect of variable water content (2-6 wt.%), major element composition (Mg-andesites to Mg-basalt), and oxygen fugacity (FMQ to FMQ+2) are given in the Appendix (Supplemental Figures 11 and 12). In our model, clinopyroxene enters as a liquidus phase at 1285 °C followed by garnet at 1210 °C. During garnet clinopyroxenite fractionation, 55-80% of the Fe in the crystallizing cumulate for each step is sequestered by garnet (Fig. 6a, b). After ~50% garnet clinopyroxenite fractionation, amphibole saturates at 940 °C, becoming the dominant Fe-bearing phase in the cumulate assemblage, clinopyroxene crystallization ceases, and garnet modal abundances decrease rapidly. Plagioclase does not saturate until 840 °C.

From these major element and modal constraints, we constructed a simple mass balance model to constrain the Fe isotope evolution of both the melt and cumulate during fractional crystallization:

$$\delta^{56}Fe^{i+1}_{melt} = \delta^{56}Fe^{i}_{melt} + \Delta^{56}Fe_{melt\text{-}cumulate}{}^{i+1}(1\text{-}f^{i+1})$$

where *f* is the fraction of Fe in the melt relative to the system at each fractionation step, *i*. As we have no isotopic constraints for primary Andean basalts, we use an initial $\delta^{56}Fe$ of 0.0‰. Our model shows that garnet clinopyroxenite crystallization should result in significant cumulate-melt fractionation ($\Delta^{56}Fe_{melt\text{-}cumulate}$ = +0.07 to +0.17‰) and an early interval of isotopically light cumulate production (Fig. 6c). Continued removal of isotopically light Fe from garnet crystallization drives more evolved melts to heavier $\delta^{56}Fe$ compositions, with >60% of the initial Fe in the system lost to garnet fractionation between ~1200 and 800°C (Fig. 6b).

Our model results suggest garnet clinopyroxenite fractionation should produce an isotopically light lower crust and an isotopically heavy amphibole-bearing middle to upper-crust. Such isotopic stratification of the arc crust has been observed in oceanic settings by previous studies of cumulate xenoliths (Lesser Antilles: Cooper and Inglis, 2022; Central Aleutians: Sosa et al., in revision) and differs significantly from the relatively uniform isotopic composition observed in the Mercaderes xenoliths (whole-rock $\delta^{56}Fe$ = –0.02 to +0.11‰, with 86% of all samples between +0.03‰ and +0.11‰.). This model, and all performed sensitivity tests, also fail to reproduce the observed Fe isotope trends of minerals separated from Mercaderes rocks (Fig. 6d; Supplemental Figure 11).

4.6.2.2 Amphibole dehydration melting (Model B)

We now turn to the hypothesis that the Mercaderes xenolith suite may instead represent a prograde metamorphic sequence. Using Perple_X and a representative diorite whole-rock composition (sample XC-MG-5), we constructed a model in which our protolith is brought to higher pressure and temperatures along the Mercaderes geothermal gradient (Fig. 7a). We use an initial $Fe^{+3}/\Sigma Fe$ = 0.30 and water content of 1.2 wt.%, which we consider an appropriate estimate for a diorite protolith containing ~60% amphibole with ~2 wt.% structurally bound water.

The melts generated in this model should not segregate from the protolith until interconnected channels are established within the residue. Estimates of the necessary melt volume required to attain channelization vary from 2-10 wt.% (e.g., Wolf and Wyllie, 1991; Vigneresse et al., 1996), and we chose 7 wt.% as a reasonable estimate (same value used by Bowman et al.,

2021). Assuming incomplete melt segregation during extraction (e.g., Sawyer, 2014), we leave 0.5 wt.% melt in the residue after each extraction event. Sensitivity tests were also performed for this model, in which we varied water content (0.5-1.5 wt.% H_2O), diorite composition, oxidation state ($Fe^{+3}/\Sigma Fe$ = 0.15-0.30), the threshold at which melt is extracted. (4-10 wt.% melt), $<F>_{amph}$ (211-253 N/m), $<F>_{cpx}$ (210-244 N/m), and the amount of melt left in the residue after each extraction event (0.1-1.0 wt.% melt) (Supplemental Figure 13).

We use an initial Fe isotope composition of $\delta^{56}Fe$ = +0.062‰ (average diorite value). Amphibole dehydration melting begins at 806 °C (Fig. 7b), with amphibole exhausted from the residue by 1094 °C after ~27 wt.% melt extraction. Plagioclase is fully consumed by 1124 °C (Fig. 8b). At 2 GPa and 1300 °C, the residue is composed completely of garnet and clinopyroxene with $\delta^{56}Fe$ = 0.029‰ (Fig. 7c), and a total of 35 wt.% melt has been extracted. The relatively uniform $\delta^{56}Fe$ of the modeled residue from 800 to 1300 °C is consistent with most measured Mercaderes xenoliths (Fig. 7c). Our model also reproduces the observed trends in amphibole, garnet and clinopyroxene Fe isotope chemistry (Fig. 7d). The residue experiences little isotopic change because the melts generated are Fe-poor below ~1100 °C (1-6% FeO_T) and most of the Fe remains in the solid, with FeO_T in the residue increasing from 10.6 wt.% at 800 °C to 13.5 wt.% at 1300 °C (normalized anhydrous). These results imply that the Andean crust in the Mercaderes region has a near-constant Fe isotope composition from ~2 to ~0.6 GPa (~70 to 21 km below the surface, assuming a pressure-to-depth conversion of 35 km/GPa), contrary to the expectation that garnet fractionation should create an isotopically light lower crust if crystallizing from a typical mantle melt.

The dramatic difference in the isotopic evolution of modeled cumulates and residues arises from the contrasting behavior of Fe in each system. Between 1300 and 800 °C, 75% of the initial melt in the system crystallizes and 95% of the initial Fe is consumed by cumulates in Model A (Fig. 8c). In contrast, because the melts formed in the amphibole dehydration model are generally Fe-poor andesites below 1125 °C, when the majority (28 wt.%) of melt generation occurs, only 21% of the initial Fe in the system is lost to the melt between 1300 and 800 °C in Model B (Fig. 8d). The modal dominance of garnet in the crystallizing cumulates between 1210 and 940 °C in

Model A also results in greater melt-solid isotopic fractionation ($\Delta^{56}Fe_{melt\text{-}cumualte}$ = +0.07 to +0.17‰) (Fig. 8e, g) compared to amphibole dehydration melting in Model B over the same temperature range ($\Delta^{56}Fe_{melt\text{-}residue}$ = +0.07 to +0.12‰) (Fig. 8f, h).

4.6.3 Implications for crustal structure and evolution

The possibility of lower to mid-crustal gabbros (or basalts) undergoing densification reactions in response to orogeny and burial, and the importance of such phase transitions in promoting lower-crustal delamination, has been long recognized (e.g., Kay and Kay, 1991, 1993; Wolf and Wyllie, 1993; Jull and Kelemen, 2001). Eclogite formation may create inverted density gradients and gravitational instabilities at the crust-mantle interface that promote lower-crustal delamination, either as a "peeling" (i.e., separation of dense garnet clinopyroxenite roots at a laterally propagating rift: Bird, 1979) or as "drips" (i.e., discrete packages of dense root material falling from the crustal base: Jull and Kelemen, 2001). Evidence of recent delamination has been observed and extensively studied further south in the Andean belt, where rising asthenospheric mantle has resulted in rapid tectonic uplift, changes in regional stress regime, and abrupt shifts from felsic to mafic volcanism (e.g., Mpodozis and Kay, 1992; Kay et al., 1994). Debate exists, however, as to whether eclogitization of gabbroic assemblages or crystallization and partial melting of garnet clinopyroxenite cumulates provides the impetus for delamination, as it has been argued that gabbro eclogitization is an inefficient means of generating dense mafic residues (e.g., Saleeby et al., 2003).

While our Fe isotope data favor the formation of low-MgO garnet clinopyroxenites through eclogitization, they do not discredit the existence of high-MgO garnet clinopyroxenite cumulates at the base of the Andean crust or upper-most mantle (which have been described in previous studies of the Mercaderes xenolith suite but were not measured here). Indeed, trace elements systematics of erupted lavas from the Andean NVZ show clear signs of garnet equilibration, suggesting that basalts either experienced prolonged periods of garnet fractionation or contain a strong eclogite-melt endmember component (e.g., Bryant et al., 2006). However, these garnet signatures could also be created by mixing between mantle-derived magmas and partial melts generated by amphibole dehydration reactions, which would also be in equilibrium with garnet.

Indeed, $\delta^{56}Fe$ values of the (basaltic) andesites and dacites generated in our amphibole dehydration model range from +0.08 to +0.20‰, similar to previous studies of Andean lavas from over-thickened (>45 km) regions of the Central Volcanic Zone further south (Du et al., 2023).

A more appropriate scenario might be a hybrid of the gabbro-eclogitization and cumulate models: primitive basalts may fractionate high-MgO garnet clinopyroxenites at the base of the Andean crust before ascending to mid/upper-crustal levels, where they fractionate diorites. Crustal shortening during orogeny and burial under the growing cumulate pile may drive amphibole dehydration and eclogitization of original diorite cumulates (Fig. 9). In conjunction with crystallization and densification of high-MgO garnet clinopyroxenite cumulate roots, amphibole dehydration may, therefore, also drive delamination of the Andean lower crust. At the pressures and temperatures specified by geothermobarometry and Perple_X modeling, calculated densities for the diorites and garnet clinopyroxenites range from 2.9 to 3.0 g/cm^3 and 3.4 to 3.6 g/cm^3, respectively, implying that the latter would be gravitationally unstable relative to the mantle (~3.3-3.4 g/cm^3). This densification is reflected in our Perple_X amphibole dehydration model, where eclogitization is associated with increased residue density from 3.0 to 3.5 g/cm^3 (Fig. 9d).

Recent studies have interpreted the chemistry of low MgO garnet clinopyroxenites as representative of magmatic conditions (e.g., Tang et al., 2018), but this must be done cautiously. Iron isotopes offer a powerful tool to disentangle the effects of garnet crystallization vs. gabbro/diorite eclogitization but should be integrated with robust petrographic and major/trace element characterization. While our results do not preclude the importance of deep garnet fractionation in generating the light Fe isotope compositions and HREE observed in lavas from thickened arc sections, they do suggest that amphibole dehydration reactions may represent an important, previously overlooked source of these signatures. Future work on Fe isotopes in high-MgO garnet clinopyroxenites from continental arcs is clearly warranted, as our dataset does not cover the full compositional diversity seen in these suites. Critically, our new Fe isotope data from the Mercaderes suite support previous studies that have suggested that gabbro densification has played an important role in the development of the lower Andean crust (e.g., Kay and Kay, 1991, 1993; Weber et al., 2002). This means that not all garnet clinopyroxenites suites will display light

Fe isotope signatures because they are not all formed through lower-crustal crystallization-differentiation. In over-thickened continental arc settings, where eclogitization reactions may dominate, the crust may not show the same isotopic stratification observed in thin oceanic arcs composed of igneous cumulates (e.g., Central Aleutians: Sosa et al., in revision; Lesser Antilles: Cooper and Inglis, 2022).

4.7 CONCLUSIONS

Iron isotope analyses of lower to mid/upper-crustal xenoliths from the Mercaderes region of the Colombian Andes reveals a narrow compositional range of $\delta^{56}Fe$ = –0.02 to +0.11‰. The $\delta^{56}Fe$ of mid to upper-crustal diorites ($\delta^{56}Fe$ = +0.05 to +0.06‰) overlaps the range observed in the lower-crustal garnet clinopyroxenites ($\delta^{56}Fe$ = –0.02 to +0.07‰), implying that, at least regionally, the Fe isotope composition of the Andean crust ~70 to 21 km below the surface is not vertically unstratified. This is inconsistent with previous theories and thermodynamically-based fractional crystallization modeling, which suggest that extensive garnet clinopyroxenite crystallization from primitive arc basalts should form an isotopically low $\delta^{56}Fe$ crustal root. The lack of correlation between the lithology of the Mercaderes xenoliths and their Fe isotope ratio, major element composition, or trace element composition is also inconsistent with a purely cumulate origin. Our preferred explanation for the Fe isotope data is that the Mercaderes suite represents a prograde metamorphic sequence in which amphibole dehydration reactions drive the densification of diorite cumulates to form garnet clinopyroxenite residues. As our data are limited to “low-MgO” garnet clinopyroxenites (i.e., MgO <13 wt.%), they do not preclude the formation of clinopyroxene-rich high-MgO garnet clinopyroxenites at the base of the Andean crust through igneous processes. Rather, we suggest that garnet pyroxenite suites from thick arcs may represent an amalgamation of igneous and metamorphic processes acting concurrently. Primitive basaltic melts may fractionate high-MgO garnet clinopyroxenite cumulates at the base of the crust before rising to crystallize mid/upper-crustal diorite or gabbros. Partial melting and densification of the high-MgO pyroxenite root and eclogitization of mid/upper-crustal diorite protoliths in response to crustal

shortening and burial may act in tandem to promote lower-crustal delamination in a self-feeding mechanism. Fe isotopes provide a promising tool to disentangle igneous and metamorphic processes and should receive greater attention in future studies of lower-crustal structure and chemistry.

4.8 ACKNOWLEDGMENTS

We thank C. Ma (Caltech) for assistance with the EMPA, T M. Present (Caltech) for his help with XRF spectroscopy, O. Wilner (Caltech) for help with the ICP-MS, R. Grigoryan (Caltech) for support with the Neptune, and K. McCarty (Pomona) and N. F. Dalleska (Caltech) for their help with LA-ICP-MS. This work was supported by NSF grant EAR 1943629 awarded to C. Bucholz. E.S.S. was supported by the National Science Foundation Graduate Research Fellowship under Grant No. DGE-1745301.

4.9 REFERENCES

Anderson, J. L., & Smith, D. R. (1995). The effects of temperature and fO2 on the Al-in-hornblende barometer. *American Mineralogist,* 80(5-6), 549-559.

Beard, B. L., & Johnson, C. M. (2004). Fe isotope variations in the modern and ancient earth and other planetary bodies. *Reviews in Mineralogy and Geochemistry,* 55(1), 319-357.

Beyer, C., Frost, D. J., & Miyajima, N. (2015). Experimental calibration of a garnet–clinopyroxene geobarometer for mantle eclogites. *Contributions to Mineralogy and Petrology,* 169, 1-21.

Bird, P. (1979). Continental delamination and the Colorado Plateau. *Journal of Geophysical Research: Solid Earth,* 84(B13), 7561-7571.

Blatter, D. L., Sisson, T. W., & Hankins, W. B. (2023). Garnet stability in arc basalt, andesite, and dacite - an experimental study. *Contributions to Mineralogy and Petrology,* 178(6), 33.

Bloch, E., Ibañez-Mejia, M., Murray, K., Vervoort, J., & Müntener, O. (2017). Recent crustal foundering in the Northern Volcanic Zone of the Andean arc: Petrological insights from the roots of a modern subduction zone. *Earth and Planetary Science Letters,* 476, 47-58.

Blundy, J. D., Falloon, T. J., Wood, B. J., & Dalton, J. A. (1995). Sodium partitioning between clinopyroxene and silicate melts. *Journal of Geophysical Research: Solid Earth,* 100(B8), 15501-15515.

Bowman, E. E., Ducea, M. N., & Triantafyllou, A. (2021). Arclogites in the subarc lower crust: Effects of crystallization, partial melting, and retained melt on the foundering ability of residual roots. *Journal of Petrology,* 62(12), egab094.

Bryant, J. A., Yogodzinski, G. M., Hall, M. L., Lewicki, J. L., & Bailey, D. G. (2006). Geochemical constraints on the origin of volcanic rocks from the Andean Northern Volcanic Zone, Ecuador. *Journal of Petrology* 47(6), 1147-1175.

Bucholz, C. E., & Spencer, C. J. (2019). Strongly peraluminous granites across the Archean–Proterozoic transition. *Journal of Petrology,* 60(7), 1299-1348.

Cooper, G. F., Davidson, J. P., & Blundy, J. D. (2016). Plutonic xenoliths from Martinique, Lesser Antilles: Evidence for open system processes and reactive melt flow in island arc crust. *Contributions to Mineralogy and Petrology,* 171, 1-21.

Cooper, G. F., & Inglis, E. C. (2022). A crustal control on the Fe isotope systematics of volcanic arcs revealed in plutonic xenoliths from the Lesser Antilles. *Frontiers in Earth Science,* 9, 795858.

Craddock, P. R., & Dauphas, N. (2010). Iron isotopic compositions of geological reference materials and chondrites. *Geostandards and Geoanalytical Research,* 35(1), 101-123.

Daczko, N. R., Clarke, G. L., & Klepeis, K. A. (2001). Transformation of two-pyroxene hornblende granulite to garnet granulite involving simultaneous melting and fracturing of the lower crust, Fiordland, New Zealand. *Journal of Metamorphic Geology,* 19(5), 549-562.

Dauphas, N., Janney, P. E., Mendybaev, R. A., Wadhwa, M., Richter, F. M., Davis, A. M., ... & Foley, C. N. (2004). Chromatographic separation and multicollection-ICPMS analysis of iron. Investigating mass-dependent and-independent isotope effects. *Analytical Chemistry,* 76(19), 5855-5863.

Dauphas, N., Pourmand, A., & Teng, F. Z. (2009). Routine isotopic analysis of iron by HR-MC-ICPMS: How precise and how accurate? *Chemical Geology* 267(3-4), 175-184.Dauphas, N., Roskosz, M., Alp, E. E., Neuville, D. R., Hu, M. Y., Sio, C. K., ... & Cordier, C. (2014). Magma redox and structural controls on iron isotope variations in Earth's mantle and crust. *Earth and Planetary Science Letters,* 398, 127-140.

Dodge, F. C. W., Lockwood, J. P., & Calk, L. C. (1988). Fragments of the mantle and crust from beneath the Sierra Nevada batholith: Xenoliths in a volcanic pipe near Big Creek, California. *Geological Society of America Bulletin,* 100(6), 938-947.

Du, D. H., Tang, M., Li, W., Kay, S. M., & Wang, X. L. (2022). What drives Fe depletion in calc-alkaline magma differentiation: Insights from Fe isotopes. *Geology,* 50(5), 552-556.

Ducea, M., & Saleeby, J. (1998). A case for delamination of the deep batholithic crust beneath the Sierra Nevada, California. *International Geology Review,* 40(1), 78-93.

Ducea, M. N., Chapman, A. D., Bowman, E., & Triantafyllou, A. (2021a). Arclogites and their role in continental evolution; part 1: Background, locations, petrography, geochemistry, chronology and thermobarometry. *Earth-Science Reviews,* 214, 103375.

Ducea, M. N., Chapman, A. D., Bowman, E., & Balica, C. (2021b). Arclogites and their role in continental evolution; part 2: Relationship to batholiths and volcanoes, density and foundering, remelting and long-term storage in the mantle. *Earth-Science Reviews,* 214, 103476.

Gianola, O., Costa, B., Ferri, F., Gilio, M., Petrelli, M., Murri, M., ... & Cesare, B. (2023). Melt inclusions in arclogitic xenoliths constrain the genesis of the lower continental arc crust beneath the Northern Volcanic Zone, Colombia. *Journal of Petrology,* 64(6), egad038.

Graham, C. M., & Powell, R. (1984). A garnet–hornblende geothermometer: Calibration, testing, and application to the Pelona Schist, Southern California. *Journal of Metamorphic Geology,* 2(1), 13-31.

Green, T. H., & Ringwood, A. E. (1968). Genesis of the calc-alkaline igneous rock suite. *Contributions to Mineralogy and Petrology,* 18(2), 105-162.

Greene, A. R., DeBari, S. M., Kelemen, P. B., Blusztajn, J., & Clift, P. D. (2006). A detailed geochemical study of island arc crust: The Talkeetna arc section, south–central Alaska. *Journal of Petrology,* 47(6), 1051-1093.

Hawthorne, F. C., Oberti, R., Harlow, G. E., Maresch, W. V., Martin, R. F., Schumacher, J. C., & Welch, M. D. (2012). Nomenclature of the amphibole supergroup. *American Mineralogist,* 97(11-12), 2031-2048.

Holland, T., & Blundy, J. (1994). Non-ideal interactions in calcic amphiboles and their bearing on amphibole-plagioclase thermometry. *Contributions to Mineralogy and Petrology,* 116, 433-447.

Holycross, M., & Cottrell, E. (2023). Garnet crystallization does not drive oxidation at arcs. *Science,* 380(6644), 506-509.

Jagoutz, O., Müntener, O., Burg, J. P., Ulmer, P., & Jagoutz, E. (2006). Lower continental crust formation through focused flow in km-scale melt conduits: The zoned ultramafic bodies of the Chilas Complex in the Kohistan Island arc (NW Pakistan). *Earth and Planetary Science Letters,* 242(3-4), 320-342.

Jagoutz, O. E., Burg, J. P., Hussain, S., Dawood, H., Pettke, T., Iizuka, T., & Maruyama, S. (2009). Construction of the granitoid crust of an island arc part I: Geochronological and geochemical constraints from the plutonic Kohistan (NW Pakistan). *Contributions to Mineralogy and Petrology,* 158, 739-755.

Jagoutz, O., Müntener, O., Schmidt, M. W., & Burg, J. P. (2011). The roles of flux-and decompression melting and their respective fractionation lines for continental crust formation: Evidence from the Kohistan arc. *Earth and Planetary Science Letter,s* 303(1-2), 25-36.

Jull, M., & Kelemen, P. Á. (2001). On the conditions for lower crustal convective instability. *Journal of Geophysical Research: Solid Earth,* 106(B4), 6423-6446.

Kay, R. W., & Mahlburg-Kay, S. (1991). Creation and destruction of lower continental crust. *Geologische Rundschau,* 80, 259-278.

Kay, R. W., & Kay, S. M. (1993). Delamination and delamination magmatism. *Tectonophysics,* 219(1-3), 177-189.

Kay, S. M., Coira, B., & Viramonte, J. (1994). Young mafic back arc volcanic rocks as indicators of continental lithospheric delamination beneath the Argentine Puna plateau, central Andes. *Journal of Geophysical Research: Solid Earth,* 99(B12), 24323-24339.

Lee, C. T. A., & Anderson, D. L. (2015). Continental crust formation at arcs, the arclogite "delamination" cycle, and one origin for fertile melting anomalies in the mantle. *Science Bulletin,* 60(13), 1141-1156.

Lee, C. T. A., Cheng, X., & Horodyskyj, U. (2006). The development and refinement of continental arcs by primary basaltic magmatism, garnet pyroxenite accumulation, basaltic recharge and delamination: Insights from the Sierra Nevada, California. *Contributions to Mineralogy and Petrology,* 151, 222-242.

Lewis, M. J., Bucholz, C. E., & Jagoutz, O. E. (2021). Evidence for polybaric fractional crystallization in a continental arc: Hidden Lakes mafic complex, Sierra Nevada batholith, California. *Contributions to Mineralogy and Petrology,* 176, 1-27.

Lewis, M. J., Ryan-Davis, J. R., & Bucholz, C. E. (2023). Mafic intrusions record mantle inputs and crustal thickness in the eastern Sierra Nevada batholith, California, USA. *Geological Society of America Bulletin,* 136, 1808-1826. https://doi.org/10.1130/B36646.1.

Li, D. Y., Xiao, Y. L., Li, W. Y., Zhu, X., Williams, H. M., & Li, Y. L. (2016). Iron isotopic systematics of UHP eclogites respond to oxidizing fluid during exhumation. *Journal of Metamorphic Geology,* 34(9), 987-997.

Liang, W., Huang, J., Zhang, G., & Huang, F. (2022). Iron isotopic fractionation during eclogite anatexis and adakitic melt evolution: Insights into garnet effect on Fe isotopic variations in high-silica igneous rocks. *Contributions to Mineralogy and Petrology,* 177(3), 33.

Li, Q. W., Zhao, J. H., Wang, Q., Zhang, Z. F., An, Y. J., & He, Y. T. (2020). Iron isotope fractionation in hydrous basaltic magmas in deep crustal hot zones. *Geochimica et Cosmochimica Acta,* 279, 29-44.

Marxer, F., Ulmer, P., & Müntener, O. (2022). Polybaric fractional crystallization of arc magmas: An experimental study simulating trans-crustal magmatic systems. *Contributions to Mineralogy and Petrology,* 177(1), 3.

Mpodozis, C., & Kay, S. M. (1992). Late Paleozoic to Triassic evolution of the Gondwana margin: Evidence from Chilean Frontal Cordilleran batholiths (28 S to 31 S). *Geological Society of America Bulletin,* 104(8), 999-1014.

Müntener, O., & Ulmer, P. (2018). Arc crust formation and differentiation constrained by experimental petrology. *American Journal of Science*, 318(1), 64-89.

Nie, N. X., Dauphas, N., Alp, E. E., Zeng, H., Sio, C. K., Hu, J. Y., ... & Spear, F. S. (2021). Iron, magnesium, and titanium isotopic fractionations between garnet, ilmenite, fayalite, biotite, and tourmaline: Results from NRIXS, ab initio, and study of mineral separates from the Moosilauke metapelite. *Geochimica et Cosmochimica Acta,* 302, 18-45.

Ravna, K. (2000). The garnet–clinopyroxene Fe^{2+}–Mg geothermometer: An updated calibration. *Journal of Metamorphic Geolog,y* 18(2), 211-219.

Ridolfi, F. (2021). Amp-TB2: An updated model for calcic amphibole thermobarometry. *Minerals,* 11(3), 324.

Ringuette, L., Martignole, J., & Windley, B. F. (1999). Magmatic crystallization, isobaric cooling, and decompression of the garnet-bearing assemblages of the Jijal sequence (Kohistan terrane western Himalayas). *Geology,* 27(2), 139-142.

Rodriguez-Vargas, A., Koester, E., Mallmann, G., Conceição, R. V., Kawashita, K., & Weber, M. B. I. (2005). Mantle diversity beneath the Colombian Andes, northern volcanic zone: Constraints from Sr and Nd Isotopes. *Lithos,* 82(3-4), 471-484.

Rubatto, D., Burger, M., Lanari, P., Hattendorf, B., Schwarz, G., Neff, C., ... & Günther, D. (2020). Identification of growth mechanisms in metamorphic garnet by high-resolution trace element mapping with LA-ICP-TOFMS. *Contributions to Mineralogy and Petrology,* 175(7), 61.

Rudnick, R. L., & Fountain, D. M. (1995). Nature and composition of the continental crust: A lower crustal perspective. *Reviews of Geophysics,* 33(3), 267-309.

Saleeby, J., Ducea, M., & Clemens-Knott, D. (2003). Production and loss of high-density batholithic root, southern Sierra Nevada, California. *Tectonics,* 22(6).

Sawyer, E. W. (2014). The inception and growth of leucosomes: Microstructure at the start of melt segregation in migmatites. *Journal of Metamorphic Geology,* 32(7), 695-712.

Sen, C., & Dunn, T. (1994). Dehydration melting of a basaltic composition amphibolite at 1.5 and 2.0 GPa: Implications for the origin of adakites. *Contributions to Mineralogy and Petrology,* 117(4), 394-409.

Spear, F. S., & Selverstone, J. (1983). Quantitative PT paths from zoned minerals: Theory and tectonic applications. *Contributions to Mineralogy and Petrology,* 83(3-4), 348-357.

Stowell, H., Tulloch, A., Zuluaga, C., & Koenig, A. (2010). Timing and duration of garnet granulite metamorphism in magmatic arc crust, Fiordland, New Zealand. *Chemical Geology,* 273(1-2), 91-110.

Tang, M., Erdman, M., Eldridge, G., & Lee, C. T. A. (2018). The redox "filter" beneath magmatic orogens and the formation of continental crust. *Science Advances,* 4(5), eaar4444.

Vigneresse, J. L., Barbey, P., & Cuney, M. (1996). Rheological transitions during partial melting and crystallization with application to felsic magma segregation and transfer. *Journal of Petrology,* 37(6), 1579-1600.

Weber, M. B. I. (1998) *The Mercaderes Río Mayo xenoliths, Colombia: Their bearing on mantle and crustal processes in the Northern Andes*. PhD thesis. University of Leicester (United Kingdom).

Weber, M. B., Tarney, J., Kempton, P. D., & Kent, R. W. (2002). Crustal make-up of the northern Andes: Evidence based on deep crustal xenolith suites, Mercaderes, SW Colombia. *Tectonophysics,* 345(1-4), 49-82.

Williams, H. M., Peslier, A. H., McCammon, C., Halliday, A. N., Levasseur, S., Teutsch, N., & Burg, J. P. (2005). Systematic iron isotope variations in mantle rocks and minerals: The effects of partial melting and oxygen fugacity. *Earth and Planetary Science Letters,* 235(1-2), 435-452.

Williams, H. M., Nielsen, S. G., Renac, C., Griffin, W. L., O'Reilly, S. Y., McCammon, C. A., ... & Halliday, A. N. (2009). Fractionation of oxygen and iron isotopes by partial melting processes: Implications for the interpretation of stable isotope signatures in mafic rocks. *Earth and Planetary Science Letters,* 283(1-4), 156-166.

Wolf, M. B., & Wyllie, P. J. (1991). Dehydration-melting of solid amphibolite at 10 kbar: Textural development, liquid interconnectivity and applications to the segregation of magmas. *Mineralogy and Petrology,* 44(3-4), 151-179.

Wyllie, P. J., & Wolf, M. B. (1993). Amphibolite dehydration-melting: Sorting out the solidus. *Geological Society, London, Special Publications,* 76(1), 405-416.

Yamamoto, H., & Yoshino, T. (1998). Superposition of replacements in the mafic granulites of the Jijal complex of the Kohistan arc, northern Pakistan: Dehydration and rehydration within deep arc crust. *Lithos,* 43(4), 219-234.

Yoshino, T., & Satish-Kumar, M. (2001). Origin of scapolite in deep-seated metagabbros of the Kohistan Arc, NW Himalayas. *Contributions to Mineralogy and Petrology,* 140(5), 511-531.

Zhao, G., Cawood, P. A., Wilde, S. A., & Lu, L. (2001). High-pressure granulites (retrograded eclogites) from the Hengshan Complex, North China Craton: Petrology and tectonic implications. *Journal of Petrology,* 42(6), 1141-1170.

Zieman, L., Ibañez-Mejia, M., Rooney, A. D., Bloch, E., Pardo, N., Schoene, B., & Szymanowski, D. (2023). To sink, or not to sink: The thermal and density structure of the modern northern Andean arc constrained by xenolith petrology. *Geology,* 51(6), 586-590.

Zieman, L. J., Ibañez-Mejia, M., Tissot, F. L., Tompkins, H. G., Pardo, N., & Bloch, E. M. (2024). Zirconium stable isotope fractionation during intra-crustal magmatic differentiation in an active continental arc. *Geochimica et Cosmochimica Acta,* 365, 53-69.

4.10 FIGURES AND CAPTIONS

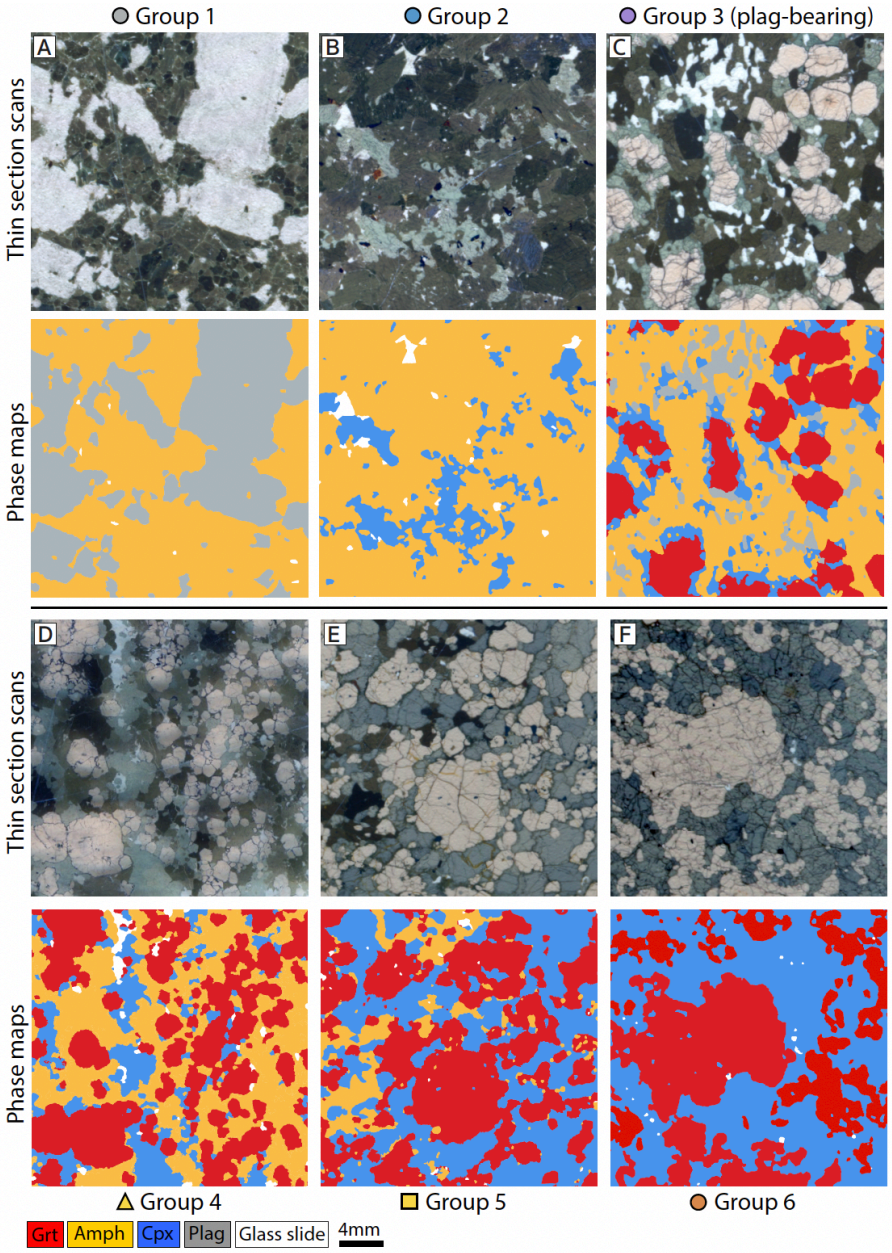

Figure 1: Partial thin section scans (rows 1 and 3) and corresponding micro-XRF phase maps (rows 2 and 4) of selected Mercaderes xenoliths. **A)** Group 1: diorite XC-M-1. **B)** Group 2: plagioclase-bearing garnet clinopyroxene hornblendite XC-M-4. **C)** Group 3: clinopyroxene hornblendite XC-MP1-4. **D)** Group 4: garnet clinopyroxene hornblendite XC07-1/17. **E)** Group 5: garnet hornblendite clinopyroxenite XC-MG-4. **F)** Group 6: garnet clinopyroxenite XC-MG-2.

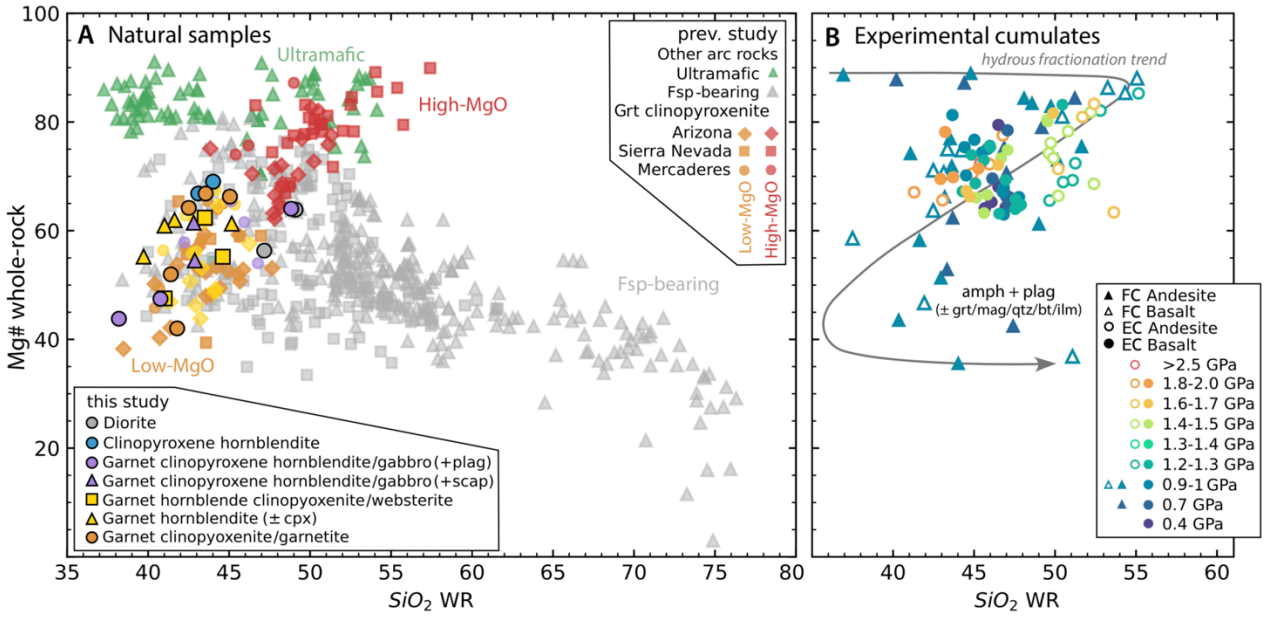

Figure 2: Whole-rock SiO_2 wt.% versus molar Mg# for (**A**) natural rocks and (**B**) experimental cumulates. Previously studied garnet-bearing plutonic xenoliths whole-rock data are from Mercaderes (circles; Weber, 1998; Bloch et al., 2017), Arizona (Erdman et al., 2016), Sierra Nevada (squares; Lee et al., 2006). Garnet-free plutonic xenoliths from oceanic arcs are from the Central Aleutians (Sosa et al., *in revision*) and Lesser Antilles (Cooper et al., 2016). Plutonic whole-rock data from exhumed oceanic and continental arcs include that from Kohistan (Jagoutz et al., 2006, 2009, 2011), Talkeetna (Greene et al., 2006), and Sierra Nevada batholith (as compiled in Lewis et al., 2023). Opaque symbols with black borders represent plutonic data from this study, while the literature data are represented by transparent symbols without borders. High and low-MgO garnet clinopyroxenites are classified after Erdman et al. (2016). Hydrous arc fractionation trend and fractional (FC) and equilibrium (EC) crystallization experimental data are from Müntener and Ulmer and references therein. Experimental data ≥ 2 GPa is from Holycross and Cottrell (2023).

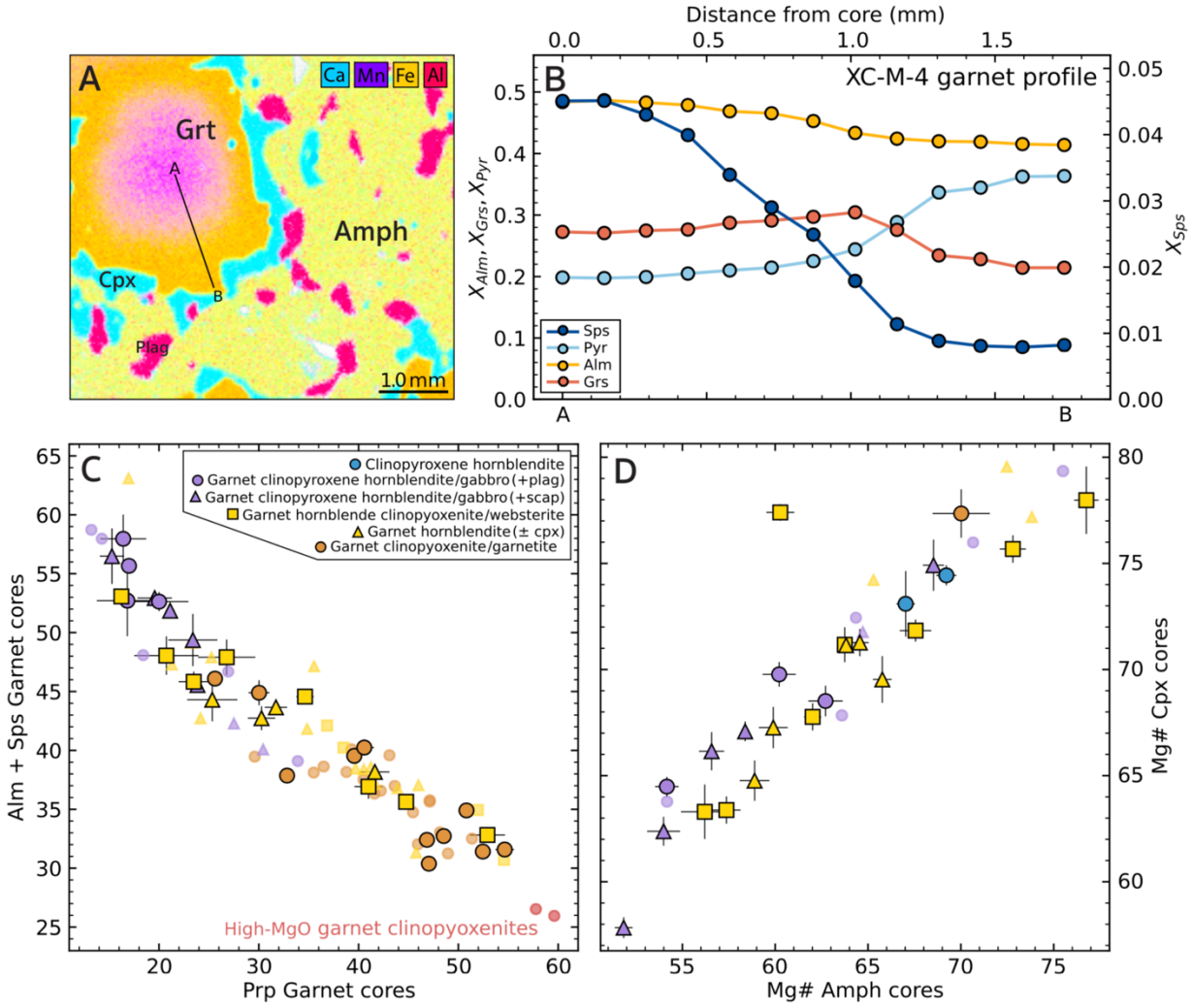

Figure 3: Summary of core mineral chemistry for the Mercaderes xenoliths. **A)** Section of micro-XRF element map of plagioclase-bearing garnet hornblende clinopyroxenite XC-M-4 for Ca, Mn, Fe, and Al. The marked garnet transect corresponds to the compositional profile in **(B)**, which shows the core-to-rim zoning typical in Mercaderes garnets from compositional group 3 in terms of spessartite, pyrope, almandine, and grossular mole fractions. **C)** Average core pyrope content of garnet vs almandine + spessartite content. **D)** Average core Mg# for amphibole vs average core Mg# for coexisting clinopyroxene. Literature data (Weber, 1998; Bloch et al., 2017; Zieman et al., 2023; Gianola et al., 2023) are represented by transparent symbols without borders.

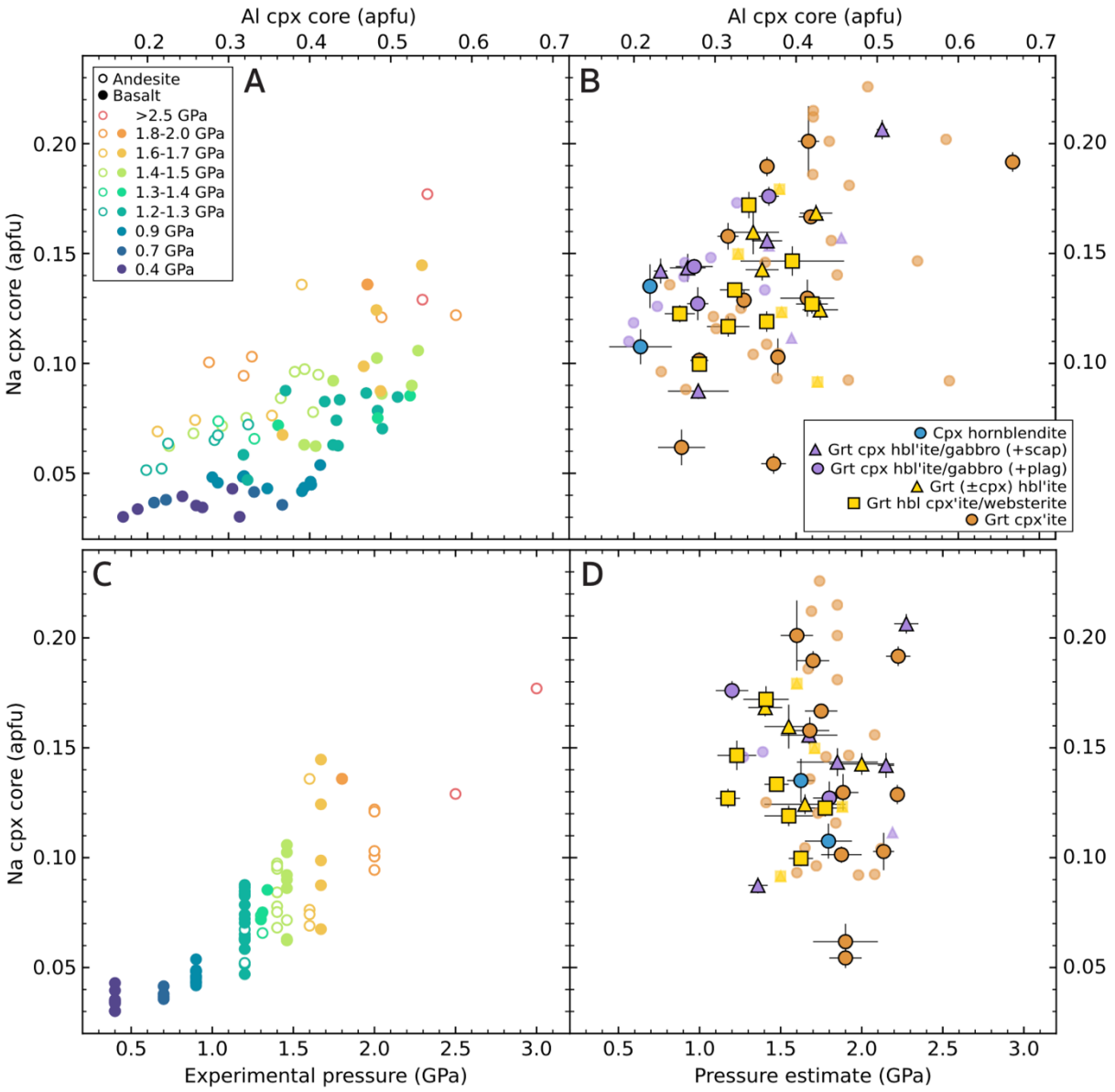

Figure 4: Clinopyroxene compositions from Mercaderes xenoliths compared to clinopyroxenes from experimental studies. Upper panels: clinopyroxene Al vs. Na for experimental studies (Blatter et al., 2013, 2023; Nandedkar et al., 2014; Ulmer et al., 2018; and Holycross and Cottrell, 2023) (**A**) and Mercaderes xenoliths (**B**). Lower panels: sample pressure estimate vs clinopyroxene Na for experimental studies (**C**) and Mercaderes xenoliths (**D**). Na and Al are given in atoms per formula unit (apfu). Literature data (Weber et al., 2002; Bloch et al., 2017; Zieman et al., 2023) are represented by transparent symbols without borders in (**B**) and (**D**).

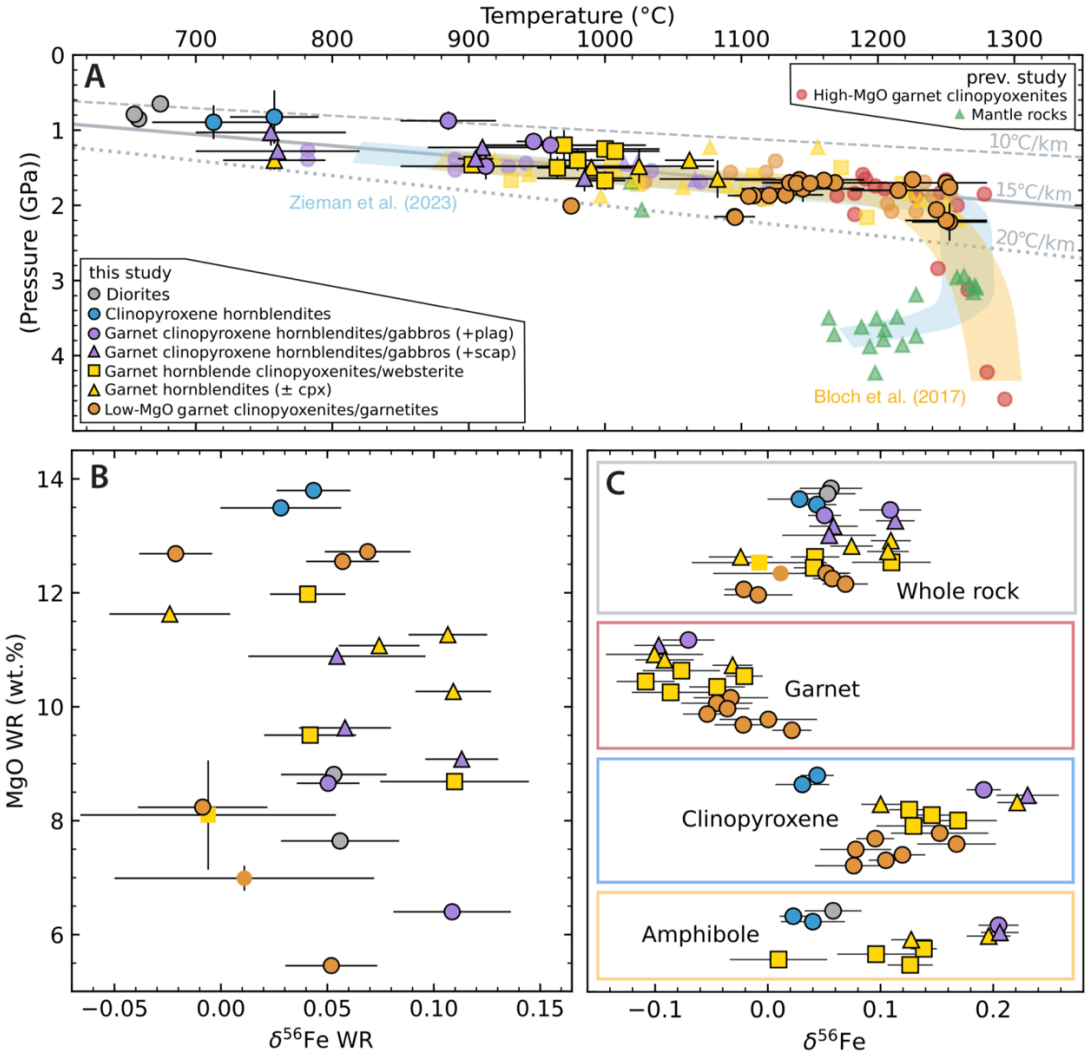

Figure 5: Fe isotope data and pressure/temperature estimates for Mercaderes xenoliths. **A)** Maximum *P-T* estimates for Mercaderes xenoliths. Literature data (Bloch et al., 2017; Zieman et al., 2023) are represented in opaque symbols. For pressure-temperature estimates obtained through garnet-clinopyroxene or amphibole-plagioclase geothermobarometry, error bars represent the range obtained by simultaneously solving the geothermometer and barometer while varying mineral compositions for each sample (see the Appendix for details). Geotherm gradients are calculated assuming a 35km per GPa pressure-to-depth conversion. **B)** Whole-rock δ^{56}Fe vs. MgO. **C)** From top to bottom panel, Fe isotope data for whole-rock powders, garnet, clinopyroxene, and amphibole from Mercaderes samples, organized by lithological groups. The greatest $\Delta^{56}Fe_{cpx\text{-}gar}$ and $\Delta^{56}Fe_{amph\text{-}gar}$ are observed in the lower-temperature Group 2 samples (grt + cpx + amph + plag/scap), while the least inter-mineral Fe isotope fractionation is seen in the Group 6 samples (grt + cpx). Symbols without black borders in **(B)** and **(C)** represent whole-rock compositions calculated from mineral chemistry, modes, and densities.

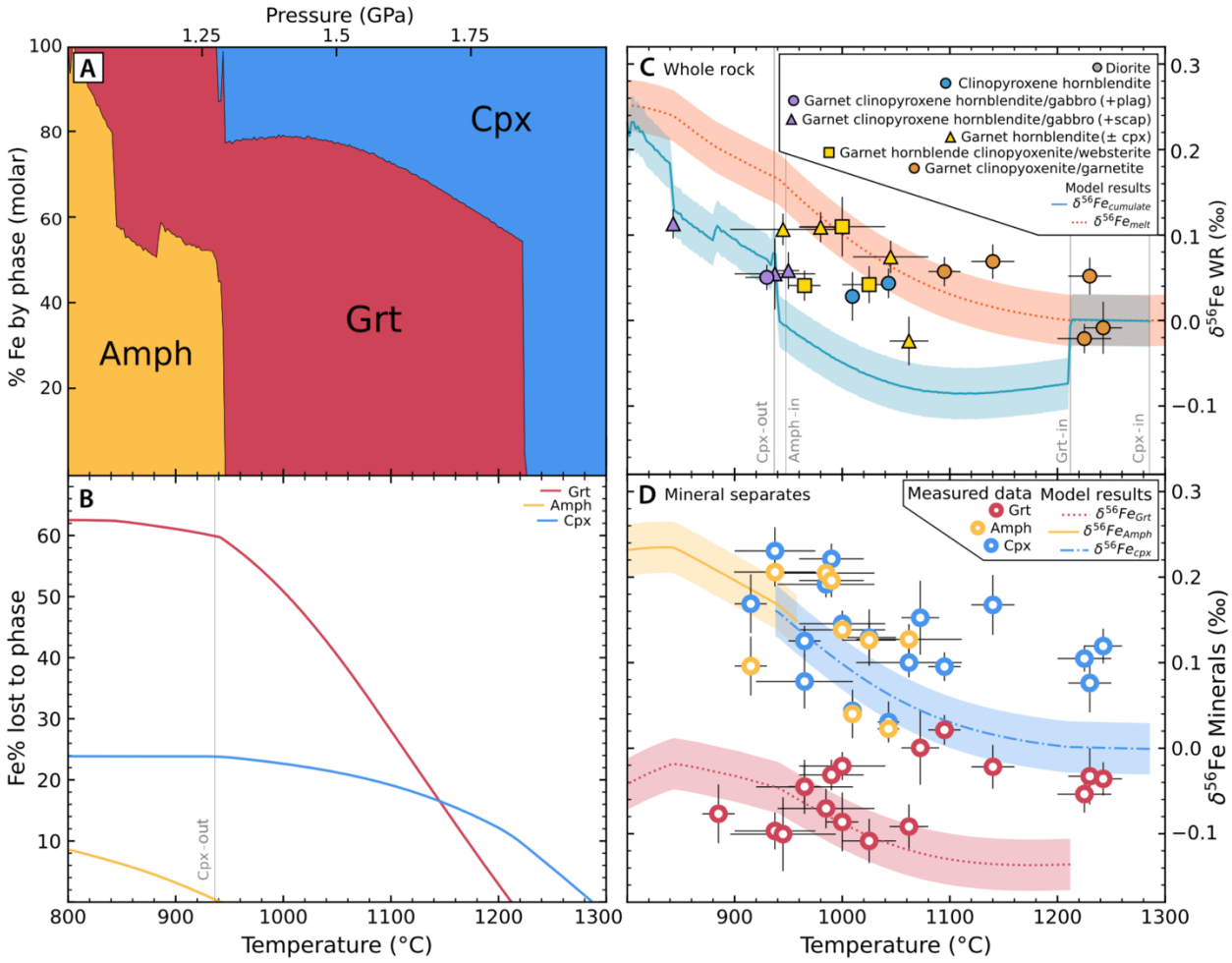

Figure 6: Fractional crystallization Fe isotope model results. **A)** Distribution of Fe between coexisting clinopyroxene, garnet, and amphibole in instantaneous fractionated cumulate. **B)** Cumulative percentage of initial Fe in the melt removed through fractionation of each phase in the model. **C)** Isotopic evolution of a basaltic melt with an initial δ^{56}Fe of 0.0‰ (dotted line) and Fe isotope composition of the complementary instantaneous cumulate (solid line). **D)** Model results for Fe isotope composition coexisting of amphibole (solid line), clinopyroxene (dot-dashed line), and garnet (dotted line) in cumulate compared to measured mineral separates. Shaded transparent fields represent 0.03‰ variability in δ^{56}Fe in (**B**) and (**C**).

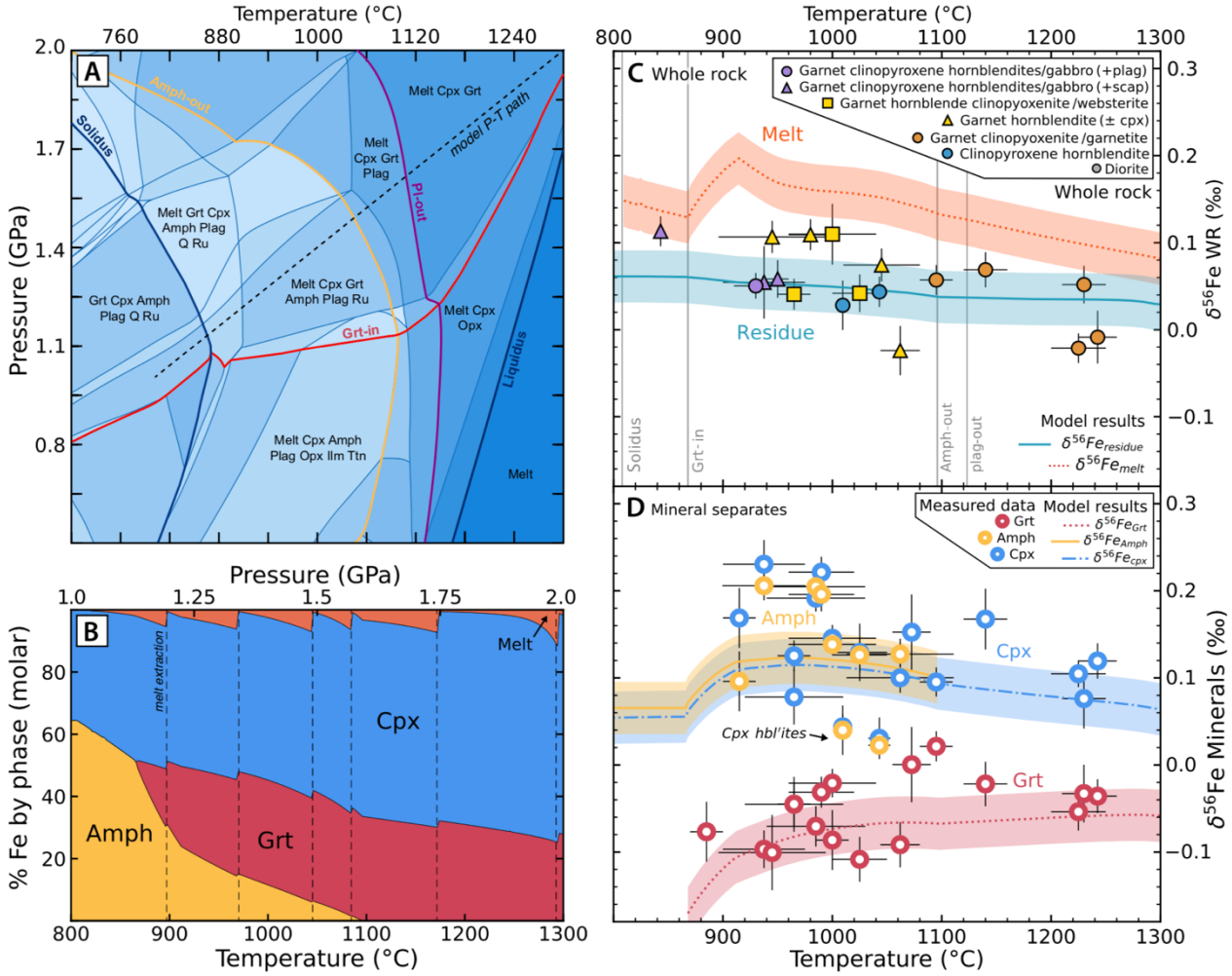

Figure 7: Amphibole dehydration partial melting Fe isotope model results. **A)** Perple_X pseudosection made with the whole-rock composition of diorite XC-MG-5, assuming initial $Fe^{+3}/\Sigma Fe$ of 0.3 and 1.2 wt.% H_2O. The dashed line in (**A**) represents the metamorphic path followed in (**B**), (**C**), and (**D**). **B)** Distribution of Fe between coexisting melt, clinopyroxene, garnet, and amphibole during prograde metamorphism. Dashed vertical lines represent melt extraction events. **C)** Fe isotope evolution of metamorphic residue (solid line) and complementary partial melts (dotted line) assuming an initial δ^{56}Fe of +0.062‰. Measured whole-rock Fe isotope compositions and temperature estimates for Mercaderes xenoliths are shown for comparison. **D)** Model results for Fe isotope composition of coexisting amphibole (solid line), clinopyroxene (dot-dashed line), and garnet (dotted line) in residue compared to measured mineral separates. Shaded transparent fields represent 0.03‰ variability in δ^{56}Fe in (**A**) and (**B**).

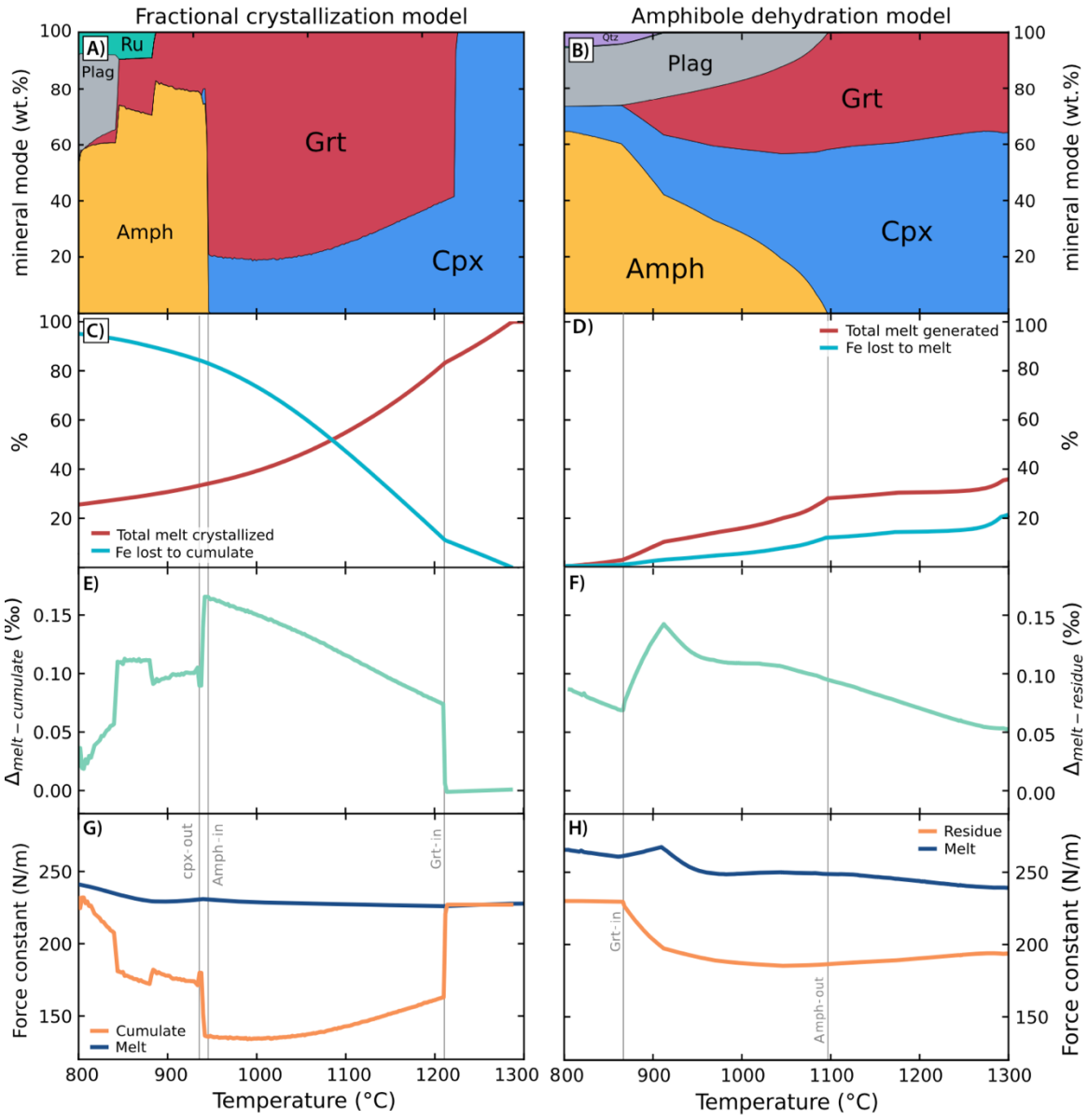

Figure 8: Comparison between fractional crystallization and amphibole dehydration models. **A)** instantaneous modal mineral abundances (wt.%) of fractionated cumulate. **B)** Modal abundance of coexisting phases in the metamorphic residue of the amphibole dehydration model. The increased isotopic fractionation between the melt and solid for the two models is also shown in plots of $\langle F \rangle_{melt}$ vs. $\langle F \rangle_{solid}$ and $\Delta^{56}Fe_{melt\text{-}cumulate}$ for the fractional crystallization (**C**, **E**) and amphibole dehydration (**D**, **F**) models. **G)** Total amount of melt crystallized and percentage of initial Fe lost to the fractionating cumulate. **H)** Total melt generated and percentage of initial Fe from the diorite protolith lost to the melt in the amphibole dehydration model.

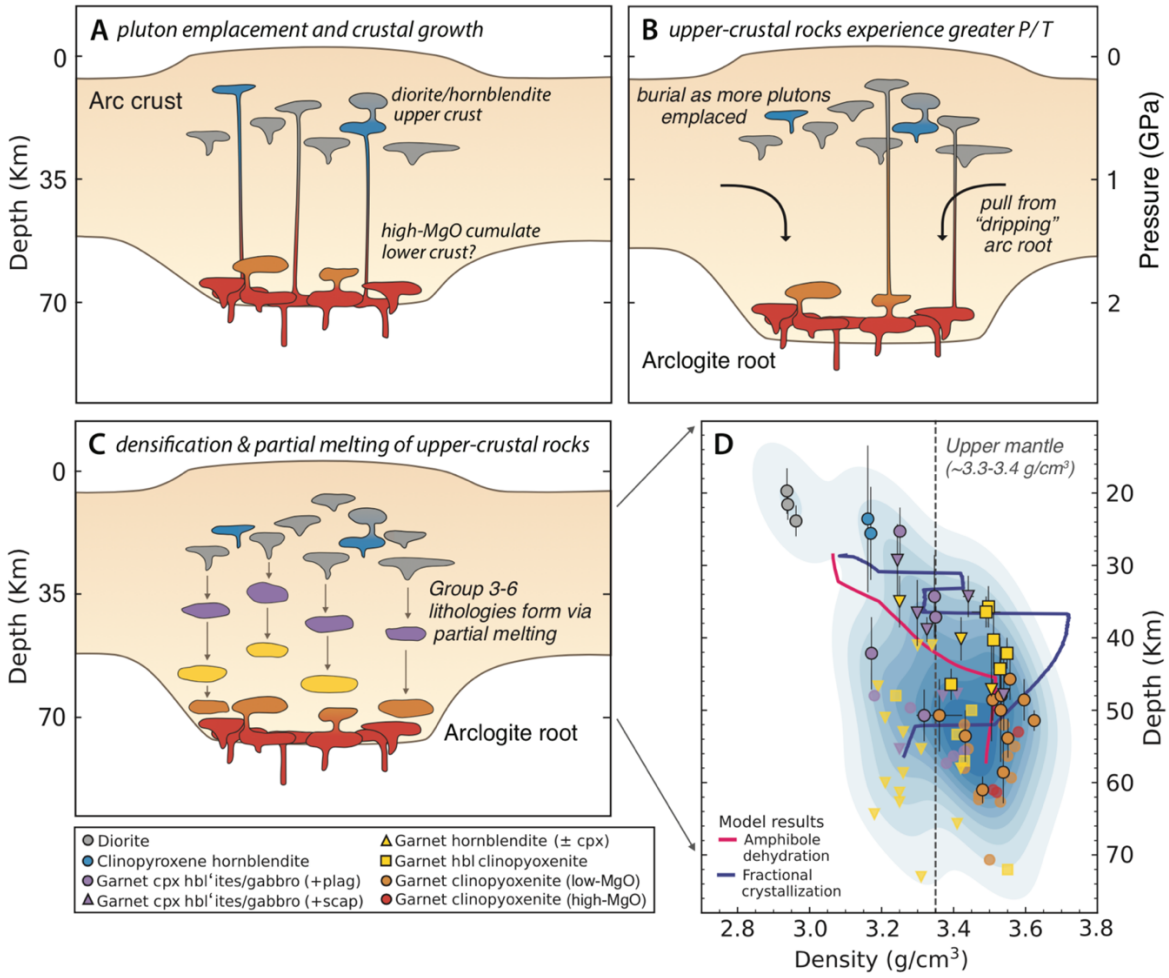

Figure 9: Schematic illustration of crustal formation (**A-C**) and density structure (**D**) of the Mercaderes crust. **A)** Initial emplacement of diorite and hornblendite protoliths. In this model, some garnet clinopyroxenites may form at the base of the Andean crust as igneous cumulates. **B)** Upper-crustal plutons begin to experience greater pressures and a downward "pull" in response to 1) burial as additional garnet-free igneous assembles are emplaced above and 2) the downward pull of dense garnet clinopyroxenite roots as they begin to delaminate in a "lithospheric-drip" type model. **C)** Upper-crustal plutons undergo amphibole dehydration (i.e., densification) reactions in response to increased pressure and temperature, resulting in the formation of garnet-bearing residues (i.e., compositional Groups 3-6). **D)** Density structure of the Mercaderes inferred from geothermobarometry and Perple_X modeling using a 35 km/GPa pressure-to-depth conversion. Xenolith densities were calculated using the *meemum* Perple_X function. Densities of fractional crystallization and partial melting Perple_X models are also shown for context, with both resulting in the formation of gravitationally unstable arclogite roots relative to the underlying mantle (~3.3-3.4 g/cm^3)

4.11 TABLES

Table 1: Rock classification scheme

Plotting symbol	Mineral content by group		Rock name
	Plagioclase/scapolite-rich		
●	**1** Hbl + plag		Diorite
	Amphibole-bearing		
●	**2** Hbl + cpx	Cpx < hbl	Clinopyroxene hornblendite
●	**3** Grt + hbl + cpx + plag	Cpx < hbl, plag < 10%	Plagioclase-bearing garnet hornblende clinopyroxenite
		Cpx < hbl, plag > 10%, cpx < 5%	Garnet hornblende gabbro
▲	Grt + hbl + cpx + scap (± plag)	Cpx < hbl, plag > 10%, cpx > 5%	Garnet clinopyroxene hornblende gabbro
		Cpx < hbl	Scapolite-bearing garnet hornblende clinopyroxenite
■	**4** Grt + hbl (± cpx)	Cpx < hbl	Garnet (± cpx) hornblendite
▲	**5** Grt + hbl + cpx + opx	Cpx > hbl (vol%)	Garnet hornblende websterite
	Grt + hbl + cpx		Garnet hornblende clinopyroxenite
	Amphibole-poor		
●	**6** Grt + cpx		Garnet clinopyroxenite (low-Mg) group)
	Grt + cpx + plag (± scap)	Grt > 75% (vol%)	Clinopyroxene garnetite

Table 1: Classification scheme used for Mercaderes xenoliths. The numbers and symbols in the left-hand columns correspond to the lithological groups given in section 4.1, and the symbols for those groups are used throughout the figures. Abbreviations are: grt, garnet; cpx, clinopyroxene; opx, orthopyroxene; scap, scapolite, plag, plagioclase; and hbl, hornblende. Note that the following assemblages are classified differently in Weber et al. (2002): grt + hbl + cpx + plag: feldspar-bearing pyribolites; grt + hbl + cpx + scap: scapolite-bearing pyribolites; grt + cpx ± plag ± scap: pyriclasites/pyrigarnites.

APPENDIX TO CHAPTER 4

4.12 Additional information on methods

Petrography: For each XRF session on the Bruker M4 Tornado μ-EDXRF spectrometer, six to eight thin sections (mounted on either 27 × 46 mm or 1" round glass slides) were loaded into the spectrometer and placed under a 20-mbar vacuum. Each thin section was mapped individually using a step size of 30 μm and a 10 ms dwell time per measurement. X-ray conditions during analysis were a 50 kV voltage, 599 μA beam current, and 30 μm beam diameter. Depending on the dimensions and size of the mapped area, each thin section map took between 2 and 4 hours to acquire. For the principal component analysis (PCA) calculations used to determine mineral modes, the software groups individual measurements into phases based on similarities in the relative intensity of measured elements. For the Mercaderes samples, we found the software was best able to distinguish between the phases observed through optical petrography (i.e., garnet, clinopyroxene, orthopyroxene, amphibole, scapolite, plagioclase, and titanite) when we performed the PCA with Al, K, Ca, Mn, Fe, Cr, Na, Ti, and Mg.

Mineral chemistry (major and trace element): For major element electron microprobe analyses, a 15 kV acceleration voltage, 25 nA beam current, and a 1-10 μm spot size (1.0 μm for garnet, pyroxene, and plagioclase, 10 μm for amphibole) were used. Peak and background count times for all measured elements and a list of EPMA standards are given in Supplemental Data File 3 (Ch4-T3). In general, 15 to 50 core analyses and 5 to 20 rim analyses were collected for each major phase in every sample. The electron microprobe data was reduced using a modified ZAF procedure (CITZAF, Armstrong, 1995). The detection limits for these conditions were: <0.01 wt.% for Si, Al, Mg, Ca, K, and Cl, <0.02 wt.% for Ti, Fe, Na, Cr, Mn, and <0.03 wt.% for F. For trace element LA-ICP-MS analyses, sample surfaces were pre-ablated for 10 seconds for each analysis. Data were collected for 30 seconds, totaling 40 seconds of ablation, followed by 40 seconds of washout. Each laser shot was performed at a 10 Hz repetition rate, and we used a He carrier gas. An 80 μm spot size was used for both analytical sessions. Typically, 3-10 core analyses and 2-6 rim analyses

were generally obtained for each phase in each sample. Every fifteen to twenty unknown sample measurements were bracketed with analysis of standards NIST 610 and BCR-2, which were used to construct calibration curves.

Chemical purification of Fe and presentation of data: All samples were digested in a mixture of concentrated HF and HNO_3 in a 2:1 ratio at 100 °C for 5 hours. These samples were fully dried and redigested in concentrated HCl and HNO_3 in a 3:1 ratio at 140 °C for 12 hours before being fully dried again. For the final digestion step, samples were fluxed in concentrated HCl and HNO_3 at 140 °C for 12 hours, but in a 2:1 ratio. Samples were then completely dried and fluxed in concentrated HCl at 180 °C for two days before being brought into a 6 M HCl solution before column chemistry. Samples were loaded into 10 mL polyethylene chromatography columns filled with 1 mL of BioRad AG1-X8 200-400 mesh anion exchange resin. Matrix elements were flushed from the columns with 8 mL of 0.4 M HCl before 8 mL of 0.4 M HCl was passed through the column to recapture the purified Fe. We performed column chemistry twice to ensure all matrix elements were removed from the purified sample. To ensure a complete matrix match between the samples and our IRMM-524b standard solution, samples were fully dried and fluxed for 12 hours in concentrated HNO_3 at 140 °C before being dried and taken up in 5 mL of 0.3 M HNO_3 run acid. Samples were fluxed in run acid at 130 °C for 12 hours prior to the start of the analytical session.

Because more measurements are made of the IRMM-524b standard than any sample during standard bracketing, the standard deviation of IRMM-524b better represents the true uncertainty of the session (Dauphas et al., 2009), and we thus opted to report errors based on the standard deviation of the IRMM-524b standard rather than the samples [error = $2*SD_{IRMM\text{-}524b}/(n_{sample})^{0.5}$]. Errors were also recalculated using the standard deviation of each sample [error = $2*SD_{sample}/(n_{sample})^{0.5}$] and are given in Supplemental Data File 3 (Ch4-T15). For $\delta^{56}Fe$, the errors calculated using the two methods are consistently within 0.025‰ of each other, with errors calculated from the 2SD of the standard generally 0.005‰ higher than those calculated using sample 2SD.

4.13 Temperature, pressure, and density estimates for Mercaderes xenoliths

For samples containing garnet and clinopyroxene, pressure and temperature were estimated by simultaneously solving the geothermometer of Ravna (2000) and geobarometer of Beyer et al. (2015). For samples with core-to-rim zoning, these calculations were performed separately with electron microprobe data taken from the core, mantle, and rim of both phases. Within each zone (i.e., all core, mantle, or rim points), the geothermometer and geobarometer were solved multiple times, varying and garnet and clinopyroxene composition (particularly, Mn, Ca, Fe, and Mg in garnet and Fe, Mg, and Al in clinopyroxene). The range in P-T determined for grain cores, mantle, and rims for each sample represents the compositional variation observed in each zone. We used a similar method to evaluate the uncertainty in our pressure-temperature calculations for amphibole-plagioclase thermometry (Holland and Blundy, 1994) and barometry (Anderson and Smith, 1995), where the geothermometer and geobarometer were solved simultaneously while varying amphibole and plagioclase compositions.

For the samples where the observed $\Delta^{56}Fe_{cpx\text{-}gar}$ and $\Delta^{56}Fe_{amph\text{-}gar}$ were used to estimate appropriate force constants for clinopyroxene and amphibole, we also constrained temperature by constructing pseudosections with Perple_X for each sample using whole-rock compositions. From these pseudosections, the stability fields of garnet, clinopyroxene, and (when present) amphibole were extracted, along with the endmember components of jadeite, calcium tschermakite, diopside, pyrope, grossular, and almandine. Isopleths of these endmember components were then compared to measured mineral chemistry for each sample and used to generate maps in pressure-temperature space of the root-mean-square error (RMSE). The results of these calculations are shown in Supplemental Figures 1 and 2, with the red areas indicating a high RSME and blue areas a low RMSE (i.e., a better fit for the measured data). Appropriate temperature estimates for calculating clinopyroxene and amphibole force constants were determined by combining these models with the mineral equilibria geothermobarometry.

Using these pressure-temperature estimates and whole-rock compositions (either measured whole-rock values or estimated values calculated using mineral chemistry and modes), we used the

meemum function in Perple_X to estimate mineral densities at the equilibrium pressure and temperature for each sample. These modeling results were then used to estimate bulk densities for the xenoliths at depth (Supplemental Data File 3, Ch4-T9).

4.14 Inter-mineral Fe isotope fractionation

Clinopyroxene-garnet Fe isotope fractionation similar to that observed in the Mercaderes xenoliths ($\Delta^{56}Fe_{cpx\text{-}gar}$ = +0.07 to +0.33‰) are also seen in eclogites from the Swiss Alps ($\Delta^{56}Fe_{cpx\text{-}gar}$ = 0.29±0.14; Beard and Johnson, 2004); Bohemian Massif ($\Delta^{56}Fe_{cpx\text{-}gar}$ = +0.27 to +0.42‰; Beard and Johnson, 2004); the Dabie orogen belt, China ($\Delta^{56}Fe_{cpx\text{-}gar}$ = +0.13 to +0.48‰; Li et al., 2016); the North Qaidam metamorphic belt, China ($\Delta^{56}Fe_{cpx\text{-}gar}$ = +0.1 to +0.37‰, ave. = +0.27‰; Liang et al., 2022); eclogite xenoliths from kimberlite pipes ($\Delta^{56}Fe_{cpx\text{-}gar}$ = 0.0 to +0.34‰, ave. = +0.18‰; Williams et al 2009); and garnet peridotites from the Czech Republic ($\Delta^{56}Fe_{cpx\text{-}gar}$ = 0.24 to +0.31‰; Beard and Johnson, 2004) (Supplemental Figure 8a). Mantle-derived garnet websterite from the Cameroon Line ($\Delta^{56}Fe_{cpx\text{-}gar}$ = +0.03 to +0.08‰; Williams et al., 2005) and metasomatized garnet peridotite from the Kaapvaal Craton ($\Delta^{56}Fe_{cpx\text{-}gar}$ = +0.01 to +0.11‰; An et al., 2017) show less clinopyroxene-garnet fractionation than is observed in the Mercaderes samples.

Although Fe isotope data of coexisting amphibole and clinopyroxene are scarce in the literature, low degrees of inter-mineral fractionation similar to those observed in the Mercaderes samples ($\Delta^{56}Fe_{amph\text{-}gar}$ = +0.23 to +0.30‰) have been reported in augite syenite from the Ilímaussaq Complex ($\Delta^{56}Fe_{cpx\text{-}amph}$ = –0.03 ± 0.05‰; Schoenberg et al., 2009), a garnet pargasite websterite from the Cameroon Line ($\Delta^{56}Fe_{cpx\text{-}amph}$ = –0.04 ± 0.08‰; Williams et al., 2005), cumulate xenoliths from Adak Island ($\Delta^{56}Fe_{cpx\text{-}amph}$ = –0.01 to +0.01‰; Sosa et al., 2023), and metasomatized spinel lherzolite from the North China Craton ($\Delta^{56}Fe_{cpx\text{-}amph}$ = –0.03 to +0.01‰; Zhao et al., 2015) (Supplemental Figure 8b). Greater clinopyroxene-amphibole isotopic fractionation is observed in retrograde eclogites from the Dabie orogen belt, China ($\Delta^{56}Fe_{cpx\text{-}amph}$ = +0.13 ± 0.10‰; Li et al., 2016).

Inter-mineral isotopic fractionation between coexisting amphibole and garnet ranges from $\Delta^{56}Fe_{amph\text{-}gar}$ = +0.10 to +0.30‰ and is consistently higher in the hornblendite (± scapolite/plagioclase) xenoliths ($\Delta^{56}Fe_{amph\text{-}gar}$ = +0.23 to +0.30‰) than the clinopyroxenite specimens ($\Delta^{56}Fe_{amph\text{-}gar}$ = +0.10 to +0.17‰) (Supplemental Figure 8c) While Fe isotope data for coexisting amphibole and garnet are also scarce in the literature, previous studies have reported levels of amphibole-garnet fractionation similar to our Mercaderes samples ($\Delta^{56}Fe_{amph\text{-}gar}$ = +0.23 to +0.30‰) in banded iron formations ($\Delta^{56}Fe_{amph\text{-}gar}$ = +0.29 to +0.43‰; Ye et al., 2020), retrograde eclogite ($\Delta^{56}Fe_{amph\text{-}gar}$ = +0.09 to +0.25‰; Li et al., 2016), and one garnet pargasite websterite ($\Delta^{56}Fe_{amph\text{-}gar}$ = +0.12 ± 0.11‰; Williams et al., 2005).

4.15 Additional modeling information

Force constants: As discussed in the text, amphibole and clinopyroxene force constants were estimated from their observed Fe isotope fractionation with coexisting garnet using the equation:

$$\Delta^{56}Fe_{B\text{-}A} = \delta^{56}Fe_B - \delta^{56}Fe_A = 2853[\langle F\rangle_B - \langle F\rangle_A]/T^2$$

The amphibole and clinopyroxene force constants calculated for each sample are shown as a function of their equilibrium temperature estimate in Supplemental Figure 9a. If our temperature estimates were not associated with Fe isotope equilibrium, and Fe diffusion continued to lower temperatures, we would expect to see strong correlations between our calculated force constant estimates and temperature. The lack of any such correlations suggests that the temperatures used in calculations are appropriate estimates. This is not surprising given the relatively slow diffusivity of Fe in garnet and clinopyroxene (Fig. S9b). Using the pre-exponential factor (D_0) and activation energy (E) of Fe in garnet and clinopyroxene, we can use the Arrhenius equation to estimate the Fe diffusion coefficient as a function of temperature:

$$D(T) = D_0 e^{(-E/RT)}$$

where T is temperature in Kelvin and R is the gas constant. We use D_0 = 3.5×10-9 m^2/s and E = 274.19 kJ/mol for garnet (Ganguly et al., 1998) and $D_0 = 6.22\times10^{-15}$ m^2/s and E = 161.5 kJ/mol for clinopyroxene (Azough and Freer, 2000). As we know the grain sizes of clinopyroxene and garnet in the xenoliths, we can calculate the time it would take Fe to diffuse from crystal cores to rims as a function of temperature from the relationship:

$$x \sim [D(T)t]^{0.5}$$

which can be rearranged to:

$$t \sim x^2/D(T)$$

where t is time in seconds. Grain radii (x) range from 0.5 to 4 mm for clinopyroxene and from 0.5 to 6 mm for garnet in the samples used for these calculations. In Supplemental Figure 9b, we calculate time scales of Fe diffusion as a function of temperature over these length scales. These back-of-the-envelope calculations show that, over time scales relevant for the xenolith suite being incorporated into the host melt and brought to the surface (days to weeks), Fe should not be lost from clinopyroxene or garnet due to diffusive exchange, as this would take on the order of thousands of years.

Fractional crystallization modeling: The starting composition for the Perple_X fractional crystallization model represents an average of four primitive Colombian basalt compositions taken from the GEOROC Northern Andean Volcanic Zone basalt/basaltic andesite compilation (Fig. S10). These data are from Marriner and Millward (1984) (sample GV 100C), Kerr et al. (1996) (sample AN173), and Villagomez et al. (2011) (samples DV111 and DV112). These samples have 9-10 wt.% MgO, high Ni (115-250 ppm), and high Cr (200-460 ppm). This basalt was fractionated along the Mercaderes geothermal gradient from 1300 °C and 2 GPa to 800 °C and 1 GPa. We started our model with an initial fO_2 of FMQ+1 and a water content of 3 wt.%.

We also ran eight sensitivity tests for this model, varying the initial water content (2-6 wt.%), composition (Mg-andesite to high-Mg basalt), amphibole and clinopyroxene force constant estimates ($<F>_{amph}$ from 211 to 253 N/m, $<F>_{cpx}$ from 210 to 244 N/m), and oxygen fugacity (FMQ to FMQ+2). The results of these tests are shown in Supplemental Figure 11, both in terms of the bulk Fe isotope composition of the cumulate and the composition of the constitute minerals. All models start with an initial δ^{56}Fe of 0.0‰. While some of these models reproduce specific characteristics of the Mercaderes suite (e.g., relatively unfractionated bulk δ^{56}Fe, observed modal mineralogy), none of them reproduced all the observed characteristics of the Mercaderes suite.

Models run at higher water contents (> 4 wt.% H_2O) produced less fractionated Fe isotope trends with respect to bulk rock compositions (0.18 - 0.20‰ variability in whole-rock δ^{56}Fe, Fig. S11a). This results from a lowering of the liquidus temperature (from 1330 °C at 2 wt.% H_2O to 1190 °C at 6 wt.% H_2O), a decrease in the temperature interval of garnet-dominated fractionation (occurring over a 350 °C temperature range at 2 wt.% H_2O and a 140 °C temperature range at 6 wt.% H_2O), and slightly earlier amphibole saturation (920 °C at 2 wt.% H_2O vs. 950 °C at 6wt% H_2O) with increased water content. As a result, the amount of garnet relative to amphibole and clinopyroxene fractioned is lower in these more hydrous systems. While higher water contents during crystallization may result in less isotopically fractionated cumulates overall, models with >4 wt.% H_2O do not produce plagioclase over the investigated pressure-temperature range, in contrast to the observed Mercaderes petrography. These more hydrous models also fail to reproduce the observed trends in garnet Fe isotope chemistry (i.e., increasingly negative δ^{56}Fe with decreasing temperature, Fig. S11b).

Relatively unfractionated bulk rock compositions (0.19‰ variability in whole-rock δ^{56}Fe) are also produced when we use a more mafic starting composition (sample 014B; Grösser et al., 1989) (Fig. S11c). Compared to the average Colombian basalt composition used in the main text, this starting composition has slightly more MgO (10.2 wt.% vs 9.1 wt.%), resulting in increased clinopyroxene fractionation relative to garnet. As our clinopyroxene force constant (227 N/m) is

closer to the force constant of the melt in this model (225 to 240 N/m) than that of garnet (110 N/m), increased clinopyroxene fractionation relative to garnet results in less melt-cumulate fractionation over the investigated pressure-temperature range. In general, these models suggest that fractional crystallization over a range of fO_2s, water contents, and initial starting compositions will result in isotopically fractionated cumulate composition and isotopically heavy late-stage melts (Fig. S12). Prolonged garnet fractionation at high pressures and temperatures depleted later-stage melts in light isotopes of Fe, resulting in the production of isotopically heavy amphibole-bearing cumulates and lower pressures and temperatures.

Amphibole dehydration model: In testing the sensitivity of our amphibole dehydration model, we varied the initial $Fe^{3+}/\Sigma Fe$ ratio from 0.15 to 0.30, the initial water content from 0.5 to 1.5 wt.% H_2O, the starting composition (diorite XC-MG-5, XC-M-1, or an average of the two samples), amphibole and clinopyroxene force constant estimates ($\langle F \rangle_{amph}$ from 211 to 253 N/m, $\langle F \rangle_{cpx}$ from 210 to 244 N/m), the threshold at which melt is extracted from the residue (4 to 10 wt.% melt), and the amount of melt remaining in the residue after each melt extraction event (1 to 0.1 wt.% melt). The results of these sensitivity tests, with respect to the residue composition, are shown in Supplemental Figure 13. While we vary the initial H_2O content from 0.5 to 1.5 wt.% to assess the effects of water content more robustly on these models, we do not consider the full extent of this range to be strictly appropriate. Given that F and Cl concentrations in amphibole from the diorite is either at or below our detection limits, we assume the primary volatile species in the amphibole structure is water (~2 wt.% H_2O). As diorite contains 50-60% amphibole and 40-50% plagioclase, and assuming plagioclase contains negligible water, we consider initial water contents of 1.0-1.2 wt.% as the most appropriate estimates for our model and thus opt to use a value of 1.2 in the model presented in the main text.

All models show similar trends, with the solidus varying from 664 to 920 °C and the total amount of melt generated varying from 34 to 41 wt.%. Amphibole and plagioclase are exhausted from all metamorphic residues between 1058-1210 °C and 1084 - 1270 °C, respectively. The final

metamorphic product is a residue composed entirely of garnet and clinopyroxene. Partial melting results in limited isotopic depletion of the original metamorphic protolith for all models, with $\delta^{56}Fe$ of the residue decreasing by 0.02 to 0.03‰ (Fig. S13). With respect to major elements, partial melting results in a decrease in Na and Ti concentrations and an increase in Fe and Mg. The final metamorphic residues produced at 2 GPa and 1300 °C are similar in major element contents to the Mercaderes garnet clinopyroxenite, albeit with slightly higher Na_2O (Fig. S14). Both major fractional crystallization and amphibole dehydration models also produced metamorphic residues that would be gravitationally unstable with respect to the underlying mantle (Figure 9 of main text).

4.16 Supplemental figures to main text

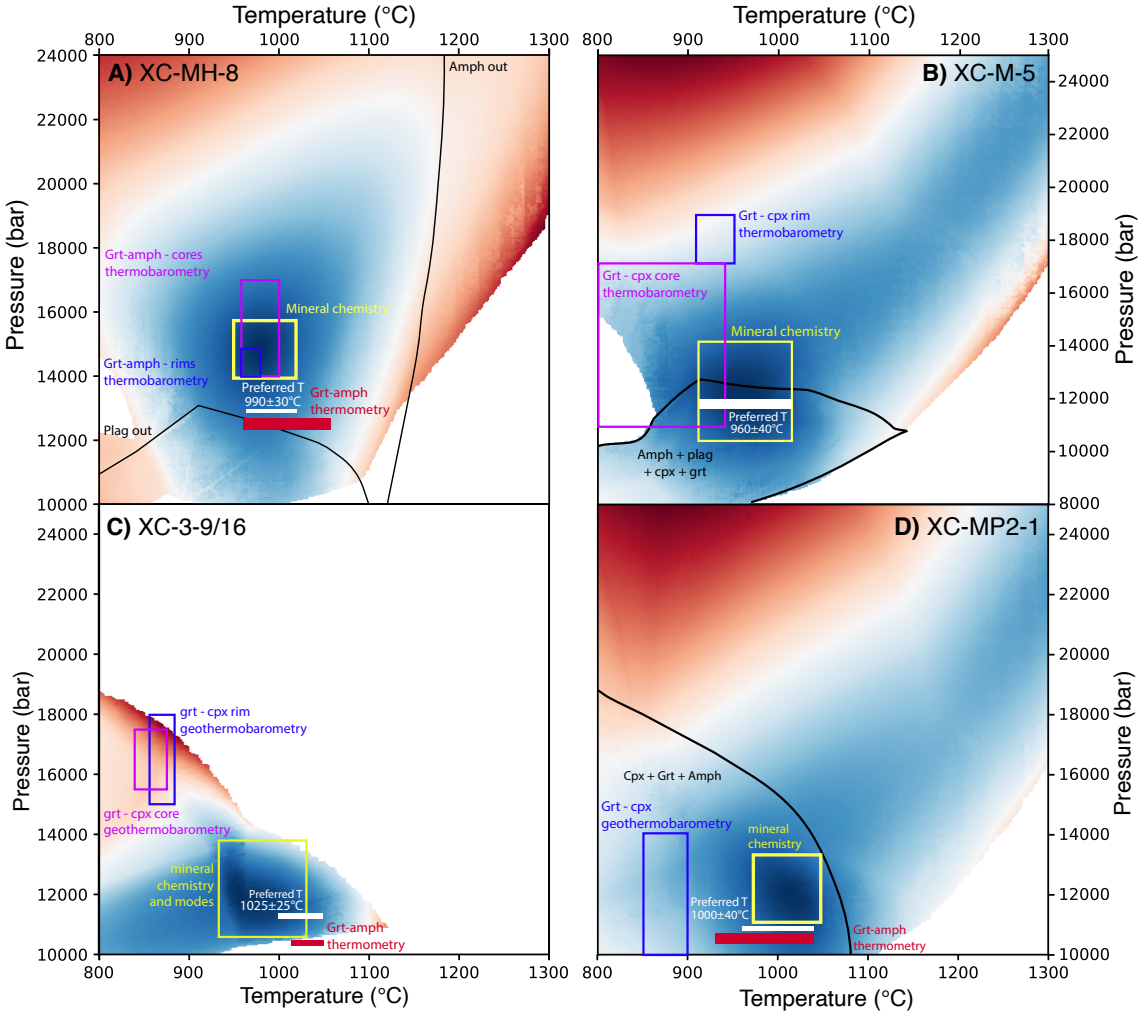

***Supplemental Figure 1*:** Map of RMSE in pressure-temperature space for garnet and clinopyroxene compositions and mineral modes for samples used to calculate $\langle F \rangle_{amph}$ from $\Delta^{56}Fe_{amph\text{-}gar}$. Colored boxes denote the equilibrium pressure-temperature range for the sample as indicated by mineral equilibria thermobarometry and white bars indicate the temperature range used to calculate the amphibole force for each sample. **A)** XC-MH-8: using a temperature of 990 ± 30 °C we calculate $\langle F \rangle_{amph}$ = 237 ± 6 N/m for this sample. **B)** XC-M-5: for this sample we use a temperature estimate of 960 ± 40 °C and calculate $\langle F \rangle_{amph}$ = 257 ± 5 N/m. **C)** XC-3-9/16: using a temperature estimate of 1025 ± 25 °C we calculated $\langle F \rangle_{amph}$ = 249 ± 5 N/m for this sample. **D)** XC-MP2-1: for this sample we used a temperature of 1000 ± 40 °C and calculated $\langle F \rangle_{amph}$ = 200 ± 6 N/m. All errors come from the uncertainties in temperature estimates. The weighted average of these values, $\langle F \rangle_{amph}$ = 232 ± 21, is used in modeling.

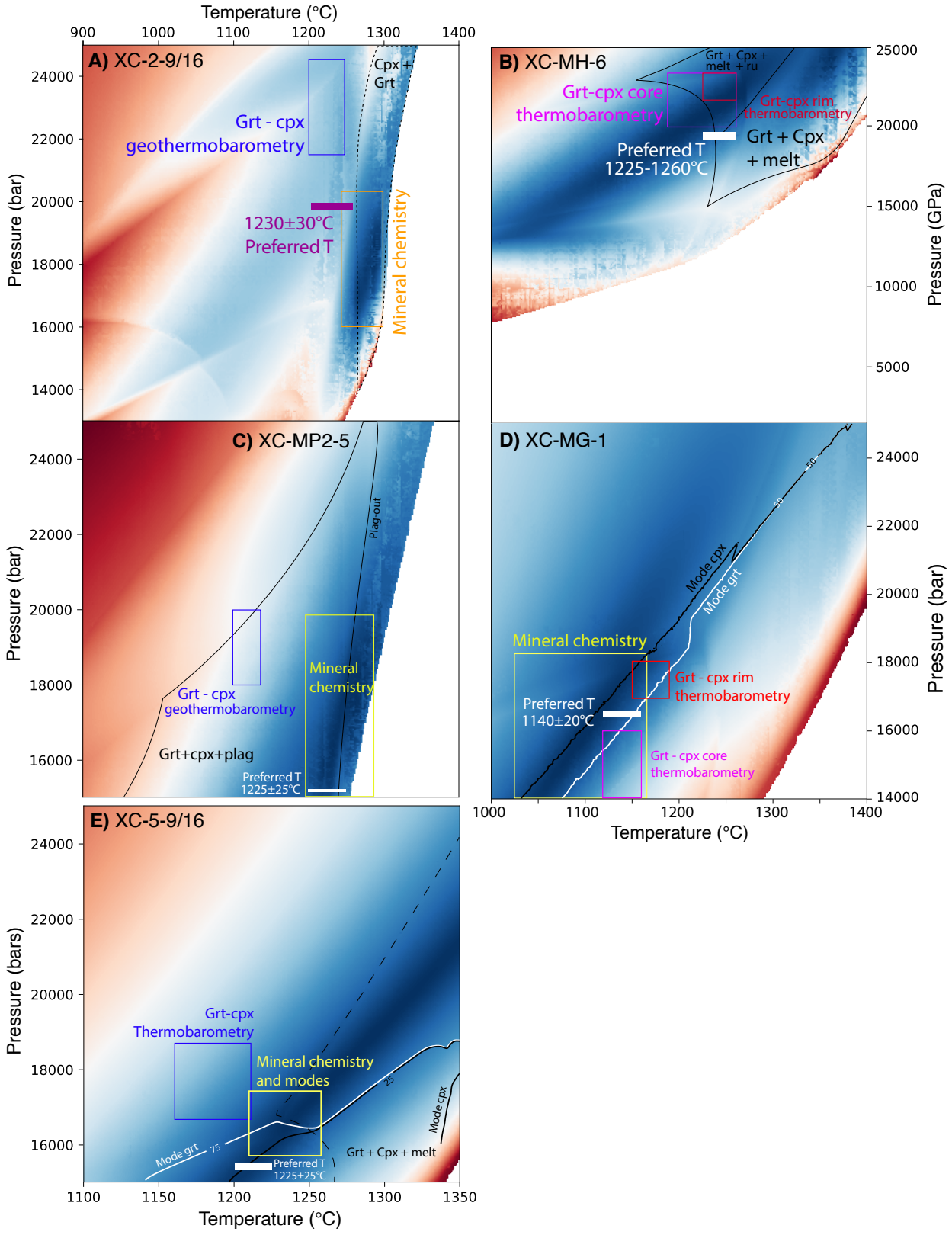
A) XC-2-9/16
Cpx + Grt
Grt - cpx geothermobarometry
1230±30°C Preferred T
Mineral chemistry
B) XC-MH-6
Grt + Cpx + melt + ru
Grt-cpx core thermobarometry
Grt-cpx rim thermobarometry
Preferred T 1225-1260°C
Grt + Cpx + melt
C) XC-MP2-5
Plag-out
Grt - cpx geothermobarometry
Mineral chemistry
Grt+cpx+plag
Preferred T 1225±25°C
D) XC-MG-1
Mode cpx
Mode grt
Mineral chemistry
Grt - cpx rim thermobarometry
Preferred T 1140±20°C
Grt - cpx core thermobarometry
E) XC-5-9/16
Grt-cpx Thermobarometry
Mineral chemistry and modes
Mode grt
Mode cpx
Grt + Cpx + melt
Preferred T 1225±25°C
Temperature (°C)
Pressure (bar)
Pressure (GPa)
Pressure (bars)

Supplemental Figure 2 **(previous page):** Map of RMSE in pressure-temperature space for garnet and clinopyroxene compositions and mineral modes for samples used to calculate $\langle F \rangle_{cpx}$ from $\Delta^{56}Fe_{cpx\text{-}gar}$. **A)** XC-2-9/16: using a temperature of 1230 ± 30 °C we calculated $\langle F \rangle_{cpx}$ = 243 ± 4 N/m for this sample. **B)** XC-MH-6: while the RMSE map does not allow us to further constrain temperature for this sample, the P-T conditions given by thermobarometry are consistent with the results of Perple_X modeling, and using a temperature range of 1225 – 1226 °C, we calculate $\langle F \rangle_{cpx}$ = 235 ± 5 N/m for this sample. **C)** XC-MP2-5: for this sample, garnet-clinopyroxene thermobarometry indicated lower temperatures than are indicated by our Perple_X modeling, likely due to uncertainties in cpx Fe+2. Instead, we use a temperature estimate of 1225 °C and estimate a $\langle F \rangle_{cpx}$ of 228 ± 6 N/m. **D)** XC-MG-1: for this sample, we use a temperature estimate of 1140 ± 20 °C and calculate $\langle F \rangle_{cpx}$ = 243 ± 4 N/m. **E)** XC-5-9/16: using an estimated temperature of 1225 ± 25 °C, we calculate $\langle F \rangle_{cpx}$ = 235 ± 4 N/m for this sample. The weighted average of these results yields a clinopyroxene force constant of 227±17 N/m.

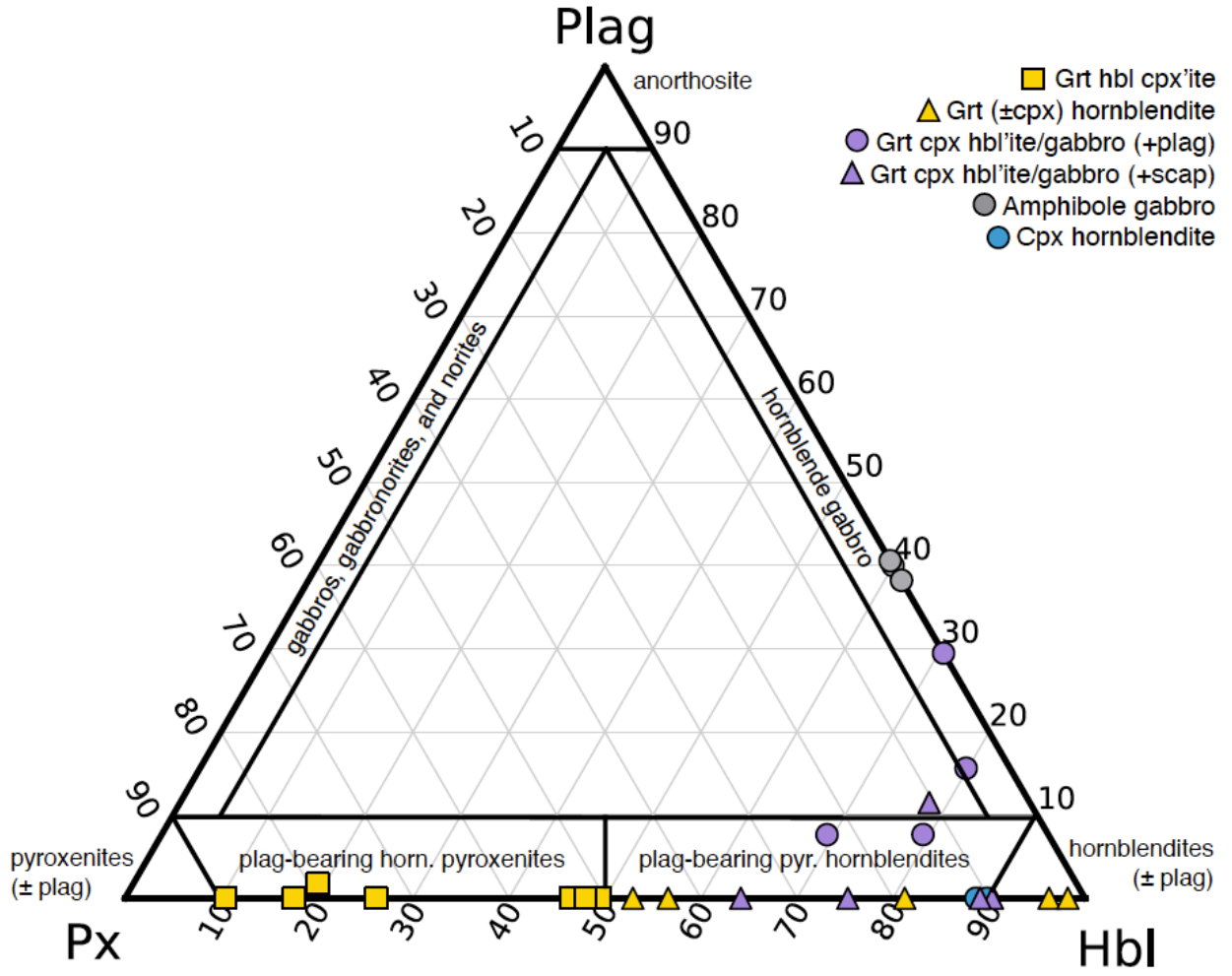

***Supplemental Figure 3*:** Classification of Mercaderes xenoliths on IUGS plagioclase (plag), pyroxene (px), and hornblende (hbl) ternary. Rocks containing only garnet and clinopyroxene are not shown but would plot on the apex of the pyroxene region of the ternary.

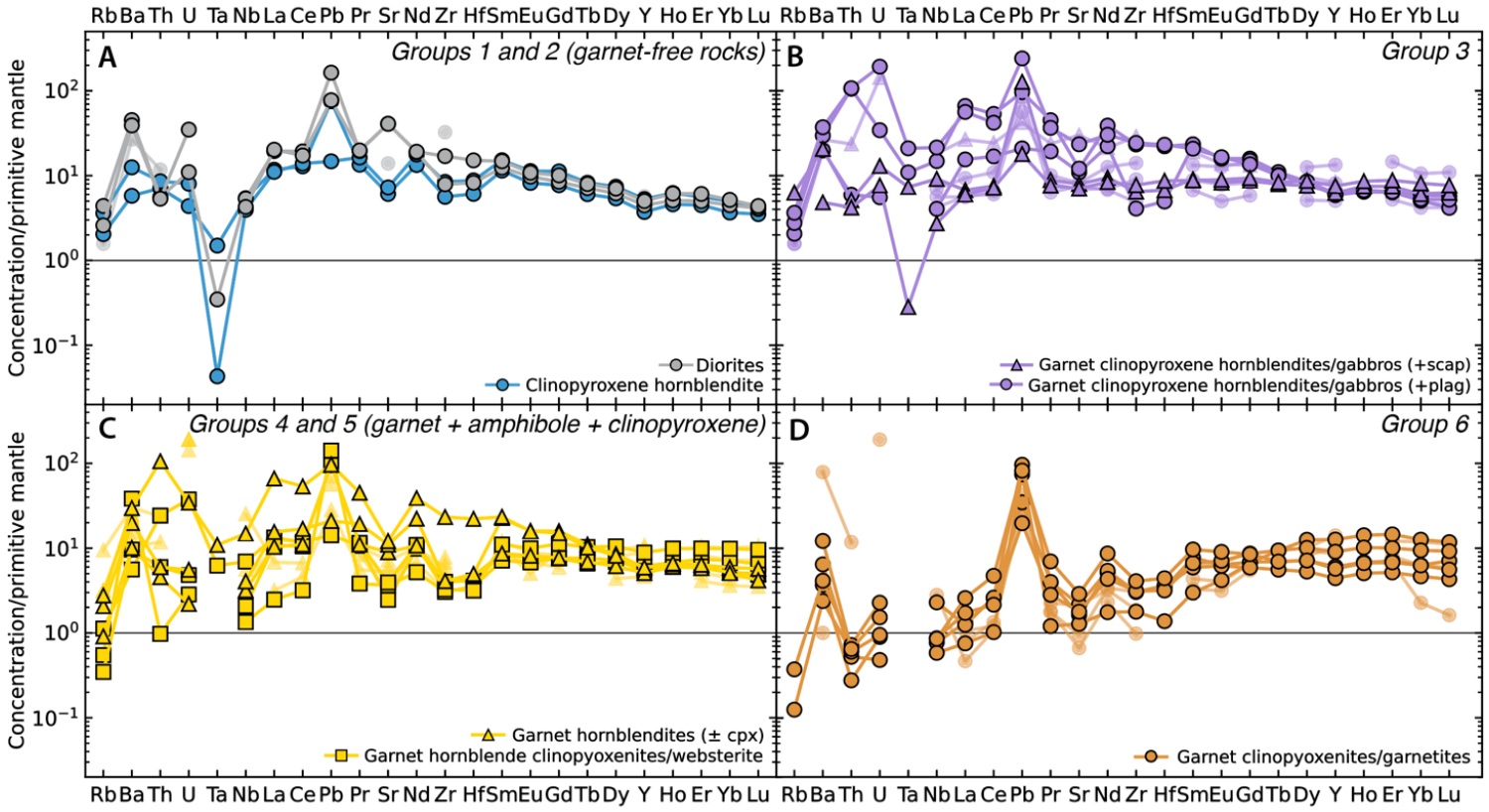

Supplemental Figure 4: Whole-rock trace element chemistry from Mercaderes xenoliths. **A)** Diorites and clinopyroxene hornblendites. **B)** Plagioclase or scapolite-bearing garnet clinopyroxene hornblendites and gabbros. **C)** Garnet hornblendites (± cpx) and garnet hornblende clinopyroxenites. **D)** Garnet clinopyroxenites. Data from Weber (1998) are represented by transparent symbols without borders.

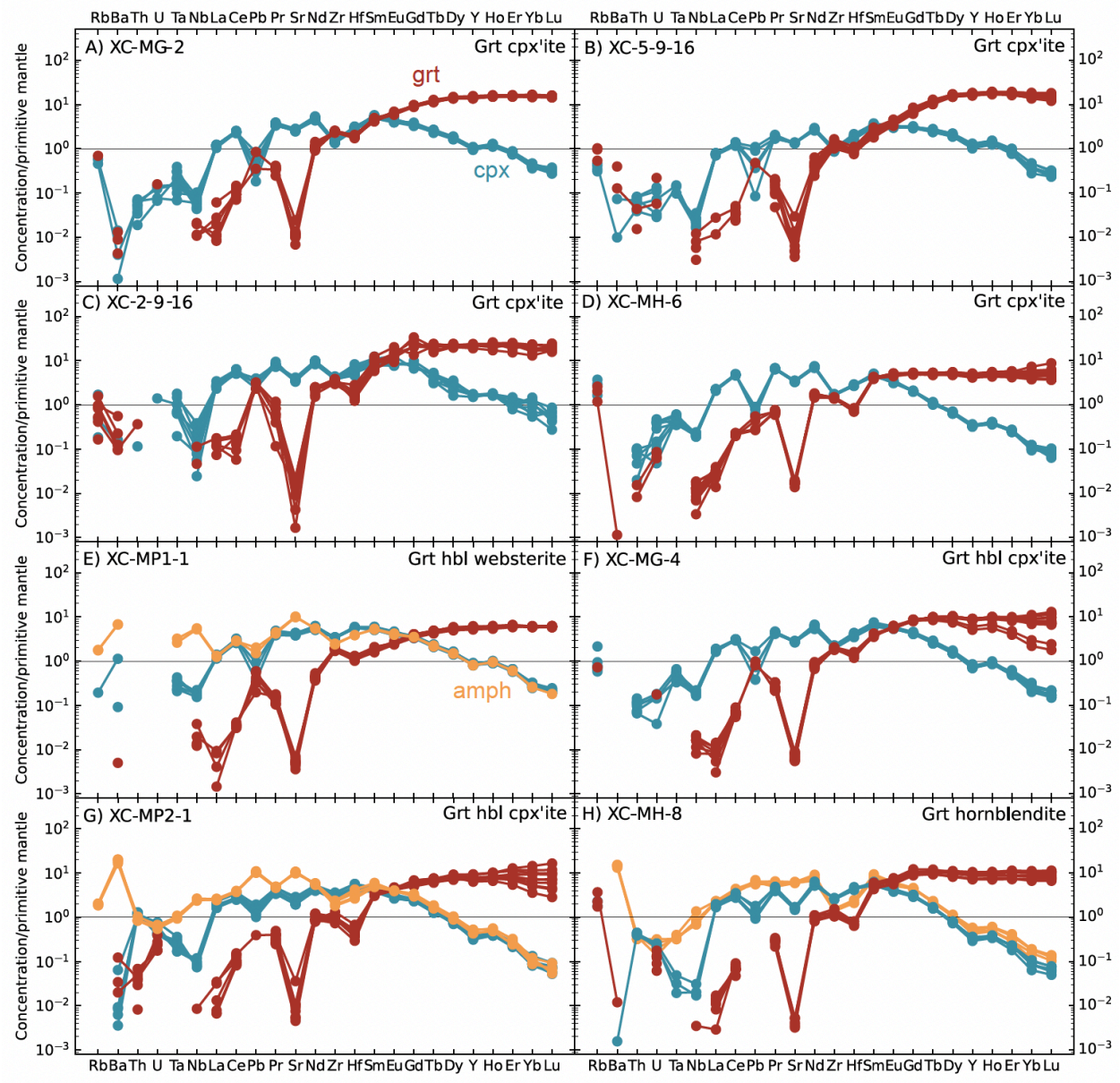

Supplemental Figure 5: Core and rim trace element garnet (red), clinopyroxene (blue), and amphibole (orange) mineral chemistry for Mercaderes xenoliths. **A)** Garnet clinopyroxenite XC-MG-2. **B)** Garnet clinopyroxenite XC-5-9-16. **C)** Garnet clinopyroxenite XC-2-9-1. **D)** Garnet clinopyroxenite XC-MH-6. **E)** Garnet hornblende websterite XC-MP1-1. **F)** Garnet hornblende clinopyroxenite XC-MG-4. **G)** Garnet hornblende clinopyroxenite XC-MP2-1. **H)** Garnet hornblendite XC-MH-8. Unless noted, there is no systematic difference between core and rim compositions.

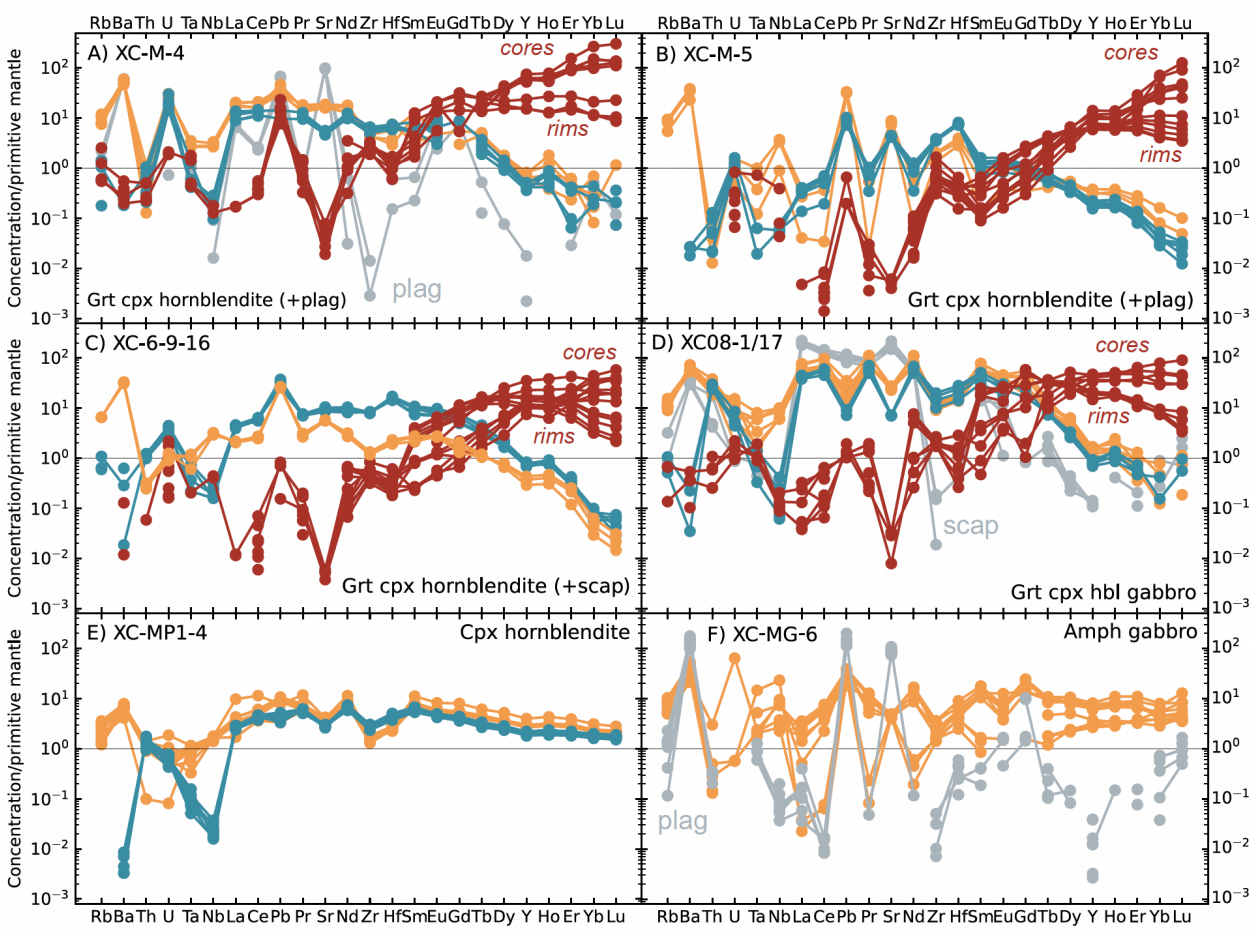

Supplemental Figure 5: Core and rim trace element garnet (red), clinopyroxene (blue), amphibole (orange), plagioclase (grey, labeled), and scapolite (grey, labeled) mineral chemistry for Mercaderes xenoliths. **A)** Plagioclase-bearing garnet clinopyroxene hornblendite XC-M-4. **B)** Plagioclase-bearing garnet clinopyroxene hornblendite XC-M-5. **C)** Scapolite-bearing garnet clinopyroxene hornblendite XC-M-4. **D)** Garnet clinopyroxene hornblende gabbro XC08-1/17. **D)** Clinopyroxene hornblendite XC-MP1-4. **E)** Diorite XC-MG-6. Unless noted, there is no systematic difference between core and rim compositions.

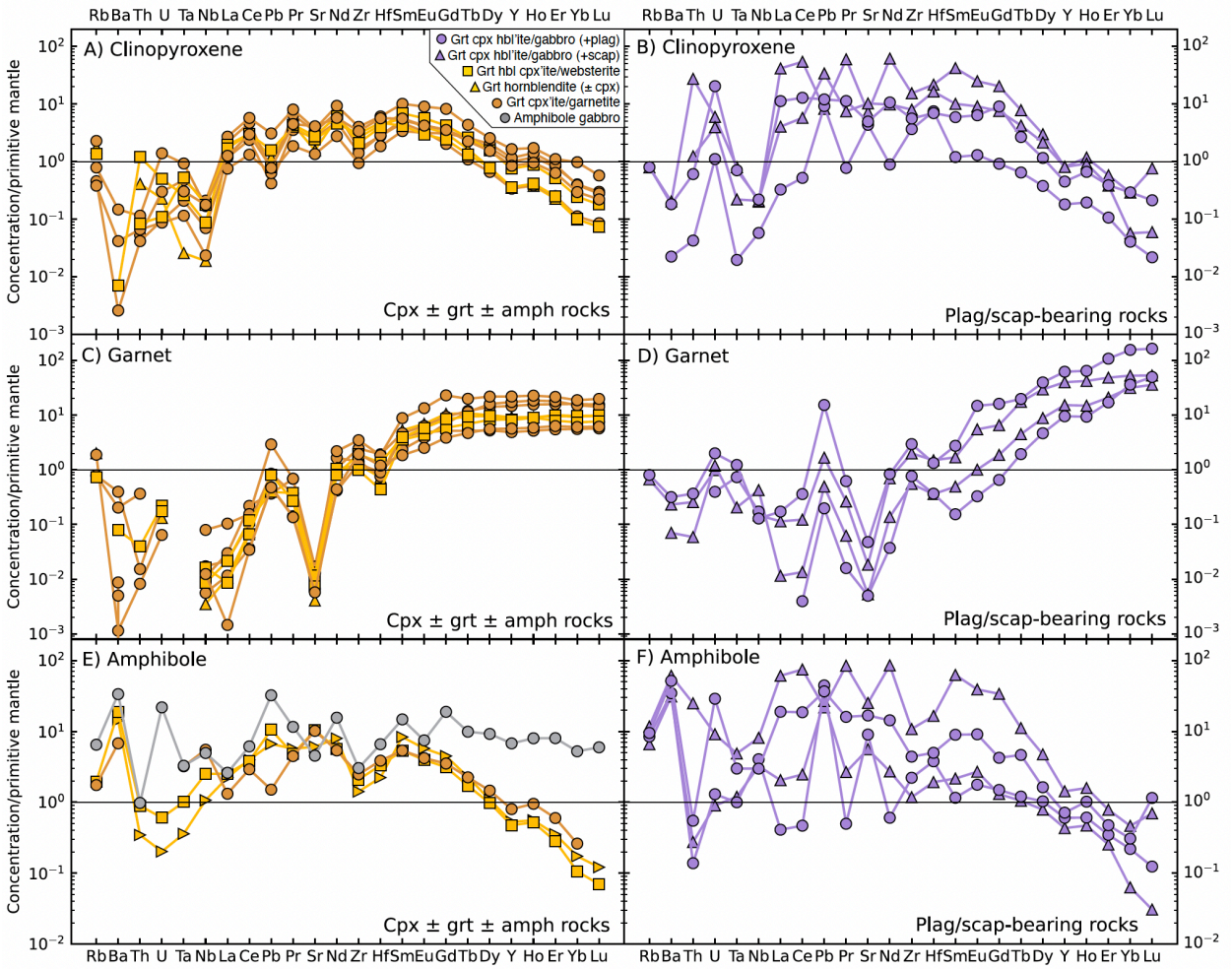

Supplemental Figure 6: Summary of trace element average core mineral chemistry. Primitive mantle normalized spider diagrams for Mercaderes clinopyroxene (**A** & **B**), garnet (**C** & **D**), and amphibole (**E** & **F**) cores. Data for minerals from the plagioclase/scapolite-bearing garnet clinopyroxene hornblendites and gabbros (Group 2) are shown separately (panels **B**, **C**, and **D**) to emphasize the disequilibrium trace element patterns of these samples.

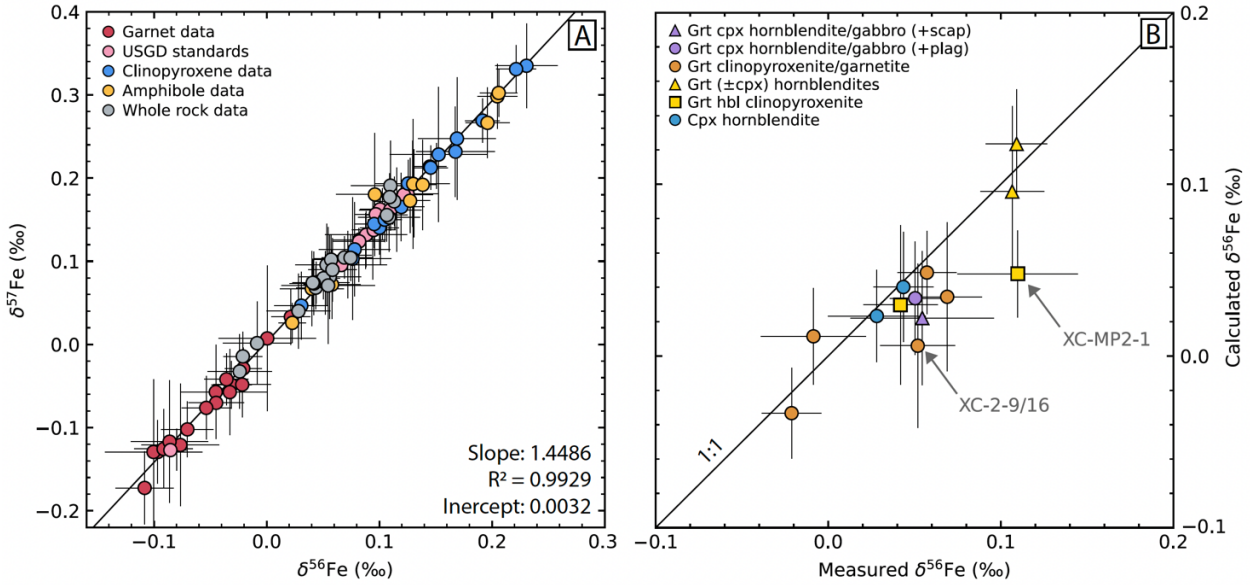

Supplemental Figure 7: Quality assessment of Fe isotope data. **A)** δ^{56}Fe vs. δ^{57}Fe (‰) of all measured samples. A linear regression through the data gives a slop of 1.4486 and an intercept of 0.0032, in excellent agreement with the expected mass-dependent fractionation (δ^{57}Fe ≈1.5 × δ^{56}Fe, Dauphas et al., 2017) and illustrating the accuracy of our Fe isotope measurements. **B)** Measured vs calculated whole-rock Fe isotope composition of Mercaderes samples. Whole-rock compositions were calculated using the modes, densities, major element chemistry, and measured δ^{57}Fe of minerals for each sample. Apart from samples XC-2-9/16 and XC-MP2-1, the measured and calculated values are within error of each other (~0.03‰).

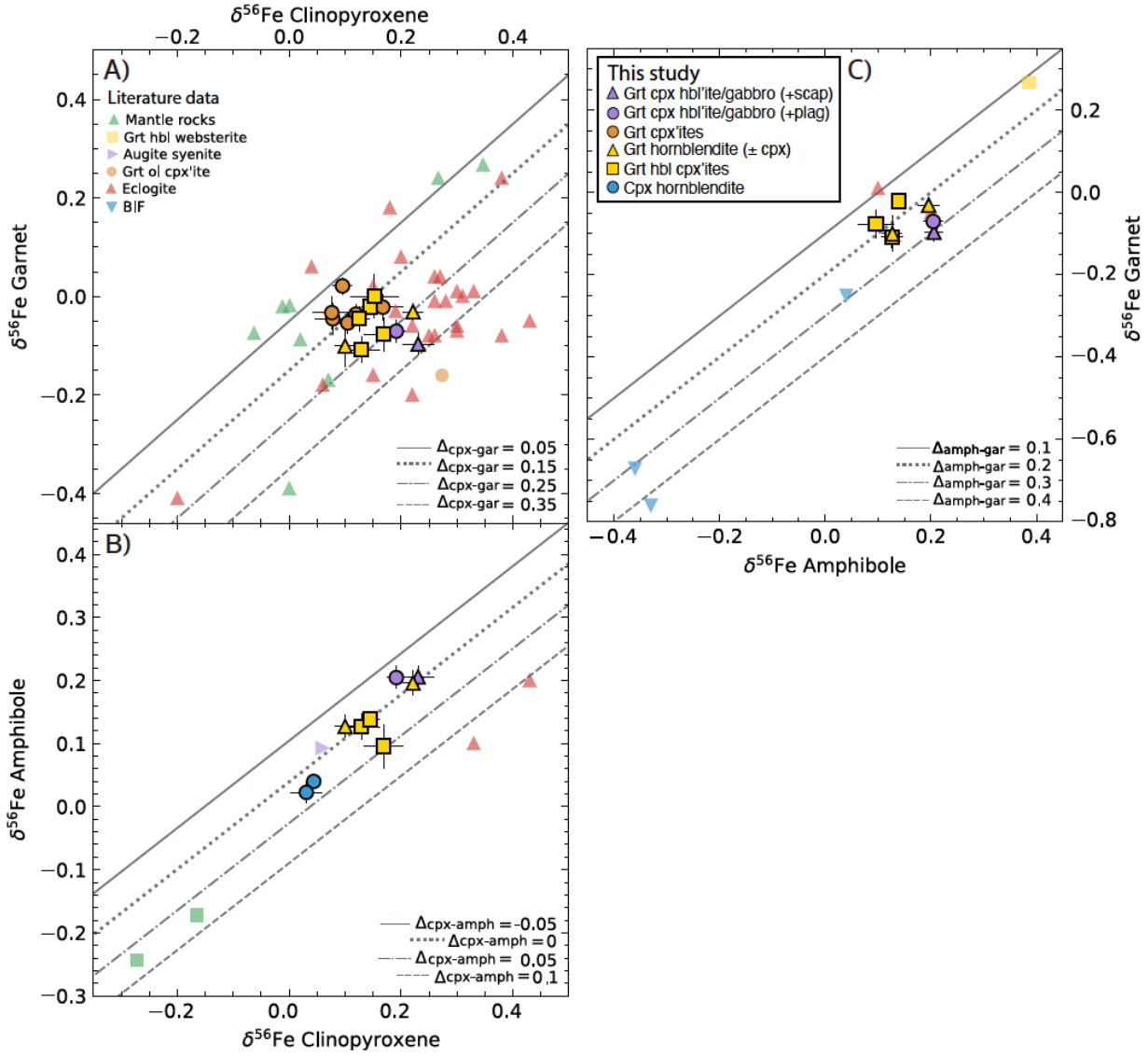

Supplemental Figure 8: Inter-mineral Fe isotope fractionation for garnet, amphibole, and clinopyroxene mineral separates from Mercaderes compared to literature data. Eclogite data is from Beard and Johnson (2004), Williams et al. (2009), Li et al. (2016), and. Liang et al. (2022). Mantle garnet peridotite, websterite, and clinopyroxenite data are from Williams et al. (2005), Beard and Johnson (2004), and An et al. (2017). Banded iron formation (BIF) data is from Ye et al. (2020). Syenite data is from Schoenberg et al. (2009).

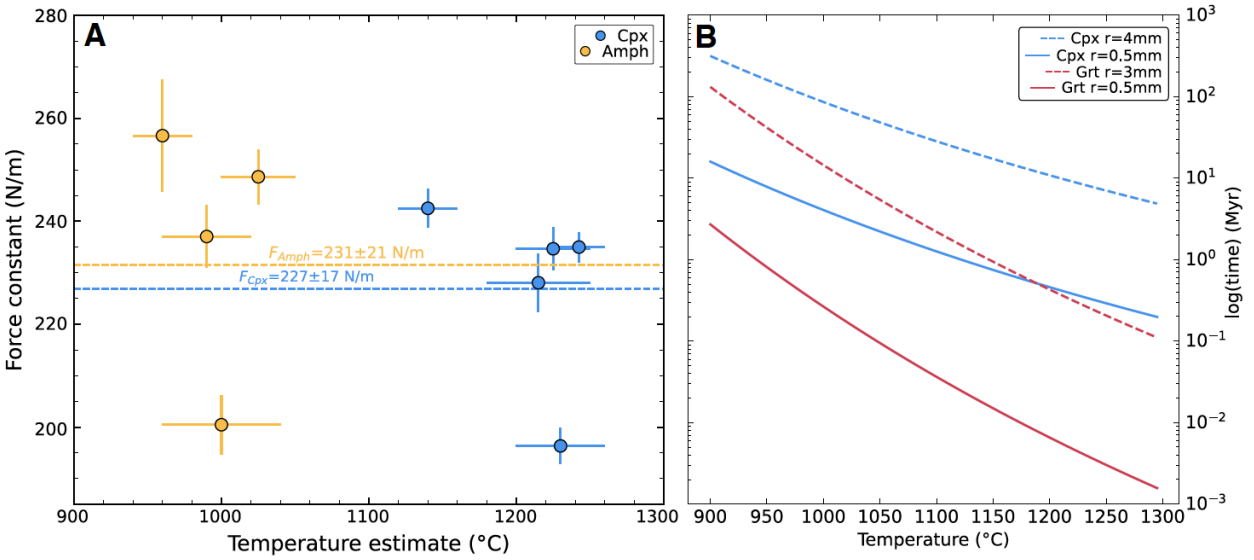

Supplemental Figure 9: **A)** Force constant estimates for amphibole and clinopyroxene as a function of equilibrium temperature for the Mercaderes xenoliths. **B)** Time scales (shown as log millions of years) for Fe to diffuse from clinopyroxene and garnet crystals with radii ranging from 0.5 to 4 mm and 0.5 to 4 mm, respectively.

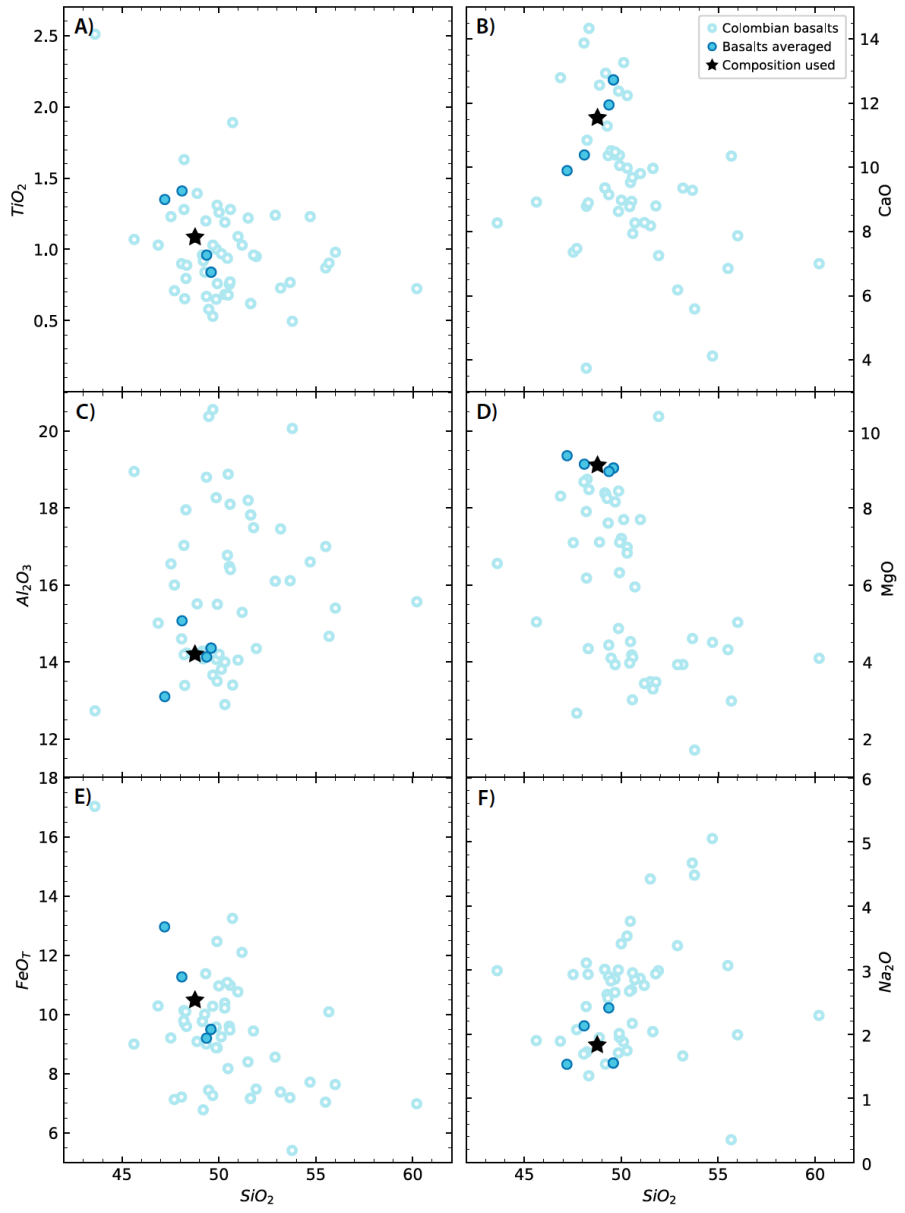

Supplemental Figure 10: Lava used in fractional crystallization modeling. Open circles represent Pre-compiled Northern Andean Volcanic Zone basalt/basaltic andesite compilation from GeoRoc. Filled circles represent high-MgO (9-10 wt.% MgO) basalts averaged to form the starting composition used in our fractional crystallization model (filled star). The basalt compositions we averaged are from Marriner and Millward (1984), Kerr et al. (1996), and Villagomez et al. (2011).

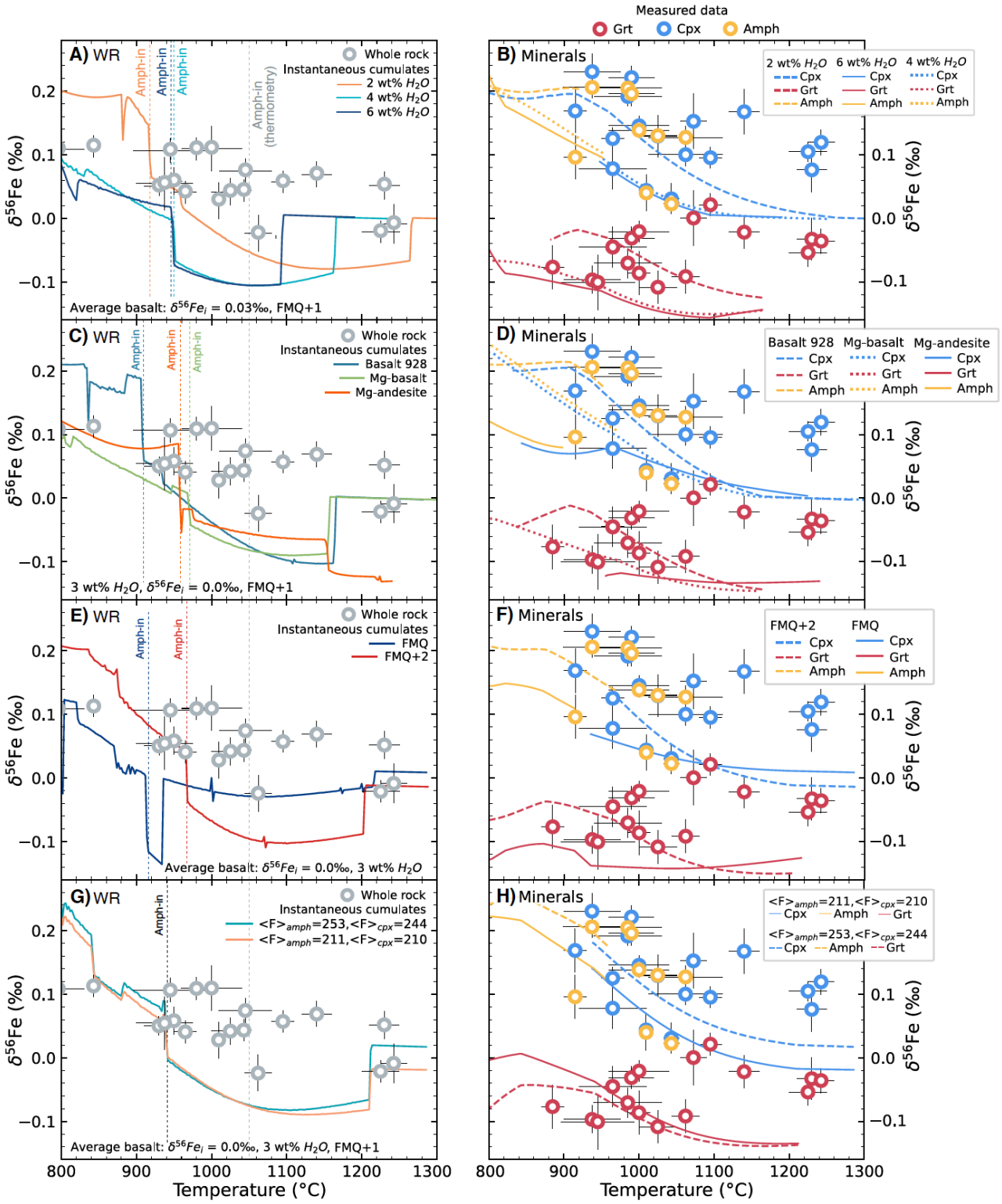
Measured data
Grt
Cpx
Amph
A) WR
Whole rock
Instantaneous cumulates
2 wt% H_2O
4 wt% H_2O
6 wt% H_2O
Amph-in
Amph-in
Amph-in
Amph-in (thermometry)
Average basalt: $\delta^{56}Fe_i$ = 0.03‰, FMQ+1
B) Minerals
2 wt% H_2O 6 wt% H_2O 4 wt% H_2O
Cpx
Grt
Amph
C) WR
Basalt 928
Mg-basalt
Mg-andesite
3 wt% H_2O, $\delta^{56}Fe_i$ = 0.0‰, FMQ+1
D) Minerals
Basalt 928 Mg-basalt Mg-andesite
E) WR
FMQ
FMQ+2
Average basalt: $\delta^{56}Fe_i$ = 0.0‰, 3 wt% H_2O
F) Minerals
FMQ+2 FMQ
G) WR
<F>$_{amph}$=253,<F>$_{cpx}$=244
<F>$_{amph}$=211,<F>$_{cpx}$=210
Average basalt: $\delta^{56}Fe_i$ = 0.0‰, 3 wt% H_2O, FMQ+1
H) Minerals
δ^{56}Fe (‰)
Temperature (°C)

Supplemental Figure 11: (previous page) - sensitivity tests for fractional crystallization models. Oxygen fugacity, melt composition, and water content are varied in these models. Dotted vertical lines denote the temperature and which amphibole enters the crystallizing assemblage for each model and are compared to the minimum temperature at which mineral equilibria thermometry and Perple_X model for the Mercaderes samples suit suggest amphibole should enter the assemblage (~1050 °C). **A)** Whole-rock instantaneous Fe isotope composition of cumulates for fractional crystallization of an average Colombian basalt at FMQ+1 for 2, 4, and 6 wt.% initial H_2O. Complementary mineral Fe isotope compositions for each model are shown in **(B)** and compared to measured mineral values. **C)** Whole-rock instantaneous Fe isotope cumulate compositions from fractional crystallization models of Mercaderes basalt 928 (Weber, 1998), an average Colombian high-Mg andesite, and a representative Colombian Mg-basalt (sample 014B; Grösser et al., 1989). Complementary mineral Fe isotope compositions for these models are given in **(D)**. The effects of varying oxygen fugacity from FMQ to FMQ+2 on the instantaneous Fe isotope cumulate composition of our average Colombian basalt with 3 wt.% initial H_2O is shown in (**E**), with the complementary Fe isotope compositions of minerals in the cumulates shown in **(F)**. The force constants for amphibole and clinopyroxene are varied in **(G)** and **(F)** to reflect the uncertainties in our estimates, with $\langle F \rangle_{amph}$ ranging from 211 to 253 N/m and $\langle F \rangle_{cpx}$ from 210 to 244 N/m. All other model parameters are the same as in Figure 6 of the main text.

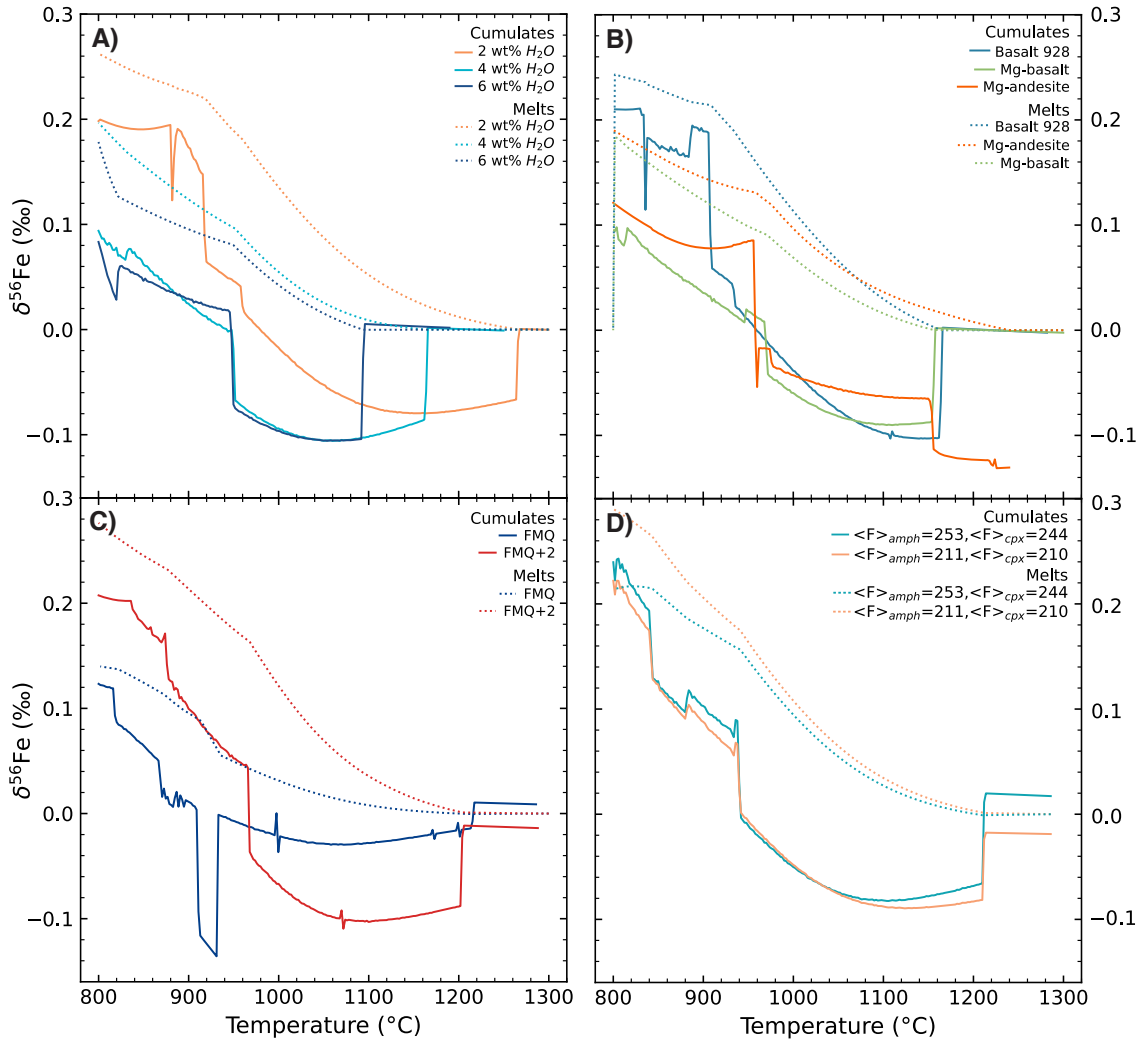

Supplemental Figure 12: Evolution of cumulates (solid lines) and their parental melts (dotted lines) in Perple_X fractional crystallization modeling in sensitivity tests. **A)** Cumulate and melt Fe isotope composition for fractional crystallization of an average Colombian basalt at FMQ+1 for 2, 4, and 6 wt.% initial H_2O. **B)** Cumulate and melt δ^{56}Fe for fractional crystallization of Mercaderes basalt 928 (Weber, 1998), an average Colombian high-Mg andesite, and a representative Colombian Mg-basalt (sample 014B; Grösser et al., 1989), all with an initial H_2O of 3 wt.%. **C)** Cumulate and melt Fe isotope composition for fractional crystallization of an average Colombian basalt with 3 wt.% H_2O varying fO_2 from FMQ to FMQ+2. **D)** Fe isotope composition of cumulates and melts varying $\langle F \rangle_{amph}$ from 211 to 253 N/m and $\langle F \rangle_{cpx}$ from 210 to 244 N/m. All other model parameters are the same as in Figure 6 of the main text (average Colombian basalt from Supplemental Figure 10 used as starting composition, with 3 wt.% H_2O, and fO_2 = FMQ+1).

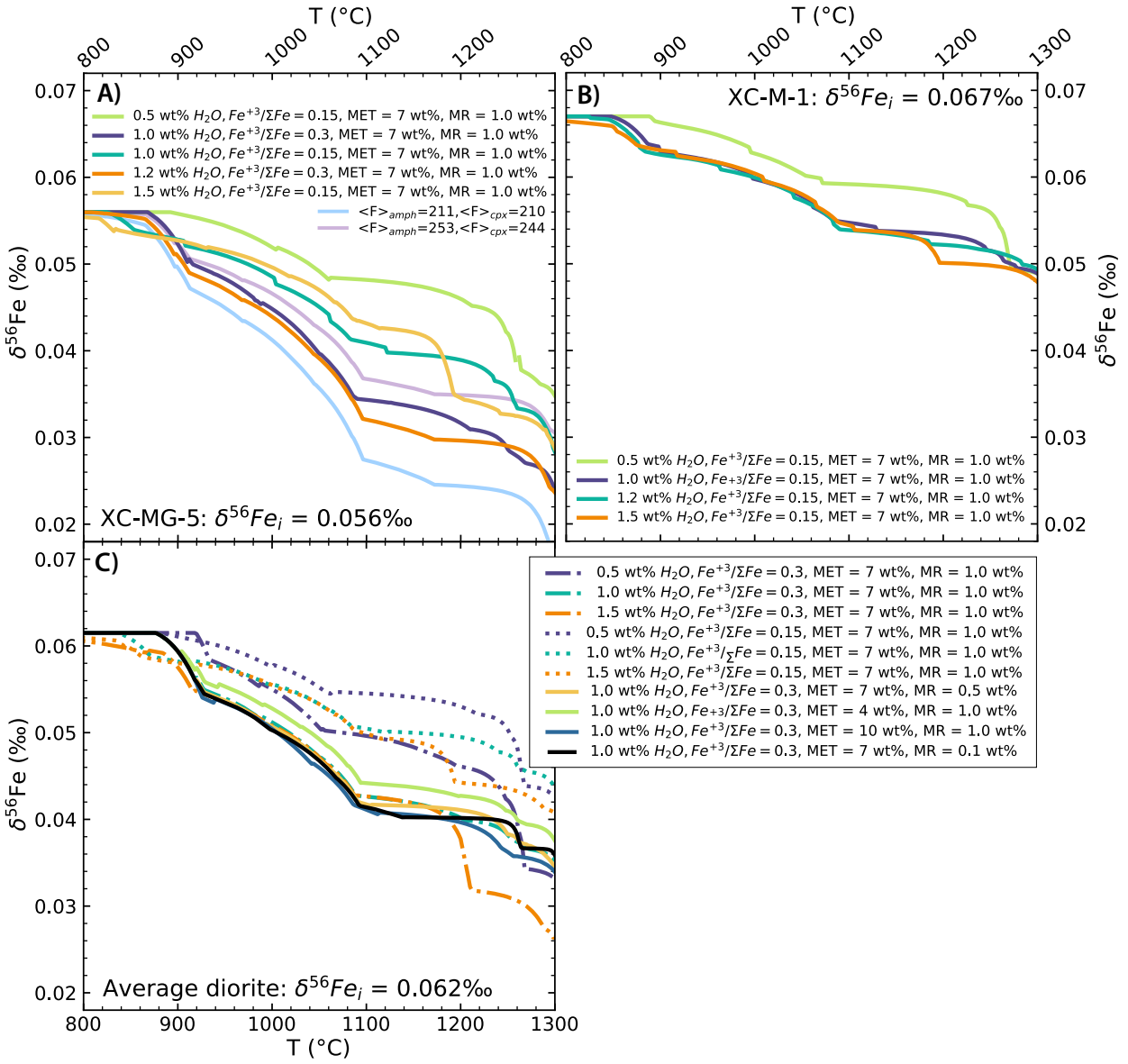

Supplemental Figure 13: Sensitivity tests for amphibole dehydration model showing the range of possible metamorphic residue compositions. Initial composition (XC-M-1, XC-MG-5, or average Mercaderes diorite), initial water content (0.5-1.5 wt.%), initial $Fe^{+3}/\Sigma Fe$ (0.15-0.3), melt mass extraction threshold (MET) (4-10 wt.%), and the mass of melt left in the residue after each extraction event (MR) (0.1 to 1 wt.%) are varied in these models. In (**A**), for the test where we vary $<F>_{amph}$ and $<F>_{cpx}$, all parameters except force constant are the same as they are in the model we present in Figure 7 of the main text.

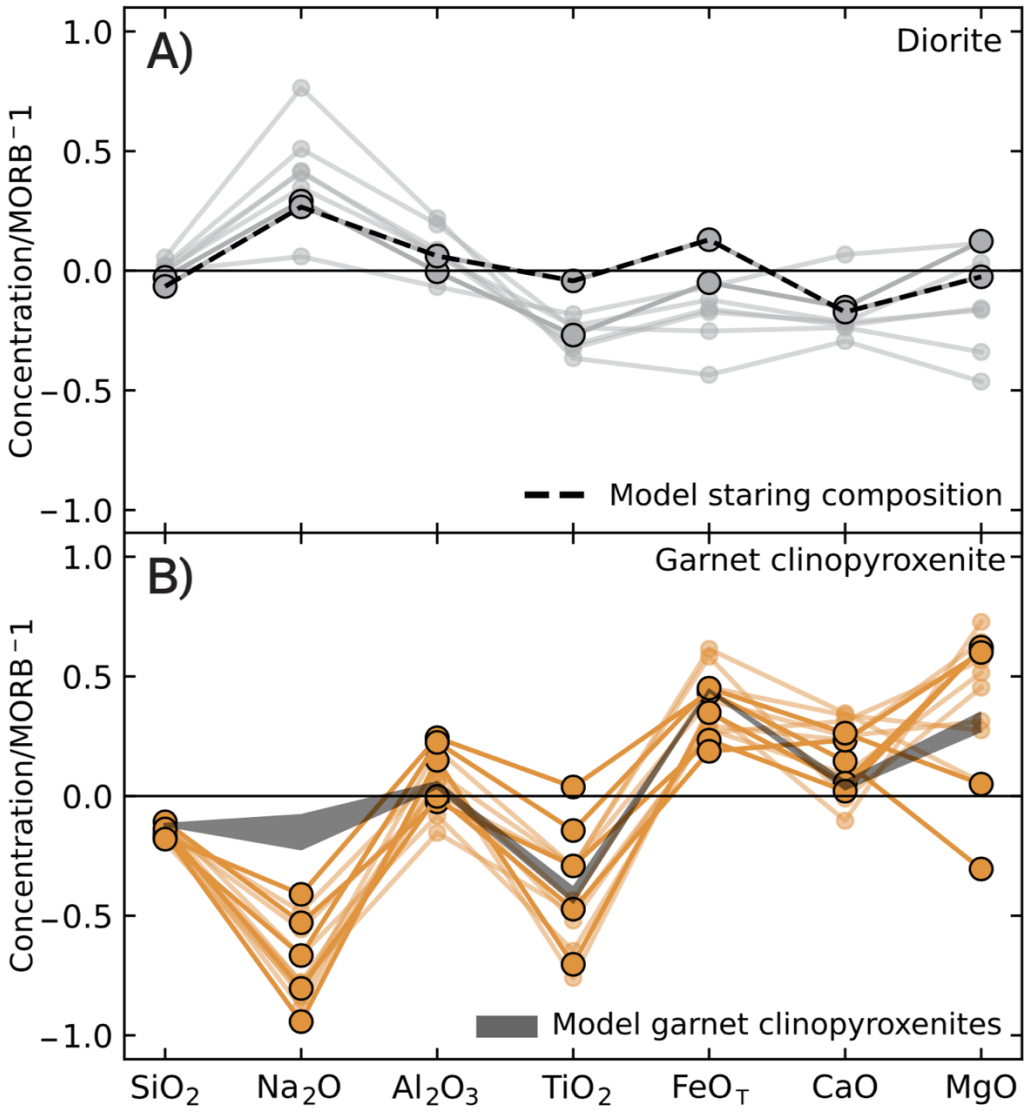

***Supplemental Figure 14*:** Major element whole-rock composition of (**A**) diorite and (**B**) garnet clinopyroxenites from suite Mercaderes. Dashed line in (**A**) represents the starting composition for the amphibole dehydration partial melting model, and shaded field in (**B**) represents garnet clinopyroxenite compositions from the model after 35% melt extraction (by mass). Literature data (Weber et al., 1998; Bloch et al., 2017) is represented by opaque symbols and lines. All data normalized to MORB (Klein et al., 2004). While our amphibole dehydration model does not fully reproduce the depletions in sodium observed in Mercaderes garnet clinopyroxenite relative to diorite, it does accurately reproduce the major element chemistry with respect to SiO_2, Al_2O_3, TiO_2, FeO_T, CaO, and MgO.

4.17 Additional sample information

Below are several additional plots, microscope photos, and XRF maps that were not discussed in the main text but provide additional context and information about the sample suite.

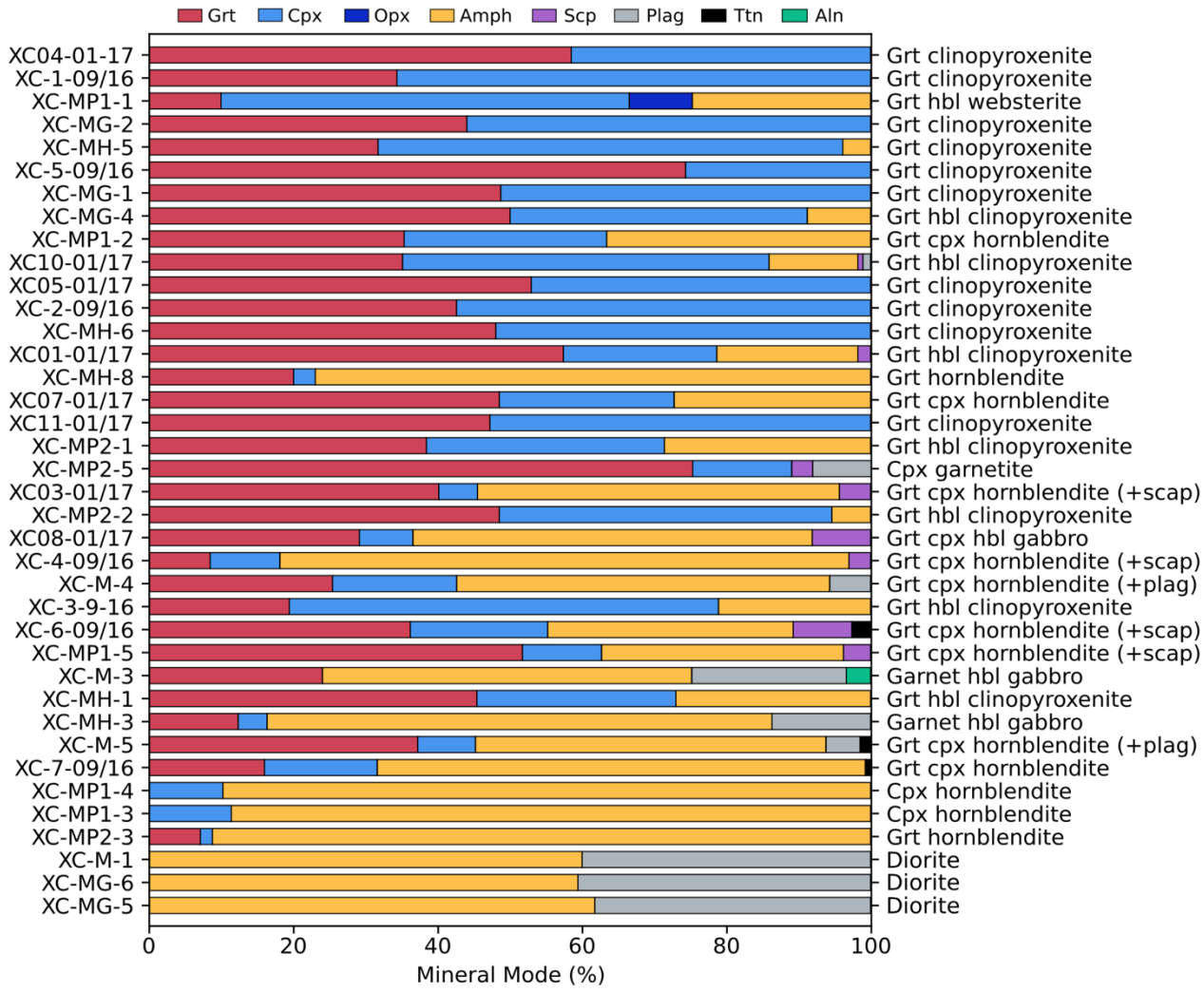

Supplemental Figure 15: Mineral modes of Mercaderes xenoliths, listed in order of decreasing Mg# of garnet cores followed by Mg# of clinopyroxene and then amphibole. Mineral abbreviations are: *Grt*, garnet; *cpx*, clinopyroxene; *opx*, orthopyroxene; *scap*, scapolite, *plag*, plagioclase; and *Hbl*, hornblende.

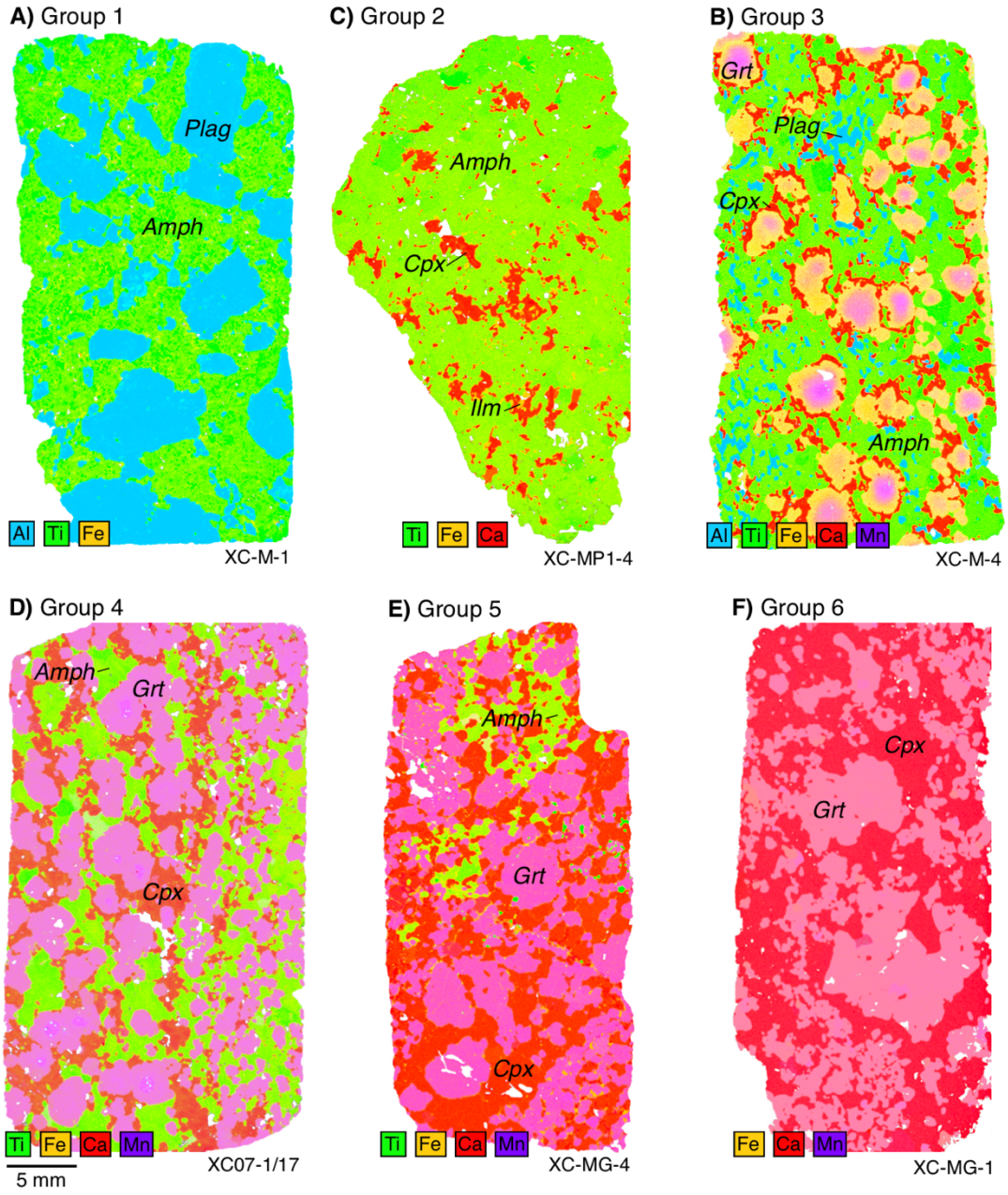

***Supplemental Figure 16*:** micro-XFR element maps of selected Mercaderes xenoliths. **A)** Group 1: Al-Ti-Fe map of diorite XC-M-1. **B)** Group 2: Al-Ti-Fe-Ca-Mn map of plagioclase-bearing garnet clinopyroxene hornblendite XC-M-4, showing core-to-rim Mn zoning in garnets. **C)** Group 3: Ti-Fe-Ca map of clinopyroxene hornblendite XC-MP1-4. **D)** Group 4: Ti-Fe-Ca-Mn map of garnet clinopyroxene hornblendite XC07-1/17. **E)** Group 5: Ti-Fe-Ca-Mn garnet hornblendite clinopyroxenite XC-MG-4. **F)** Group 6: Fe-Ca-Mn map of garnet clinopyroxenite XC-MG-2.

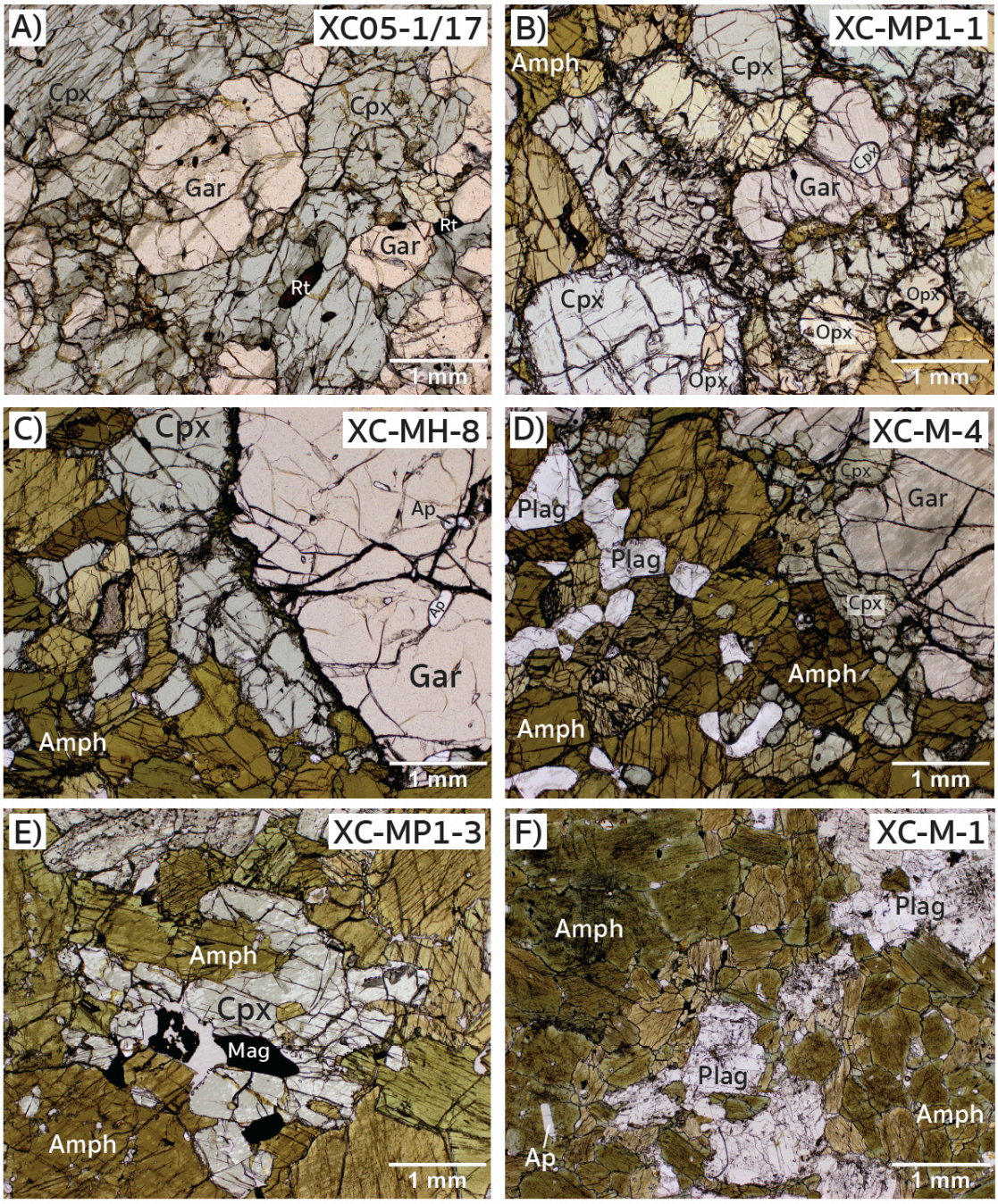

Supplemental Figure 17: Photomicrographs of Mercaderes xenoliths in plane-polarized light. **A)** Garnet clinopyroxenite XC05-1/17. **B)** Garnet hornblende websterite XC-MP1-1. **C)** Garnet hornblendite XC-MH-8. **D)** Plagioclase-bearing garnet clinopyroxene hornblendite XC-M-4, showing cpx corona around garnet. **E)** Clinopyroxene hornblendite. **F)** Diorite XC-M-1.

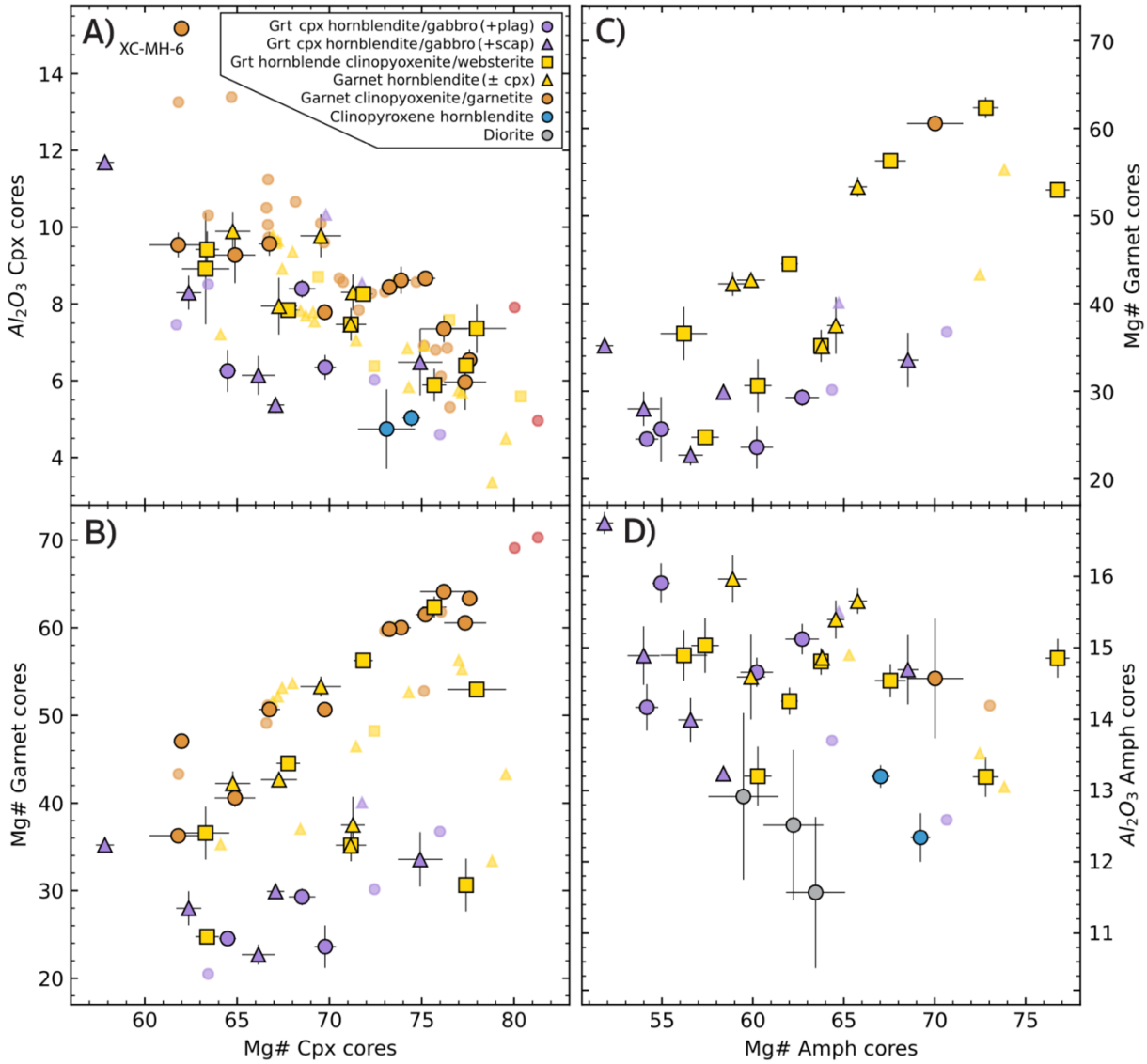

Supplemental Figure 18: Additional data for core mineral chemistry from the Mercaderes xenoliths. **A**) Average core Mg# vs. Al_2O_3 (wt.%) for clinopyroxene. **B**) Average core Mg# for clinopyroxene vs average core Mg# for coexisting garnet. **C**) Average core Mg# for amphibole vs average core Mg# for coexisting garnet. **D**) Average core Mg# vs. Al_2O_3 (wt.%) for amphibole. Literature data (Weber, 1998; Bloch et al., 2017; Zieman et al., 2023; Gianola et al., 2023) are represented by transparent symbols without borders. Garnets from the plagioclase-free assemblages have higher core Mg# than those from the plagioclase and scapolite-bearing rocks and are offset to clinopyroxene Al_2O_3 and a given Mg#. Apart from this, all lithological groups display surprisingly consistent mineral chemistry, with no apparent trends in clinopyroxene Mg#, amphibole Mg#, or amphibole Al_2O_3 and lithology.

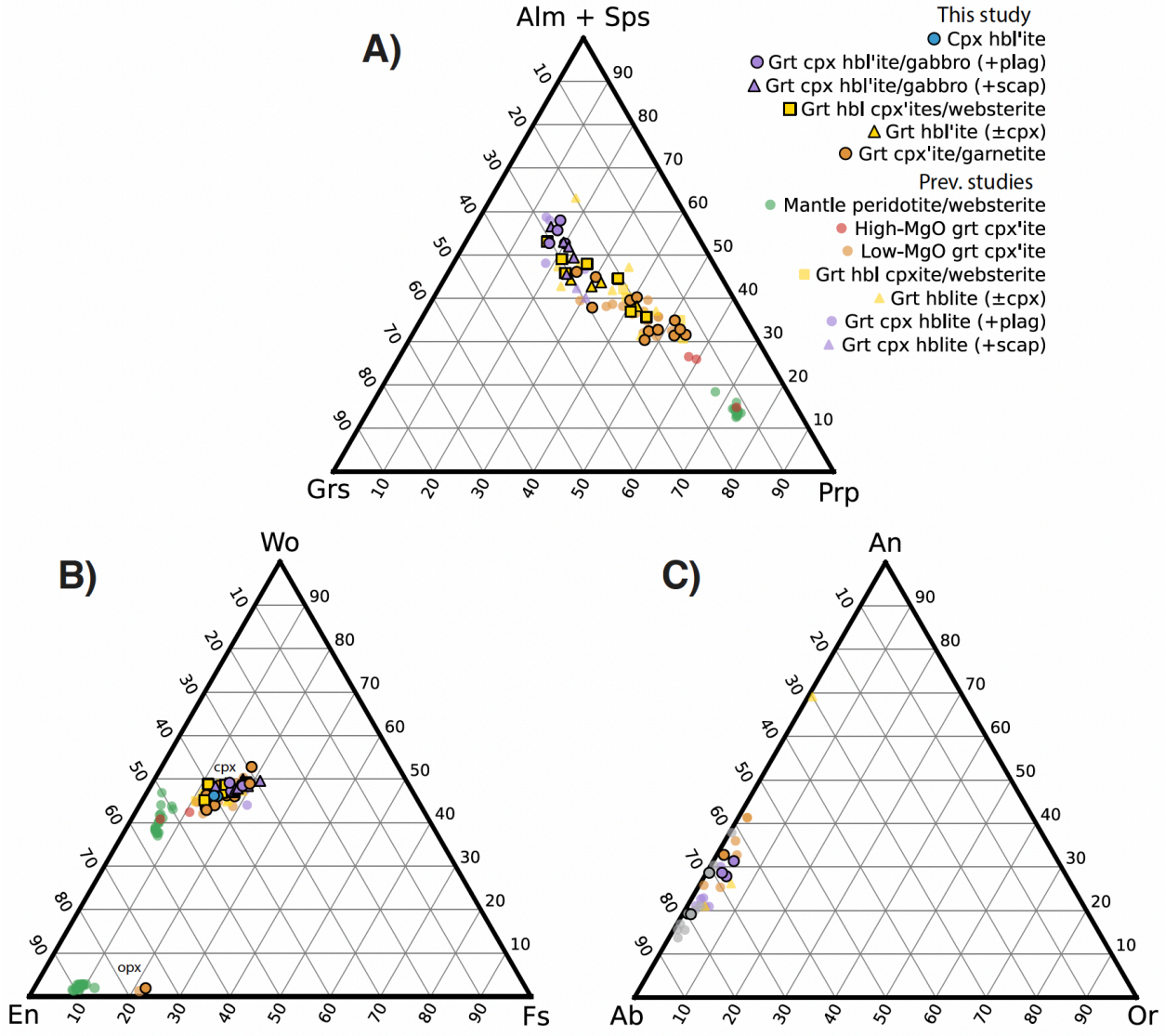

***Supplemental Figure 19*:** Mineral chemistry ternary diagrams for garnet, clinopyroxene, and amphibole. **A)** Garnet ternary diagram for Mercaderes xenoliths. **B)** Pyroxene enstatite-ferrosilite-wollastonite ternary diagram for Mercaderes xenoliths. **C)** Plagioclase ternary diagram for Mercaderes xenoliths. Literature data (Weber, 1998; Bloch et al., 2017; Zieman et al., 2023; Gianola et al., 2023) are represented by transparent symbols without borders.

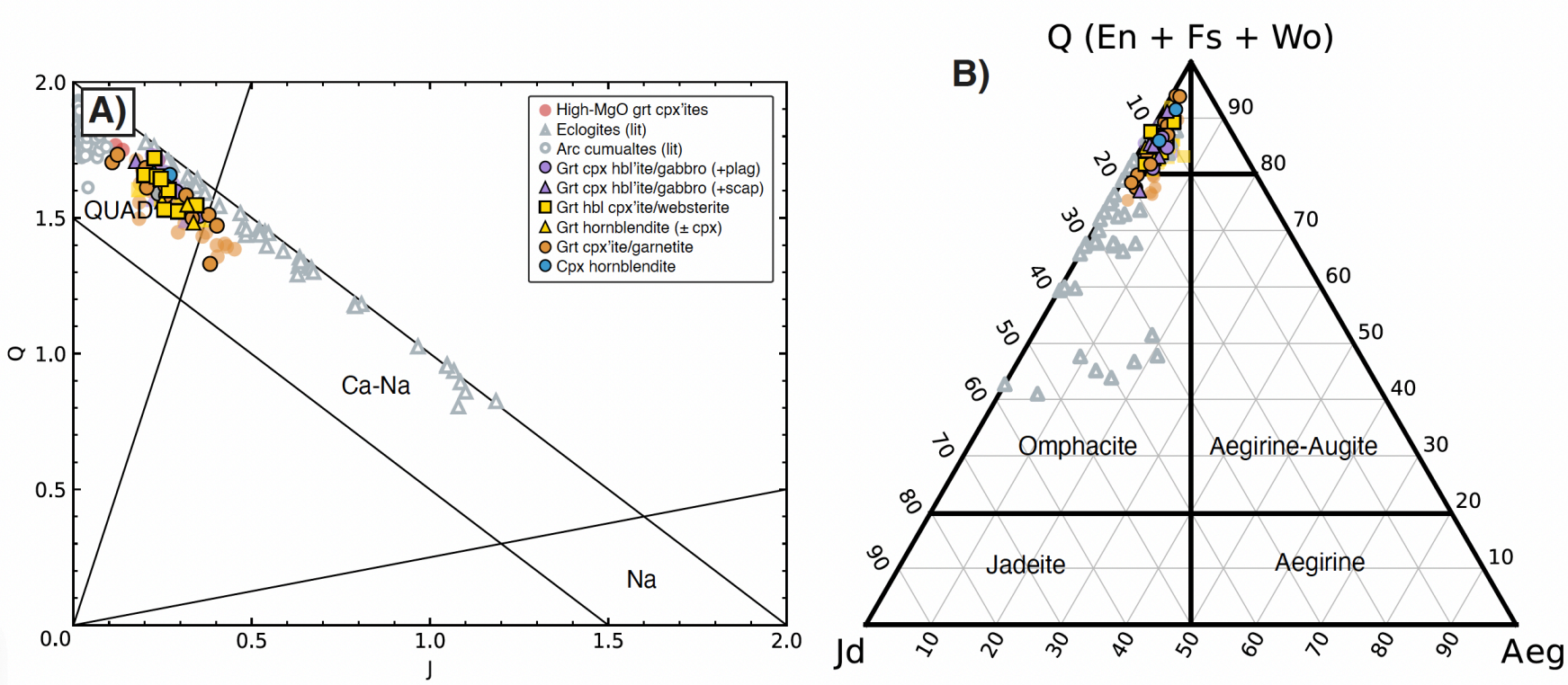

***Supplemental Figure 20*:** Clinopyroxene core compositions from Mercaderes xenoliths following the nomenclature of Morimoto (1989)**. A)** Clinopyroxene core compositions on Q-J classification diagram (where Q = Fe + Mg + Ca and J = 2 × Na in apfu: Morimoto, 1989). **B)** Clinopyroxene core compositions on the Ca-Na pyroxene ternary. Mercaderes literature data (Weber, 1998; Bloch et al., 2017; Zieman et al., 2023; Gianola et al., 2023) are represented by transparent symbols without borders. Other arc data (open circle) are from Kohistan (Jagoutz et al., 2007), Talkeetna (DeBari and Coleman, 1989; Greene et al., 2006), Lesser Antilles (Cooper et al., 2016) and Central Aleutians (Sosa et al., 2023). Eclogite data are from Aoya (2001), Tsujimori (2002), Schmickler et al. (2004), Viljoen et al. (2005, 2010), Williams et al. (2009), Tappe et al. (2011), and Pernet-Fisher et al. (2014).

4.18 Additional references

An, Y., Huang, J. X., Griffin, W. L., Liu, C., & Huang, F. (2017). Isotopic composition of Mg and Fe in garnet peridotites from the Kaapvaal and Siberian cratons. *Geochimica et Cosmochimica Acta* 200, 167-185.

Aoya, M. (2001). P–T–D path of eclogite from the Sambagawa belt deduced from combination of petrological and microstructural analyses. *Journal of Petrology* 42(7), 1225-1248.

Armstrong, J. T. (1995). Citzaf-a package of correction programs for the quantitative Electron Microbeam X-Ray-Analysis of thick polished materials, thin-films, and particles. *Microbeam Analysis* 4(3), 177-200.

Azough, F., & Freer, R. (2000). Iron diffusion in single-crystal diopside. *Physics and Chemistry of Minerals* 27, 732-740.

Beard, B. L., & Johnson, C. M. (2004). Inter-mineral Fe isotope variations in mantle-derived rocks and implications for the Fe geochemical cycle. *Geochimica et Cosmochimica Acta* 68(22), 4727-4743.

Dauphas, N., John, S. G., & Rouxel, O. (2017). Iron isotope systematics. *Reviews in Mineralogy and Geochemistry* 82(1), 415-510.

DeBari, S. M., & Coleman, R. G. (1989). Examination of the deep levels of an island arc: Evidence from the Tonsina ultramafic-mafic assemblage, Tonsina, Alaska. *Journal of Geophysical Research: Solid Earth* 94(B4), 4373-4391.

Ganguly, J., Cheng, W., & Chakraborty, S. (1998). Cation diffusion in aluminosilicate garnets: Experimental determination in pyrope-almandine diffusion couples. *Contributions to Mineralogy and Petrology* 131, 171-180.

Grösser, J. R. (1989). Geotectonic evolution of the Western Cordillera of Colombia: New aspects from geochemical data on volcanic rocks. *Journal of South American Earth Sciences* 2(4), 359-369.

Jagoutz, O., Müntener, O., Ulmer, P., Pettke, T., Burg, J. P., Dawood, H., & Hussain, S. (2007). Petrology and mineral chemistry of lower crustal intrusions: The Chilas Complex, Kohistan (NW Pakistan). *Journal of Petrology* 48(10), 1895-1953.

Kerr, A. C., Tarney, J., Marriner, G. F., Nivia, A., Klaver, G. T., & Saunders, A. D. (1996). The geochemistry and tectonic setting of late Cretaceous Caribbean and Colombian volcanism. *Journal of South American Earth Sciences* 9(1-2), 111-120.

Klein, E. M. (2003). Geochemistry of the igneous oceanic crust. *Treatise on Geochemistry* 3, 659.

Li, D. Y., Xiao, Y. L., Li, W. Y., Zhu, X., Williams, H. M., & Li, Y. L. (2016). Iron isotopic systematics of UHP eclogites respond to oxidizing fluid during exhumation. *Journal of Metamorphic Geology* 34(9), 987-997.

Liang, W., Huang, J., Zhang, G., & Huang, F. (2022). Iron isotopic fractionation during eclogite anatexis and adakitic melt evolution: Insights into garnet effect on Fe isotopic variations in high-silica igneous rocks. *Contributions to Mineralogy and Petrology* 177(3), 33.

Marriner, G. F., & Millward, D. (1984). The petrology and geochemistry of Cretaceous to Recent volcanism in Colombia: The magmatic history of an accretionary plate margin. *Journal of the Geological Society* 141(3), 473-486.

Morimoto, N. (1989). Nomenclature of pyroxenes. *Mineralogical Journal* 14(5), 198-221.

Pernet-Fisher, J. F., Howarth, G. H., Liu, Y., Barry, P. H., Carmody, L., Valley, J. W., ... & Taylor, L. A. (2014). Komsomolskaya diamondiferous eclogites: Evidence for oceanic crustal protoliths. *Contributions to Mineralogy and Petrology* 167, 1-17.

Schmickler, B., Jacob, D. E., & Foley, S. F. (2004). Eclogite xenoliths from the Kuruman kimberlites, South Africa: Geochemical fingerprinting of deep subduction and cumulate processes. *Lithos* 75(1-2), 173-207.

Schoenberg, R., Marks, M. A., Schuessler, J. A., von Blanckenburg, F., & Markl, G. (2009). Fe isotope systematics of coexisting amphibole and pyroxene in the alkaline igneous rock suite of the Ilímaussaq Complex, South Greenland. *Chemical Geology* 258(1-2), 65-77.

Sosa, E. S., Bucholz, C. E., Barickman, M. H., VanTongeren, J. A., Setera, J. B., Kay, S. M., & Kay, R. W. (2023). Petrology and geochemistry of Adak Island plutonic xenoliths: Implications for primitive magma generation and crustal differentiation in the Aleutian Island arc. *Journal of Petrology* 64(10).

Tappe, S., Smart, K. A., Pearson, D. G., Steenfelt, A., & Simonetti, A. (2011). Craton formation in Late Archean subduction zones revealed by first Greenland eclogites. *Geology* 39(12), 1103-1106.

Tsujimori, T. (2002). Prograde and retrograde PT paths of the late Paleozoic glaucophane eclogite from the Renge metamorphic belt, Hida Mountains, southwestern Japan. *International Geology Review* 44(9), 797-818.

Viljoen, K. S., Schulze, D. J., & Quadling, A. G. (2005). Contrasting group I and group II eclogite xenolith petrogenesis: Petrological, trace element and isotopic evidence from eclogite, garnet-websterite and alkremite xenoliths in the Kaalvallei kimberlite, South Africa. *Journal of Petrology* 46(10), 2059-2090.

Viljoen, F., Dobbe, R., Harris, J., & Smit, B. (2010). Trace element chemistry of mineral inclusions in eclogitic diamonds from the Premier (Cullinan) and Finsch kimberlites, South Africa: Implications for the evolution of their mantle source. *Lithos* 118(1-2), 156-168.

Villagómez, D., Spikings, R., Magna, T., Kammer, A., Winkler, W., & Beltrán, A. (2011). Geochronology, geochemistry and tectonic evolution of the Western and Central cordilleras of Colombia. *Lithos* 125(3-4), 875-896.

Williams, H. M., Peslier, A. H., McCammon, C., Halliday, A. N., Levasseur, S., Teutsch, N., & Burg, J. P. (2005). Systematic iron isotope variations in mantle rocks and minerals: The effects of partial melting and oxygen fugacity. *Earth and Planetary Science Letters* 235(1-2), 435-452.

Ye, H., Wu, C., Brzozowski, M. J., Yang, T., Zha, X., Zhao, S., ... & Li, W. (2020). Calibrating equilibrium Fe isotope fractionation factors between magnetite, garnet, amphibole, and biotite. *Geochimica et Cosmochimica Acta* 271, 78-95.

Zhao, X. M., Zhang, H. F., Zhu, X. K., Zhu, B., & Cao, H. H. (2015). Effects of melt percolation on iron isotopic variation in peridotites from Yangyuan, North China Craton. *Chemical Geology* 401, 96-110.